Transactions of the ASME®

Journal of Engineering for Gas Turbines and Power

Published Quarterly by The American Society of Mechanical Engineers

VOLUME 121 • NUMBER 2 • APRIL 1999

TECHNICAL PAPERS

Internal Combustion Engines

Gas Turbines: Aircraft

Gas Turbines: Ceramics

Gas Turbines: Combustion & Fuels

(Contents continued on outside back cover)

Technical Editor
H. D. NELSON (2001)

Associate Technical Editors
Advanced Energy Systems
M. J. MORAN (1999)
G. REISTAD (2002)
Fuels and Combustion Technologies
S. GOLLAHALLI (2001)
Gas Turbine (Review Chair)
D. WISLER (2001)
Gas Turbine
D. COOKE (1999)
M. MIGNOLET (2002)
J. PETERS (1999)
Internal Combustion Engines
D. ASSANIS (1999)
Nuclear
R. DUFFEY (2001)
Power
D. LOU (2002)

BOARD ON COMMUNICATIONS
Chairman and Vice President
R. K. SHAH

OFFICERS OF THE ASME
President, **W. M. PHILLIPS**

Executive Director, **D. L. BELDEN**

Treasurer, **J. A. MASON**

PUBLISHING STAFF
Managing Director, Engineering
CHARLES W. BEARDSLEY

Director, Technical Publishing
PHILIP DI VIETRO

Managing Editor, Technical Publishing
CYNTHIA B. CLARK

Managing Editor, Transactions
CORNELIA MONAHAN

Production Coordinator
COLIN MCATEER

Production Assistant
MARISOL ANDINO

Transactions of the ASME, Journal of Engineering for Gas Turbines and Power (ISSN 0742-4795) is published quarterly (Jan., April, July, Oct.) for $205.00 per year by The American Society of Mechanical Engineers, Three Park Avenue, New York, NY 10016. Periodicals postage paid at New York, NY and additional mailing offices. POSTMASTER: Send address changes to Transactions of the ASME, Journal of Engineering for Gas Turbines and Power, c/o THE AMERICAN SOCIETY OF MECHANICAL ENGINEERS, 22 Law Drive, Box 2300, Fairfield, NJ 07007-2300.

CHANGES OF ADDRESS must be received at Society headquarters seven weeks before they are to be effective. Please send old label and new address.

PRICES: To members, $40.00, annually: to nonmembers, $205.00. Add $40.00 for postage to countries outside the United States and Canada.

STATEMENT from By-Laws. The Society shall not be responsible for statements or opinions advanced in papers or . . . printed in its publications (B7.1, par. 3).

COPYRIGHT © 1999 by The American Society of Mechanical Engineers. Authorization to photocopy material for internal or personal use under circumstances not falling within the fair use provisions of the Copyright Act is granted by ASME to libraries and other users registered with the Copyright Clearance Center (CCC) Transactional Reporting Service provided that the base fee of $3.00 per article is paid directly to CCC, Inc., 222 Rosewood Dr., Danvers, MA 01923. Request for special permission or bulk copying should be addressed to Reprints/Permission Department.

INDEXED by Applied Mechanics Reviews and Engineering Information, Inc. Canadian Goods & Services Tax Registration #126148048

This journal is printed on acid-free paper, which exceeds the ANSI Z39.48-1992 specification for permanence of paper and library materials.♾ ™

♲ 85% recycled content, including 10% post-consumer fibers.

Downloaded 03 Jun 2010 to 171.66.16.159. Redistribution subject to ASME license or copyright; see http://www.asme.org/terms/Terms_Use.cfm

(Contents continued)

P. F. Flynn
Cummins Engine Company Inc.,
1900 McKinley Avenue, Box 2005,
Columbus, IN 47202

Pursuing Customer Satisfaction—An Abridged Technical History of Cummins Engine Development

The paper presents a brief overview of the technical and market development activity undertaken by Cummins Engine Company. The process of identifying customers, demonstrating product capability to those customers, and developing the engines to meet evolving customer needs is portrayed. These activities facilitated the growth and expansion of Cummins Engine Company from a small manufacturer of single-cylinder engines for water pumping, to the largest independent diesel engine manufacturer in the world. The period of time covered is the 77 years of operation from 1919 to 1996.

Introduction

Cummins' story, as well as many other financially viable organizations today, is one of perceiving and responding to the needs of customers as they evolve over time. Cummins Engine Company found its roots in the creative genius and mechanical aptitude of Clessie Cummins, chauffeur and handyman of banker W. G. Irwin in Columbus, Indiana.

Clessie in his readings was exposed to the engine developments that were being publicized out of Europe, especially those of inventor, Rudolph Diesel (Cummins, 1967, Cummins, 1976). These publications plus other information about engine development in Europe prompted the organization of Cummins Engine Company in February 1919. The intent of the company at that time was to manufacture an engine known as the ''HVID'' engine in the US.

Activity began quickly, and the first 2.6 horsepower single-cylinder hopper-cooled horizontal engine (Fig. 1), operating at 600 RPM, was completed in April 1919 (Cummins, 1947). From this early development, other variants of these horizontal single-cylinder engines were completed. Figure 2 presents a time line that highlights important events in Cummins' technical history and the evolution of various engine parameters.

From these small beginnings, the company evolved to what it is today by identifying potential customers and setting out to satisfy their needs.

The following text tells this story with regard to the following three arbitrary perspectives: the identification of customers and their needs, the development of the mechanical and durability aspects of the products, and the evolution of product performance. This separation is entirely arbitrary as all three aspects of development are entwined in many ways, but this separation allows some focus of the discussion as opposed to a pure chronological history.

Customers and Their Needs

The consistent outlook of customers over time has been the requirement to serve their power needs with products that provide reliable power at the most reasonable cost in a compact package that fits the customers' installation requirements.

The first engines were horizontal stroke single-cylinder engines suitable for use in pumping water and other light industrial chores. This engine was first sold at the 1919 Indiana State Fair. One of the major problems for the small company was identifying themselves to potential customers.

In 1920 and 1921, 1.5, 3, 6, and 8 horsepower versions of this early single-cylinder engine were offered for sale through the Sears Roebuck catalog. The engine was offered with a money back guarantee. Although it is not clear what the causes for return were (one can speculate on a range of causes between inadequate performance by the engines and the shrewd economics of the purchasers), over half of the engines were returned, making the business aspects of the endeavor a catastrophe.

Following these experiences with horizontal engines, efforts began to focus on manufacture of engines with a vertical stroke. Several configurations were developed as a model ''F'' (Fig. 3) in the range from 7 to 15 horsepower per cylinder. These engines were used to power shrimp fishing trawlers and other industrial applications (Cummins, 1927). These engines were well received, even with their early problems of combustion system carboning. The engine might require combustion system cleaning several times per day.

It was in the late 1920s that Clessie Cummins began to envision the application of the diesel to automotive transport. Since there had been no mobile vehicle applications of diesels to date, the introduction of the diesel to potential customers was a significant problem. To introduce the diesel engine to the public, Clessie Cummins and his colleagues set upon a series of diesel automotive demonstrations.

The first of these demonstrations happened on Christmas Day 1929 with the completion of a 4-cylinder model ''U'' engine installation in a Packard limousine (Fig. 4). After demonstrating this engine for a short while in Columbus, it was decided that this diesel car should go to New York City for a demonstration at the New York Auto Show (Cummins, 1930). The car was successfully driven to New York City. Following the successful interactions at the New York Auto Show, the next demonstration pursued was the world's land speed record for such a vehicle. The record was established at Daytona Beach, Florida. The speed reached in this demonstration was 80.389 mph.

To attract additional attention, a 4-cylinder model ''U'' engine was installed in the first Cummins-powered race car and taken to Daytona Beach in February 1931 to re-establish the land speed record at 100 mph. Following completion of the runs in Daytona Beach, this same race car (Fig. 5) was entered

---

Contributed by the Internal Combustion Engines Division and presented at the 1996 Fall Technical Conference of the ASME Internal Combustion Engine Division, Springfield, OH, October 20–23, 1996. Manuscript received by the ASME Headquarters August 1, 1996. Associate Technical Editor: D. Assanis.

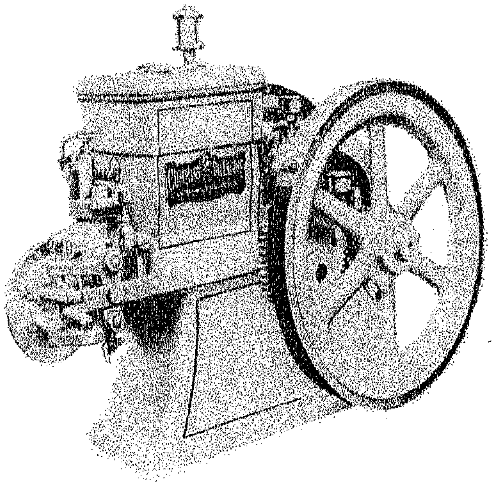

Fig. 1 Original "HVID" engine

into the Indianapolis 500 Mile Race on Memorial Day in Indianapolis. Special rule waivers were obtained so that the engine could be admitted to the race if it could qualify at a speed higher than 70 mph. The car entered the race. When the race had finished, the car averaged 86.5 mph against a winning speed of 96 mph, and it had run the entire 500 miles without stopping.

The next demonstration was the installation of another model "U" engine into a 2.5 ton "Indiana" truck. This truck was later used for a New York City to Los Angeles (3220 miles) run carrying the race car as part of its load.

The next episode of engine development and automotive demonstrations was completed shortly after the first model "H" engine was built. The engine, installed in the "Indiana" truck, was used for an endurance demonstration. Starting December 18, 1932 the truck, with a large tank of fuel and general supplies, started a run at the Indianapolis raceway. The engine was refueled by an oil truck running alongside and finally completed its endurance trial on Christmas Day after 14,600 miles nonstop. The engine was also used in the 1934 Cummins entry in the Indianapolis 500 Race.

Through the World War II years, the application of Cummins engines to military trucks (Fig. 6) provided a boost to the diesel engine reputation. The exposure that was afforded to those who had the opportunity to drive such military trucks provided a group of interested potential customers for diesel automotive power.

During this period the distributor network that had been set up to service engines in the field became an important attribute of the company. The distributors provided the mechanism to repower highway trucks by removing existing gasoline engines and substituting Cummins diesel power.

Since the existing equipment manufacturers supplied and serviced only gasoline engines, this network of distributors served a key role in accessing potential customers. These customers required the backup on a broad range of engineering services. The Cummins engineering organization developed sophisticated skills around automotive engine applications.

The skills that evolved out of this customer interface included dealing with the special gearing and cooling needs of automotive engines. Also important was the understanding of a wide variety of environmental exposures that engines might encounter. The variations in temperature, altitude, and ambient dust conditions provided critical challenges to the engineering organization.

After serving individual owners in the repower segment of the market, by 1950 relationships had developed with a variety of original equipment manufacturers in the bus and truck market. These OEM's were using the model "J" engine as a pilot diesel engine for vehicles to decide whether or not to offer the

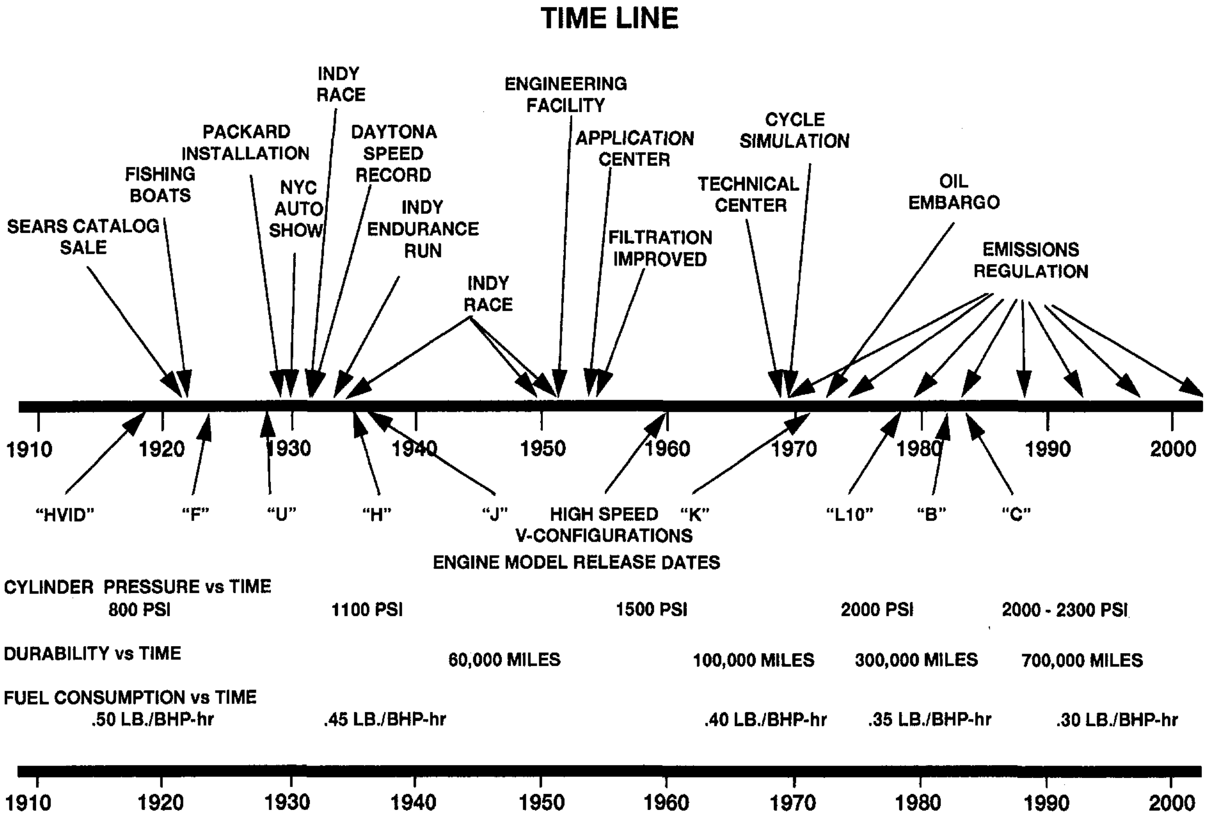

Fig. 2 Historical events and product progress

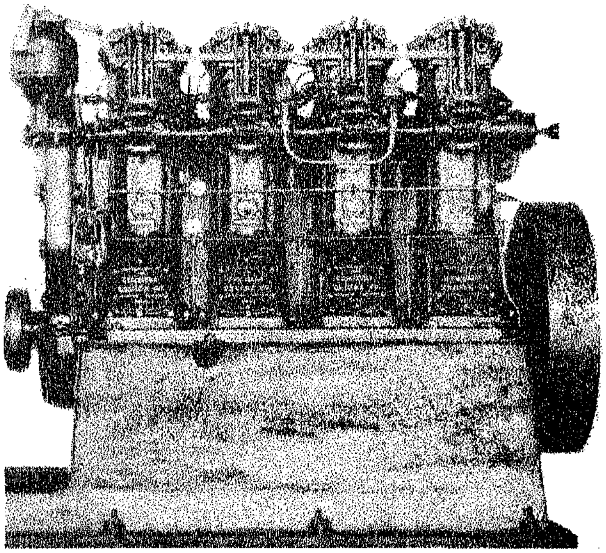

Fig. 3 Model "F" engine

engine in their product line. At that point in time, the automotive engine was offered with a 100,000 mile or one year warranty.

The passage of the Interstate Highway Bill in 1956 was a major event in the ever-increasing dieselization of the U.S. highway truck fleet. Companies such as Cummins realized that the type of roads that would be built in response to this bill, and the evolving nature of the transport infrastructure, provided a major opportunity for added diesel use in over-the-road trucking. It became obvious that truck speeds and loads would continue to increase, and the need to operate continuously at high load and speed with the new road system would prove very difficult for the competing gasoline engines.

These high loads and high speeds essentially deeded the over-the-road truck fleet to the diesel engine industry. The combination of poor fuel economy and decreased engine durability caused by the high load factors on gasoline engines provided a clear advantage in operating cost for companies that used diesel engines.

To function properly, since the major companies were not producing diesel engines for their trucks, Cummins had to assume the role of a diesel engine division for some of the truck companies. The work was supported from a special vehicle applications center completed in 1956.

Cummins Engine Company developed a vehicle mission simulator that allowed mapping of critical US highway routes and selection of transmission, axle, and engine combinations to service customer needs in the most effective way.

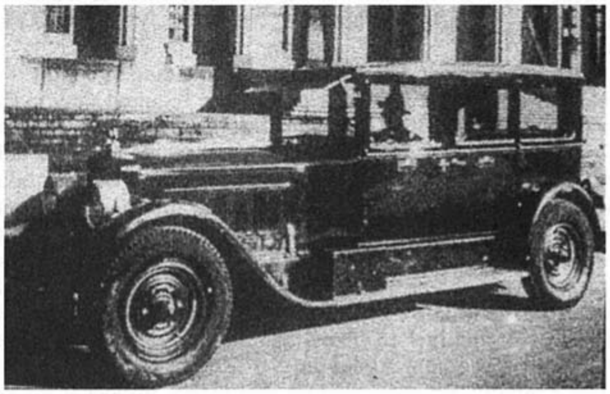

Fig. 4 Diesel powered packard

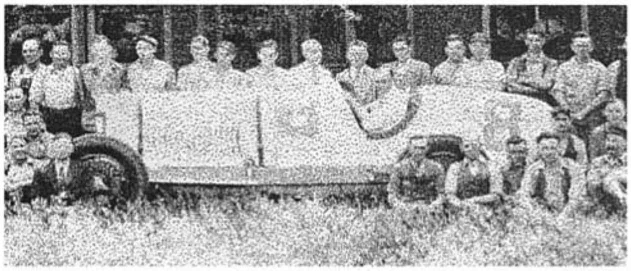

Fig. 5 Diesel powered Indy race car from 1931 race

This focus on the heavy-duty truck market provided a growth rate that continually strained the company's resources through the 1950s, 60s, and early 70s. In the early 1970s it became clear that activities in heavy-duty trucking alone would not continue to supply the future growth desired. Thus, the company embarked upon a long-term program to broaden the product line and pursue a wide variety of new markets. The product line was expanded to larger and smaller engines. Customer needs in agricultural, industrial, mining, marine, and power generation markets were identified, and special teams set about the task of meeting the needs of these new customers. In all markets the problem remains one of identifying special needs of customers and turning those needs into duty cycle, performance, and durability specifications for engine development programs. These proven approaches continue to serve new market entries today.

Mechanical and Durability Needs

All early Cummins engines had problems with the reliability of the fuel system and the combustion process. Since fuel specifications for diesel fuel didn't exist, the wide range of fuels encountered caused injection and combustion problems. An additional problem with the multicylinder engines was that of providing a steady and equal supply of fuel to each of the cylinders.

Early on, the engineers concluded that to be successful the fuel metering and delivery portions of the fuel system needed to be separated so each could be dealt with independently. This would allow the specific problems associated with the injector and fuel metering process to be handled in ways that suited each process.

In the period between 1923 and 1927, literally thousands of explicit modifications and attempts to redesign the fuel system to avoid problems of uneven fuel delivery, carboning of injectors, and inconsistent power output were completed. In addition, several combustion chamber variations were tried, including what became known as a ''sneezer'' piston (Fig. 7), to eliminate smoke and high exhaust temperatures associated with not completing the burning process fast enough in the cylinder.

Stepping back from these problems, it is clear that although engine builders are addressing these problems at greater levels

Fig. 6 Cummins-powered military trucks

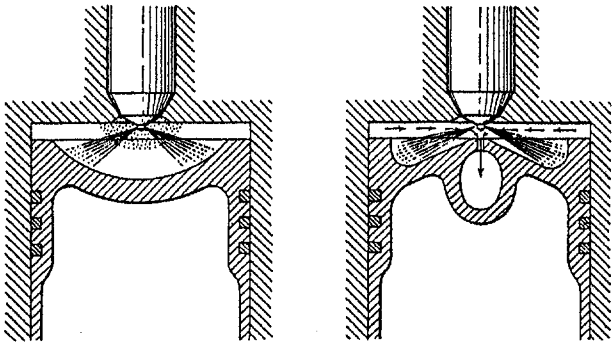

Fig. 7 Standard and "sneezer" pistons

of sophistication today, these are the problems that continue to require the attention of diesel engineers.

Early vertical stroke engines, namely model ''F'' engines, had been constructed of individual cylinders and heads with a camshaft assembly attached to the side. As such, the lubrication of the engine was divided between oils used in the crankcase and greases used on the camshaft. This exterior camshaft drive configuration was especially troublesome in those ambient environments where dirt and grime could enter the camshaft cavity and cause camshaft wear.

While trying to define appropriate new engine configurations, a great many experiments were run evaluating the characteristics of both 2-stroke and 4-stroke cycle engine configurations. At the end of these efforts, a series of decisions that would play a key role in Cummins Engine Company's success for the next several decades were reached. These decisions included (1) use of a cam-driven unit injector to inject fuel at relatively high pressures directly into cylinders; (2) application of fuel metering devices that were separate from the injection process, and, therefore, controlled to deliver the appropriate fuel charge to each cylinder; (3) redesign of the engine configuration to include the camshaft and valve operating gear within the engine, thus lubricated with oil and preventing the wearable moving parts from exposure to the outside atmosphere (Cummins, C. L. 1930). These conclusions were first incorporated into the design and development of the model ''H'' engine, which was a $4\frac{7}{8}$ inch bore, 6 inch stroke engine operated at 1800 RPM.

The fuel injection system (Fig. 8) was a unit injector with a distributor type metering system using a single plunger to meter fuel. The fuel was then routed to the various injectors by a disc distribution system. This type of distributor supply pump was used until it proved to be inadequate at high engine speeds. A new fuel system, later to become known as the PT fuel system, replaced this system in the 1950s.

The creation of the engine development laboratories in Columbus in the early 1950s was the beginning of the application of real science to the art of diesel engine development. The work that could be carried out in test cells used for engine research and development allowed the acquisition of the company's first pressure-volume diagrams. This work identified the loads that components of the engine were required to carry. The new laboratory provided an environment to apply strain gauges to critical engine parts and diagnose failures in engine structure. These understandings would lead to lighter and stronger engine configurations. Crank shaft torsional vibration problems were attacked through measurement and analysis. The success of these early technical approaches built confidence in top management with regard to the application of science and technology to engine development.

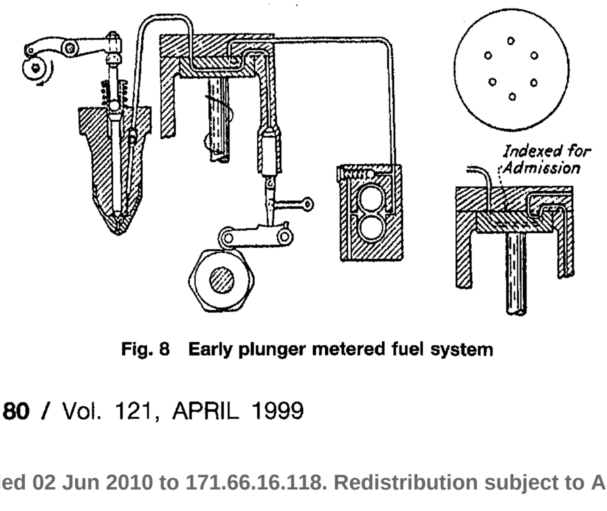

Fig. 8 Early plunger metered fuel system

The need to support customers using Cummins engines in trucks required a clear understanding of the technical support need of vehicular engines. A familiarity with the installation and maintenance needs of engines in a variety of vehicles was developed. The company worked hard on developing cooling standards and the means of appropriately filtering air, oil, and water in the engine. The development of these filtration processes, both in terms of air and lubricant, were key aspects in developing the durability of the engines to the levels that are known today.

The filtration needs of engines were explored through a special series of tests in Cummins facilities and other tests completed in cooperation with Southwest Research. Those tests clearly indicated the impact of fine ingested dust on engine life. This understanding lead to the development of efficient filtration systems for the engines and birth of the Fleetguard Division of Cummins Engine Company.

The adaptation of paper filters to the intake air in diesel engines was key to extending the life of the piston, rings, and liners. Wear reduction of cylinder components allowed the development of the capability to manage oil consumption. During this period of time, the lube oil consumption of engines began to drop drastically. Starting at a level of around 150 miles per quart, improvements gradually decreased oil consumption, so that now engines consume less than a quart every several thousand miles.

The 1960s brought a focus on improving technology to improve engine life. During that period of time, programs were started with durability goals of 350,000 to 500,000 miles to overhaul. To achieve such goals, engineers began to work harder on the technical detail of bearings, pistons, crankshafts, connecting rods, etc. More detailed stress analysis on key components yielded improved engine life without increasing engine cost.

In the mid 1960s, the company decided to invest in future technology for all of our markets and committed to build the Cummins Technical Center. The Technical Center, which was completed in the early 1970s, was a facility that would provide 88 test cells, in-house cold room testing, in-house altitude testing, computers for simulation, and laboratories for sophisticated technology development. In the late 1960s and early 1970s, there was a large recruiting effort to bring specialists and technology to the company. The specialists were hired with advanced degrees from all over the world in areas of materials, mechanical design, stress analysis, thermal analysis, cycle simulation, etc.

The development of a technical understanding of engine mechanical detail, and how it related to the required duty cycle, enabled a wide range of engine mechanical improvements. These fundamental mechanical analyses, combined with field test duty cycle information, allowed the evolution of probabilistic design methods that could predict the life of such critical components as cranks and connecting rods. The knowledge of bearing load capability and crankshaft fatigue requirements provided a basis for critical engine configuration decisions that would be confronted in the 1970s. As customers demanded more power and fuel economy, and the government demanded control of exhaust emissions, the choice between large displacement naturally aspirated engines and highly turbocharged engines became critical.

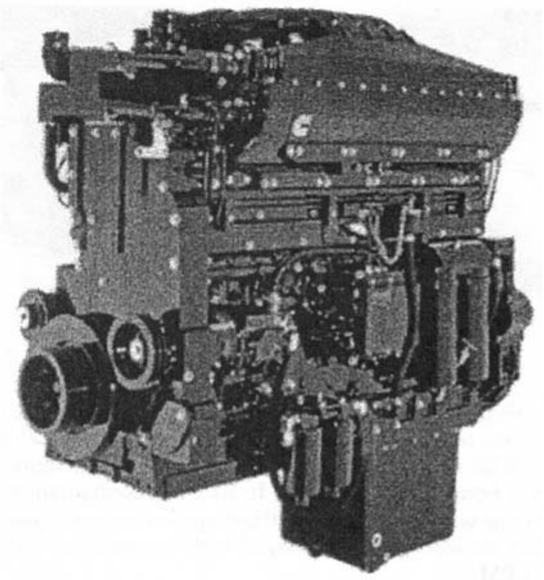

Fig. 9 "K" engine

The 6-cylinder inline configuration had additional space for bearing area to handle higher cylinder pressures. At that time, new processes and material capabilities were developing. This allowed the increase in power of the 14 liter model "NH" engine and thereby reduced its specific weight and size. There were rapid advancements in all mechanical technology areas.

Investments in a noise facility helped in understanding the mechanical and combustion force contributions to engine noise and allowed the design of an engine crankcase and cover system to control noise without adding exterior treatment.

In the late 1960s, it appeared the evolving US highway system and the outlook in Europe would require truck powers to be regulated. Expectations were that horsepower per ton regulations would create a need for very large automotive engines. This perception, combined with the need to broaden our product line in higher horsepower industrial markets (Butler, 1974) triggered the design of a family of engines that were 6.5 inch stroke by 6.5 inch bore called the model "K" engines (Fig. 9).

The initial focus was a 6-cylinder engine, which was an extremely compact design being no longer than the 14 liter model "NH" engine (Hoefflin, 1980) to serve the very high end of the automotive market. The 12 and 16-cylinder versions of the same engine, combined with more highly rated 6-cylinder versions, served to meet the evolving markets in mining and power generation.

The new technical capability, both in terms of manpower and computers, enabled extensive use of finite element stress analysis to optimize the configuration of crankshafts and camshafts. Investments in materials technology allowed Cummins to introduce innovations like induction-hardened crankshaft fillets, and the production processes required to reliably produce well-controlled crank strengths. This was possible because processes were developed in-house and controlled in our own manufacturing plants. Especially important during this period was the development of the understanding of cam materials and camshaft loads, and how they could be managed.

As the 1970s evolved, Cummins found itself very well served by the investments in technology. The understandings about combustion, gleaned from simulation and analysis of dynamometer tests, highlighted the need for improved injection characteristics. Improved camshafts to handle these higher injection pressures and mechanical structures to carry higher loads were required.

One key observation with regard to the combustion processes in the 1970s was that eventually the engine would need to control both the amount of fuel injected and the timing of injection. These elements were important in terms of maintaining our ability to satisfy customer needs for power, while maintaining fuel economy and meeting exhaust emissions regulations.

This function was attacked with three different approaches. The first approach was to use movements of the mechanical system to manage injection pressure and timing variations. Figure 10 shows this mechanical design as implemented and released in 1981 on our 475 horsepower 2-stage turbocharged model "NH" engine (Robinson, 1982).

The second approach was to use a variable length hydraulic tappet inside the injector train. Management of the filling and emptying of the tappet accomplished advance and retard of injection timing. The third approach was electronic management of the process. Thus, the initial efforts to control injection timing electronically were started. Figure 11 depicts the internal configurations of these three types of injectors.

During the last half of the 1970s, a second round of emissions legislation with a new transient test cycle was put forth by EPA. This new approach to emissions regulation required a better understanding of the engine combustion phenomena and a commitment to large investment in test and diagnostic equipment to measure emissions. Data obtained in this time frame showed that engines with good fuel economy had NOx emissions above the 10 grams/brake HP–Hr proposed standard. When injection pressures were raised and injection characteristics improved, optimum performance for the engine was obtained with a NOx emission of about 8 grams/brake HP–Hr.

At this time, as the pressures of emissions materialized and the limitations of *V* configuration engines became obvious, it became clear that investments would have to be made in a smaller displacement version of a 6-cylinder inline heavy-duty engine and that precipitated a design of the 10 liter configuration. The engine was introduced in 1982 as the model "L10" (Fig. 12), and has since evolved to be the model "M11". The engine was first introduced with the PT fuel system and later with electronically controlled fuel injection. This same evolution occurred on both the 14 liter model "NT" engine and the 19 liter model "K," with the time horizons of these modifications coinciding with the emissions requirements in the markets served.

Improved understanding of materials has allowed engineers to extend the life of designs. The development of understanding of the key capabilities of ceramics during the 1980s allowed development of load carrying members within the injector train

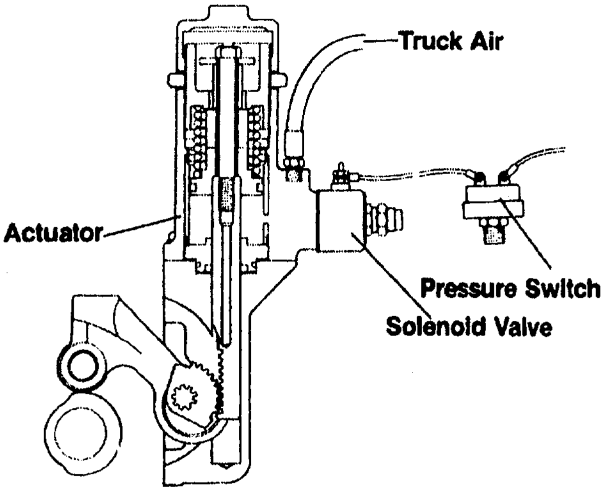

Fig. 10 Mechanical variable timing actuator

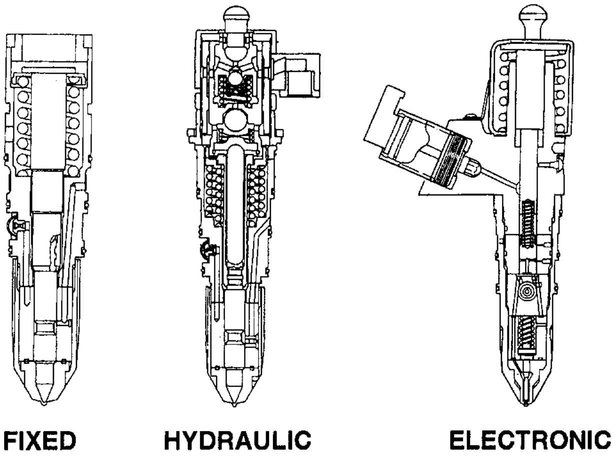

Fig. 11 Fixed timed, hydraulically timed, and electronically controlled injectors

to sustain our basic injector design without increasing injector diameter. Since the early 1990s, the highest loads in the injector train have been handled by a ceramic injector link. This application of ceramics was allowed because of the combined capacity for carrying extremely high loads, and the tribological capability to operate at these high loads with minimum wear against the other metallic components. These incremental improvements continue to the present with a focus on more integrated designs that have the same good mechanical characteristics while being manufactured at lower cost.

Product Performance Attributes

With regard to product performance, customers have always sustained a desire for the highest power out of the smallest package at the best fuel economy that the technology could deliver. In the early days of the company, the diesel attracted customers with its ability to handle the wide range of fuels that were encountered.

The need to package power compactly was even more important in the mobile vehicle markets that were pursued starting in the early 1930s. This pursuit of higher power density was the focus of the models ''H'' and ''J'' engines designed during the 1930s.

The power of the model ''H'' engine was raised from 115 horsepower at 1800 RPM to 125 horsepower, and then later to 150 horsepower in naturally aspirated configurations. The same engine was offered in a supercharged configuration at 200 horsepower. This engine later evolved to the NH series engine with $5\frac{1}{8}$ inch bore × 6 inch stroke. In its early configurations, the NH engine was developed at 200 horsepower naturally aspirated and 275 horsepower turbocharged with an operating speed of 2100 RPM.

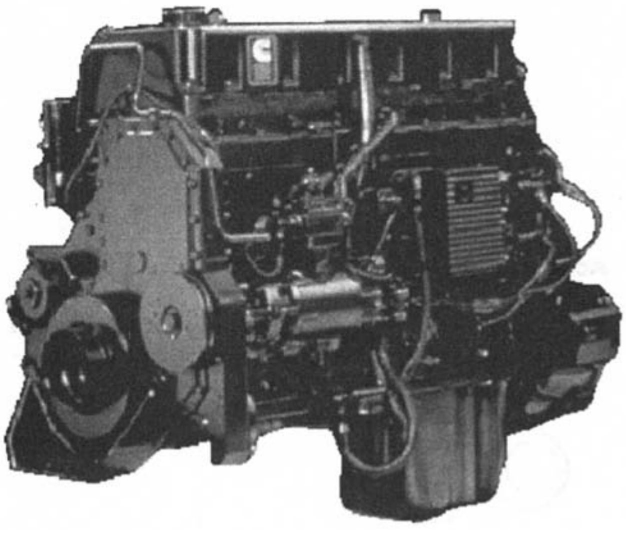

Fig. 12 L10 engine

Fig. 13 1952 Cummins-powered Indianapolis race car

To support the increasing horsepower needs of industrial customers, a *V* version of the model ''H'' engine was developed to service the markets between 400 and 550 horsepower (Kahlenbeck, 1968). The engine was offered both in naturally aspirated and turbocharged configurations and found applications in heavy-duty mine trucks. This configuration was later rated as high as 800 horsepower.

In the spring of 1950, experiences gained in preparing an entry for the Indianapolis 500 Mile Race set some beacons for the company's design of future engines (Miller, 1950). The capability to apply a large supercharger to the engine and more than double the horsepower output of the engine for the race set ever-increasing expectations in terms of the performance potential for diesel engines. Experiments with the engine at operating speeds up to 4000 RPM proved that reasonable combustion processes could be created at higher engine speeds. This high speed operation clearly demonstrated the worth of 4-valve heads when applied to such engines.

During the late 1940s and early 50s, industrial applications demonstrated the need for altitude compensation. Since engines at that time were either naturally aspirated or supercharged, intake manifold pressures of the engines were locked at some fixed ratio compared to ambient pressure. Thus, as engines were operated at higher altitudes, reducing ambient pressure caused high exhaust smoke and high exhaust temperatures. These circumstances spurred the interest and the application of turbochargers to diesel engines and initiated a turbocharger development program inside the company. Although it was to be a long time before turbochargers would be considered a reliable component in automotive markets, they rapidly proved their worth in terms of extending engine power.

In 1952 a new version of the model ''J'' engine was entered into the Indianapolis 500 Race (Fig. 13). This time the engine was turbocharged, and because of the relief of the displacement constraints, the engine was able to achieve powers that were large enough to make the car very competitive. The engine was rated 430 horsepower at 4000 RPM (Reiners, 1951). This power level allowed the engine to qualify for the pole position in the race with a qualifying speed of 138.01 mph. At the start of the race, the car proved to be very competitive. As the race progressed, power loss and visible smoke increase were obvious to the drivers, mechanics, and pit crew. The engine completed 71 of the 200 laps to make 500 miles and thus placed 27th in the field.

Evaluating the configuration and what had caused the problem, the engineers discovered that the turbocharged engine, with the low front air intake, had been aspirating rubber particles off the track as the tires wore. These rubber particles had found

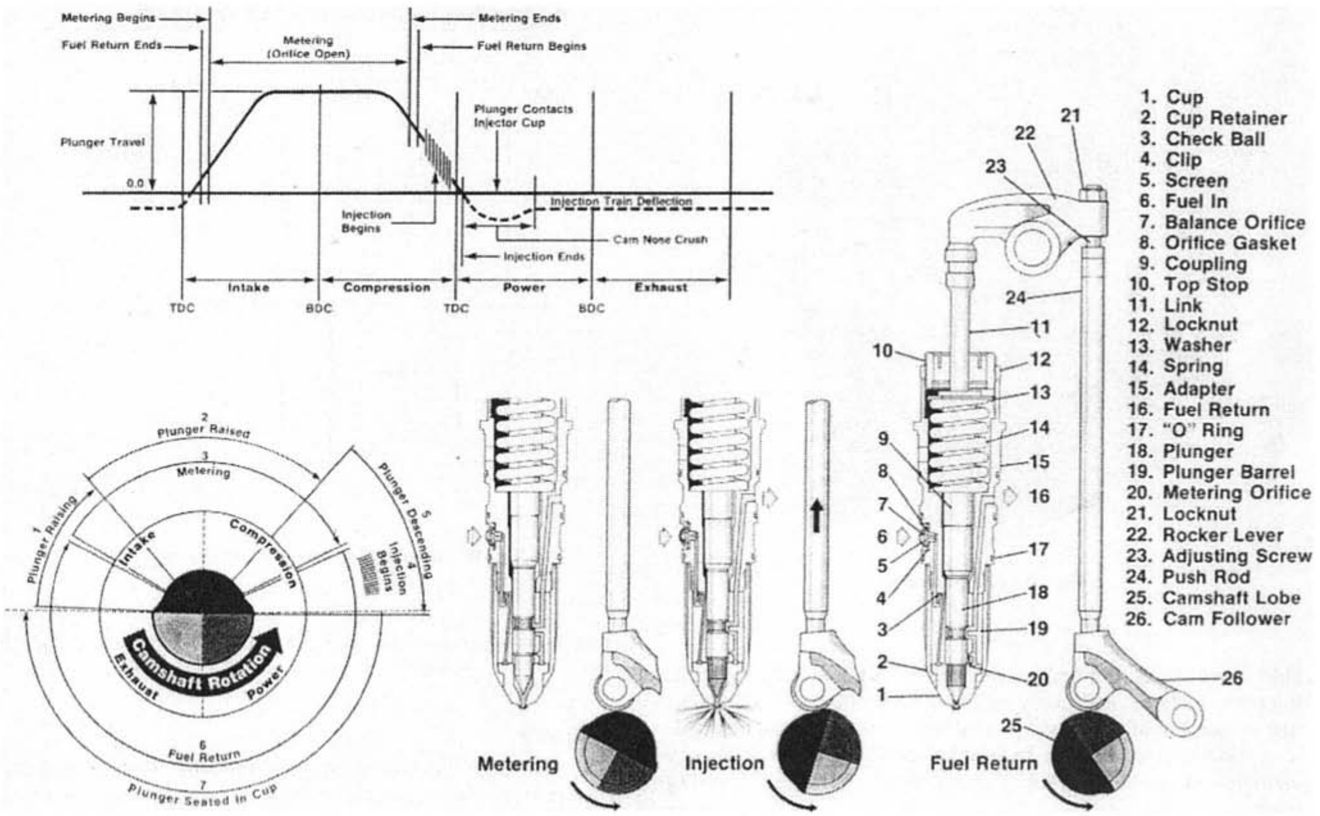

Fig. 14 PT fuel system operations

their way to the turbocharger inlet and eventually blocked the turbocharger limiting its breathing capability. Needless to say, these relative successes, in terms of obtaining high speeds and being competitive overall, prompted the race officials to disallow the technical variations that had been allowed previously for diesel engines. As such, it has not been possible to enter a competitive diesel race car in the Indianapolis 500 since that date.

During the 1950's, the success of the turbocharged engine at the Indianapolis 500 Race fostered the application of the turbocharger to the highly rated industrial product line. Also, there were increases in the bore of the model "H" engine to bring it to its present day displacement of 14 liters.

A large amount of work was focused on the development of the PT fuel system (Fig. 14). The system, while maintaining the benefits of the centrally located unit injector, provided the engine with a simple regulated fuel pump pressure that provided fueling as a function of orifice open time in the injector cavity itself. The fuel system was calibrated by controlling orifice sizes feeding the injectors and relied on shaping fuel pump regulation curves to obtain torque control and governing.

The focus of activities during that period was on the application of diesel engines to line-haul automotive applications. To meet the application needs of these mobile vehicular engines, it was necessary to deal with climatic and altitude conditions over all the continental United States. To appraise the impact of climatic conditions, Cummins developed a cold room at the Columbus facility and began to use altitude test chambers of military test facilities.

Late in the 1950s, as roads continued to improve and trucks increased in size, users began to demand more horsepower from engines. To meet that need and still use naturally aspirated engines, Cummins embarked upon design and development of a line of short stroke *V* configuration naturally aspirated engines.

These engines were capable of operating at higher speeds and the *V* configuration provided a compact package in which engine displacement could be maximized (Butler, 1971). The combination of high speeds and large displacements that could be designed into this *V* configuration engine (Fig. 15) allowed the trucking industry to address needs for additional power. Work was continuing on industrial engines with turbochargers, but turbocharger applications had only reached a modest acceptance on the open highway truck engines. The *V* configuration, while making extremely efficient use of space for producing power, limited the space for bearings and structural load carrying capability.

Late in the 1960s the country's concern for environmental pollution began to surface. In the 1970 Clean Air Act, the Environmental Protection Agency initiated smoke regulations and later the NOx and hydrocarbons regulations. This environmental legislation focused the company's attention on the engine combustion process. Smoke was the first difficult problem confronted. It was especially difficult for the high-speed naturally aspirated designs that had been developed during the 1960s to meet the new smoke control requirements.

After exploring options to improve smoke, it became clear that turbocharging provided a major benefit. The turbocharger could be used to improve smoke and increase power at modest cost. So, in the early 1970s there was a rapid change to turbocharged engines. By 1975 nearly all Cummins automotive engines were turbocharged. This commitment to turbocharging required the development of engines to sustain higher cylinder pressures and development of turbochargers that operated efficiently over a wide speed range. This adaptation was easier for engines with a modest speed range, such as the 6-cylinder model "NH" engine.

The new computational capabilities, arising from technology investments, allowed the development of large scale engine simulations. These simulations allowed performance attributes of a wide variety of components and design elements of engines to be evaluated analytically before ever running in the test cell. These simulations eventually grew to be accurate and depend-

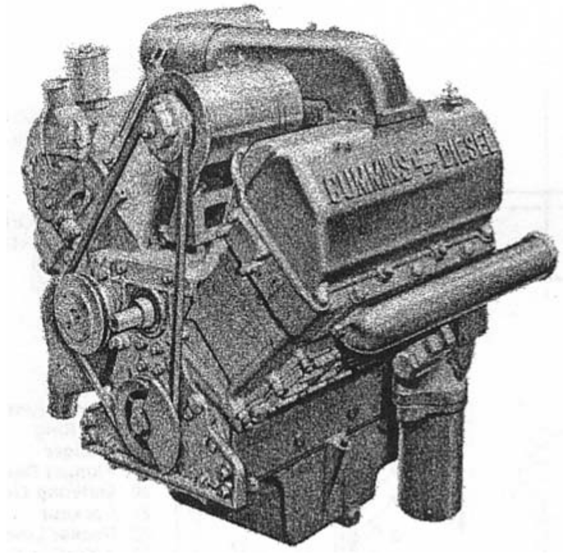

Fig. 15 V6-200 engine

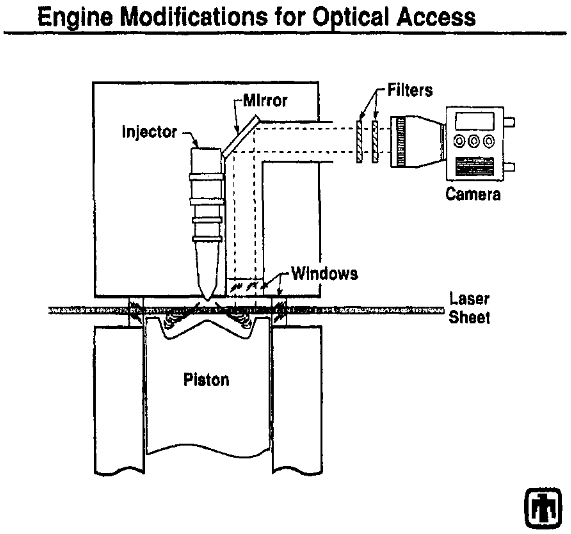

Fig. 16 Combustion research facility laser rig

able when designing camshafts, valves, air handling systems, injection systems, and many other engine systems. Understanding the science of the power production in-cylinder, the mechanics of the engine, and the hydraulics in fuel systems were key elements in evolving designs to accommodate ever-increasing loads.

In 1973 with the fuel embargo and rising fuel prices, fuel economy became even more important. Deregulation of the trucking industry increased pressures on operating costs and further heightened concerns for engine first cost and fuel consumption.

With regard to fuel economy and power, the evolving capabilities of the turbocharger proved to be important in the design approach. While the increase in cylinder pressures provided the capability to operate at relatively lean air-fuel ratios to control smoke, turbocharging also afforded the capability to burn more fuel in a combustion chamber of the same surface area and volume, thus improving the engine's innate efficiency. As turbocharger capabilities improved, the improved turbomachinery provided contributions to fuel economy improvements. These gains arose from the positive pressure differential that could be sustained across the engine. The standard cycle became a compounded one, with a diesel cycle surrounded by a low pressure gas turbine cycle.

To manage both NOx and particulates, it was necessary to increase the injection pressure, control the start of injection to manage NOx, and complete combustion rapidly so as not to trap unburned particulates in the combustion process late in the cycle. The injection event modifications and injection pressure increases that were required to do this, combined with efficiency improvement in turbomachinery, actually improved fuel economy as engine emissions were lowered.

The process of managing performance and emissions has evolved from a process of empirically manipulating the injection and combustion processes, to one that requires an understanding of the detailed evolution of the burning process in the cylinder. To increase the depth of understanding, Cummins has worked with a wide variety of government laboratories to improve its simulation analysis and diagnostic capability. Laser diagnostics completed at the Sandia Combustion Research Facility (Fig. 16) have been applied to combustion inside actual operating diesel engines to determine the time and places where combustion starts, particulates are formed, and the processes and places in which NOx is formed inside the engine. These more detailed understandings created expectations for continuing improvement with the methods that existed for the last 75 years.

Summary

The efforts of Cummins Engine Company have for the last 75 years been focused on a process of recognizing customers and their needs. Once customers have been identified, the company has applied the available scientific tools to build engines to satisfy those needs. This process required the adaptation of technical tools from other industries and the development of special capabilities for the industrial sectors being served.

It appears looking into the future that engine builders will be able to continue to serve customers with compact high power density configurations that will evolve and to meet the ever more stringent emissions requirements demanded by the public. The diesel engine remains into the foreseeable future the most efficient mobile fossil fuel burning power plant. Diesel engines will continue to serve markets well into the next century by meeting customer needs.

Acknowledgments

The author wishes to express his appreciation to Cummins Engine Company for allowing access to the detailed as yet unpublished historical records of the corporation, and especially to Bill Schwab, whose recollections of the technical work of Cummins Engine Company over the last 50 years helped identify key technical breakthroughs.

References

Butler, J. L., Dugan, R. W., and Kemp, E. H., 1971, "Cummins V504 and V555 Engines," SAE Paper 710131, Society of Automotive Engineers, Inc., presented at the Automotive Engineering Congress, Detroit, Michigan, January 11–15, 1971.

Butler, J. L., Garrett, J. H., and Hoch, J. L., 1974, "Cummins K-Series Engines," SAE Paper 740036, Society of Automotive Engineers, Inc., presented at the Automotive Engineering Congress, Detroit, Michigan, February 25–March 1, 1974.

Cummins, C. L., 1927, "Development of the Automotive Diesel Oil-Engine," *SAE Journal,* No. 4, Vol. XXI, Oct., pp. 388–392.

Cummins, C. L., 1930, "Diesel Engines for Automobiles," *SAE Journal,* No. 3, Vol. XXVII, Sep., pp. 285–289.

Cummins, C. L., 1967, *My Days With the Diesel,* Chilton Company, Philadelphia, PA, (published simultaneously in Toronto, Canada, by Ambassador Books, Ltd. Library of Congress Catalog Card Number 67-11846).

Cummins, Jr., C. L., 1976, *Internal Fire,* Carnot Press, Lake Oswego, OR.

Cummins, D. J., 1947, "A Brief Outline of the Developments of the Cummins Diesel Engine," paper presented at a meeting of the Western Michigan Section of the Society of Automotive Engineers on January 23, 1947.

Hoefflin, C. W., 1980, "Evolution of the NT-855 Engine," SAE Paper 800922, SAE/SP-80/467 802.50, Society of Automotive Engineers, Inc., Warrendale, PA.

Kahlenbeck, P. R., 1968, "Cummins VTA-1710 800 HP Engine," SAE Paper 680602, presented at the SAE National Combined Farm Construction and Industrial Machinery, Powerplant, and Transportation Meetings, Milwaukee, Wisconsin, September 9–12, 1968.

Miller, J. C., and Boll, C. R., 1950, "The New Model JBS-600 Cummins Diesel Engine," Paper No. 492, paper presented at the SAE National West Coast Meeting, Biltmore Hotel, Los Angeles, California, August 14–16, 1950.

Reiners, N. M., and Schmidt, R. C., 1951, "The Experimental High Speed Cummins Diesel Engine 4000 RPM-345 HP-401 cu. in.," Paper No. 626, paper presented at the SAE Summer Meeting, French Lick Springs Hotel, French Lick, Indiana, June 3–8, 1951.

Robinson, R. H., and Schnapp, J. P., 1982, "Cummins NTC-475 Series Turbocharged Engine," SAE Paper 820982, paper presented at the West Coast International Meeting, San Francisco, California August 16–19, 1982.

Simulation and Experimental Analysis of Diesel Fuel-Injection Systems With a Double-Stage Injector

A. E. Catania
Mem. ASME

C. Dongiovanni

A. Mittica

C. Negri

E. Spessa

Dipartimento di Energetica,
Politecnico di Torino,
C. so Duca degli Abruzzi 24,
Torino, Italy

A double-spring, sacless-nozzle injector was fitted to the distributor-pump fuel-injection system of an automotive diesel engine in order to study its effect on the system performance for two different configurations of the pump delivery valve assembly with a constant-pressure valve and with a reflux-hole valve, respectively. Injection-rate shapes and local pressure time histories were both numerically and experimentally investigated. The NAIS simulation program was used for theoretical analysis based on a novel implicit numerical algorithm with a second-order accuracy and a high degree of efficiency. The injector model was set up and stored in a library containing a variety of system component models, which gave a modular structure to the computational code. The program was also capable of simulating possible cavitation propagation phenomena and of taking the fluid property dependence on pressure and temperature, as well as flow shear and minor losses into account. The experimental investigation was performed on a test bench under real operating conditions. Pressures were measured in the pumping chamber at two different pipe locations and in the injector nozzle upstream of the needle-seat opening passage. This last measurement was carried out in order to determine the nozzle-hole discharge flow coefficient under nonstationary flow conditions, which was achieved for the first time in a sacless-nozzle two-stage injector over a wide pump-speed range. The numerical and experimental results were compared and discussed.

Introduction

The performance of a high-pressure fuel-injection system and its effects on diesel engine combustion can be strongly influenced by the injector characteristics (Aoyama et al., 1990; Beck and Chen, 1990). Double-spring injectors that allow a two-stage lift injection are capable of reducing the engine combustion noise, i.e., the roughness of engine operation (Greeves and Wang, 1990; Russel et al., 1990). In addition, reduced-sac and sacless-nozzle injectors can reduce the emissions of exhaust hydrocarbons. These are caused by undesirable combustion processes occurring for the fuel fraction delivered by the sac chamber when the injector is closed (Andoh and Shiraishi, 1986).

A dual-spring sacless-nozzle injector was installed in the distributor-pump fuel-injection system of an automotive diesel engine and its effects on the system performance were numerically and experimentally analyzed for two different configurations of the pump delivery-valve assembly: one with a constant-pressure valve, and the other with a reflux-hole valve. The theoretical analysis was carried out using the system simulation program NAIS that had been previously developed, extensively tested, and validated. This is based on a novel implicit numerical algorithm with a second-order accuracy and a high degree of efficiency. The computational code has a modular structure and a flexibility given by a wide library with a variety of system component models (Catania et al., 1995). It is also capable of simulating possible cavitation occurrence and propagation, taking the dependence of fluid properties on pressure and temperature, as well as flow shear and minor losses into account. The program, which is of more general application, was used to study local details of the complex flow phenomena in injection systems and also to analyze the effects of specific components on the system performance (Catania et al., 1992, 1993, 1994a, 1994b).

The experimental investigation was carried out at pump speeds ranging from 500 rpm to 2000 rpm on a test bench of the type usually used in industry for assessing diesel injection equipment. A high speed data acquisition unit was used to record pressure time histories at different locations in the system along with the needle lift, the injection rate, and the fuel quantity injected per cycle. Pressures were measured in the pumping chamber at two pipe locations (one close to the delivery valve assembly, and the other close to the injector) and also inside the injector nozzle at a point ahead of the needle-seat opening passage.

This last pressure measurement was also performed for determining the nonstationary values of the injector-nozzle-hole discharge flow coefficient, so as to take the effects of liquid compressibility, flow unsteadiness, and needle-valve dynamics into account. These values were obtained with the support of the numerical model by solving the equation of mass conservation in the injector tip region, using, as input data, the following measured quantities: pressure at the needle-seat opening passage, needle lift, and injection rate.

Fuel Injection System

Figure 1 shows the double-spring sacless-nozzle injector under study. The two-stage lift injection is achieved through the consecutive action of the two springs as follows. At the first opening stage, only one spring (the first spring in the figure) works against the axial force which the pressurized fuel applies to the needle surface, while at the second stage of the needle lift, both springs are active. The enlargement at the top left of Fig. 1 evidences the stroke ends defining the maximum ampli-

---

Contributed by the Internal Combustion Engine Division and presented at the 18th Fall Technical Conference of the ASME Internal Combustion Engine Division, Fairborn, OH, October 20–23, 1996 Manuscript received by the ASME Headquarters July 16, 1998. Associate Technical Editor: D. Assanis.

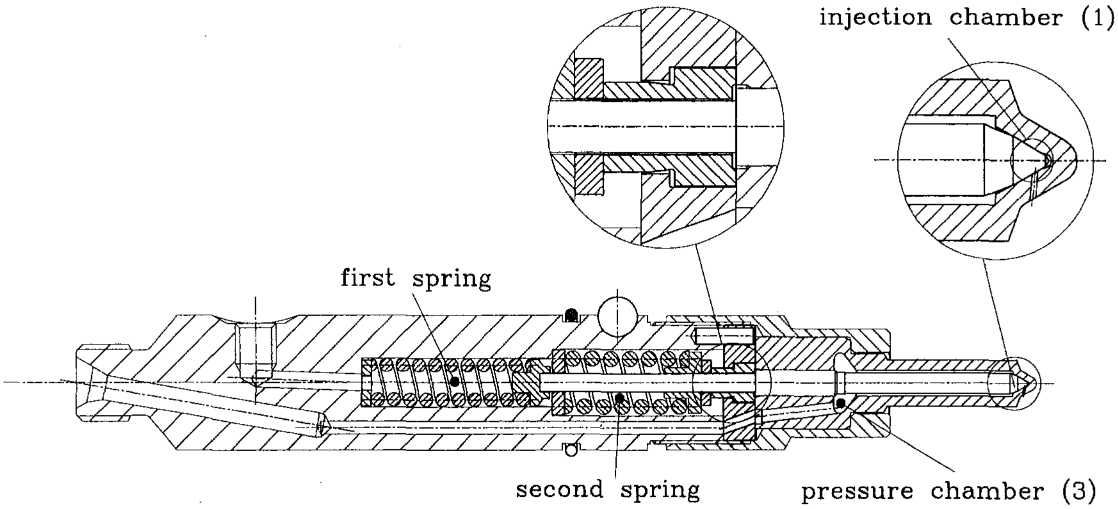

Fig. 1 Double-stage sacless-nozzle injector

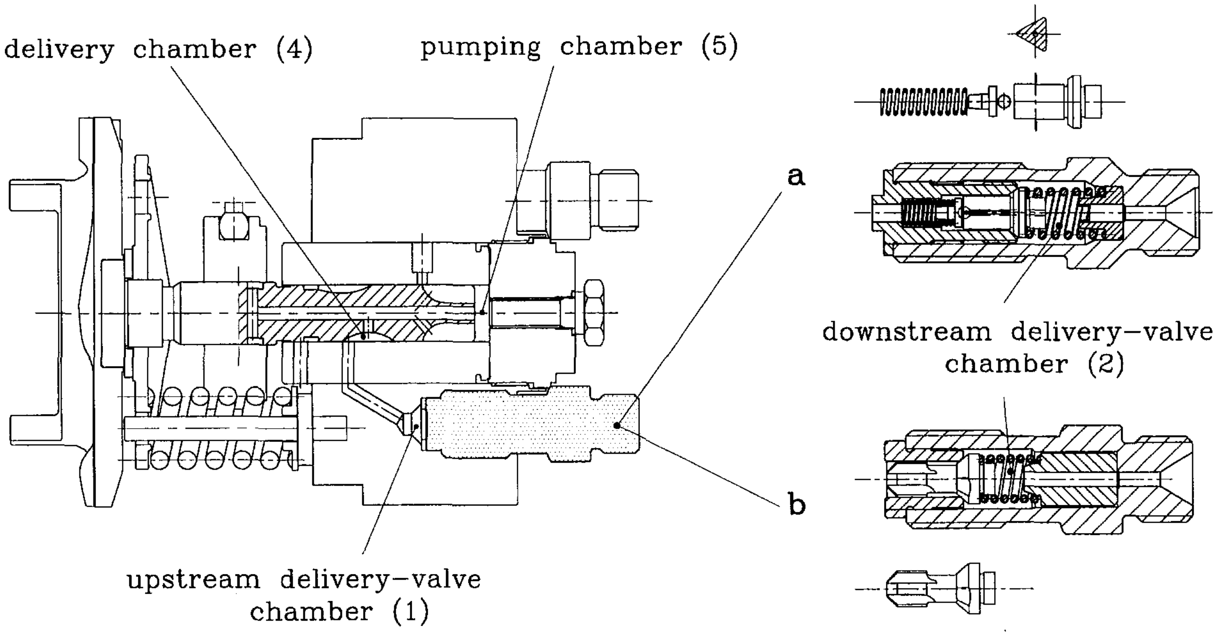

Fig. 2 High-pressure portion of the pump and delivery-valve assembly with constant-pressure valve (*a*) and reflux-hole valve (*b*)

Nomenclature

A = flow area
a = wave propagation speed; mixture celerity
d = pipe diameter
E = bulk modulus of elasticity
F = spring force
k = spring rate
l = lift; stroke
m = mass; mobile element
n = pump angular speed
P = plunger
p = pressure; average cross-sectional pressure
Q = flow rate; injection rate
S = surface
t = time
u = average cross-sectional velocity
V = volume
x = axial distance along pipe; lift
α = average cross-sectional void fraction
β = damping
Γ = gas/vapor production rate per unit volume
Δt = time increment
Δx = distance increment
ϑ = cam angle
μ = discharge flow coefficient
ρ = density; mixture density
τ = wall shear stress

Subscripts

0 = reference value
b = back-flow direction; seats
c = pumping chamber
e = injection environment
f = feed-flow direction
h = injector nozzle holes
i = pump interior
l = liquid phase
M = maximum value
m = mobile element: valve; needle
n = needle
p = plunger
pd = pipe location at the delivery-valve assembly
pi = pipe location at the injector inlet
s = sac chamber
sp = needle-seat passage
v = gaseous/vaporous phase; valve

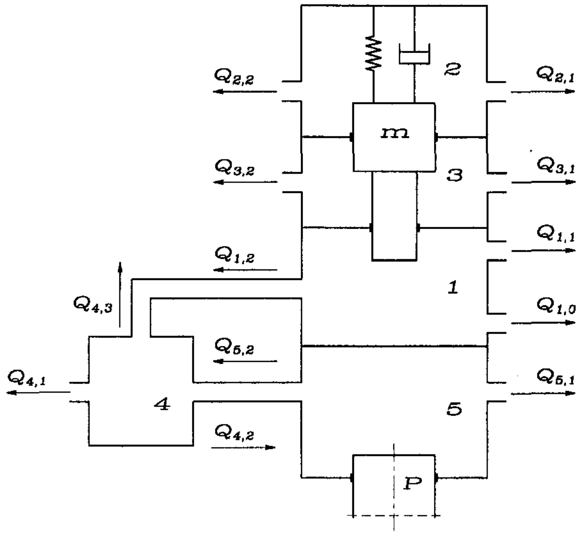

Fig. 3 Mathematical model of pump and injector

tude of the needle lift during the first and the second opening stages. Such a dual-spring device produces an injection rate distribution with a gradual slope that is capable of reducing the roughness in diesel engine operation. The injector-tip enlargement at the top right of Fig. 1 shows the typical design of a sacless nozzle.

The injector was fitted to an automotive diesel injection system with a Bosch-VER 286/1 distributor-type pump as is described in the technical report of Bosch (1981). The high pressure pump body is drawn in Fig. 2 giving evidence to the plunger and to the delivery valve assembly. This was alternatively equipped with a constant-pressure delivery valve (Fig. 2(*a*)) and with a reflux-hole valve (Fig. 2(*b*)). The constant-pressure valve is made up of two valves: the feed and the back-flow valves. More specifically, the feed-flow valve presents a hole along its axis whose opening and flow area are controlled by the back-flow pressure-calibrated valve (this opens for a back-flow pressure of ≈6 MPa). The reflux-hole valve presents a flat in the collar forming a return-flow restriction with the seat. The delivery valves are open during the injection phase, when the fluid flows from the pump to the injector. At the end of injection, consequent to the opening of the spill port in the pump plunger, the flow inverts its direction from the injector back to the valve. The back-flow valve-controlled hole and the permanently open reflux hole have the purpose of attenuating the back-flow pressure-wave reflection at the delivery valve head after its closure, so as to avoid the reopening of the injector nozzle. Nevertheless, an excessive damping of the pressure-wave reflection can be undesirable in order to hinder the cavitation that may arise from the depression wave subsequent to the spill-port opening. These two valves were expected to be little or no cavitation inducing, and, hence, their effects were compared to each other in this respect, for the considered injector equipment.

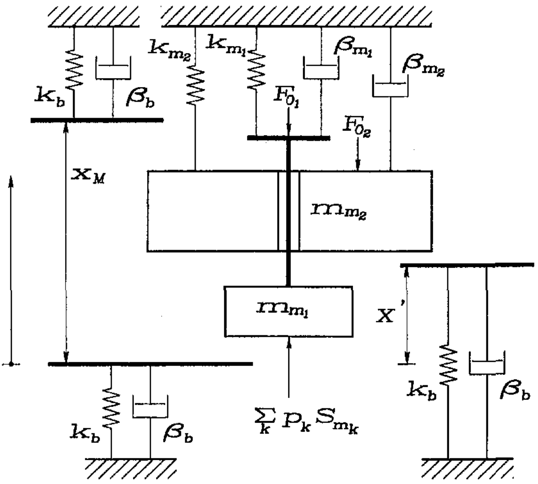

Fig. 4 Second-order dynamic model of double-stage injector

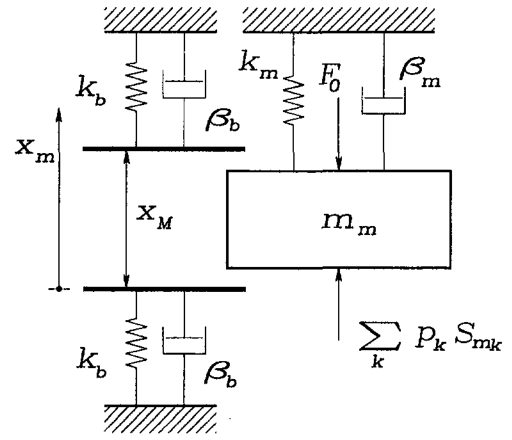

Fig. 5 Second-order dynamic model of reflux-hole delivery valve

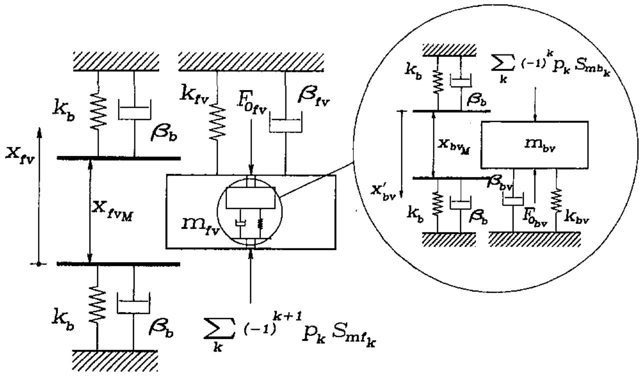

Fig. 6 Second-order dynamic model of constant-pressure delivery valve

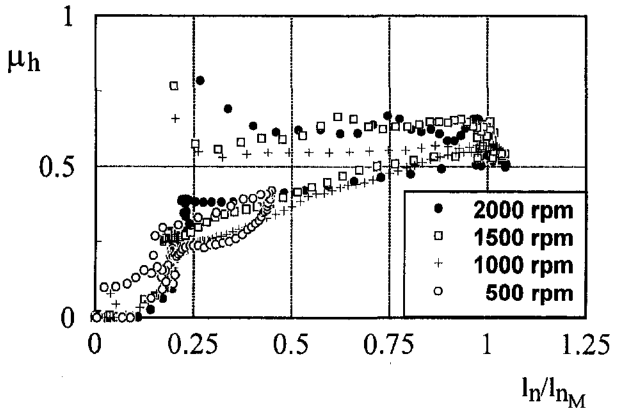

Fig. 7 Discharge flow coefficient of the sacless-nozzle double-stage injector

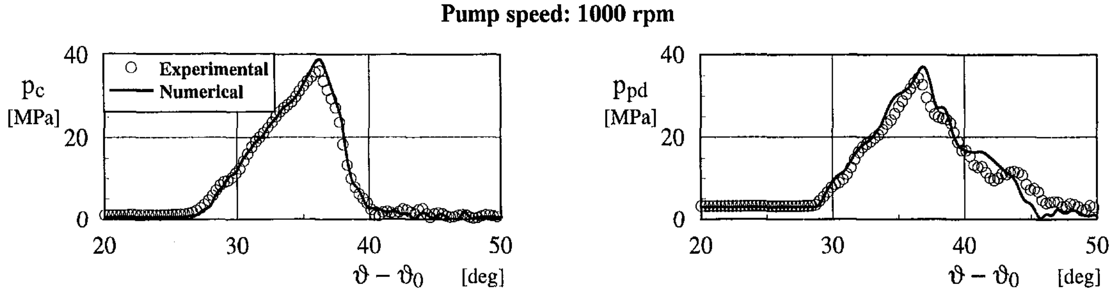

a - pumping chamber pressure

b - pipe pressure at the delivery outlet

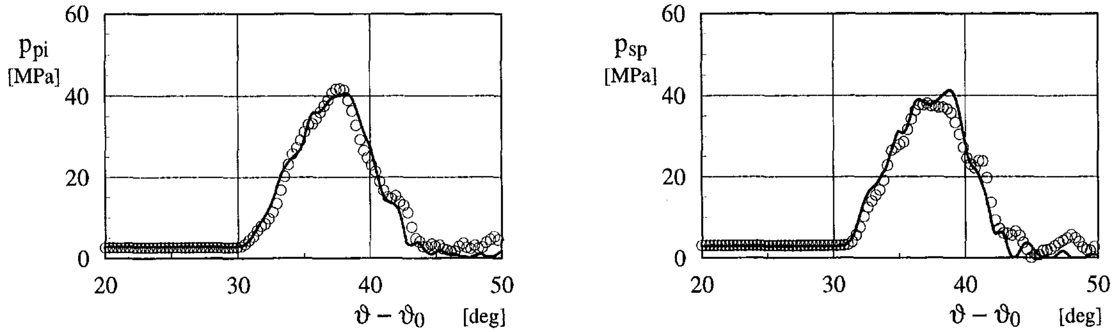

c - pipe pressure at the injector inlet

d - pressure at the needle-valve seat

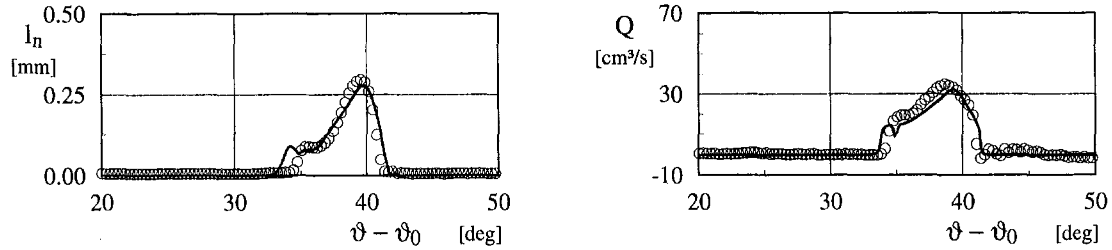

e - needle lift

f - injection rate

Fig. 8 Numerical and experimental results for the injection pump configuration with constant-pressure valve

Mathematical Model

Pipe Flow. The fluid flowing through the delivery pipe, connecting the pump with the injector, is ordinarily in the liquid state, but it becomes a liquid and vapor-phase mixture whenever cavitation occurs. Therefore, the transient pipe-flow conservation equations are written, in general, for a homogeneous, bubbly, two-phase fluid, so that the pure-liquid flow equations can be directly derived as a particular case. Cavitation is described by a dependent variable termed void fraction that is defined as the volume of the vaporous component per unit volume of the mixture. A virtually isothermal flow is considered, requiring only mass and momentum conservation equations for simulation. An average cross-sectional representation of mixture velocity, pressure, void fraction and component densities is employed. The details of pipe-flow model equations and related assumptions are reported and discussed elsewhere (Catania et al., 1992, 1993, 1994a). In summary, the conservation of mass for the vapor and liquid phases and the mixture momentum balance, under negligible body forces, are written in the following matrix form (Catania et al., 1992):

$$\frac{\partial \mathbf{w}}{\partial t} + [A]\frac{\partial \mathbf{w}}{\partial x} = \mathbf{H} \tag{1}$$

where

$$\mathbf{w} = \begin{bmatrix} u \\ p \\ \alpha \end{bmatrix} \quad [A] = \begin{bmatrix} u & \dfrac{1}{\rho} & 0 \\ \rho a^2 & u & 0 \\ \alpha\left(1 - \dfrac{\rho a^2}{\rho_v a_v^2}\right) & 0 & u \end{bmatrix}$$

$$\mathbf{H} = \begin{bmatrix} -\dfrac{4\tau}{\rho d} \\ \dfrac{\Gamma}{\rho_v}\left(1 - \dfrac{\rho_v}{\rho_l}\right)\rho a^2 \\ \dfrac{\Gamma}{\rho_v}\left[1 - \alpha\left(1 - \dfrac{\rho_v}{\rho_l}\right)\dfrac{\rho a^2}{\rho_v a_v^2}\right] \end{bmatrix}$$

The mixture density ρ is defined as $\rho = \alpha\rho_v + (1 - \alpha)\rho_l$, where α is the void fraction; a_v and a_l are the isothermal wave propagation speeds of the gas/vapor and liquid, respectively; the variable a is given by

$$\frac{1}{\rho a^2} = \frac{\alpha}{\rho_v a_v^2} + \frac{1 - \alpha}{\rho_l a_l^2} \tag{2}$$

and expresses the wave propagation speed of the mixture, as

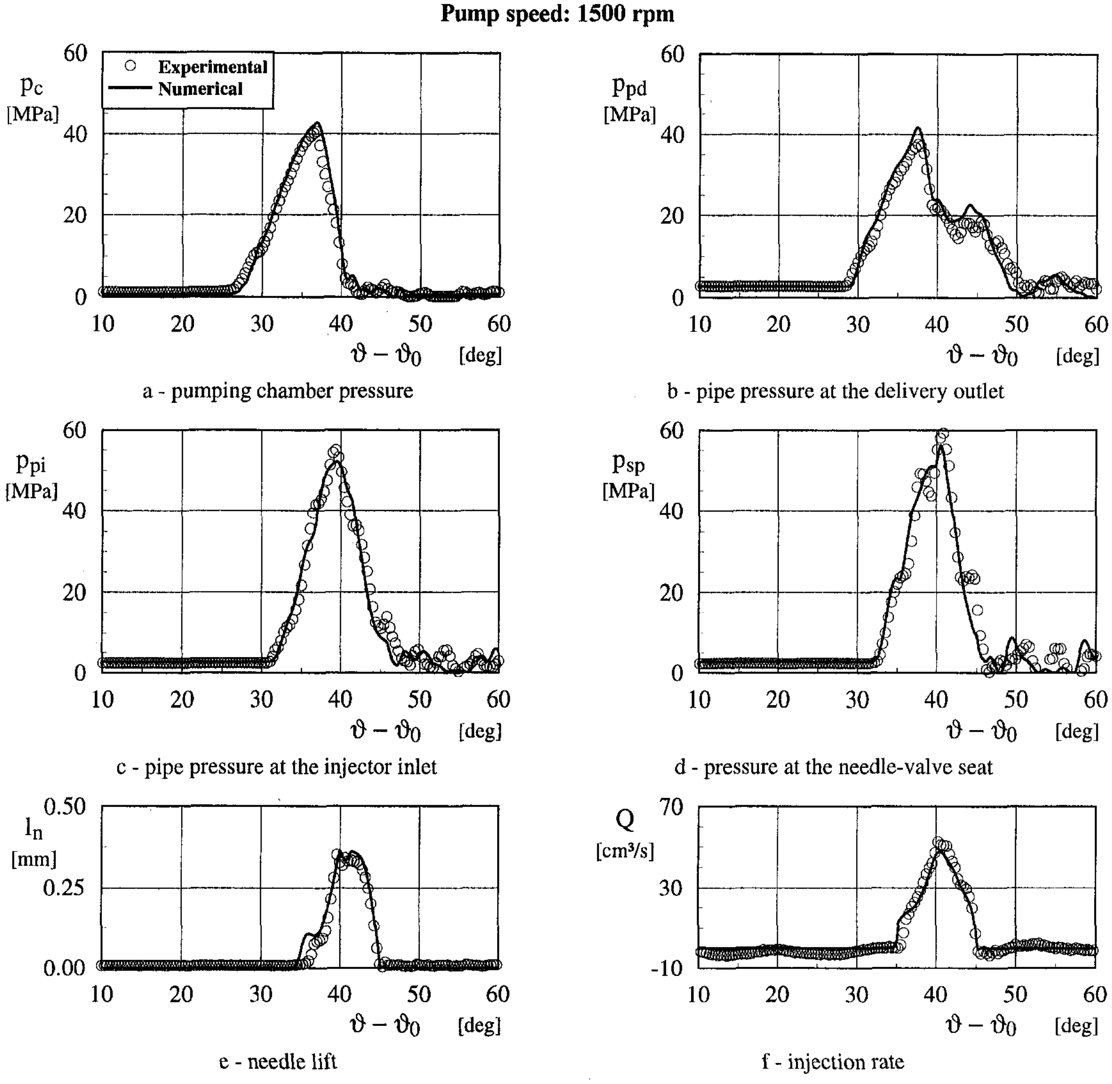

a - pumping chamber pressure

b - pipe pressure at the delivery outlet

c - pipe pressure at the injector inlet

d - pressure at the needle-valve seat

e - needle lift

f - injection rate

Fig. 9 Numerical and experimental results for the injection pump configuration with constant-pressure valve

can be deduced from the eigenvalues λ of the matrix $[A]$: $\lambda_{1,2} = u \pm a$, $\lambda_3 = u$.

Pump, Injector and Valves. The flow and wave-propagation phenomena through the injector drilled passages (Fig. 1) and along the internal and outlet ducts of the distributor pump (Fig. 2) were simulated according to the foregoing pipe-flow model. A conventional lumped mass model was applied to write the continuity and compressibility equations that allow for flow rates through the isobaric chambers of the injector and pump indicated in Figs. 1 and 2, as is detailed by Catania et al. (1994a, 1995). These chambers are numbered according to Fig. 3, so that, with reference to the chamber j, one can write the following:

$$\sum_{k=1-\delta_{j1}}^{2+\delta_{j4}} Q_{j,k} + V_{0_j}\zeta_j = \delta_{j5} S_p\left(x_p\zeta_j + \frac{dx_p}{dt}\right) + (-1 + \delta_{j4} + \delta_{j5})^j S_{m_j}\left(x_m\zeta_j + \frac{dx_m}{dt}\right) \qquad j \neq j_0, \quad j = 1, 2, 3, 4, 5 \qquad (3)$$

where, for $k = 0, 1$

$$Q_{j,k} = \frac{p_j - p_{j,k}}{|p_j - p_{j,k}|}\,\mu_{j,k}A_{j,k}\sqrt{\frac{2}{\rho}\,|p_j - p_{j,k}|} \qquad j = 1, 2, 3, 4, 5$$

and, for $k = 2, 3$, $Q_{j,k}$ expresses the volumetric flow rates from the chambers to the internal connecting lines and to the pressure pipe,

$$\delta_{jk} = \begin{cases} 1 & j = k \\ 0 & j \neq k \end{cases}$$

$$\zeta_j = \begin{cases} \dfrac{1}{E_l}\dfrac{dp_j}{dt} & p_j > p_v \\[2ex] \left(\dfrac{\rho_l}{\rho_v - \rho_l} + \alpha_j\right)^{-1}\dfrac{d\alpha_j}{dt} & p_j = p_v. \end{cases}$$

E_l is the elasticity modulus of the liquid, and p_v is the vapor pressure. In Eq. (3), the terms containing ζ_j designate the accumulation terms, the other terms indicate the chamber volume reduction, or increase, due to the displacement x of the element surface S.

The differential equations for the pump and injector can be derived from Eq. (3) by putting for the pump, $j_0 = 3$ and

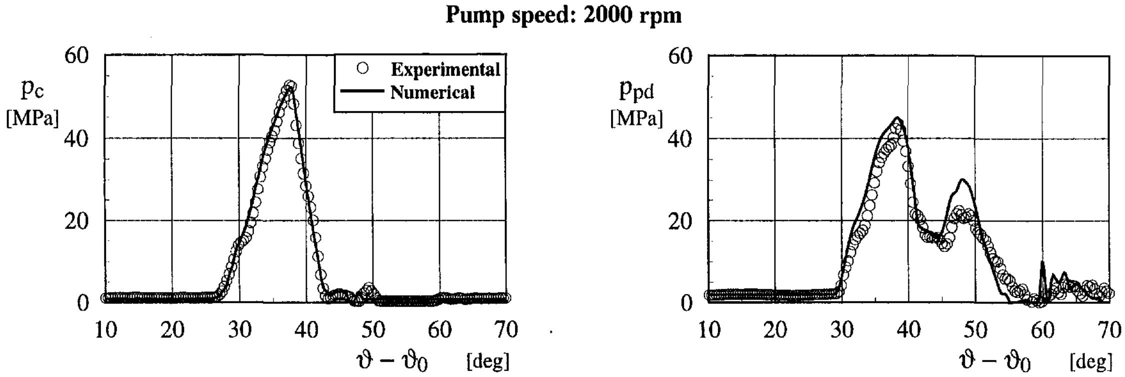

a - pumping chamber pressure

b - pipe pressure at the delivery outlet

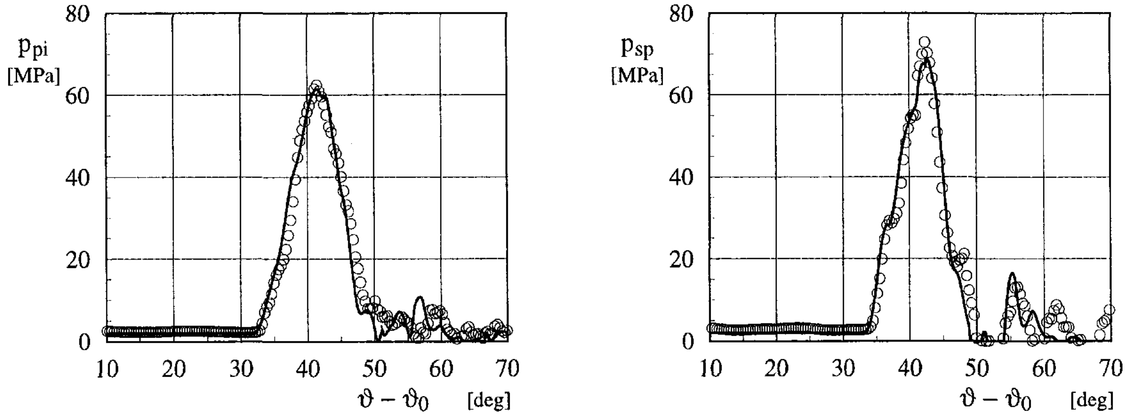

c - pipe pressure at the injector inlet

d - pressure at the needle-valve seat

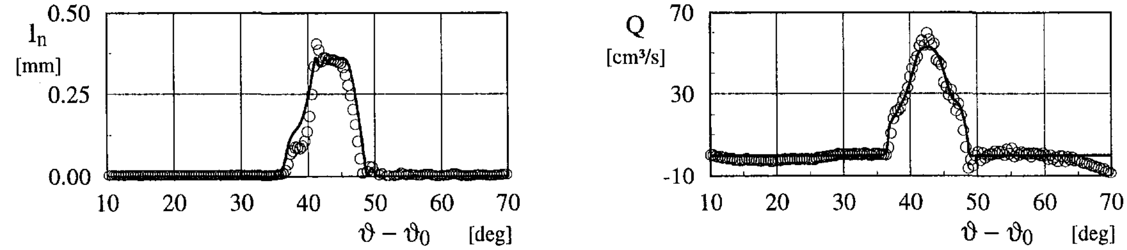

e - needle lift

f - injection rate

Fig. 10 Numerical and experimental results for the injection pump configuration with constant-pressure valve

$Q_{1,0} = 0,\ Q_{1,1} = -Q_{2,1},\ p_{1,1} = p_2,\ p_{2,1} = p_1,\ p_{4,1} = p_i,\ p_{5,1} = p_i,$

and for the injector, $j_0 = 2, 4, 5$ and

$$Q_{1,2} = 0,\ Q_{3,1} = -Q_{1,1},\ p_{1,0} = p_e,\ p_{1,1} = p_3,\ p_{3,1} = p_1.$$

The dynamics of the injector needle (Fig. 1) and of the reflux-hole delivery valve (Fig. 2(*b*)) are simulated through the second-order linear-system models of Figs. 4 and 5, respectively, given by the following ordinary differential equation:

$$\bar{m}_m \frac{d^2 x_m}{dt^2} + \bar{\beta}_m \frac{dx_m}{dt} + \bar{k}_m x_m + \bar{F}_0 + \sum_{\substack{k=1 \\ k \neq j_0}}^{3} (-1)^k p_k S_{m_k} = 0 \quad (4)$$

where $\bar{F}_0$, $\bar{m}_m$, $\bar{k}_m$, and $\bar{\beta}_m$, are defined in what follows.

For the model of the injector needle, using the subscripts 1 for the first spring and 2 for the second spring (Fig. 4):

$$x_m < 0 \quad \bar{F}_0 = F_{0_1} \quad \bar{m}_m = m_{m_1}$$

$$\bar{k}_m = k_{m_1} + k_b \quad \bar{\beta}_m = \beta_{m_1} + \beta_b$$

$$0 \le x_m < x' \quad \bar{F}_0 = F_{0_1} \quad \bar{m}_m = m_{m_1}$$

$$\bar{k}_m = k_{m_1} \quad \bar{\beta}_m = \beta_{m_1}$$

$$x' \le x_m < x_0' \quad \bar{F}_0 = F_{0_1} + F_{0_2} - k_{m_2}x' - k_b x_0'$$

$$\bar{m}_m = m_{m_1} + m_{m_2} \quad \bar{k}_m = k_{m_1} + k_{m_2} + k_b$$

$$\bar{\beta}_m = \beta_{m_1} + \beta_{m_2} + \beta_b$$

$$x_0' \le x_m < x_M \quad \bar{F}_0 = F_{0_1} + F_{0_2} - k_{m_2}x' \quad \bar{m}_m = m_{m_1} + m_{m_2}$$

$$\bar{k}_m = k_{m_1} + k_{m_2} \quad \bar{\beta}_m = \beta_{m_1} + \beta_{m_2}$$

$$x_M < x_m \quad \bar{F}_0 = F_{0_1} + F_{0_2} - k_{m_2}x' - k_b x_M \quad \bar{m}_m = m_{m_1} + m_{m_2}$$

$$\bar{k}_m = k_{m_1} + k_{m_2} + k_b \quad \bar{\beta}_m = \beta_{m_1} + \beta_{m_2} + \beta_b$$

with $x' = x_0' - F_{0_2}/k_b$;

for the reflux-hole valve model (Fig. 5):

$$x_m < 0 \quad \bar{F}_0 = F_0 \quad \bar{k}_m = k_m + k_b \quad \bar{m}_m = m_m \quad \bar{\beta}_m = \beta_m + \beta_b$$

$$0 \le x_m \le x_M \quad \bar{F}_0 = F_0 \quad \bar{k}_m = k_m \quad \bar{m}_m = m_m \quad \bar{\beta}_m = \beta_m$$

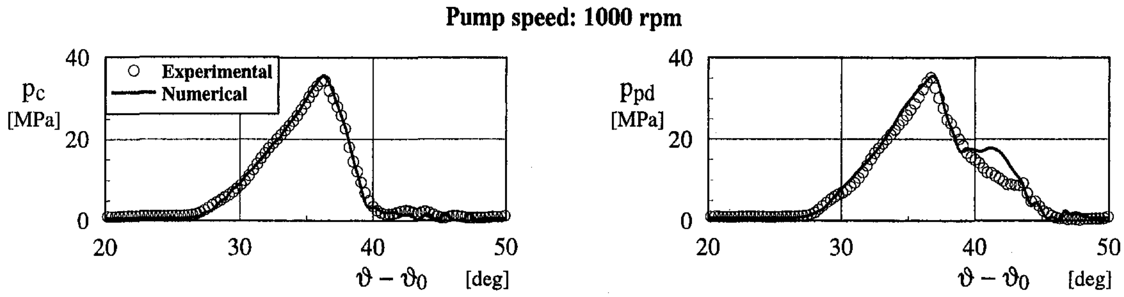

a - pumping chamber pressure

b - pipe pressure at the delivery outlet

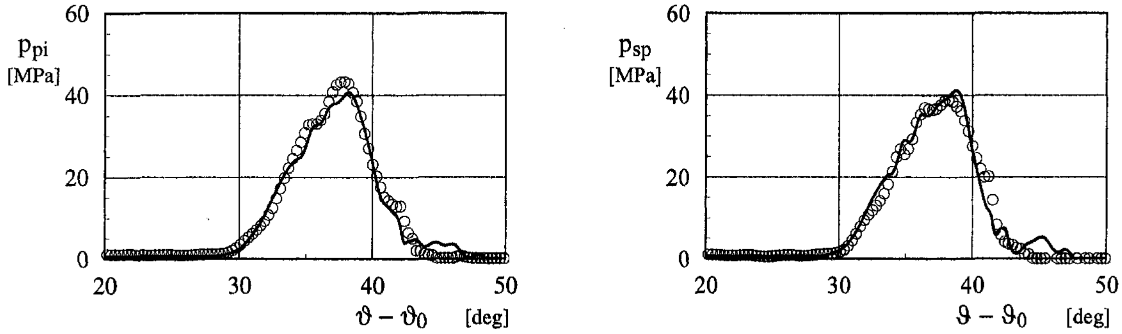

c - pipe pressure at the injector inlet

d - pressure at the needle-valve seat

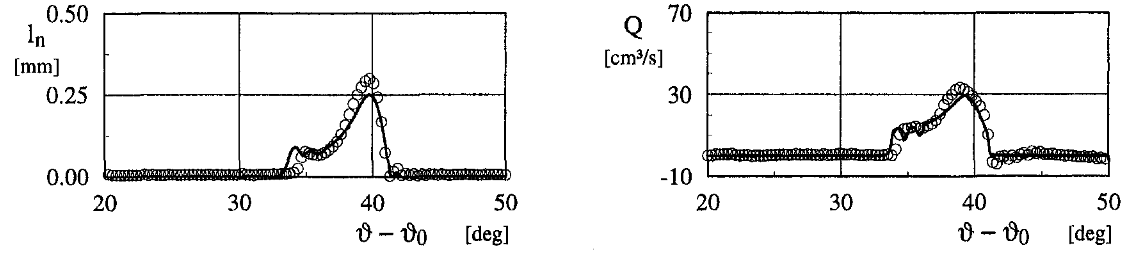

e - needle lift

f - injection rate

Fig. 11 Numerical and experimental results for the injection pump configuration with reflux-hole valve

$$x_M < x_m \quad \bar{F}_0 = F_0 - k_b x_M \quad \bar{k}_m = k_m + k_b$$

$$\bar{m}_m = m_m \quad \bar{\beta}_m = \beta_m + \beta_b .$$

With reference to Fig. 6, the dynamic equilibrium equations of the constant-pressure delivery valve, for both feed and backflow directions, are:

$$m_{fv}\frac{d^2x_{fv}}{dt^2} + \bar{\beta}_{fv}\frac{dx_{fv}}{dt} + \bar{\beta}_{bv}\frac{dx'_{bv}}{dt} + \bar{k}_{fv}x_{fv} + \bar{k}_{bv}x'_{bv} + \bar{F}_{0_{fv}} + \bar{F}_{0_{bv}} = \sum_{\substack{k=1\\ k\neq j_0}}^{3}(-1)^{k+1}p_k S_{mf_k} \quad (5)$$

$$m_{bv}\left(\frac{d^2x'_{bv}}{dt^2} - \frac{d^2x_{fv}}{dt^2}\right) + \bar{\beta}_{bv}\frac{dx'_{bv}}{dt} + \bar{k}_b x'_{bv} + \bar{F}_{0_{bv}} = \sum_{\substack{k=1\\ k\neq j_0}}^{3}(-1)^{k}p_k S_{mb_k} \quad (6)$$

where

$$x_{fv} < 0 \quad \bar{k}_{fv} = k_{fv} + k_b \quad \bar{F}_{0_{fv}} = F_{0_{fv}} \quad \bar{\beta}_{fv} = \beta_{fv} + \beta_b$$

$$0 \leq x_{fv} < x_{fv_M} \quad \bar{k}_{fv} = k_{fv} \quad \bar{F}_{0_{fv}} = F_{0_{fv}} \quad \bar{\beta}_{fv} = \beta_{fv}$$

$$x_{fv_M} \leq x_{fv} \quad \bar{k}_{fv} = k_{fv} + k_b \quad \bar{F}_{0_{fv}} = F_{0_{fv}} - k_b x_{fv_M}$$

$$\bar{\beta}_{fv} = \beta_{fv} + \beta_b$$

and

$$x'_{bv} < 0 \quad \bar{k}_{bv} = k_{bv} + k_b \quad \bar{F}_{0_{bv}} = F_{0_{bv}} \quad \bar{\beta}_{bv} = \beta_{bv} + \beta_b$$

$$0 \leq x'_{bv} < x_{bv_M} \quad \bar{k}_{bv} = k_{bv} \quad \bar{F}_{0_{bv}} = F_{0_{bv}} \quad \bar{\beta}_{bv} = \beta_{bv}$$

$$x_{bv_M} \leq x'_{bv} \quad \bar{k}_{bv} = k_{bv} + k_b \quad \bar{F}_{0_{bv}} = F_{0_{bv}} - k_b x_{bv_M}$$

$$\bar{\beta}_{bv} = \beta_{bv} + \beta_b .$$

Geometric and mechanical quantities relevant to the model, such as lengths, volumes, masses, spring preloads and rates, and others, were thoroughly measured. For example, the spring rates were evaluated by correlating the axial spring deformation to the intensity of the compression force acting on the spring, so that, with specific reference to the models of Figs. 4–6, the following values were obtained: $k_{m_1} = 147.5$ N/mm, $k_{m_2} = 179.3$ N/mm, $k_m = 3.1$ N/mm, $k_{fv} = 14.0$ N/mm, and $k_{bv} = 6.0$ N/mm.

Numerical Algorithm

Backward Differentiation Formulas (BDF) implicit multistep schemes of the second-order accuracy were selected to discretize the ordinary differential equations in the models of the pump, injector, and valve dynamics because they are suitable for problems of the stiff type. A second-order BDF approxima-

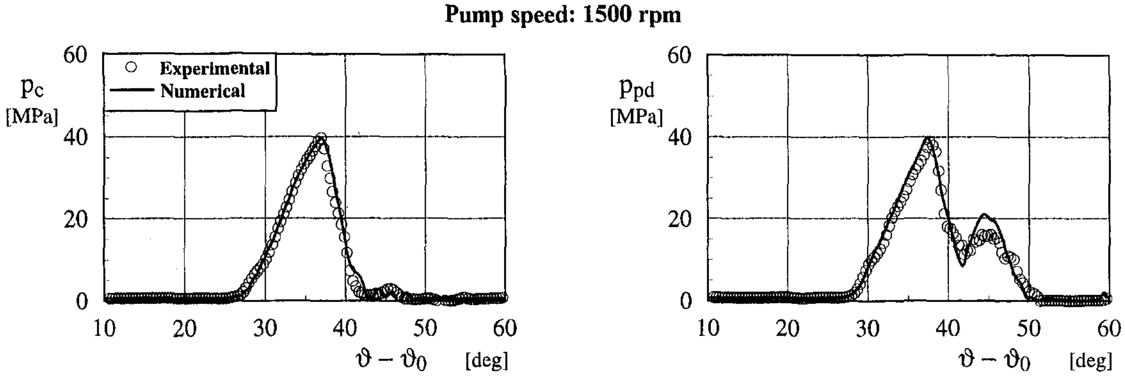

a - pumping chamber pressure

b - pipe pressure at the delivery outlet

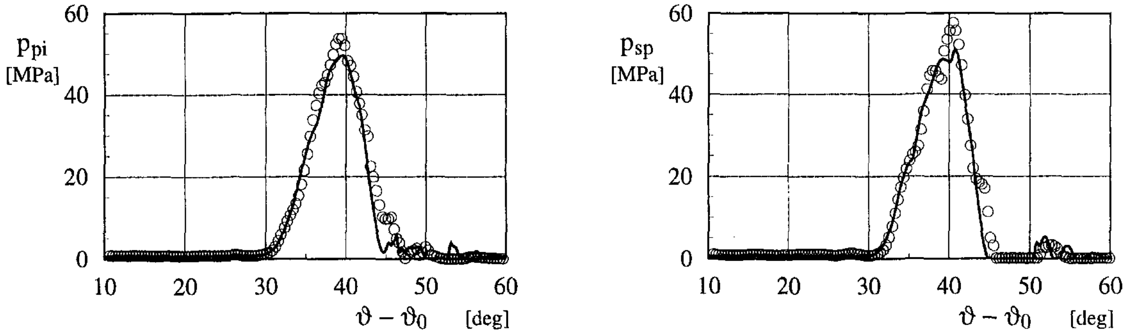

c - pipe pressure at the injector inlet

d - pressure at the needle-valve seat

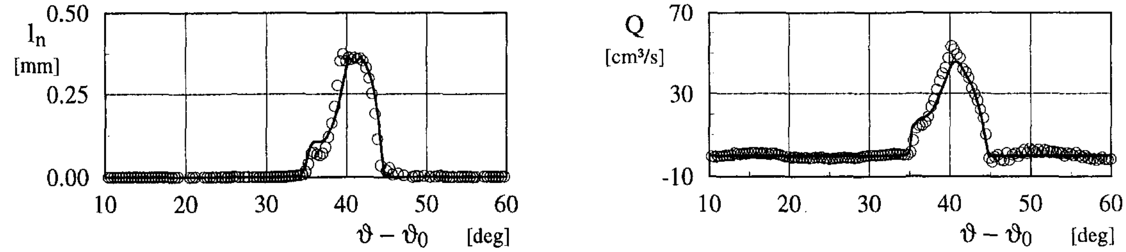

e - needle lift

f - injection rate

Fig. 12 Numerical and experimental results for the injection pump configuration with reflux-hole valve

tion to the first-order time derivative of any time function y, at the instant $n + 1$, is given by

$$\left(\frac{dy}{dt}\right)^{n+1} = \frac{1}{\Delta t}\left(\frac{3}{2}y^{n+1} - 2y^{n} + \frac{1}{2}y^{n-1}\right). \qquad (7)$$

The three-time level[1] Trapezoidal Space, Backward Time (TSBT) implicit finite-difference scheme of the second-order accuracy, proposed by Catania et al. (1996), was used to discretize the pipe-flow partial differential equations, as follows:

$$\left\{\frac{3}{2}[I] + \frac{\Delta t}{\Delta x}([A]_i^{n+1} + [A]_{i-1}^{n+1})\right\}\mathbf{w}_i^{n+1}$$

$$+ \left\{\frac{3}{2}[I] - \frac{\Delta t}{\Delta x}([A]_i^{n+1} + [A]_{i-1}^{n+1})\right\}\mathbf{w}_{i-1}^{n+1} = 2(\mathbf{w}_i^{n} + \mathbf{w}_{i-1}^{n})$$

$$- \frac{1}{2}(\mathbf{w}_i^{n-1} + \mathbf{w}_{i-1}^{n-1}) + \Delta t(\mathbf{H}_i^{n+1} + \mathbf{H}_{i-1}^{n+1}) \qquad (8)$$

where the time-stepping coordinate in the computational grid is indicated by the superscript and the spatial coordinate by the subscript, $\Delta t = t^n - t^{n-1}$ and $\Delta x = x_i - x_{i-1}$ being the time and space-interval of the grid, respectively.

The finite-difference analogues to the ordinary differential equations of the pump and injector and to the partial differential equations of the pipe flow led to a system of nonlinear algebraic equations. This system was solved using the Newton–Raphson iterative method, which transforms it into a linear form. The solution of the linear equation system is obtained using a very fast direct method proposed and detailed elsewhere (Catania et al., 1992, 1993, 1994a).

Injection Pressure and Nozzle-Hole Flow Coefficient

The pressure in the sacless-nozzle tip ahead of the holes is defined as the injection pressure. The direct measurement of this quantity in a commercial injector is an extremely hard task, especially for an automotive diesel engine, due to the tiny dimension of the nozzle tip. Therefore, the injection pressure was derived from tests carried out under actual engine conditions by integrating the experimentation with modeling. During these tests, piezometric data in the nozzle were acquired upstream of the needle-seat opening passage; the fuel injection rate and the needle lift were also measured as functions of

---

[1] It is also sometimes referred to as a two-step scheme, with reference to the time-stepping coordinate (Catania et al., 1994b).

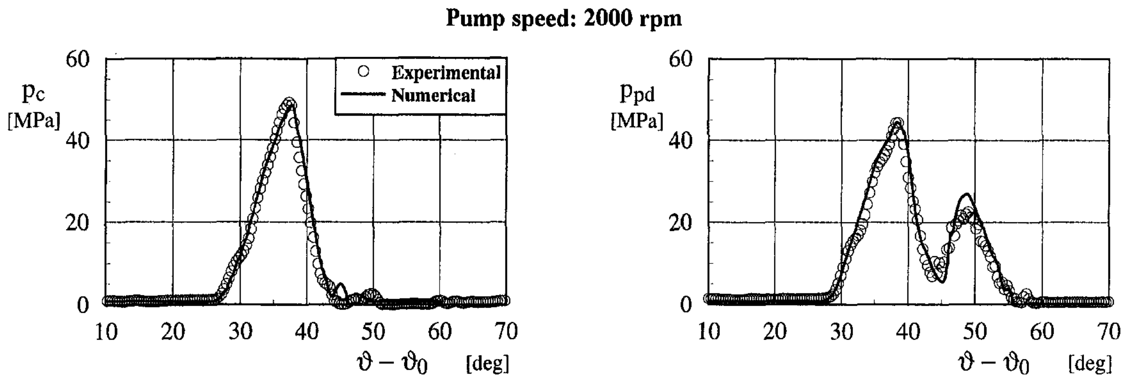

a - pumping chamber pressure

b - pipe pressure at the delivery outlet

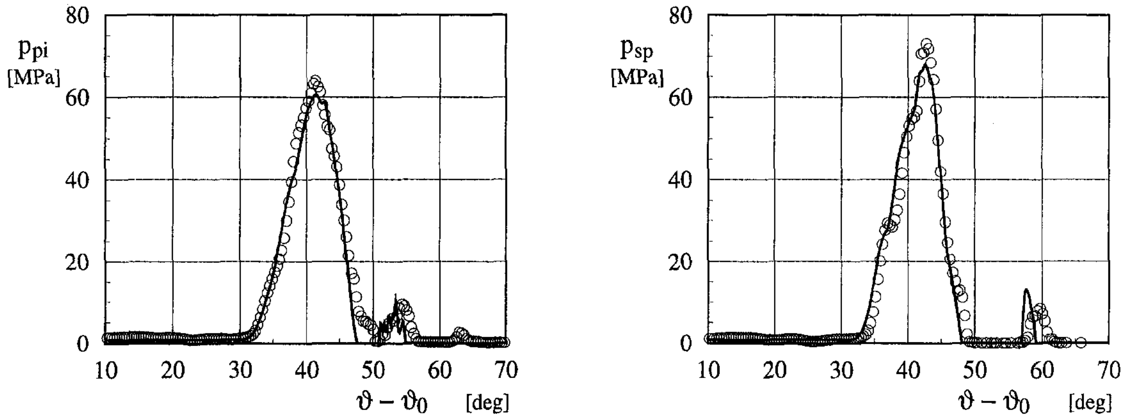

c - pipe pressure at the injector inlet

d - pressure at the needle-valve seat

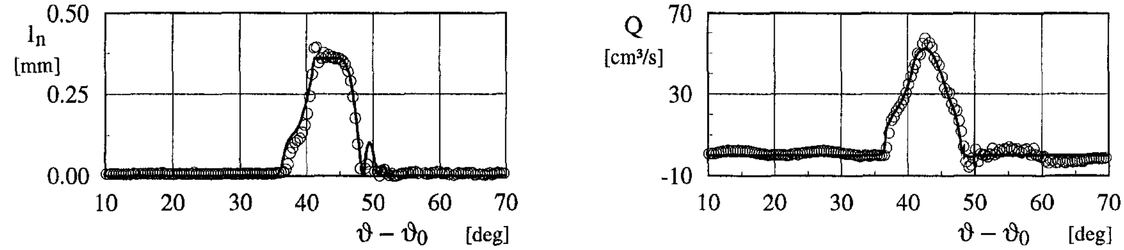

e - needle lift

f - injection rate

Fig. 13 Numerical and experimental results for the injection pump configuration with reflux-hole valve

time. The obtained experimental data were introduced as known variables in the continuity equation model written for the sac chamber developing during the needle lift. The injection pressure was thus determined as the solution of this equation. Its uncertainty was taken to be virtually the same as the overall uncertainty ascribed to the experimental results. The experimental uncertainty was prudentially estimated to be less than ±10 percent (Catania et al., 1994a, b).

The discharge coefficient μ_h of the injector-nozzle holes was conventionally defined as the ratio between the actual flow rate discharged and the ideal one evaluated by means of the pressure difference across the holes according to

$$\mu_h = Q\left(\frac{p_s - p_e}{|p_s - p_e|} A_h \sqrt{\frac{2|p_s - p_e|}{\rho_l}}\right)^{-1} \qquad (9)$$

where Q is the injected volumetric flow rate, A_h is the geometric cross-sectional area of the nozzle holes, p_s is the injection pressure, and p_e is the nozzle back pressure. In order to take the unsteadiness and compressibility flow effects as well as the dynamic effects of the needle lift, the injection pressure and volumetric flow rate used in Eq. (9) were those derived from the abovementioned tests. The discharge coefficient was then obtained from Eq. (9) for a back pressure equal to the ambient pressure. It has to be pointed out that, in the presence of a Bosch indicator, which was used to measure the injection rate, an average back pressure higher than the ambient pressure occurred downstream from the nozzle holes. However, the injection rate was virtually independent of back pressure (Bosch, 1966; Bower and Foster, 1991; Takamura et al., 1992). A similar result was found for the pressures in the injection systems as well as for the needle lift. This was in agreement with previous findings for a reduced-sac-nozzle injector (Catania et al., 1994a, b). Therefore, it is the flow coefficient that depends on the nozzle-hole back pressure.

Results

Figure 7 plots the distributions of the nonstationary flow coefficient of the double-stage sacless-nozzle injector versus needle lift, as were determined for the pump equipment with the reflux-hole valve at the indicated speeds. However, the delivery valve was found to have a negligible influence on the distributions of μ_h. During the injector opening, a continuously increasing trend of μ_h is shown by Fig. 7, with different patterns before and after the end of the first-stage lift ($l_n/l_{n_M} \approx 0.20$). This trend is typical of sacless nozzles. Similar deductions to those reported by Catania et al. (1994a, b) for a single-stage reduced-sac-nozzle injector can be inferred from Fig. 7 at the maximum needle lift and during the injector closure, in relation to pressure and needle-dynamic effects. An analytical fit of the test-derived μ_h values was applied for the injection-system numerical simulation. The virtually negligible dependence on engine speed shown by the figure and also the fact that the needle valve did not reach its lift end at 500 rpm were taken into account. It is interesting to observe that an average value $\mu_h \approx 0.5-0.6$ can be deduced from Fig. 7 in the main part of the needle lift at the different speeds except at the lowest one, where a much smaller value is obtained. However, an average value $\mu_h \approx 0.7$ resulted for the single-spring reduced-sac nozzle injector (Catania et al., 1994b).

Figures 8–13 show, for both delivery valve assemblies, the numerical and experimental distributions of the following quantities versus pump-cam-plate angle ($\vartheta-\vartheta_0$): pumping-chamber pressure (p_c), pipe pressure at the delivery valve outlet (p_{pd}), pipe pressure at the injector inlet (p_{pi}), pressure at the needle seat opening passage (p_{sp}), needle lift (l_n), and injection rate (Q). These results refer to the pump-shaft angular speeds indicated at the top of each figure, that is 1000 rpm, 1500 rpm, and 2000 rpm. The injection rate was normalized through the average quantity of fuel injected per cycle, which was measured by means of a burette. The experimental results were obtained as the ensemble average of 40–50 cycles. The flow coefficient of the back-flow valve, as well as of the feed flow and reflux-hole valves, used in the simulation program was derived from tests carried out under steady-state flow conditions.

The generally good agreement between the computed and measured quantities substantiates the validity of the mathematical model for the double-stage sacless-nozzle injector.

The double spring effects, which can be inferred from the patterns of l_n and Q, particularly at the early stage of injection, are remarkable at low pump speeds and reduce by increasing the speed.

The distributions of p_{pd}, p_{pi}, and p_{sp} show the presence of cavitation in the delivery pipe and in the injector nozzle. It is worthwhile to recall that cavitation occurs, usually after the closure of the injector needle valve, whenever the fluid pressure collapses to the vapor pressure, that is almost zero in the pressure time-histories of the figures.

By comparing the results of Figs. 8–10 to those of Figs. 11–13, a slight influence of the valve on the injection system performance can be deduced, with specific reference to the injection rate shape. However, for the constant-pressure valve, a less intense cavitation was generally observed with respect to the reflux-hole valve, as can be deduced in particular from the distributions of p_{sp} at the highest speeds. The noncavitating trend of the system behavior with the constant-pressure delivery valve stems from the relatively high value of the residual pressure in the delivery pipe at the end of the injection phase, due to the calibration pressure of the back-flow valve.

Figure 14 plots the computed distributions of the injection pressure versus cam angle at the indicated pump speeds. For comparison, the test-derived distributions of p_s are also reported in the figure. These were determined from the measured time histories of the pressure at the needle-seat passage, of the injection rate and needle lift, as is specified in the previous section. Since p_s was numerically predicted by simulating the whole injection system and the nozzle-hole flow coefficient was obtained from the test-derived values of p_s, the results of Fig. 14 give a further indication of the numerical model accuracy.

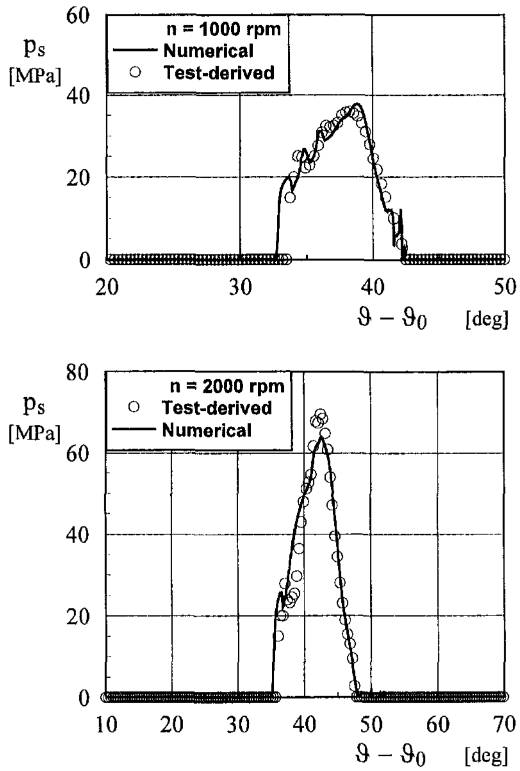

Fig. 14 Injection pressure

Conclusion

A double-stage sacless-nozzle injector was installed in an automotive diesel injection system and its effects on the system performance were numerically and experimentally investigated for the distinct pump configurations with a constant-pressure and a reflux-hole delivery valve.

The injector model was validated over a wide pump-speed range and included in the library of the previously developed NAIS program for injection system simulation.

The nonstationary discharge flow-coefficient distributions which were determined under real test conditions showed the effects of both sacless nozzle and two-lift injection, without a sensible dependence on the delivery valve type and also on the pump speed, though the needle valve did not reach its lift end at 500 rpm.

The effects of the injector springs on the needle lift and injection rate shape were less substantial at higher speeds.

A slight influence of the valve on the injection system performance was observed, with specific reference to the injection rate. However, the cavitation occurring in the injector nozzle, for the configuration with the constant-pressure valve, was less intense than that observed with the reflux hole valve, particularly at higher speeds.

Acknowledgments

This work was financially supported by MURST (Ministero dell'Università e della Ricerca Scientifica e Tecnologica) and in part by C.N.R. (Consiglio Nazionale delle Ricerche) under PS (Progetto Speciale) "Study of Thermo-Fluid-Dynamic Processes and Techniques for Reduction of Pollutant Emissions from IC Reciprocating Engines," Contribution No. 95.00079.CT07.

The authors would like to thank the C.R.F. (Centro Ricerche Fiat) for permission to use its experimental facilities. The technical assistance of Messrs. R. Antonioli, M. Danzero, E. Rigon and D. Varesio of the C.R.F. is also acknowledged.

References

Andoh, H., and Shiraishi, K., 1986, "Influence on Injection and Combustion Phenomena by Elimination of Hole Nozzle Sac Volume," SAE Paper No. 860416.

Aoyama, T., Mizuta, J., and Oshima, Y., 1990, "NO_x Reduction by Injection Control," SAE Paper No. 900637.

Beck, N. J., and Chen, S. K., 1990, "Injection Rate Shaping and High Speed Combustion Analysis—New Tools for Diesel Engine Combustion Development," SAE Paper No. 900639.

Bosch, W., 1966, "The Fuel Rate Indicator: A New Measuring Instrument for Display of the Characteristics of Individual Injection," SAE Paper No. 660749.

Bosch, R., 1981, "Distributor-Type Fuel Injection Pump Type VE—Technical Description D 5/2," GmbH, Bosch Automotive Equipment Division K5.

Bower, G. R., and Foster, D. E., 1991, "A Comparison of the Bosch and Zeuch Rate of Injection Meters," SAE Paper No. 910724.

Catania, A. E., Dongiovanni, C., and Mittica, A., 1992, "Implicit Numerical Model of a High-Pressure Injection System," ASME JOURNAL OF ENGINEERING FOR GAS TURBINES AND POWER, Vol. 114, pp. 534–543.

Catania, A. E., Dongiovanni, C., and Mittica, A., 1993, "On the Numerical Simulation of High-Pressure Injection Equipment," (in Italian) *ATA Automotive Engineering,* Vol. 46, pp. 338–354.

Catania, A. E., Dongiovanni, C., Mittica, A., Badami, M., and Lovisolo, F., 1994a, "Numerical Analysis Versus Experimental Investigation of a Distributor-Type Diesel Fuel-Injection System," ASME JOURNAL OF ENGINEERING FOR GAS TURBINES AND POWER, Vol. 116, pp. 814–830.

Catania, A. E., Dongiovanni, C., Mittica, A., Spessa, E., and Lovisolo, F., 1994b, "Study of Unsteady Flow Phenomena in an Automotive Diesel Injection System," Proceedings, XXV FISITA Congress, International Academic Publishers, Beijing, Vol. 1, pp. 124–137.

Catania, A. E., Dongiovanni, C., Negri, C., and Spessa, E., 1995, "Models for Automotive High-Pressure Injection System Simulation under Stationary and Transient Operating Conditions," (in Italian) Proceedings, 50th ATI Congress, SGEditoriali, Padova, Vol. 2, pp. 1301–1313.

Catania, A. E., Dongiovanni, C., Mittica, A., and Spessa, E., 1996, "Transient Flow and Cavitation Simulation in an Automotive Diesel Injection System Using a Novel Second-Order Accurate Implicit Finite-Difference Scheme," Report PTDE 428/MA, presented at the 17th ASME ETCE, Internal Combustion Engine Symposium, New Orleans, LA.

Greeves, G., and Wang, C. H. T., 1990, "Two-Stage Lift Injection and HSDI Combustion," SAE Paper No. 905025.

Russel, M. F., Young, C. D., and Nicol, S. W., 1990, "Modulation of Injection Rate to Improve Direct Injection Diesel Engine Noise," SAE Paper No. 900349.

Takamura, A., Ohta, T., Fukushima, S., and Kamimoto, T., 1992, "A Study on Precise Measurement of Diesel Fuel Injection Rate," SAE Paper No. 920630.

Limitations of Rigid Body Descriptions for Heavy-Duty Diesel Engine Vibration

D. M. W. Hoffman[1]

D. R. Dowling

Department of Mechanical Engineering and
Applied Mechanics,
The University of Michigan,
2019 W. E. Lay Automotive Lab,
Ann Arbor, MI 48109-2121

Internal combustion engine vibration modeling commonly relies on assuming the engine is a linearly reacting rigid body, thereby ignoring rotating, reciprocating, and nonsolid engine components. Limitations of this approach are identified from a series of experiments on a heavy-duty in-line six-cylinder Diesel engine typical of Class VIII trucks. Measurement of all three orthogonal vibration force components were made at each of three engine mounts during standard impact-excitation modal identification tests on the quiescent engine and during engine operation. The running-engine vibration forces, measured throughout the test engine load and speed operating envelope, were projected onto the quiescent-engine rigid body modes to determine the modal content and residual vibration as a function of frequency. Modal decomposition results for the running engine show that the quiescent-engine rigid body modes, with modal frequencies between 5.6 and 26.3 Hz, account for 80 percent or more of the measured engine vibration forces for all engine speeds and loads in a bandwidth from zero to 200 Hz. The likely origins of the residual vibration within this bandwidth are discussed.

1 Introduction

Oscillating mechanical loads from piston-driven internal combustion (IC) engines are frequently the main source of vibration in transportation systems. These loads are commonly transmitted to the vehicle structure through the engine mounts and to the vehicle powertrain through the engine flywheel. Noise and vibration must be considered during vehicle design and development because excess levels typically decrease customer perception of quality and durability in civilian vehicles and degrade crew readiness and communication in military vehicles. The simplest approach to modeling engine vibration assumes the engine to be a linearly reacting, harmonically excited rigid body attached at known points to a rigid foundation through elastic isolation elements. However, a running IC engine is not a rigid body—it contains moving fluids, possesses finite flexural stiffnesses, and includes rotating and reciprocating components. Moreover, a running engine is not excited by a single frequency (harmonically). Combustion pressure forces and the constraining loads on moving components cause broadband and multiple-frequency excitations. In spite of the increasing market, regulatory, and military driven need to predict and control vibration and noise, clear engineering guidelines for the validity of the rigid engine approximation have not been identified. This paper explores the range of validity of this approximation for engine mount vibration loads produced by a heavy-duty Diesel engine through experimental modal analysis of both the quiescent and running engine. Although important for torsional vibration analysis of vehicle powertrains (Zhengchang and Anderson, 1988), torsional vibration loads produced by the engine's rotating components are not addressed here.

Most testing and analyses of engine noise and vibration are undertaken with the laudable objective of reducing or eliminating noise and vibration transmission from the engine to the vehicle structure (Priede, 1992; Swanson et al., 1994; Suh and Smith, 1997). Harmonic analyses and experiments are commonly conducted assuming that the engine block and its components form a rigid body in order to properly choose the engine mount locations and isolator properties. This rigid body approximation is typically used to optimize the engine mounting system at primary firing at engine idle. For passenger cars and aircraft, efforts to reduce vibration transmission from the engine have included (1) optimization of the engine mounts for vibration absorption or isolation at natural frequencies of the vehicle suspension system or structure (Johnson and Subhedar, 1979; Geck and Patton, 1984; Ford, 1985; Hata and Tanaka, 1987; Ashrafiuon and Nataraj, 1992; Snyman et al., 1995), (2) reduction of engine-to-structure vibration transmission to prevent in-cabin vibration and noise (Radcliffe et al., 1983; Matsuda et al., 1987; Müller et al., 1995), and (3) identification of engine inertial properties and isolator modulii (Butsuen et al., 1986; Okuma et al., 1989). Although most exploit the rigid body assumption, none of these previous studies have directly addressed the limitations of this assumption for a running engine. A recent review of engine mount vibration isolation strategies (Brach, 1997) highlights many of their inherent limitations.

While the basic engineering approaches exploited in previous passenger-car studies (Himelblau and Rubin, 1961; Smollen, 1966) form a useful basis for heavy-duty engine research, engine component inertias and engine mount locations typically differ significantly between passenger-car and heavy-duty engines so any extension of passenger-car engine results to heavy-duty engines is not trivial. Compared to their widespread prevalence and high economic importance, there is a relative dearth of published investigations relevant to engine vibration for heavy-duty trucks (Class VIII), off-highway construction equipment, and military vehicles. Schmitt and Leingang (1976) and Walker and Foscolos (1997) have addressed isolator design for heavy-duty engines based on harmonic excitation. In the precursor to the current study (Winton and Dowling, 1997), modal decomposition at two operating points showed that increasing engine speed and load decreased the accuracy of a description of the running-engine mount vibration forces in terms of quiescent-engine modes. The present study includes 200 Hz bandwidth measurements at thirteen engine operation points and separately identifies the effects of increasing engine load, engine speed, and measurement bandwidth. These findings should guide the development of computer models (i.e., Nor-

---

[1] née Winton.

Contributed by the Internal Combustion Engine Division. Manuscript received by the ASME Headquarters March 23, 1998. Associate Technical Editor: D. Assanis.

ling, 1978; Shiao et al., 1994; Bretl, 1995) of civilian and military vehicles and vehicle systems for prediction of passenger and crew comfort, as well as vehicle durability. Furthermore, unpublished accelerometer data (Reinhart, 1997) suggests significant flexible engine-structure response of a heavy-duty engine operating at high load conditions. In particular, the 4.5 order of that engine was shown to drive the first engine-block torsion mode well below this mode's natural frequency. In light of these findings, the purpose of this paper is to assess the applicability limits of the rigid engine assumption by quantifying nonrigid engine residual force vibration.

The results presented here are based on measured vibration forces from a heavy-duty in-line six-cylinder Diesel engine supported on standard elastomeric isolators and yield clear guidelines for the applicability of the rigid engine assumption. Measured quiescent-engine modes are taken to represent the rigid body description of the engine. Measured running-engine vibration forces are assumed to be typical for modern Class VIII truck engines. The residuals determined by this research provide a bound for the accuracy of the linearly reacting rigid body model assumption, since the experimentally determined quiescent-engine vibration modes are essentially guaranteed to be more accurate than modes predicted a priori from engine design parameters alone. The experimental modes include the following: all possible component configuration details; quiescent-engine load and frequency-accurate isolator modulii; corrections for nonmount engine attachments that carry shunt forces, such as air intake and exhaust lines; and corrections for nonsolid engine components, such as oil and coolant. All of these factors may lead to inaccuracy in a priori predicted vibration modes. In particular, elastomeric isolator elements commonly have nonlinear behavior (Harris and Stevenson, 1987).

A complete rigid body mathematical model of an engine and its mounting system is ultimately coupled and nonlinear when rotating crankshaft gyroscopic dynamics are included in the formulation. However, because the results in this paper are based purely on experimental force output of both the running and quiescent engine, a mathematical development of the input forces to the engine block is unnecessary. Here, the running-engine mount forces are decomposed into a linear combination of measured quiescent-engine modes, thus dividing the response of the running engine into nominally rigid and nonrigid engine motions. The unknown vibrational input from the engine mechanics, which includes gyroscopic effects, simply excites either of these motions.

The results of this paper span the operating envelope of the test engine and indicate the presence of nonrigid body behavior at all operating points throughout the 200 Hz bandwidth. The observed dependence on engine speed, engine load, and measurement bandwidth are discussed. The remainder of this paper is divided into three sections. The next section, Section II, details the experimental setup and data reduction techniques, which are illustrated with measurements taken at rated speed and full load for the test engine (2100 RPM, 1654 N-m). Section III presents the root-mean-square force and residual vibration results. The final section, Section IV, provides a summary of this study and the main conclusions drawn from it.

2 Experimental Technique

This experimental study is based on engine mount force measurements and modal analysis of a quiescent and operating Class VIII truck engine. A detailed description of the apparatus and data reduction technique has been given elsewhere (Winton and Dowling, 1997); therefore, the summary in the following few paragraphs is brief.

The experiments were conducted in an engine test cell on a four-stroke in-line six-cylinder heavy-duty Diesel engine. Engine parameters are given in Table 1. The load torque produced by the engine was absorbed by an electric dynamometer attached to the engine through a flexible driveshaft (Dana Corp., Spicer Series 1810, part no. 907912). The engine was supported by three diagnostic mounts (two rear mounts and one front mount) incorporating elastomeric isolation elements and three-component strain-gauge load cells. The rear mounts each employed one isolator (Lord Corp. CB 2204-2) and one three-component 22,240 N (5,000 lbf) vertical capacity load cell (AMTI MC5-3-5000). The front mount employed two isolators (Lord Corp. SSB33-1000-4) and a three-component 44,480 N (10,000 lbf) vertical capacity load cell (AMTI MC5-4-10000). Figure 1 shows a schematic of the setup along with the coordinate system used in the data reduction. Left and right sides of the engine are denoted, and the dark blocks indicate the three engine mounts. Direct measurement of forces alleviated the need to monitor or estimate isolator modulii during investigations. The nine load cell outputs (three per mount) were amplified with AMTI signal conditioners, low pass filtered below 1.05 kHz, and 16-bit digitized at 2.1 kHz for 5 seconds using Tektronix data acquisition hardware, LabVIEW software (from National Instruments), and a PC-type computer.

Experimental data was acquired in two stages. First, the warmed-up but quiescent engine was subjected to standard impact hammer modal analysis with output force measurements replacing the usual accelerometer or proximity probe measurements. In this procedure, the mounted engine is treated as a linear system subjected to a uniform broadband excitation (the hammer blow). The resulting measured response (the nine force components verses time) contains information about the natural vibrations (modes) of the system. The modal frequency, modal damping, and modal force signature for each mode were extracted from the nine force outputs by Fourier analyzing the data and subsequently using commercial curve-fitting software (STAR system software from Spectral Dynamics, Inc.). For the current study, the force measurements produce modal force signatures instead of the usual modal displacements or mode shapes. The impact-test modes, having the six lowest modal

Table 1 Test engine parameters

Engine Type:	In-line 6-cylinder; 4-stroke; DI Diesel
Displacement:	12.7 liters (774 cu. in.)
Rated Power:	350 kW (470 BHP) @ 2100 RPM
Rated Maximum Torque:	2100 N-m (1550 ft-lbf) @ 1200 RPM
Approximate Engine Idle:	600 RPM
Air System (test setup):	Turbocharged, water-to-air charge cooling
Nominal Weight (dry):	11,700 N (2630 lbf)
Nominal Weight (wet):	12,240 N (2752 lbf)
Weight as mounted in test setup (wet):	15,060 N (3386 lbf)
Length:	1.4 m (57 in)
Width:	0.86 m (34 in)
Height:	1.3 m (50 in)

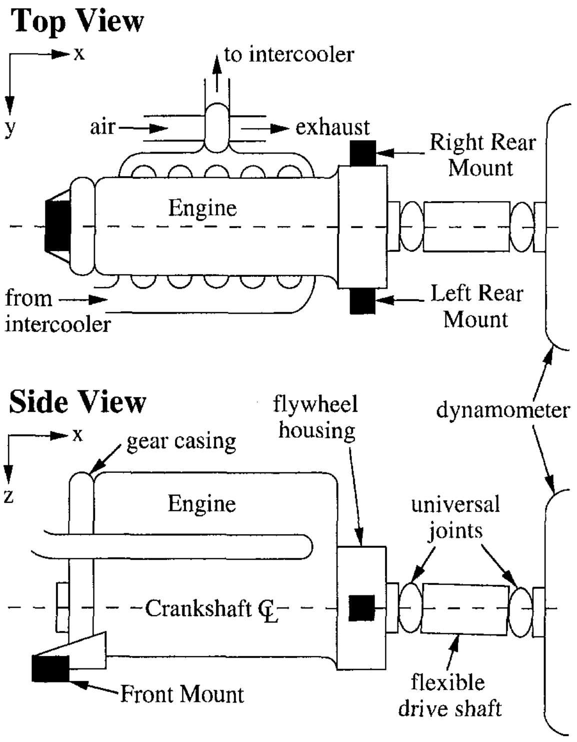

Fig. 1 Schematic of the experimental setup. Force components were measured with respect to the *x-y-z* axes shown. The dark blocks correspond to the engine mount locations.

frequencies, were assumed to represent the engine's rigid body natural vibration modes. The six modal frequencies lie between 5.6 and 26.3 Hz. The modal dampings are mainly produced by a combination of elastomeric and fluid mechanical effects. Each modal signature is a nine-element complex vector with one component for each force direction at each engine mount. A tabulation of measured modal parameters is provided in Table 2. The modal signature magnitudes are dimensionless and are normalized such that the square root of the sum of its nine components squared equals one. Sample plots illustrating the modal analysis procedure appear in Winton and Dowling (1997). Note that the relatively coarse resolution of the three-point measurement configuration, although appropriate for this study, may allow some flexible engine motions to masquerade as rigid body modes.

In the second stage of data acquisition, the engine was run at thirteen different operating points spanning its load and speed ranges. The data acquisition rate and duration was the same as in the quiescent-engine modal testing. A sample time history is shown in Fig. 2 for the vertical load on the right rear engine mount at rated speed and full load (2100 RPM and 1654 N-m). The magnitude reflects engine weight, mean torque load, and peak-to-peak oscillations of approximately 1000 N. This signal, along with the eight other signals, were then Fourier analyzed to determine the complex force amplitude in each direction at each engine mount in the frequency range from zero to 200 Hz. As a result of this specific engine setup, measured vibration levels above 200 Hz were not considered because they were contaminated with a vibration of the engine mounting structure. A sample force amplitude spectrum up to 200 Hz is shown in Fig. 3 for the vertical load on the right rear engine mount at rated speed and load. The first engine order at 2100 RPM is 35 Hz, and most of the measured force oscillations have frequencies below the fifth engine order (175 Hz). Ideally, an in-line six-cylinder four-stroke engine with even firing generates third, sixth, ninth, etc. order firing torques. The vibration resulting at orders other than these arise from the complex excitation of engine components or accessories and from the nonrigid behavior of the engine. For example, the large vibration contribution at first engine order may be due to rotational imbalance of the crankshaft system.

The measured spectral force outputs were then least-square projected onto the six quiescent-engine modes at each discrete frequency to determine the modal content of the running engine as a function of frequency. Figure 4 shows the modal content of the running engine at rated speed and full load. Again, the first engine order is 35 Hz; therefore, the bandwidth from zero to 200 Hz contains the first five engine orders. The modes are arranged in ascending order according to modal frequency (see Table 2). The height of the various peaks quantifies the relative

Table 2 Experimentally determined modal parameters

	Mode #1	Mode #2	Mode #3	Mode #4	Mode #5	Mode #6
Frequency (Hz)	5.68	9.76	12.84	13.53	20.98	26.25
Damping (% of Critical)	6.61	5.42	5.24	4.39	3.47	3.49
Left Rear:						
X- Magnitude	0.0843	0.2720	0.0647	0.2460	0.0763	0.0311
X- Phase (degrees)	-159	-15	-128	176	-6	170
Y- Magnitude	0.2350	0.0705	0.1700	0.4543	0.0120	0.0138
Y- Phase	11	-92	-5	174	140	-161
Z- Magnitude	0.5704	0.4746	0.4770	0.0542	0.1917	0.0444
Z- Phase	-168	-18	13	-14	177	-22
Right Rear:						
X- Magnitude	0.0691	0.2808	0.1791	0.0795	0.0743	0.0170
X- Phase	-25	-9	-166	-15	-179	-177
Y- Magnitude	0.2546	0.0839	0.1979	0.4915	0.0138	0.0147
Y- Phase	12	-79	-5	173	141	-151
Z- Magnitude	0.5669	0.5671	0.3999	0.4872	0.2189	0.0664
Z- Phase	3	-13	18	-5	-4	-24
Front:						
X- Magnitude	0.0566	0.5128	0.4029	0.2864	0.0204	0.0291
X- Phase	-105	-4	-157	-179	-67	89
Y- Magnitude	0.4651	0.0531	0.0535	0.1730	0.9479	0.0226
Y- Phase	9	28	139	-2	180	82
Z- Magnitude	0.0427	0.1499	0.5857	0.3647	0.0682	0.9953
Z- Phase	104	-167	21	-5	0	178

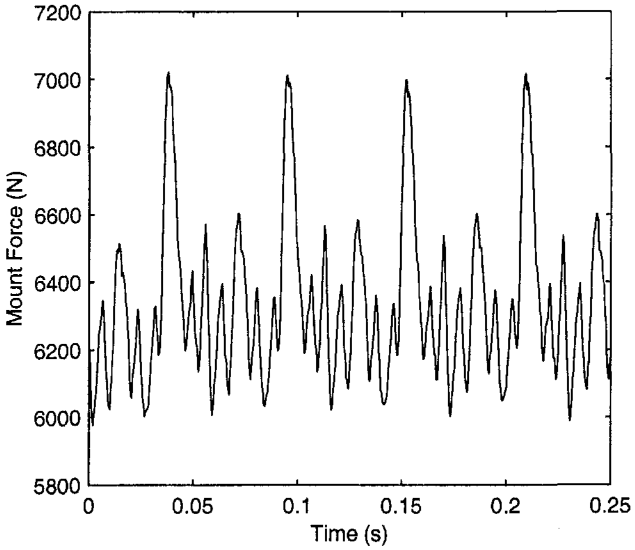

Fig. 2 Measured vertical force verses time on the right rear mount at 2100 RPM and full load 1654 N-m. The magnitude of the numbers on the vertical axis reflect the weight of the engine, the mean torque loading, and superimposed oscillations.

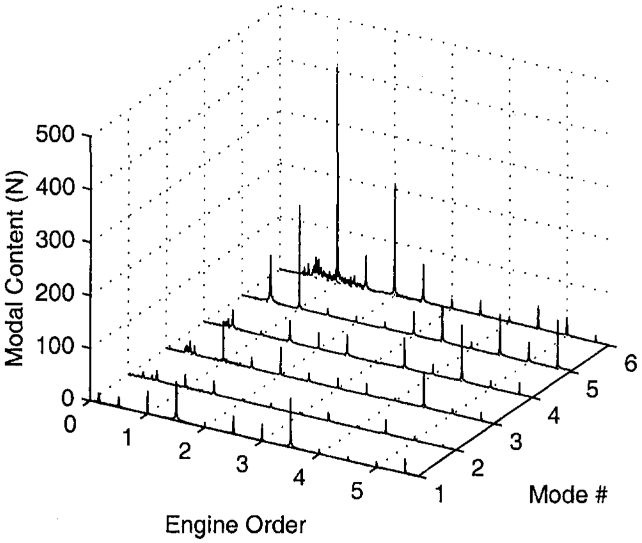

Fig. 4 Modal content of the test engine running at 2100 RPM and full load 1654 N-m. The engine order axis spans the frequency range from zero to 200 Hz. The modes are arranged in ascending order according to natural frequency. The height of the various peaks shows the relative contribution of that mode at that frequency to the overall state of engine vibration.

contribution of that mode at that frequency to the overall vibration state of the engine. Although not shown in Fig. 4, the modal content at all frequencies beyond approximately the eighth engine order (280 Hz) is nearly but not quite zero.

The accuracy of the rigid engine assumption was assessed at the thirteen load and speed engine operating points by examining the difference between the actual measured vibration amplitudes and the modal decomposition; the general assumption is that vibratory characteristics not accounted for by the six lowest quiescent-engine modes result from nonrigid engine behavior. An intermediate measure of the associated error with a modal decomposition of the engine was quantified by a root-mean-square discrete frequency residual, R_f, that depends on the frequency of interest, f:

$$R_f^2(f) = \frac{\sum_{i=1}^{3}\sum_{j=1}^{3} \|M_{ij}(f) - \sum_{k=1}^{6} a_k(f)\phi_{ijk}\|^2}{\sum_{i=1}^{3}\sum_{j=1}^{3} \|M_{ijk}(f)\|^2}, \qquad (1)$$

where R_f^2 is the mean-square discrete frequency residual, i is the direction number ($x = 1$, $y = 2$, $z = 3$), j is the mount number (left rear = 1, right rear = 2, front = 3), $M_{ij}(f)$ is the measured complex force amplitude in direction i on mount j, k is the mode number, a_k is the complex least-square linear weighting of quiescent-engine mode k at frequency f, and ϕ_{ijk} is the quiescent-engine modal force signature (the force amplitude in direction i on mount j re-

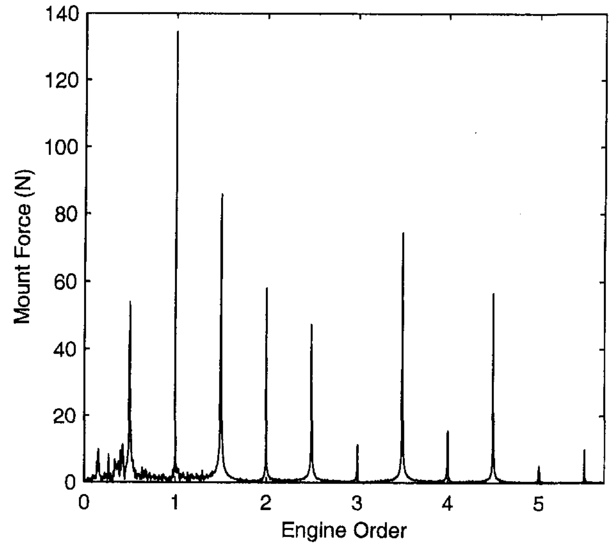

Fig. 3 Measured spectral amplitude verses frequency for the vertical force on the right rear mount at 2100 RPM and full load 1654 N-m. This is merely the discrete-time Fourier transform of the data in Fig. 2. First engine order is 35 Hz.

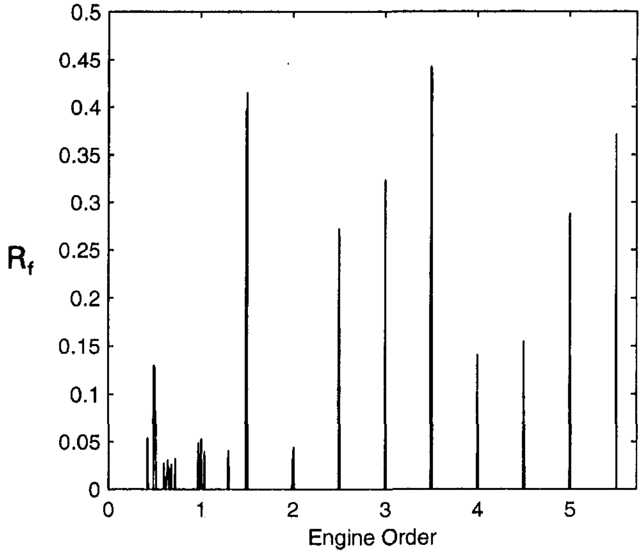

Fig. 5 Root-mean-square discrete frequency residual versus discrete frequency (evaluated as engine order). First engine order is 35 Hz. R_f is filtered to zero when the maximum modal content at that frequency is less than 20 N.

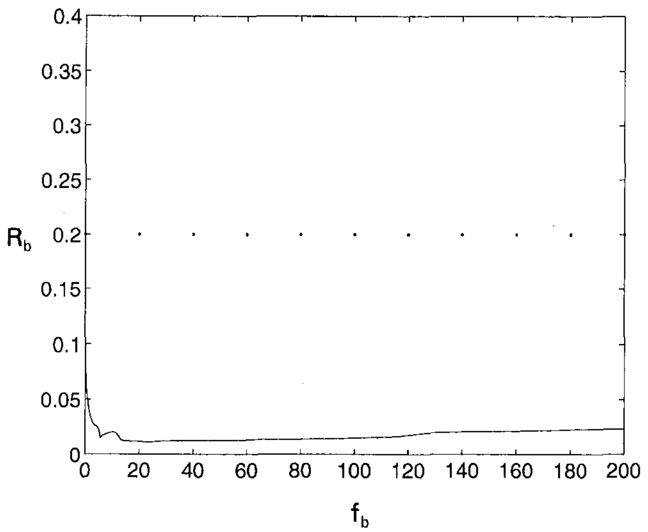

Fig. 6 Root-mean-square bandwidth residual verses bandwidth for the impact test data. The minimum of the curve occurs at the bandwidth that contains the six lowest quiescent engine natural frequencies. The small defect at 10 Hz is believed to be caused by a flexible driveshaft torsional oscillation.

sulting from unit excitation of quiescent-engine mode k). The value of R_f represents the fraction of vibration force at a specific frequency unaccounted for by the six lowest quiescent-engine modes. For an ideal linearly reacting rigid engine, R_f would be zero. Figure 5 shows the root-mean-square (rms) discrete frequency residual at rated speed and full load and has been filtered to zero when the maximum modal content at that frequency is less than 20 N. While this discrete frequency residual is useful in evaluating the vibration of the engine at a specific frequency, it indicates large residual values at frequencies where the vibration level does not significantly contribute to the overall vibration of the engine. Therefore, a better representation for the residual of the rigid engine approximation is evaluated over a range of frequencies.

The measured modal decomposition difference was then quantified by a root-mean-square bandwidth residual, R_b, that depends on the analysis bandwidth, f_b:

$$R_b^2(f_b) = \frac{\displaystyle\int_0^{f_b} \{\sum_{i=1}^{3}\sum_{j=1}^{3} \|M_{ij}(f) - \sum_{k=1}^{6} a_k(f)\phi_{ijk}\|^2\}\,df}{\displaystyle\int_0^{f_b} \{\sum_{i=1}^{3}\sum_{j=1}^{3} \|M_{ijk}(f)\|^2\}\,df}, \quad (2)$$

where R_b^2 is now the mean-square bandwidth residual, and f_b is the integration bandwidth. The value of R_b represents the fraction of overall vibration force within bandwidth f_b, which is unaccounted for by the six lowest quiescent-engine modes. For an ideal linearly reacting rigid engine, R_b would be zero. When $R_b(f_b) \ll 1$, a rigid body description is presumed accurate in the bandwidth f_b. A value of $R_b = 1$ implies that the six lowest modes are irrelevant to the measured state of engine vibration. As shown in the next section, R_b tends to increase with increasing engine speed, engine load, and measurement bandwidth beyond the frequency of the first engine order. A threshold of $R_b = 0.2$ was chosen to discriminate between acceptable ($R_b < 0.2$) and unacceptable ($R_b > 0.2$) regimes for the linearly reacting rigid engine assumption. The choice of $R_b = 0.2$ was made based on the accuracy level typically expected from a priori engineering models of mechanical systems. Naturally, more or less stringent thresholds can be applied.

For all tests, the engine was either in operation or in a ready-to-run condition. This meant that shunt forces could be transmitted through the additional engine attachments necessary for intake air, exhaust, load torque, coolant, etc. While these extra connections were all made through appropriate flexible couplings to minimize their influence, it was recognized that such engine attachments could mildly influence the experimental modal frequencies, modal dampings, modal force signatures, and effective vibration excitation source since they amount to additional weak resilient engine mounts. However, it is very doubtful that the extra attachments could mask the primary results given their relatively low stiffness compared to the three load-bearing diagnostic engine mounts. If an external engine attachment was brought into vibrational resonance, its main effect on the engine would be to force one or more rigid or flexural engine modes at the external attachment's resonant frequency. Compared to the more flexible intake air, coolant, and charge cooler attachments, the exhaust attachment is one accessory that visually appears to resonate during engine operation around 700 RPM. All remaining attachments were observed or believed to resonate below the idle condition (600 RPM). Since R_b is sensitive only to mismatches between measured vibrations and their decomposition into the six lowest quiescent-engine modes, even if the extra engine attachments resonate after the engine is struck or while it is running, the attachments merely provide a small alteration to the effective internal or external engine excitation source.

To assess the validity of the experimental modes, R_b was evaluated for the impact-hammer data for $0 < f_b < 200$ Hz. The results are displayed in Fig. 6. The minimum in this curve, $R_b \approx 0.012$, occurs at about 30 Hz, a bandwidth that includes the six lowest quiescent-engine natural frequencies. The

Table 3 Root-mean-square engine mount vibration forces

Speed (RPM)	Load (N-m) ±5	Left Rear Mount (N) X	Y	Z	Right Rear Mount (N) X	Y	Z	Front Mount (N) X	Y	Z
750	27	39.5	174	149	99.6	182	72.2	103	140	243
750	813	42.8	144	98.8	70.5	151	146	45.4	234	157
1200	27	60.4	53.7	109	43.2	55.1	105	37.5	321	360
1200	813	57.8	50.8	83.5	54.9	53.5	126	34.6	304	393
1200	1654	91.4	72.6	97.9	89.0	73.6	169	72.1	314	588
1200	2061	95.3	84.0	123	71.5	81.9	213	79.7	343	455
1650	27	80.6	53.4	56.0	80.8	54.8	112	50.8	207	891
1650	813	75.4	92.0	63.4	81.7	101	141	53.0	230	810
1650	1654	136	99.5	119	138	110	214	132	318	805
1650	1993	163	138	117	152	140	272	95.6	337	811
2100	27	132	54.7	68.9	129	49.1	108	62.0	291	340
2100	813	303	97.2	72.3	234	73.1	152	89.3	417	429
2100	1654	284	114	108	277	111	240	151	611	470

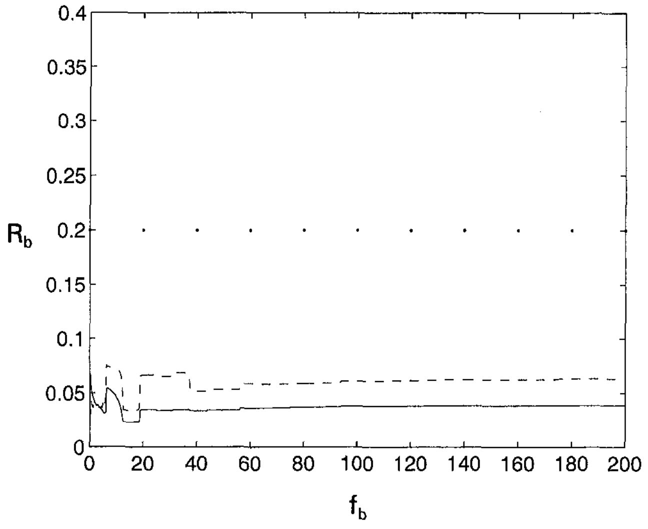

Fig. 7 Root-mean-square bandwidth residual verses bandwidth at 750 RPM: engine load = 27 N-m (——); engine load = 813 N-m (----). The rigid engine assumption is acceptable when $R_b < 0.2$; the dots at $R_b = 0.2$ denote this threshold. The full rms bandwidth residual changes by only about 50 percent although the load changed by a factor of 30.

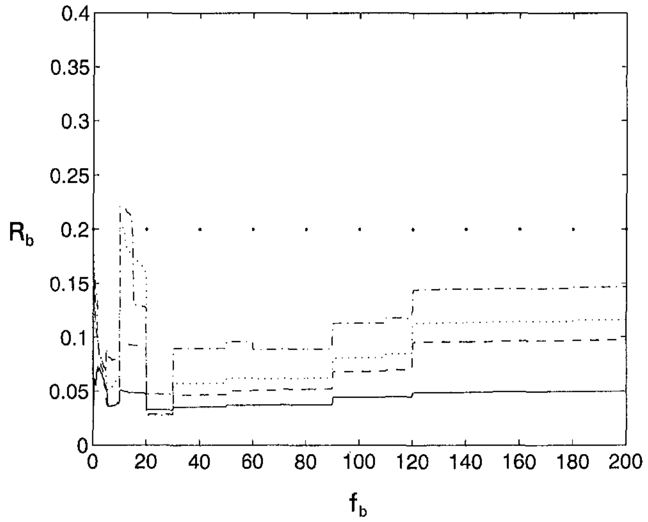

Fig. 8 Root-mean-square bandwidth residual verses bandwidth at 1200 RPM: engine load = 27 N-m (——); engine load = 813 N-m (----); engine load = 1654 N-m (· · ·); engine load = 2061 N-m (– · – · – ·). The rigid engine assumption is acceptable when $R_b < 0.2$; the dots at $R_b = 0.2$ denote this threshold. The full rms bandwidth residual changes by only a factor of three although the load changes by a factor of 76.

smallness of this result represents the noise level in these experiments and suggests that the accuracy and internal consistency of the six lowest measured modes (assumed herein to represent the engine rigid body vibration modes) is good. However, the small peak in R_b seen near $f_b = 10$ Hz in Fig. 6, which probably arises from a flexible driveshaft torsional vibration, produces some minor deleterious effects when excited by the running engine. The driveshaft natural frequency was estimated to be between 5 and 9 Hz, and a resonance is visually verified during engine shutdown near 400 RPM. For bandwidths greater than 30 Hz, the rms bandwidth residual increases until 200 Hz where it becomes 0.025. The increase in R_b above 30 Hz is expected because the experimental modal description was truncated after the six lowest modes, and any additional excited vibration modes of the engine system increase the residual.

3 Experimental Results

Engine vibration measurements were made at thirteen operating points. The data includes four speeds: just above idle (low speed, 750 RPM), peak-torque speed (mid-speed, 1200 RPM), moderate high speed (1650 RPM), and rated speed (2100 RPM). In addition, five load torques were investigated: 27 N-m (20 ft-lbf), 813 N-m (600 ft-lbf), 1654 N-m (1220 ft-lbf), 1993 N-m (1470 ft-lbf), and 2061 N-m (1520 ft-lbf). Only the two lowest loads could be sustained at every engine speed. A quantitative summary of the measured root-mean-square engine mount forces is contained in Table 3. A general trend of increasing rms loads with increasing engine load was observed. Although the engine internal dynamics remain kinematically similar, the combustion pressure excitation differs as does the measured vibratory response when engine load and speed are changed; therefore, the general trend mentioned above is not universally valid for each force component on every mount.

Results for the rms bandwidth residual vibration are shown in Figs. 7, 8, 9, and 10 which display the low speed, mid-speed, moderate-high and rated speed results, respectively. All of these plots share a few common elements. First of all, in spite of their appearance, the data has not been lumped into discrete frequency bins. R_b is calculated every 0.2 Hz from 0 to 200 Hz bandwidth. The staircase character of the various curves occurs because the dominant engine excitation is at integer and half-integer multiples of the first engine order. Because there is little or no excitation between these engine harmonics, $R_b(f_b)$ is essentially constant between them. Second, the value of R_b near $f_b = 0$ is relatively large compared to its value near $f_b \approx$ 40 to 50 Hz. This feature of the plots is not significant and is primarily due to experimental uncertainty. When f_b is small and does not include several engine excitation frequencies, the denominator in (2) is small compared to its value when f_b does include significant engine excitation. Therefore, at small f_b, any mismatch between the measurements and the modal decomposition is amplified relative to the same size mismatch when f_b is larger. Third, the jagged minimum in R_b obtained just above first engine order (10 Hz $< f_b <$ 40 Hz) shows that the rigid body modes of the engine provide a reasonable description of engine vibration near their natural (modal) frequencies. Fourth, R_b typically increases at the 0.5 and 1.5 engine orders, indicating

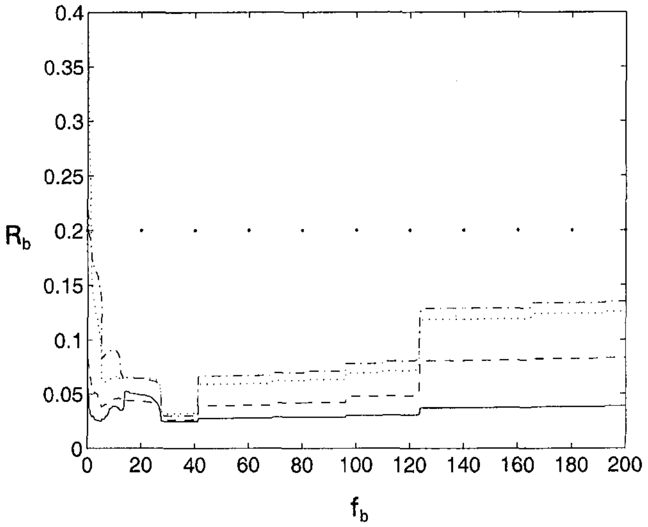

Fig. 9 Root-mean-square bandwidth residual verses bandwidth at 1650 RPM: engine load = 27 N-m (——); engine load = 813 N-m (----); engine load = 1654 N-m (· · ·); engine load = 1993 N-m (– · – · – ·). The rigid engine assumption is acceptable when $R_b < 0.2$; the dots at $R_b = 0.2$ denote this threshold. The full rms bandwidth residual changes by only a factor of 3.5 although the load changes by a factor of 74.

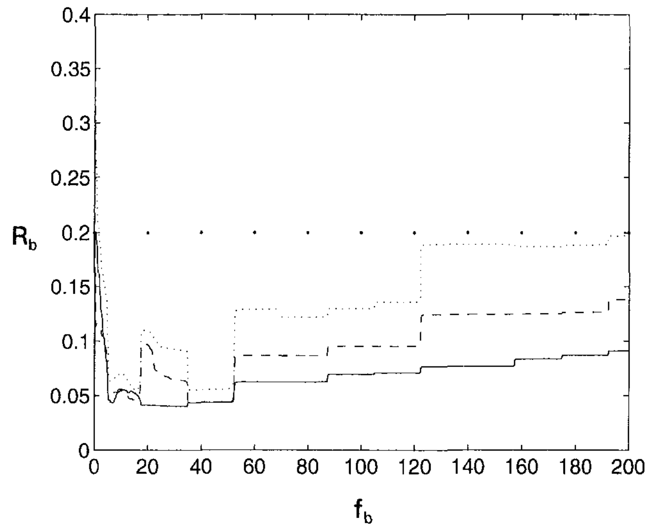

Fig. 10 Root-mean-square bandwidth residual verses bandwidth at 2100 RPM: engine load = 27 N-m (——); engine load = 813 N-m (----); engine load = 1654 N-m (· · ·). The rigid engine assumption is acceptable when $R_b < 0.2$; the dots at $R_b = 0.2$ denote this threshold. The full rms bandwidth residual changes by only a factor of 2.2 although the load changes by a factor of 61.

the presence of nonrigid body behavior at these engine harmonics. However, the relative vibration at these harmonics are typically smaller than the overall vibration level of the running engine. Fifth, all the curves show an increase in R_b near 90 Hz and 120 Hz which indicates significant nonrigid body behavior at these higher frequencies. Sixth, R_b reaches a constant value beyond $f_b \approx 120$ Hz on each plot. This is largely due to the reduction of running engine excitation in this regime (as evidenced by Fig. 4), so both the numerator and denominator of (2) remain constant as f_b increases beyond 120 Hz. And finally, the dotted horizontal line on these plots displays the $R_b = 0.2$ threshold.

Figures 7 through 10 show trends in the rms bandwidth residual vibration as engine speed and load are varied. In particular, R_b is found to depend strongly on engine speed. Consider the low load R_b curves in Figs. 7 through 10 (solid lines). In Fig. 7, the low load R_b curve is similar to the impact-excitation results in Fig. 6. Figures 8, 9, and 10 show the low load rms bandwidth residual rising with every increase in speed. This progression, covering a ratio of 2.8 between the lowest and highest speeds (750 and 2100 RPM), produces a change in the full bandwidth residual from 0.04 to 0.09. Similarly, for the moderate load case, the full bandwidth residual increases from 0.06 to 0.14.

The measured load dependence of R_b is similar but much less dramatic. Consider the results in Figs. 8, 9, and 10. In all figures, the full bandwidth residual increases at most by a factor of three as the load is varied from 27 to 1654 N-m, a dynamic range of more than 60. For example, in Fig. 7 at 750 RPM, the full rms bandwidth residual changes by only about 50 percent, although the load changed by a factor of 30. In Fig. 8 at 1200 RPM, the full rms bandwidth residual changes by only a factor of three although the load changes by a factor of 76. In Fig. 9 at 1650 RPM, the full rms bandwidth residual changes by only a factor of 3.5 although the load changes by a factor of 74. In Fig. 10 at 2100 RPM, the full rms bandwidth residual changes by only a factor of 2.2 although the load changes by a factor of 61. Hence, the accuracy of a rigid body modal decomposition of the running engine is much less sensitive to increases in engine load compared to increases in engine speed. In addition, an anomalously high value of R_b is found near $f_b = 10$ Hz in Fig. 8. This peak's location matches the minor defect location noted near $f_b = 10$ Hz in Fig. 6. At 1200 RPM, the half engine order, a typical excitation frequency for a four-stroke engine, is 10 Hz. Therefore, the anomalous peak in Fig. 8 apparently results from the running engine exciting an undocumented nonrigid engine degree of freedom at this frequency. However, the anomalously high R_b at 10 Hz does not persist past the first engine order at 20 Hz and does not make an important contribution to the full bandwidth value of R_b at 200 Hz.

Using a threshold value of R_b at 0.20 shows that the rigid body approximation is acceptable throughout the test engine's entire operating range in a bandwidth from zero to 200 Hz. This result is important because it validates the use of a linearly reacting rigid engine approximation up to a bandwidth of 200 Hz when considering the overall force vibration of the engine.

4 Conclusions

This experimental study was undertaken to determine the applicability limits of the linearly reacting rigid engine assumption for heavy-duty Diesel engine vibration as a function of engine speed, engine load, and measurement bandwidth. The linear rigid body character of the test engine, mounted in the standard three-point configuration on standard vibration isolators, was assumed to be captured by the six lowest-frequency natural vibration modes determined from an experimental modal analysis of the test engine in a ready-to-run state. Differences between measured running-engine vibration forces and the projection of these forces onto the quiescent engine modal force signatures have been used to assess the accuracy of the rigid engine assumption during engine operation. A threshold value corresponding to approximately 20 percent error in the rigid engine assumption was used to substantiate this assumption's applicability to overall engine mount force vibration simulation.

The main results contained in Figs. 7 through 10 lead to the following two main conclusions:

1 The linearly reacting rigid engine assumption is acceptable for analysis bandwidths up to approximately 200 Hz, independent of the engine speed and the engine load. Although nonlinear and nonrigid body behavior always exists within this analysis bandwidth, its overall contribution does not invalidate the linearly reacting rigid body assumption's applicability to the running engine up to a 200 Hz analysis bandwidth.
2 Compared to engine speed, the engine load dependence of the accuracy is comparatively mild. This result suggests the persistence of linear vibration behavior through most of the engine's operating envelope.

The observed dependence of the rigid body assumption's accuracy on engine speed is believed to result from the time-varying nature of the engine system resulting from the rotation and reciprocation of internal engine components, as well as from the motion of nonsolid parts such as oil and coolant. The accuracy's dependence on engine load and analysis bandwidth likely results from the flexibility of the engine block. The relatively higher engine speed sensitivity of the rigid engine assumption's accuracy suggests that the first enhancement of a linearly reacting rigid engine vibration model would be inclusion of time-varying engine characteristics to account for moving internal component dynamics. Compared to the engine speed sensitivity, the observed mild load dependence on the accuracy suggests that a second enhancement should be the inclusion of at least one engine block flexibility mode.

It should be noted that for heavy-duty engines, like the test engine of this study, the first flexural mode of the engine block alone would lie above 200 Hz (Reinhart, 1997). With the incorporation of a typical transmission to the engine system, this estimated flexural mode natural frequency would decrease, and the resulting engine force vibrations could have a larger effect on the accuracy assessment within the 200 Hz measurement bandwidth used in this analysis.

While the rms bandwidth residual defined in this paper is not directly applicable as an iterative design tool, it is appropriate for understanding the applicability limits of the linearly reacting rigid engine approximation typically used in engine mount force simulations. Naturally, some care must be exercised when extending the conclusions of this paper to V-type or passenger-car engines.

Acknowledgments

This research was supported by the United States Army Tank-Automotive Research Development and Engineering Center (TARDEC) through the Automotive Research Center (ARC) under contract no. DAAE07-94-C-R094 with The University of Michigan. The authors wish to recognize the contributions of Steve Hoffman and Kevin Morrison who were largely responsible for the construction and maintenance of the experimental setup.

References

Ashrafiuon, H., and Nataraj, C., 1992, "Dynamic-Analysis of Engine-Mount Systems," *Journal of Vibration and Acoustics,* Vol. 114, pp. 79–83.

Brach, R. M., 1997, "Automotive Powerplant Isolation Strategies," SAE Paper No. 971942.

Bretl, J., 1995, "Advancements in Computer Simulation Methods for Vehicle Noise and Vibration," SAE Paper No. 951255.

Butsuen, T., Okuma, M., and Nagamatsu, A., 1986, "Application of Direct System Identification Method for Engine Rigid Body Mount System," SAE Paper No. 860551.

Ford, D. M., 1985, "An Analysis and Application of a Decoupled Engine Mount System for Idle Isolation," SAE Paper No. 850976.

Hata, H., and Tanaka, H., 1987, "Experimental Method to Drive Optimum Engine Mount System for Idle Shake," SAE Paper No. 870961.

Geck, P. E., and Patton, R. D., 1984, "Front Wheel Drive Engine Mount Optimization," SAE Paper No. 840736.

Harris, J., and Stevenson, A., 1987, "On the Role of Non-Linearity in the Dynamic Behavior of Rubber Components," *International Journal of Vehicle Design,* Vol. 8, pp. 553–577.

Himelblau, H., and Rubin, S., 1961, "Vibration of a Resiliently Supported Rigid Body," chap. 3 in *Shock and Vibration Handbook,* 2nd Ed., C. Crede and C. Harris, eds., McGraw-Hill Book Co., New York.

Johnson, S. R., and Subhedar, J. W., 1979, "Computer Optimization of Engine Mounting Systems," SAE Paper No. 790974.

Matsuda, A., Yasutaka, H., Junzo, H., 1987, "Vibration Analysis of a Diesel Engine at Cranking and Idling Modes and Its Mounting System," SAE Paper No. 870964.

Müller, M., Siebler, T. W., and Gartner, H., 1995, "Simulation of Vibrating Vehicle Structures as Part of the Design Process of Engine Mount Systems and Vibration Absorbers," SAE Paper No. 952211.

Norling, R. L., 1978, "Continuous Time Simulation of Forces and Motion Within an Automotive Engine," SAE Paper No. 780665.

Okuma, M., Ohara, T., and Nagamatsu, A., 1989, "Application of a New Experimental Identification Method to Engine Rigid Body Mount System," SAE Paper No. 891139.

Priede, T. 1992, "Noise and Vibration Control of the Internal Combustion Reciprocating Engine," chap. 19 in *Noise and Vibration Control Engineering,* L. L. Beranek, and I. L. Vér, eds., John Wiley & Sons, New York.

Radcliffe, C. J., Picklemann, M. N., Hine, D. S., and Spiekermann, C. E., 1983, "Simulation of Engine Idle Shake Vibration," SAE Paper No. 830259.

Reinhart, T. E., 1997, private communication, Cummins Engine Company, Inc., Columbus, IN.

Schmitt, R. V., and Leingang, C. J., 1976, "Design of Elastomeric Vibration Isolation Mounting Systems for Internal Combustion Engines," SAE Paper No. 760431.

Shiao, Y.-J., Pan, C.-H., and Moskwa, J. J., 1994, "Advanced Dynamic Spark Ignition Engine Modeling for Diagnostics and Control," *International Journal of Vehicle Design,* Vol. 15, pp. 578–596.

Suh, C.-H., and Smith, C. G., 1997, "Dynamic Simulation of Engine-Mount Systems," SAE Paper No. 971940.

Smollen, L. E., 1966, "Generalized Matrix Method for the Design and Analysis of Vibration-Isolation Systems," *Journal of the Acoustical Society of America,* Vol. 40, pp. 195–204.

Snyman, J. A., Heyns, P. S., and Vermeulen, P. J., 1995, "Vibration Isolation of a Mounted Engine Through Optimization," *Mechanism & Machine Theory,* Vol. 30, pp. 109–118.

Swanson, D. A., Miller, L. R., and Norris, M. A., 1994, "Multidimensional Mount Effectiveness for Vibration Isolation," *AIAA Journal of Aircraft,* Vol. 31, pp. 188–196.

Walker, S. R., and Foscolos, J. G., Jr., 1997, "Optimization of Vibration Isolators for Marine Diesel Engine Applications," SAE Paper No. 971937.

Winton (Hoffman), D. M. and Dowling, D. R., 1997, "Modal Content of Heavy-Duty Diesel Engine Block Vibration," SAE Paper No. 971948.

Zhengchang, X., and Anderson, R. J., 1988, "A New Method for Estimating Amplitudes of Torsional Vibration for Engine Crankshafts," *International Journal of Vehicle Design,* Vol. 9, pp. 252–261.

On the Concept of Separate Aftercooling for Locomotive Diesel Engines

T. Uzkan

M. A. Lenz

General Motors Corporation,
Electro-Motive Division,
P.O. Box 10381,
LaGrange, IL 60525

This paper describes a patented cooling system concept for a turbocharged diesel engine. In particular, it defines a cooling system having the capability of transferring some of the cooling capacity of engine jacket and engine oil cooling to cool the cylinder inlet air when more than the cooling capacity built into the system through the size of the radiators and fans is needed. This increased aftercooling will improve the engine performance and reduce emission levels. The cooling capacity of a locomotive is essentially determined by the radiator and fan size, among other factors, and is designed to cool the engine within acceptable metal temperatures at a specified maximum ambient temperature and at the maximum engine power. On the other hand, at lower ambient temperatures or engine power levels, the cooling needs of the engine will be less than this maximum cooling capacity of the cooling system. There remains some excess capacity. This paper describes the concept called the ''Separate Aftercooling System'' that uses some of this excess cooling capacity to cool the engine inlet air at the aftercoolers. It shows the feasibility of such a system, describes the order of magnitude of benefits that can be expected from such a system, and outlines the implementation of this concept to EMD built Locomotives.

Introduction

Diesel-electric railway locomotives develop their tractive effort (driving force) through a mechanical-to-electrical-to-mechanical transmission system. The power to propel the locomotive is developed first by the high powered diesel engine. The diesel engine drives the generator, that converts the mechanical energy to electrical energy. The electrical energy is then transferred to traction motors, which convert the electrical energy back to mechanical energy in order to drive axles connected to the drive wheels. The friction between the drive wheels of the locomotive and the rail provides the traction for causing the movement of the locomotive and the railway cars.

Economic and safety considerations place requirements on the durability, reliability and the operation life of the engine and its components. In turn, these requirements impose restrictions on the maximum operating temperature of the engine components in order to sustain the operating life. If the engine components are exposed to temperatures higher than the set maximum operating temperature during the operation of the engine, then it is necessary to reduce the temperature of components to an acceptable level by providing engine cooling. Therefore, all diesel-electric locomotives incorporate some procedure for cooling the engine.

In a locomotive engine, the cooling of the engine components is usually provided by the water cooling system, although some cooling is also provided by the lubricating oil. Figure 1 shows a representative engine, the EMD 16-710 Engine, used extensively in present day locomotives. Figure 2 shows a block diagram of the basic components of a typical engine water cooling system of many types of locomotives. A typical modern locomotive, the SD70MAC locomotive is shown in Fig. 3. The general characteristics of the 16-710 engine and the SD70MAC locomotives are summarized in Table 1 [1, 2]. The heat generated by the engine is transferred to the water circulating through the water loop of the cooling system. The water pump provides the water circulation and transfers the heated water from the engine, through the water loop to the radiators. The system has fans (either hot-side or cold-side fans) that drive ambient air through the radiator to transfer the heat of the water in the water loop to the surrounding air. The cooled water is then circulated through the other engine system components, such as an oil cooler and then back to the engine. A water tank is usually built into the system as the make-up water supply, to fill components, and for other purposes. The specific operation, as well as the different variations of the system components in the above described water cooling system, is well known.

For a given engine cylinder size, the power of the engine can be increased by burning more fuel in the cylinder. To burn this increased amount of fuel, more air needs to be supplied to the cylinder. In modern internal combustion engines, particularly in all modern locomotive diesel engines, this air is supplied by the use of a turbocharger that compresses the ambient air to a higher pressure and increases its density. This compression also increases the temperature of the air, which is not desirable as it reduces the volumetric efficiency (an air breathing characteristic of the engine). The supply of cool air into the engine cylinders is also important to decrease the engine emission levels. Therefore, an aftercooler is used to transfer heat from the air coming out of the turbocharger, to the water in the cooling loop. This air cooling at the aftercooler improves the engine efficiency and reduces the engine emissions and is a well known trend [3].

Sizing of the cooling system components is influenced by various parameters such as the characteristics of the components and operational considerations. For any particular engine, there is a maximum design limit of the engine cooling water temperature in order to maintain the temperatures of the components of the engine below a threshold limit for reliable and durable operation. Usually the engine manufacturer sets and recommends this maximum engine water temperature limit as part of its design process. For a set maximum water temperature and maximum ambient air temperature in which the locomotive is expected to operate, the size of the components, such as radiators, fans, and circulation pumps, can be chosen. For the chosen components, there is a maximum amount of heat that the cooling

---

Contributed by the Internal Combustion Engine Division and presented at the Fall Technical Conference of the ASME Internal Combustion Engine Division, Madison, WI, September 28–October 1, 1997. Associate Technical Editor: D. Assanis.

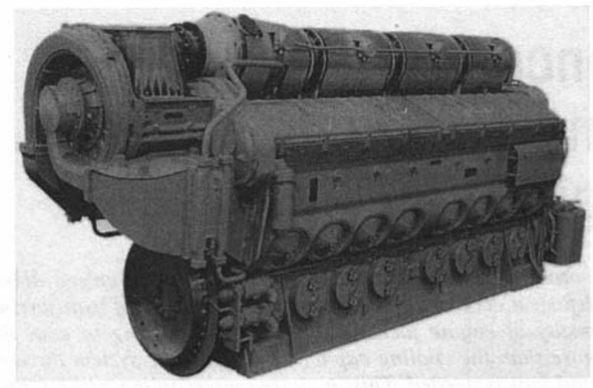

Fig. 1 EMD 16-710 engine

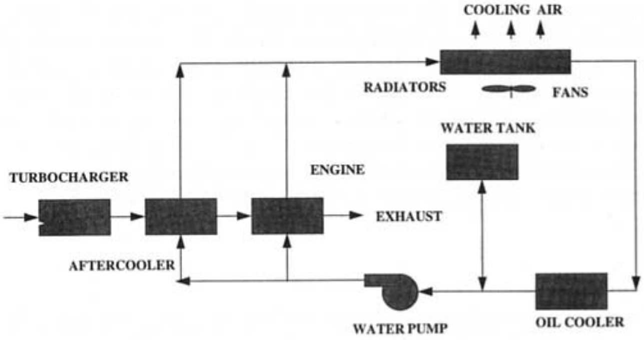

Fig. 2 Turbocharged, aftercooled engine cooling system

system can transfer to the ambient air at the maximum ambient air temperature. This is usually called as the ''cooling capacity'' of the system. At the maximum engine power limit of operation, the heat given to the circulating water at the engine, oil cooler and at the aftercooler should not exceed the cooling capacity at the radiators and fans. Otherwise, the temperatures of the engine components would continue to increase and exceed the maximum allowable temperature limit.

Among the several parameters that affect the cooling capacity of the engine cooling system is the temperature difference between the water and the air entering the radiator. The larger this difference, the higher the amount of heat transfer from the coolant water to the ambient air. Therefore, when a system is designed for a given maximum ambient temperature and maximum engine power level, the cooling capacity at the radiators would be more than necessary to cool the engine within the desired limits at a lower ambient temperature. The maximum cooling capacity designed into the engine cooling system for maximum engine load at maximum ambient air temperature is more than enough to cool the engine at lower loads and ambient temperatures.

There are several requirements that an engine cooling system is expected to conform to. Among others, the system is first to maintain the engine water temperatures below the specified design limit. Present cooling systems are all sized to satisfy this basic requirement. In addition, what is needed is the capability of increased aftercooling of the engine air, to improve the engine performance and emissions. Therefore, a cooling system is envisioned such that when excess cooling capacity is available, and it is directed to cool the engine inlet air at the aftercooler. When the excess capacity is needed again, all of the cooling capacity could be directed to engine cooling again. This concept is called the separate aftercooling system (SAC System). Such a system is developed, patented [4], implemented, and operated.

Figure 4 shows the schematic arrangement of the concept. There are two different loops in the SAC system (one for the main engine and the other for the aftercooler) working independently at low ambient temperatures, where a large portion of the systems total cooling capacity is allocated to the aftercooling. Each system has its own radiators and pumps. At higher ambient temperatures and loads, the cooling capacity allocated to the engine loop is not enough to bring the engine components' temperatures to within desired limits. When that condition is reached, as determined by the use of water temperature sensors, a linking valve is opened by the valve controller under the command of a control computer. Some of the hot water on the engine loop is transferred to the colder aftercooler loop, and the same amount of cold water is transferred to the hotter engine loop. In this way, some of the heat load of the engine loop is transferred to the aftercooler loop to be dissipated to the air at the aftercooler radiator. This way, a portion of the total cooling capacity installed in the aftercooler loop is allocated to the engine loop at hot ambient conditions, and to the aftercooler loop at cold ambient conditions. This controlled transfer of the cooling capacity to one loop or the other is the main and essential characteristic of the SAC system.

There are other engine cooling systems described in the literature for turbocharged engines. In Stang et al. [5] a coolant system is described with an aftercooler and a turbocharger with a loop having a temperature sensitive control thermostat. Melchinor [6] describes a supercharged engine having a cooling system with a radiator for cooling the coolant circulating in the system and another radiator for the supercharger. Musick et al. [7] describes a cooling system which has the capability of self adjusting the cooling of an internal combustion engine. Roettgen et al. [8] described a cooling system for a turbocharged diesel

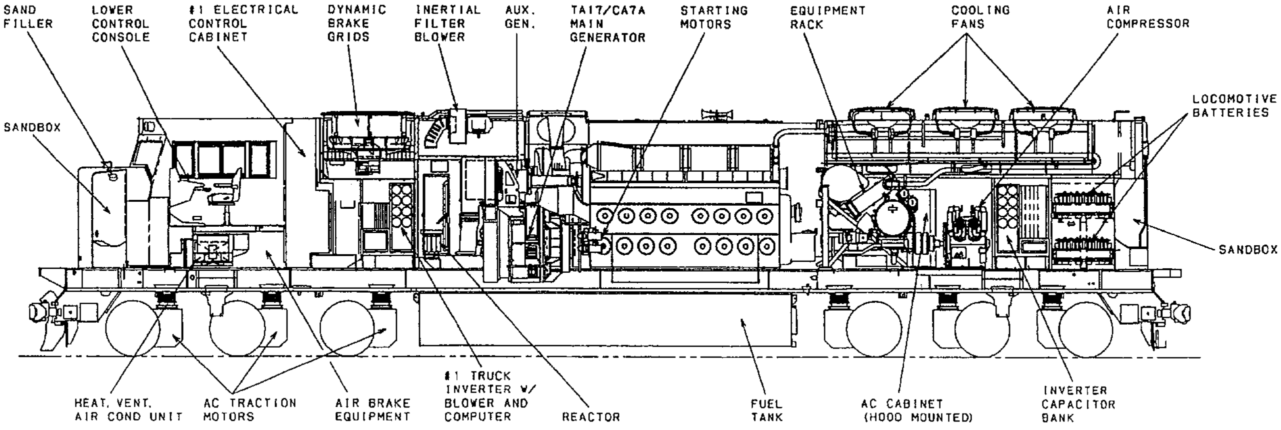

Fig. 3 Equipment location in an SD70MAC Locomotive

Table 1 General information about SD70MAC Locomotive and 710G3B-EC Engine

SD70MAC Locomotive:	
Nominal Locomotive Power:	4000 HP
Total Loaded Weight:	415,000 lbs
Dimensions:	H = 15′ 7.75″, W = 10′7.81″, L = 74′
Speeds:	
Min Continuous @ Full Power:	9.3 mph
Max Continuous:	70 mph
Main Engine:	710G3B-EC
Main Generator:	TA17-6/CA7A
Traction Alternator:	TA17-6, Max Volt 2600, 1500 Amp
Companion Alternator:	CA7A, 230 V AC
Traction Motors:	6, 3 Phase, 500 KW, 2027 VAC, 3220 rpm
710G3B-EC Engine:	
Number of Cylinders:	16
Engine Type:	Two Stroke, Turbocharged
Cylinder Arrangement:	45 Deg V Type
Compression ratio:	16:1
Displacement per Cylinder:	710 cu. inch
Cylinder Bore & Stroke:	9 1/16″, 11″
Full and Idle Speeds:	904 rpm and 200–300 rpm

engine with an aftercooler and an oil cooler. Crofts Sr. [9] describes an engine cooling system with an engine, a radiator, and an aftercooler. The temperature of the coolant passing through the aftercooler is regulated automatically. In reference [10], Nagle et al. describe a split temperature regulating system, where a portion of the engine cooling water circulated through a second radiator for enhanced aftercooling. The division is controlled by using control valves. McTaggard [11] is describing a turbocharged and aftercooled engine coolant system radiator details, for the split cooling system of [10], where there are two sequential radiators. Some of the coolant cooled in the first radiator is passed through a second radiator, to cool it more for the aftercooler loop. Uzkan [12] describes a cooling system for a turbocharged, aftercooled engine, where the engine-out water temperature is held constant at the maximum allowable temperature by derating the engine through a control system.

Detailed Description of the SAC Concept

On Figure 4, the schematic diagram of a basic SAC system of internal combustion engine water cooling is shown. There are two separate cooling water loops, one for the main engine cooling and the other is for the aftercooler cooling loop. The main engine cooling loop includes a water pump, the main engine, the main engine radiator, the oil cooler, and the main engine loop water tank. The aftercooler cooling loop has a water pump, the aftercooler heat exchanger, the aftercooler radiator, and the aftercooler loop water tank. The fans force the ambient air through both of the radiators sequentially. Each of these components operate in the same manner to the like components as described above with reference to Fig. 2.

Additionally, there are two valves shown on Fig. 4 linking the main engine cooling loop to the aftercooler cooling loop. The opening of these valves are controlled by the valve controllers, which are under the control of the computer. The linking valve A links the output of the aftercooler pump to the input of the main engine pump. Similarly, valve B links the output of the main engine water pump to the inlet of the aftercooler water pump. These locations are merely chosen to describe the system operation easily. The system components will be designed in such a way that the main engine loop will have a high water temperature, i.e., 170–180°F, and the aftercooler loop water will have much lower temperature under operation at moderate ambient temperatures. If the valves are completely shut off, then, there will not be any flow from the main engine loop to the aftercooler cooling loop through valve B and from the aftercooler cooling loop to the main engine cooling loop through the valve A. If the valves are open, then the cold water in the aftercooler loop will flow from the outlet of the pump, which has a high pressure, to the main pump inlet, where the pressure is lower. Conversely, the same amount of water will flow from the main engine cooling system from the outlet of the main pump to the inlet of the aftercooler pump. At steady-state operation, the amount of hot coolant flow from the main engine loop to the aftercooler loop will be equal to the amount of the cold coolant flow from the aftercooler loop to the main engine loop. This amount of coolant flow per unit time transferred from one loop to the other is to be referred as the ''linking flow rate.'' Although the linking flow rates, from one loop to the other and the reverse are the same, the amount of heat transferred from one loop to the other will be different due to the temperature difference of the coolant in the loops. Therefore, there will be a net heat transfer from the main engine cooling loop to the aftercooler cooling loop. The amount of the heat transferred per unit time will be referred as the ''convected heat rate''.

The system operation is as follows. At low ambient temperatures, the linking valves are both completely closed and there is no linking flow. The cooling loops are not connected through coolant and perform as if they are two independent loops. The size of the system components are designed such that a cooling capacity larger than conventional designs is allocated to the aftercooler loop at the expense of the main engine loop. As an example, the main engine loop capacity may be just enough to cool the engine operating at the maximum power level at about 70°F. This is chosen mainly for the safe and reliable operation of the engine continuously, at moderate ambient temperature condition. For the purpose of allocating a cooling capacity to the aftercooling loop as high as possible, a lower value may be selected. Depending on the size of the radiators, fans, and pumps, there will be an ambient air temperature $T1$, such that when the locomotive is working at this ambient, and at full power level, the coolant temperature in the main engine loop will reach to a design upper limit $T2$ and that the reliability of the engine will not be compromised. This limit temperature $T2$, will be referred as the ''valve opening temperature'' in the sequel. When the valve opening temperature limit is reached, as measured by the temperature sensors, the control computer would activate the valve controllers and open the valves. By the opening of the valves, some cold coolant from the aftercooler loop is transferred to the main loop and the same amount of hot coolant is transferred from the main loop to the aftercooler loop. As the ambient air temperature increases, the valves would open more, the amount of the linking flow rate

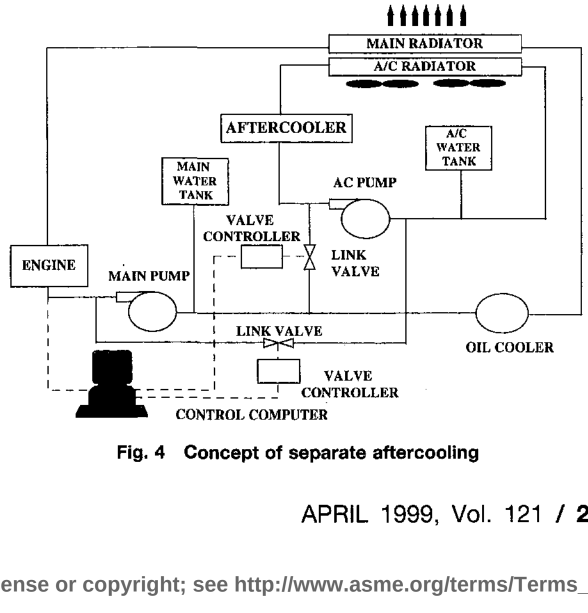

Fig. 4 Concept of separate aftercooling

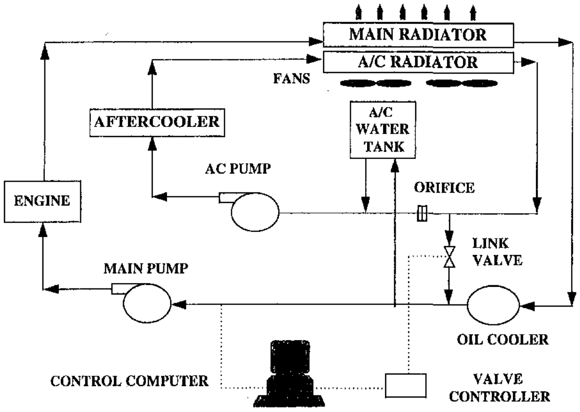

Fig. 5 SD80MAC separate aftercooling system

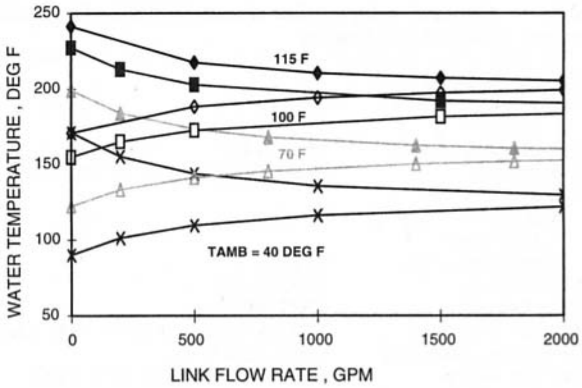

Fig. 6 Predicted engine and A/C inlet water temperatures

will increase, the coolant temperature in the main engine loop would be kept within the allowable design limits, while the temperature of the coolant in the aftercooler loop increases. Practically, through this convective mass transfer, some of the cooling capacity designed into the aftercooler radiator is effectively transferred to cool the coolant in the main engine cooling loop. At the maximum ambient air temperature that the engine is specified to operate, the coolant temperatures in both of the loops can be made to be practically the same, so that both the top and bottom radiators, are cooling both of the coolants in the loops to stay within the maximum allowable engine coolant temperatures. With this methodology, the cooling capacity built in the system is allocated to the different loops in a controlled manner. At low ambient temperatures, the cooling capacity at the main engine cooling loop is chosen to operate the engine at the desired temperature ranges, and the remaining capacity can all be allocated to cool the inlet air. At high ambient temperatures, the cooling capacity allocated to the main engine cooling system can be increased, as necessary, to keep engine temperatures within desired limits, and the cooling capacity allocated to the aftercooling loop can be decreased. This control of cooling capacity allocation through the use of flow linking is the essential contribution of this idea.

The simple description given above is for ease in communication and the application is in no way limited to this description. Different modifications of the above described process can provide the desired results without departing from the scope of the basic idea, as described in reference [4] in further detail.

On Fig. 5, the schematic arrangement of a modified separate aftercooling system is shown. This system is different than the previously described system in Fig. 4 in many ways. As before, there are two separate coolant flow loops, one loop is for the main engine and the other loop is for the aftercooling. As in the previous case, each loop has the same components. There are also some differences between the system shown on Fig. 5 and the one described on Fig. 4. There is only one linking valve in the system between the outlet of the aftercooler radiator and the inlet of the main engine water pump. There is also one water tank, which has connections to both loops. Moreover, an orifice is introduced into the aftercooling loop, before the water pump, to increase the pressure of the coolant at the linking valve connection to the aftercooler loop. At low ambient temperatures, the linking valve is closed. There is no flow through the linking valve and the two loops are working separately and independently. The cooling capacity designed into the system by the choice of the size of the radiators and by the fans is such that the aftercooler loop water temperature is much lower than the main engine cooling loop. At higher ambient air temperatures, when the cooling capacity of the main radiator will not be enough to cool the engine loop, and the engine loop temperature goes beyond the designed limit, the sensor signals to the computer that in turn generates a command to actuate the valve actuator and the linking valve starts to open. As the pressure at the linking loop where the linking valve is connected is made high by the use of the orifice, the flow of linking water will be from the aftercooler loop to the main loop. The same amount of hot coolant will flow from the main loop to the water tank, and from the water tank to the aftercooler loop. With an increase in the linking valve opening, the linking flow rate will increase, and therefore, the amount of heat transferred from the main loop to the aftercooler loop. The system components can be selected in such a way that at the maximum allowable ambient temperature condition, the aftercooler loop water temperature, can be at the same or at a different temperature as the main engine cooling loop.

The performance of such a SAC system is estimated by using the available system performance modeling tools. The trends are given on Figs. 8 and 9, in terms of the percentage decrease of the engine brake-specific fuel consumption (lb/hp/hr) and in terms of the percentage decrease in the NOx emissions as a function of the linking flow rate for different ambient air temperatures and at constant, maximum engine power level. The amount of gains are estimated to be high enough for practical applications with economic incentives.

There are several other modifications and/or options possible from the schematic arrangement described in Figs. 4 and 5 covered by this concept. Further details can be found in reference [4]. Another important application of the SAC concept is the heating of the aftercooler loop coolant by transferring heat from the engine loop to the aftercooler loop to eliminate aftercooler core or aftercooler radiator freezing. At very low ambient temperatures, or for applications with a low turbocompressor pressure ratio, the temperature of the inlet air can be too low for stable operation of the compressor or the heat load in the aftercooler loop can not be high enough to eliminate

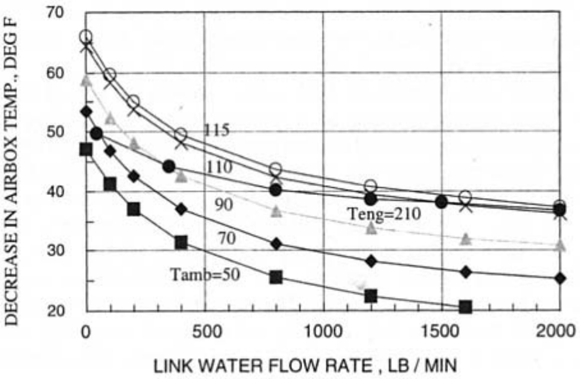

Fig. 7 Predicted decrease in airbox temperature

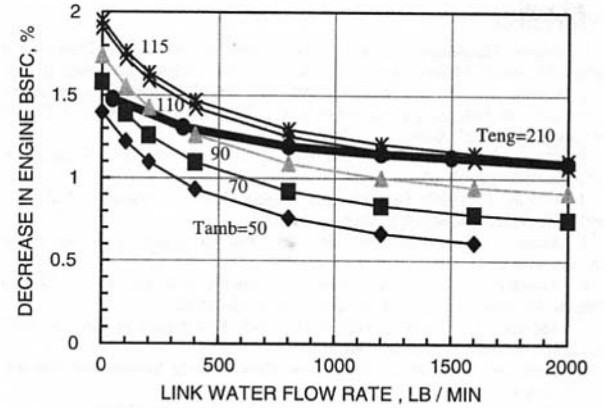

Fig. 8 Predicted decrease in engine BSFC

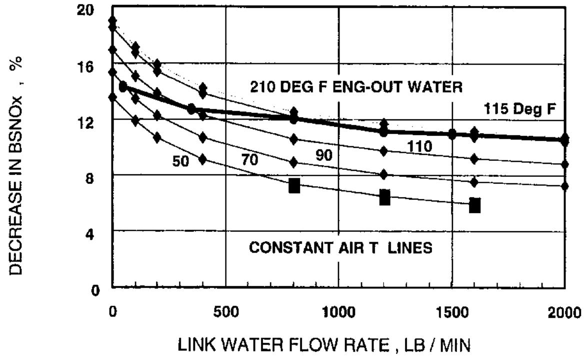

Fig. 9 Predicted decrease in BSNOx versus link flow

possible freeze in the aftercooler radiators. In such a case, by opening the linking valve, heat can be transferred from the main engine to the aftercooler loop, the airflow rate through the compressor could be reduced as well as the freezing of the radiators can be eliminated.

Concept Validation

In a conventional cooling system, as shown on Fig. 2, the cooling water temperature at the engine inlet and the aftercooler core inlet are the same. Moreover the objective of the SAC system is to decrease the water temperature at the after cooler core inlet. Therefore, the coolant temperature difference between the engine inlet and aftercooler core inlet is a good indicator of the effectiveness of the SAC concept.

On Fig. 6, the predicted engine inlet and aftercooler core inlet water temperatures are given as a function of the link flow rate, for 60, 80, 90, and 100°F ambient air temperature conditions. The vertical distance between the engine inlet and AC core inlet curves (for the same ambient temperature) is an indication of the effectiveness of SAC system. For 60°F, and zero link flow, this difference is about 58°F, but for 90°F ambient and 400 lb/min water flow, the difference is about 24°F. This is for a particular locomotive application. Even at 100°F ambient, there is more than 20°F temperature difference for this application.

Figure 7 shows the decrease in the airbox air temperature as a function of the link flow rate, for certain ambient air temperatures (50, 70, 90, 110, and 115°F) and for certain engine inlet air temperatures permitted (190, 200, and 210°F) as a function of link flow rate. In this design, for 90°F ambient and 190°F engine water temperature, the decrease in the airbox air temperature would be about 34°F.

Figure 8 shows the analytically predicted BSFC improvements we would expect from SAC system application, as a function of the link flow rate. For this application, the predictions indicate a gain of about 1.1–1.4 percent. Figure 9 shows the predicted emissions improvements for the same application indicating that about 10–12 percent decrease in BSNOx. These trends are worth the effort of implementing the SAC concepts.

Demonstration of Feasibility and Implementation

At EMD the separate aftercooling method of engine cooling has been successfully implemented on several locomotive models within the last two years. Among these are the SD80MAC, SD70MAC, and SD90MAC locomotive models. Other SAC system designs are at different stages of completion. At the time of writing this paper, there are more than 235 locomotives with SAC cooling system built and delivered to customers and are operational in the field. There is not any evidence or demonstration of nonperformance of the SAC concept. The feasibility, durability, and the operational reliability of this basic idea is proven by these applications in the field. There are also very serious efforts in improving and enhancing the implementation of the SAC concept for different purposes and to reduce the cost and weight of the locomotive.

To demonstrate the feasibility and application of the concept, Fig. 10 is prepared, where the difference of the inlet water temperatures at the main engine inlet and the aftercooler core inlet is plotted as a function of engine speed. This is actual locomotive test data for the SD80MAC locomotives. The engine notch position (engine load) is also changing with engine speed. Each data point is for a specific notch position. In this plot, curve (a) is for high ambient air temperature and link valve full open position. It indicates that for the Notch 4 to Notch 8 operation region, the water temperature at the inlet of the aftercooler is maintained about 26.5°F lower than the inlet water to the main engine. curve (b) is for low ambient link valve fully closed operation conditions. It indicates that the same temperature difference is about 46°F in the average. It is clear that the concept is feasible and works.

It is also important to mention that EMD engineering has developed the necessary design analysis tools for these systems, and was able to design and deliver even the first locomotive without going through the prototype testing phase of a new product or system. This has reduced the time and cost of system development. Only a check and finalization of the size of orifices is required through testing of a new design, after the prototype locomotive is built and ready to deliver.

Conclusions

The idea of separate aftercooling, that is the possibility of transferring some of the cooling capacity, designed into the

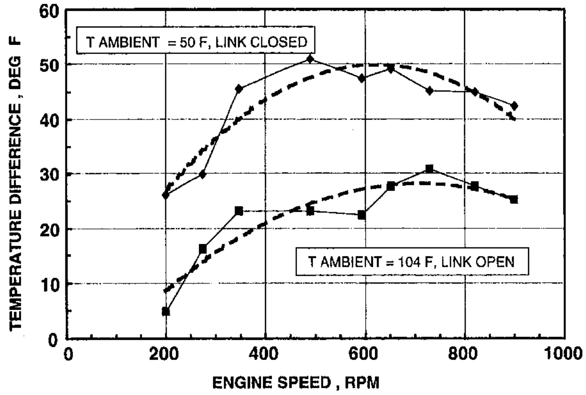

Fig. 10 Measured engine and aftercooler inlet water temperature difference

engine cooling system by the size of its radiators and fans, from engine cooling to inlet air cooling is conceived and developed. Using analytical methods, the feasibility of the concept is proven and the benefits expected from the application of the concept are estimated. Using this method, it is reasonable to expect about 1 to 1.5 percent improvement in BSFC and about 8–12 percent reduction in NOx emissions. Test results on locomotives confirmed the benefits expected from the application of the idea. The SAC system is applied to several state of art locomotive models and over 235 locomotives built and operated in the field for more than a year and a half, without any negative implication attributable to the SAC concept. The concept is feasible, practical, beneficial, and is working.

Analytical tools are also developed at EMD to design such a system without resorting to new prototype testing and development, by using the same characteristics of components as used in the conventional cooling system designs. Moreover, using these analytical tools, modified versions of the basic SAC idea is possible and under considerations.

References

1 Engine Maintenance Manual, 1994, Model 710G3B Engine, Document No. EE000003, General Motors Corporation, Electro-Motive Division, LaGrange, IL 60525.

2 Locomotive Service Manual, 1995, SD70MAC Locomotive, Document # SO936445, 1st Edition, General Motors Corporation, Electro-Motive Division, LaGrange, IL 60525, USA.

3 Heywood, J. R., 1988, *Internal Combustion Engine Fundamentals*, McGraw-Hill, New York.

4 Uzkan, T., 1997, Turbocharged Engine Cooling Apparatus, U.S. Patent #5598705 (other patent applications pending).

5 Stang, J. H. and Yamaguchi, H., 1982, Two Loop Engine Cooling System, U.S. Patent #4,325,219.

6 Melchior, J. F., 1984, Supercharged Internal Combustion Engine Equipped With an Air Intercooling System, U.S. Patent #4,485,624.

7 Musick, D. R., and Howell, E. H., 1985, Self-Adjusting Cooling System for Diesel Engines, U.S. Patent #4,517,929.

8 Roettgen, L. A., et al., 1985, Low Flow Cooling System and Apparatus, U.S. Patent #4,520,767.

9 Crofts, J. G., 1985, Cooling System, U.S. Patent #4,550,692.

10 Nagle, J. A., et al., 1995, Split Temperature Regulating System and Method for Turbocharged Internal Combustion Engine, U.S. Patent #5,415,147.

11 McTaggart, L. E., 1993, Controlled Cooling System For A Turbocharged Internal Combustion Engine, U.S. Patent #5,201,285.

12 Uzkan, T., 1995, Locomotive Engine Cooling System, U.S. Patent #5,392,741.

J. M. Clarke
clarkjm@cat.com

W. G. Berlinger

Caterpillar Inc.,
Engine Research Department,
P. O. Box 1875,
Technical Center, Building F,
Peoria, IL 61656-1875

A New Compression Ignition Engine Concept for High Power Density

A new compression ignition (CI) engine concept has been identified which greatly improves power density over conventional CI engines. This paper reviews the scaling laws as they apply to power density (power/crate volume) and derives a parameter reflecting the compactness of any engine design. The new concept is compared to existing engines on the basis of this parameter. Ideal cycle analysis of the multistage thermodynamic processes inherent in the new arrangement leads to the expectation that this engine will be more efficient than current engines. Real cycle simulations and concept design work have confirmed that efficiency can be at least as high as current engines while size is much reduced. Design and analysis are continuing in order to establish that the durability and low emissions will be competitive with modern CI engines.

Introduction

Smaller lighter spark ignition engines enabled the success of automobiles and powered flight. Size and weight reductions allowed the more efficient compression ignition engines to be used for road vehicles (Cummins, 1970). More recent developments leading to smaller engines include the widespread application of turbocharging (Zinner, 1978) and the use of rotary pistons (Wankel, 1965; Clarke, 1972; Yamamoto, 1981). Other features being equal, a smaller, lighter engine is generally preferable and may extend the range of application.

The concept described here is more suitable than the rotary piston machines for high cylinder pressure and hence more amenable to turbocharging and to high efficiency. Therefore, subject to satisfactory completion of the design and development phases, this concept offers an exceptional mix of small size and high efficiency. These features would allow the fuel savings of the CI engine to be available to a much wider range of users.

The idea is patented (Clarke, 1995).

Mechanical Arrangement

Figure 1 is a schematic transverse section of a module of a compact compression ignition (CCI) engine. The modules can be stacked along the shafts in the manner of the cylinders of an in-line engine. Referring to Fig. 1, the housing contains geared counter-rotating shafts to which the high pressure pistons are attached by journal bearings. There are no wrist pins. The low pressure piston contains the high pressure cylinder and is reciprocated in the manner of a "scotch yoke" on the slider bearings which are integral with the high pressure pistons. The lower portion of the low pressure piston forms a reciprocating piston used for induction and part of the compression. The upper portion forms a similar but larger piston used for part of the expansion and the exhaust. The end of compression, the combustion and the start of the expansion occur between the opposed high pressure pistons. Intake valves, possibly self-acting, are located in the lower housing surface. Exhaust valves, possibly hydraulically activated, are located in the upper housing surface. Transfer ports, opened and closed by a sleeve, are located between the low and high pressure cylinders.

To achieve the necessary asymmetric port timing this sleeve rocks about its axis as the low pressure piston reciprocates. The mechanisms for imparting this rocking motion and injecting the fuel are the subject of continuing design selection (see Design Issues).

The operation of the engine is as follows. Referring to Fig. 2, combustion occurs near minimum volume in the combustion space. This minimum volume defines the crank angle origin. The high pressure gas expands for about 90 crank degrees, until the exhaust space has near zero volume, the exhaust transfer port opens and the gas transfer process starts. At 135 degrees both the combustion and exhaust spaces are expanding but the exhaust space does so faster and most gas transfers to it. At 180 degrees the exhaust transfer port closes. The larger portion of gas which is now confined in the exhaust space continues to expand until at 270 deg the exhaust valves open and the exhaust stroke starts. At 450 (90) deg the exhaust stroke is completed. Returning to the situation at 270 deg, the induction space has near zero volume, intake valves open and induction starts. This continues until 450 (90) deg when the intake valves close. Compression then occurs in the induction space until at 180 deg the inlet transfer valve opens and for about the next 90 deg this gas transfers into the combustion space (mixing with the retained gas) while being further compressed. At 270 deg the inlet transfer closes and compression of the fresh charge diluted with retained exhaust continues for the next 90 deg until combustion starts and the cycle repeats.

This arrangement has the following important mechanical advantages over the usual slider-crank mechanism:

1. Complete balance of all pistons can be achieved by weights on the shafts, even for a single module.
2. Structural efficiency is higher because the piston area exposed to maximum pressure is much less than the piston area used for induction.
3. Generous shaft and bearing dimensions and absence of gasket and wrist pins permit higher firing pressure.

The reasons for the inherently high power density and high thermodynamic efficiency are developed in the following sections.

Power Density and the Scaling Laws

Reciprocating engines span powers from below 0.3 kilowatt to above 30,000 kilowatt; a range of over 5 orders of magnitude.

Contributed by the Internal Combustion Engine Division (ICE) of THE AMERICAL SOCIETY OF MECHANICAL ENGINEERS for publication in the ASME JOURNAL OF ENGINEERING FOR GAS TURBINES AND POWER.

Manuscript received by the ICE August 1, 1996; final revision received by the ASME Headquarters January 12, 1999. Associate Technical Editor: D. Assanis.

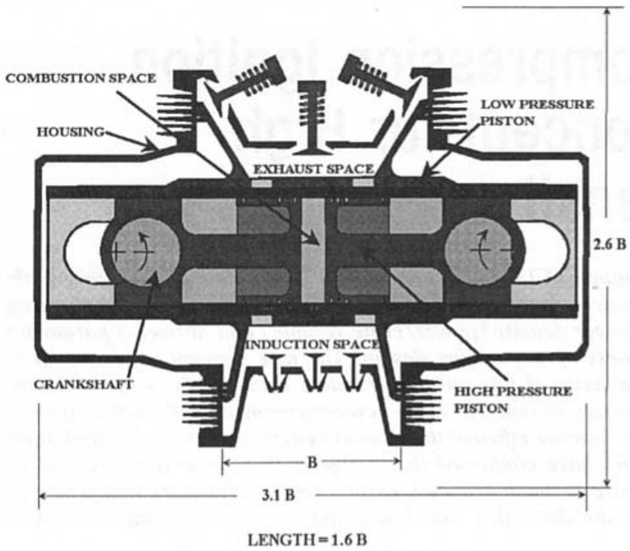

Fig. 1 Transverse section through a module of the compact compression ignition engine

The power density (power/crate volume) of the low power units is much greater than the larger ones even though the latter make more use of turbocharging and multi-cylinder configurations to increase their power density. This small engine advantage is a consequence of the "square-cube law". This asserts that exact scale replicas of engines increase their power with the square of their linear dimension while their volume and weight increase with its cube. This "law" follows from the use of a uniform range of piston speeds across the 100,000 fold range of reciprocating engine powers as shown in Fig. 3 (McMahon and Bonner, 1983).

One of the reasons for that uniformity is that inertia induced stresses are equal for scaled mechanisms operating at the same linear speed. Another reason is that vibration mode frequencies remain a fixed multiple of engine firing frequency. Also, according to dimensionless groups developed for fuel spray penetration data (Naber and Siebers, 1996), even the development of fuel spray penetration within a combustion chamber remains the same in terms of crankshaft angle. By eliminating the scaling factor from the two equations expressing the square-cube law it follows:

$$\text{Power/Volume} = D/\sqrt{\text{Power}} \tag{1}$$

In Eq. 1 the parameter, D, depends on engine design and is near constant for scaled engines. (It is exactly constant for engines which obey the square-cube law exactly.) The use of higher boost pressure, higher piston speed and multiple cylinders in V configuration are the principle ways in which conventional engine designs increase the value of the parameter D. But it can be increased further by adopting unconventional designs. Figure 4 shows the power density parameter, over a 50-fold power range for engines made by Caterpillar. The higher values for the more powerful engines result from higher inlet manifold air densities through turbocharging and typically more cylinders in V configuration.

Appendix 1 gives a derivation from conventional definitions of the following formula:

$$D = \left(\frac{\text{FAR}\cdot\eta_V\cdot\rho_I\cdot V_P}{\text{SFC}\cdot St}\right)^{3/2}\cdot G \tag{2}$$

In Eq. 2 the dimensionless group, $G = A_P^{1.5}/V_c$, is the geometric factor. Traditionally G is increased by adding cylinders and moving from in-line to V configurations. Because of the square-root effect, it requires a 4-fold increase in the number of cylinders to achieve a 2-fold increase in G.

The use of sophisticated "high D" engines in the larger sizes is an application requirement. For instance to achieve the same power to weight ratio, hence equal hill climb speed, in a large truck as in a small one requires a higher D engine in the larger unit.

Table 1 shows representative numerical values consistent with Eq. 2 and Fig. 3 for a truck type CI engine and a more power-dense large engine for locomotive use.

Typically, fuel air ratio, FAR, volumetric efficiency, η_V, and piston speed, V_P, are close to physical limits imposed by aerodynamic, mechanical or chemical requirements so they are not available for large increases. Nor is specific fuel consumption, SFC, available for large reductions. Any major change in the power density parameter, D, therefore depends on some combination of increased inlet density, ρ_I, geometric factor, G, and possibly conversion to a 2-stroke.

Adding turbochargers raises $(\rho_I)^{1.5}$ much faster than it lowers the geometric parameter, G, and is a well known approach.

The CCI concept increases G from about 0.02 to as high as 0.10 while reducing St from 4 to 2. The combined effect of these two changes, with other parameters equal is a multiplication of D by $5 \times 2^{1.5} = 14.1$. Practical considerations limit the increase to less than this, but design studies confirm that it remains high.

Traditional measures such as increasing the speed and the number of cylinders can only increase power density by evolutionary improvements. The new mechanism improves the space efficiency of the air induction process which leads to large power density improvements.

Ideal Cycle Analysis and the CCI Cycle

Conventional two and four stroke engines aim to remove nearly all combustion products prior to compression. The cycle used by the CCI configuration retains a substantial portion (typically 40 percent) of the exhaust in the high pressure cylinder for the next cycle. (The fuel to air ratio, FAR, used here is the overall value for the engine.) Exhaust retention actually increases the oxygen mass in the cylinder but decreases its concentration. The net effect is to decrease both the flame tempera-

Nomenclature

A_P = area of induction piston
CCI = compact compression ignition
CI = compression ignition
D = size independent power density parameter
DARPA = defense advanced research projects agency
FAR = fuel to air mass ratio into engine
G = dimensionless geometric parameter
L_C = combustion loss/heat supplied
L_E = exhaust loss/heat supplied
L_M = mixing loss/heat supplied
SFC = specific fuel consumption
St = strokes, (4 for 4-stroke, 2 for 2-stroke)
TACOM = tank automotive command
V_C = crate volume, length*width*height
V_P = mean piston speed
m = mass during combustion/mass induced
η_V = volumetric efficiency
η_T = thermal efficiency, work/heat supplied
ρ_I = air density to induction cylinder

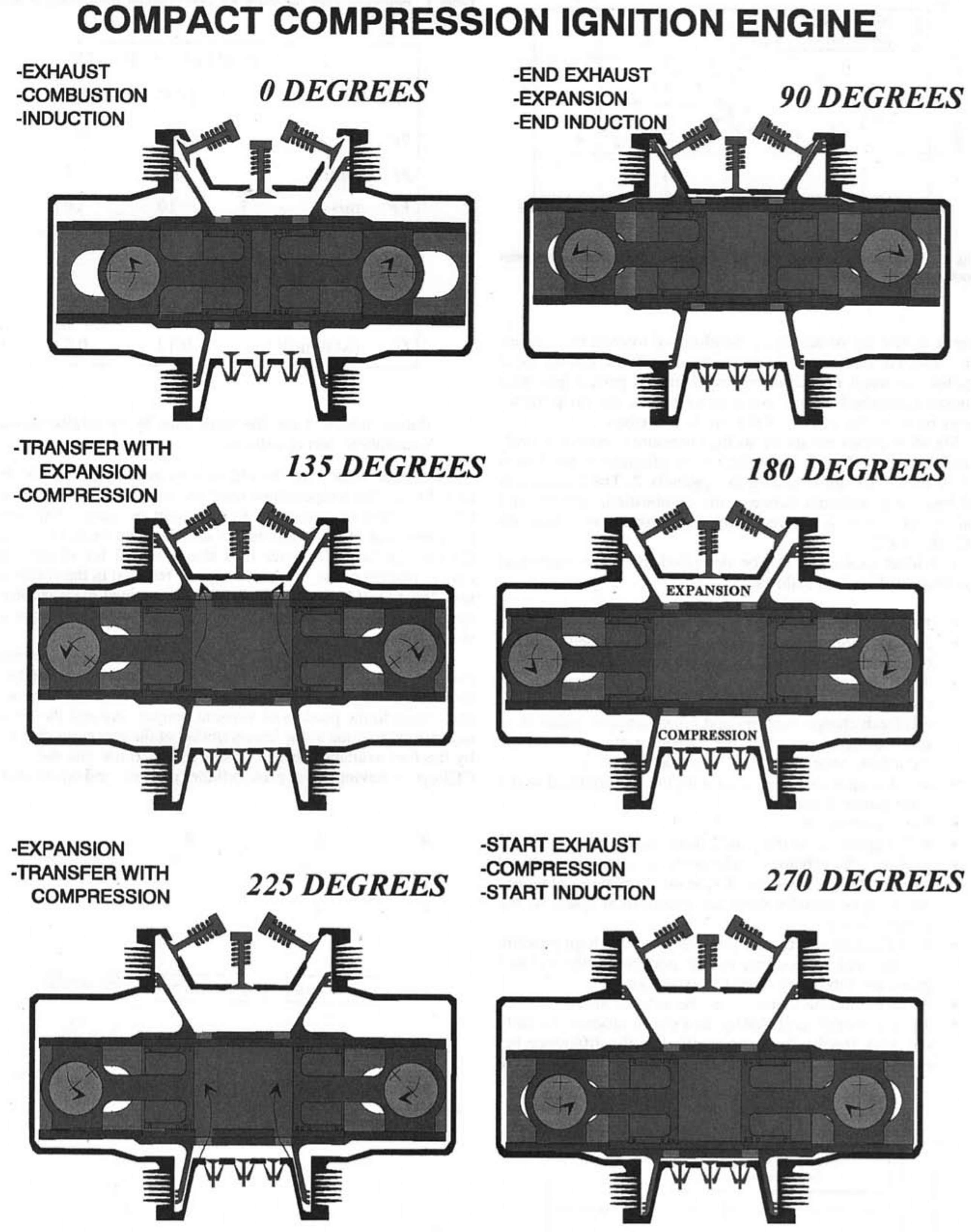

Fig. 2 Compact compression ignition engine operating cycle

ture rise and the average temperature rise relative to an engine with the same fuel rate and no retained exhaust.)

In conventional engines such a level of exhaust retention would reduce power unacceptably. But in this engine the space needed to accommodate that gas is only required in the high pressure chamber, so it does not detract from the induction space. It is the induction space which controls the air flow capacity and hence the power of the engine. Clearly this retained exhaust also increases temperatures during compression. It is not obvious however whether this is good for the thermody-

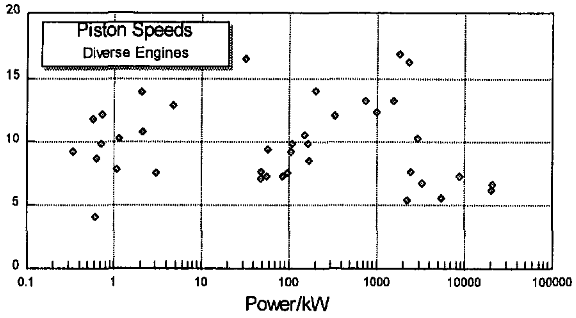

Fig. 3 Reciprocating piston speeds do not change systematically with engine power

namic efficiency or not. It is, therefore, of interest to compare an idealized version of the new cycle with the classic ideal cycles. As usual the idealizations assume a perfect gas with constant specific heat, no heat transfer losses, and crisp transitions between the phases of the cyclic processes.

Six ideal cycles are shown as log (pressure) versus log (volume) circuits in Fig. 5. Formulae for the efficiencies and losses of all the cycles are tabulated in Appendix 2. The distribution of lost work potential between the combustion, exhaust and mixing processes is derived from a "Second Law" analysis (Clarke, 1976).

The ideal CCI cycle can be described using the numerical notation on Fig. 5 as follows:

- 1–2 Compression in the induction space.
- 2–3 The high pressure volume with its retained combustion products merges with the compressed charge.
- 3–4 Compression continues with the induction space and combustion spaces joined through open inlet transfer ports and fresh charge transfers and mixes into the combustion space contents until at 4 the transfer ports close and the induction space has "zero" volume.
- 4–5 Compression continues with the gas confined to the combustion space.
- 5–6 Combustion.
- 6–7 Expansion in the combustion space.
- 7–8 At 7 the exhaust transfer ports open with the exhaust space at "zero" volume. Expansion continues while exhaust gases transfer from the combustion space to the exhaust space.
- 8–9 The exhaust transfer ports close so that high pressure volume and the corresponding portion of the exhaust gases are subtracted from the expansion.
- 9–10 Expansion continues in the exhaust space.
- 10–1 The cycle is closed by the exhaust process. Actually the work involved in process 10–1 is the difference between the flow work done on the engine by the atmosphere during induction and the work done by the engine on the atmosphere during exhaust.

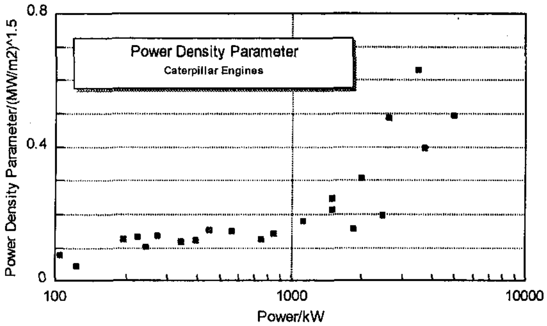

Fig. 4 Power density parameter, *D*, for Caterpillar engines

Table 1 Representative numbers for conventional turbocharged and aftercooled CI engines

		6 cyl in-line	16 cyl V
FAR		1/30	1/30
η_V		0.9	0.9
ρ_I	kg/m^3	2.5	4
V_P	m/s	10	10
SFC	g/(kW.h)	190	200
St		4	4
G		0.02	0.04
D	(MW/m^2)$^{1.5}$	0.13	0.5

Numerical values for the efficiencies and losses are shown in Table 2. The temperatures used are based on cycles having the same ratio of maximum to minimum pressure (200) and the same heat (fuel) addition per unit induced mass of air. In the case of the CCI cycles it is also assumed for illustration that 37 percent of the combustion gas is retained in the combustion space ($m/(1 + m) = 0.37$). As the retained mass fraction approaches zero the CCI cycle approaches the other full expansion cycles.

In Table 2 the losses, L_c, L_e and L_m, are the combustion, exhaust, and mixing losses expressed as fractions of the fuel available energy. They are calculated using second law analysis and equate to the product of ambient temperature and the internal entropy rise due to the irreversibility of the processes divided by the fuel available energy. These results show that the ideal CCI cycles having equal peak cylinder pressure and equal over-

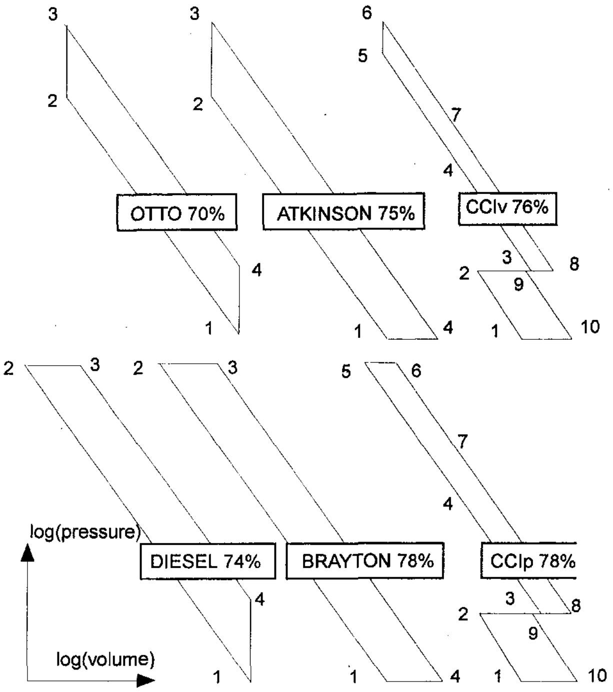

Fig. 5 Classic and CCI cycles compared for equal maximum pressure and fuel to air ratio

Table 2 Efficiencies and losses for six ideal cycles having equal peak pressure and heating quantity

	Otto	Atkinson	CCI_V	Diesel	Brayton	CCI_P
T_{max}, K	3041	3041	2945	2829	2829	2829
Eff, %	69.7	74.8	76.3	74.0	78.0	78.0
L_C, %	16.4	16.4	13.4	14.9	14.9	12.7
L_E, %	13.9	8.8	8.0	11.1	7.1	7.2
L_M, %	0	0	2.3	0	0	2.1

all fuel air ratio are equal to or better than the classic full expansion cycles (Atkinson and Brayton). These in turn are better than the cycles we currently use (Otto and Diesel) for which the expansion and compression ratios are equal. In the constant volume combustion CCI cycle the added mixing loss partially negates the reduced combustion loss. In the constant pressure combustion CCI cycle the mixing loss exactly negates the lower combustion loss. Note that all columns of Table 2 add to 100 percent, because the available work of the heat is fully accounted for in the losses and work done.

A further advantage of the two-stage process in the CCI engine concerns the geometry of the combustion space. The diesel cycle in the above comparison requires a compression ratio of 44 which implies either an excessive stroke or a combustion chamber with very poor surface to volume ratio. The constant volume CCI cycle on the other hand has a geometric compression ratio in the combustion cylinder of 8.

Design Issues

The design of this concept has been taken as far as is required for thermodynamic simulation. However the injection and cooling schemes need further work to decide between two approaches.

The first uses an internal sleeve as a liner for the high pressure pistons. The sleeve contains cooling passages and is oscillated, to open and close the transfer ports, as the low pressure piston reciprocates by an arm linked to the housing. In this concept the injector is integral with the arm and is fed both with fuel and actuating hydraulic power through the pivots of the link.

The second uses a pair of sleeves external to the high pressure cylinder liner to control the transfer ports. Oscillation of each sleeve is achieved by wire straps (or toothed rack) joining the periphery of the sleeve to the housing. In this concept the injector tip is mounted directly in the low pressure piston and its reciprocation is used to power the fuel injection. In this way neither camshaft nor hydraulic methods are needed to inject fuel.

Simulation

After concept design work allows engine proportions and transfer port areas to be evaluated, it is possible to estimate the engine performance using nearly standard engine simulation programs. A modular simulation program was adapted for that purpose (Sandford, 1996). Figure 6 and Table 3 show some results from simulation of a turbocharged and aftercooled two-module arrangement aimed at on-highway truck applications.

Table 3 also shows results from simulation of a modified design aimed at a naturally aspirated configuration. This design is appropriate for applications where the specific power benefits of turbocharging and multiple modules yield to the need for simplicity and low cost. Note that the FAR values shown in Table 3 are for the overall engine, the retained gas increases the oxygen mass in the cylinder while reducing the oxygen mole fraction. The low volumetric efficiencies are the result of the need to expand residual air in the induction space clearances before the induction begins. The resulting power density parameter, D, is much larger than could be obtained conventionally at these boost levels.

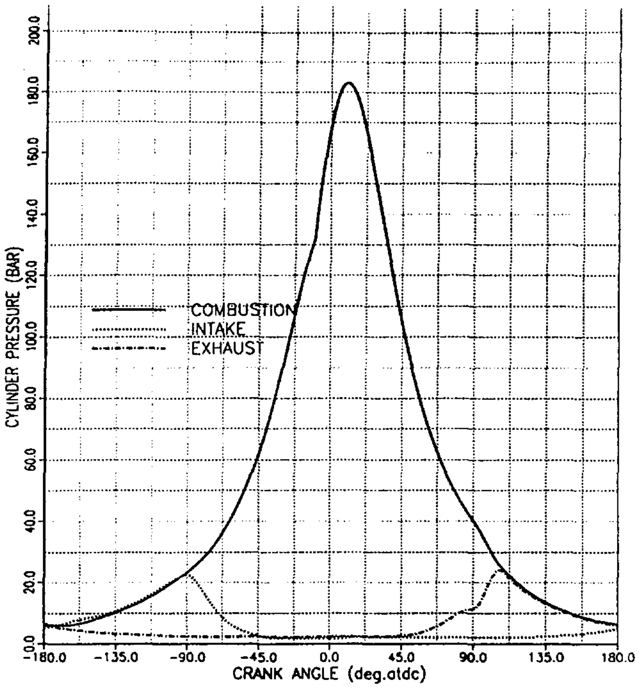

Fig. 6 Simulated pressure versus crank angle for a turbocharged aftercooled two-module CCI truck engine

Comparing the values of D for the CCI engines in Table 3 with the values for conventional engines in Table 1 shows that the CCI concept in single module naturally aspirated form yields twice the power density of a turbocharged six cylinder CI engine.

Application Benefits Over Conventional Engines

Although over half the nation's petroleum derived fuel is used in spark ignited automobile engines, it has not yet been the practice to utilize many of the more fuel efficient CI engines in that application. Obstacles to the use of conventional CI engines include their size, cost, noise and perceived emissions.

Table 3 Simulated performance and power density of two CCI engines

		Turbocharged aftercooled 2-module CCI	Naturally aspirated 1-module CCI
FAR		1/22.4	1/19.2
η_V		0.76	0.69
ρ_I	kg/m³	2.5	1.2
V_P	m/s	4.8	6.1
SFC	g/(kW.h)	183	211
St		2	2
G		0.076	0.091
D	$(MW/m^2)^{1.5}$	0.616	0.307

Size is clearly reduced by this configuration. It appears that even a naturally aspirated single module CCI is as small as a multi-cylinder turbocharged conventional CI engine of equal power.

Cost savings can be reasonably anticipated from the single fuel injection system, the smaller size and the natural aspiration.

Noise is reduced by the high temperature at the end of compression leading to very little premixed combustion. The combustion chamber is more isolated from the housing than for typical engines. Exhaust blow-down is less violent due to the extra expansion volume. Vibration due to piston motion can be eliminated by crank mounted balance weights. The counter-rotating shafts provide a further vibration reduction feature because they prevent speed changes, such as those caused by individual firings, from causing reactions on the engine mountings.

Emissions expectations are also promising. The inherent Exhaust Gas Retention (EGR) of the CCI engine may reduce NOx or, at least, help the NOx to SFC tradeoff. Although the NOx production might be expected to rise with the higher average combustion temperatures, it is apparent from the ideal cycle analyses that the maximum temperature of the cycle is not being raised by the exhaust retention. This is because the larger mass of gas moderates both the temperature and pressure rise from combustion of the same fuel quantity. Also the temperature rise due to locally stoichiometric combustion is reduced by the oxygen dilution from the retained exhaust products. Exhaust gas recirculation is an established method of reducing NOx in conventional engines, but it cannot be applied at high power because the reduced quantity of fresh charge limits engine power. In the CCI engine the fresh charge quantity is controlled by the induction space. The combustion space has to be larger to accommodate the retained exhaust but this makes very little contribution to engine size. The result is that large quantities of exhaust can be recirculated by retention, even at high power, without compromising engine power and without the use of external pipes.

If this CCI engine concept adequately addresses these issues it would save billions of dollars per annum in the nation's fuel costs through its use in automobiles.

Conclusions

1. A new and compact CI engine configuration has been identified.
2. A power density parameter, D, independent of engine size has been derived. It includes the dimensionless geometric factor, G. This factor is about 0.02 for 6 in line engines, about 0.04 for current multi-cylinder V configurations. It rises to between 0.05 and 0.10 for the CCI concept.
3. A study of ideal thermodynamic cycles suggests that CCI engines derive an efficiency advantage from their higher average combustion temperatures and lower average exhaust temperatures.
4. Simulations show that even with conservative estimates of piston speed and volumetric efficiency in a practical CCI engine the power density is still improved. According to Tables 1 and 3, a naturally aspirated single-module CCI engine can be half the volume of a turbocharged 6 in-line conventional unit. Similarly a turbocharged and aftercooled two-module CCI engine can be more compact than a more highly boosted 16 cylinder Vee conventional unit.
5. The CCI engine, even in its simplest single module naturally aspirated version, appears to offer size, cost, noise and possibly emission advantages over conventional CI engines. This may extend the use of efficient CI engines in automobiles and many other applications.

Acknowledgments

The authors acknowledge with gratitude the support given to this work by DARPA and TACOM. Structural analysis and cycle simulation were greatly helped by a subcontract with Lotus Engineering, England. The permission from Caterpillar to publish this paper is much appreciated.

References

Clarke, J. M., Walker, D. F., and Hamilton, P. H., 1972, "A New Class of Rotary Piston Machines Suitable for Compressors, Pumps and Internal Combustion Engines," I. Mech. E. Proceedings, Volume 186, 62/72.

Clarke, J. M., 1976, "The Thermodynamic Cycle Requirements for Very High Rational Efficiencies," I. Mech. E C53/76, pp. 121–129.

Clarke, J. M., 1995, "Dual Compression and Dual Expansion Internal Combustion Engine and Method Therefor," US. Patent 5,456,219.

Cummins, C. L., 1970, "Diesels from the Woodshed," SAE SP-357.

McMahon, T. A., and Bonner, J. T., 1983, *On Size and Life,* Scientific American Books, W. H. Freeman and Company, New York.

Naber, J. D., and Siebers, D. L., 1996, "Effects of Gas Density and Vaporization on Penetration and Dispersion of Diesel Sprays," SAE 960034, SP-1159, pp. 59–88.

Sandford, M. H., 1996, *Multi-Cylinder Engine Simulation (MICES) User's Handbook,* Lotus Engineering, Norwich, England.

Wankel, F., 1965, *Rotary Piston Machines,* Iliffe Books Ltd., London.

Yamamoto, K., 1981, *Rotary Engine,* Sankaido Co. Ltd., Tokyo.

Zinner, K., 1978, *Supercharging of Internal Combustion Engines,* Springer-Verlag, Berlin.

APPENDIX 1

Derivation of Power Density Parameter, *D*

Nomenclature

A_P	Total area of induction pistons
M_A	Air mass rate to engine
M_F	Fuel mass rate to engine
P	Power of engine
St	Strokes per induction stroke (4 for 4-stroke, 2 for 2-stroke)
V_C	Crate volume of engine ($L \times W \times H$)
V_P	Mean piston speed (2 × Stroke × RotationFreq.)
ρ_I	Density of induced air

Defining Relations

$$\mathrm{SFC} = M_F/P \quad \text{Specific fuel consumption} \tag{3}$$

$$\eta_V = M_A/(\rho_I A_P V_P/St) \quad \text{Volumetric efficiency} \tag{4}$$

$$\mathrm{FAR} = M_F/M_A \quad \text{Overall Fuel air ratio} \tag{5}$$

$$D = P^{3/2}/V_C \quad \text{Power density parameter} \tag{6}$$

$$G = A_P^{3/2}/V_C \quad \text{Geometric compactness parameter} \tag{7}$$

Expressions for Power Density Parameter. Eliminating the extensive variables (P, M_A, M_F) from Eq. 3–6 yields:

$$D = \left(\frac{\mathrm{FAR}\cdot\eta_V\cdot\rho_I\cdot V_P\cdot A_P}{\mathrm{SFC}\cdot St}\right)^{3/2}\cdot\frac{1}{V_C}$$

Factorizing to separate geometric variables, and using Eq. 7 yields:

$$D = \left(\frac{\mathrm{FAR}\cdot\eta_V\cdot\rho_I\cdot V_P}{\mathrm{SFC}\cdot St}\right)^{3/2}\cdot G$$

Note that D has units of (Energy flux)$^{3/2}$. For numerical work with engines (MW/m^2)$^{3/2}$ units are used.

APPENDIX 2

Formulae for Efficiencies and Losses

Applying the heat engine analogy for internal combustion engines the following efficiency and loss formulae can be derived using standard thermodynamic principles. Temperatures, T_x, and volumes, V_x are subscripted with the numbers shown on Fig. 5. Gamma, γ, is the ratio of specific heats and is assumed to be 1.4. L_C, L_E and L_M are the internal losses from combustion, exhaust and mixing expressed as fractions of the heat supplied.

Otto

$$c = T_2/T_1 \quad h = T_3/T_2$$

$$\eta_T = 1 - \frac{1}{c} \quad L_C = \frac{\ln(h)}{c(h-1)} \quad L_E = \frac{h - 1 - \ln(h)}{c(h-1)}$$

Atkinson

$$c = T_2/T_1 \quad h = T_3/T_2 \quad \eta_T = 1 - \frac{\gamma(h^{1/\gamma} - 1)}{c(h-1)}$$

$$L_C = \frac{\ln(h)}{c(h-1)} \quad L_E = \frac{\gamma(h^{1/\gamma} - 1) - \ln(h)}{c(h-1)}$$

CCI (Constant Volume Combustion)

$$c = T_5/T_1 \quad h = T_6/T_5 \quad m = V_8/V_9 \quad r = m - (m-1)h^{1/\gamma}$$

$$\eta_T = 1 - \frac{\gamma(h^{1/\gamma} - 1)}{c(h-1)r} \quad L_C = \frac{\ln(h)}{c(h-1)}$$

$$L_E = \frac{\gamma}{c(h-1)} \left(\frac{(h^{1/\gamma} - 1)}{r} - \frac{\ln(h^{1/\gamma}/r)}{m} \right)$$

$$L_M = \frac{1}{c(h-1)} \left(\frac{\gamma \ln(h^{1/\gamma}/r)}{m} - \ln(h) \right)$$

Diesel

$$c = T_2/T_1 \quad h = T_3/T_2$$

$$\eta_T = 1 - \frac{h^\gamma - 1}{c\gamma(h-1)} \quad L_C = \frac{\ln(h)}{c(h-1)}$$

$$L_E = \frac{1}{c\gamma(h-1)} (h^\gamma - 1 - \gamma \ln(h))$$

Brayton

$$c = T_2/T_1 \quad h = T_3/T_2$$

$$\eta_T = 1 - \frac{1}{c} \quad L_C = \frac{\ln(h)}{c(h-1)} \quad L_E = \frac{h - 1 - \ln(h)}{c(h-1)}$$

CCI (Constant Pressure Combustion)

$$c = T_6/T_{10} \quad h = T_6/T_5 \quad m = V_8/V_9 \quad r = m - (m-1)h$$

$$\eta_T = 1 - \frac{1}{c} \quad L_C = \frac{r \ln(h)}{c(h-1)}$$

$$L_E = \frac{1}{c(h-1)} (h - 1 + r \ln(r/h)/m)$$

$$L_M = \frac{-r}{c(h-1)} (\ln(h) + \ln(r/h)/m)$$

M. Vittal

J. A. Borek

D. A. Marks

A. L. Boehman

Department of Energy and
Geo-Environmental Engineering,
The Pennsylvania State University,
University Park, PA 16802-5000

D. A. Okrent

Rupprecht and Patashnick Company, Inc.,
25 Corporate Circle,
Albany, NY 12203

A. P. Bentz

JBL Associates, Inc.,
P.O. Box 7191,
Groton, CT 06340-7191

The Effects of Thermal Barrier Coatings on Diesel Engine Emissions

This study has characterized the influence of thermal barrier coatings (TBCs) applied to combustion chamber surfaces on the emissions from an indirect injection (IDI) diesel engine. The TBCs were applied to the piston crown, the cylinder head (fire deck) and the valves of a single cylinder Yanmar TS-180 IDI diesel utility engine. The gaseous and particulate emissions from the baseline (uncoated) and ceramic-coated engine were analyzed to assess the changes in the combustion process caused by the coatings. The results of these analyses show two clear trends during operation of the baseline and ceramic-coated engine. First, comparison of the emissions from the four modes of operation for the baseline (uncoated) engine shows that particulate matter emissions (on a g/kWh basis) are highest at low load-low speed (mode 4) conditions. At low load-low speed conditions (modes 3 and 4), particulate matter decreases substantially with the TBCs present. Second, these observations combined with thermal and morphological analyses of the particulate matter show that the TBCs reduce particulate mass by reducing the volatile organic content of the particulate.

Introduction

Diesel Engine Emissions. Reduction of emissions from diesel engines is becoming increasingly important, both because of increasing concerns among the public about the environment and because regulatory agencies are promulgating ever more stringent emissions legislation. While marine diesel engines have not been targeted for emissions reduction with as much vigor as on-highway vehicles, a need remains to address marine emissions as well. For example, recent efforts have attempted to reduce NO_x emissions from marine diesel engines by selective catalytic reduction of NO_x (Gibson and Groene, 1991). Understanding and minimizing diesel engine emissions is essential to the US maritime community in light of the likely increased dependence on diesel powerplants due to their flexibility of fuel requirements, high efficiency, low maintenance and high availability in the marketplace (Karaszewski and Schaefer, 1991). Because they rely on diesel powered vessels, the U.S. Coast Guard has an interest in strategies for reducing emissions from existing diesel engines in their fleet.

Particulate and NO_x emissions are the primary concern for diesel engines, owing to the nature of the compression-ignition process and diesel fuel composition. The control of diesel vehicle emissions is a particularly challenging problem due to the presence of solid particulates in the exhaust, in addition to the gas phase pollutants. Diesel exhaust contains a mixture of gas, liquid and solid phases made up of organic and inorganic compounds (Johnson et al., 1994). Gas phase emissions include NO_x, CO, vapor phase hydrocarbons, and SO_2. Liquid phase emissions consist of condensed hydrocarbons and sulfates with hydration. The solid phase is composed primarily of small (10–80 nm) spherical carbon particles. The particulate matter emitted by diesel vehicles is an agglomeration of the solid spheres that are coated with adsorbed sulfates and condensed hydrocarbons (called the SOF, or soluble organic fraction). When inhaled, the easily respirable particles are eventually trapped in the bronchial passages and alveoli of the lungs where the sulfates and soot particles may interact synergistically to cause certain bronchial diseases and lung dysfunction (Hippeli and Elstner, 1990). Polynuclear aromatic hydrocarbons (PAH) are present in the SOF and contribute to the overall carcinogenic effect of diesel particulates as well (Bagley et al., 1996). These PAH compounds are just one component of the diverse polycyclic organic matter which is present in both the gas and particulate phases of diesel exhausts (Health Effects Institute, 1993).

Exhaust particulate emissions from diesel engines are typically ten times greater than those from gasoline engines (Lies et al., 1986). In order to decrease toxic exhaust emissions, diesel engines are required to meet increasingly stringent particulate emission standards (Docekal et al., 1992). To control diesel particulate emissions, as well as increase engine performance, efforts have focused on in-cylinder improvement of the combustion process by design modifications, although considerable research and development have been devoted to exhaust aftertreatment (traps and oxidation converters) and fuel modifications (low aromatic and low sulfur). In diesel engine development, emissions reductions have been achieved through higher fuel injection pressures, exhaust gas recirculation, turbocharging and modifications of combustion chamber geometry (Neeft et al., 1996). Another method being considered is the insulation of selected parts of the combustion chamber with thermal barrier coatings (TBCs).

Thermal Barrier Coatings. Insulating the combustion chamber walls of a diesel engine has been investigated as a means to increase its thermal efficiency (Bryzik et al., 1983). In a typical diesel engine, only 30–40 percent of the entering fuel chemical energy is converted to useful power output. The remainder is divided approximately evenly between the coolant and the exhaust stream. Cooling engine components is necessary to protect them against thermal stresses which can otherwise cause engine failure. Thermal insulation of the combustion

---

Contributed by the Internal Combustion Engine Division (ICE) of THE AMERICAN SOCIETY OF MECHANICAL ENGINEERS for publication in the ASME JOURNAL OF ENGINEERING FOR GAS TURBINES AND POWER.

Manuscript received by the ICE February 21, 1998; final revision received by the ASME Headquarters December 29, 1998. Associate Technical Editor: D. Assanis.

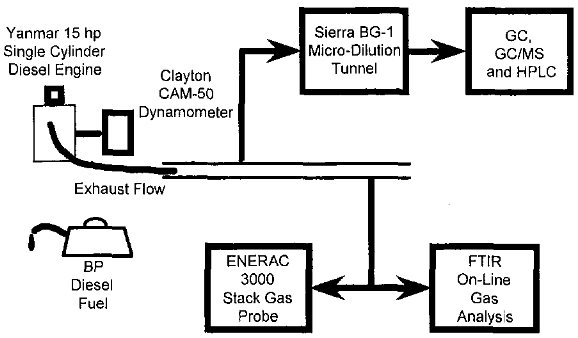

Fig. 1 Schematic of engine test cell

chamber seeks to protect the engine components from thermal stresses by decreasing the heat transfer between the working fluid and the cylinder walls. Thus, energy that would otherwise have been rejected to the coolant is exchanged for increased shaft work. For this reason, such an engine is sometimes referred to as an ''adiabatic,'' or, more commonly, a low heat rejection (LHR) engine.

Typically, ceramic materials are used to insulate the combustion chamber walls. The use of thin thermal barrier coatings has superseded the use of thick coatings and monolithic ceramic inserts (Kamo et al., 1989). The first use of thermal barrier coatings was for relatively minor roles, in aircraft engine performance (Brindley, 1995). The concept of thermal barrier coatings for diesel engines began in the mid 1970s by Kvernes at the Central Institute for Industrial Research in Oslo, Norway (Fairbanks, 1995). Since then, several advanced ceramics have been investigated for heat insulation of combustion chamber walls. Among the desirable material properties are low thermal conductivity and good high temperature strength. It has been difficult to find a material to satisfy both criteria. Partially stabilized zirconia is a popular choice because of its low thermal conductivity, although silicon nitride has better high temperature strength.

It is to be expected that heat insulation of the combustion chamber walls will have an effect not only on performance but also on emissions. There is substantial literature on adiabatic and LHR engines, with a thorough review provided by Amann (1988). However, Assanis et al. (1991) assert that the picture presented by the literature on the effects of thermal barrier coatings is unclear and that more in-depth studies of performance and emissions are needed. Using a two-stroke direct injection (DI) diesel engine that was rebuilt with coated piston crowns, cylinder head fire decks and exhaust valves, Voss et al. (1997) found a reduction in the dry soot fraction of the total particulate matter (i.e., the volatile fraction of the particulate matter increased). Voss et al. further observed that a combination of a ceramic-coated engine followed by a diesel oxidation catalyst led to a net decrease in total particulate emissions. However, in this work we show by examination of particulate morphology and composition that condensable hydrocarbon adsorbed onto the particulates is significantly reduced in the presence of TBCs. Enhanced oxidation of the condensable hydrocarbon substantially alters the volatile content of the particulate, shifting toward lower volatile content and a higher dry soot fraction.

Thermoanalytical methods (or thermal analysis) for determining the composition of particulate emissions have been developed. Cuthbertson et al. (1979) and Shore and Cuthbertson (1985) have described a thermogravimetric analyzer (TGA) for achieving a simple separation of diesel particulate components. Their method consists of collecting particulate matter on a disposable filter using a constant volume sampling (CVS) tunnel. The filter-borne particulate is then heated according to a set program. When their analyzer was interfaced with a flame ionization detector, additional data on the hydrocarbon fraction could be obtained. They found thermogravimetry to be a useful tool for diesel engine development. More recently, Zinbo and co-workers (1990, 1995) have described a thermogravimetric method for determining the volatile fraction of particulate from both diesel and SI engines. Their method involved collection of particulate on PTFE-bonded glass-fiber membrane filters which were then heated in inert gas or air. Key to their analysis was the fact that the PTFE-bonded membrane filters decomposed cleanly in a temperature range 450–600°C in N_2. This permitted the membrane mass to be subtracted out to yield the TGA profile of the particulate alone. They compared their TGA results to analysis by solvent extraction/chromatography and found good correlation. Arai (1993) used thermal analysis in a study of diesel oxidation catalysts. He absorbed SOF from solution on to a piece of catalyst which was then crushed to obtain test samples. Thermal analysis on these samples yielded TGA and DTA (differential thermal analysis) profiles which he used to estimate the SOF oxidation temperature. Very recently, an online thermoanalytical method for measuring the volatile fraction in diesel exhaust particulates has also been developed (Okrent, 1996). The Series 5100 Diesel Particulate Measurement System from R&P Co., Albany, NY, is based on this method. It is convenient and fast because it incorporates particulate collection and analysis procedures in a single unit.

In this paper, we present a detailed comparison between engine operation with and without thermal barrier coated engine parts. By operating the same engine with and without coatings present, the extraneous influence of many engine operating factors has been removed from the study. However, no attempt was made to maintain constant compression ratio. Particulate matter and gaseous emissions are compared for the two engine configurations, with emphasis placed on the particulate mass. The objectives of this study were to determine quantitatively the influence of thermal barrier coatings on the emissions from marine diesel engines and to evaluate the potential benefits of using thermal barrier coatings to reduce particulate emissions from diesel-powered Coast Guard vessels. To achieve this goal, particulate matter has been collected from an engine with and without thermal barrier coated parts, and the particulate matter has been subjected to mass, thermal and microscopic analyses. Gaseous emissions and engine operating conditions were also monitored. Where possible, the experimental observations have been interpreted in terms of combustion mechanisms to clarify our understanding of the influence of the thermal barrier coatings.

Experimental

A schematic of the engine test cell is shown in Fig. 1 and specifications of this engine are listed in Table 1. As seen in the figure, the engine was coupled to a Clayton waterbrake dynamometer. The dynamometer torque was measured using a strain gauge load cell and the speed was monitored using a 60-tooth gear assembly. The exhaust, lube oil, and coolant tempera-

Table 1 Engine specifications

Parameter	Type / Value
Make	Yanmar
Model	TS180C
Type	Prechamber
No. of cylinders	1
Bore * stroke (mm)	102*106
Displacement (l)	.866
Continuous rating output (kW/rpm)	11.2/2200
Compression ratio (baseline)	19.5

Table 2 Engine test matrix

	Mode 1	Mode 2	Mode 3	Mode 4
Speed (RPM)	2200	2002	1760	1386
% Rated Speed	100	91	80	63
Power (HP)	12.26	8.77	5.32	2.03
% Rated Power	81.7	58.5	35.5	13.5

tures were also measured to monitor engine operation. The temperature of the exhaust gas was monitored with a type-K thermocouple mounted in the exhaust manifold. The data acquisition system was a Gateway 2000 P-5/100 MHz computer with a DAS-8/PGA data acquisition and control board from Keithley Metrabyte. The computer was set up to log real-time engine speed, engine torque, engine power, and exhaust, lube oil, and coolant temperatures.

The piston crown, cylinder head, and valves were given thin thermal barrier coatings (300 μm thick) by Turbine Components Corporation of Branford, CT. The parts were given a bond coat of NiCoCrAly, followed by a top coat of Metco prealloyed, yttria stabilized zirconia. The cylinder liner was not coated, as this would have raised significant tribological and coating durability concerns. No attempt was made to maintain a fixed compression ratio. Instead identical engine components were used where the only difference was the presence of the ceramic coating on the aforementioned surfaces. Assuming that the combustion chamber consists of a simple cylindrical surface, we estimate that the compression ratio changed from 19.5 to 21.6 between the baseline and ceramic-coated configurations. However, the actual difference in compression ratio was most likely negligible because the baseline (uncoated) engine acquired a significant carbon deposit during the break-in period, which would increase the baseline compression ratio. The Coordinating Research Council considers a ''trace to light'' combustion chamber deposit to be of 200 to 400 μm thickness (Megnin and Choate, 1994). During the break-in period, the ceramic-coated surfaces resisted formation of significant carbon deposits. So, the ''in-use'' compression ratios of the baseline and ceramic-coated engines were probably similar in magnitude. If the carbon deposit on the baseline engine increased to even a ''medium'' rating (1.59 mm), the ceramic-coated engine could result in lower ''in use'' compression ratio.

The test procedure was chosen so as to match the typical duty cycle of a diesel engine for marine applications. The International Standard (ISO 8178, Part 4) was consulted for guidance. Table 2 shows the test matrix used in this work. It is based broadly on cycle E3 (''Marine Applications,'' heavy-duty propulsion engines) described in ISO 8178, Part 4. There are four modes, a mode being a part of the test cycle with defined speed and torque.

A protocol was established to effect the changeover from the baseline (metal) configuration to the ceramic-coated configuration. The same piston rings and fuel injector were used for both configurations. However, for each changeover, the cylinder head gasket was replaced with a new (identical) gasket to ensure quality of the seal between the head and the cylinder block. The lube oil and coolant were also changed, although lubricant consumption was not monitored. The lube oil was SAE 10W-30 Motor Oil from Valvoline and the coolant was Prestone Antifreeze/Coolant. Each time the lube oil was changed, the engine was run for 8 hours to break in the new oil. The oil temperature in the engine typically took up to an hour to reach steady state. Thus, an hour-long warm-up period was always used to prepare the engine for testing. A low-sulfur Diesel fuel from BP Oil was used in all tests.

The gaseous portion of the exhaust was analyzed using the ENERAC Model 3000E Integrated Emissions System. The ENERAC gas analyzer is based on electrochemical sensors and measures NO, NO_2, CO, combustibles, SO_2 and O_2 concentrations. The ENERAC reports NO, NO_2, SO_2, and CO concentrations on a ''ppm'' basis and the O_2 and combustibles concentrations on a percent basis. The reported accuracy of the instrument is as follows: ±2 percent of the reading for NO, NO_2, and CO, and ±0,2 percent for O_2. The instrument continuously monitored these emissions and print-outs of values were taken three times during the ten minute test cycle to ensure that a steady state had been reached. In selected cases, CO and NO_x were also measured using a NICOLET Magna-IR 550 Spectrometer to allow a direct comparison to be made between the measurement techniques. These measurements were intended to help the Coast Guard evaluate the efficacy of using the ENERAC probe for shipboard emissions analysis.

Diesel exhaust particulates were collected on Pallflex TX40HI20WW filters using a Sierra Instruments Model BG-1 Micro-Dilution Test Stand. Basically, a dilution tunnel for diesel particulate sampling is designed to simulate the atmospheric dilution process. In a full dilution system the total exhaust gas flow from the engine is mixed with a quantity of dilution air. Such configurations are impractical and uneconomical for large engines that have very high exhaust flow rates. Therefore, there has been a trend towards micro-dilution systems which incorporate a fractional sampling device wherein only a portion of the total exhaust is extracted, diluted to achieve a maximum temperature of 52°C, then passed thorough a pair of filters (Diesel Progress, 1993).

The BG-1 allows for the specification of total flow rate and dilution flow rate. The total flow rate was set at 50.0 standard liters/minute (SLPM) and the dilution flow rate was set at 41.7 SLPM. These settings yield a sample flow rate of 8.3 SLPM, and, thus, a dilution rate of 5.0. Sierra Instruments quotes a precision of ±1.02 percent for the sample flow reading at a dilution ratio similar to the one employed in this experiment. The precision of the mass flow controllers was verified daily by performing an internal calibration check and, if necessary, recalibration.

Particulates were collected for ten minutes at each mode. The International Standard (ISO/DIS 8178-1.2) stipulates that the temperature of the collection filters should be below 52°C, a minimum of 2.3 mg of soot should be collected, the pressure drop increase during the test should not exceed 25 kPa, and the filters should not tear. The flowrates were adjusted by trial and error until these criteria were satisfied completely. All runs reported here complied with these requirements.

For each trial, two filters were used. Particulate was collected on the primary filter and the secondary filter served as a back up to collect any particulate that should pass through the primary filter. Particulate material was not found on the backup filter following any test. Before each test, the filter pairs were allowed to equilibrate in a humidity controlled environment of 45 percent relative humidity for at least one hour as per the ISO standard. The filter pairs were then weighed using a Sartorius microbalance with an accuracy of ±2 μg. After sampling the filters were again allowed to equilibrate in the humidity-controlled chamber and then weighed again.

Thermal analysis and electron microscopy of diesel particulates from this engine were performed using a Series 5100 Diesel Particulate Measurement System and a JOEL Scanning Electron Microscope, respectively. The Series 5100 Diesel Particulate Measurement System from R&P Co. was attached to the exhaust stack by means of a heated sample tube. The instrument cycle has two phases which are controlled by an instrument computer. During the collection phase, the system draws a sample of particulate-laden gas from the exhaust and routes it to a quartz filter. As the gas passes through the filter, particulate is trapped and filtered exhaust gas is vented out of the device. During the analysis phase, the collected sample is heated according to a user-defined temperature program. As the filter temperature increases, volatiles leave the filter, enter the gas

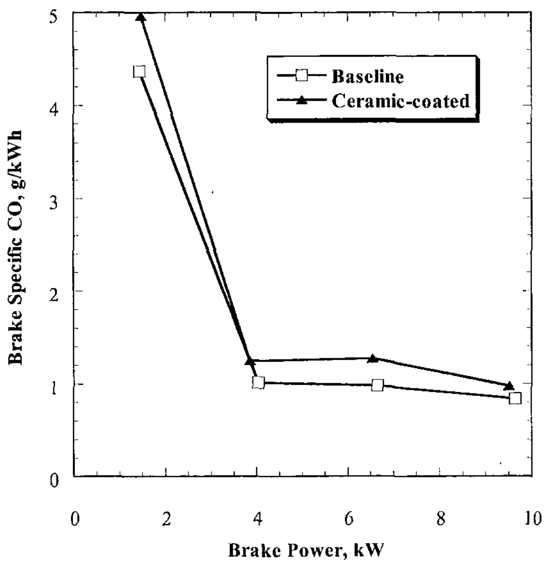

Fig. 2 Variation of brake specific carbon monoxide emissions with power for the baseline (□) and ceramic-coated (▲) configurations

stream, and travel to an afterburner set for 750°C. Oxidation of the carbonaceous materials produces CO_2, which is read by an NDIR CO_2 analyzer. The instrument computer converts the reading into a carbon concentration (mg of carbon per ml of exhaust gas collected). The collection and analysis parameters used in this work were as follows. Particulate-laden exhaust gas was sampled at a rate of 8.0 liters/min for 60 sec at engine operating Modes 1 and 2, and 120 sec at Modes 3 and 4. The collection temperature was 75°C. After collection, the filter temperature was ramped from 200 to 750°C at a rate of 5°C/min. The CO_2 concentration data at each temperature were downloaded from the instrument to a PC for graphing and analysis.

Three different scanning electron microscopes were used to examine particulate morphology, an ISI SX 40-ABT and an ISI SX 40 for preliminary analyses and a JEOL JSM-6300 FV for final analyses. The ISI SX 40-ABT was used first to perform an energy dispersive x-ray analysis (i.e., elemental analysis). The ISI SX 40 was then used to take photographs of the microscopic structure of the particulate sample (i.e., structural analysis). A JEOL JSM-6300 FV scanning electron microscope, equipped with a full function Oxford Instruments electron dispersive spectrometry (EDS) detector and analysis system, then was used to repeat both analyses with higher resolution. The results presented here were obtained on the JEOL SEM, which allowed magnification up to 120,000× compared to only 10,000× on the ISI SEMs.

To prepare the particulate samples for SEM analysis, the particulate laden Pallflex filters were dried for 1 h at 80°C under vacuum to remove moisture (this was performed after the total particulate mass was determined). Drying the filters at 80°C reduced the volatility of the particulate samples and enhanced the stability of the SEM probe and imaging system. Small quantities of particulate matter were placed on test stands to permit the SEM analysis. For the ISI SEM, a carbon test stand was used. For the JEOL SEM, an aluminum test stand was used. In both situations, a vacuum safe double-sided adhesive tape was used to mount the particulate samples on the test stands. In order to take photographs with the scanning electron microscopes, it was necessary to coat the samples with gold, a conducting medium. This was done by using a BIO-RAD SC500 sputter coater.

Results and Discussion

Results are presented on a brake specific basis (per kWh) and are presented against engine output (kW). Note that mode

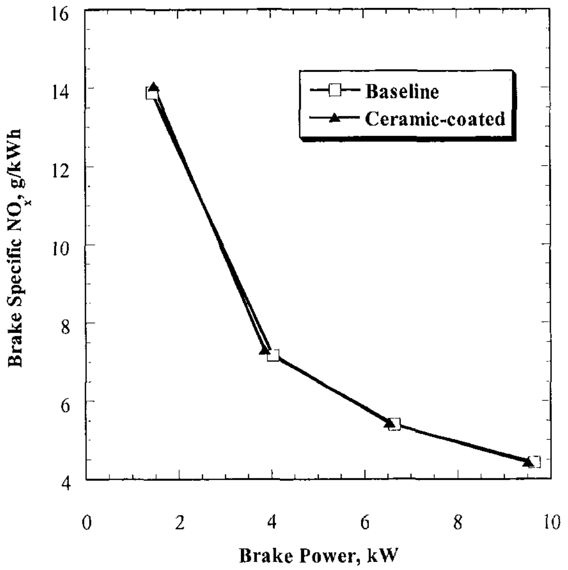

Fig. 3 Variation of brake specific NO_x emissions with power for the baseline (□) and ceramic-coated (▲) configurations

1 represents a high speed/high load condition, with load and speed decreasing with increasing Mode number. Emissions of CO and NO_x exhibited the same trends for both the baseline and ceramic-coated engines. As shown in Fig. 2, brake specific CO emissions decreased sharply from Mode 4 to Mode 3 (i.e., as load increases), and slightly thereafter. Brake specific NO_x emissions decreased with increasing power as shown in Fig. 3. For all modes, CO emissions were higher for the ceramic-coated engine, while NO_x emissions were the same for both configurations. The exhaust temperature (Fig. 4) was higher for the ceramic-coated engine over the full range of power settings.

It was expected that CO emissions would be lower for the ceramic-coated engine since the higher temperatures of the combustion gas and chamber walls should increase the rate of oxidation reactions leading to the complete combustion product, CO_2 (Thring, 1986). However, for all modes there was a slight increase in brake specific (BS) CO emissions for the ceramic-coated engine. Higher CO concentrations were also reported by researchers at the Southwest Research Institute (Dickey, 1989)

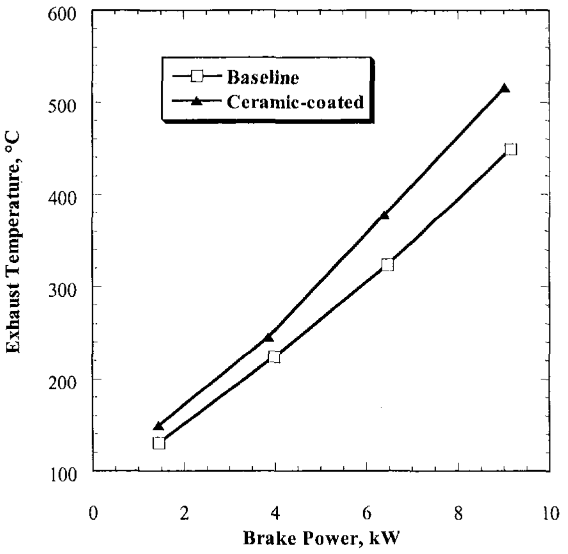

Fig. 4 Variation of exhaust temperature with power for the baseline (□) and ceramic-coated (▲) configurations

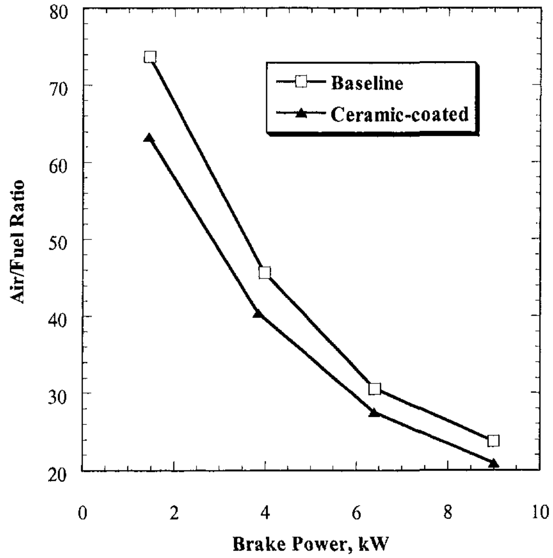

Fig. 5 Variation of air/fuel ratio with power for the baseline (□) and ceramic-coated (▲) configurations

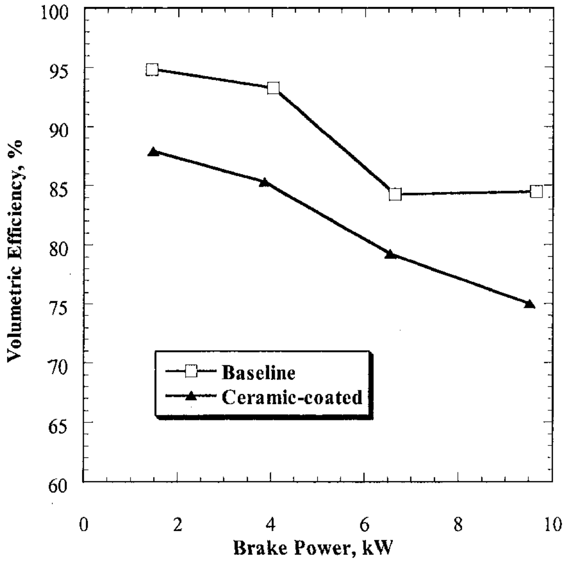

Fig. 7 Variation of volumetric efficiency with power for the baseline (□) and ceramic-coated (▲) configurations

for an LHR engine at high loads. One potential explanation lies in the strong relationship between CO emissions and the air/fuel ratio. As the air/fuel ratio decreases, CO emissions increase, particularly below stoichiometric (Heywood, 1988). Figure 5 shows the variation of air/fuel ratio for the baseline and ceramic-coated engines. It is clear that for all modes the air/fuel ratio was lower for the ceramic-coated engine, thus explaining the higher CO concentrations in the exhaust. However, the sharp increase in BSCO emissions at mode 4 for both configurations is harder to explain. Since diesel engines always operate on the lean side of stoichiometric, one would expect that CO emissions should vary little with air/fuel ratio. It is possible that combustion at this mode was highly degraded because of lower temperatures resulting in slower kinetics. This is also borne out by Fig. 6 which shows that the brake specific fuel consumption for mode 4 was inordinately high in both cases.

The thermal barrier coating caused no significant change in the brake specific NO_x emissions. There was a marked decrease in $BSNO_x$ in both cases as power was increased. It may be expected that the ceramic-coated engine would have higher NO_x emissions due to the higher combustion temperatures and indeed other researchers have found an increase in NO_x emissions for LHR engines (Siegla and Alkidas, 1989). However, NO_x emissions are a function of both temperature and pressure of the burned gas. On the one hand, the higher temperatures in the LHR engine accelerate NOx formation. On the other hand, the shift from premixed to diffusion combustion in the LHR engine results in lower peak pressures (Assanis et al., 1991). Due to these two competing factors, there may be a trade-off between the temperature and pressure effects on the NO_x formation rate. The most likely explanation for the observed consistency in NO_x emissions from the baseline and ceramic-coated engine arises from the IDI engine configuration. As noted by Heywood (1988), most of the NO forms within the prechamber and is then transported into cylinder where the NO concentration is frozen through rapid mixing with the surrounding air. The prechamber was not given a TBC coating, and thus the opportunity for differences to arise between the two engine configurations, with regard to NO_x emissions was reduced.

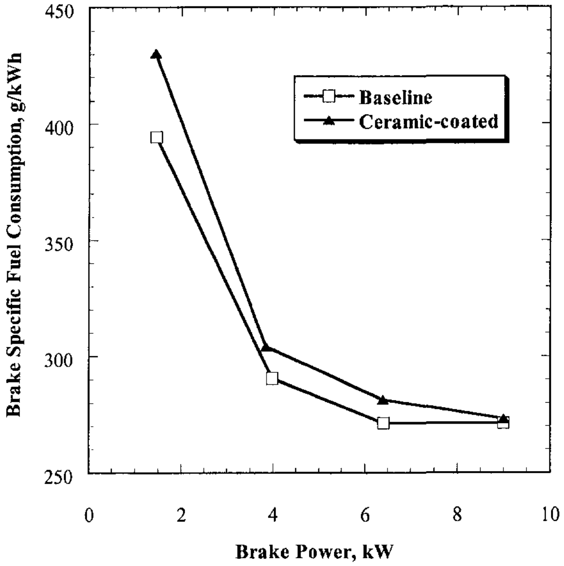

Fig. 6 Variation of brake specific fuel consumption (BSFC) with power for the baseline (□) and ceramic-coated (▲) configurations

The decrease in $BSNO_x$ with increased power may appear to be counter intuitive since NO_x levels generally increase with decreasing air/fuel ratios that accompany increases in power (Heywood, 1988). However, in diesel combustion much of the fuel burns at near stoichiometric conditions, and, thus, the effect of air/fuel ratio is minimized. Thus, provided changes in pressure and temperature do not greatly affect the level of emissions, NO_x should be proportional to the mass of fuel injected (Heywood, 1988). This is supported by the correspondence between the BSFC and $BSNO_x$ trends in Figs. 3 and 6.

The volumetric efficiency was determined using the oxygen concentrations provided by the gas analysis. This result is shown

Table 3 Comparison between ENERAC 3000E and Nicolet Magna 500 FTIR spectrometer measurements on baseline engine

Species	NO (ppm)	CO (ppm)
Mode 1		
ENERAC	471	138
FTIR	440	228
Mode 4		
ENERAC	296	170
FTIR	239	220

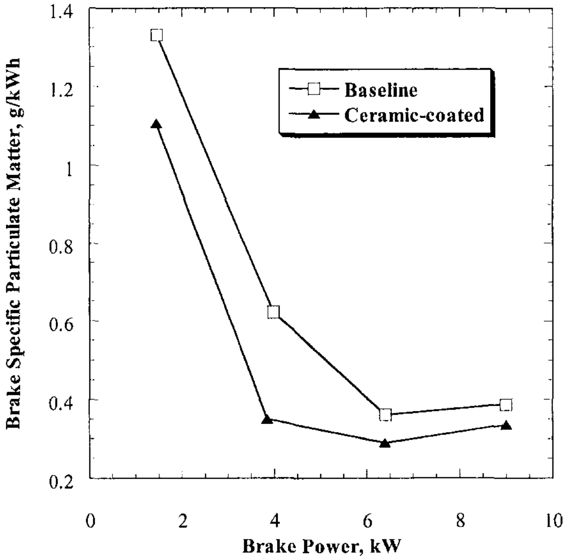

Fig. 8 Variation of brake specific particulate matter emissions with power for the baseline (□) and ceramic-coated (▲) configurations

in Fig. 7. For both the ceramic-coated and baseline engines, the volumetric efficiency decreased with increased power. The volumetric efficiency of the ceramic-coated engine was lower in all operating modes due to higher in-cylinder temperatures.

The CO and NO measurements provided by the ENERAC were compared against those determined using FTIR spectrometry (Table 3). Using quick-connects, the ENERAC's probe was simply reconfigured to send a sample to the gas cell of the FTIR. The ENERAC's probe consists of the sampling tube, a small pump and a desiccant pack to dry the sample gas. The effluent from the probe was directly routed to the FTIR spectrometer, and in this manner, gas samples with the same pretreatment history were passed to both analyzers. The discrepancy between the FTIR and ENERAC measurements CO and NO cannot be explained at this time, and requires further study. The EPA has issued a conditional certification for the ENERAC 3000E. The difficult challenge of performing exhaust gas analyses on-board maritime vessels necessitates the use of portable analyzers such as the ENERAC, so additional study of these discrepancies is warranted.

The EPA defines particulates as solid or liquid (except for water) that collects on a filter at or below 52°C (Amann, 1988). Diesel particulates are made up primarily of carbonaceous soot with some adsorbed hydrocarbons. Particulate formation in diesel engines is a complex and not fully understood process. From

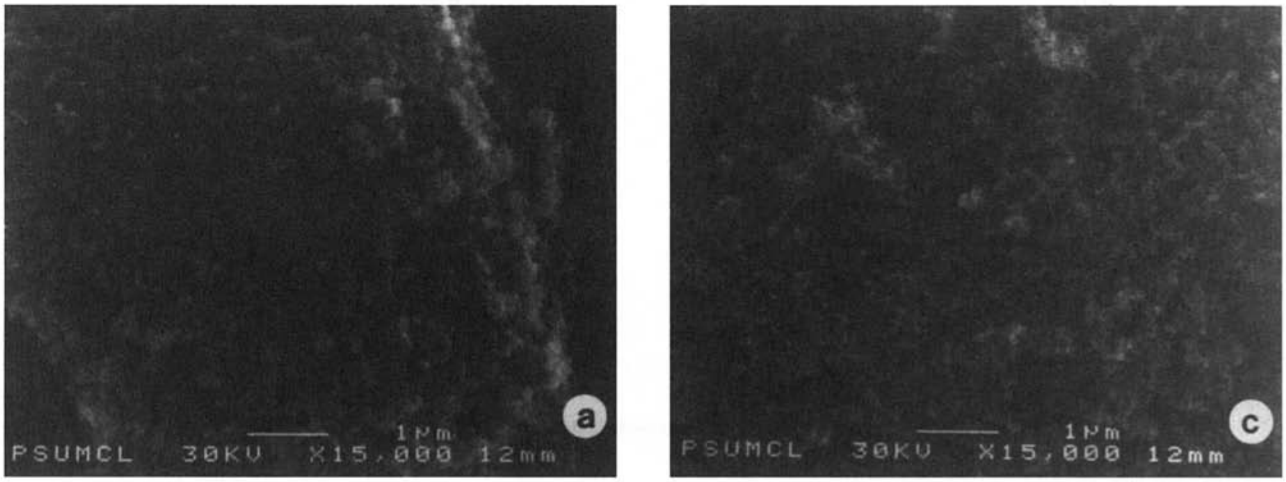

MODE 1 - Uncoated Engine

MODE 1 - Thermal Barrier Coated Engine

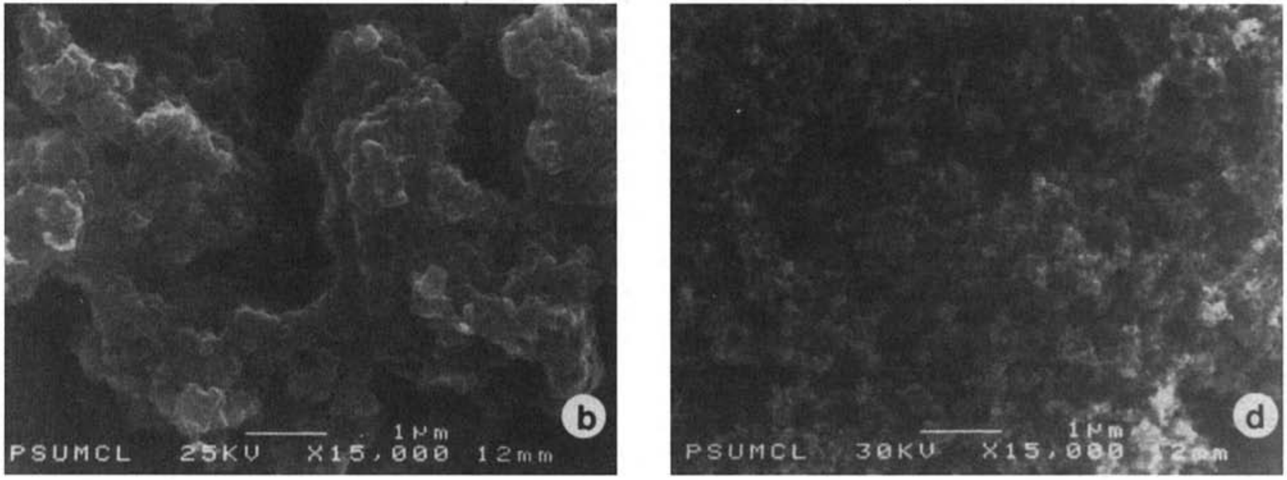

MODE 4 - Uncoated Engine

MODE 4 - Thermal Barrier Coated Engine

Fig. 9 SEM Micrographs of particulate matter from the uncoated and thermal barrier coated engine, at 15,000× magnification for two engine operating conditions

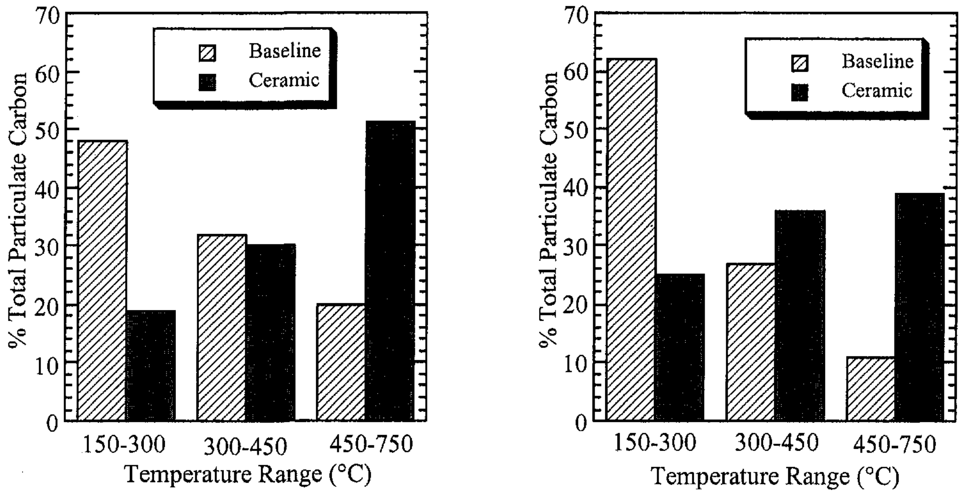

(a) Mode 1 (9.1 kW, 2200 RPM)

(c) Mode 3 (4.0 kW, 1760 RPM)

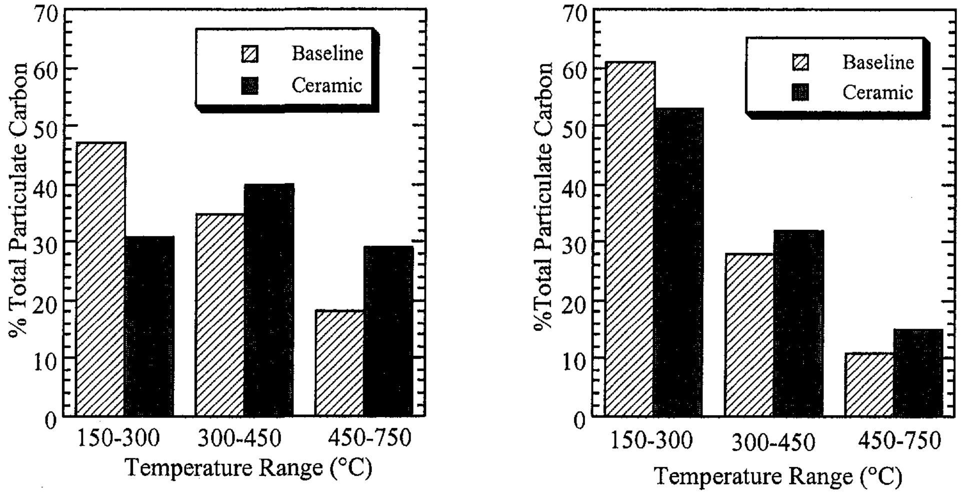

(b) Mode 2 (6.5 kW, 2000 RPM)

(d) Mode 4 (1.5 kW, 1390 RPM)

Fig. 10 Compositional difference between exhaust particulates from the baseline and ceramic-coated engine configurations

what is known, soot formation can be considered to occur in four stages: nucleation, surface growth, agglomeration, and adsorption/condensation (Heywood, 1988). The mass of soot in the exhaust gas is a function of the relationship between formation and oxidation. Both formation and oxidation rates are increased in the coated engine due to the higher temperatures and improved air to fuel mixing (Alkidas, 1989). In the case of most LHR engines, the increase in oxidation rate is greater than the increase in formation rate.

The higher oxidation rates led to decreased brake specific particulate matter emissions in the ceramic-coated engine as shown in Fig. 8. At light loads (modes 3 and 4) the decrease in particulate emissions from the ceramic-coated engine (relative to the baseline engine) was greater than at high loads (modes 1 and 2). This is because at light loads a greater fraction of the fuel energy is lost to the coolant (Amann, 1988). Thus, the decrease in energy rejection to the coolant due to the ceramic coating is greater at lighter loads, and a larger decrease in particulate emissions is realized.

The increased oxidation rates are a direct consequence of the insulation provided by the ceramic coating, and appear to affect the amount of condensable hydrocarbons that bind the primary soot and soot aggregate particles together. This conclusion is supported (for the engine used in the present study) by the reduction in particulate mass, by analyses of particulate morphology and by thermal analyses of particulate composition. For the baseline engine, the structure of the mode 4 (low load) particulate matter showed significant agglomeration of primary soot particles into layers bound by condensed hydrocarbons, as shown in Fig. 9(*a*). For the ceramic-coated engine, the structure of mode 4 particulates was more granular (Fig. 9(*b*)), wherein the primary soot particles had aggregated into smaller structures and more closely resembled the particulate matter from mode 1 (high load) in Figs. 9(*c*) and 9(*d*). Furthermore, as shown in Figs. 10(*a–d*), thermal analysis of the particulate matter demonstrates that the ceramic-coated engine shifts the composition of the particulate matter toward more dry soot and less volatile content. This shift is especially evident in mode 1 (Fig. 10(*a*)) where the largest shift from volatile to dry soot content is observed.

Conclusions

The data and observations reported here support the following conclusions for the single cylinder IDI diesel engine used in this study. Over the four mode ISO 8178 type E3 test, thermal barrier coatings: increased CO emissions slightly; increased the exhaust temperature; increased specific fuel consumption; decreased the air/fuel ratio; and reduced particulate emissions on both a raw and a brake-specific basis. The decrease in particulate mass emissions is largest at lower load conditions, due to reduced heat rejection to the coolant, and a corresponding increase in oxidation of soot and condensable hydrocarbon species. Both thermal and morphological analysis of the particulate matter support the conclusion that oxidation of condensable hydrocarbons is a primary reason for the reduction in particulate mass emissions. In addition, additional work is needed to determine the source of the discrepancies between FTIR and ENERAC gas analyzers. While the NO measurements were in relatively good agreement, the CO measurements were not. If this portable system is to be used for on-board exhaust analyses for marine diesel vessels, these discrepancies should be addressed.

Acknowledgments

The authors wish to thank the Coast Guard R&D Center for its "in-kind" support of this work. The authors wish to acknowledge support received from the Fuel Science Program, the Department of Materials Science and Engineering, and the College of Earth and Mineral Science at Penn State. Also, the authors wish to thank Dr. Rafal Sobotowski of BP Oil Company, Cleveland, OH, who supplied fuels for this research project.

References

Amann, C. A., 1988, "The Low-Heat-Rejection Diesel (Also Called the 'Adiabatic Diesel')," in *Advanced Diesel Engineering and Operation*, S. D. Haddad, ed., Ellis Horworth, Chichester, UK, pp. 173–239.

Alkidas, A. C., 1989, "Performance and Emissions Achievements With an Uncooled Heavy-Duty Single Cylinder Diesel Engine," SAE Technical Paper 890144.

Arai, M., 1993, "Thermal Analysis for the Evaluation of SOF Oxidation Temperature by Diesel Catalyst," SAE Technical Paper 930134.

Assanis, D., Wiese, K., Schwarz, E., and Bryzik, W., 1991, "The Effects of Ceramic Coatings on Diesel Engine Performance and Exhaust Emissions," SAE Technical Paper 910460.

Bagley, S. T., Baumgard, K. J., Gratz, L. D., Johnson, J. H., and Leddy, D. G., 1996, "Characterization of Fuel and Aftertreatment Device Effects on Diesel Emissions," Health Effects Institute, Research Report No. 76, Cambridge, MA.

Brindley, W. J., 1995, "Foreword," Proceedings, Thermal Barrier Coating Workshop, March 27–29, 1995, NASA Conference Publication 10170, National Technical Information Service, Washington, D.C., p. iii.

Bryzik, W., and Kamo, R., 1983, "TACOM/Cummins Adiabatic Engine Program," SAE Technical Paper 830314.

Cuthbertson, R. D., Stinton, H. C., and Wheeler, R. W., 1979, "The Use of a Thermogravimetric Analyser for the Investigation of Particulates and Hydrocarbons in Diesel Engine Exhaust," SAE Technical Paper 790814.

Dickey, D. W., 1989, "The Effect of Insulated Combustion Chamber Surfaces on Direct-Injected Diesel Engine Performance, Emissions and Combustion," SAE Technical Paper 890292.

Docekal, B., Krivan, V., and Pelz, N., 1992, "Trace and Minor Element Characterization of Diesel Soot," *Fresenius Journal of Analytical Chemistry*, Vol. 343, pp. 873–878.

Fairbanks, J. W., 1995, "Thermal Barrier Coatings Application in Diesel Engines," Proceedings, Thermal Barrier Coating Workshop, March 27–29, 1995, NASA Conference Publication 10170, National Technical Information Service, Washington, D.C., p. 11.

Gibson, J., and Groene, O., 1991, "Selective Catalytic Reduction on Marine Diesel Engines," *Automotive Engineering*, Vol. 99, pp. 19–88.

Health Effects Institute, 1993, *Research Priorities For Mobile Air Toxics*, HEI Communications Number 2, Health Effects Institute, Cambridge, MA.

Heywood, J. B., 1988, *Internal Combustion Engine Fundamentals*, McGraw-Hill, New York, pp. 567–596.

Hippeli, S. C., and Elstner, E. F., 1990, "Influence of Diesel Soot Particles and Sulfite on Functions of Polymorphonuclear Leukocytes," *Free Rad. Res. Comms.*, Vol. 11, pp. 29–38.

International Standards Organization, 1992, "ISO 8178-4, RIC Engines—Exhaust Emission Measurement; Part 4: Test Cycles for Different Engine Applications," Working Document.

Johnson, J. H., Bagley, S. T., Gratz, L. D., and Leddy, D. G., 1994, "A Review of Diesel Particulate Control Technology and Emission Effects—1992 Horning Memorial Award Lecture," SAE Technical Paper 940233.

Kamo, R., Assanis, D. N., and Bryzik, W., 1989, "Thin Thermal Barrier Coatings for Engines," SAE Technical Paper 890143.

Karaszewski, Z. J., and Schaefer, W. F., 1991, "Marine Diesel Propulsion Plants for the U.S. Navy: Requirements for Geared Medium-Speed Engines," *Marine Technology*, Vol. 28, pp. 276–301.

Lies, K. H., Hartung, A., Postulka, A., Gring, H., and Schultz, J., 1989, "Carcinogenic and Mutagenic Effects of Diesel Engine Exhaust," Proceedings, International Satellite Symposium, Toxic Effects of Emissions from Diesel Engines, Tsukubaka, Japan, pp. 65–84.

Marks, D. A., and Boehman, A. L., 1997, "The Influence of Thermal Barrier Coatings on Morphology and Composition of Diesel Particulates," SAE Technical Paper 970756.

Megnin, M. K., and Choate, P. J., 1994, "Combustion Chamber Deposit Measurement Techniques," SAE Technical Paper 940346.

Neeft, J. P. A., Makee, M., and Moulijn, J. A., 1996, "Diesel Particulate Control," *Fuel Processing Technology*, Vol. 47, pp. 1–69.

Okrent, D. A., 1996, "Description of an On-Line Method for Measuring the Ratio of Soot to Organics in Diesel Exhaust Particulates," SAE Technical Paper 960252.

Shore, P. R., and Cuthbertson, R. D., 1985, "Application of a Tapered Element Oscillating Microbalance to Continuous Diesel Particulate Measurement," SAE Technical Paper 850405.

Siegla, D. C., and Alkidas, A. C., 1989, "Evaluation of the Potential of a Low-Heat-Rejection Diesel Engine to Meet Future EPA Heavy-Duty Emission Standards," SAE Technical Paper 890291.

Thring, R. H., 1986, "Low Heat Rejection Engines," SAE Technical Paper 860314.

Vittal, M., Borek, J. A., Boehman, A. L., and Okrent, D. A., 1997, "The Influence of Thermal Barrier Coatings on the Composition of Diesel Particulate Emissions," SAE Technical Paper 972958.

Voss, K., Cioffi, J., Gorel, A., Norris, M., Rotolico, T., and Fabel, A., 1997, "Zirconia Based Ceramic, In-Cylinder Coatings and Aftertreatment Oxidation Catalysts for Reduction of Emissions from Heavy Duty Diesel Engines," SAE Technical Paper 970469.

Zinbo, M., Korniski, T. J., and Weir, J. E., 1995, *Ind. Eng. Chem. Res.*, Vol. 34, p. 619.

Zinbo, M., Skewes, L. M., Hunter, C. E., and Schuetzle, D., 1990, *Thermochim. Acta*, Vol. 166, p. 267.

A Contribution to the Analysis of Turbulence Anisotropy and Nonhomogeneity in an Open-Chamber Diesel Engine

E. Spessa
Dipartimento di Energetica,
Politecnico di Torino,
Torino, Italy

Further investigation of the turbulence time-frequency spectral structure and its anisotropy and nonhomogeneity has been carried out in the combustion chamber of an automotive diesel engine with a high-squish reentrant in-piston-bowl and a helical intake port. An advanced HWA technique was applied for turbulence measurements along the injector axis, under motored engine conditions in the speed range of 600–3000 rpm. Autospectral density functions of each fluctuating velocity component, as was determined by a specific sensor-wire orientation, were evaluated in consecutive crank-angle correlation intervals during the induction, compression, and early expansion strokes. In order to study the speed dependence of the turbulence-structure anisotropy and nonhomogeneity in different portions of the engine cycle, time-scales of cycle-resolved and conventional turbulent fluctuations were analyzed as functions of the engine speed for different wire orientations, measurement locations, and correlation intervals. Anisotropy and nonhomogeneity were generally significant at low engine speeds, whereas a tendency towards isotropy and homogeneity was found by increasing the speed. With specific reference to the bowl-generated turbulence, spectral anisotropy was remarkable at all speeds in the reverse-squish flow, close to the cylinder-head wall. However, spectral nonhomogeneity was the main feature of the direct-squish flow at low engine speeds.

Introduction

In-cylinder turbulence characteristics are significantly coupled with combustion in spark ignition engines (Daneshyar and Hill, 1987; Floch et al., 1995) and also with fuel-air mixing in diesel engines (Ikegami, 1990; Timoney and Smith, 1996; Smith and Timoney, 1997). Magnussen and Hjertager (1976), Heywood (1988), Smith and Timoney (1997) showed that the combustion rate is affected by the dissipation rate of eddies, and that the fluctuating motion plays a major role in fuel-air mixing in high-speed direct-injection (DI) engines. Besides, high-frequency and intense turbulence can be useful in DI automotive diesel engines at the latest combustion stages, so as to enhance the mixing of soot-particle-laden regions with the excess air and to promote their burn up (Konno et al., 1992). Therefore, experimental investigation of in-cylinder turbulence properties is of great interest to develop advanced combustion systems for automotive DI engines. Owing to the difficulties of taking velocity measurements in real-engine geometry and operating conditions, results obtained in unmodified production engines under motored conditions can be of high technical-scientific value (Lancaster et al., 1976; Catania et al., 1992a; Witze, 1994; Catania et al., 1995).

In-cylinder flow studies have been carried out using both hot wire anemometry (HWA) and laser Doppler velocimetry (LDV). Comments on the advantages and drawbacks of HWA versus LDV are reported by Catania et al. (1992a, 1995). However, the very high frequency response of HWA and its capability of giving a continuous velocity signal in each engine cycle, make this technique appropriate for cycle-resolved and time-frequency spectral analysis of turbulence, particularly at high speeds and when the velocity-data acquisition is not restricted to small parts of the engine cycle. Besides, any probe-induced flow perturbation may be negligible, even for turbulence intensity and frequency (Catania et al., 1995; Spessa, 1995).

The present work is part of a research program (Catania et al., 1992a; Catania et al., 1995) aimed at investigating the distinct and combined effects of intake and combustion systems on the fluid dynamics of new automotive engine concepts, with specific reference to in-cylinder turbulence properties and their control at the end of the compression stroke. The paper deals with a further investigation of the turbulence-structure anisotropy and nonhomogeneity in the combustion chamber of an automotive diesel engine with a reentrant in-piston bowl and a helical intake duct, under motored conditions. An advanced HWA technique, using homemade single and multiple-sensor probes (Catania et al., 1994; Spessa, 1995) was applied for instantaneous air-velocity measurements in a crank-angle interval ranging from 30 deg before the intake-stroke TDC to 60 deg after the compression-stroke TDC. Therefore, it was possible to study the direct and reverse-squish flows that were produced by the bowl. The instantaneous velocity measurements of Catania and Spessa (1996), Catania et al. (1996) were completed and analyzed in the speed range of 600–3000 rpm, at the distances of 2 mm, 5 mm, and 9 mm from the cylinder-head wall along the injector axis, for the three wire orientations in the radial, tangential, and axial directions of the cylinder reference frame.

The spectral analysis of the nonstationary engine turbulence was performed by evaluating the average statistical properties of turbulence in the crank-angle correlation intervals which the fluctuation data records were divided into (Catania and Mittica; 1990). The anisotropy and nonhomogeneity of the turbulence time-frequency spectral structure as well as their speed dependence throughout the engine cycle were studied by analyzing the autospectra and time scales of cycle-resolved and conventional turbulence components, which were determined from the differently oriented wires at the considered measurement locations.

Contributed by the Internal Combustion Engine Division and presented at the 19th Fall Technical Conference of the ASME Internal Combustion Engine Division, Madison, Wisconsin, September 27–October 1, 1997. Manuscript received by the ASME Headquarters July 16, 1998. Associate Technical Editor: D. Assanis.

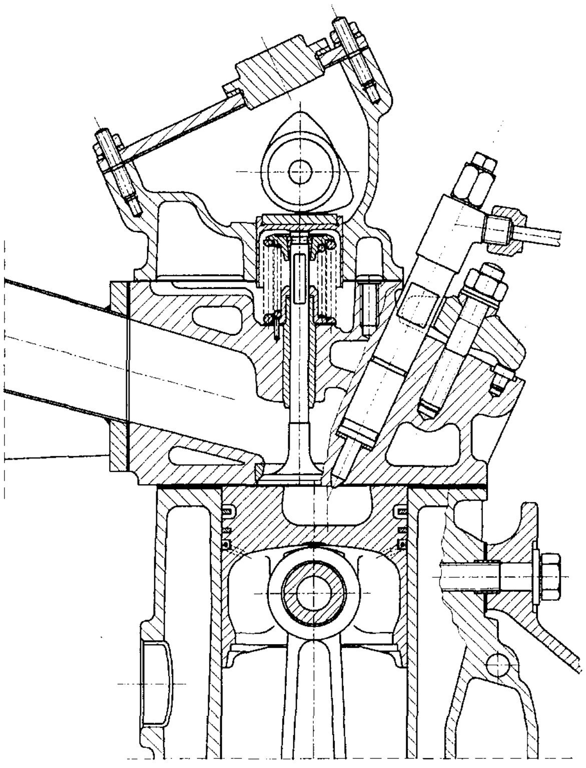

Fig. 1 Test engine

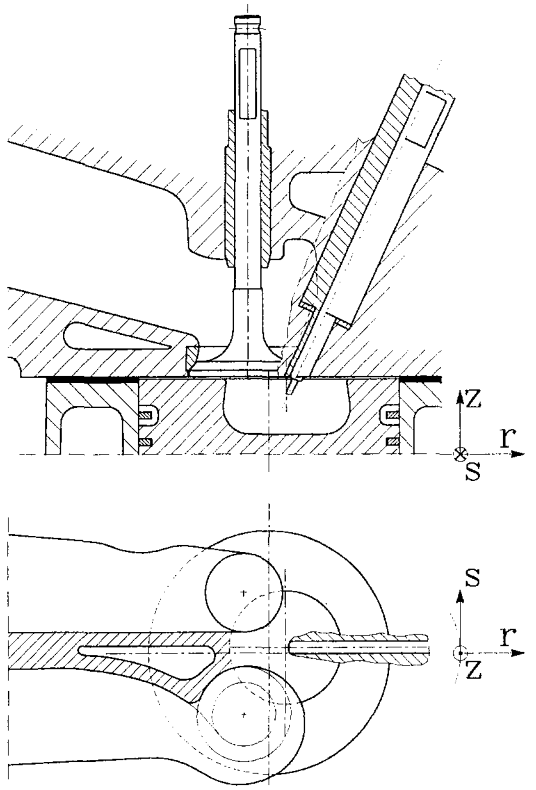

Fig. 2 Schematic of the engine with probe setup

Measurement Equipment and Procedure

Test Engine. The tested engine (Figs. 1 and 2) was the four-stroke, direct-injection single cylinder reported by Catania et al. (1995) and Spessa (1995). It was derived from an automotive diesel engine at the Fiat Research Center. The engine had a high-squish reentrant in-piston bowl of the conical type (Fig. 2(*a*)) and a helical inlet port (Fig. 2(*b*)). Figure 3 shows the measurement locations in the combustion bowl with their distances from the cylinder-head wall.

The main engine specifications are as follows:

displacement:	427 cm^3
bore:	79.5 mm
stroke:	86 mm
compression ratio:	18
connecting rod length:	140.5 mm
inlet valve diameter:	31.5 mm
maximum inlet valve lift:	8.1 mm
inlet valve opening:	5 deg BTDC
inlet valve closure:	55 deg ABDC
exhaust valve opening:	55 deg BBDC
exhaust valve closure:	5 deg ATDC
speed range:	600–3500 rpm
swirl ratio:	3.5

The engine was driven by an electrical motor through a speed regulator of the belt type.

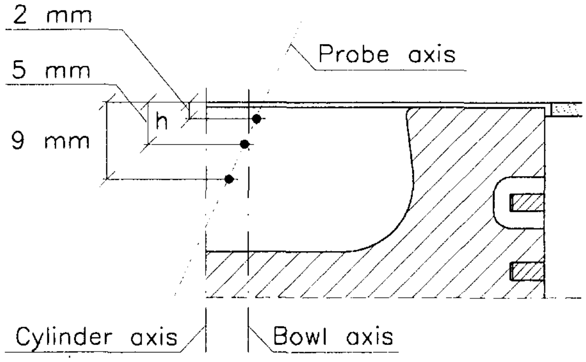

Fig. 3 Measurement locations

Nomenclature

E = normalized autospectral density function
f = frequency
h = measurement location distance from cylinder head
n = engine speed
r, s, z = reference directions
R = autocorrelation coefficient
t = time
T = time interval
u = turbulence fluctuation
u' = turbulence intensity
$\tilde{u}$ = low-frequency velocity fluctuation
w = window function
δ_τ = micro time-scale of cycle-resolved turbulence
ϵ = ensemble-average of cycle-resolved turbulence
λ_τ = micro time-scale of conventional turbulence
Λ_τ = macro time-scale of conventional turbulence
τ = separation time
θ = crank angle
Θ, Φ = crank-angle interval

Subscripts

0 = reference quantity
E = ensemble average
i = index referring to engine cycle
uu = cycle-resolved turbulence
$u_E u_E$ = conventional turbulence

HWA Data Acquisition and Processing. The anemometric probe (Fig. 2) was accommodated in the injector seat so that the probe axis was coincident with the injector axis. The measurement location could be changed by means of a micrometric device, allowing for sensor-wire displacement along the injector axis with an accuracy of ±0.05 mm.

The experimental technique, which was based on a constant-temperature HWA, and the probes used in this study were detailed by Spessa (1995). The probe sensing wires were oriented along the radial (r), tangential (s), and axial (z) directions in the reference frame of Fig. 2.

Since the anemometer output voltage depends on the heat exchange between the sensor wire and its environment, it was necessary to measure the in-cylinder gas pressure and temperature, as well as the prong-tip temperature, in addition to the air velocity. The pressure was taken by a piezoelectric transducer housed in the glow plug seat. For the gas temperature, the same anemometric probe was alternately used as a thermometric one, owing to the high repeatability of the temperature trace (Catania et al., 1995; Spessa, 1995). The prong-tip temperature, where the sensing wire is welded, was measured by means of a thermocouple, one of its leads being a prong.

An automatic system was used for high-frequency in-cylinder data acquisition (Spessa, 1995). It was equipped with a high-speed memory buffer and three 12-bit analog-to-digital converter cards for the contemporary acquisition of three signals. The acquisition process was governed by a crank-shaft driven encoder, which was provided with 1800 angular divisions, generating an impulse every 0.2 crank-angle degrees. An acquisition controller was interfaced with the system and the data capture was managed by a specifically developed software. The maximum sample rate was 500 kHz, 190 kHz, or 120 kHz per channel conforming to data acquisition from one, two, or three different sources, respectively, at the same time.

The instantaneous velocity U_i sensed by the wire was computed from the anemometer output signal by means of the analytical-numerical method detailed by Catania et al. (1995) and by Spessa (1995), which is based on the heat transfer equations for the anemometric and thermometric wires. This technique allows one to avoid the almost impracticable calibration of each probe for each condition of gas pressure and temperature as well as of prong temperature in the engine environment.

Turbulence Spectral Analysis

The definitions of nonstationary turbulence statistical properties and the procedures for their evaluation and analysis in an engine cylinder were developed, detailed, and discussed elsewhere (e.g., Catania and Mittica, 1989, 1990; Catania et al., 1992a). Those of interest for the present study are recapitulated in what follows.

Velocity Fluctuations. Both cycle-resolved and conventional turbulence were considered for investigation. The time-average filtering (TAF) procedure (Catania and Mittica, 1989, 1990) was applied to each instantaneous-velocity data record in order to separate the in-cycle nonstationary mean velocity from the turbulent fluctuation about it, within the cycle-resolved analysis. This procedure is based on the interpolation of the mean value obtained by time averaging the velocity in consecutive crank-angle intervals throughout the engine cycle, so as to yield a cycle-resolved turbulent fluctuation with a zero mean value, either as a time or virtually as an ensemble-averaged value. Ensemble averaging of the instantaneous velocity was used for conventional data reduction. The turbulent fluctuation about the ensemble-averaged velocity will be referred to as the instantaneous velocity fluctuation or the conventional turbulence.

The following decomposition was applied to the instantaneous velocity fluctuation $u_{i,E}(t)$ (Catania and Mittica, 1989; Catania et al., 1992a)

$$u_{i,E}(t) = u_i(t) + \tilde{u}_i(t) - \epsilon(t) \approx u_i(t) + \tilde{u}_i(t), \qquad (1)$$

where $u_i(t)$ is the cycle-resolved turbulent fluctuation, $\tilde{u}_i(t)$ is the so-called low-frequency cyclic fluctuation of the mean velocity, and $\epsilon(t)$, which is the ensemble average of $u_i(t)$, is a negligible term, depending on the filtering procedure used (Catania and Mittica, 1989).

Time-Frequency Spectral Functions. The Eulerian temporal autocorrelation coefficient of the cycle-resolved turbulent fluctuation $u_i(t)$ in the period T, centered on the instant t_0, can be defined as (Catania and Mittica, 1990)

$$R_{uu}(T, t_0, \tau) = \frac{1}{u'^2}\left\langle \frac{1}{T-\tau}\int_{t_0-T/2+\tau/2}^{t_0+T/2-\tau/2} u_i(t-\tau/2)u_i(t+\tau/2)dt \right\rangle . \qquad (2)$$

The separation-time variable τ in the correlation interval T ranges from zero to $\tau_{\max} = T/2$. The factor u'^2, normalizing the autocorrelation function to unity at $\tau = 0$, is the square of the cycle-resolved turbulence intensity u' in T

$$u' = \sqrt{\langle \overline{u_i^2} \rangle} . \qquad (3)$$

The overscore is used to indicate a short time-averaging operation (Catania and Mittica, 1989). The brackets $\langle\ \rangle$ designate an ensemble average over a large number of sample records. The autocorrelation coefficient given by Eq. (2), being an even function of τ independent of the instant t in the period T, makes the standard approach for stationary flows (Bendat and Piersol, 1986) suitable for the spectral analysis of nonstationary turbulence in the subrecords into which the fluctuation data record is divided.

The normalized energy spectral density function of $u_i(t)$ in T can thus be obtained from Eq. (2) in the form

$$E_{uu}(T, t_0, f) = 4\int_0^{\tau_{\max}} R_{uu}(T, t_0, \tau)w(\tau)\cos(2\pi f\tau)d\tau, \qquad (4)$$

where f is the frequency, and $w(\tau)$ is a window function of the rectangular or Hamming type. In order to analyze the temporal variation of the turbulence structure, the engine cycle was divided into consecutive correlation crank-angle intervals Φ, each corresponding to the period T in Eqs. (2) and (4). The interval Φ should be long enough to provide statistical validity of the results, but, at the same time, short enough to include a negligible effect of turbulence time dependence. Based on the results of previous studies (Catania and Mittica, 1990; Catania et al., 1992a), an interval $\Phi = 60$ deg was used for turbulence spectral analysis.

Although Eqs. (2), (3), and (4) are written for the cycle-resolved turbulent fluctuation, similar expressions can be derived (Catania et al., 1992a) for any of the other terms in Eq. (1). The symbols $R_{u_E u_E}$ and $E_{u_E u_E}$ (the dependence on time variables is omitted for simplicity) express the autocorrelation and autospectral coefficients of $u_{i,E}(t)$, respectively.

Eulerian Scales. The micro time scale of $u_i(t)$ in T is given by (Catania and Mittica, 1990)

$$\delta_\tau(T, t_0) = \frac{1}{\sqrt{2\pi^2\int_0^{f_{\max}} f^2 E_{uu}(T, t_0, f)df}}, \qquad (5)$$

where $f_{\max}$ is the maximum frequency for which $E_{uu}(T, t_0, f)$ is still finite and significant ($f_{\max}$ is less than or at least equal to the Nyquist frequency associated to the sample data). This parameter can be considered to be an average statistical measure of the most rapid changes that occur in the fluctuations of $u_i(t)$ during the period T and, therefore, it is directly related to the highest turbulence frequencies.

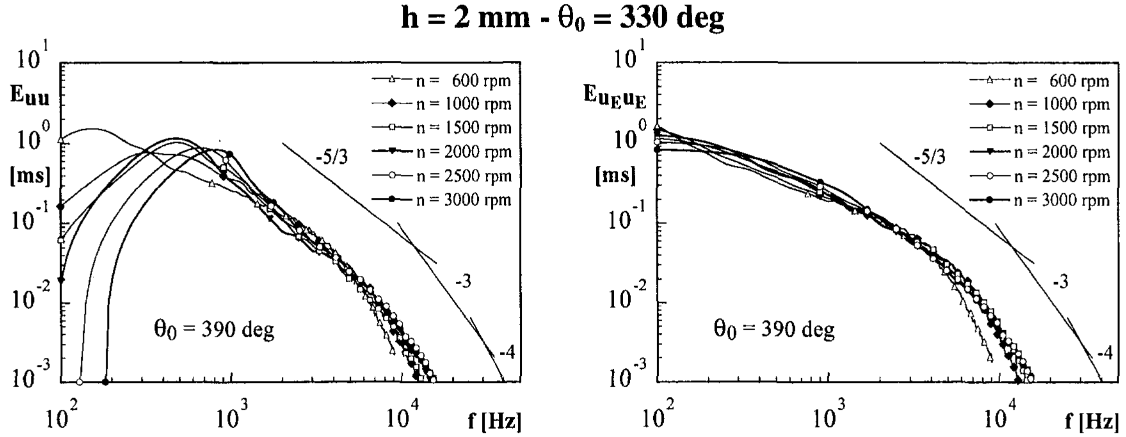

radial wire

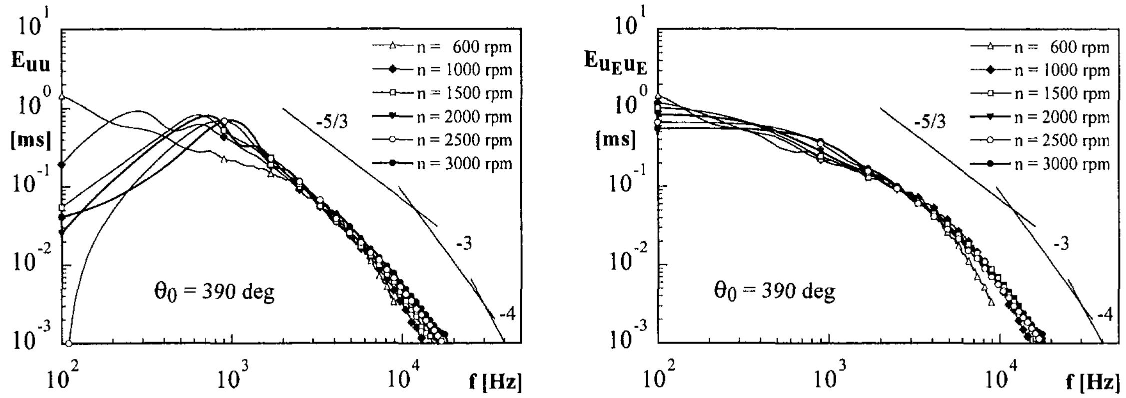

tangential wire

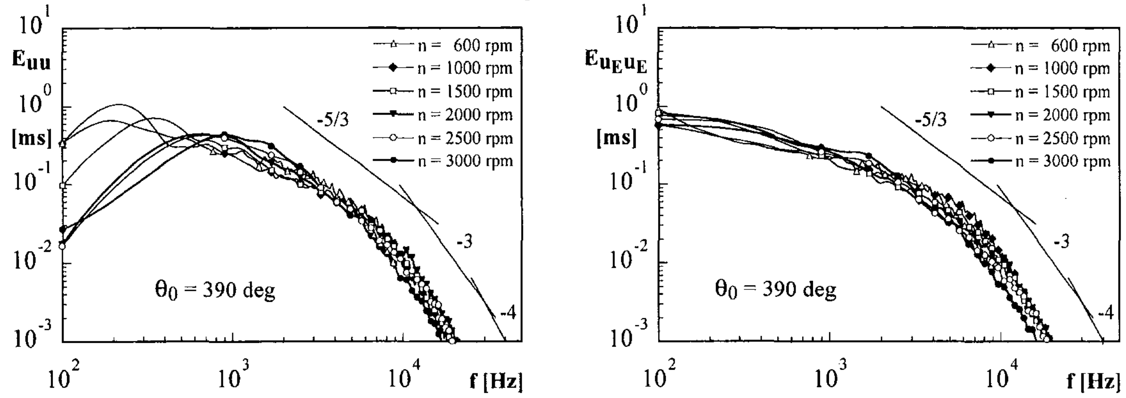

axial wire

Fig. 4 Normalized autospectral density functions of cycle-resolved (left column) and conventional (right column) turbulence obtained from wires oriented along the radial, tangential, and axial directions at the indicated engine speeds (*n*)

Similarly, for the instantaneous velocity fluctuation

$$\lambda_T(T, t_0) = \frac{1}{\sqrt{2\pi^2 \int_0^{f_{\max}} f^2 E_{u_E u_E}(T, t_0, f)\, df}} . \qquad (6)$$

Another turbulence time scale can be defined on the analogy of integral time scale in stationary flows by taking the integral of R over τ from 0 to $\tau_{\max}$, when R has positive values and decays over a sufficiently long period. Since this is generally the case for the conventional turbulence (Catania and Mittica, 1990; Catania et al., 1992a), then

$$\Lambda_T(T, t_0) = \int_0^{\tau_{\max}} R_{u_E u_E}(T, t_0, \tau) w(\tau) d\tau, \qquad (7)$$

which can be considered to be a rough measure of the longest connection in the random behavior of $u_{i,E}(t)$ in T.

Experimental Uncertainties

The experimental uncertainty sources and the precision of the measured velocities were analyzed elsewhere (Catania, 1985; Spessa, 1995). Based on the average deviations of repeated measurement sets and on previous findings, an uncertainty of up to ±8 percent could generally be ascribed to the velocity.

Guidelines for evaluating the random error of the autocorrelation and autospectrum function estimates are given by Bendat and Piersol (1986) and recapitulated by Catania et al. (1992a). The statistical uncertainty of the autocorrelation function estimate depends on the reciprocal square root of the following quantities: the Nyquist frequency of sample data, the correlation-interval length, and the number of data records. Based on the minimum number of acquired data records, a precautionary range for the normalized random error of the autocorrelation coefficient may extend from ≈0,5 percent, at separation time h = 2 mm - θ0 = 390 deg

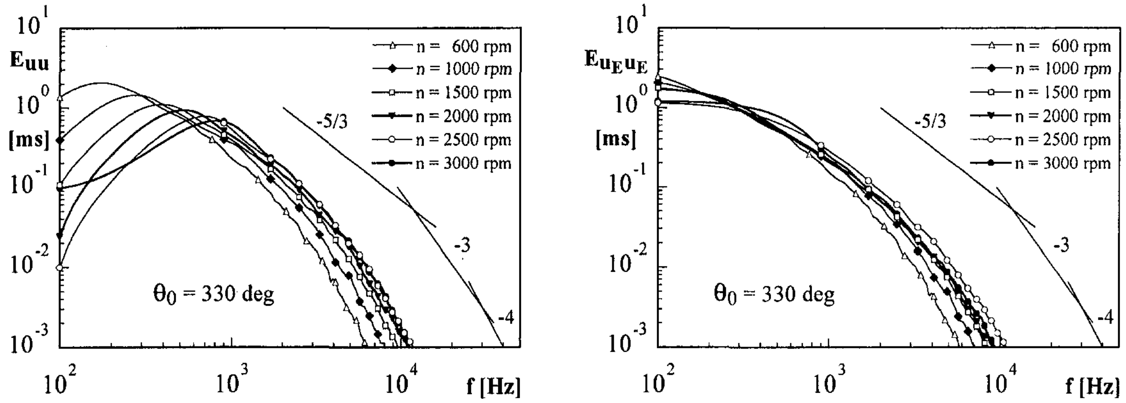

radial wire

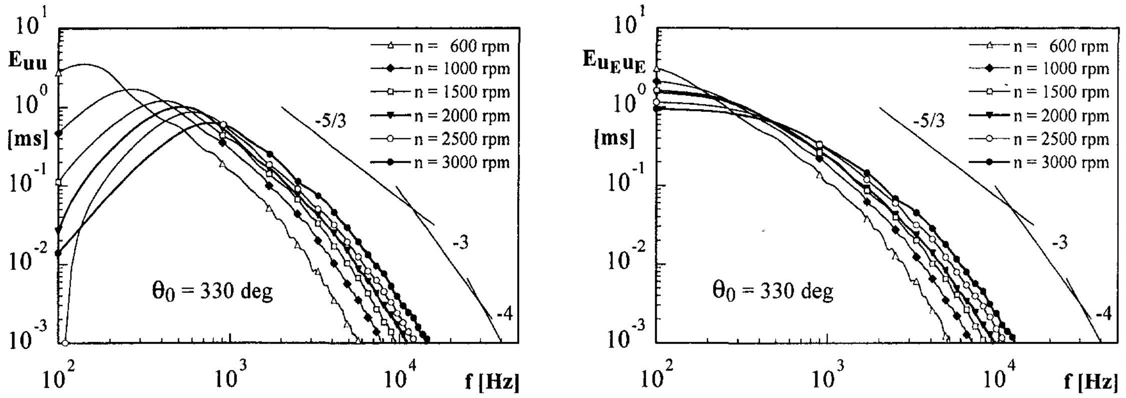

tangential wire

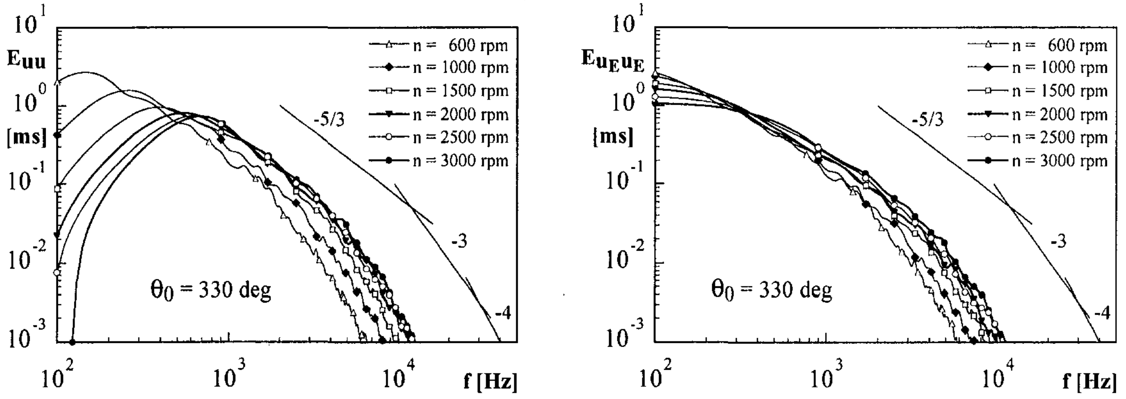

axial wire

Fig. 5 Normalized autospectral density functions of cycle-resolved (left column) and conventional (right column) turbulence obtained from wires oriented along the radial, tangential, and axial directions at the indicated engine speeds (n)

close to zero, to ≈10 percent, at large separation time where the coefficient approaches zero. Accordingly, the normalized random error of the autospectrum is proportional to the reciprocal square root of the number of data records and so may be taken as less than ≈6 percent in the present results.

However, the overall uncertainty can be expected not to influence the result implications and related conclusions.

Experimental Results and Discussion

The criteria for selection of the time-averaging interval used within the TAF procedure to filter the instantaneous velocity data were discussed by Catania and Mittica (1989) and the sensitivity of turbulence quantities to this interval was examined by Catania et al. (1992a). A crank-angle averaging interval $\Theta = 12-15$ deg was thus chosen, so that $\epsilon(t) = \langle u_i(t) \rangle \approx 0$.

The results reported in what follows were derived from velocity data acquired with radial (r), tangential (s), and axial (z) sensing wires, that is, by means of wires oriented along the radial, tangential, and axial directions, respectively, in the cylinder reference frame of Fig. 2.

The algorithm of Rader (1970) and Rabiner et al. (1979), suitably modified by Catania and Mittica (1989), was applied for autospectrum function estimation by Eq. (4).

Figures 4 and 5 show, as an example, the autospectral density coefficients of the cycle-resolved (left column) and conventional (right column) turbulence at $h = 2$ mm, for the three-wire orientations at the indicated engine speeds (n) and in the correlation intervals $\Phi = 60$ deg centered on $\theta_0 = 330$ deg (direct squish phase, Fig. 4) and $\theta_0 = 390$ deg (reverse squish phase, Fig. 5). The autospectral functions obtained during the induction and compression strokes as well as at other measure-

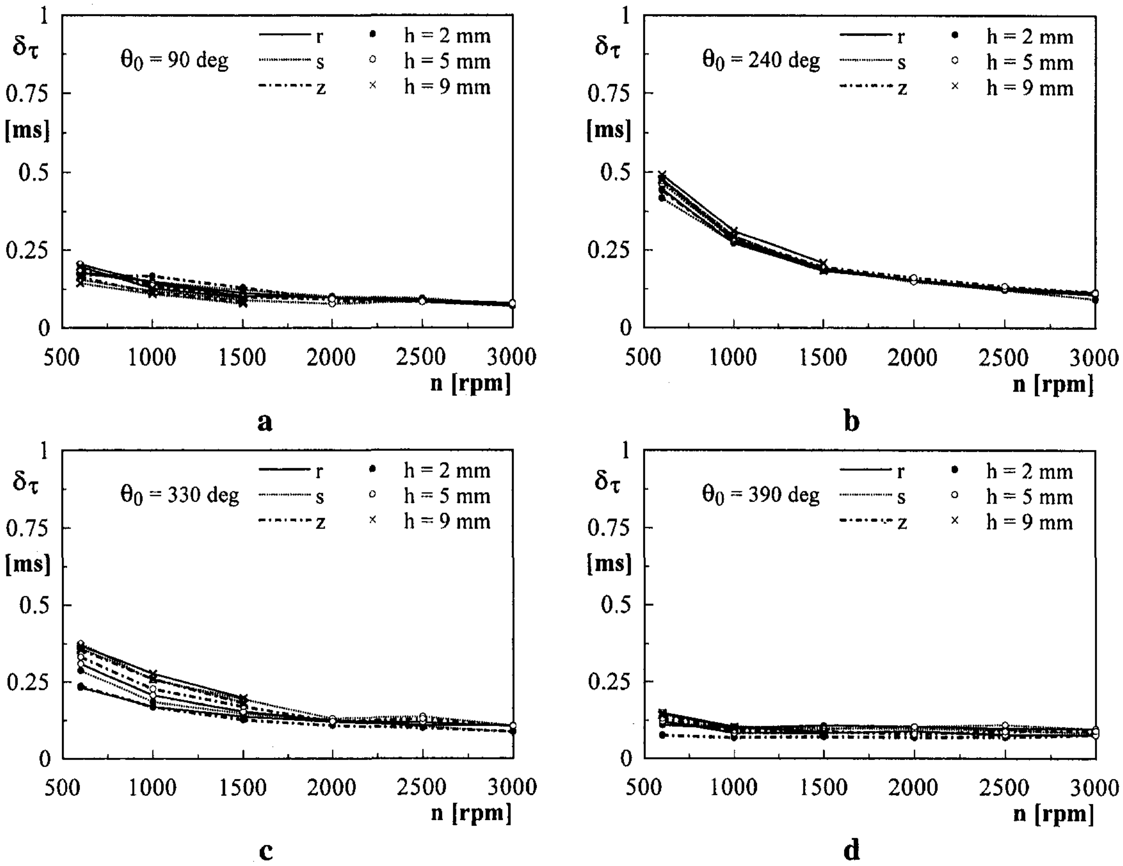

Fig. 6 Micro time-scale distributions of cycle-resolved turbulence obtained from wires oriented along the radial (*r*), tangential (*s*), and axial (*z*) directions at the indicated measurement locations (*h*) as functions of the engine speed

ment locations are reported by Spessa (1997). As illustrated by Figs. 4 and 5, logarithmic scales were used for giving emphasis to the high-frequency range. The slopes −5/3, −3, and −4 were also marked for analogy purposes with wave-number spectra (Catania et al., 1992a). It is useful to recall (Lesieur, 1987) that the Kolmogorov $k^{-5/3}$ inertial range of the wave number spectrum was deduced within the energy cascade concept and verified in the small scales of a flow with sufficiently high Reynolds number. The Kraichnan k^{-3} and the Saffman k^{-4} wave number spectra can be predicted within the "enstrophy[1]" cascade concept which applies to environments with high local vorticity gradients and thus a strong eddy interaction, implying a high flux of vorticity into the small scales. Such may be considered to be the in-cylinder environment during the induction and squish-flow phases, where wall-flow and wake-flow interactions, flow stratification, and interference occur. The results about the $f^{-5/3}$, f^{-3}, and f^{-4} ranges of the frequency spectrum as well as their dependence on engine speed, wire orientation, and measurement location, were discussed by Catania and Spessa (1996), Catania et al. (1996), Spessa (1997).

Figures 6–7 report the micro time-scale distributions versus engine speed of both cycle-resolved (Fig. 6) and conventional (Fig. 7) turbulence, obtained from the same velocity data records, for the three wire orientations (r, s, z) and measurement locations (h = 2 mm, h = 5 mm, and h = 9 mm). The time-scale distributions are reported for the correlation intervals centered on θ_0 = 90 deg (main induction at intake-valve maximum lift, Figs. 6(*a*) and 7(*a*)), θ_0 = 240 deg (mid compression, Figs. 6(*b*) and 7(*b*)), θ_0 = 330 deg (direct squish, Figs. 6(*c*)), and 7(*c*)), and θ_0 = 390 deg (reverse squish, Figs. 6(*d*) and 7(*d*)). The patterns of δ_τ and λ_τ are consistent with the autospectra of Figs. 4 and 5 and with those reported by Spessa (1997), taking in mind that the lowest time-scale values are related to the highest turbulence frequency content and conversely, the highest time-scale values correspond to the lowest turbulence frequency content.

The distributions of δ_τ and λ_τ in Figs. 6 and 7 basically show a decreasing trend against a speed increase. Therefore, the turbulence frequency content shows a generally increasing trend with the engine speed for all of the fluctuation components. In the main part of the compression stroke such an increase is virtually proportional to the engine speed, whereas in the other phases of the engine cycle the frequency content of the turbulence components grows less than linearly with the speed, according to the previous findings of Catania and Spessa (1996). In particular, during the reverse-squish phase (Figs. 6(*d*) and 7(*d*)), at h = 2 mm the micro time-scales are virtually independent of the engine speed. However, farther from the cylinder-head wall and in the low-speed range, these scales show to slightly decrease by increasing the engine speed. As can be inferred from the distributions of δ_τ, the highest frequency and finest structures of turbulence are in a virtually unrelaxed state at high speeds, according to previously obtained results from a different automotive engine with a shallow in-piston bowl (Catania et al., 1992a).

Figures 6 and 7 show an anisotropic spectral structure in the low speed range (600–1500 rpm) and a general tendency towards isotropy by increasing the engine speed. However, at high speeds a low anisotropy level in the conventional-turbulence structure can still be observed during the main part of the compression stroke (Fig. 7(*b*)), most likely due to stratification and compression effects. Such an anisotropy tends to disappear with the onset of high-frequency squish-generated turbulence (Fig. 7(*c* and *d*)).

---

[1] The "enstrophy" (Lesieur, 1987) is defined as the variance of the vorticity.

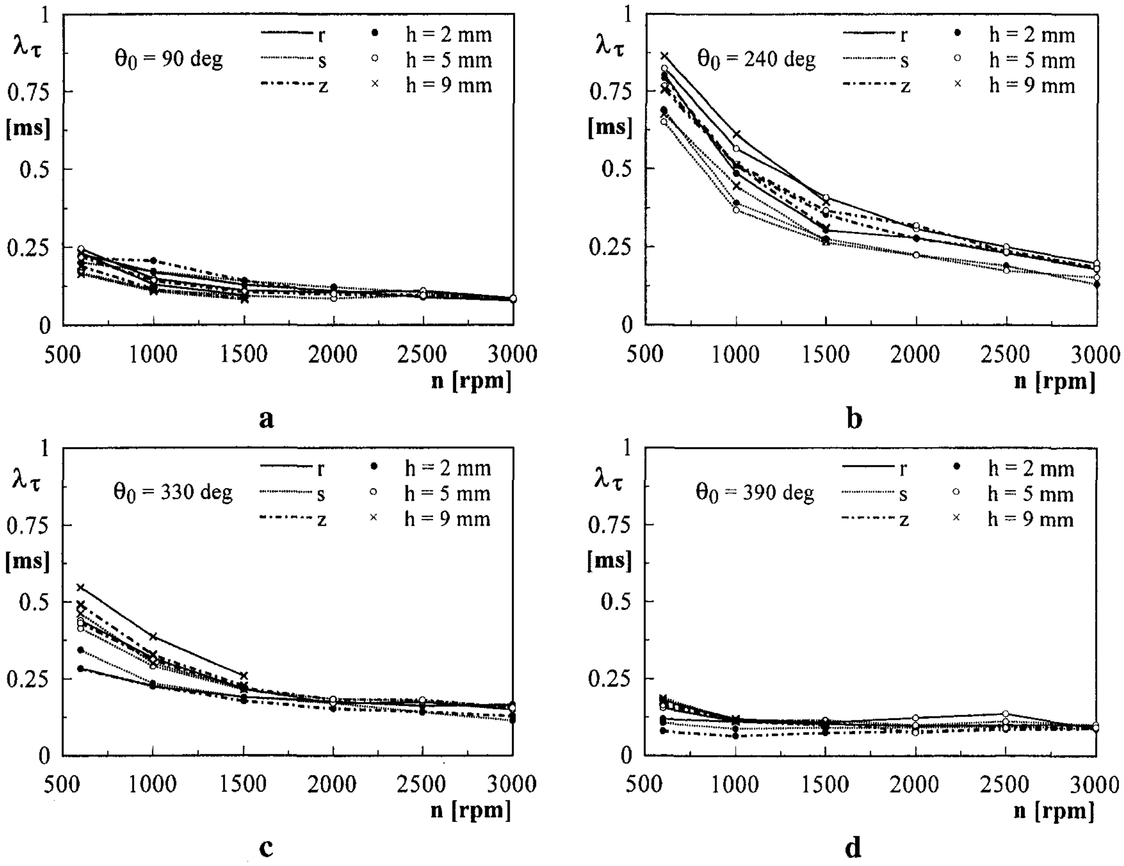

Fig. 7 Micro time-scale distributions of conventional turbulence obtained from wires oriented along the radial (*r*), tangential (*s*), and axial (*z*) directions at the indicated measurement locations (*h*) as functions of the engine speed

More specifically, during the induction stroke ($\theta_0 = 90$ deg, Figs. 6(*a*) and 7(*a*)) in the low speed range (600–1500 rpm) at $h = 5$ mm and $h = 9$ mm the smallest time-scale values of both cycle-resolved (Fig. 6(*a*)) and conventional (Fig. 7(*a*)) turbulence generally pertain to the axial and radial velocity components, which are sensed by the tangential wire. However, close to the cylinder head ($h = 2$ mm) at $n = 600$ rpm turbulence structure appears to be isotropic, though at $n = 1000$ rpm and $n = 1500$ rpm the axial component shows its highest frequencies. In the high speed range (2000–3000 rpm) a general tendency towards isotropy is apparent in the turbulence time-frequency structure at all of the measurement locations.

During the main part of the compression stroke ($\theta_0 = 240$ deg, Figs. 6(*b*) and 7(*b*)), the small-scale turbulence fine structures (Figs. 6(*b*)) are virtually isotropic, whereas the conventional turbulence (Fig. 7(*b*)) shows anisotropy in the whole speed range. The highest λ_τ values pertain to the tangential velocity component for all of the measurement locations. The lowest λ_τ values belong to the radial velocity component at $h = 5$ mm and $h = 9$ mm and to the axial and radial components at $h = 2$ mm. The anisotropy shown by the distributions of λ_τ is consistent with the large shift to low frequencies shown by the conventional turbulence autospectra (Spessa, 1997) and can also be ascribed to the spectral anisotropy in the so-called mean-flow cyclic fluctuation (Catania et al., 1996).

Both the direct ($\theta_0 = 330$ deg, Figs. 6(*c*) and 7(*c*)) and reverse ($\theta_0 = 390$ deg, Figs. 6(*d*) and 7(*d*)) squish flows proved to be sources of high-frequency turbulence with high intensity (Catania et al., 1995; Catania and Spessa, 1996). In addition, it can be inferred from the figures that the reverse squish flow gives rise to turbulence with higher frequency content than that produced by the direct squish flow. During the squish phases, anisotropy in the frequency structure of turbulence does not show a well defined trend with the engine speed, owing to the complexity of flow in the presence of instabilities and piston dynamic effects (Catania et al., 1996). Such a spectral anisotropy appears to be relatively less significant during the direct-squish phase (Figs. 6(*c*) and 7(*c*)), depending on measurement location and engine speed. More specifically, for the considered speeds, the conventional turbulence (Fig. 7(*c*)) is virtually isotropic at $h = 5$ mm and the cycle-resolved turbulence (Figs. 6(*c*)) shows to be isotropic both at $h = 5$ mm and $h = 9$ mm. At $h = 2$ mm (as can also be inferred from the autospectra of Fig. 4), both cycle-resolved and conventional turbulence show isotropy for $n = 1000$–1500 rpm, whereas for the other engine speeds anisotropy is evidenced by the fact that the radial velocity component generally has the lowest frequency content.

During the reverse-squish phase (Figs. 6(*d*) and 7(*d*)) both conventional and cycle-resolved turbulence exhibit a spectral anisotropy which is generally more significant close to the cylinder-head wall (consistent with the autospectra of Fig. 5) for all of the considered engine speeds. More specifically, at $h = 2$ mm the δ_τ and λ_τ, values of the radial component are lower than those of the tangential and axial flows, supporting the finding of a high shear flow layer perpendicular to the cylinder axis at the bowl rim around TDC (Catania et al., 1996). At $h = 5$ mm a slightly higher frequency content in the cycle-resolved turbulence pertains to the tangential velocity component in the whole speed range, whereas the highest frequencies in the conventional turbulence structure can be ascribed to the tangential ($n = 600$, 1500, 3000 rpm) or axial ($n = 1000$ rpm) or radial ($n = 2000$, 2500 rpm) velocity components. At $h = 9$ mm the results of Figs. 6(*d*) and 7(*d*) show a virtually isotropic turbulence frequency structure.

As far as turbulence nonhomogeneity is concerned, a stratification in the frequency content of the fluctuating motion is

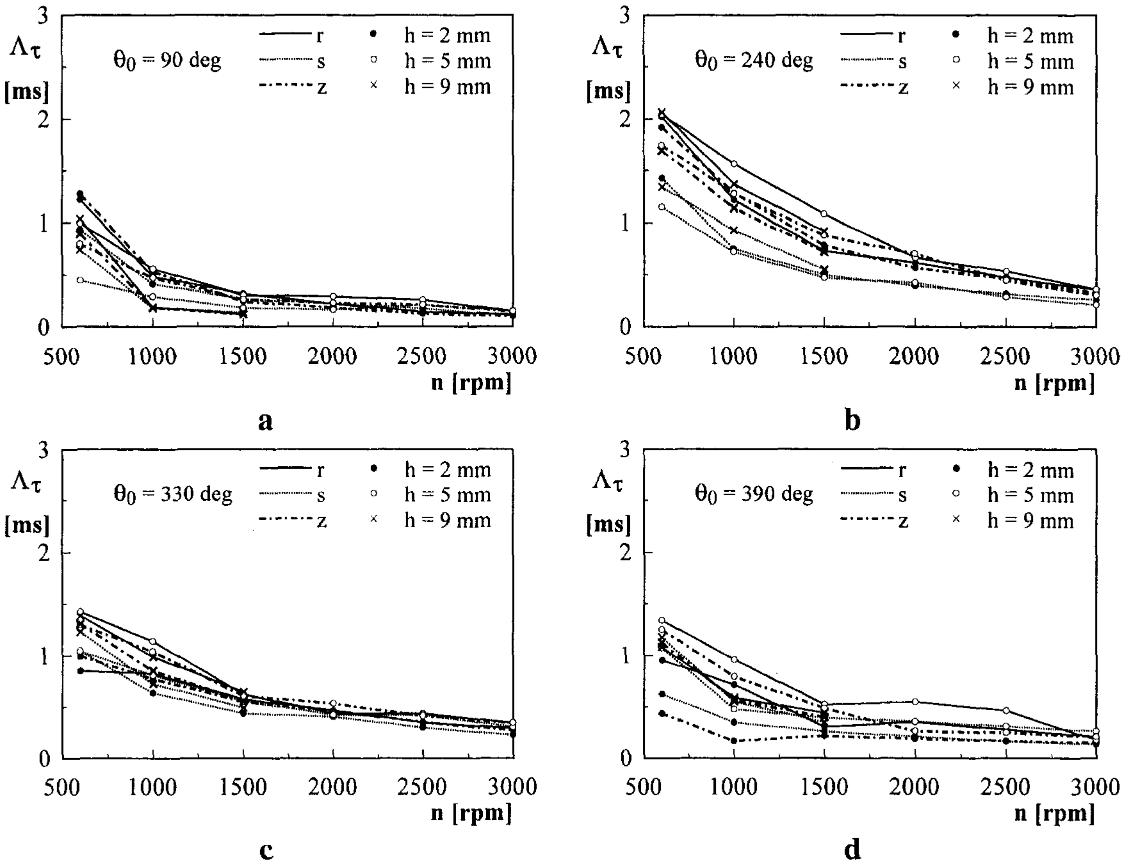

Fig. 8 Macro time-scale distributions of conventional turbulence obtained from wires oriented along the radial (*r*), tangential (*s*), and axial (*z*) directions at the indicated measurement locations (*h*) as functions of the engine speed

generally observed at low speeds (Figs. 6 and 7). However, a tendency towards homogeneity can be inferred from these figures by considering an increase of the engine speed. In more detail, during the induction stroke (Figs. 6(*a*) and 7(*a*)) the frequency content of both cycle-resolved and conventional turbulence slightly heightens the farther the distance from the cylinder head. Such a heightening is more evident for the radial and axial flow components which are detected by the tangential wire. During the compression stroke, nonhomogeneity in turbulence spectral structure is still apparent for the conventional turbulence (Fig. 7(*b*)) whereas the small-scale turbulence fine structures (Fig. 6(*b*)) are virtually homogeneous in the whole speed range. During the direct-squish (Figs. 6(*c*) and 7(*c*)) and reverse-squish (Figs. 6(*d*) and 7(*d*)) phases a sensible nonhomogeneity is apparent in both cycle-resolved and conventional turbulence spectral structures. The highest frequencies are detected close to the cylinder-head wall. Such a spectral nonhomogeneity is more pronounced during the direct-squish phase (Figs. 6(*c*) and 7(*c*)) in the low-speed range.

The interest of the above findings to the combustion-system design in DI diesel engines stems mainly from the fact that a significant reduction of smoke and particulate emissions can be caused by the generation of intense and high-frequency turbulence in the late combustion stages (Konno et al., 1992; Catania et al., 1994). The results also suggest that the turbulence required for successful and ''clean'' combustion is not almost exclusively generated by the fuel spray (Konno et al., 1992) with a partial contribution from the collapse of bulk air flow structures such as swirl (Plee and Ahmad, 1983; Bazari, 1992). In fact, a major role can be played by the high-frequency bowl-generated jet flows and by their interaction with the swirl flow during the last part of compression and the early part of the expansion stroke. Therefore, in high-speed DI diesel engines greater attention should be drawn to the combustion bowl design so as to achieve the maximum benefit from the influence of bowl-generated turbulence on combustion.

Figure 8 plots the distributions of the integral time scale Λ_τ for the conventional turbulence, as were derived from the same velocity data referred to in Figs. 6 and 7. It is worth recalling that the integral time scale may be interpreted as a rough indication of the transit time of lower-frequency larger-structures in their relative motion with respect to the ensemble-averaged velocity. In the main part of compression (Fig. 8(*b*)), this scale approaches a roughly linear inverse dependence on the engine speed. On the reverse-squish flow phase (Fig. 8(*d*)), at low speeds, Λ_τ presents a more sensible decreasing trend versus engine speed than that observed for Λ_T. Furthermore, the lower-frequency and larger turbulence structures mainly have higher anisotropy and nonhomogeneity levels than those of the finer structures during the induction (Fig. 8(*a*)) and reverse-squish (Fig. 8(*d*)) phases.

Comments on the relevance of turbulence studies in the cylinder of motored engines to firing conditions are given by Catania and Mittica (1989) with a wide literature review concerning the similarity of turbulent flow patterns before combustion under motored and firing conditions. It can be expected that the reported results hold in firing conditions before injection (Catania and Spessa, 1996). Furthermore, the fuel-spray interaction with the in-cylinder air flow may constitute an additional source of anisotropy and nonhomogeneity in turbulence structure. This interaction needs to be studied particularly at low speeds, where anisotropy and nonhomogeneity are more pronounced.

Conclusion

The time-frequency spectral structure of turbulence with particular reference to its anisotropy and nonhomogeneity was further investigated along the injector axis in the combustion chamber of a production DI diesel engine under motored conditions at speed of practical interest. The main results for cycle-resolved and conventional turbulence, which were obtained over the crank-angle interval from 30 deg before intake TDC to 60 deg after compression TDC, can be summarized as follows.

1 Basically, the turbulence spectral structure presents anisotropy and nonhomogeneity in the low-speed range, with a tendency towards isotropy and homogeneity by increasing the engine speed, although a low anisotropy level can still occur at high speeds during compression for conventional turbulence. The micro time-scale δ_τ generally shows slighter anisotropy and nonhomogeneity levels with respect to λ_τ, indicating a virtually isotropic and homogeneous structure of the cycle-resolved small-scale turbulence along the engine cycle at all speeds except the lowest ones.

2 During the induction stroke, anisotropy, and nonhomogeneity arise at low speeds and the turbulence frequency content slightly heightens the farther the distance from the cylinder-head wall.

3 During the main part of the compression stroke, anisotropy persists in the conventional-turbulence structure extending to the whole speed range, whereas nonhomogeneity mainly tends to reduce in the high-speed range.

4 The direct-squish flow generates high-frequency turbulence with a slight anisotropy, depending on engine speed and measurement location, and with a significant nonhomogeneity mainly in the low-speed range.

5 The reverse-squish flow is source of higher frequency turbulence than that induced by direct squish. The spectral anisotropy is more significant close to the cylinder-head wall for all speeds. Besides, the turbulence structure is nonhomogeneous and shows its highest frequencies close to the cylinder-head wall.

6 The distributions of the integral time scale Λ_τ for the conventional turbulence highlight the presence of low-frequency large structures in the fluctuating motion. Higher anisotropy and nonhomogeneity levels than those of the high-frequency fine structures mainly occur during the induction stroke and the reverse-squish phase.

Acknowledgments

This work was financed by the MURST (Ministero dell'Università e della Ricerca Scientifica e Tecnologica) and in part by the CNR (Consiglio Nazionale delle Ricerche) under PS (Progetto Speciale) "Study of Thermo-Fluid-Dynamic Processes and Techniques for Reduction of Pollutant Emissions from IC Reciprocating Engines," Contribution No. 96.02280.CT07.

References

Bazari, Z., 1992, "A DI Diesel Combustion and Emission Predictive Capability for Use in Cycle Simulation," SAE Paper No. 920462.

Bendat, J. S., and Piersol, A. G., 1986, *Random Data: Analysis and Measurement Procedures*, 2nd Ed., John Wiley & Sons, New York.

Catania, A. E., 1985, "Induction System Effects on the Fluid-Dynamics of a D.I. Automotive Diesel Engine," ASME Paper No. 85-DGP-11.

Catania, A. E., and Mittica, A., 1989, "Extraction Techniques and Analysis of Turbulence Quantities from In-Cylinder Velocity Data," ASME JOURNAL OF ENGINEERING FOR GAS TURBINES AND POWER, Vol. 111, pp. 466–478.

Catania, A. E., and Mittica, A., 1990, "Autocorrelation and Autospectra Estimation of Reciprocating Engine Turbulence," ASME JOURNAL OF ENGINEERING FOR GAS TURBINES AND POWER, Vol. 112, pp. 357–368.

Catania, A. E., Dongiovanni, C., and Mittica, A., 1992a, "Time-Frequency Spectral Structure of Turbulence in an Automotive Engine," Paper No. 920153. *Journal of Engines*, SAE, Vol. 101, pp. 221–244.

Catania, A. E., Dongiovanni, C., Mittica, A., Molina, G., and Spessa, E., 1994, "Cycle-Resolved HWA Measurements with Single and Dual-Sensor Probes in an Open-Chamber Automotive Engine," *Proceedings, COMODIA 94*, JSME, Tokyo, pp. 437–444.

Catania, A. E., Dongiovanni, C., Mittica, A., Molina, G., and Spessa, E., 1995, "A New Test Bench for HWA Fluid-Dynamic Characterization of a Two-Valved In-Piston-Bowl Production Engine," Paper No. 952467, *Journal of Engines*, SAE, Vol. 104, Sect. 3, pp. 2301–2324.

Catania, A. E., and Spessa, E., 1996, "Speed Dependence of Turbulence Properties in a High-Squish Automotive Engine Combustion System," SAE Paper No. 960268, *Journal of Engines*, SAE, Vol. 105, Sect. 3, pp. 313–334.

Catania, A. E., Dongiovanni, C., Mittica, A., Negri, C., and Spessa, E., 1996, "Turbulence Spectrum Investigation in a DI Diesel Engine With a Reentrant Combustion Bowl and a Helical Inlet Port," SAE Paper No. 962019. *Journal of Engines*, SAE, Vol. 105, Sect. 3, pp. 2205–2226.

Daneshyar, H., and Hill, P. G., 1987, "The Structure of Small-Scale Turbulence and Its Effect on Combustion in Spark Ignition Engines," *Prog. Energy Combust. Sci.*, Vol. 13, pp. 47–73.

Floch, A., Van Frank, J., and Ahmed, A., 1995, "Comparison of the Effects of Intake-Generated Swirl and Tumble on Turbulence Characteristics in a 4-Valve Engine," SAE Paper No. 952457, *Diagnostics in Diesel and SI Engines*, SAE SP-1122, pp. 69–85.

Heywood, J. B., 1988, *Internal Combustion Engine Fundamentals*, McGraw-Hill International Editions, New York.

Ikegami, M., 1990, "Role of Flows and Turbulent Mixing in Combustion and Pollutant Formation in Diesel Engines," *Proceedings, COMODIA 90*, JSME, Tokyo, pp. 49–58.

Konno, M., Chikahisa, T., and Murayama, T., 1992, "Reduction of Smoke and NO_x by Strong Turbulence Generated During the Combustion Process in D.I. Diesel Engines," SAE Paper No. 920467, *Reducing Emissions from Diesel Combustion*, SAE SP-895, pp. 111–119.

Lancaster, R. D., Krieger, R. B., Sorenson, S. C., and Hull, W. L., 1976, "Effects of Turbulence on Spark-Ignition Engine Combustion," Paper No. 760160, *Trans. SAE*, Vol. 85, pp. 689–710.

Lesieur, M., 1987, *Turbulence in Fluids*, Martinus Nijhoff Publishers, The Netherlands.

Magnussen, B. F., and Hjertager, B. H., 1976, "On Mathematical Modelling of Turbulent Combustion With Special Emphasis on Soot Formation and Combustion," paper presented at the 16th Symposium (International) on Combustion, The Combustion Institute, Pittsburg, PA.

Plee, S. L., and Ahmad, T., 1983, "Relative Roles of Premixed and Diffusion Burning in Diesel Combustion," SAE Paper No. 831733.

Rabiner, L. R., Schafer, R. W., and Dlugos, D., 1979, "Correlation Method for Power Spectrum Estimation," *IEEE Programs for Digital Signal Processing*, IEEE, Piscataway, NJ.

Rader, C. M., 1970, "An Improved Algorithm for High Speed Autocorrelation with Applications to Spectral Estimation," *IEEE Trans. Audio Electroacoustics*, Vol. AU-18, No. 4, pp. 439–441.

Smith, W. J., and Timoney, D. J., 1997, "On the Relative Roles of Fuel Spray Kinetic Energy and Engine Speed in Determining Mixing Rates in D.I. Diesel Engines," ASME JOURNAL OF ENGINEERING FOR GAS TURBINES AND POWER, Vol. 119, pp. 212–217.

Spessa, E., 1995, "Experimental Investigation of Turbulent Flow Properties in a Diesel Engine Cylinder by an Innovative HWA Technique," (in Italian) Ph.D. thesis, Politecnico di Torino.

Spessa, E., 1997, "A Contribution to the Analysis of Turbulence Anisotropy and Nonhomogeneity in an Open-Chamber Diesel Engine," ICE-Vol. 29-2, Book. No. H1099B.

Timoney, D. J., and Smith, W. J., 1996, "Influences of Fuel Injection and Air Motion Energy Sources on Fuel-Air Mixing Rates in a D.I. Diesel Combustion System," SAE Paper No. 960035, *Diesel Engine Combustion Processes*, SAE SP-1159, pp. 89–101.

Witze, P. O., 1994, "In-Cylinder Diagnostics for Production Spark-Ignition Engines," in *Unsteady Combustion*, F. E. Culick, M. V. Heitor, and J. H. Whitelaw, Eds., Kluwer Academic Publishers, Dordrecht, The Netherlands.

D. R. Reddy

C. J. Steffen Jr.

K. B. M. Q. Zaman

Turbomachinery and
Propulsion Systems Division,
NASA Lewis Research Center,
MS 5-11,
21000 Brookpark Road,
Cleveland, OH 44135

Computation of Three-Dimensional Compressible Flow From a Rectangular Nozzle With Delta Tabs

A three-dimensional viscous flow analysis is performed using a time-marching Reynolds-averaged Navier-Stokes code for a 3:1 rectangular nozzle with two delta tabs located at the nozzle exit plane to enhance mixing. Two flow configurations, a subsonic jet case and a supersonic jet case using the same tab configuration, which were previously studied experimentally, are computed and compared with the experimental data. The experimental data include streamwise velocity and vorticity distributions for the subsonic case, and Mach number distributions for the supersonic case, at various axial locations downstream of the nozzle exit. The computational results show very good agreement with the experimental data. In addition, the effect of compressibility on vorticity dynamics is examined by comparing the vorticity contours of the subsonic jet case with those of the supersonic jet case which were not measured in the experiment.

Introduction

Noise reduction through enhanced mixing between the nozzle exhaust and the ambient air stream has received a great deal of attention recently in the design of subsonic as well as supersonic propulsion systems. One of the strategies to enhance the mixing is to place passive control devices such as small vortex generators, or tabs, at the nozzle exit plane—thereby generating streamwise vortical structures that increase the effectiveness of the mixing process. This paper deals with the computation of flowfield from a rectangular nozzle with a pair of delta tabs placed on the narrow edges at the exit of the nozzle.

There has been an ongoing experimental investigation of tabbed nozzles at the NASA Lewis Research center for the past five years with emphasis placed upon furthering the understanding of the vorticity dynamics. Recently, we have applied an incompressible Navier-Stokes code to complement the experimental effort in an attempt to provide an efficient alternative for extensive parametric studies in the subsonic flow regime (Steffen et al., 1995). In order to assess the effect of compressibility on the mixing phenomena, which might be significant in the high speed research (HSR) applications, we need a compressible Navier-Stokes code that has been validated for the types of flows relevant to HSR configurations. A three-dimensional compressible Navier-Stokes code that has been in extensive use for the last fifteen years by the Aerospace companies and government agencies is NPARC (NPARC Alliance Technical Team, 1994) which continues to be developed and supported by a joint alliance between NASA Lewis Research Center and Arnold Engineering Development Center, U.S. Air force. The main objective of this study is to assess the NPARC code for the compressible jet mixing flow from a rectangular nozzle with delta tabs using experimental data obtained in-house in an open jet facility (Zaman, 1996a). Two sets of experimental data, a subsonic jet case and a supersonic jet case using the same tab configuration, are considered for this study. The experimental data include streamwise velocity and vorticity contours for the subsonic jet case, and Mach number contours for the supersonic jet case at various axial locations in the mixing region of the flowfield. Another objective, in addition to code assessment, is to examine the effect of compressibility on vorticity dynamics by comparing the vorticity contours of the subsonic jet case with those of the supersonic jet case which were not measured in the experiment.

Background

Bradbury and Khadem (1975) were among the first to study the effect of tabs on circular jet mixing. They examined the effects of nozzle boundary layer, number of square tabs, circumferential variation of flow angle at the nozzle exit, etc. on the mixing phenomenon in the flowfield downstream. More recently, Samimy et al. (1993) reported several key observations in the study of tabbed circular jets. They observed that the flowfield downstream of the nozzle exit contained a primary streamwise component of vorticity along each side of the tab and that a significant pressure difference had to exist across the tab for the vortical structures to affect the downstream flow. Zaman et al. (1994) postulated that the high pressure region directly upstream of the tab, called "pressure hill" was responsible for the dominant streamwise vorticity. Bohl and Foss (1995) have also documented the pressure hill effect and this has been further investigated by Reeder (1994) for tab configurations positioned either inside or outside of the nozzle exit plane.

In related efforts, others (Ho and Gutmark, 1987; Hussain and Hussain, 1989) have reported that jets with an elliptic cross section can undergo axis switching, a term referred to an exchange of major and minor axes of the elliptically shaped jet stream, which resulted in an enhanced mixing of the jet flow with the ambient airstream. Zaman (1996b) has studied the effect of tabs for a rectangular nozzle and inferred that streamwise vortex pairs produced by the tabs have a considerable influence on the axis switching phenomenon as well as the jet spreading.

Flow Configuration

The flow configuration considered for the present study was experimentally investigated by Zaman (1996a and 1996b). This

---

Contributed by the International Gas Turbine Institute and presented at the International Gas Turbine & Aeroengine Congress & Exhibition, Orlando, FL, June 2–5, 1997. Manuscript received by the ASME Headquarters July 1, 1997. Paper No. 97-GT-257. Associate Technical Editor: H. A. Kidd.

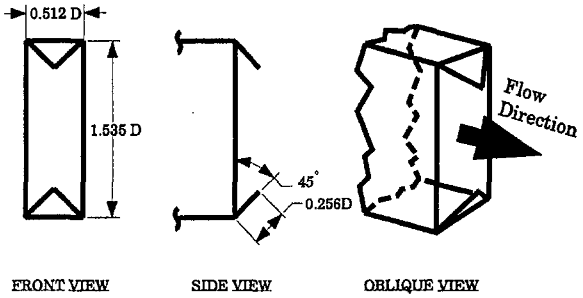

Fig. 1 A 3:1 rectangular nozzle fitted with two delta tabs

is shown schematically in Fig. 1. It is a convergent nozzle discharging into a quiescent ambient air. The nozzle cross section is a 3:1 rectangle and the delta tabs are placed at the nozzle exit plane inclined at 45° outward. Note that D is the equivalent diameter of the rectangular cross section. For the configuration considered for this study, the base of the delta tab spans the entire width (i.e., the narrow edge) of the nozzle. This configuration produced the maximum mixing enhancement compared to certain other configurations. The area blockage due to the presence of the tabs is about 6 percent of the nozzle exit area per tab (12 percent total), which results in about 5 percent deterioration in the nozzle performance (Zaman, 1996a). As mentioned earlier, two flow regimes were tested with this setup. The first was a subsonic jet case with a Mach number of 0.3 at the nozzle exit. The equivalent diameter for this case was 2.5 inches. The second case was an underexpanded supersonic jet with a "jet Mach number" of 1.63 which was run with a geometrically similar but smaller nozzle. The equivalent diameter for this case was 0.58 inches. The Reynolds number based on the sonic speed and the equivalent diameter was 1.34×10^6 for the subsonic case, and 0.992×10^6 for the supersonic case.

For the subsonic case, hot wire anemometer was used to obtain streamwise velocity and vorticity contours in the cross plane at various axial locations from the nozzle exit. For the supersonic jet case, Pitot pressure measurements were obtained to yield the cross plane Mach number contours at different axial locations. Further details of the experiment and error estimates can be found in Zaman (1996a, b). The scope of the present study is to assess the predictive capability of NPARC in simulating the relevant flow physics through a detailed comparison of the solution with the available data and also examine the effects of compressibility on the vorticity field. It is worth pointing out here that for the supersonic jet case the Pitot pressure measurements were only taken in the subsonic region ($X/D > 9.0$). While Mach number distributions were computed for a tabbed rectangular jet with 2:1 aspect ratio (Lee and Sova, 1995), the present computations not only provide a direct comparison with the available experimental data, but also examine the velocity and vorticity distributions in the supersonic mixing region.

Numerical Method

As mentioned previously, the numerical flow solver chosen for this study is a time-marching full Navier-Stokes code, called NPARC (NPARC Alliance Technical Team, 1994). The code was originally developed as AIR3D by Pulliam and Steger (1980); Pulliam (1984) later added the artificial dissipation of Jameson (Jameson et al., 1981) and called the code ARC3D. Cooper et al. (1987) adapted the code for internal flows of propulsion application and named the code PARC3D which was subsequently renamed NPARC when an alliance was formed between NASA, LeRC, and AEDC to jointly develop and support the code.

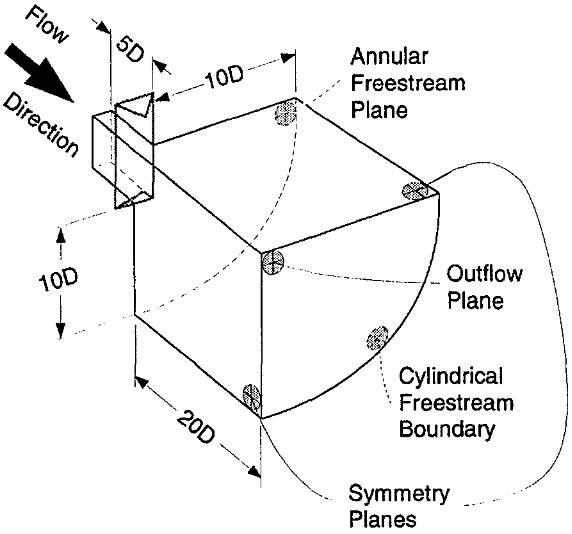

Fig. 2 Geometric description of the computational domain

NPARC solves the full three-dimensional Reynolds-averaged Navier-Stokes equations in strong conservation form using Beam and Warming approximate factorization. The discretization employs central differencing on a generalized curvilinear coordinate system with implicit and explicit second and fourth order artificial dissipation. The fourth order dissipation is added as a background damping to prevent odd and even point decoupling. The second order dissipation is added primarily to smooth out oscillations in regions of pressure gradients associated with shock waves. There are several options available in the NPARC code to modify the amount of artificial dissipation added as described above. The option used in the present computations provides for an appropriate anisotropic model for the dissipation coefficients as suggested by Siclari et al. (1989). Thus, the amount of the added artificial dissipation becomes more a function of the coordinate direction, which depends on the local velocity component in each direction. A detailed description of all the available options of artificial dissipation treatment can be found in the report of Cooper and Sirbaugh (1989).

In the present study, for the subsonic case, the second order dissipation was not added; for the supersonic case, the second order dissipation coefficient used was 0.25, which is a default value in the code. For both subsonic as well as the supersonic case, the default value of 0.64 was used for the fourth order dissipation coefficient. The value of α used in the expression for the anisotropy of the second order dissipation was 0.2 for the present computations (1 corresponds to isotropy and 0 corresponds to full anisotropy). A nonzero value for α is recommended (Cooper and Sirbaugh, 1989) since in practice $\alpha = 0$ often leads to slow convergence and instability. To simplify the solution of the block pentadiagonal system of discretized

Nomenclature

D = equivalent diameter of nozzle exit cross section
X = axial distance downstream from nozzle exit
k = turbulent kinetic energy
y^+ = normal distance scaled by wall shear
α = exponent for anisotropy in second order dissipation expression
ϵ = turbulent dissipation

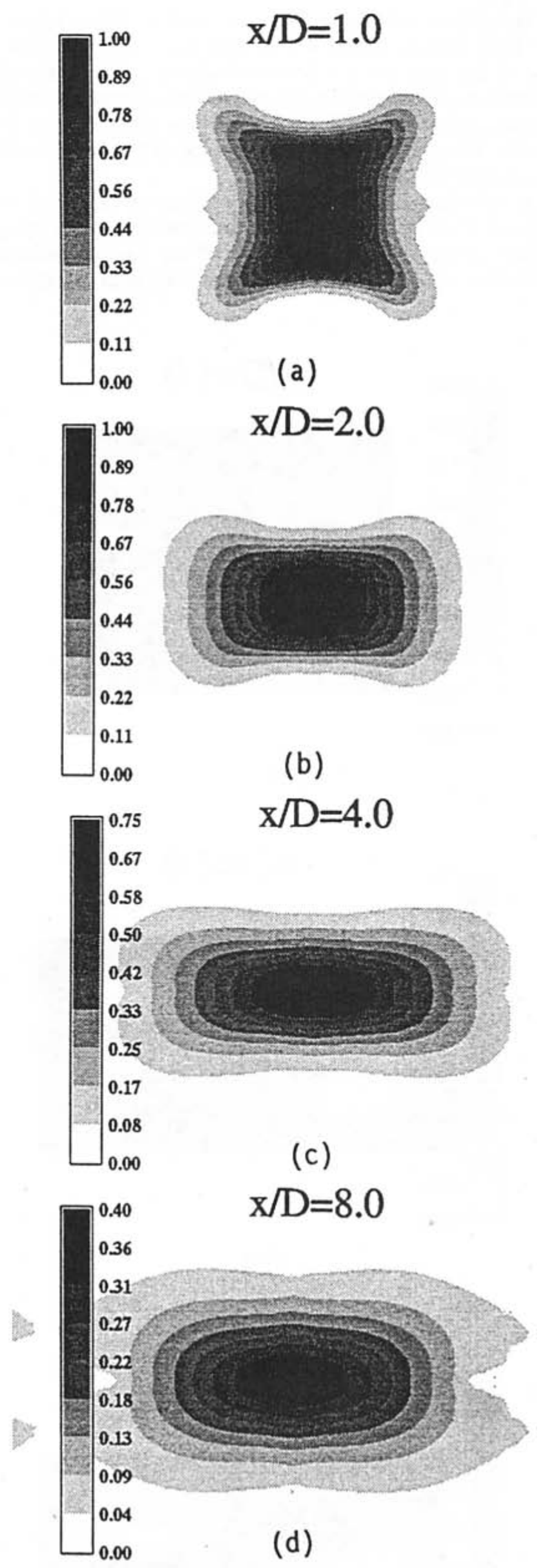

Fig. 3 Streamwise velocity contours: computed (subsonic)

equations, the block implicit operators are diagonalized by decomposing the flux Jacobians, resulting in a scalar pentadiagonal system. The loss of time accuracy from the diagonalization does not affect the spatial accuracy of the steady-state solution (Pulliam, 1984). NPARC also has a multi-block capability to enable the treatment of the flow domain as a collection of several blocks, each block containing its own boundary conditions with all the necessary interface conditions with the adjoining blocks.

A number of turbulence models ranging in complexity from zero-equation to two-equation formulations are available in the NPARC code. The turbulence model chosen for this study is a one-equation model developed by Spalart and Allmaras (1992),

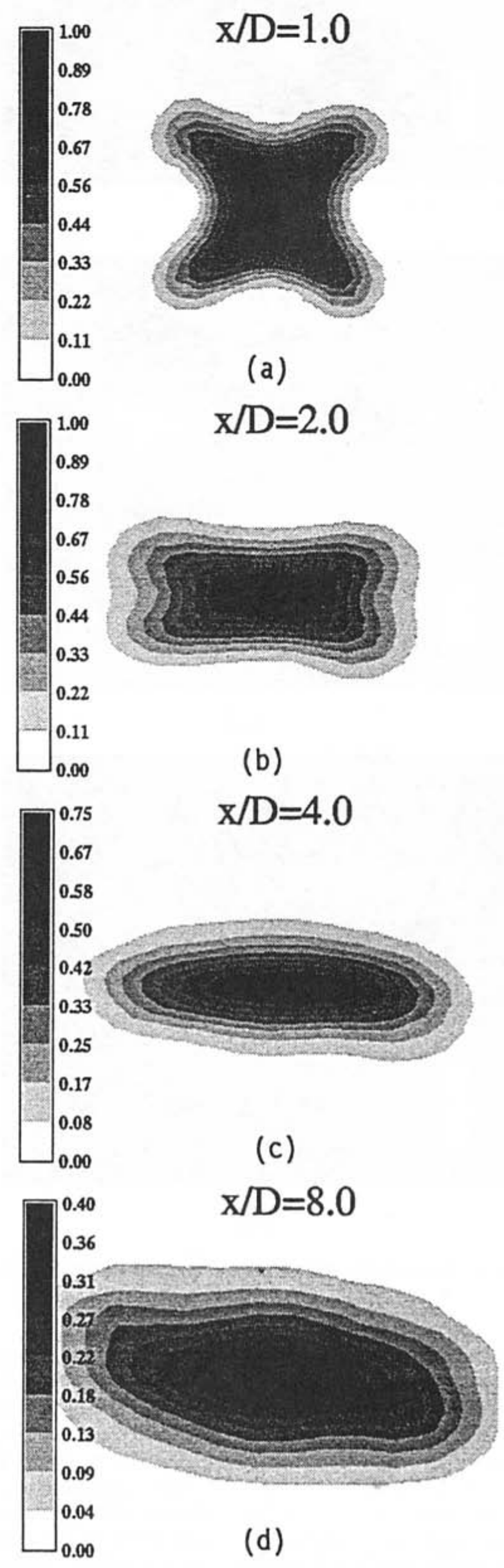

Fig. 4 Streamwise velocity contours: experiment (subsonic)

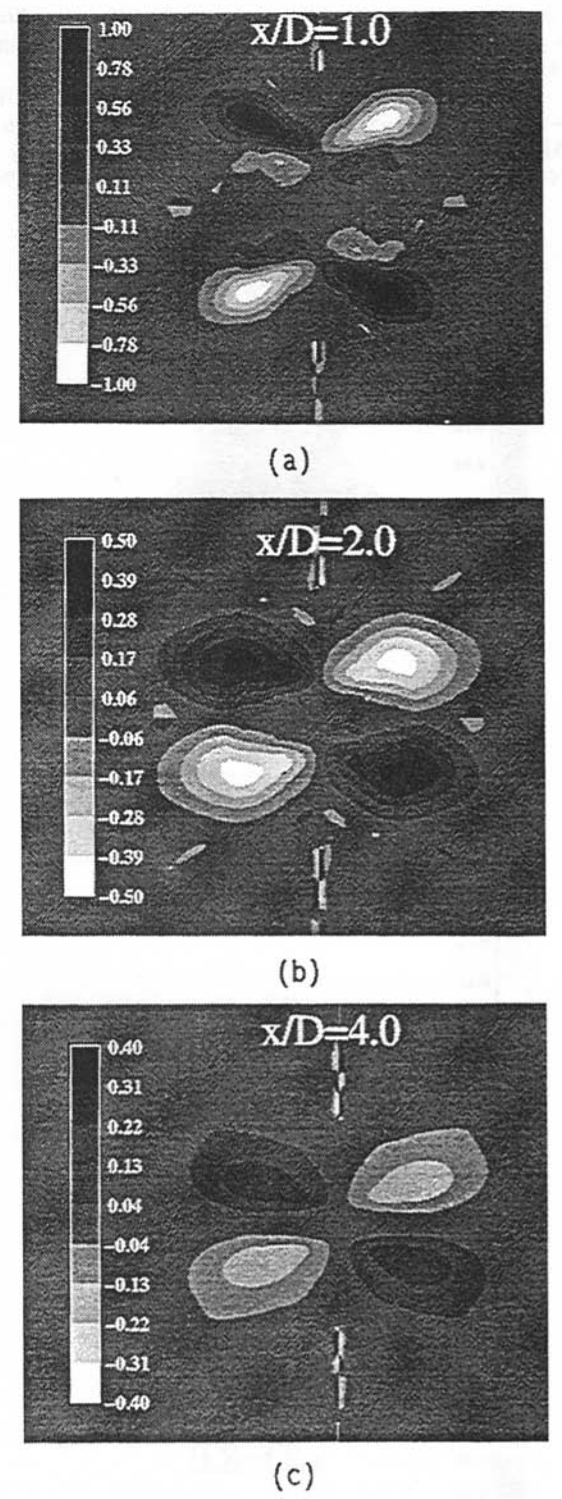

Fig. 5 Streamwise vorticity contours: computed (subsonic)

which is considered to be in the medium range of complexity using one partial differential equation for the transport of turbulent viscosity. The most compelling reason for the selection of this model over others is that it has been found to be more stable compared to the two-equation models. Attempts to use the k-ϵ model in this code for this flow configuration have been unsuccessful due to stability problems with the turbulence transport equations. In addition, as pointed out in the studies of Steffen et al. (1995) and Bradbury and Khadem (1975), the effect of streamwise vorticity introduced by the tabs is so dominant in the flowfield that resolution of wall boundary layers and shear layer mixing which would have been crucial in the absence of the tabs has not been considered to be that critical. Furthermore, the standard k-ϵ model has been known to overpredict three-dimensional jet spreading (see for example, Pope (1978)). These factors led to the choice of the simpler turbulence model stated above.

The code has been verified by several investigators for a variety of flow configurations demonstrating the accuracy of the flow solver and the limitations of the various turbulence models that were incorporated into the code over the period of

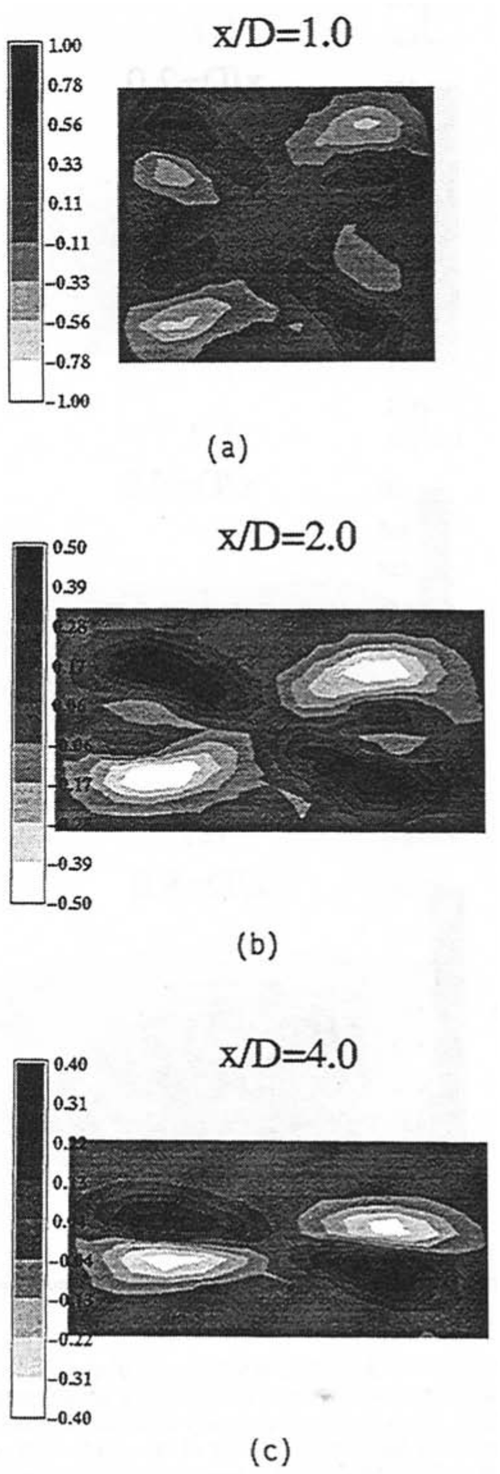

Fig. 6 Streamwise vorticity contours: experiment (subsonic)

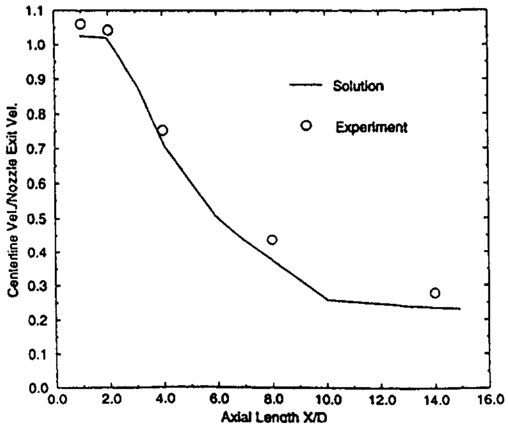

Fig. 7 Centerline velocity distribution (subsonic)

its evolution. Following are some of the recent studies that are relevant to the flow configurations considered here. DeBonis (1992) applied NPARC to study the mixing performance of a mixer/ejector nozzle for a future supersonic transport application using a zero-equation algebraic turbulence model. Georgiadis and Yoder (1994) examined three types of nozzle configurations with flow characteristics similar to those considered for supersonic transport program using a zero-equation and a two-equation turbulence models. DeBonis et al. (1995) validated NPARC for two-dimensional and axisymmetric nozzle afterbody flows at transonic speeds using two-equation and zero-equation turbulence models to predict separation in the flowfield. Reddy (1995) used NPARC to study the three-dimensional flow field of a crossing, glancing shocks/turbulent boundary layer interaction configuration to assess the predictive capability of NPARC using a zero-equation turbulence model for high speed aircraft inlet application. Khavaran and Georgiadis (1996) applied NPARC using a two-equation turbulence model and simplified noise source correlation terms derived from acoustic analogy to predict the three-dimensional directivity of noise for a Mach 1.5 elliptic jet as well as a round jet.

The physical domain is modeled by a five block, structured, generalized curvilinear coordinate mesh created with GRIDGEN (Steinbrenner and Chawner, 1995) software. Since the flowfield has symmetry in both cross-stream directions, only one fourth of the full flowfield is computed with symmetry imposed in the vertical as well as the transverse direction, see Fig. 2. The total number of grid points in the computation is 306,350 with appropriate clustering of nodes employed to resolve the boundary layers and shear layers in the flowfield. The grid clustering is done such that on an average it yields a y^+ of about 10 which is required by the turbulence model used in this study. The same degree of clustering is used in the shear layer mixing region downstream of the nozzle exit.

The boundary conditions are imposed by selecting from the choice of options available in the code. The inflow and outflow boundaries are located at $5D$ upstream and $20D$ downstream of the nozzle exit plane with inflow and outflow conditions imposed at these boundaries, see Fig. 2. It is worth mentioning here that the convergent portion of the nozzle upstream of the nozzle throat has not been considered in the computations. The inflow boundary is assumed to be the throat section slightly upstream of the nozzle exit. For the supersonic case, the inflow boundary is fixed at the initial values (Mach 1.0) and at the outflow boundary, which is subsonic, free stream static pressure is imposed, and all the other flow variables are extrapolated from the upstream flow region. For the subsonic jet case, total pressure and total temperature are specified at the inflow boundary with all the other flow quantities computed from within the flow downstream of the boundary. The lateral and transverse farfield boundaries, located at $10D$ away from the nozzle walls, as well as the cross-stream plane surrounding the nozzle exit have the free stream conditions imposed. The free stream conditions imposed are similar to the subsonic inflow condition that would allow the quiescent air to be entrained into the computational domain. The total pressure and temperature on these boundaries are the ambient static pressure and temperature. The nozzle walls and the tab are modeled as no slip surfaces.

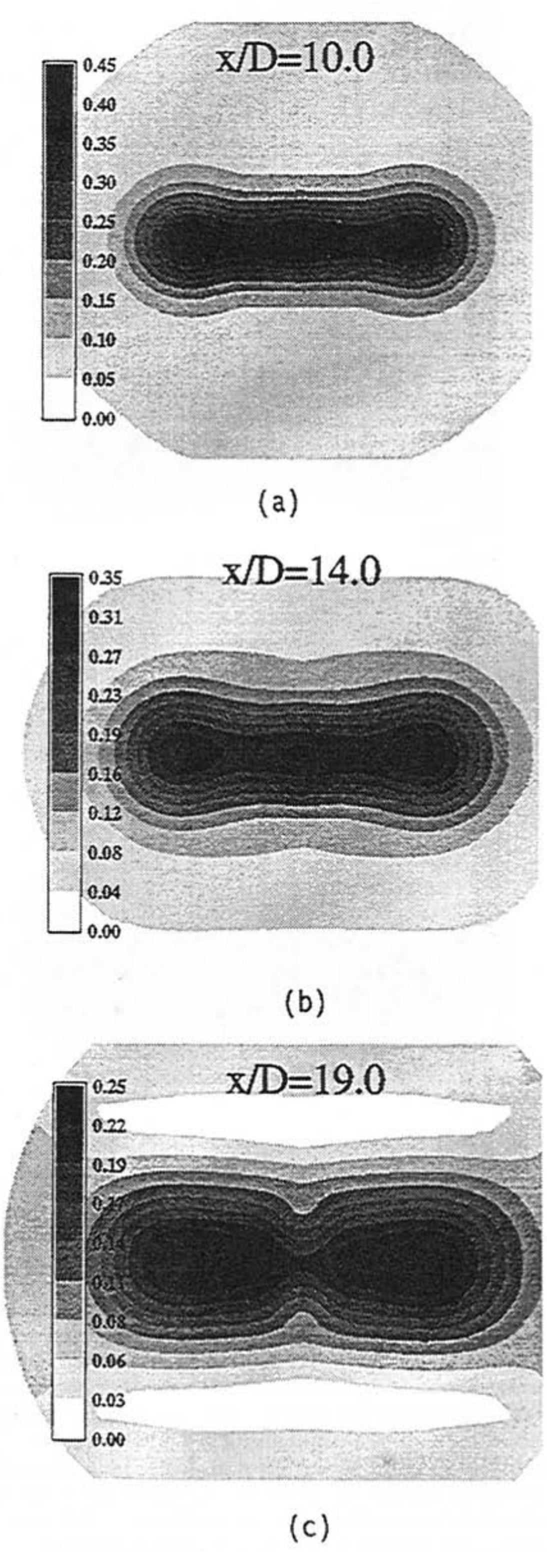

Fig. 8 Mach number contours: computed (supersonic)

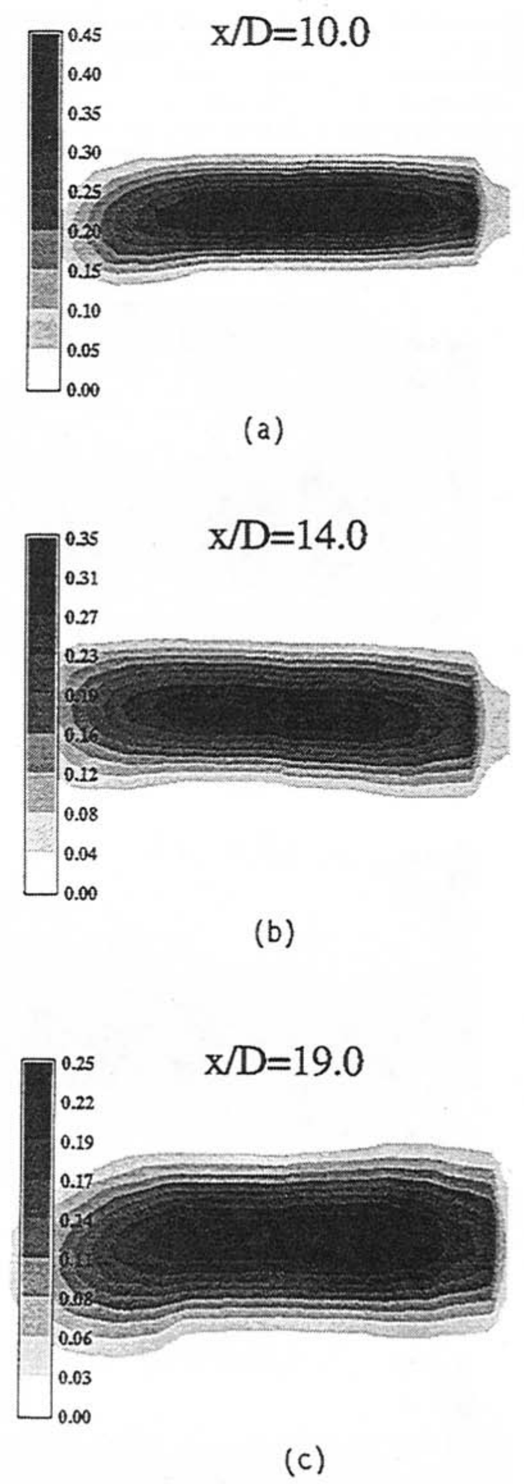

Fig. 9 Mach number contours: experiment (supersonic)

The size of the numerical grid for the computation is selected based on a mesh resolution study which was presented in Steffen et al. (1995). That study was carried out in a manner consistent with that specified by Roache (1994) for the incompressible flow code which has the same formal second order accuracy as that of NPARC. A very similar grid density that produced grid-independent solution of Steffen et al. (1995) has been used in the present computations. In the present study, the flow solution is considered converged when the residuals of the mean flow equations dropped by five orders of magnitude (final residual values were about 10^{-6}). The run time for the computation of each of the flow regimes is about 15 hours on Cray C90 computer.

Results and Discussion

Three-dimensional solutions are obtained for the two flow cases of subsonic and supersonic jet conditions, with the same nozzle configuration, that correspond to the experimental runs. The subsonic flow results will be discussed first followed by the supersonic results. The results from both cases are compared with the available experimental data. All results are normalized by the equivalent diameter and the streamwise velocity along the jet center line at the nozzle exit plane. The contour maps are presented in such a way that the experimental data and the computational results at each streamwise location are plotted on the same physical scale and contour scale.

Figure 3(a–d) shows the contour plots of streamwise velocity for the subsonic jet case at four different axial (X/D) locations downstream of the nozzle exit and the corresponding contour plots from the experimental data are shown in Figs. 4(a–d). The nozzle exit plane is denoted by $X/D = 0.0$. The figures show good agreement between the solution and the experimental data. A slight asymmetry observed in the experimental data is attributed to a large scale recirculation present in the laboratory environment (Zaman, 1996b). The comparison also shows that the evolution of the jet cross section into a four lobed shape and eventually to an oval shape, as well as the axis switching by which the major axis of the oval cross section aligns with the short dimension of the nozzle cross section are well predicted by the computation.

A detailed comparison of streamwise vorticity contours, for the subsonic case, are presented in Figs. 5(a–c) and 6(a–c) at three of the four axial locations where streamwise velocity is presented. Since vorticity is a derived quantity, the agreement between the solution and the data is not expected to be as good since differentiation amplifies the errors in the mean flow quantities. The computed results show reasonably good agreement with the experimental data both in extent and magnitude. However, the computed results show a faster decay of peak vorticity compared to the experimental data. We believe that this rapid diffusion is due primarily to the excess diffusion from the turbulence model. This was also observed in the solution obtained using the k-ϵ turbulence model with the incompressible code presented in Steffen et al. (1995). It can also be seen that the computations have captured the dominant flow features that govern the streamwise vorticity dynamics. This is evident from the shape and location of the streamwise vortical structures that

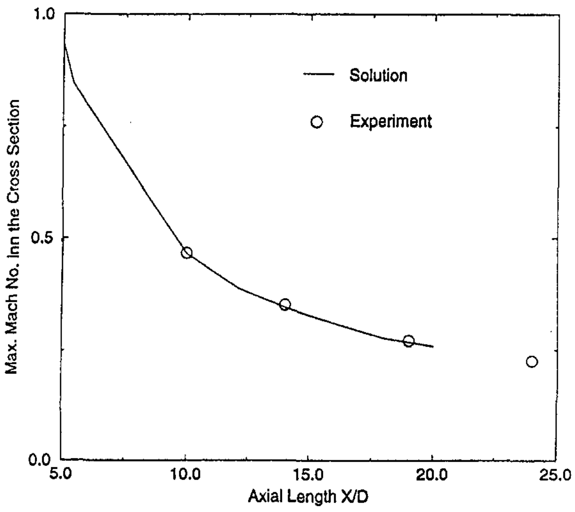

Fig. 10 Axial distribution of peak mach number (supersonic)

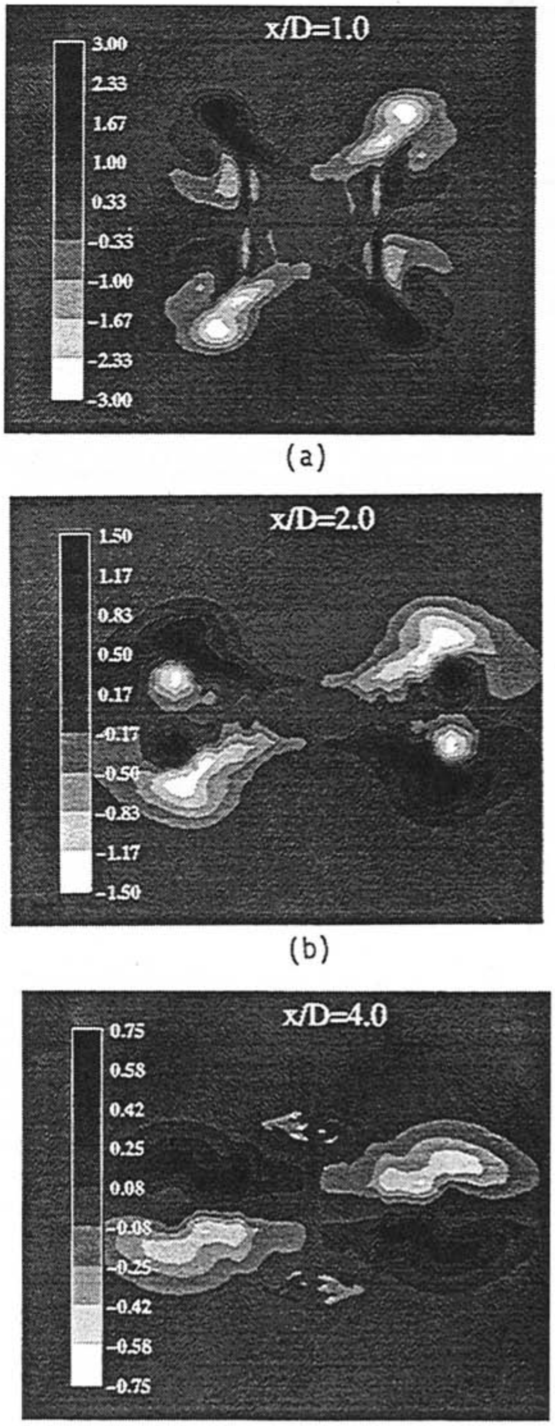

(a)

(b)

(c)

Fig. 11 Streamwise vorticity contours: computed (supersonic)

compare well with those of the experimental data. Note that at $X/D = 1$, the primary vortex pair and the secondary vortex pair of smaller amplitude and opposite sense are also captured in the computed results. The secondary vorticity decays rapidly in the experiment as well as computation. The streamwise velocity decay along the centerline is shown in Fig. 7 in comparison with the experimental data. Very good agreement is observed between the solution and the data.

Figures 8(*a–c*) and 9(*a–c*) present the comparison between computations and experimental data for the case of supersonic jet in the form of Mach number contours at three different axial locations downstream of the nozzle exit plane. Again, good agreement is observed between computed results and the experimental data. A discrepancy can be seen at $X/D = 19$ where the computed contours show a slight dip in the middle of the flowfield indicating an incipient bifurcation of the jet which was observed for other supersonic tabbed nozzles (Zaman et al., 1994). It is not clear why this tendency appears in the computed results, but not in the experiment. However, it is worth noting that the lateral extent of the jet spreading and the peak velocity magnitudes are well predicted by the computation. A slight asymmetry in the experimental data is again attributable to the large scale circulation in the laboratory. A quantitative comparison of the jet decay is presented in Fig. 10, which shows the axial distribution of Peak Mach number at any given cross plane in comparison with the corresponding experimental values. The comparison shows excellent agreement between the solution and the data.

Figures 11(*a–c*) show the computed streamwise vorticity contours at three different axial locations from the nozzle exit for the supersonic jet case. As mentioned earlier, corresponding experimental data is not available for comparison. Examining these plots and comparing them with the corresponding contour plots of the subsonic jet case (Figs. 6(*a–c*)), the following observations can be made. The magnitude of the streamwise vorticity is about three times higher compared to that of subsonic case. This large difference is for the most part due to the lack of a consistent normalizing velocity value for subsonic as well as supersonic jets. In the present comparisons, velocity at the nozzle exit plane is used for the nondimensionalization. This value for the subsonic case is 0.3 times the sonic speed where as for the supersonic case it is the sonic speed based on the local temperature at the exit (throat). The fact that the local temperatures are different and, as the supersonic jet expands the velocity increases and decreases through the expansion/shock cells, it is very difficult to determine a velocity scale which would provide a consistent comparison between the subsonic and supersonic cases. Overall, however, the vorticity distributions are quite similar for the subsonic and supersonic cases. This is consistent with the similar spreading and axis switching observed in both flow regimes. In the supersonic case the vortical structures appear more elongated and the secondary vortical structures are more pronounced (especially at $X/D = 2$) compared to the subsonic case. From these differences it can be inferred that, for the delta tab configuration considered in this study, the supersonic jet case shows higher spreading compared to the subsonic jet case. A conclusive evidence of the above inference can be established when further measurements are available for the supersonic case.

Summary

Three-dimensional viscous flow solutions have been obtained for two flow configurations of a 3:1 rectangular nozzle with two delta tabs to assess the capability of NPARC to predict the dominant flow features governing the mixing enhancement mechanism in the tabbed nozzle flowfields. Comparison of the computed results with experimental data shows that NPARC can predict the complex flow features that influence the vorticity dynamics and the resulting mixing enhancement for subsonic as well as supersonic jets. This is evidenced by the resolution of the primary and secondary vortical structures in both cases. In addition, comparison of the computed streamwise vorticity field of the supersonic jet case with that of the subsonic jet case shows a similar but somewhat more pronounced effect of the tabs in the supersonic case. The present study provides a strong support that the NPARC code can now be used for parametric studies of various tab configurations for use in the design of high speed nozzles.

Acknowledgments

The authors would like to thank Jim Sirbaugh of NYMA, Inc. for his valuable help in setting up the multiblock grid structure for NPARC and for his suggestions regarding the selection of the turbulence model. The computations have been carried out on the NASA Aeronautics Consolidated Supercomputing Facility's (ACSF) Cray C90 computer.

References

Bohl, D., and Foss, J., 1995, "Characteristics of the Velocity and Streamwise Vorticity Fields in a Developing Tabbed Jet," AIAA Paper 95-0102.

Bradbury, L. J. S., and Khadem, A. H., 1975, "The Distortion of a Jet by Tabs," *Journal of Fluid Mechanics*, Vol. 70, pp. 801–813.

Cooper, G. K., Jordan, J. L., and Phares, W. J., 1987, "Analysis Tool for Application to Ground Testing of Highly Underexpanded Nozzles," AIAA Paper 87-2015.

Cooper, G. K., and Sirbaugh, J. R., 1989, *PARC Code: Theory and Usage*, AEDC-TR-89-15, Arnold Engineering Development Center, Tullahoma, TN.

DeBonis, J. R., 1992, "Full Navier-Stokes Analysis of a Two-Dimensional Mixer/Ejector Nozzle for Noise Suppression," AIAA Paper 92-3570.

DeBonis, J. R., and Georgiadis, N. J., 1995, "Validation of the NPARC Code for Nozzle Afterbody Flows at Transonic Speeds," AIAA Paper 95-2614.

Georgiadis, N. J., and Yoder, D. A., 1994, "Use of Navier-Stokes Methods for the Calculation of High-Speed Nozzle Flow Fields," AIAA Paper 94-3212.

Ho, C.-M., and Gutmark, E., 1987, "Vortex Induction and Mass Entrainment in a Small-Aspect-Ratio Elliptic Jet," *Journal of Fluid Mechanics*, Vol. 179, p. 383.

Hussain, F., and Hussain, H. S., 1989, "Elliptic Jets. Part 1. Characteristics of Unexcited and Excited Jets," *Journal of Fluid Mechanics*, Vol. 208, pp. 257–320.

Jameson, A., Schmidt, W., and Turkel, E., 1981, "Numerical Solutions of the Euler Equations by Finite Volume Method Using Runge-Kutta Time Stepping Schemes," AIAA 81-1259.

Khavaran, A., and Georgiadis, N. J., 1996, "Aeroacoustics of Supersonic Elliptic Jets," AIAA Paper 96-0641.

NPARC Alliance Technical Team, 1994, *A User's Guide to NPARC*, NPARC Alliance Technical Team, Arnold Engineering Development Center, Arnold Airforce Base, TN.

Lee, H. W., and Sova, G., 1995, private communication, Rockwell Aerospace, Seal Beach, CA.

Pope, S. B., 1978, "An Explanation of the Turbulent Round-Jet/Plane-Jet Anomaly," *AIAA Journal*, Vol. 16, No. 3, pp. 279–281.

Pulliam, T. H., and Steger, J. L., 1980, "Implicit Finite-Difference Simulations of Three-Dimensional Compressible Flow," *AIAA Journal*, Vol. 18, pp. 159–167.

Pulliam, T. H., 1984, "Euler and Thin Layer Navier-Stokes Code: ARC2D, ARC3D," notes for CFD User's Workshop, The University of Tennessee Space Institute, Tullahoma, TN, March 12–16.

Reddy, D. R., 1995, "3-D Navier-Stokes Analysis of Crossing Glancing Shocks/Turbulent Boundary Layer Interactions," *Computers & Fluids*, Vol. 24, No. 4, pp. 435–445.

Reeder, M. F., 1994, "An Experimental Study of Mixing Enhancements in Jets with Vortex Generating Tabs," Ph.D. dissertation, Ohio State University, Columbus, OH.

Roache, P. J., 1994, "Perspective: A Method for Uniform Reporting of Grid Refinement Studies," *Journal of Fluids Engineering*, Vol. 116.

Samimy, M., Zaman, K. B. M. Q., and Reeder, M. F., 1993, "Effects of Tabs at the Nozzle Lip on the Flow and Noise Field of an Axisymmetric Jet," *AIAA Journal*, Vol. 31, No. 4, pp. 609–619.

Siclari, M. J., DelGuidice, P., and Jameson, A., 1989, "A Multigrid Finite Volume Method for Solving the Euler and Navier-Stokes Equations for High Speed Flows," AIAA Paper 89-0283.

Spalart, P. R., and Allmaras, S. R., 1992, "A One-Equation Turbulence Model for Aerodynamic Flows," AIAA Paper 92-0439.

Steffen, C. J., Jr., Reddy, D. R., and Zaman, K. B. M. Q., 1995, "Analysis of Flowfield from a Rectangular Nozzle with Delta Tabs," AIAA Paper 95-2146.

Steibrenner, J. P., and Chawner, J. R., 1995, *Users Manual for GRIDEN*, Version 10, Pointwise, Inc., Bedford, TX.

Zaman, K. B. M. Q., Reeder, M. F., and Samimy, M., 1994, "Control of an Axisymmetric Jet Using Vortex Generators," *Physics of Fluids*.

Zaman, K. B. M. Q., 1996, "Spreading Characteristics and Thrust of Jets from Asymmetric Nozzles," AIAA Paper 96-0200.

Zaman, K. B. M. Q., 1996, "Axis Switching and Spreading of an Asymmetric Jet: The Role of Coherent Structure Dynamics," *Journal of Fluid Mechanics*, Vol. 316, pp. 1–27.

D. M. Costura

P. B. Lawless

S. H. Fankel

Thermal Science and Propulsion Center,
School of Mechanical Engineering,
Purdue University,
1003 Chaffee Hall,
West Lafayette, IN 47907-1003

A Computational Model for the Study of Gas Turbine Combustor Dynamics

A dynamic combustor model is developed for inclusion into a one-dimensional full gas turbine engine simulation code. A flux-difference splitting algorithm is used to numerically integrate the quasi-one-dimensional Euler equations, supplemented with species mass conservation equations. The combustion model involves a single-step, global finite-rate chemistry scheme with a temperature-dependent activation energy. Source terms are used to account for mass bleed and mass injection, with additional capabilities to handle momentum and energy sources and sinks. Numerical results for cold and reacting flow for a can-type gas turbine combustor are presented. Comparisons with experimental data from this combustor are also made.

Introduction

Due to the inherent dynamics of the fluid system, the transient performance of a gas turbine engine can differ significantly from that predicted from quasi-steady operating assumptions. The consequences of these dynamics can be quite dramatic, including unexpected crossing of the compressor surge line while transitioning between operating points. Beyond the surge line, compressor rotating stall and surge serve as the forcing functions for a complex dynamic interaction between the engine components. These unsteady operating cycles are of particular interest, as they result in substantially reduced performance and durability. Since it is impossible to guarantee that an engine can avoid such behavior during its operational lifetime, recovery from rotating stall and surge is an important issue facing the gas turbine designer. Because of this, significant efforts have been made to accurately simulate the performance of a compressor undergoing a surge transient (Hale and Davis, 1992). As these techniques have matured, the focus increasingly has shifted toward extending these methods to encompass the entire engine, and, thus, capture the important compressor-combustor interactions that occur during engine surge (Garrard et al., 1995; Garrard, 1995). One of the more challenging tasks in this effort is the modeling of combustor behavior.

In the earliest days of gas turbine engine development, combustor design was regarded as somewhat of a "black art," typically involving labor intensive parametric testing. As the "art" evolved into more of a science, rule-based design techniques relying on experimental correlations became an important part of the initial design phase (Lefebvre, 1983). More recently, as industry was challenged by ever more stringent requirements for performance and emissions, advanced computational modeling has played an important role in the design sequence. Ideally, a combustor model would address the actual physical processes, including the effects of three-dimensional, turbulent, viscous reacting flow. Unfortunately, such models require vast computational resources that prohibit their use as a design tool. As a result, numerous efforts have been made over the past 35 years to produce simplified models to predict gas turbine combustor performance (Lefebvre, 1983). These models and numerical techniques have primarily focused on the simulation of steady flow in combustors, with particular emphasis in the past 20 years on pollution (Mellor, 1976; Gupta and Lilley, 1994). Considering the modeling difficulties experienced in steady flow, it is not surprising that little effort has been directed on addressing the added complexity of the transient behavior of the combustor. Unfortunately, the limited knowledge in this area has proven a key difficulty in modeling dynamic gas turbine engine behavior, especially post-stall dynamics.

Pryzbylko (1985) identified the important role the combustor played in determining an engines ability to recover from surge. He also presented one of the first discussions concerning modeling efforts in post-stall engine dynamics which addressed the desired features of a post-stall dynamic combustor model. Coincident with Pryzbylko's discussion of transient engine modeling, Davis (1986) modified a one-dimensional, time dependent stage-by-stage axial compressor model to describe the behavior of a high-speed compression system during post-stall events. This model was finite-volume based, and solved the one-dimensional Euler equations. It incorporated a time-lagged source term treatment to provide a dynamic stage characteristic in the rotating stall region. This treatment alleviated the problems associated with applying the quasi-steady assumption to events such as rotating stall and surge which were primary concerns of Pryzbylko.

To capture the effect of the combustor on system stability, further refinements of this model introduced a set of control volumes representing the combustor geometry. Heat released from the reaction was evenly distributed throughout the entire combustor section, with the presence of a flame based upon fixed equivalence ratio criterion. Similar to the approach taken for the compressor model, an ignition delay was imposed which lagged the heat release during re-light with a time constant taken from experimental measurements, analogous to the treatment of the turbomachinery terms that were included.

Over the last decade, the work of Davis evolved into the Aerodynamic Turbine Engine Code (ATEC) whose latest results are presented by Garrard (1995). This type of model has demonstrated its effectiveness in characterizing the dynamics of the gas turbine, albeit with certain limitations. One of these limitations is the accuracy with which the model can characterize the combustor behavior. The simple quasi-steady heat release formulation employed in the model has limited ability to accurately predict heat release, flame-out, re-light, and fuel migration in the combustor. Despite these limitations, the current models have shed new light on the importance of the compressor-combustor interaction during the engine surge event.

To improve the accuracy of such engine simulations, it is evident that an improved combustor model is necessary. A key

---

Contributed by the International Gas Turbine Institute and presented at the International Gas Turbine and Aeroengine Congress and Exhibition, Stockholm, Sweden, June 2–5, 1998. Manuscript received by the ASME Headquarters April 1, 1998. Paper No. 98-GT-342. Associate Technical Editor: R. Kielb.

to producing this improved model is the ability to model fuel transport, as this is critical to the calculation of the local equivalence ratio. As this local equivalence ratio is the basis for all of the empirical combustor dynamic calculations of the ATEC model, in itself including fuel transport would be a significant improvement. However, a significant additional benefit of adding fuel transport modeling is the ability to incorporate finite rate chemical kinetics which allows for the prediction of both the magnitude and location of the heat release due to combustion, thus removing significant empiricism from the analysis.

The objective of the research discussed herein is to develop a computational combustor model based on finite-rate chemistry for incorporation into a dynamic gas turbine engine model. The goal of the model under development focuses on characterizing the type of dynamic events typical of aircraft engine operation. Initial verification of this model was accomplished by comparison to step-combustor studies (Costura et al., 1997). As favorable agreement was achieved, computational studies herein are now focused on realistic gas turbine combustor geometry. Specifically, the model that is developed will be exercised against the geometry of a can-type gas turbine combustor currently being tested at Purdue as part of this research effort.

Technical Approach

As the objective of this work is to develop a dynamic combustor model for incorporation into the ATEC full gas turbine engine simulation code, the same modeling philosophy and numerical approach used in ATEC (Garrard, 1995) is employed here. The model is then evaluated on the geometry from a can type gas turbine combustor which has been tested at Purdue (Costura, 1997).

Governing Equations. The unsteady quasi-one-dimensional Euler equations, supplemented with the species mass conservation (neglecting molecular transport), are numerically integrated using a first-order characteristic-based, explicit finite-difference method (Kneile and Hale, 1995). The governing equations, expressed in vector conservative form, are

$$\frac{\partial \vec{U}}{\partial t} + \frac{\partial \vec{F}}{\partial x} = \vec{G} \qquad (1)$$

$$\vec{U} = \begin{bmatrix} S\rho \\ S\rho u \\ SE \\ S\rho Y_i \end{bmatrix} \qquad (2)$$

$$\vec{F} = \begin{bmatrix} S\rho u \\ S(\rho u^2 + P) \\ S(E + P)u \\ S\rho Y_i u \end{bmatrix} \qquad (3)$$

$$\vec{G} = \begin{bmatrix} \dot{m}_b + \dot{m}_{inj} \\ P\dfrac{dS}{dx} + F_{\text{blade}} + F_b - F_l - F_s \\ W_s + \dot{Q}_{\text{chem}} + \dot{H}_b + \dot{H}_{inj} + \dot{E}_{ign} \\ \dot{m}_b Y_i + \dot{m}_{inj} Y_i + \dot{\omega}_i \end{bmatrix}, \qquad (4)$$

where ρ, u, E, P, Y_i, and S are the density, velocity, total energy (sensible, chemical and kinetic), pressure, i^{th} species mass fraction, and cross-sectional area, respectively. The source vector G contains mass, momentum, energy, and species source/sink rate terms per unit length. In the conservation of mass equations (total and individual species), $\dot{m}_b$ represents the mass transfer rate across boundaries other than the inlet or exit (such as secondary or dilution air addition), and $\dot{m}_{inj}$ represents mass addition due to fuel injection. In the momentum equation, the first term is due to the cross-sectional area variation, while the remaining terms are due to blade forces (not used here), bleed momentum losses, flow losses, and skin friction losses, respectively. In the energy equation, the source terms represent shaft power (not used here), chemical energy release, enthalpy gain due to mass addition and thermal energy deposition due to ignition, respectively. In the species mass conservation equation, the source terms represent mass addition due to dilution air and fuel injection, and the chemical production term. Under the assumption of an ideal gas mixture and cold air-standard assumptions, the equation of state is

$$P = (\gamma - 1)\left(E - \frac{\rho u^2}{2}\right), \qquad (5)$$

where γ is the ratio of the specific heats.

The formulation and major assumptions of the model are made to be consistent with the ATEC approach and may be extended and relaxed in future work.

Combustion Model. Hydrocarbon fuel combustion is modeled with a single-step, global chemical reaction mechanism based upon the work of Westbrook and Dryer (1981), which is of the following form:

$$C_xH_y + (x + y/4)O_2 \rightarrow xCO_2 + (y/2)H_2O. \qquad (6)$$

After testing numerous mixtures of fuel and oxidizer, Westbrook and Dryer were able to develop a set of reaction rate parameters that provided excellent agreement between experimental and predicted flame speeds and flammability limits. The reaction rate equation used takes the form of the Arrhenius equation:

$$\dot{\omega}_{C_xH_y} = \frac{d[C_xH_y]}{dt} = -A\exp\left(-\frac{E_a}{RT}\right)[C_xH_y]^a[O_2]^b, \qquad (7)$$

where the parameters R_u, A, E_a, a, and b, represent the universal gas constant, pre-exponential factor, activation energy, and concentration exponents, respectively. The last four terms are the parameters that were adjusted to match experimental data accumulated during their studies. The study performed by these authors was primarily based upon temperatures in excess of 1000 K which are typically encountered in steady flames. In transient simulations, where ignition phenomena are important, using a constant activation energy, E_a, can lead to undesirable results. Of primary concern is the low temperature kinetics which dominate during this period of the combustion process. Generally, in order to describe an ignition event, significant modifications need to be implemented to produce a stable solution (Winowich, 1990).

Ignition is dependent upon the formation of free-radical species that develop as a result of the ignition source, usually a spark. These free-radicals are not modeled in a global one-step combustion mechanism because these species are simply intermediate products that are subsequently decomposed as the reaction reaches, ideally, completion characterized by the ultimate production of carbon dioxide and water vapor. With their absence, there is no physical mechanism for ignition delay which in turn causes extremely rapid increases in chemical heat release often driving computational models to instability. The following methods have been proposed and tested to overcome this weakness in the chemical model:

- Incorporation of a minimal number of additional chemical reactions. Typically at least 5–7 chemical equations involving generally ten additional chemical species are necessary to have the desired effect (Vlachos, 1996; Egolfopoulos et al., 1992).
- A two-step chemistry mechanism which divides the overall reaction rate into disparate temperature ranges. When the local temperature is below a lower temperature threshold, a low temperature global mechanism is used to model

Fig. 1 Photograph of combustor liner

ignition events. For high temperature combustion, typically over 1100 K, the models use another single step global mechanism. Finally, while in the region between the lower threshold and high temperature regime, a representative average of the two rates is employed (Kong and Reitz, 1993; Ayoub and Reitz, 1997).

- Modification of one or more of the reaction rate parameters while still using a single global chemical kinetics mechanism (Winowich, 1990; Segal and Haj-Harra, 1994; Chitsomboon and Notham, 1991).

In this study, the last method was chosen, as the primary motivation for using a quasi-one-dimensional model is to balance the computational workload with the requirement for a physics-based dynamic model. Thus, the inclusion of more than a half-dozen additional species conservation equations was not regarded as a worthwhile investment of computational resources in this context. And although the use of multiple global kinetics mechanisms over a few temperature regimes does not increase the computational time significantly, the approach has been used principally in multidimensional analysis of complex flows. Without any documented efforts in one-dimensional flows, the data base presented in the literature was not directly applicable. Thus, upon evaluation of the probability of success, this technique was viewed with less enthusiasm than the single mechanism implementation.

The principle task in implementing the single global kinetics method was to determine which particular parameter to vary. Previous studies focused mainly on adjusting the activation energy (Chitsomboom and Northam, 1991; Segal and Haj-Hariri, 1994) and pre-exponential terms (Winowich, 1990). Aly (1991) varied each of these parameters for a generic Arrhenius equation, and studied the effect upon the reaction rate. It is important to note that aside from ignition, a steady-state physical characteristic needs to be addressed, namely the distribution of the reaction zone. Reaction models are calibrated to provide an accurate comparison to experimentally measured flame thickness. However, the flame thickness measured is usually based on an opposed jet flame experiment for which the flame is a thin sheet rather than the distributed shape present in a combustor or afterburner. Aly found that modifying either the pre-exponential factor or activation energy spreads the reaction zone as they are decreased and increased respectively. This demonstrated that modifying either of these parameters would produce the desired stretching of the flame as well as compensating for the ignition effects. Thus, the choice was narrowed down to two parameters: activation energy and the pre-exponential factor. Ultimately, a parabolic dependence of the activation energy on temperature was selected, primarily because the reaction rate is more sensitive to changes in activation energy than changes in the pre-exponential factor. The parabolic relationship was clipped to a constant value below a critical low temperature limit and above a high temperature limit (500 K and 2500 K in these studies).

Numerical Approach. Numerical integration of the governing equations is achieved using an explicit, first-order, finite-difference approximation to the flux-split characteristic form of the hyperbolic partial differential equations (Kneile and Hale, 1995). The finite-difference equation for this scheme is

$$\left(\frac{\Delta\vec{U}}{\Delta t}\right)_j = I^{+}_{j-1/2}\left[\vec{G}_{j-1/2} - \frac{(\vec{F}_j - \vec{F}_{j-1})}{(x_j - x_{j-1})}\right] + I^{-}_{j+1/2}\left[\vec{G}_{j+1/2} - \frac{(\vec{F}_{j+1} - \vec{F}_j)}{(x_{j+1} - x_j)}\right], \quad (8)$$

where first-order Euler integration is used to advance the solution in time. In this equation, the I matrices pre-multiplying the square bracketed terms on the right hand side involve the eigenvalues of the Jacobian matrix and the + and − superscripts indicate right-running and left-running characteristics, respectively. Notice that the fluxes are evaluated at the grid points whereas the I matrices and the source term vector are evaluated at the cell interfaces. In order to evaluate these quantities at the cell interface, variables are approximated by Roe averages (Hirsch, 1990). A stable time step for the scheme is chosen as the more restrictive of a CFL based time step and a chemistry based time step (Drummond et al., 1996). More details and a derivation of the method are given by Costura (1997).

Boundary Conditions. Characteristic-based boundary conditions, extended for reacting flow, are enforced at the inlet and exit of the computational domain (Kneile and Hale, 1995). At the inlet, total temperature, total pressure, and species mass fractions are specified. At the outlet, either static pressure, mass flow rate, or Mach number are specified. Characteristic equations corresponding to the outgoing characteristics at the exit, i.e., the u and $u + a$ (where a is the sound speed), and outgoing characteristics at the inlet, i.e., the u-a, are computed based on a subsonic boundary assumption. The boundary conditions are developed in order to be fully functional with a full engine simulation, including events such as engine surge. For this purpose, during reverse flow the inlet boundary condition is transitioned to a static pressure boundary condition. Upon resumption of forward flow, the upstream stagnation boundary conditions are increased at a user specified rate until the values match those specified before the reverse-flow event was encountered (Garrard, 1995). Essentially, this is similar to a compressor recovery in the full engine simulation.

Results and Discussion

The combustor liner geometry to be evaluated is shown in Fig. 1. This is a simple, swirl, and cross jet stabilized can-type

Table 1 Flow splitting information at test operating point

Physical Location	%
Inlet Swirl Slots	8.0
1st Primary Row	16.0
2nd Primary Row	23.5
3rd Primary Row	31.0
1st Secondary Row	40.3
2nd Secondary Row	49.6
3rd Secondary Row	59.0
Dilution/Annulus	100.0

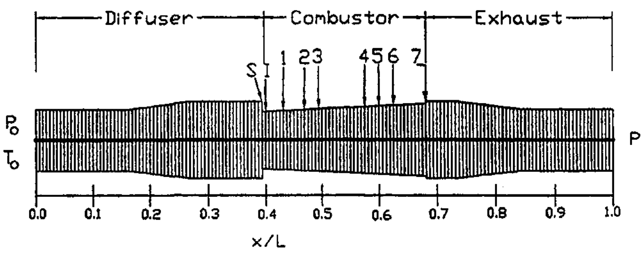

Fig. 2 Computational grid, physical diagram, and boundary conditions for test combustor geometry

combustor that is undergoing testing as part of this research effort. The experimentally determined flow splits for this combustor are presented in Table 1, and further details on the geometry and experimental data are given by Costura (1997). The combustor is liquid fueled. In the experimental studies, the combustor was fired with ethyl alcohol, due to the need for a high volatility fuel to minimize the effects of spray quality. This introduces some error due to the large latent heat of vaporization, however, which is not currently modeled in the code.

Steady-State Simulation. Numerical predictions for the experimental combustor geometry under nonreacting (cold) flow conditions are first examined. For this test case, the inlet total temperature, pressure and mass flow rate are 311 K, 275.6 kPa, and 0.272 kg/s, respectively. Injection of gaseous ethyl alcohol occurs just upstream of the primary zone at a rate of 22.7 L/hr to coincide with the experimental testing. Figure 2 shows the geometry, computational grid, and boundary conditions, where 161 uniformly spaced grid points are employed in the simulations. The S and I indicators correspond to the swirler and fuel injector locations. The numbers indicate liner holes. The percentage of air that passes through the swirler slots and the primary, intermediate, and dilution liner holes is measured in the laboratory and specified in the code. Losses associated with the swirlers are not accounted for in this preliminary test and the slot air injection is specified with zero streamwise momentum. Constant inlet total temperature, pressure, and exit static pressure are enforced. Steady state is achieved after 0.25 s. Figure 3 shows the steady-state velocity distribution within the combustor. The velocity decreases as the flow enters the diffuser and again when the flow is split before it enters the swirlers and the primary zone. The velocity increases as fuel is injected and as air is reintroduced into the combustor through the liner holes. The velocity increases further as the flow enters the exhaust section and exits the combustor at a slightly higher velocity than when it entered due to the additional fuel mass.

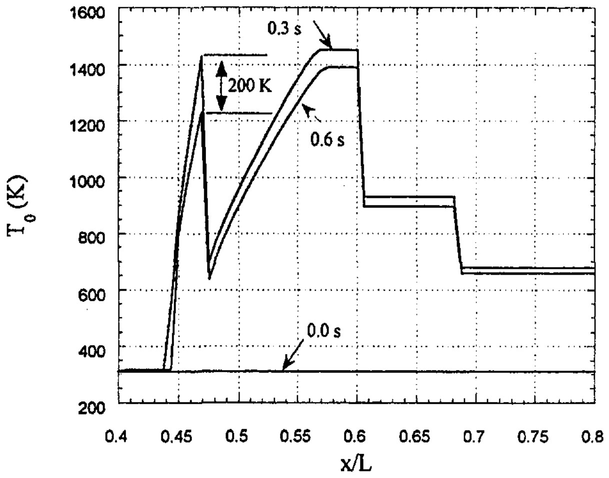

Fig. 4 Total temperature profiles for steady reacting flow

Simulations of steady-state reacting flow are next examined. Initial conditions for this test case were identical to the cold flow study with the exception of the dilution air splits. In this test case, the three rows of the primary zone, and the three rows of the secondary zone were lumped into one injection port for each group with the amount of dilution air in each zone remaining the same as the cold flow case.

At the beginning of the simulation fuel begins to be injected at a constant equivalence ratio of 1.81 which approximates the primary zone equivalence ratio calculated in the laboratory tests, and the ignitor is activated to elevate the ignitor control volume by 200 K. Figure 4 shows temperature profiles at 0.30 and 0.60 s for the portion of the computational domain between $x/L = 0.4$ and $x/L = 0.8$. Until the ignitor source term is deactivated at 0.30 s, the solution reaches a steady state following the ignition event. When the ignitor source term is removed, the primary zone temperature decreases by 200 K as the flow reaches a second-steady solution indicated by the profile given at 0.60 s. The predicted exit temperature is in good agreement with the experiments, with an exit temperature between 650 K and 700 K observed in the data.

Figure 5 presents a trace of the total temperature at $x/L = 0.56$ which is located just downstream of the primary zone. Once again the effect of turning off the ignitor is seen at 0.30 s, with the

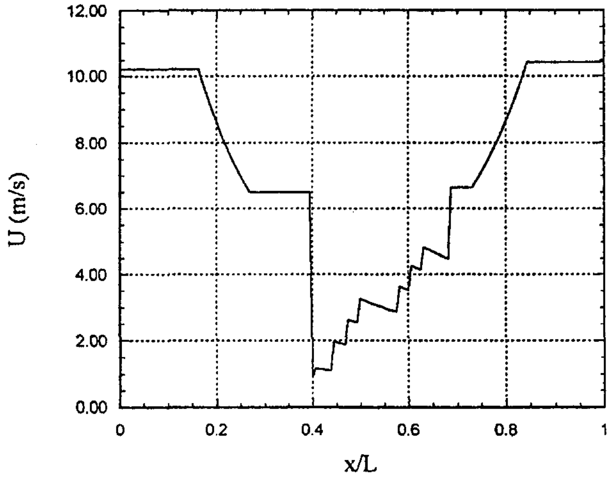

Fig. 3 Steady-state velocity profile for cold flow test

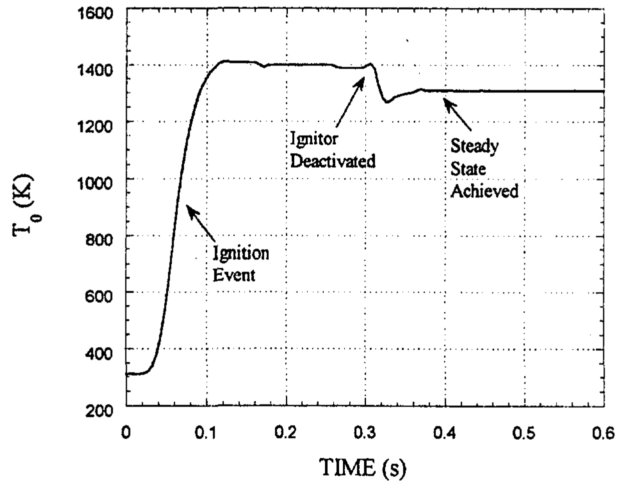

Fig. 5 Total temperature trace at $x/L = 0.56$ for steady reacting flow test case

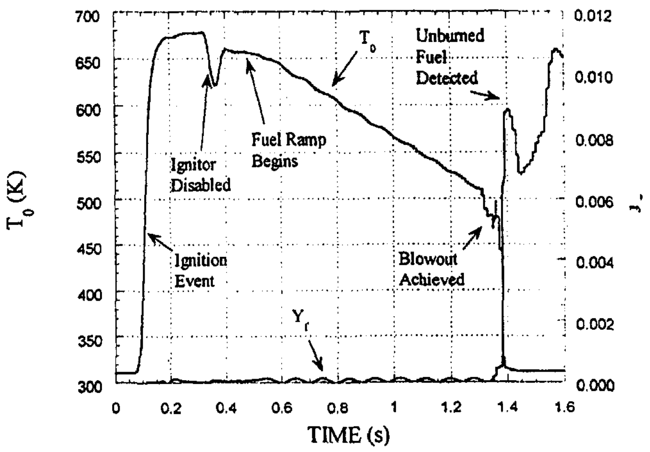

Fig. 6 Exit total temperature trace and fuel mass fraction trace for the lean blowout transient test case

temperature profile dropping nearly 100 K before becoming stable at approximately 1300 K. Since the primary zone dilution air has been added, only 50 K of the temperature drop can be attributed to the ignitor. The remainder of the temperature drop is due to a slight shift in the temperature profile where the reaction zone has elongated due to the absence of the preheat provided by the ignitor source term. In other words, at this location the fuel is no longer completely burned as it was in the previous steady state solution presented at 0.30 s.

Lean Blow Out Simulation. Results from a lean blow out simulation are achieved with initial conditions identical to the previous test case with the ignitor source term turned off at 0.30 s. At 0.40 s, the fuel injector mass flow rate is reduced to decrease the equivalence ratio at a rate of 1.0 per s. A plot of the exit total temperature trace is given in Fig. 6. Over the period from 0.40 to 1.30 s, there is a gradual decline in exit temperature as the fuel flow rate is decreased. After a brief transient event at approximately 1.35 s, lean blowout is achieved at a primary zone equivalence ratio of 0.8, as indicated by the sharp decline in exit temperature. The exit fuel mass fraction trace also provided in Fig. 6 indicates the presence of unburned fuel as a result of the injector remaining active until the end of the simulation.

Upon achieving lean blowout, a large disturbance is evident in the mass flow rate which is presented in Fig. 7. Following the spike, a self-sustaining oscillation is evident with an approximate frequency of 100 Hz. This may be explained by a brief reverse flow event that occurs just upstream of the combustion liner where the secondary air is extracted. This event causes the secondary air source term to shut off, due to the current numerical formulation of the source term, until the flow recovers. The subsequent occurrence of reverse flow oscillations induced at this axial location corresponds to the exact frequency of the exit mass flow rate oscillations, which would suggest that the source term is driving the flow into this perpetual instability.

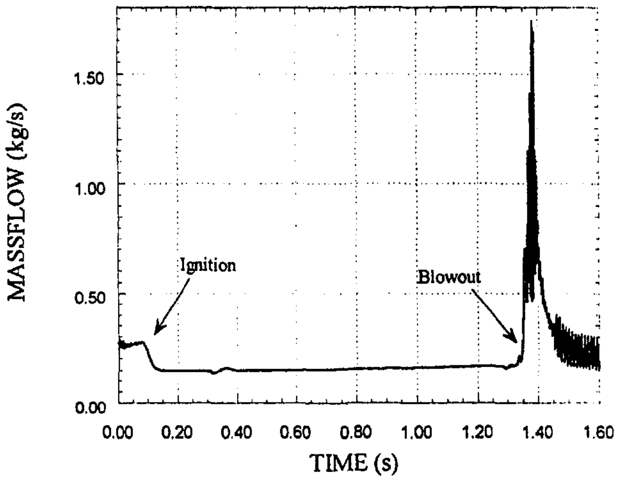

Fig. 7 Exit mass flow rate trace for lean blowout transient

An experimental test of lean blowout in this combustor has been performed (Costura, 1997) with an equivalence ratio change identical to the above simulation. In Fig. 8, data from high response thermocouples located in the primary zone of the combustor and the exit plane are shown. Here the primary zone temperatures are used primarily as an indication of flame position, as radiation effects are significant and reduce temperature accuracy. However, it is clear that primary zone temperatures are similar to those predicted previously in Fig. 4. Of significance in the lean blow out transient is the change in character of the primary zone trace at t = 13.4 s, followed by a sharp decay in primary zone temperature. This occurs at an exit temperature of 450 K, and is consistent with termination of flame in the primary zone. This exit temperature value compares favorably to the 500 K value indicated by the simulation at lean blowout.

Conclusions

A combustor model was developed to study gas turbine dynamics. The model was tested for both cold and hot flow in can-type gas turbine combustor geometry. Comparisons to the available experimental data were favorable. Results from the combustor model and transient combustor test data show that

1 cold flow simulations performed with the test combustor geometry demonstrated the models ability to provide a stable solution while diverting large quantities of mass flow required to model the effect of flow splitting
2 in addition to the detection of unburned fuel and decreasing exit temperature, lean blowout simulations showed similarities to the behavior exhibited in the experimental data

In addition, the current studies have illuminated the need for a revision of the current secondary mass flow model, as this proved inadequate to provide accurate results for large scale flow disturbances such as that resulting from lean blowout. In addition, although adequate for a first approximation, the assumptions of infinite mass transfer rate between the extraction and injection ports and fixed flow split information in this model need to be re-evaluated in the future. In order to alleviate these

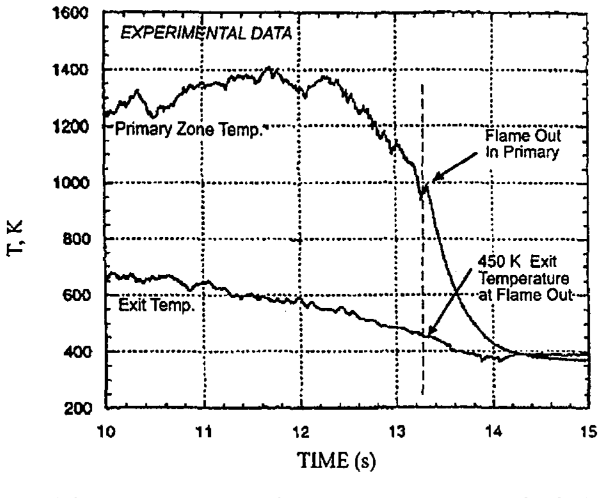

Fig. 8 Exit total temperature and primary zone temperature for the lean blowout testing over the period t = 10.0 s until t = 15.0 s

concerns, it should be possible to parallel process the secondary air passage using the extraction node as the inlet boundary and the final injection port as the exit boundary. The intermediate injection holes would then be calculated as bleed terms based upon the pressure differential across the liner interface.

As a broader range of data from the experimental program becomes available, it is foreseen to continue to exercise and develop this model against that database, with a focus on rich blow out and reverse flow events.

Acknowledgments

This work was supported by the Arnold Engineering Development Center under the Joint Dynamics Air-Breathing Propulsion Simulation (JDAPS) working group. The authors would like to thank Dr. Milt W. Davis and Dr. Doug Garrard of Sverdrup Technology, Inc, AEDC Group, for their assistance with this project.

References

Aly, S.L., 1991, "Flame Structure and Reaction Kinetics: The Effects of the Pre-exponential Frequency Factor, Reaction Order, and Activation Energy," *Applied Energy,* Vol. 37, pp. 139–150.

Ayoub, N.S., and R.D. Reitz, 1997, "Multidimensional Modeling of Fuel Effects and Split Injections on Diesel Engine Cold-Starting," *Journal of Propulsion and Power,* Vol. 13, No. 1, pp. 123–130.

Chitsomboon, T., and G.B. Northam, 1991, "Computational Fluid Dynamics Prediction of the Reacting Flowfield Inside a Subscale Scramjet Combustor," *Journal of Propulsion and Power,* Vol. 7, No. 1, pp. 44–48.

Costura, D.M., 1997, "A Computaional and Experimental Study of Gas Turbine Combustor Dynamics," M.S. thesis, Purdue University, West Lafayette, IN.

Costura, D.M., Velez, T.A., Lawless, P.B., and Frankel, S.H., 1996, "A Model for Combustor Dynamics for Inclusion in a Dynamic Gas Turbine Engine Simulation Code," AIAA-97-3336.

Davis, M.W., 1986, "A Stage-by-Stage Post-Stall Compression System Modeling Technique: Methodology, Validation, and Application," Ph.D. dissertation, Virginia Polytechnic Institute and State University, Blacksburg, VA.

Drummond, J.P., Rogers, R.C., and Hussaini, M.Y., 1996, "A Detailed Numerical Model of a Supersonic Reacting Mixing Layer," AIAA-86-1427.

Egolfopoulos, F.N., Du, D.X., and Law, C.K., 1992, "A Study on Ethanol Oxidation Kinetics in Laminar Premixed Flames, Flow Reactors, and Shock Tubes," Proceedings, Twenty-Fourth Symposium (International) on Combustion, The Combustion Institute, Pittsburgh, PA, pp. 833–841.

Garrard, G.D., Davis, M.W., Jr., and Hale, A.A., 1995, "Recent Advances in Gas Turbine Engine Dynamic Models Developed Through JDAPS," ASME Paper 95-GT-146.

Garrard, G.D., 1995, "ATEC: The Aerodynamic Turbine Engine Code for the Analysis of Transient and Dynamic Turbine Engine System Operations," Ph.D. dissertation, The University of Tennessee, Knoxville, TN.

Hale, A.A., and Davis, M.W., 1992, "Dynamic Turbine Engine Compressor Code DYNTECC—Theory and Capabilities," AIAA Paper 92-3190.

Hirsch, C., 1990, *Numerical Computation of Internal and External Flows,* John Wiley & Sons, New York.

Kong, S.C., and Reitz, R.D., 1993, "Multidimensional Modeling of Diesel Ignition and Combustion using a Multistep Kinetics Model," ASME JOURNAL OF ENGINEERING FOR GAS TURBINES AND POWER, Vol. 115, pp. 781–789.

Kneile, K.R., and Hale, A.A., 1995, "Appendix C: Numerical Solution to the Governing Equations," Appendix C in Garrard, Ph.D. dissertation, The University of Tennessee, Knoxville, TN.

Lefebvre, A.H., 1983, *Gas Turbine Combustion,* Taylor & Francis, London.

Mellor, A.M., 1976, "Gas Turbine Engine Pollution," *Prog. Energy Combust. Sci.,* Vol. 1, pp. 111–133.

Przybylko, S.J., 1985, "Application of System Identification Techniques to Poststall Combustor Dynamics," AIAA Paper 85-1353.

Segal, C., and Haj-Hariri, H., 1994, "Effects of the Chemical Reaction Model on Calculations of Supersonic Combustion Flows," *Journal of Propulsion and Power,* Vol. 11, No. 3, pp. 565–568.

Vlachos, D.G., 1996, "Reduction of Detailed Kinetic Mechanisms for Ignition and Extinction of Premixed Hydrogen/Air Flames," *Chemical Engineering Science,* Vol. 51, No. 16, pp. 3979–3993.

Westbrook, C.K., and Dryer, F.L., 1981, "Simplified Reaction Mechanisms for the Oxidation of Hydrocarbon Fuels in Flames," *Combustion Science and Technology,* Vol. 27, pp. 31–43.

Winowich, N.S., 1990, "Numerical Prediction of Turbulent Flame Stability in Premixed/Prevaporized (HSCT) Combustors," National Aeronautics and Space Administration Contractor Report NASA-CR-188991.

New Nondimensional Parameters in Fluid Mechanics and Their Application to Turbine Flowmeter Data Analysis

S. Mozumdar

O. Islam

AlliedSignal Engines,
P. O. Box 52181, MS 302-201,
Phoenix, AZ 85072-2181

Dimensional analysis has been used in experimental fluid mechanics for over a hundred years. Controllable and uncontrollable variables in an experiment can be efficiently organized into nondimensional groups or parameters. Such nondimensional parameters are used for geometric scaling, and for developing dynamic similitude in experimental processes. Commonly used nondimensional parameters in fluid mechanics include Reynolds number, Mach number, Froude number, Weber number, Strouhal number, etc. Most modern text books and technical papers discuss the use of Buckingham Pi theorem for developing the nondimensionalization process. An often ignored and somewhat older technique is the Rayleigh method. Both the Pi theorem and the Rayleigh method are founded on the principle of dimensional homogeneity, and require some experience in the grouping of physical variables. The present paper uses the Rayleigh method to develop two new nondimensional parameters. A discussion is presented about the use of the parameters in the application of turbine flowmeter calibration and test data analysis. It is shown that data analysis for turbine flowmeters is considerably simplified by the use of the new parameters.

1 Introduction

The basic principle of the operation of turbine flowmeters in fluid flow measurement has been in use for over 400 years (Baker, 1991). The early uses were more for the measurement of speed and distance-log than for fluid volumetric flow-rate. A typical present-day flowmeter consists of a bladed rotor supported by bearings in a housing with a magnetic (mag), or modulated carrier (RF) pick-off to generate pulses corresponding to the rotation of the rotor in the fluid stream. The frequency of the pulse-stream is proportional to the flow velocity, within some limitations of operating conditions. Thus, when installed in a pipe, the volumetric flowrate can be determined from the measurement of the output frequency. The volume flowrate can be converted to mass flowrate if the fluid density is known. Turbine flowmeters are widely used in the industries of aerospace, oil and gas, automobile, etc., because of their reasonable cost, good accuracy, operational simplicity, and durability in field usage.

Turbine flowmeters are calibrated to determine the frequency-flowrate relationship. This relationship is a function of the temperature and pressure of the fluid which affect fluid properties, and the geometric dimensions of the meter. In general, the operating conditions are different from the calibration-conditions, thus requiring the development of a correlation technique. The correlation model is used to process the calibration data, as well as the meter output frequency in operation, to determine the volume flowrate at operating conditions. Several models are used for the characterization of the frequency-flowrate relationship. The most comprehensive model is the Strouhal-Roshko characterization (Mattingly, 1992). Despite recent attempts to standardize this model (SAE, 1997), it is the least frequently used because of the inherent complexity in translating it into an algorithm for automated data acquisition systems (ADAS). This led to the current effort to develop a new correlation model.

The following sections give a brief overview of the existing correlation models with their limitations, and describe the development of the new models resulting in two new nondimensional parameters. Sample case studies using the new parameters are presented with suggested use of the parameters in other areas of applied fluid mechanics.

2 Existing Correlation Models

Several correlation models are used to characterize the frequency-flowrate relationship for a turbine flowmeter. It is an acceptable practice to consider the fundamental dimensions in applied mechanics as Mass (M), Length (L), and Time (T). Assuming incompressible operating conditions and negligible mechanical and electromagnetic forces (viz. negligible bearing and magnetic drag) for a flowmeter, the controllable parameters are the volumetric flowrate (Q, with the associated dimension of L^3T^{-1}), the fluid density (ρ, with the dimension of ML^{-3}), and the fluid absolute viscosity (μ, with the dimension of $ML^{-1}T^{-1}$). The uncontrollable parameters are the meter bore-diameter (D, with the dimension of L), and the output frequency (f, the response function and a characteristic of the meter, with the dimension of T^{-1}). It may then be stated (Hochreiter, 1957) that a correlation model can be developed on the basis of the functional relationship

$$Q = fn(f, D, \rho, \mu). \tag{1}$$

A methodically developed model for dynamic similitude of the characteristics of a meter must include these five dimensional parameters. The goal of the correlation model is to develop the characteristics to determine the unknown variable Q from a measurement of the response variable f. It may be noted that conditions (viz. temperature and pressure) that affect ρ also affect μ. Hence, it is a common practice to combine μ and ρ into the ratio of the two, the kinematic viscosity, ν, with the dimension of L^2T^{-1}. Both ρ and μ, and hence ν, are strong functions of temperature, but are weak functions of pressure. Following is a brief description of the existing correlation models.

Contributed by the International Gas Turbine Institute and presented at the International Gas Turbine and Aeroengine Congress and Exhibition, Stockholm, Sweden, June 2–5, 1998. Manuscript received by the ASME Headquarters April 1, 1998. Paper No. 98-GT-486. Associate Technical Editor: R. Kielb.

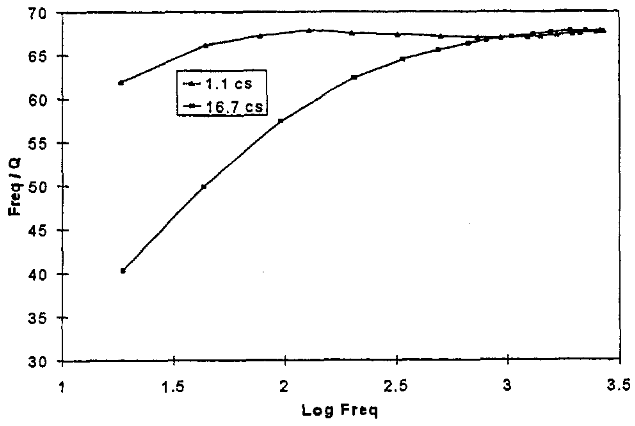

Fig. 1 Constant *K*-factor model

2.1 The Constant K-factor Model. The ratio of f and Q is often referred to as the meter K-factor (with the dimension of L^{-3}). It is identical to the ratio of the number of pulses counted over a period of time to the volume flow through the meter over the same time. This model assumes that the meter K-factor is constant over the entire range of the meter in a specific application. This range is also commonly referred to as the linear range of a flowmeter at a specific fluid viscosity. While it may be possible to carefully fine-tune a flowmeter for such linear operation over a limited range, the model suffers from serious limitations. As is evident from Eq. (1), the other three parameters, viz., D, ρ, and μ (alternatively, D and ν) must remain constant over the range of operation. Hence, the calibration must be done at the same ν as the application fluid (preferably using the same fluid), and the operating temperature and pressure must be held constant.

Figure 1 shows the typical K-factor characteristics of a 0.4–40 Liters per Minute (LPM) turbine flowmeter with RF pickoff. The K-factor is plotted against f at two different ν's, and the plots are generated from calibration data referenced to 15.5°C. The upper curve is at a ν of 1.1 cs and the lower one is at 16.7 cs. The significant difference between the two curves indicates that the constant K-factor model is valid only at one fixed viscosity. In addition, at the lower ν of 1.1 cs, the linear range of the flowmeter is approximately 80 to 2700 Hz, with a tolerance band of ± 1.5 percent. The corresponding turn-down ratio is 34:1. However, at the higher viscosity of 16.7 cs, the linear range is narrowed to approximately 795 to 2600 Hz (i.e., a turn-down ratio of 3:1), keeping the same tolerance band of ± 1.5 percent. Thus, it is extremely important, for this model to be applied, to calibrate the meter at the viscosity (ν) of application, determine the linear range with an acceptable tolerance band of uncertainty, and ensure that the conditions of operation do not result in a change in the viscosity of the fluid. It is a simple model to use in an ADAS, when the resulting measurement uncertainties can be tolerated. However, dynamic similitude is lost in this dimensional model and, when the limitations are not adhered to, the errors in the measured flowrate can climb to several percentage points.

2.2 The Universal Viscosity Curve (UVC) Model. This model characterizes the K-factor as a function of the ratio f/ν (with the associated dimension of L^{-2}). A characteristic curve is created by plotting the K-factor in the y-axis and the ratio f/ν in the x-axis, thus taking into account the effect of kinematic viscosity. This is a dimensional correlation model since both the K-factor and f/ν are dimensional quantities. However, as is evident from Eq. (1), along with the assumption of incompressibility, only D has to be held constant for the model to be valid. Typically, the flowmeter is calibrated in fluids of two or more ν's covering the expected operational range of ν. The characteristic curves (K-factor versus f/ν) are then plotted from the calibration data, and the curves are blended manually to create a single characteristic curve, i.e., the UVC.

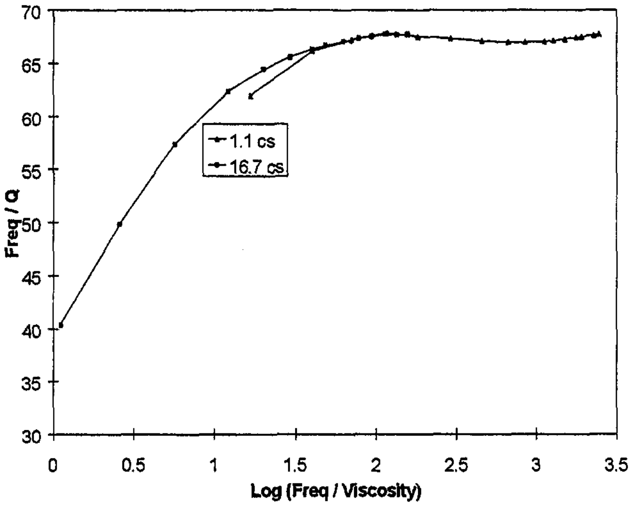

Fig. 2 UVC model step 1

Figure 2 shows the first step towards generating the UVC characteristics for the same flowmeter with the same calibration data as in section 2.1. The effect of viscosity is now taken into account by using it as a factor in the X-axis. The blended UVC is generated by eliminating the portion of the low viscosity curve that falls away from the continuum, and is shown in Fig. 3. This leads to some risk of compromising accuracy when using this model at low-viscosity low-flow conditions, which is the part of the curve dropped off while generating the UVC. Even though dynamic similitude is lost, the model works when there is no significant change in D, and it fails when D changes, usually due to changes in pressure and temperature, both of which have relatively small effects on D. The model involves manual intervention to blend the curves. The blended UVC is nonlinear in nature resulting in the added complexity of digitizing the curve to create a look-up table in an ADAS. In general, the nature of the curve has been found to be different even within the same family and size of flowmeters. In addition, if the range of viscosity of the application fluid is large, it requires several calibrations at intervals of viscosity to generate the blended UVC.

2.3 The Strouhal-Roshko (St-Ro) Characterization Model. The basic parametric relationships of this nondimensional model were first developed by V. P. Head in 1950 and

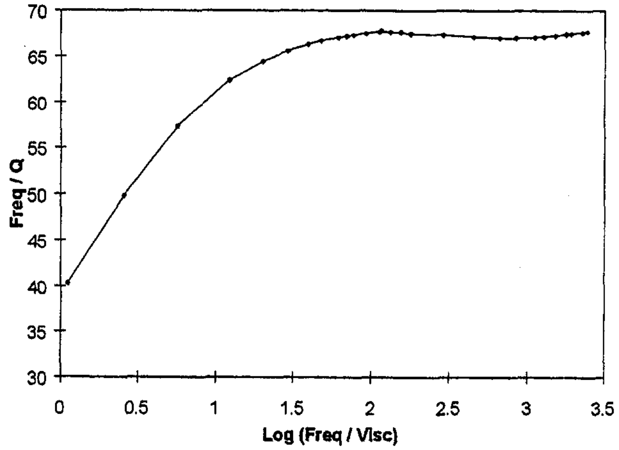

Fig. 3 Universal viscosity curve (UVC)

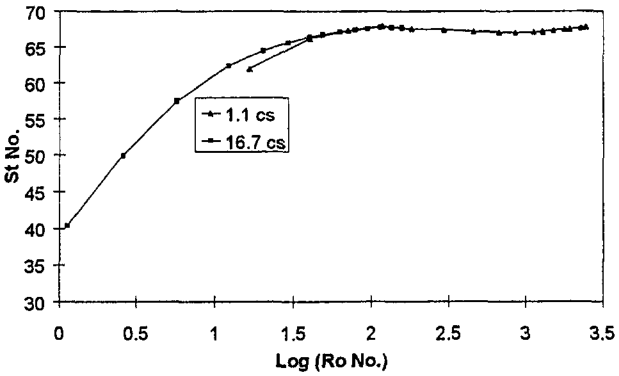

Fig. 4 St-Ro characterization

documented in an unpublished Research Report at Fisher & Porter Company. This is the most comprehensive correlation model and has been widely reported in the available literature (Hochreiter, 1957; Shafer, 1961; Craft, 1992; Mattingly, 1992; Ruffner and Olivier, 1994). This was also included in a recently published *Aerospace Recommended Practice* (SAE, 1997) in an effort to standardize fuel flow calculation procedures while using turbine flowmeters. The model was developed by using Buckingham Pi theorem (Buckingham, 1915). A detailed discussion of this theorem is available in most modern text books in *Fluid Mechanics* in the section on nondimensionalization. Applying the theorem to the five parameters of Eq. (1), two nondimensional parameters may be obtained,

$$\text{Strouhal Number St} = f * D^3/Q \tag{2}$$

$$\text{Roshko Number Ro} = f * D^2/\nu. \tag{3}$$

The relationship between the two numbers gives the flowmeter characteristic as

$$\text{St} = fn(\text{Ro}). \tag{4}$$

Since the St-Ro characterization involves all the five parameters of Eq. (1), it provides dynamic similitude through the nondimensionalization process. It may be noted that the only difference between this model and the UVC model discussed in section 2.2 is in the introduction of the D terms in Eqs. (2) and (3). Typically, the flowmeter is calibrated in fluids of two or more ν's covering the expected operational range of ν. The measured bore diameter, adjusted for the calibration conditions, is recorded. It may be noted that the measured D at the reference conditions, D_{ref} acts as a scaling factor, with appropriate exponents, for both St and Ro. Hence, D_{ref} can be set to unity without sacrificing the nondimensional characteristics of the correlation model. The St-Ro characterization is plotted for each calibration and the curves are blended manually, or using some analytical curve fitting technique like the cubic-spline algorithm.

Figure 4 shows the St-Ro characterization using the earlier calibration data. Since the calibration was performed at a temperature close to the reference temperature, the difference between Fig. 2 and Fig. 4 is minimal. It may be noticed in Fig. 4 that the curves at the two viscosities tend to form a continuum except for the low-viscosity low-flow area that tends to fall away. This is the region of the meter operation where the mechanical forces are no longer negligible compared to the fluid forces. It is difficult to characterize this region because the magnitude of the mechanical forces depends on the lubricity of the fluid and the mechanical condition of the bearings, in addition to the fluid viscosity. To avoid this region and stay on the continuum of the characteristic curve, the concept of $f_{\min}$ was introduced (Olivier, 1995). Based on the observation of calibration data, $f_{\min}$ was defined as the minimum frequency above which the flowmeter stayed on the continuum, and below which the meter should not be used. However, $f_{\min}$ depends on the viscosity of the fluid, and it has to be determined for each viscosity—by calibrating the meter at a higher viscosity, plotting the St-Ro curves and then manually determining the point of falling away. This technique limits the operational range of the meter by running it above the lower cut-off frequency, $f_{\min}$ thus keeping the St-Ro characteristic on the continuum. The resulting curve is similar to the UVC, but is restricted from falling into the low flow departure area. Multiple calibrations are required over the range of viscosity expected during the application, including at least one viscosity above the range for the determination of $f_{\min}$. Also, like the UVC, the curve has been found to be different even within the same family and size of flowmeters. Each such uniquely nonlinear curve needs digitization to generate a look-up table for applications using an ADAS.

3 New Correlation Models

The St-Ro model, as discussed in section 2.3 above, was developed using the Pi theorem. An often ignored and somewhat older nondimensionalization technique is the Rayleigh method (Rayleigh, 1899). Applying this method, Eq. (1) may be restated as,

$$Q = K_1 * f^a * D^b * \rho^c * \mu^d, \tag{5}$$

where K_1 is a dimensionless constant, and a, b, c, and d are exponents of the variables. Substituting the dimensions of the various parameters, the dimensional equation is obtained as,

$$M^0 L^3 T^{-1} = M^{(c+d)} L^{(b-3c-d)} T^{(a+d)}. \tag{6}$$

Now, using the principle of dimensional homogeneity, both sides of Eq. (6) may be balanced to yield,

$$\left.\begin{aligned} c + d &= 0 \\ b - 3c - d &= 3 \\ a + d &= 1 \end{aligned}\right\}. \tag{7}$$

Equation (7) is a set of three equations with four unknowns. Hence, it may be solved for three of the unknowns in terms of the fourth. Thus, four correlation models can be developed. However, when a, b, and c are expressed in terms of d, and, when a, b, and d are expressed in terms of c, the resulting nondimensional groups are similar to the St-Ro model described in section 2.3. Hence, the St-Ro model falls out as a subset of the four models resulting from the Rayleigh approach. This leaves us with two additional possible models, which have not been reported yet.

3.1 New Correlation Model 1. The terms of Eq. (7) may be rearranged to express a, c, and d in terms of b, and substituted in Eq. (5). After simplifying, the following expression may be obtained,

$$(Q * f^{0.5}/\nu^{1.5}) = K_1 * \{f * D^2/\nu\}^{b/2}. \tag{8}$$

The nondimensional group on the right side of Eq. (8) is Ro as defined in Eq. (3). The group on the left side is a new nondimensional group, which may be called Islam Number (Is),

$$\text{Islam number} \quad \text{Is} = Q * f^{0.5}/\nu^{1.5}. \tag{9}$$

Thus, Eq. (8) may be restated as,

$$\text{Is} = K_1 * \text{Ro}^{b/2}. \tag{10}$$

This, then, is a new correlation model involving all the five parameters of Eq. (1), resulting in a functional relationship between Is and Ro. A careful study of Eq. (10) reveals that in the logarithmic domain, the Is-Ro characterization may be expected to be linear, or close to linear, depending on the variation of the exponent b. An application of this model to the same calibration data for the 0.4–40 LPM flowmeter is discussed in section 4.

3.2 New Correlation Model 2. As shown in section 3.1 above, the terms of Eq. (7) may also be rearranged to express b, c, and d in terms of a. Substitution of the results in Eq. (5), and simplification yield,

$$Q/(D*\nu) = K_1*\{f*D^2/\nu\}^a. \tag{11}$$

The nondimensional group on the right side is the familiar Ro. The group on the left side of Eq. (11) is yet another new group which may be called Mozumdar number (Mo),

$$\text{Mozumdar number} \quad \text{Mo} = Q/(D*\nu). \tag{12}$$

Hence, Eq. (11) can be rewritten as,

$$\text{Mo} = K_1*\text{Ro}^a. \tag{13}$$

This is a second new correlation model involving all the five parameters of Eq. (1). The functional relationship between Mo and Ro may be expected to be linear, or close to being such, in the logarithmic domain depending on the variation of the exponent, a. An application of this model to the same calibration data is discussed in the following section.

4 Application of New Correlation Models

The same calibration data set from the 0.4–40 LPM turbine flowmeter is used to generate Fig. 5, which shows the Is-Ro characterization in the logarithmic domain as given in section 3.1. As expected, it is close to a straight line. The minor departure from a straight line may be compensated for by using a simple polynomial algorithm of higher order. When data from two or more viscosities are combined into a single set, a fifth order polynomial has been found to yield good results.

Proceeding as before, and reprocessing the data for the Mo-Ro correlation, the model shown in Fig. 6 is obtained. As expected, in the logarithmic domain, this characterization is also close to a linear representation of the functional relationship between the parameters. In addition, for combined data from two or more viscosities, a fifth order polynomial has been found to yield good results.

In applications where a ±1.5 to ±2 percent curve-fit uncertainty can be accepted, either of the Is-Ro, and the Mo-Ro correlations may be used as linear first order models, i.e., a straight line fit may be used. Where a higher order of accuracy is desired, the fifth order polynomial may be used. It has also been found that both the models hold for families of flowmeters of different sizes. In addition, where the variation in fluid viscosity is large, it is possible to establish the correlations with fewer calibrations at different viscosities.

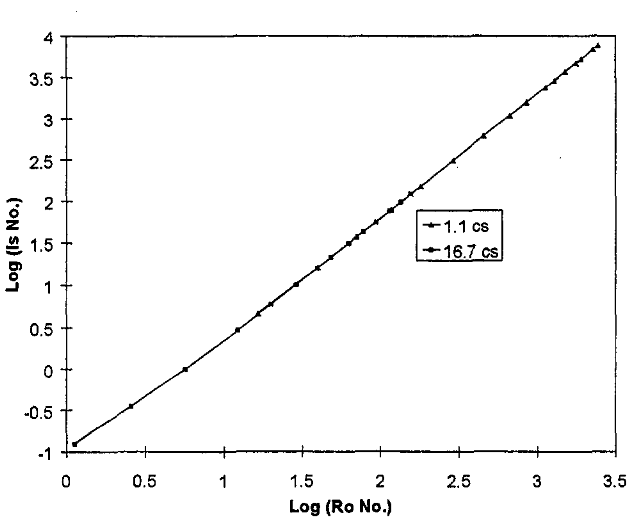

Fig. 5 Is-Ro characterization

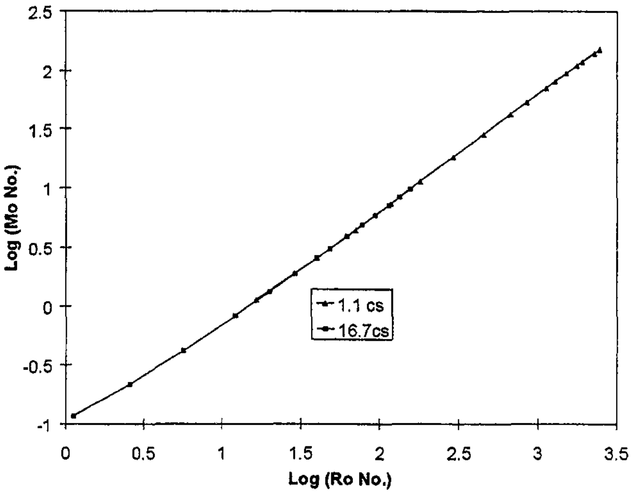

Fig. 6 Mo-Ro characterization

5 Summary and Conclusions

Two new correlation models have been developed for turbine flowmeter data analysis. This was achieved by adopting a systematic approach using the Rayleigh method along with the principle of dimensional homogeneity resulting in two new nondimensional parameters.

Nondimensional parameters may be created by the combination, or by the manipulation of existing nondimensional parameters. For example, Roshko number can be arrived at by the multiplication of Strouhal number and Reynolds number (Craft, 1992; Mattingly, 1992; Ruffner and Olivier, 1994). Similarly, multiplying the numerator and the denominator of an existing nondimensional number by two parameters of identical dimensions can also lead to a new nondimensional parameter. It may be noted that the mere creation of nondimensional parameters does not lead to the development of effective correlation models in experimental fluid mechanics. The development of correlation models requires a methodical and systematic approach. Evidently, the different approaches to dimensional analysis are not comprehensive. Most fluid dynamicists believe that the Buckingham Pi theorem is the most effective means of dimensional analysis, and, hence, it has become the method of choice. However, the Pi theorem requires considerable insight into the physics of a process along with experience in grouping controllable and uncontrollable variables in an application. There is great confusion about the rules concerning the number of dimensional parameters while applying the Pi theorem (Granger, 1985). Though generally avoided, the Rayleigh method is easier to apply than the Pi theorem. In the present application, the St-Ro characterization, originally developed using the Pi theorem, came out as a subset of the correlations from the approach using the Rayleigh method. However, the vice versa is not true, i.e., neither the Is-Ro, nor the Mo-Ro correlation could be arrived at using the Pi theorem.

The new correlation models have been successfully applied to several flowmeters of different sizes. Both the models overcome many of the limitations of the existing models. It may be recognized that while the new models offer significant benefits over the existing models, they do not, by themselves, change the measurement uncertainties. As in the St-Ro characterization, the new Is-Ro and the Mo-Ro models capture all the parameters from Eq. (1), within the assumptions of incompressibility and the negligibility of mechanical forces compared to fluid forces. In specific, the new models reduce the required number of calibrations over the operating range of the application fluid, and simplify the algorithm for ADAS, thus providing the potential to reduce curve-fit errors.

The newly formed Is number is a nondimensional combination of three physical parameters, viz. fluid kinematic viscosity, frequency, and volume flowrate. Thus, Is number may be used in other applications where these physical parameters come into play, e.g., in Karman vortex street or other vortex shedding phenomena. Similarly, Mo number is also a nondimensional combination of three physical parameters, viz., fluid kinematic viscosity, volume flowrate, and a characteristic linear dimension-like diameter, or length. Hence, Mo number may also be used in other applications where these parameters play a role in the flow phenomena.

In conclusion, it may be noted that both the new correlation models lead to considerable simplifications in the analysis of turbine flowmeter data. The authors have not recommended one model over the other as this may depend on operational simplicity in a specific application. However, both the models can be effectively used with relatively simple polynomial curve-fit algorithms in automated data acquisition systems.

Acknowledgments

The authors acknowledge the support of the management of the Engineering Laboratory at AlliedSignal Engines to complete the present work, and appreciate the clearance from AlliedSignal to publish the material in this paper.

References

Baker, R. C., 1991, "Review: Turbine and Related Flowmeters: 1. Industrial Practice," *Flow Measurement Instrumentation,* Vol. 2, Butterworth-Heinemann Ltd., Oxford, U.K., pp. 147–161.

Buckingham, E., 1915, "Model Experiments and the Forms of Empirical Equations," *Trans. ASME,* Vol. 37, pp. 263–296.

Craft, D. W., 1992, "High Accuracy Fuel Flowmeter: Final Report—Phase IIC and Phase III, The Mass Flowrate Calibration of High Accuracy Fuel Flowmeters," NASA CR 187108.

Granger, R. A., 1985, *Fluid Mechanics,* Holt, Reinhart, and Winston, New York.

Hochreiter, H. M., 1957, "Dimensionless Correlation of Coefficients of Turbine-Type Flowmeters," ASME 57-A-63.

Mattingly, G. E., 1992, "The Characterization of a Piston Displacement-Type Flowmeter Calibration Facility and the Calibration and Use of Pulsed Output Type Flowmeters," *Journal of Research of the National Institute of Standards and Technology,* Vol. 97, No. 5, pp. 509–531.

Olivier, P. D., 1995, "Determination of Turbine Flowmeter Turndown," Proceedings, NCSL Workshop & Symposium, National Conference of Standards Laboratories, Boulder, Colorado, pp. 739–745.

Rayleigh, L., 1899, "On the Viscosity of Argon as Affected by Temperature," *Proc. Royal Soc.,* London, pp. 68–94.

Ruffner, D. F., and Olivier, P. D., 1992, "Improved Turbine Meter Accuracy by Utilization of Dimensionless Data," Proceedings, NCSL Workshop and Symposium, National Conference of Standards Laboratories, Boulder, CO, pp. 599–607.

Shafer, M. R., 1961, "Performance Characteristics of Turbine Flowmeters," ASME 61-WA-25.

Society of Automotive Engineers, 1997, "Turbine Flowmeter Fuel Flow Calculations," *Aerospace Recommended Practice,* SAE ARP 4990.

M. Dilzer

C. Gutmann

A. Schulz

S. Wittig

University of Karlsruhe,
Institut für Thermische
Strömungsmaschinen,
Universität Karlsruhe, Kaiserstr. 12,
D-76128 Karlsruhe, Germany

Testing of a Low Cooled Ceramic Nozzle Vane Under Transient Conditions

At the Institut für Thermische Strömungsmaschinen, University of Karlsruhe (ITS), a design technology has been introduced to reduce the mechanically and especially the thermally induced stresses in ceramic components. The concept is based on a three-layered construction (outer ceramic shell, heat insulating layer, and metallic core) and an optimization of the thicknesses of the single layers, in order to obtain a homogenous temperature distribution in the ceramic structure. The optimization is performed by finite element analyses in combination with failure probability calculations. This methodology has been applied to increase the reliability of a first stage Sintered Silicon Carbide (SSiC) ceramic nozzle vane of a stationary gas turbine (70 MW/1400°C). As a result it was found that the mechanically and thermally induced loads have been reduced considerably and do not exceed 100 MPa, thus achieving adequate life based upon failure probability calculations. Even in a trip situation (fuel cutoff), when the highest loads do occur, the calculations demonstrate a significantly reduced failure probability. The results of the finite element analyses were verified by simulating the typical operating conditions after fuel cutoff in a test rig.

Introduction

Due to the favourable properties of ceramics at high temperatures, there are considerable efforts to replace thermally high loaded metallic gas turbine components by ceramic parts. The use of ceramics in gas turbine engines allows higher operating temperatures and/or requires a smaller amount of cooling air, which leads to higher thermal efficiencies.

So far the brittleness and the inability to reduce stresses by plastic deformation have for the most part prevented ceramic components from being applied to gas turbines. In order to achieve sufficient reliability and durability these unfavorable properties have to be taken into account. Hence, there ought not just be a simple substitution but a new design has to be developed.

In recent years there have been a lot of undertakings to introduce ceramic nozzle vanes to stationary gas turbines [1, 2, 3, 4]. But, so far there has been no systematic adjustment of the shape of the ceramic component with respect to thermally and mechanically induced loads.

At the Institut für Thermische Strömungsmaschinen (ITS), a new design concept, taking advantage of the excellent high temperature properties of ceramic materials while compensating for their deficiencies, has been worked out and applied to a first stage ceramic nozzle vane (SSiC) of a 70 MW, 1400°C class stationary gas turbine [5]. The adjustment of the wall thicknesses of the ceramic shell and the heat insulating layer according to the local thermal loadings leads to a more uniform temperature distribution in the ceramic component. This results, if compared with conventional design concepts, in a significant reduction of the thermally induced stresses in the hybrid constructed stator vane.

A finite element analysis shows that the load remains far below the characteristic fracture strength of the considered SSiC-material for continuous engine operation as well as for emergency shutdown. At the same time the reliability has been raised substantially, so that even under severe transient thermal boundary conditions (trip) a satisfactory failure probability is to be obtained (ITS fracture statistics code CERITS) [6].

For an experimental verification of the applied design method it is necessary to simulate the thermal loadings that occur during the trip of the engine. Therefore, a test rig, which causes thermal stresses in the ceramic structure equal to those induced by the temperature drop during the fuel cutoff in real engines, has been built up.

This paper deals with the results of the experimental investigations with respect to the thermal shock behavior of the optimized ceramic nozzle vane.

Construction and Stress Analysis of the Hybrid Ceramic Nozzle Vane

The previously presented design methodology for thermally high loaded ceramic components [5] has been applied to improve the reliability of a first stage ceramic nozzle vane for a stationary gas turbine. The specifications for the engine and the ceramic stator are shown in Table 1.

In order to ensure that wide parts of the nozzle vane are accessible for the inner cooling, it was decided to change the outline form of the vane profile; especially the trailing edge region is rather inapplicable for an optimum cooling configuration. Therefore, the angle between the ceramic shells at the trailing edge was enlarged. This resulted in a slightly thicker vane profile (Fig. 1), if compared to the original metallic guide vane.

The finite element model of the untwisted three-layered hybrid ceramic guide vane is shown in Fig. 1. The ceramic shell protects the metallic core from contact with the high temperature corrosive hot gas flow. The heat insulating layer insures that there is balanced temperature distribution in the ceramic shell and it compensates the different thermal expansions as well. Since there has been an assumption of symmetry at vane mid height the model can be reduced to one half of the nozzle vane.

The boundary conditions have been ascertained and implemented to the computation model. It was found that the stresses induced by mechanical loads do have negligible importance. The dominant loads are the thermally induced stresses due to different thermal expansions.

Contributed by the International Gas Turbine Institute and presented at the International Gas Turbine and Aeroengine Congress and Exhibition, Stockholm, Sweden, June 2–5, 1998. Manuscript received by the ASME Headquarters April 1, 1998. Paper No. 98-GT-116. Associate Technical Editor: R. Kielb.

Table 1 Specifications of the gas turbine and the first stage ceramic guide vane

Gas Turbine	
Rating [MW]	70
Pressure Ratio [1]	approx.17
Mass Flow [kg/s]	approx. 200
Turbine Inlet Temperature [K]	1673
Cooling Temperature [K]	673

Ceramic Nozzle Vane	
Material	Sintered Silicon Carbide
Design Concept	Hybrid + Load Oriented
Relative Cooling Mass Flow	<2% of Core Mass Flow
Vane Height [mm]	60
Chord Length [mm]	58

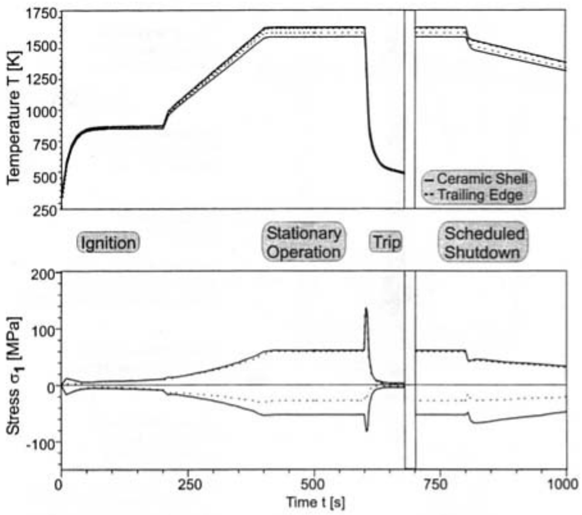

Fig. 2 Maximum and minimum temperatures and stresses in the ceramic shell (optimized hybrid nozzle vane)

The results for the optimized low-cooled ceramic guide vane are shown in Fig. 2. The minimum and maximum temperatures and stresses are presented for the full operating cycle of the engine (ignition stationary operation, trip, and scheduled shutdown). If compared with the results of a previously performed finite element analysis of a conventionally designed (directly cooled) ceramic nozzle vane with induced maximum stresses of more than 400 MPa, it becomes clear that the stress level in the ceramic shell of the optimized hybrid vane is very low, for both the continuous and the transient operation, when the most severe loads do occur. The maximum tensile stresses remain below 75 MPa and 135 MPa for continuous operation and trip, respectively. Failure probability calculations (CERITS [6]) demonstrate sufficient reliability for engine operation. The time dependent (slow crack growth) failure probability determination led to $P_f = 0.84 \times 10^{-4}$ considering 10,000 hours of continuous operation. Taking into account the loads induced during the trip of the engine failure probability (fast fracture mode) was found to be $P_f = 0.81 \times 10^{-4}$.

Test Rig

From the stress analyses it was found that the maximum stresses occur during the trip of the engine. Consequently there is a demand for a test facility, that is able to simulate the transient thermal boundary conditions taking place after fuel cutoff in real engines.

To simplify the producing of practical test specimens it has been decided to examine the thermal shock resistance of vane profiles without inner and outer side walls (Fig. 3). This ought to be acceptable since a finite element analysis has been performed in order to indicate the influence of the side walls on the stress distribution in the ceramic vane profile. The results of this comparison demonstrate that there is a small dependence of the stress distribution on the ceramic side walls.

A test rig has been built up as shown in Fig. 4. Inside the heating zone an electric furnace allows to heat up the ceramic nozzle vane to a maximum temperature of 1773 K. The inner cooling of the unit under test is achieved by a cooling air flow through small tubes attached to the outer side of the metallic cantilever (Fig. 5). A variation of the inside diameter and the distance between the single tubes makes it possible to adjust the

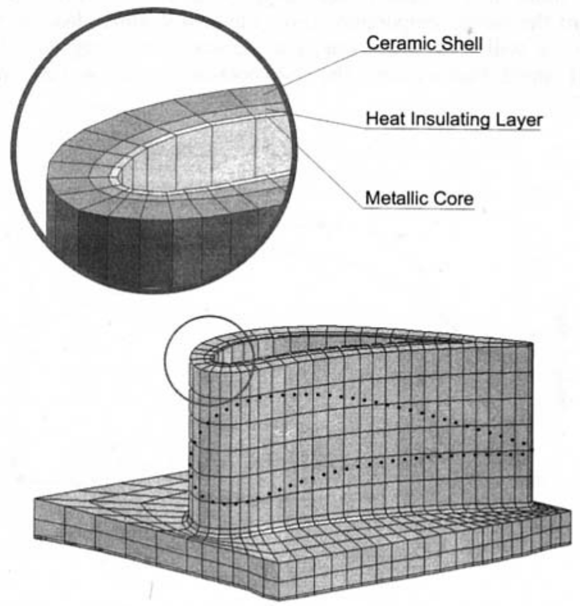

Fig. 1 Finite-element model of the hybrid ceramic nozzle vane

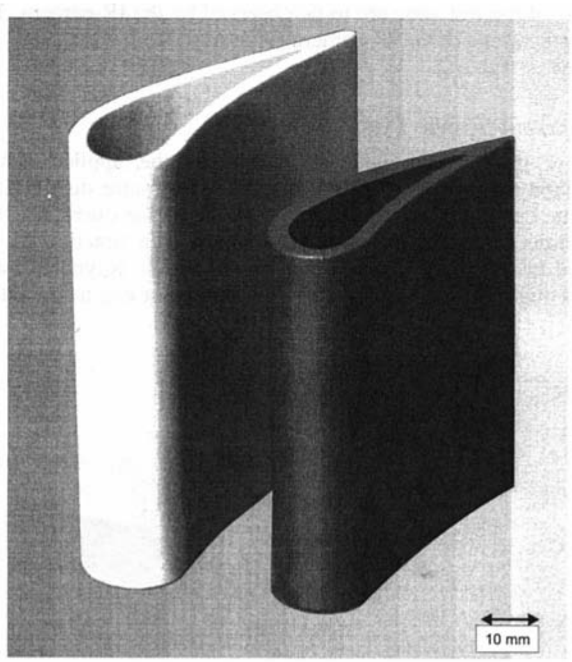

Fig. 3 Test specimen before (l.) and after (r.) the sintering process

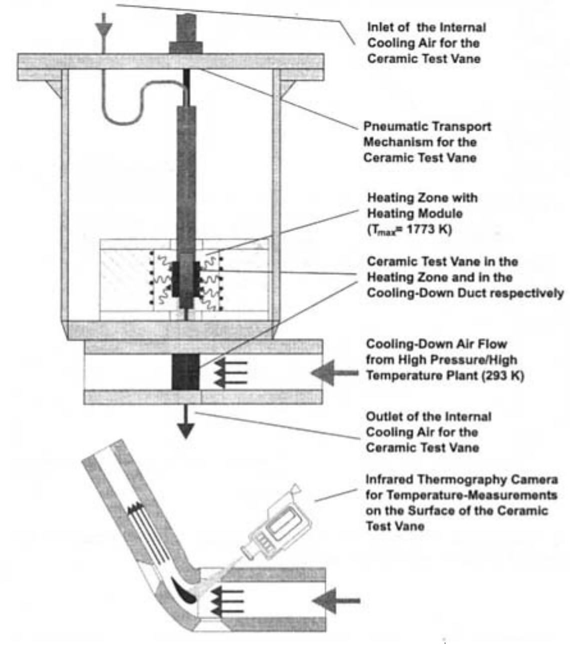

Fig. 4 Schematic drawing of the test rig

local temperature according to real engine continuous operation. After the heat up process the tested vane profile is moved into the cooling-down duct using a pneumatic transport mechanism. Inside the cooling-down section the main air flow (T = 293 K, p_{max} = 1 MPa) causes a temperature drop in the tested ceramic vane profile, similar to the trip situation in real engines.

The design of the sidewalls of the cooling-down duct has been carried out carefully in order to achieve a realistic flow around the tested vane profile. This is necessary to obtain coincidence with respect to the local heat transfer coefficients on the surface of the vane for the experiment and real engine operation.

During the cooling-down process, the surface temperature distribution of the ceramic vane is recorded by infrared radiation thermography. Three sapphire glass windows have been installed to observe the unit under test from three different perspectives as shown in Fig. 6. Thus, it is guaranteed that many parts of the test vane are to be observed by the IR-camera. The specifications of the IR-camera (Agema 900) that was used are listed in Table 2.

Thermal Shock Tests

For the experimental verification of the applied design method there is a need for identical temperature distributions in the ceramic shell for experiment and engine operation. The time-dependent temperature distribution is a function of the local heat transfer coefficients. Therefore, the Reynolds numbers ought to be reproduced in the test rig. For engine operation the main flow Reynolds number (based on the chord length of the vane) is Re_1 = 670,000. This Reynolds number was chosen for the tests and kept constant for all experiments. The boundary conditions for the thermal shock tests are listed in Table 3.

Due to the fixed temperatures of the main and the cooling gas flow (approximately 400 K lower than the compressor output temperature of 673 K), the conditions for the unit under test are more severe than in real engines. If cooling down starts from the same temperature level the temperature drop in the test rig will exceed the one, that occurs in real engines after fuel cutoff. Furthermore, the test specimen is exposed to a real

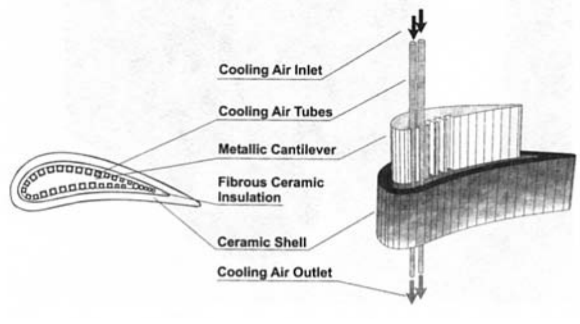

Fig. 5 Internal cooling of the ceramic test vane

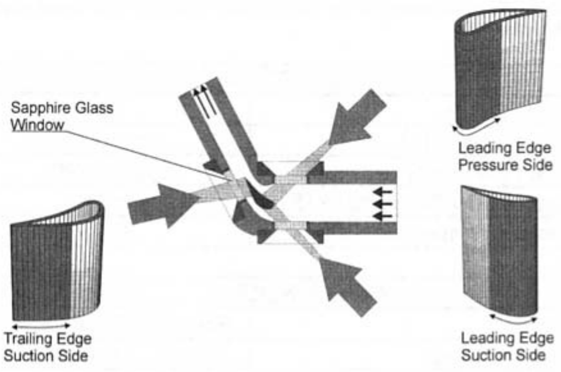

Fig. 6 Perspectives for the IR-camera measurements

Table 2 Specifications for the Agema 900 IR-camera

IR-Camera (Agema 900)	
Temperature Sensor	2-5.6 μm (Stirling-Cooled)
Resolution	0.6 * 0.6 mm^2
Picture Frequency	30 s^{-1}
Data Acquisition Frequency	approx. 5 Pictures * s^{-1}

Table 3 Boundary conditions for the thermal shock tests

Main Flow	T_{Main}	293 K
	$p_{Main,max}$	1 MPa
Cooling Flow	T_{Cool}	293 K
	$p_{Cool,max}$	0.7 MPa
Heating Zone	$T_{Heating,max}$	1773 K

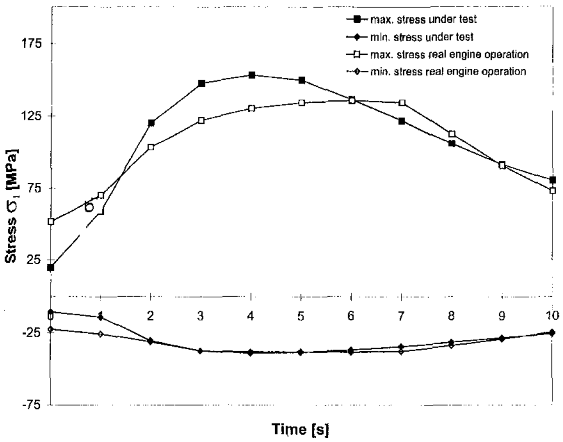

Fig. 7 Timedependent stresses under testing conditions and for real engine operation (trip)

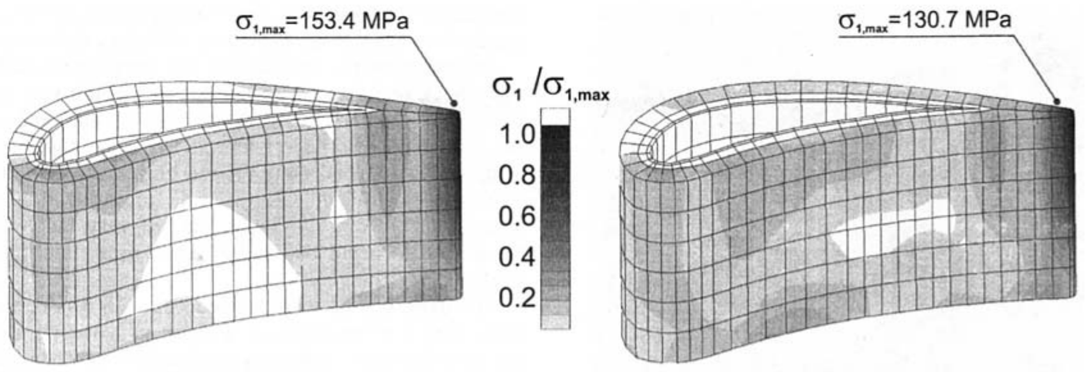

Fig. 8 Stress distribution in the ceramic vane profile 4 seconds after the start of the thermal shock test (l.) and 4 seconds after the fuel cutoff for real engine operation (r.)

temperature step while the actual gas flow cools down with appreciable temperature gradients during the trip situation.

With regard to this, the following test procedures will be used:

- —$\mathrm{Re}_{\mathrm{Main},1}$ = 670,000 (adjustment of the local heat transfer coefficients)
- —increasing the temperature of the ceramic nozzle vane profile in the heating zone step by step and thermal shocking afterwards
- —determination of the surface temperature with infrared radiation thermography
- —visual inspection of the test specimen after each experiment

Results

Thermal shock tests of ceramic vane profiles have been performed as described before. Before the test specimen were displaced into the cooling-down duct they were heated and held at temperature in the furnace until there was no temperature change on the outside of the metallic core (see Fig. 5). The temperature level in the heating zone was increased in approximately 50 K increments. For each temperature level at least three tests were performed, in order to observe the ceramic vane profile from each perspective (Fig. 6).

A finite element analysis of the time-dependent temperature and stress distribution in the test specimen throughout the thermal shock test has been carried out.

A comparison of the calculated stress distribution under test (furnace temperature of 1323 K and boundary conditions as described before) and for the trip situation of real engine operation is shown in Fig. 7. The maximum load of the test specimen is approximately 155 MPa, which is about 10 percent higher than it was calculated for engine operation. The stress distributions in the ceramic vane profile four seconds after the start of the thermal shock test and the fuel cutoff, respectively, are presented in Fig. 8.

The similarity of the local stresses for both unit under test and vane profile during the trip situation is obvious. For both cases the maximum stresses do occur at the mid-height of the trailing edge. The loads for the other parts of the ceramic profile remain significantly below this maximum. This demonstrates that the performed thermal shock tests are well suited to estimate the reliability of the optimized ceramic vane profile.

Figure 9 shows the maximum temperatures during the thermal shock tests. In order to compare the induced temperature gradients with those under real engine operation (trip) it was decided to describe them using a dimensionless temperature $T_{v,0}$ as defined below.

$$T_{v,0} = \frac{T_{\mathrm{vane}} - T_{\mathrm{cool}}}{T_{\mathrm{vane,max}} - T_{\mathrm{cool}}} \qquad (1)$$

There is very good agreement between the finite element analysis for the experiment and the infrared thermography measurements. Also it has been shown that the induced temperature gradients are very much the same as those that are calculated for the trip situation in real engines. In both cases the temperature of the ceramic vane profile changes with approximately 80 K/s within the first 10 seconds.

So far the experiments have been carried out with three ceramic vane profiles. The induced loads for the test specimen have been increased step by step as described before. One specimen was fractured under testing conditions that have been significantly below the aimed load of about 150 MPa. It was concluded that the reason for this failure has been an incorrect adjustment of the pneumatic transport mechanism, which resulted in a knocking of the test specimen while moving through the slot between heating zone and cooling-down duct.

The other ceramic vane profiles survived a multitude of experiments with maximum induced loads of approximately 150 MPa. No visible damage was observed. For one of the test specimen a number of tests with increasing loads was performed. This vane profile endured additional thermal shock tests until the induced tensile stresses exceeded 250 MPa. It was fractured in the fourth experiment that was performed with induced stresses of about 250 MPa.

Before the failure took place the ceramic shell showed no signs of damage. Only a slight change of the test specimen's color at the trailing edge was to be observed (Fig. 10). This might have been caused by a reaction of the vane profile with gases that have been diffused from the furnace insulation mate-

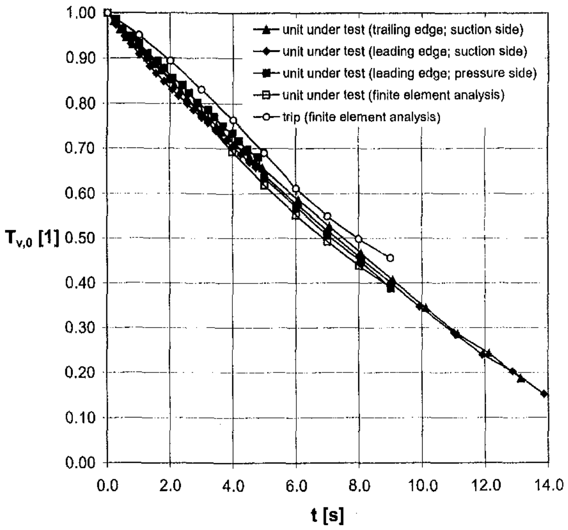

Fig. 9 Dimensionless maximum temperatures under testing conditions (T_{furnace} = 1323 K) and for real engine operation (trip)

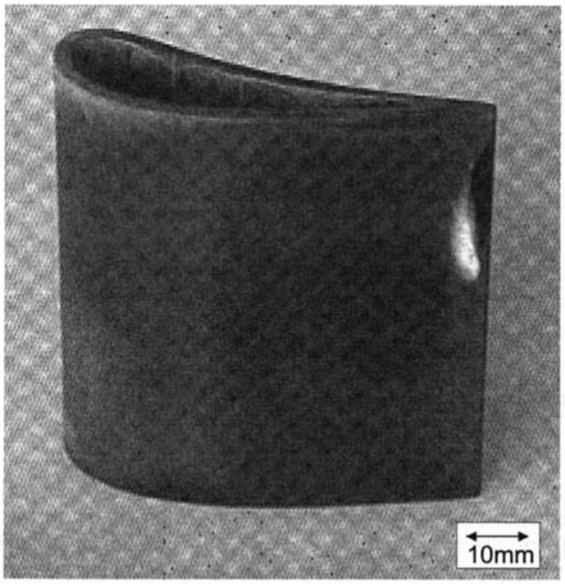

Fig. 10 Test specimen after a series of thermal shock tests

rial. A detailed examination of this layer showed that its thickness is less than 0.5 μm, which should have had no noticeable effect on the strength of the tested unit.

For a final assessment of the design method it is absolutely necessary to perform additional experiments in order to generate statistically significant information about the thermal shock behavior of the thermally optimized ceramic stator vane. But it can already be affirmed that this design method is a means to reduce thermally induced stresses considerably, and, therefore, increases the reliability of ceramic components.

Conclusions

A three-layered hybrid ceramic first stage nozzle vane for a stationary gas turbine has been optimized in order to improve the reliability. The applied method, which is based on an adaption of the local thicknesses of the single layers according to the thermal boundary conditions, is carried out by finite element analyses. At the same time the outline form of the vane profile has been adapted to make sure that many parts become accessible for the internal cooling system.

The performed finite element analyses are pointing out that the induced stresses in the ceramic component have been more than halved, if compared with conventional design concepts. The dominating thermally induced loads have been reduced considerably and remain even during transient operation of the engine low enough to guarantee sufficient failure probability.

An experimental verification has been performed. The thermal shock resistance of SSiC ceramic guide vane profiles has been proved in a test rig. Starting from stationary conditions the test specimens have been cooled down rapidly to ambient temperature. It was found (based on a finite element analysis) that the experimental setup is well suited for inducing thermal stresses in the test specimen that are very much the same as those that do occur during the fuel cutoff situation in real engines.

The experiments were carried out with 3 ceramic vane profiles. One was fractured as a result of a wrong alignment for the test specimen transport mechanism, after having endured only some experiments with rather small stress loadings. The others withstood a large number of thermal shock tests with induced tensile stresses up to 150 MPa, without any visible damage. This stress level was found to be the maximum load which occurs after fuel cutoff during the trip of the engine. For one of this two test specimen the induced loads have been increased step by step until it was fractured after the fourth experiment with induced stresses of approximately 250 MPa.

Thus, it is demonstrated, though based on a small amount of experimental data, that the applied design method, taking into account the specific demands of ceramic materials, is a powerful tool to increase the reliability of ceramic components.

The achieved improvement might contribute to bridge the gap between ceramics in the laboratory and near-term commercial gas turbine applications.

Acknowledgments

The authors are grateful to the AG TURBO (Arbeitsgemeinschaft Turbomaschinen, Turbotherm II), which supported this work.

References

1 Nakakado, K., Machida, T., Miyata, H., Hisamatsu, T., Mori, N., and Yuri, I., 1995, "Strength Design and Reliability Evaluation of a Hybrid Ceramic Stator Vane for Industrial Gas Turbines," ASME JOURNAL OF ENGINEERING FOR GAS TURBINES AND POWER, Vol. 117, pp. 245–250.

2 Tsuchiya, T., Furuse, Y., Yoshino, S., Chikami, R., Tsukagoshi, K., and Moro, M., 1995, "Development of Air-Cooled Ceramic Nozzles for a Power Generating Gas Turbine," ASME Paper 95-GT-105.

3 Machida, T., Nakayama, M., Wada, K., Hisamatsu, T., Yuri, I., and Watanabe, K., 1996, "Development of Ceramic Stator Vane for 1500°C Class Gas Turbine," ASME Paper 96-GT-459.

4 Wenglarz, R., Calcuttawala, S., and Pope, E., 1997, "Ceramic Vane Demonstration in an Industrial Gas Turbine," ASME Paper 97-GT-155.

5 Gutmann, C., Schulz, A., and Wittig, S., 1996, "A New Approach for a Low-Cooled Ceramic Nozzle Vane," ASME Paper 96-GT-232.

6 Stürmer, G., Schulz, A., and Wittig, S., 1991, "Life Time Prediction for Ceramic Gas Turbine Components," ASME Paper 91-GT-96.

Characterization of Fatigue Mechanisms of Thermal Barrier Coatings by a Novel Laser-Based Test

U. Rettig

U. Bast

D. Steiner

M. Oechsner

Siemes AG,
ZT MF2, Otto-Hahn-Ring 6,
Munich, Germany, 81739

The use of high performance ceramic thermal barrier coatings in stationary gas turbines requires fundamental knowledge of their fatigue behavior under high temperature gradients and thermal cycling. An experimental method based on rapid laser heating complemented with finite-element calculations was developed in order to identify the major damage mechanisms and to obtain a data set for reliability assessment of thermal barrier coatings for temperature and stress fields similar to gas turbine conditions. The observed failures are strongly related to the pretreatment procedures such as annealing under high temperature gradients and isothermal long-term oxidation. The vertical crack patterns observed close to the top surface of the Zirconia coating are generated at the moment of rapid cooling. These cracks are induced by high biaxial tensile stresses caused by the temperature gradient and the stress reversion after relaxation of compressive stresses at high temperatures. The long-term fatigue behavior is decisively determined by two processes: (1) the porous Zirconia loses its damage tolerant properties by densification, and (2) the growth of an oxide layer at the bond coat degrades adhesion and produces localized stress fields at the interface. Cyclic loads increase the length of existing in-plane cracks and delaminations rather than enlarging their number. Misfit of the crack flanks and wedge effects are the driving forces for continued crack propagation. These experimental results are discussed in terms of fracture mechanics.

Introduction

To increase the efficiency of stationary gas turbines and to reduce the emissions, efforts are being made to cut down on the amount of cooling air required whilst at the same time increasing the temperature of the hot gas. This means that components in the hot gas zone of turbine engines have to withstand surface temperatures in excess of 1200°C. One way of achieving this is the use of ceramic coatings with low thermal conductivity. The coatings, which normally consist of partially-stabilized ZrO_2, are applied by atmospheric plasma spraying (APS) or electron beam physical vapor deposition (EB-PVD).

The protective effect of ceramic thermal barrier coatings (TBC's) will be used in the design of future stationary gas turbines. This means that the coating will have to retain its heat barrier effect over the complete service life of the component in order to reduce the temperatures on the interface of the component to a level which the metallic substrate can tolerate.

The many years of experience of coating systems used on aircraft engines cannot simply be transferred to stationary turbine conditions. One reason for this are the very different operating cycles. In contrast to aircraft engines which are only subjected to high loads during the short take-off phase, stationary gas turbine engines are run at full load over very long operating periods. Furthermore, the sizes of the components used are very different. This means that there are different requirements for the design of thermal barrier coatings and it's not clear from the outset whether the same damage mechanisms operate under the specific load conditions. Prediction models have to be able to suitably reflect the damage processes in the coated component under service conditions.

The aim of the investigations presented here is to detect the determinant damage mechanisms of cyclic thermal fatigue of thermal barrier coatings systems by using quantitative characterization and fracture mechanics modeling and to determine criteria for the assessment of various coatings on the basis of fracture mechanics. There is also the need to develop a test procedure for validation of the established criteria, selection of coatings, and for quality assurance of the coating system used. These requirements are determined by the temperature and stress conditions on actual components in gas turbines (linings in combustion chambers and hot gas ducts, first stage vanes, and rotor blades). The long operating durations under stationary temperature gradients and specific loading during trips require particular consideration.

Basis and Method of Experiments

The functional failure of thermal barrier coatings in the form of delamination of the coating is preceded by crack damage due to critical stresses in the coating system. Fracture mechanics using theoretical modeling describe the onset and propagation of the crack resulting from the applied loadings and the properties of the materials. The loading of ceramic thermal barrier coatings result mainly from

— prolonged use at high temperatures
— thermally induced mechanical stresses due to the thermal expansion mismatch of the metallic substrate and ceramic coating and/or inhomogeneous temperature distribution
— processes at the interface to the metallic substrate which are mainly associated with oxidation of the bond coat

The formation and generation of cracks are predicted by comparing the available energy release rate with a critical energy release rate. The critical energy release rate is a property of the material that in thermal barrier coatings is anisotropic and

---

Contributed by the International Gas Turbine Institute and presented at the International Gas Turbine and Aeroengine Congress and Exhibition, Stockholm, Sweden, June 2–5, 1998. Manuscript received by the ASME Headquarters April 1, 1998. Paper No. 98-GT-336. Associate Technical Editor: R. Kielb.

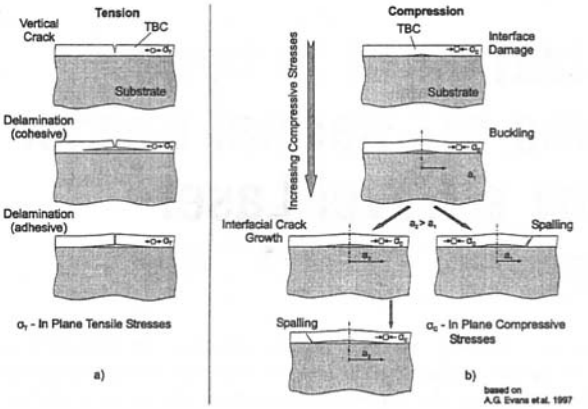

Fig. 1 Schematic representation of crack damage to thermal barrier coatings under tensile (*a*) and compressive stresses (*b*)

changes over time under service conditions. Sintering of the thermal barrier coating or the additional stresses in the interface zone due to oxidation of the bond coat and formation of an additional oxide layer (thermally grown oxide, TGO) [1] lead to an increase in the elastic energy density. Damage accumulation due to the relaxation of local stress peaks, cyclic effects or phase changes due to temperature or stress lower the critical energy release rate. Changes in local stresses are not only associated with time dependent changes in temperature distribution, but are also linked to time-dependent changing material properties and the growth of the oxide coating during stationary temperature loading.

From the fracture mechanics point of view, the crack propagation in a surface coating can be described under (biaxial) tensile, and also compressive, stresses (Fig. 1). Both stress conditions can occur in coated components under the operating conditions within a gas turbine cycle. The fracture criterion for the corresponding crack configuration provides the conditions for the occurrence of vertical cracks and also cohesive and/or adhesive delamination cracks [2, 3].

The aim of the experiment was to transfer those stress distributions present in TBCs during the operation of gas turbines, at least qualitatively, to model trials in order to identify the relevant damage mechanisms. This meant that the course of the damage process had to be accelerated by the use of higher temperatures and stresses in order to enable effective tests to be achieved within short periods of time. A hypothetical precondition was that this would not in principle change the character of the processes. The validity of this assumption is to be verified by suitable investigations.

The experimental test set up had to meet the following requirements. Experimental investigations should be done at various geometries (disks, cylinders) reproducibly with defined temperature and stress profiles over a large number of cycles (>1000). Radiant heating, i.e., using a powerful laser, enabled the required high temperatures (>1300°C) to be achieved, together with rapid control and variation of the temperature loading at the same time. This procedure was already successfully established for characterization of monolithic ceramics as well as ceramic coatings [4–8]. The verification of the accompanying FE analysis and control of the test meant that the temperature distributions in the coating and substrate had to be measured. Substrate cooling had to be available to increase or maintain the temperature gradients through the thickness during irradiation. In order to be able to determine the time at which load states corresponding to damage processes occurred, it was necessary to be able to detect the time at which acoustic signals generated in the samples took place and to be able to make visual observations.

An existing laser apparatus, was modified to meet these requirements (Fig. 2). A Nd:YAG laser working in continuous wave mode ($\lambda = 1.064$ μm) with an output which could be adjusted in small steps of 75 W up to a maximum of 800 W range was used as the irradiation source (maximum accessible peak power density = 130 MW/m^2). The laser beam was directed through a flexible optical fiber to the specimen. In the static irradiation mode, the infrared beam was widened by a long focal length lens, thus enabling the size of the hot spot to be easily set by the distance to the sample. A laser scanning system consisting of two electronically driven tilting mirrors enabled special temperature distributions, such as ring profiles, to be generated. The advantage of the dynamic laser beam deflection was that irradiation profiles could be achieved which were independent of the power density distribution in the laser beam, which is generally Gaussian.

The specimens were held vertical by pins which were mounted in coil springs thus enabling an almost forceless clamping. The top pin was used as an acoustic wave conductor and coupled with a sound sensor. Acoustic signals occurring in the sample were detected and, after appropriate amplification, recorded.

A fast scanning, position-indicating, pyrometer (50–1700°C) and two point pyrometers (50–800°C and 300–1400°C) were used to measure temperatures. The scanning pyrometer was used mainly on the irradiation side because that is where the steepest temperature gradients occur. A point pyrometer was usually sufficient to determine the substrate temperature at one or two points. ZrO_2 is very translucent to electromagnetic waves in the near infrared range and the pronounced reflections on the bright surface, typical for oxide ceramics, also had to be taken into account. This meant that the Nd:YAG laser power could only be coupled into the thermal barrier coating through a suitable, additionally placed absorption coating. To do this, a CoNi coating was applied in steps of 1 μm using a vapor deposition process and then oxidized for 5 h in air at a constant 700°C. Complete oxidation was checked by measuring the conductivity. Adding Ni forms a mixed oxide which suppresses the change in the oxidation stage of the Co, which is associated with a color change to pink and takes place in the CoO at approximately 900°C. The oxidized CoNi coating is very resistant to high temperatures, guarantees an adequate absorption of the Nd:YAG irradiation and has sufficient emissivity for the pyrometric temperature measurement. The phase composition and the mechanical properties of the Zirconia coating were not influenced by the applied thin oxidized CoNi film.

Cooling was achieved by a fast-flowing gas (N_2), introduced through a nozzle on to the zone to be cooled. The cooling air supply was controlled either manually or by computer as required. The combination of irradiation conditions and cooling geometry enabled the temperature profiles that could be set for the experiment to be varied over a wide range. The specimen could be observed by means of a long distance microscope. A connected video system enabled a separate assessment to be

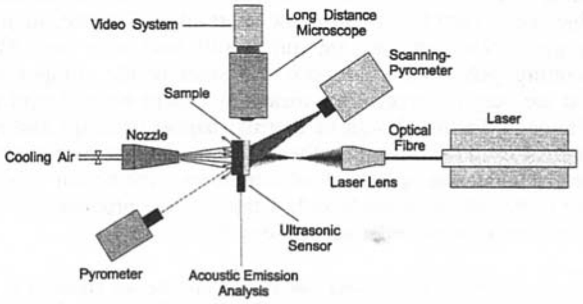

Fig. 2 Experimental test setup for defined generation of thermal loading conditions in thermal barrier coatings using laser heating and air cooling

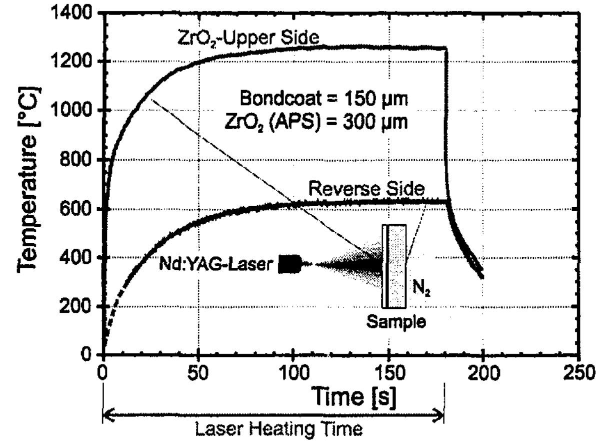

Fig. 3 Temperature course measured in the center of the specimen with a 3 minute front face irradiation at 280 W laser power and simultaneous cooling of the substrate side

made at a later time point. A PC was used to control the test apparatus and collect the data. The high reliability of the equipment and the extensive use of hardware and software in the checking mechanisms meant that the cyclic tests could be run in automatic mode without supervision.

Precise knowledge of the spatial and temporal distribution of temperature and stress/strain in the coating system is indispensable for evaluation of the experiments. For this reason, an FE model was produced parallel to the experiment analysis. The thermal calculation model for the coating specimens takes account of both the thermal conduction and the thermal irradiation as well as the heat dissipated by convection, whereby the laser irradiation was treated as a constant heat flux on the surface of the Zirconia coating. A modified Gaussian distribution was used as the power density distribution of the laser after adaptation to the temperature profiles measured in the experiment. The parameters for irradiation and convection, which were very difficult to determine experimentally, were established by iterative comparison of the calculated temperature distributions with the temperatures measured in the experiment. The time points at which the transient load states were calculated were automatically matched to the occurrence of large temperature changes. The subsequent mechanical analysis took account not only of the temperature-dependent thermoelastic material data but also the elastic-viscous creep. The load and temperature-related creep of the coatings used was measured at the Institute for Non-Metallic Inorganic Materials (INAM, Stuttgart University) [9, 10].

Care had to be taken to ensure that the level of the calculated stresses was not incorrectly interpreted because the modeling did not take account of a whole series of important material properties and reactions. For instance, APS sprayed Zirconia coatings have a very low tensile strength in the region of a maximum of 75 MPa. If the strength value is exceeded during tensile stress, a crack network forms and this leads to local relaxation of stresses. This means that the calculated tensile stresses in the order of $\geq$100 MPa are not really present and to be regarded only as an indication of a large expansion of the coating with accompanying crack patterns. The porous ZrO$_2$ material became locally compacted under pressure, particularly in conjunction with high temperatures. The associated inhomogeneous increase in the modulus of elasticity therefore resulted in substantially higher stresses for the same thermal loading.

Thermal barrier coatings produced using the APS process were investigated. IN 617 was used as the basic material for the substrate. Vacuum plasma spraying was used to apply a MCrAlY bond coat (M = Co, Ni) which was then subjected to a multistage heat treatment to improve its adhesion to the substrate. 7-wt%-Y$_2$O$_3$ partially stabilized Zirconia was used as the material for the thermal barrier coating. 5.2 mm thick circular specimens, 29 mm in diameter were utilized as a substrate to represent in-plane thermal barrier coating systems.

To investigate the effect of bond coat oxidation and thermal aging of the coating, some of the specimens were conditioned at 1000°C or 1100°C for up to 1000 h. The characteristics of the thermal barrier coatings under test were determined using metallographically prepared cross sections. Quantitative image analysis was used to determined crack length distribution of surface cracks, vertical cracks, in-plane cracks within the ZrO$_2$ coating, as well as delamination cracks at the interface, relative to the previous conditioning and the cyclical thermal laser irradiation.

Material Damage During the Laser Thermal Cycling Test

The loading, designated in the following as "front face irradiation" is characterized by heating the center of the ZrO$_2$ coating using a static spread laser beam with rear face substrate cooling taking place at the same time by blowing with air or nitrogen (T = 20°C). The irradiation time for the test evaluated in Figs. 3 and 4 was 3 min. With a laser power of 280 W. The hot spot diameter defined by the $1/e$-decay of the power density was 12 mm (peak power density $\approx$ 2 W/m^2).

An extremely high heating rate was reached on the irradiated face in the first seconds, which was due on one hand to the high power density in the center of the laser beam and on the other hand to the low thermal conductivity of the porous Zirconia at low temperatures (the part shown dotted in the initial area of the rear face temperature curve was extrapolated afterwards using FE-analysis data, because the pyrometer used did not deliver a measuring signal below 300°C). At the selected laser power, a maximum temperature of 1250°C was established on the face of the thermal barrier coating after approximately 100 s. This dropped to 750°C towards the edge of the disk (not shown in Fig. 3). The temperature difference between the front and rear faces measured at the center of the specimen in the subsequent thermally-stable condition was more than 600 K, and, therefore, greater by a factor of at least 3 than for the stationary "operational case" on the gas turbine.

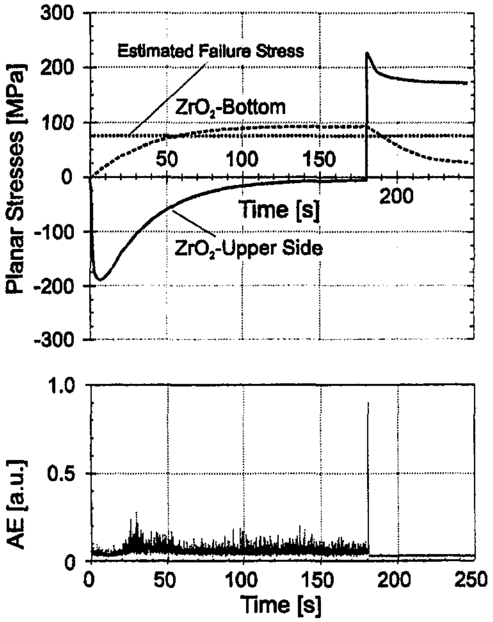

Fig. 4 Calculated course of planar stresses in the center of the disk for a single thermal shock and during the measurement of detected acoustic signals

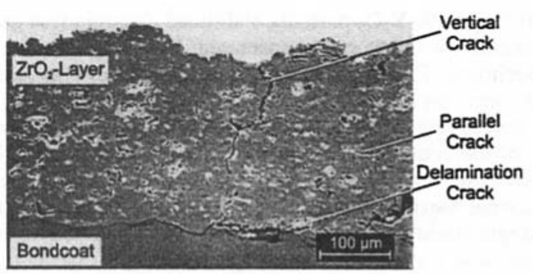

Fig. 5 Vertical cracks, parallel cracks, and the onset of delamination after cyclic thermal loading

The calculated time pattern of the planar stresses (σ_{xx}, σ_{yy}) in the center of the specimen is shown by the plot in Fig. 4 compared with the detected acoustic signals (bottom plot). In the first seconds of heating the hot Zirconia near to the surface came under pressure. The cold edge area of the ceramic and the metallic substrate which was also still cold exerted an in-plane restriction on the expanding material which was therefore compressed. Increasing substrate temperature caused the underside of the ceramic coating at the interface to the bond coat to expand due to the higher thermal coefficient of expansion of the superalloy. At the same time, the compressive stresses in the hot ZrO_2 top face reduced because of the axial temperature difference reducing in the first 100 s and because of the creep (relaxation) of the ceramic. The level of the compressive stresses depends on the diameter of the hot spot. The smaller the radius of the hot spot, the greater the induced compressive stresses for the same temperature, but because of short relaxation times the relationship is significant only for short heating shocks.

At the start of irradiation, and increasingly after approximately 15 s, the detected acoustic signals (bottom plot in Fig. 4) show that fracture processes take place in the ceramic coating which release acoustic energy. However, it was not possible to determine clearly the area of the ZrO_2 coating in which the signals were generated, because fracture processes took place both in the compressive and tensile area.

Immediately after the laser beam heating was switched off, a dramatic reversal of the in-plane stresses from slight compression to high tension took place on the top face of the thermal barrier coating. This was due both to the extremely rapid cooling by the radiation of the Zirconia surface and also because the substrate was still relatively hot due to the very high heat capacity, and, therefore, expanded. Because the level of the induced thermal stresses far exceeded the strength of the material, a network of vertical cracks developed close to the surface. This process was accompanied by strong acoustic signals (''switch-off'' peaks) whose amplitude became distinctly greater compared with the acoustic signals which occurred during the irradiation.

Because of the stress relaxation and creep that took place under compression in the hot condition, residual stresses, the level of which is limited by the strength of the material, remained in the area of the ZrO_2 coating close to the surface after cooling down had taken place [7]. Low frozen-in stresses can also not be precluded in the vicinity of the bond coat.

During the cyclic test, an adequate cooling time (2 min) was allowed to ensure that the specimen had a homogenous initial temperature before each cycle. The stress condition at the beginning of each cycle is, however, dependent on the frozen-in stresses, particularly from the preceding cycle, the momentary material parameters, and the accumulated damage state of the coating system. The residual stress state remaining after the APS coating is important only for the first cycles of the thermal fatigue test during which high temperature or long dwell times are achieved. A new residual stress condition becomes established after a few cycles. In particular, the stresses in the hot condition are compressive.

All specimens irradiated from the ceramic face showed individual cracks on the surface of the ceramic in the area of the hot focal point. These cracks were variously oriented and initially had a low spread. With an increasing number of cycles, the cracks grew to form a network.

Figure 5 shows a typical microstructure of APS-coated specimens after being subjected to a large number of cycles at high temperatures. A basic distinction is to be made between two different directions: (i) cracks which run mainly vertical to the surface, and (ii) cracks which are parallel to the surface. Very long verticals cracks which can extend to the bond coating begin at the surface and represent an extension of the depth of the crack network. Parallel cracks run both within the ceramic coating and also at the interface between the thermal barrier coating and bond coating. The latter type of crack, i.e., a delamination of the thermal barrier coating from the bond coating, is referred to here as a delamination crack.

Considered in combination with the calculated stress patterns, the acoustic emission signals (Fig. 6) recorded during the cyclic tests provide data on the temporal sequence of crack growth. This shows that the formation of the network of surface cracks and its propagation down into the material is due to the high-in-plane tensile stresses at the beginning of the cooling phase. This correlates with the occurrence of distinct acoustic signal peaks at the final time point of the laser heating. The occurrence of switch-off peaks immediately after the end of laser heating also after a large number of cycles clearly indicates that the vertical cracks partially heal due to creep and sintering processes under the influence of hot compressive stresses in the surface coating and open up again due to energy release when cooling down.

The growth of surface cracks depends largely on the oven conditioning. Where aging takes place using steep temperature

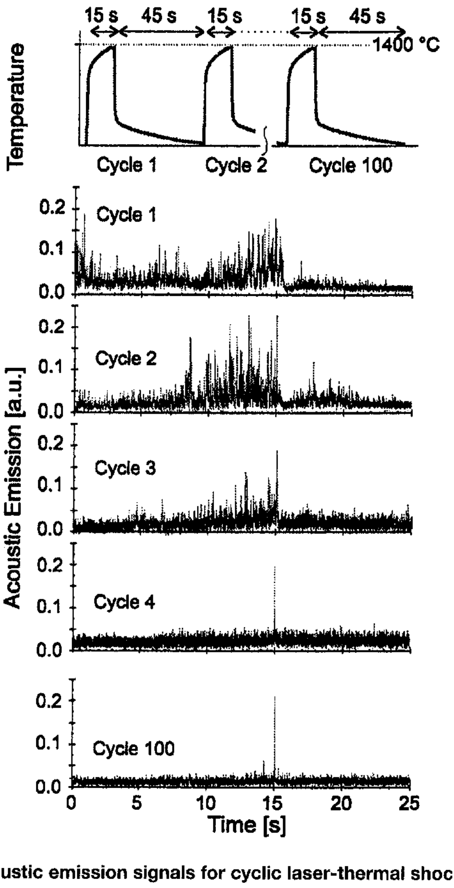

Fig. 6 Acoustic emission signals for cyclic laser-thermal shock loading

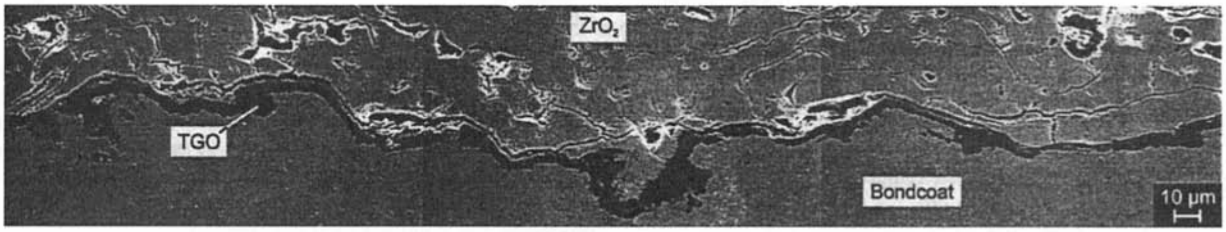

Fig. 7 Delamination cracks at the interface after laser thermal cycling on a conditioned thermal barrier coating

gradients (thermal barrier coating = 1400°C, substrate = 800°C) there is, however, a distinct compaction in the area close to the surface. The increase in the modulus of elasticity associated with this causes higher thermoelastic stresses at the same temperature loading, which makes the segmenting network finer and causes individual cracks to become distinctly wider where there is cyclic loading. Frequent, repeated opening and closing of the edges of the cracks under alternating load causes friction effects. As could be in situ observed with the long distance microscope, this led to the breakaway of small particles. These breakaway particles can act as wedges resulting in additional tensile forces at the ends of the microcracks. The length distribution of vertical cracks shows that the crack population changes only negligibly due to thermal cycling, but that a few cracks can, where there is a high number of cycles, grow to greater lengths, finally extending to the bond coat.

The amplitude and frequency of the acoustic signals during the heating phase decrease as the number of cycles increases. In-plane tensile as well as compressive stresses are present in the coating depending on the depth. Parallel cracks which are present due to the given pancake structure of the APS coating and the fact that it is applied in layers, can grow in both situations because in each case positive stress intensities are present at the end of the crack. But because higher compressive stresses are achieved than tensile stresses due to the low tensile strength of the ceramic coating, compressive stresses may have been chiefly responsible for the propagation of the in-plane cracks.

On coatings that have not been conditioned, the growth of parallel cracks triggered by thermal cycling did not lead to a shift in the cumulative maximum, but instead to an increase in the number of fewer, longer cracks. This can be explained by the fact that the short cracks join and the longer cracks thus produced can then grow more quickly. Long and wide parallel cracks were frequently, but not always side branches of the long vertical cracks. All cracks showed a tendency to spread as a result of the cyclic loading.

With increasing intensity of the preceding heat treatment the number of parallel cracks, on the other hand, increased strongly with the number of cycles, whereby the maximum damage occurred within the first 500 cycles. A further increase in the number of cycles brought about only slight changes in the crack population. Even when the oven conditioning did not have the effect of strong compaction of the ceramic, the Youngs's modulus did increase, and, thus, produced an overall higher level of thermally induced stresses. The reduction in acoustic emissions in the heating phase in line with an increase in the number of cycles supports this deduction.

The formation of delamination cracks depends on the conditioning to a much greater degree than is the case with parallel and vertical cracks. Very few delamination cracks were found on specimens which were not conditioned, even when subjected to a high number of cycles. The effect of thermal cycling expanded with increasingly intensive aging, i.e., in particular the number of longer delamination cracks increased. Enlarging the number of cycles beyond 500 led to further growth in delamination cracks in the case of long aging (1000 h) (Fig. 7). This result shows that the delamination is closely linked to the existing thickness of the TGO coating. This means that aging by cyclic laser irradiation does lead to compaction of the ceramic and correspondingly greater crack damage in the thermal barrier coating, but because of the relatively lower temperature of the bond coat results in only a slight growth in the oxide coating. The cyclic laser aging consequently promotes the growth in delamination cracks far less than a preceding oven aging. A TGO coating thickness of at least 7 to 8 μm is necessary for thermal cycling to lead to the generation and growth of delamination damage.

The behavior of thermally loaded, thicker thermal barrier coatings differed clearly from the coating previously discussed, which had a thickness up to 350 μm. To investigate the differences thermal cyclic tests on specimens with a 1000 μm APS coating were carried out. The laser power was set so that the same maximum surface temperature as for thin coatings (1300 to 1350°C) was reached and the irradiation time was also 15 s. The choice of parameters enabled a direct comparison of the different coating thicknesses. Certainly in the gas turbines, the surface temperature of thicker thermal barrier coatings is higher than for thinner thermal barrier coatings at the same hot gas temperature. This means that the surface of thicker thermal barrier coating is more heavily loaded and the viscous-elastic behavior of the material becomes even more significant.

Under tensile stress, cracks occurred on the surface the same as with the thin thermal barrier coatings. These cracks propagated heavily under the influence of the ceramic compaction in the area close to the surface and first grew in depth in the vertical direction. In contrast to the thin thermal barrier coatings, the cracks did not spread to the bond coat but instead branched off at a depth of 400 to 500 μm in a direction parallel to the surface (Fig. 8). Delamination cracks occurred within the ceramic coating. This finally led to cohesive failure of the thermal barrier coating. Delamination at the interface between the thermal barrier coating and bond coat was, however, very much less than for specimens with thin thermal barrier coatings subjected to comparable loading.

Conclusions

The results of the above investigations show and confirm that the damage and failure of thermal barrier coatings under thermal loading is influenced essentially by the following three factors:

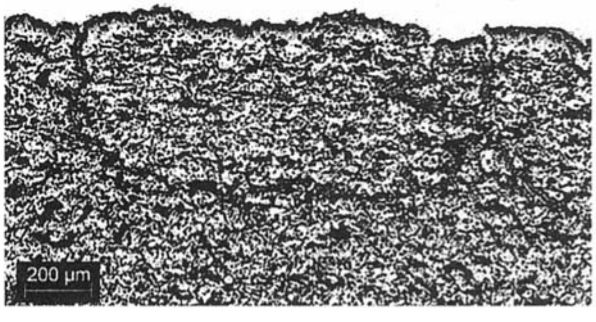

Fig. 8 Crack deflection in the area of the focal point of a 1000 μm APS coating

- changes in the modulus of elasticity and the fracture mechanics properties of the ceramic due to aging processes
- oxidation of the bond coat which encourages failure of the adhesion
- irreversible deformations which cause progress of the damage during cyclic loading

Both APS and PVD thermal barrier coatings are characterized by a high expansion tolerance in the initial condition. Therefore, they can tolerate both stationary and transient thermal expansions without macroscopic damage. The energy release rate available for crack propagation is small. The microstructure, however, changes both due to the stress application, and also the diffusion effects at high temperatures. In the case of APS coatings, this also includes compaction by the concentration of spray flecks which takes place even at relatively low temperatures and the creep and sinter effects present at high temperatures that are caused by pressure. The compaction processes take place relatively quickly at the temperatures used for the laser tests. The temperatures occurring on the gas turbines in service are lower, but are present for substantially longer periods. Because of the increase in the modulus of elasticity, the thermally induced stresses and the energy release rate of the ceramic coating increase. The threshold for supercritical crack propagation can be more readily attained.

However, the critical energy release rate also changes with increasing operating duration and material aging. The additional stresses in the area of the interface which occur in the case of TGO formation are reduced or completely relaxed by the growth of microcracks and cause a degradation in the adhesion of the thermal barrier coating. Under operational service stresses, delamination sets in leading to functional failure of the thermal barrier coating.

The aging processes described (particularly ceramic compaction and bond coat oxidation) provide a necessary precondition for crack growth, but this is also driven by special cyclic effects. Crack propagation occurs due to a quasi-stable growth of cracks of different orientation. The mismatch of the crack edges due to irreversible deformations (such as creep of the ceramic or bond coat, breakaway of small particles or plastic deformation of the substrate) causes a break up of the microstructure. But, because the interaction of the crack edges reduces with an increase in the number of cycles, crack growth slows down during cyclic loading.

These results agree very well with recently published data by Zhu et al. on thick thermal barrier coating systems for diesel engine applications [8]. With a similar experimental approach they showed that the fatigue crack growth rate is accelerated by thermal cycling at a high temperature level in combination with applied severe thermal shocks due to surface wedging processes and coating creep phenomena.

Acknowledgments

We wish to thank Messrs. M. Baatz and R. Sporer for the model development and for carrying out the Finite Element calculations. This work was supported by the BMBF in the course of the MATEC promotion program under project support number 03M0026.

References

1 G.C. Chang, Phucharoen, W., Miller, R.A., 1987, "Behavior of Thermal Barrier Coating for Advanced Gas Turbine Blades," *Surface and Coatings Technologies,* Vol. 30, pp. 13–28.

2 Kokini, K., Takeuchi, Y., 1994, "Initiation of Surface Cracks in Multilayer Ceramic Thermal Barrier Coatings Under Thermal Loads," *Material Science and Engineering* A, Vol. 189, pp. 301–309.

3 Evans, A.G., Wang, J.S., Mum, D., 1997, "Mechanism-Based Life Prediction Issues for Thermal Barrier Coating," paper presented at the TBC-Workshop, Cincinnati, OH, May 19–21, 1997.

4 Loh, R.L., Rossington, C., Evans, A.G., 1986, "Laser Technique for Evaluating Spall Resistance of Brittle Coatings," *J. Am. Ceram. Soc.,* Vol. 69, pp. 139–142.

5 Hashida, T., Takahashi, H., 1990, "Laser Irradiation Thermal Shock and Thermal Fatigue Test Procedure," Proceedings, Int. Symposium, FGM, Sendai, pp. 365–373.

6 Kirchhoff, G., Holzherr, M., Bast, U., Rettig, U., 1993, "Thermal Shock and Thermal Cycling Behavior of Silicon Nitride Ceramics," Proceedings, Int. Conf. On Silicon Nitride-Based Ceramics, Trans Tech Public. Ltd., Switzerland, pp. 605–609.

7 Pompe, W., Bahr, H.-A., Pflugbeil, I., Kirchhoff, G., Langmeier, P., Weiss, H.-J., 1997, "Laser Induced Creep and Fracture in Ceramics," *Materials Science and Engineering,* A233 (1–2), Elsevier Science, The Netherlands, pp. 167–175.

8 Zhu, D., Miller, R.A., 1997, "Investigation of Thermal Fatigue Behavior of Thermal Barrier Coating Systems," *Surface and Coatings Technology,* Vol. 94–95, pp. 94–101.

9 Thurn, G., 1997, "Hochtemperatureigenschaften und Schädigungsverhalten plasmagespritzter ZrO_2-Wärmebarrieren," thesis, Universität Stuttgart, Germany.

10 Thurn, G., Aldinger, F., Schneider, G.A., 1997, "High-Temperature deformation of Plasma-Sprayed ZrO2 Thermal Barrier Coatings," *Materials Science and Engineering A,* Vol. 233, pp. 176–182.

Assessment of Combustion Modes for Internal Combustion Wave Rotors

M. R. Nalim[1]
National Research Council,
NASA Lewis Research Center,
Cleveland, OH

Combustion within the channels of a wave rotor is examined as a means of obtaining pressure gain during heat addition in a gas turbine engine. Three modes of combustion are assessed: premixed autoignition (detonation), premixed deflagration, and non-premixed autoignition. The last two will require strong turbulence for completion of combustion in a reasonable time in the wave rotor. The autoignition modes will require inlet temperatures in excess of 800 K for reliable ignition with most hydrocarbon fuels. Examples of combustion mode selection are presented for two engine applications.

Introduction

The internal combustion wave rotor is a promising means of pressure-gain combustion. It approaches the thermodynamic ideal of constant-volume combustion, and can provide significant enhancement of gas turbine engine performance and NO_x emissions reduction. Pressure-gain combustion has been a long sought ideal. Indeed, the earliest working gas turbines had valved, pulsating combustion chambers (Foa, 1960). But while they encountered analytical obstacles and turbine flow unsteadiness, improvements in compressor technology favored the simpler, high loss, steady flow combustor. Over the years, a variety of methods have been investigated for pressure-gain combustion or compound-cycle systems with substantially steady flow to the turbine. These include pulse or valved combustors, detonation-wave combustors, wave rotors, and piston devices (Goldstein et al., 1957; Kentfield et al., 1988). Figure 1 includes a flow schematic of the concept and a T-S diagram to illustrate that constant-volume heat addition (2–3), yields a cycle with greater potential work output (3–4) than a conventional cycle (1–2–3′–4′) with the same turbine inlet temperature (TIT).

The wave rotor arguably offers the closest viable approach to this thermodynamic ideal. Simple pulse combustors have passive or no valving to control the flow and have limited pressure gain potential. On the other hand, piston machines offer tight flow control and large pressure ratios, but are mechanically complex, bulky, and heavy. A well-designed wave rotor can provide large-amplitude pressure waves and active flow control, and will be a light, compact, low-loss device with a single low-cost moving part.

Wave Rotor Background. The wave rotor is a device that utilizes unsteady waves to exchange energy directly between fluids. It consists of a number of channels arranged about an axis; by rotation the ends of the channels are periodically connected to higher and lower pressure manifolds that generate and utilize waves in the channels. The flow in the manifolds is steady, and is directed to other steady flow components. An important feature is that as varying temperature gases flow through the rotor, it experiences a mean temperature much lower than the peak cycle temperature. Low rotational speed relative to turbomachines, and simpler geometry moderates structural and material requirements.

Among its many applications (Shreeve and Mathur, 1985), the wave rotor in a gas turbine engine can increase its pressure ratio and peak cycle temperature beyond the limits of turbomachinery. It can utilize external (i.e., conventional, steady flow) combustion or internal (on rotor) combustion. This distinction is made with reference to the wave rotor; in the thermodynamic sense, combustion is always internal, i.e., within the working fluid. Past approaches have generally proposed external combustion, pressure-exchanger systems (Wilson and Paxson, 1995; Resler et al., 1994; Zauner et al., 1993), where low pressure, compressor-discharge air is further compressed in the wave rotor channels by compression or shock waves. The compression work is provided by hot gas from the external combustor, which expands in the wave rotor, and is then sent to the turbine at a lower temperature than the combustor exit. This system acts as a topping stage to increase the pressure ratio and peak temperature of the engine cycle.

Pressure-Gain Combustion in the Wave Rotor. In the internal combustion wave rotor, combustion occurs within the wave channels, each channel being periodically charged and discharged as it rotates past appropriate partial-annular inlet and outlet ports. The typical combustion and wave processes are illustrated in the wave rotor sketch in Fig. 2. The inlet manifold, which conveys compressor-discharge air, has been omitted to reveal the inlet port in the stationary end plate. The outlet manifold exhausts the flow to a turbine. The advantages of internal combustion are (a) pressure gain equivalent to a pressure exchanger, but lighter, more compact, and with less ducting and associated losses and penalties, and (b) potentially low NO_x formation, because the expansion of burned gas within the rotor minimizes the residence time at peak temperature. In common with a pressure exchanger, the internal combustion wave rotor is periodically cooled by the air flow, and, thus, can tolerate high gas temperature, and it provides wave precompression of inlet air as it is brought to rest in the channel.

Previous descriptions of this concept have focused on mechanical (Lewis, 1955) and gas dynamic (Schapker, 1958) aspects, but not combustion. If successful, wave rotor combustion could provide a quantum advance in the performance of combustion engines, by combining the best of two worlds: the thermodynamic efficiency of confined combustion in the internal combustion (IC) engine, and the power density of the turbine. Whereas ideal reciprocating IC engine performance is compromised by dynamic effects at high speed operation, the wave rotor is designed to exploit dynamic (wave) effects.

Table 1 indicates the pressure rise developed with adiabatic constant-volume combustion of some fuel/air mixtures at various initial conditions, calculated using equilibrium chemistry

---

[1] Presently at the Department of Mechanical Engineering, IUPUI, 723 W. Michigan Street, SL 260, Indianapolis, IN 46202.

Contributed by the Internal Combustion Engine Division and presented at the 31st Joint Propulsion Conference, San Diego, CA, July 1995. Manuscript received by the ASME Headquarters June 12, 1998. Associate Technical Editor: D. Assanis.

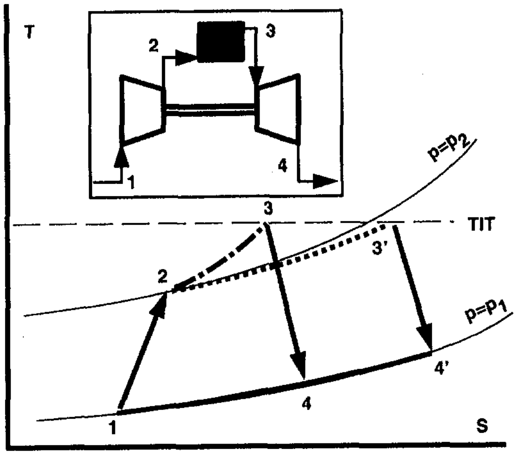

Fig. 1 Pressure-gain combustion engine cycle

and real-gas thermodynamic data. Note that the initial temperature strongly influences the pressure ratio. For simplicity, the T-S diagram of Fig. 1 ignores the necessary flow work of charging and discharging the combustion chamber(s). With accounting for flow work, the net pressure-gain ratio for a perfect constant-volume combustor (Nalim, 1998) is

$$\Pi = \Theta^{\gamma/\gamma-1}\{1 + \gamma(\Theta - 1)\}^{1/1-\gamma},$$

where Θ is the overall temperature ratio, and γ is the specific heat ratio (assumed constant). Π is less (Fig. 3) than the pressure ratio indicated in Table 1. This result must be further modified to account for nonconstant-volume combustion and wave precompression. Using numerical simulations that include these corrections and all major losses, Wilson and Paxson (1995) estimate that an optimized pressure-gain wave rotor can increase the specific power of a typical small gas turbine by 23 percent and decrease its fuel consumption by 19 percent. Similar performance is predicted by numerical simulation of internal combustion (Nalim and Paxson, 1997).

Wave-rotor combustion will have much in common with IC engine combustion. Fuel and air in a confined volume must react rapidly and reliably, but without damaging heat loading or pressure oscillations. Ignition and flame propagation behavior will depend on details of fuel and turbulence properties. Despite much research, diesel and spark ignited (SI) engine combustion phenomena remain poorly understood at the fundamental level; much of the empirical knowledge available may not apply beyond the specific engine conditions obtained.

Rapid combustion is essential to minimize residence time and rotor size. The peak flame speed in an automotive SI engine is typically limited by turbulence levels to 10–50 m/s. In the wave rotor we must and can achieve higher combustion rates, so that the time taken for combustion is not an inordinately large part of the total cycle time. This will require judicious design of the mode of combustion based on fuel properties and the wave-rotor inlet conditions over the range of operation of the engine.

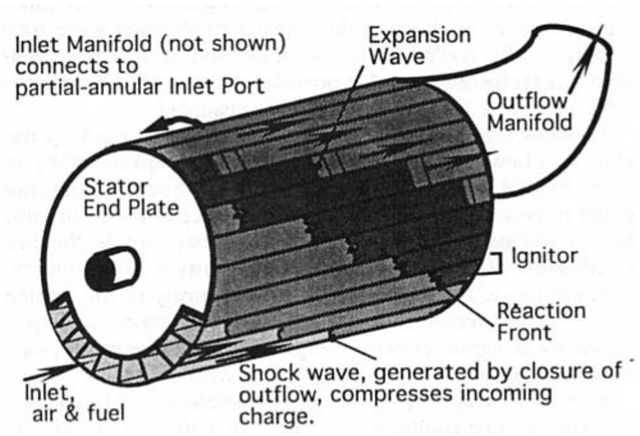

Fig. 2 Internal-combustion wave rotor sketch

Table 1 Constant volume adiabatic combustion pressure ratio

Mixture:	H_2/Air		C_3H_8/Air	
Equivalence ratio:	1.0	0.5	1.0	0.5
Initial state				
298 K, 1 atm	11.3	7.4	9.3	6.3
750 K, 1 atm	4.6	3.3	3.8	2.9
750 K, 20 atm	4.9	3.4	4.0	2.9

Combustion Modes

A novel combustion system introduces many uncertainties about possible reaction initiation, propagation, and extinction mechanisms. Varying inlet conditions modify the relative roles of chemistry, molecular diffusion, turbulence, radiation, multiphase, wall surface, and catalytic effects. For discussion, we distinguish among several typical modes of combustion of fuel and air, involving either premixed or non-premixed combustion, and different ignition mechanisms. A real combustion system may have features and behavior that combine more than one of the following idealized modes.

1. Shock-wave compression autoignition followed by a premixed reaction front, which strengthens and accelerates the shock. It may be a ''fast flame'' (Clarke, 1989), or develop into a detonation. This mode will require high initial temperature.
2. Premixed turbulent deflagration, when thermally ignited by a spark, laser, recirculated hot gas, or other means, at one or more sites. As in IC engines, flame speed will depend on turbulence intensity and scales, and on combustion temperature. Subsequent autoignition may accelerate combustion.
3. Autoignited non-premixed combustion when fuel is injected into air at (or immediately compressed to) sufficiently high temperature, as in a diesel IC engine. Some

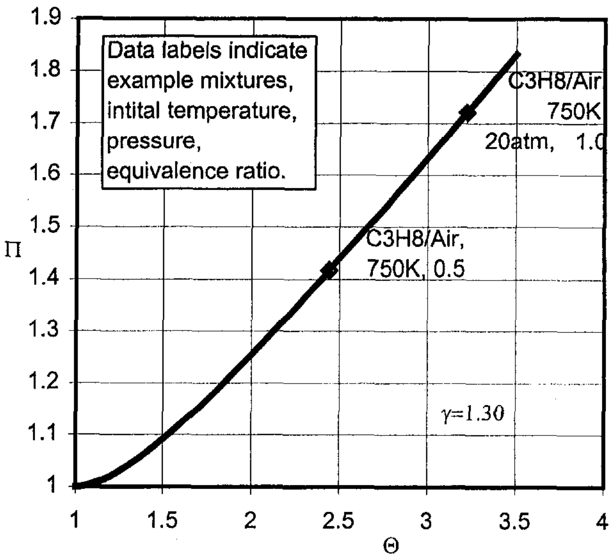

Fig. 3 Constant-volume combustion pressure gain

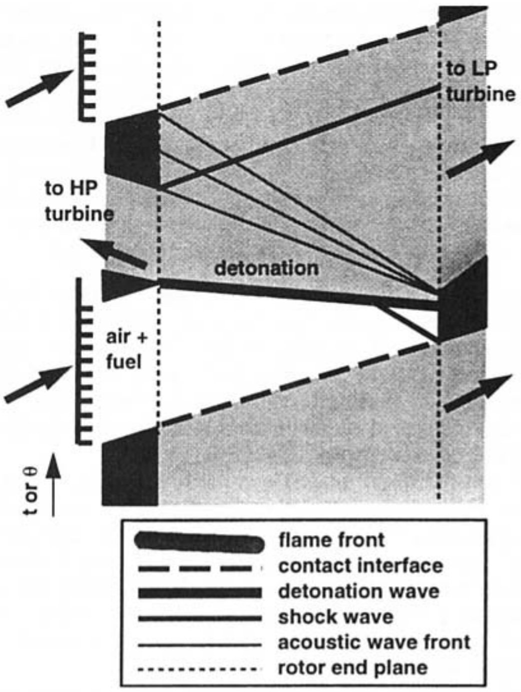

Fig. 4 Simplified wave diagram for shock-ignited detonation mode

contiguous fuel and oxygen mix and rapidly autoignite; the remainder react at a rate determined by turbulent mixing.

The unsteady flow process within the wave rotor is best illustrated by a wave diagram. This is a position–time (x-t) diagram (or time history) of the periodic process in any single channel. The vertical axis represents time t. Figures 4 and 5 are simplified wave diagrams for premixed modes. Full lines represent the trajectories of pressure waves, and broken lines represent the paths of fluid particles or interfaces. When inlet temperature is sufficiently high, the mixture will react behind the shock, ultimately forming a detonation (Fig. 4). With lower temperature, deflagrations must be initiated, possibly from each end (Fig. 5). For pressure gain, the outlet pressure is higher than the inlet pressure, unless there is a second exhaust to a low-pressure (LP) turbine (Fig. 4). Thus, the hot gas in the channel from the previous cycle may not be completely purged and could be a useful ignition source (but bewaring flashback as discussed later).

Premixed Autoignition and Detonation. Fuel properties and temperature primarily determine whether compression ignition can occur. Gaseous hydrocarbon-air mixtures at 600–900 K autoignite in a two-stage chemical process involving a ''cool flame'' (Halstead et al., 1977). Empirically, an autoignition delay time for a particular fuel/oxidant mixture is determined at given temperature and pressure conditions. At fixed conditions, the chemical autoignition time varies among common hydrocarbon fuels by about an order of magnitude. Small amounts of certain compounds (e.g., octane boosters in gasoline) can strongly affect autoignition in otherwise identical compositions.

Autoignition delay times have been measured in a variety of experimental reactors: rapid compression machines (Halstead et al., 1977), shock tubes (Burcat et al., 1971), combustion bombs, and continuous plug flow ducts (Freeman and Lefebvre, 1984; TeVelde and Spadaccini, 1981). Comparable values vary significantly and there is disagreement about the relative influence of reaction variables (such as stoichiometry). Ignition delay data must be interpreted carefully in the light of fuel specifications, experimental apparatus, and detection criteria. A sample of compiled data is presented in Fig. 5, scaling the autoignition time with the inverse of pressure to allow a reasonable comparison among experiments over a wide range of conditions.

Referring to Fig. 4, with nearly sonic inflow, the temperature will rise by a factor about 1.4 through the shock wave that stops the flow. For a 900 K hydrocarbon-air mixture adiabatically compressed to 1250 K, the chemical induction time will contract from a few milliseconds to about 0.01 ms. In comparison, the acoustic transit time will be about 0.5 ms for a half-meter long channel. For these conditions we expect immediate reaction behind the shock to form equilibrium products. When post-compression temperature is below about 1100 K, the chemical time scale will be finite relative to the acoustic time scale. For even lower temperatures (<600 K) hydrocarbon autoignition reactions are typically negligible.

Relative to the inflowing mixture, the far end plate is equivalent to a suddenly started piston. The relative velocity and the reaction enthalpy together determine whether an overdriven or a Chapman–Jouguet (C-J) detonation occurs. C-J detonation speeds for lean propane-air mixtures range 1500–2500 m/s for pressures of 1–20 atm, with weaker dependence on stoichiometry and temperature.

Detonative combustion produces a severe pressure pulse and hot, high speed flow behind the wave. Although the peak heat load is momentary and is offset by colder flows, the weight and cost of an adequately robust rotor is unknown. Another drawback is the temperature and composition sensitivity of autoignition already discussed. When inlet temperature is low (e.g., at startup), an alternative ignition method is required.

Premixed Deflagration. Turbulent flame propagation is necessary for fast burn in this mode, as in the SI engine. Sources of turbulence generation in the inflowing gas include the upstream compressor, ducting, fuel spray, the opening process, any additional turbulence generators, and the stopping shock. On board, the turbulent kinetic energy will be distributed into length scales no larger than the characteristic channel transverse dimension, b.

Since ignition can occur as soon as the inlet closes, turbulence decay is limited. (In contrast, reciprocating-engine turbulence decays considerably during piston compression, and various means—squish, swirl, tumble—are employed to enhance turbulence.) If the root-mean-square turbulence intensity is u', and the characteristic lengthscale of turbulent eddies is assumed equal to b, their characteristic timescale will be b/u'; this is a measure of their rate of decay. The extent of decay in the intake duration t_i can be characterized by the number of eddy rotations $n_d = t_i u'/b$. For small inlet Mach no. M_i, it can easily be shown

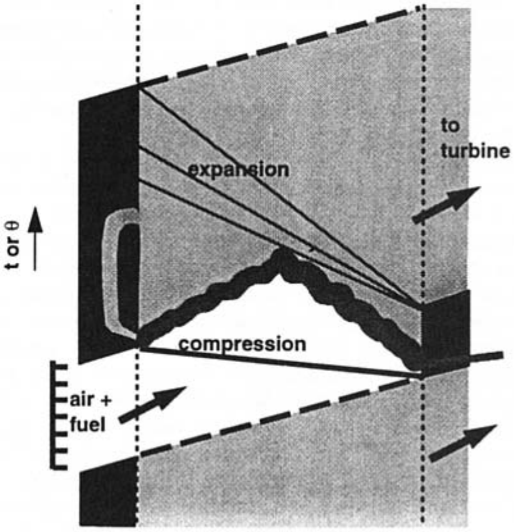

Fig. 5 Simplified wave diagram for deflagration mode

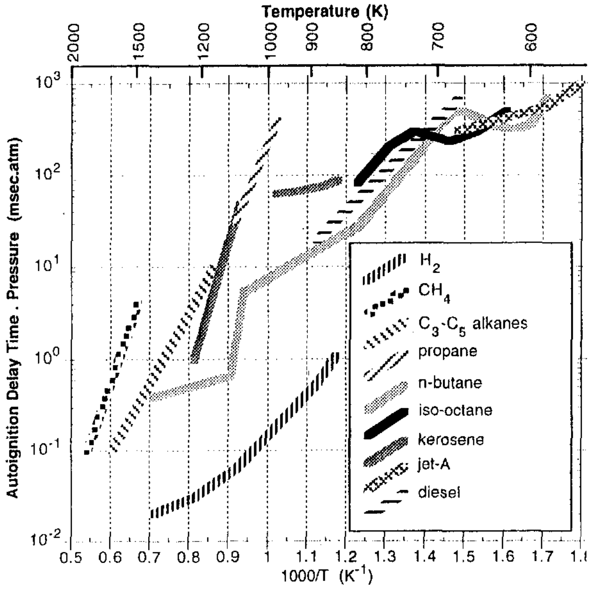

Fig. 6 Autoignition delay for common fuels (Halstead et al., 1977; Burcat et al., 1971; Freeman and Lefebvre, 1984; TeVelde and Spadaccini, 1981; Slack and Grillo, 1977; Ohta et al., 1987)

that $n_d \cong (u'/U_i)(L_i/b)(1 + M_i)$, where L_i is the filled length of the channel and U_i is the inlet velocity. For typical values of $L_i/b = 10$, $u'/U_i = 0.1$, $M_i = 0.3$, there is about one rotation, and, therefore, little decay.

Turbulent combustion can occur in a variety of regimes ranging from wrinkled laminar flames to distributed combustion. When a propagating flame can be defined, the turbulent flame speed, s_t depends on both turbulence properties and chemical kinetics. Measurements of s_t in some experiments (reviewed by Heywood, 1988) indicate that s_t is about equal to u' for moderate levels of turbulence up to twenty times the laminar flame speed, s_l. If the inlet Mach number is 0.3 and u'/U_i is 0.1, the effective flame speed is about 3 percent of the acoustic speed at inlet conditions. Increasing the turbulence intensity should boost the flame speed, but there is little data about flame propagation at very high intensities.

Ignition of a premixed gas could be by a spark, laser, recirculated or residual hot gas, or other means. Spark-ignition delay time will be governed by laminar flame kinetics until the initial flame kernel reaches the size of the turbulent eddies. Multiple or distributed ignition sites would reduce ignition delay and combustion time. Recirculation of high-pressure combustion gas from leading channels via a passage in the end wall (Fig. 5) can provide penetrating jets of hot gas for fast reaction. With proper mixture control, residual gas can provide another strong ignition source.

Limitation of TIT necessitates an overall fuel-air ratio that is considerably leaner than stoichiometric (equivalence ratios of 0.3 to 0.4). This cannot support ignition and flame for typical inlet temperatures. Lean-burn IC engines use charge stratification for reliable ignition, with the spark region nearly stoichiometric to minimize ignition delay and required ignition energy. The wave rotor charge can be easily stratified by nonuniform fuel distribution, but this may result in outflow temperature nonuniformity. Homogenization of temperature in the channel and downstream requires further investigation.

As in SI engines, autoignition can occur in the "end gas" that burns last. Some precombustion reactions normally occur as temperature rises by compression. If this causes autoignition before the flame arrives detonation may occur. Stratification for lean end gas can prevent autoignition without resort to high octane fuel.

Risks of premixing are premature ignition and flashback, particularly with high inlet temperature and hot casing-gas infiltration due to poor end-gap seals. However, typical inlet velocities far exceed flame speed and cause high strain rates near walls, discouraging flashback. Valving by rotation naturally separates the combustion chamber from the intake port. Premature ignition by residual gas can be controlled by tailoring the stoichiometry of the leading inlet gas. While flashback is unlikely, any combustion that occurs before confinement contributes absolutely no benefit from taking place in a wave rotor.

Nonpremixed Compression Ignition. Besides flashback, potential problems with premixing are uncontrolled autoignition/detonation and ignition failure for over-lean mixtures. Combustion could be accomplished rapidly without complete premixing if (a) high inlet temperature ensures short ignition delay time (physical and chemical), and (b) turbulent mixing is strong during combustion.

The non-premixed mode is similar to diesel IC engine combustion. Heat release profiles in diesel engines show that combustion occurs in two phases (Heywood, 1988): rapid combustion of fuel and air mixed before autoignition, followed by diffusion burning of the bulk of the fuel. Completion time is determined by the turbulent mixing timescale, which normally exceeds the kinetic timescale. Similar behavior is expected in the wave rotor.

High speed diesel sprays have an initial injection velocity exceeding 100 m/s, but require several milliseconds to penetrate over a few centimeters. To fully utilize the charge air and obtain good mixing, fuel should be added in the intake using multiple nozzles. A possible wave diagram for non-premixed combustion in given in Fig. 7. With continuous port injection, fuel distribution is accomplished by the flow of air rather than by spray penetration. Liquid fuel will still require high pressure injection for atomization. A likely configuration is a rail-type injector with plain orifices. Swirl orifices will not be useful unless placed some distance upstream of the inlet plane. With many injectors, the distinction from premixed combustion is admittedly blurred. For liquid fuels with good atomization we can neglect the physical delay time for a small amount of fuel to evaporate and mix. The chemical ignition time with most hydrocarbon fuels will not exceed 1 ms for conditions beyond 1000 K and 30 atm (Fig. 6). Limited by decaying cylinder turbulence, the total burn duration in today's high-speed diesels can be several milliseconds. In the wave rotor, turbulence will be intense and sustained.

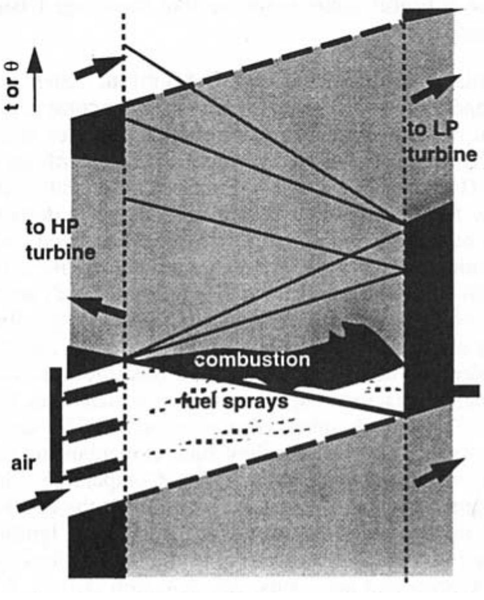

Fig. 7 Simplified wave diagram for non-premixed mode

Table 2 Engine and wave rotor design data (Wilson and Paxson, 1995; Paxson, 1995a)

	Small engine	Large engine
Base Engine		
Core Mass Flow (kg/sec)	1.8	180
Shaft Compression Ratio	7	40
Turbine Inlet Temperature (K)	1330	1780
Compressor Discharge Temp.(K)	580	930
Core Air/Fuel Mass Ratio	45.8	38.6
Pressure-exchange wave rotor		
Rotor Diameter, Length (mm)	152, 152	610, 305
Channel Height, Width (mm)	16.2, 7.6	114.6, 9.7
Wave cycle period (ms)	1.92	3.57
Relative Inlet Velocity (m/s)	~200	~300
Performance of topped engine		
Pressure Gain in wave rotor	1.232	1.204
% Increase, core specific power	23	8.7
% Decrease, SFC	18.8	8.0
Combustion initial and final states		
T_i (K)	640	1040
p_i (atm)	9.7	55.2
T_f (K)	1580	2560
p_f (atm)	16.5	94.4

Example Design Cases

Using a validated simulation code, Wilson and Paxson (1995) optimized 4-port, pressure-exchanger wave rotors (with one exhaust port) for engine sizes from about 2 to 200 kg/s core flow. The equivalent 2-port, internal combustion wave rotors, with the same inflow and outflow states, are examined here for two of those designs. The overall performance of a topped engine depends only on these states, whether combustion is internal or external.

Table 2 indicates the relevant data for these designs. The pressure-exchange cycles for the two engines are nearly identical when nondimensionalized with respect to their inlet states. Their common wave diagram, Fig. 8, shows that the hot gas present in the channel is partially recirculated to the external combustor, because complete scavenging precludes pressure gain. Only 65 percent of the hot gas in the channel at state "*f*" is exhausted; the mass flow through the combustor is increased 55 percent due to recirculation. After ram compression, unreacted fresh charge (state "*i*") will occupy 45 percent of the channel.

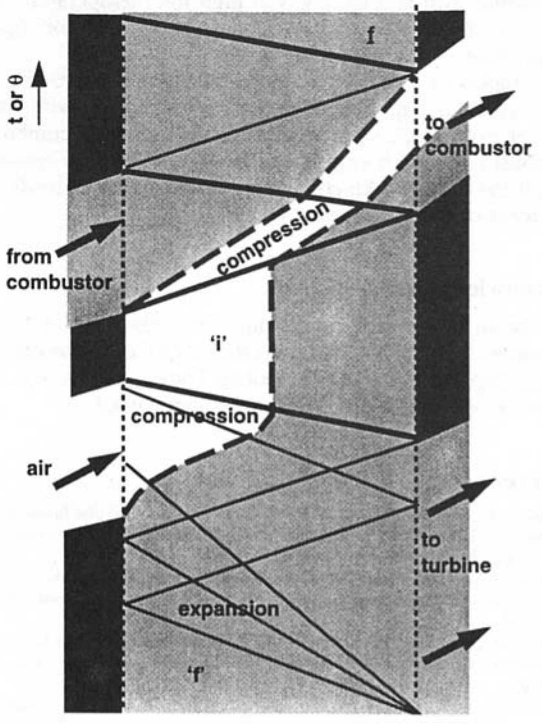

Fig. 8 Wave diagram for pressure-exchanger cycle

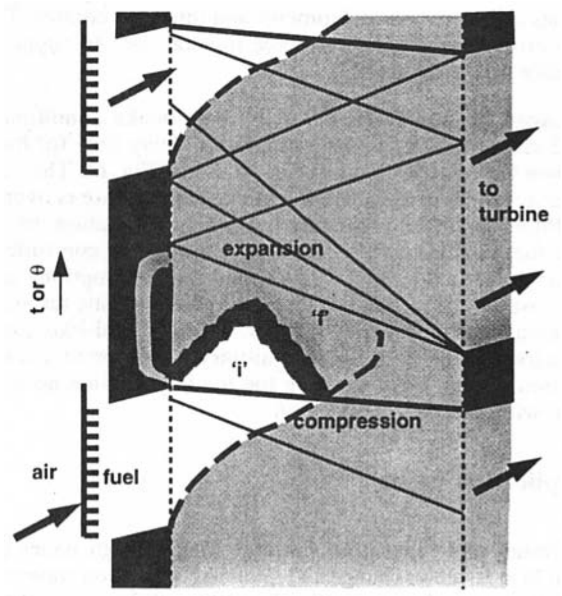

Fig. 9 Wave diagram for equivalent internal combustion cycle

Figure 9 is the wave diagram for an internal combustion wave rotor, which replicates the inlet and exhaust flows of the pressure exchanger. The strengths of the inlet compression wave and the exhaust expansion wave are also replicated; therefore, as are the states marked "*i*" and "*f*", which now represent the initial and final states of the internal combustion process. The fresh charge expands in volume by a factor of 1.4 during combustion while the pressure increases by a factor of 1.7. The actual temperatures of the initial states in the two engine designs differ greatly, dictating different combustion modes as discussed below. It is assumed that the pressure-exchanger dimensions are retained and that the fuel is a typical hydrocarbon.

Small Engine Case. Referring to Fig. 6, the autoignition delay time for the initial conditions of 640 K and 9.7 atm is about 50 ms for most hydrocarbon fuels, much longer than the 0.5 ms intake process. Therefore, only premixed deflagration is feasible, ignited by a hot gas jet at the left end wall and by residual gas on the right. The charge near the left wall is stoichiometric to ensure ignition with minimum delay. For the above initial conditions, the laminar flame speed is about 1 m/s for gasoline-like fuel. If the turbulence length scale is taken equal to the channel width (7.6 mm) the ignition delay time for a conventional electric spark is estimated to be 7 ms. This is unacceptable if the total wave-cycle time is not to exceed that of the pressure exchanger. Although a crude estimate, it is a certain indication that much stronger sources of ignition are needed, such as recirculated and residual hot gas.

If the turbulence kinetic energy in the inlet flow is assumed to be about 5 percent of the total kinetic energy (which corresponds to a drop in total pressure of about 1 percent), then $u' = 50$ m/s. At this speed, a single turbulent flame would traverse the combustible mixture (half the rotor length) in about 1.6 ms. This puts the total cycle time only slightly over that for the corresponding pressure exchanger. Although flame speed may fall off at high u', stratification and dual ignition sites will compensate. Ignition by residual gas assumes appropriate stoichiometry and interface control. There is a critical need for good experimental data to support or modify this assessment.

Large Engine Case. For the post-intake conditions of 55.2 atm and 1040 K, the autoignition delay time for hydrocarbon fuels ranges from 0.2 ms to 2 ms (Fig. 6). The intake duration is about 1 ms and the intake temperature is over 900 K. Premixing risks premature ignition or detonation. Instead, port fuel injection will allow combustion to be controlled by mixing after autoignition. With the same assumptions as the last case for the turbulence level, the characteristic turbulence timescale will be about 0.2 ms. Using diesel-like fuel, it appears feasible to complete ignition and non-premixed combustion within 2 ms, keeping the total cycle time no longer than with external combustion.

Application Issues

Design and Operation Issues. Many design issues common to pressure-exchange and internal combustion wave rotors are discussed elsewhere (Snyder, 1996; Wilson and Paxson, 1995). These include rotation speed selection and matching, alternative cycles, and off-design performance. It is evident that the concept of combustion in a wave rotor presents some unique challenges, but there are also many unexplored ideas and possibilities for design.

Stability. Compared to the pressure-exchanger cycle, on-rotor combustion and gas dynamics are closely and dynamically coupled. This creates the possibility of cycle-to-cycle variability and oscillations whose stability behavior is unknown at present. For instance, an increase in the amount of fuel in one cycle will boost combustion pressure, and thus increase the mass of air taken in during the next cycle. The evolution of this disturbance will depend partly on the fuel control system. The dynamic behavior of a pressure exchanger appears to be beneficial to a gas turbine (Paxson, 1995b), and this may be true with internal combustion as well.

Cooling. In the wave cycle of Fig. 9, the fresh charge does not completely fill the channel. Therefore, it cools only one end of the rotor, unless "reverse flow" multiple cycles are used. For example, the inlet on the left could be followed (after combustion) by an exhaust port on the left, with the inlet for the next cycle on the right. With perfect symmetry, a permanent buffer gas would remain in the rotor. Other arrangements are possible that would also provide even cooling.

Off-design. Only a single-point design is considered in the examples discussed. Over the real operating range of the engines, mixture conditions will vary considerably, affecting ignition and combustion. Guaranteed ignition at all conditions will require fuel staging (stratification), which is easily accomplished by partitioning the inlet port into zones with different steady fueling rates. Although requiring multiple manifolds, modulation of individual nozzles should allow adequate turndown. Numerical simulation of stratified combustion over a wide load range is discussed by Nalim (1997).

Leakage. Thermal issues may be exacerbated by leakage of hot or combustible gas into the rotor-housing cavity. The control of end gaps to limit leakage is required for all wave rotors, for which workable methods have been invented. Internal combustion allows more time for leakage, possibly from hotter gas, requiring tighter control.

Life. High cycle fatigue due to pressure fluctuations may be lower than in a pressure exchanger, but remain an important mechanical design issue. Temperature fluctuations are too rapid to be felt by the rotor, which will remain at a steady-state temperature.

Emissions. NO_x emissions are determined by combustion temperature, residence time, and stoichiometry. In a wave rotor, the residence time at high temperature can be kept short by properly timing the expansion that discharges the channel. Inlet stratification allows lean combustion overall and local enrichment at the ignition site, as in IC engines (Tice and Nalim, 1988; Resler, 1988). A wave rotor could also be designed to incorporate the rich stage of a Rich-Quench-Lean (RQL) low-NO_x combustion scheme (Nalim and Resler, 1995). The RQL scheme requires rapid mixing of hot rich-burn product and quench air, to minimize time at near-stoichiometric conditions. Large injection pressure drop and liner cooling are challenges. A rich-combustion wave rotor can provide (a) a self-cooled combustion chamber, (b) pressure exchange to quench air for rapid second-stage mixing, (c) immediate wave expansion cooling of the rich burn gases, and (d) lower enthalpy of exiting rich product gas, thus reducing mixing-zone stoichiometric temperature.

In a lean-burn wave rotor, there may be unburned hydrocarbons due to quenching in over-lean zones, but no significant carbon monoxide (CO). Pollutants usually formed under rich conditions, such as CO and soot are more likely in rich-burn and in non-premixed cycles. It is premature to make more detailed emissions predictions. Carbon dioxide emissions will always be reduced in proportion to the gain in efficiency.

Conclusions

Combustion within the channels of a wave rotor is a promising means of obtaining pressure gain in a gas turbine engine. Premixed deflagration and non-premixed combustion will require strong turbulence for completion of combustion in a reasonable time in the wave rotor. Sufficient turbulence is expected, with little decay.

For reliable ignition with most hydrocarbon fuels, premixed and non-premixed autoignition modes will require inlet temperatures in excess of about 800 K; otherwise, a supplementary ignition method must be provided. Rapid detonative combustion is possible with premixed gas at high inlet temperature, but it may complicate the mechanical design of the rotor. Ignition temperature is fuel dependent.

Examples of combustion mode selection are presented for two core engine applications previously designed with equivalent pressure-exchanger cycles using external combustion. Combustion in each engine can be completed in a reasonable time if the turbulent kinetic energy in the inflow exceeds about 5 percent of the total kinetic energy.

Acknowledgments

This work was performed while the author held a National Research Council–NASA Lewis Research Center Research Associateship, advised by Dr. L. Bober. The comments of L. Larosiliere, J. Wilson, and F. Hinant are appreciated.

References

Burcat, A., Scheller, K., and Lifshitz, A., 1971, "Shock-Tube Investigation of Comparative Ignition Delay Times for C1-C5 Alkanes," *Combustion and Flame*, Vol. 16, pp. 29–33.

Clarke, J. F., 1989, *Prog. Energy Combust. Sci.*, Vol. 15, pp. 241–271.

Foa, J. V., 1960, *Elements of Flight Propulsion*, John Wiley and Sons, Inc., New York.

Freeman, G., and Lefebvre, A. H., 1984, "Spontaneous Ignition Characteristics of Gaseous Hydrocarbon-Air Mixtures," *Combustion and Flame*, Vol. 58, pp. 153–162.

Goldstein, A. W., Klapproth, J. F., and Hartmann, M. J., 1957, "Ideal Performance of Valved-Combustors and Applicability to Several Engine Types," ASME Paper No. 57-A-102.

Halstead, M. P., Kirsch, L. J., and Quinn, C. P., 1977, "The Autoignition of Hydrocarbon Fuels at High Temperatures and Pressures—Fitting of a Mathematical Model," *Combustion and Flame*, Vol. 30, pp. 45–60.

Heywood, J. B., 1988, *Internal Combustion Engine Fundamentals*, McGraw-Hill, New York.

Kentfield, J. A. C., and O'Blenes, M., 1988, "Methods of Achieving a Combustion-Driven Pressure Gain in Gas Turbines," ASME JOURNAL OF GAS TURBINES AND POWER, Vol. 110, p. 704.

Lewis, R. B., 1955, "Engine Having a Rotor With a Plurality of Circumferentially-Spaced Combustion Chambers," U.S. Patent 2,705,867.

Nalim, M. R., and Resler, E. L., Jr., 1995, "Wave Cycle Design For Wave Rotor Gas Turbine Engines With Low NOx Emissions," ASME Paper No. 95-GT-245.

Nalim, M. R., and Paxson, D. E., 1997, "A Numerical Investigation of Premixed Combustion in Wave Rotors," ASME JOURNAL OF ENGINEERING FOR GAS TURBINES AND POWER, Vol. 119, p. 668.

Nalim, M. R., 1994, "Wave Cycle Design for Wave Rotor Engines with Limited Nitrogen Oxide Emissions," Ph.D. thesis, Cornell University, Ithaca, NY.

Nalim, M. R., 1997, "Numerical Study of Stratified Charge Combustion in Wave Rotors," AIAA Paper No. 97-3141.

Nalim, M. R., 1998, "Thermodynamic Limits of Pressure Gain and Work Production in Combustion and Evaporation Processes," AIAA Paper No. 98-3398.

Ohta, Y., et al., 1987, "n-Butane Ignition in a Wide Range of Temperatures," *Progress in Astronautics and Aeronautics*, Vol. 113, p. 225.

Paxson, D. E., 1995a, private communication.

Paxson, D. E., 1995b, "A Numerical Model for Dynamic Wave Rotor Analysis," AIAA Paper No. 95-2800.

Resler, E. L., Jr., 1988, "Intake Manifold Prestratified Charge," *Chem. Eng. Comm.*, Vol. 67, pp. 111–127.

Resler, E. L., Jr., Mocsari, J. C., and Nalim, M. R., 1994, "Analytic Design Methods for Wave Rotor Cycles," *AIAA J. Propulsion and Power*, Vol. 10, No. 5, p. 683.

Schapker, R. L., 1958, "Analysis of a Wave Combustor Designed for Time-Steady Inlet and Discharge Conditions," General Electric Company Technical Information Series No. DF58AGT 387, Flight Propulsion Laboratory Dept., Cincinnati, OH.

Shreeve, R. P., and Mathur, A., 1985, ed., Proceedings, ONR/NAVAIR Wave Rotor Research and Technology Workshop, Naval Postgraduate School, Monterey, CA.

Slack, M., and Grillo, A., 1977, "Investigation of Hydrogen-Air Ignition Sensitized by Nitric Oxide and Nitrogen Dioxide," NASA CR-2896.

Snyder, P. H., 1996, "Wave Rotor Demonstrator Engine Assessment," NASA CR-198496.

TeVelde, J. A., and Spadaccini, L. J., 1981, "Autoignition Characteristics of No. 2 Diesel Fuel," NASA CR-165315.

Tice, J. K., and Nalim, M. R., 1988, "Control of NO_x Emissions in Gas Engines Using Prestratified charge—Applications and Field Experience," ASME Paper No. 88-ICE-11.

Wilson, J., and Paxson, D. E., 1995, "Optimization of Wave Rotors for Use as Gas Turbine Engine Topping Cycles," SAE Paper No. 951411.

Zauner, E., Chyou, Y.-P., Walraven, F., and Althaus, R., 1993, "Gas Turbine Topping Stage based on Energy Exchangers: Process and Performance," ASME Paper No. 93-GT-58.

D. G. Nicol

P. C. Malte

Department of Mechanical Engineering,
Box 352600,
University of Washington,
Seattle, WA 98195-2600

A. J. Hamer

R. J. Roby

Combustion Science and Engineering, Inc.,
Columbia, MD

R. C. Steele

Solar Turbines, Inc.,
San Diego, CA

Development of a Five-Step Global Methane Oxidation-NO Formation Mechanism for Lean-Premixed Gas Turbine Combustion

It is known that many of the previously published global methane oxidation mechanisms used in conjunction with computational fluid dynamics (CFD) codes do not accurately predict CH_4 and CO concentrations under typical lean-premixed combustion turbine operating conditions. In an effort to improve the accuracy of the global oxidation mechanism under these conditions, an optimization method for selectively adjusting the reaction rate parameters of the global mechanisms (e.g., pre-exponential factor, activation temperature, and species concentration exponents) using chemical reactor modeling is developed herein. Traditional global mechanisms involve only hydrocarbon oxidation; that is, they do not allow for the prediction of NO directly from the kinetic mechanism. In this work, a two-step global mechanism for NO formation is proposed to be used in combination with a three-step oxidation mechanism. The resulting five-step global mechanism can be used with CFD codes to predict CO, CO_2, and NO emission directly. Results of the global mechanism optimization method are shown for a pressure of 1 atmosphere and for pressures of interest for gas turbine engines. CFD results showing predicted CO and NO emissions using the five-step global mechanism developed for elevated pressures are presented and compared to measured data.

Introduction

Due to numerical limitations, most computational fluid dynamics (CFD) codes that operate on personal workstation platforms and which consider two and three-dimensional geometries with turbulence-chemistry interactions are presently restricted to one to five-step global mechanisms to model the oxidation of the hydrocarbon fuel. Traditionally in a three-step global oxidation mechanism, the first reaction involves the oxidation of the hydrocarbon fuel (e.g., CH_4) directly to CO and H_2O, and the remaining two reactions involve the forward and reverse of the oxidation of CO to CO_2. The only species used in the global mechanism are the fuel, O_2, CO, CO_2, and H_2O. In a five-step global oxidation mechanism for hydrocarbon oxidation, H_2 is added to the list of reacting species. The fuel is oxidized to CO and H_2, and the remaining four reactions concern the forward and reverse of the water-gas shift reaction (i.e., $CO + H_2O \Leftrightarrow CO_2 + H_2$) and the oxidation of H_2 to H_2O.

A number of investigators including Dryer and Glassman (1973), referred to hereafter as DG, DuPont, Pourkashanian, and Williams (1993), referred to hereafter as DPW, Westbrook and Dryer (1984), and Jones and Lindstedt (1988) have proposed global reaction mechanisms for hydrocarbon oxidation which were developed to maximize agreement with experimentally obtained chemical information such as flame speed or species concentrations from a particular burner design. The specific chemical reactions and rate constants, which comprise these global mechanisms, are shown in Table 1. However, it is shown in Nicol (1995) that many of these existing global reaction mechanisms cannot accurately predict species concentrations under normal gas turbine operating conditions.

The three and five-step global mechanisms listed in Table 1 involve only fuel oxidation, and CO, CO_2, H_2O, and H_2 formation (H_2 formation in the five-step mechanism only); that is, they do not allow for the prediction of NO directly from the kinetic mechanism. In Nicol (1995), the concept of an NO post-processor is developed whereby a suitable species already present in the global mechanism is linked to local NO formation rates, and the CFD solver is used to solve the NO transport equations for the two or three-dimensional computational field. It was proposed that of the global mechanism species (i.e., CO, CO_2, H_2O, and O_2 in the three-step mechanism, plus H_2 in the five-step mechanism), the CO concentration is the most indicative of the free-radical chemistry, and thus, the best suited for linking to the local NO formation rate. A multi-dimensional table look-up approach, wherein a numerical look-up table containing NO formation rate data as a function of CO concentration and local fuel-air equivalence ratio is suggested as an effective means for integrating the post-processor into the CFD code. In this study, in order to avoid the added complexity and cumbersome nature of the look-up table approach, an initial attempt is made to provide a two-step global mechanism for NO formation which can be used in conjunction with a three-step global hydrocarbon oxidation mechanism (resulting in a five-step global mechanism) in order to predict NO emissions under typical gas turbine operating conditions. As the simpler and more straight forward approach of the two-step NO formation global mechanism is shown to be successful herein, the look-up table approach is not addressed in this study.

NO is known to form via three chemical pathways, termed the prompt, nitrous oxide, and Zeldovich pathways. Recent full chemical mechanisms such as the GRI 2.11 mechanism (1995) also include a NO formation pathway via NNH. It is shown in

---

Contributed by the International Gas Turbine Institute and presented at the International Gas Turbine and Aeroengine Congress and Exhibition, Stockholm, Sweden, June 2–5, 1998. Manuscript received by the ASME Headquarters April 1, 1998. Paper No. 98-GT-185. Associate Technical Editor: R. Kielb.

Table 1 A review of existing global kinetic mechanism rate expressions for methane-air combustion (units are kmoles, cubic meters, seconds, and Kelvin)

Dryer and Glassman (1973)	
$CH_4 + \frac{3}{2}O_2 \Rightarrow CO + 2H_2O$	$R = 10^{11.70} \exp\left(\frac{-24358}{T}\right)[CH_4]^{0.7}[O_2]^{0.8}$
$CO + \frac{1}{2}O_2 \Rightarrow CO_2$	$R = 10^{12.35} \exp\left(\frac{-20131}{T}\right)[CO]^{1.0}[H_2O]^{0.5}[O_2]^{0.25}$
$CO_2 \Rightarrow CO + \frac{1}{2}O_2$	$R = 10^{12.50} \exp\left(\frac{-21641}{T}\right)[CO]^{1.0}[H_2O]^{0.5}[O_2]^{0.25}$
DuPont, Pourkashanian and Williams (1993)	
$CH_4 + \frac{3}{2}O_2 \Rightarrow CO + 2H_2O$	$R = 10^{10.0} \exp\left(\frac{-12019}{T}\right)[CH_4]^{1.0}[O_2]^{1.0}$
$CO + \frac{1}{2}O_2 \Rightarrow CO_2$	$R = 10^{10.0} \exp\left(\frac{-12019}{T}\right)[CO]^{1.0}[O_2]^{1.0}$
Jones and Lindstedt (1988)	
$CH_4 + \frac{1}{2}O_2 \Rightarrow CO + 2H_2$	$R = 10^{8.48} \exp\left(\frac{-15098}{T}\right)[CH_4]^{0.5}[O_2]^{1.25}$
$CO + H_2O \Leftrightarrow CO_2 + H_2$	$R = 10^{9.44} \exp\left(\frac{-10065}{T}\right)[CO]^{1.0}[H_2O]^{1.0}$ Reverse rate calculated from equilibrium
$H_2 + \frac{1}{2}O_2 \Leftrightarrow H_2O$	$R = 10^{15.83} T^{-1.0} \exp\left(\frac{-30131}{T}\right)[H_2]^{0.25}[O_2]^{1.5}$ Reverse rate calculated from equilibrium
Westbrook and Dryer (1984)	
$CH_4 + \frac{3}{2}O_2 \Rightarrow CO + 2H_2O$	$R = 10^{9.45} \exp\left(\frac{-24358}{T}\right)[CH_4]^{-0.3}[O_2]^{1.3}$
$CO + \frac{1}{2}O_2 \Rightarrow CO_2$	$R = 10^{12.35} \exp\left(\frac{-20131}{T}\right)[CO]^{1.0}[H_2O]^{0.5}[O_2]^{0.25}$
$CO_2 \Rightarrow CO + \frac{1}{2}O_2$	$R = 10^{8.70} \exp\left(\frac{-20131}{T}\right)[CO_2]^{1.0}$

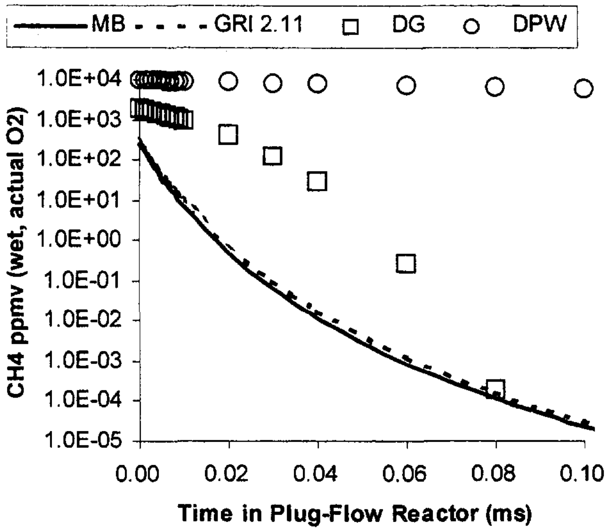

Fig. 1 Comparison of predicted methane concentrations using CRM in the PSR (0.5 ms residence time) + PFR configuration at a pressure of 1 atm, a 650 K inlet temperature, and a 0.55 fuel-air equivalence ratio. Results are shown for the full Miller and Bowman (MB) and the GRI 2.11 mechanisms, the Dryer and Glassman (DG), and the DuPont, Pourkashanian, and Williams (DPW) global mechanisms.

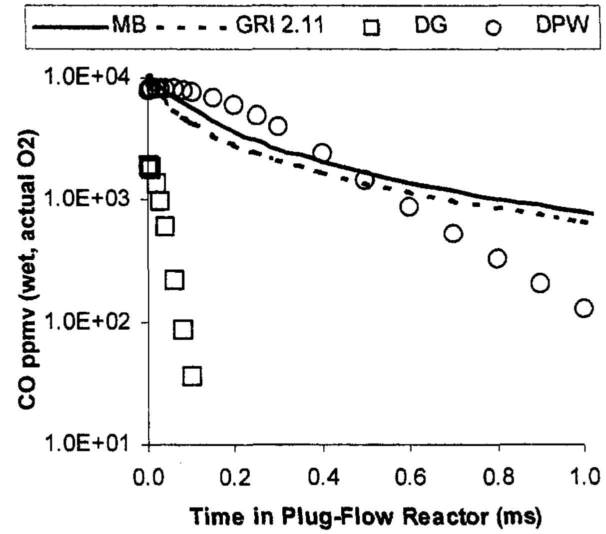

Fig. 2 Comparison of predicted carbon monoxide concentrations using CRM in the PSR (0.5 ms residence time) + PFR configuration at a pressure of 1 atm, 650 K inlet temperature, and 0.55 fuel-air equivalence ratio. Results are shown for the full Miller and Bowman (MB) and GRI 2.11 mechanisms, and the Dryer and Glassman (DG), and the DuPont, Pourkashanian and Williams (DPW) global mechanisms.

Nicol (1995) that the relative contribution of each pathway to total NO formation differs in the flame and post-flame zones of gas turbine combustion. In the flame zone, all pathways make non-negligible contributions to overall NO production; however, in the post-flame zone at long residence times, thermal NO (i.e., the Zeldovich pathway with an equilibrium O-atom concentration) is the predominant source of NO formation. The two-step global NO formation mechanism proposed herein makes use of the knowledge of the different NO formation pathway contributions in the flame and post-flame zones. Nonthermally formed NO (i.e., NO formed via prompt, nitrous oxide, NNH, and nonequilibrium Zeldovich pathways) is accounted for by one reaction step and thermal NO is accounted for by the second. The nonthermally formed NO reaction step involves a strong dependence on free-radical chemistry; i.e., on O-atom, H-atom, and OH-radical concentrations. Knowing that the CO concentration is indicative of the free-radical chemistry provides the means for incorporating nonthermal NO formation into the global mechanism. That is, the global nonthermal NO formation rate is expressed directly in terms of the CO concentration.

As a means for developing global reaction mechanisms and for understanding chemical kinetics, chemical reactor modeling (CRM) consisting of a combination of perfectly stirred reactors (PSRs) and plug flow reactors (PFRs) is shown in Nicol (1995) to be an effective numerical tool. Additionally, CRM is shown to give good agreement with measured CO and NO emissions in laboratory Jet-Stirred reactors (Nicol et al., 1995; Steele et al., 1995, 1997). In CRM, the PSR is an idealization of a back-mixed reactor with high-intensity turbulent mixing and is used to model the combustion flame zone (i.e., the zone of high free-radical concentrations). The PFR represents quasi-one-dimensional streamline flow with finite rate chemistry and is used to model the post-flame zone of combustion. CRM is used in this study as the primary numerical means for developing and assessing the accuracy of the global mechanisms.

Table 2 Baseline five-step global kinetic mechanism for methane oxidation and NO formation

$CH_4 + \frac{3}{2}O_2 \Rightarrow CO + 2H_2O$	$R_1 = 10^{A1}[CH_4]^{B1}[O_2]^{C1}\exp\left(^{-D_1}/_T\right)$
$CO + \frac{1}{2}O_2 \Rightarrow CO_2$	$R_2 = 10^{A2}[CO]^{B2}[O_2]^{C2}\exp\left(^{-D_2}/_T\right)$
$CO_2 \Rightarrow CO + \frac{1}{2}O_2$	$R_3 = 10^{A3}[CO_2]^{B3}\exp\left(^{-D_3}/_T\right)$
$N_2 + O_2 \Rightarrow 2NO$	$R_4 = 10^{A4}[CO]^{B4}[O_2]^{C4}\exp\left(^{-D_4}/_T\right)$
$N_2 + O_2 \Rightarrow 2NO$	$R_5 = 10^{A5}T^{-0.5}[N_2][O_2]^{0.5}\exp\left(^{-D_5}/_T\right)$

R_i is the forward reaction rate in kmole/m^3-sec,

10^{A_i} is the pre-exponential factor,

[X] is the species concentration in kmole/m^3, and
D_i is the activation temperature in Kelvin.

Table 3 One atmosphere five-step global kinetic mechanism for methane oxidation and NO formation. Mechanism is valid for a pressure of 1 atm, an inlet temperature of 650 K, and a fuel-air equivalence ratio range of 0.45 to 0.70 (units are kmoles, cubic meters, seconds, and Kelvin).

$CH_4 + \frac{3}{2}O_2 \Rightarrow CO + 2H_2O$	$R_1 = 10^{15.220}[CH_4]^{1.460}[O_2]^{0.5217}\exp\left(-20643/T\right)$
$CO + \frac{1}{2}O_2 \Rightarrow CO_2$	$R_2 = 10^{14.902}[CO]^{1.6904}[O_2]^{1.570}\exp\left(-11613/T\right)$
$CO_2 \Rightarrow CO + \frac{1}{2}O_2$	$R_3 = 10^{14.349}[CO_2]^{1.0}\exp\left(-62281/T\right)$
$N_2 + O_2 \Rightarrow 2NO$	$R_4 = 10^{23.946}[CO]^{0.7211}[O_2]^{4.0111}\exp\left(-53369/T\right)$
$N_2 + O_2 \Rightarrow 2NO$	$R_5 = 10^{14.967}T^{-0.5}[N_2][O_2]^{0.5}\exp\left(-68899/T\right)$

Two sets of operating conditions are used in this study. One set consists of a pressure of 1 atm; the other set consists of an elevated pressure of interest for lean-premixed gas turbine engines. Both sets consist of an inlet temperature of 650 K and a fuel-air equivalence ratio range of 0.45 to 0.70. The atmospheric pressure operating conditions are used herein for the following two purposes: (1) to provide the test conditions at which the global mechanisms are compared and evaluated against the full chemical kinetic mechanisms of Miller and Bowman (1989), hereafter referred to as MB, and the GRI 2.11 mechanism (1995), and (2) to provide conditions at which an example application of the global mechanism optimization method can be shown. The elevated pressure operating conditions are used to develop an optimized global mechanism (not shown in detail herein) that is used in conjunction with a CFD code to predict CO and NO emission from an industrial gas turbine engine.

It should be noted that it is not the intent of this work to test the goodness of the full chemical mechanisms or to compare one full mechanism against another. The full mechanisms have been validated against experimental measurements during their development and are presently widely used and recognized. In this work the full mechanisms are accepted as offering a valid starting point for the development and testing of the optimized global mechanisms.

Comparison of Existing Global Mechanisms to Full Kinetic Mechanisms

It is shown in Nicol (1995) that all of the proposed global mechanisms mentioned above are able to predict CO_2, O_2, and H_2O to within 15 percent (relative) accuracy; however, only the DG and the DPW mechanisms are able to approximate the predicted methane consumption rate to the correct order of magnitude under typical gas turbine operating conditions. The ability of the DG and the DPW mechanisms to accurately predict species under the test conditions of this study (i.e., 1.0 atm pressure, 650 K inlet temperature, 0.55 nominal mean fuel-air equivalence ratio) is determined using CRM in a PSR (with a 0.5 ms residence time) followed by a PFR configuration. The results of this analysis comparing the DG and DPW global mechanisms with the full chemical MB and GRI mechanisms are shown in Fig. 1 for the methane concentration and in Fig. 2 for the carbon monoxide concentration. In each of these figures, the leftmost point (i.e., shortest time) corresponds to the conditions existing at the PSR exit. All other points shown in the figures correspond to the conditions existing in the PFR section used to model the post-flame zone. From Fig. 1 it may be seen that the DG mechanism underpredicts the methane consumption rate in the PSR and in the early sections of the PFR; however, it overpredicts the methane consumption rate in the later stages of the PFR. The DPW mechanism predicts a CH_4 consumption rate that is uniformly too slow in both the PSR and the PFR sections. From Fig. 2 it may be seen that the DPW mechanism predicts the carbon monoxide consumption rate satisfactorily in the PSR and in the earliest sections of the PFR; however, it overpredicts the CO consumption rate in the later stages of the PFR. The DG mechanism predicts a CO consumption rate that is uniformly too fast in both the PSR and the PFR sections. The fact that in the later stages of the PFR, both mechanisms overpredict the conversion of CO to CO_2 may be explained by noting the following. In the case of the DPW mechanism, this overprediction may be attributed to the absence of the reaction, $CO_2 \Rightarrow CO + 1/2O_2$, which will act to slow the overall net CO consumption rate. Although the DG mechanism includes the above reaction, the rates for this reaction do not accurately reflect CO-CO_2 equilibrium behavior at the conditions examined, and hence, the DG mechanism also predicts an overall CO consumption rate which is too fast.

Global Mechanism "Tuning" Procedure

The goal of the global mechanism "tuning" procedure is to make the relevant species concentrations found using the global mechanism closely agree with those found using the full mechanism at the specified input conditions. The fundamental principles of the global mechanism "tuning" procedure are given in detail in Nicol (1995). In short, the "tuning" procedure involves adjusting ("tuning") the reaction rate parameters of the global mechanism (i.e., pre-exponential factor, activation temperature, and species exponents). The magnitudes of the adjustments are determined by running a chemical reactor model in an appropriate configuration at the desired operating conditions with a full kinetic mechanism to find species net formation rates as a function of reactor residence time, temperature, fuel-air equivalence ratio, etc. Chemical reactor modeling is selected as the means for generating the species formation rate data as it allows for analysis using a full kinetic mechanism while preserving numerical and computational tractability. A regression analysis is performed on the resulting species formation rate data whereby the global rate input parameters are adjusted such that the match between the species formation rates found using the global and full mechanisms is optimized. As shown below, the global reaction rate expression is of the form, $R_i = 10^{A_i}[X]^{B_i}[Y]^{C_i}\exp(-D_i/T)$, and hence, the natural logarithm of the reaction rate is given by, $\ln(R_i) = A_i \ln(10) + B_i \ln([X]) + C_i \ln([Y]) - D_i/T$. Thus, by working with the logarithm of the rate instead of with the rate directly, the regression analysis used to determine the optimized global input parameters can be simplified to a linear least-squares data fit.

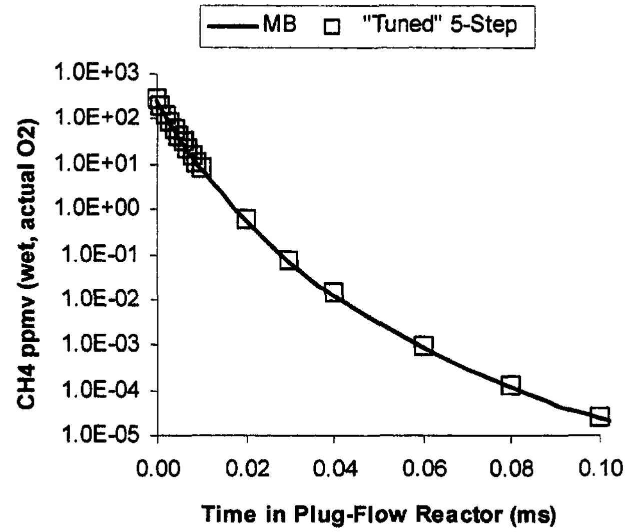

Fig. 3 Comparison of predicted methane concentrations using CRM in the PSR (0.5 ms residence time) + PFR configuration at a pressure of 1 atm, a 650 K inlet temperature, and a 0.55 fuel-air equivalence ratio. Results are shown for the full Miller and Bowman (MB) and the "tuned" five-step global mechanism.

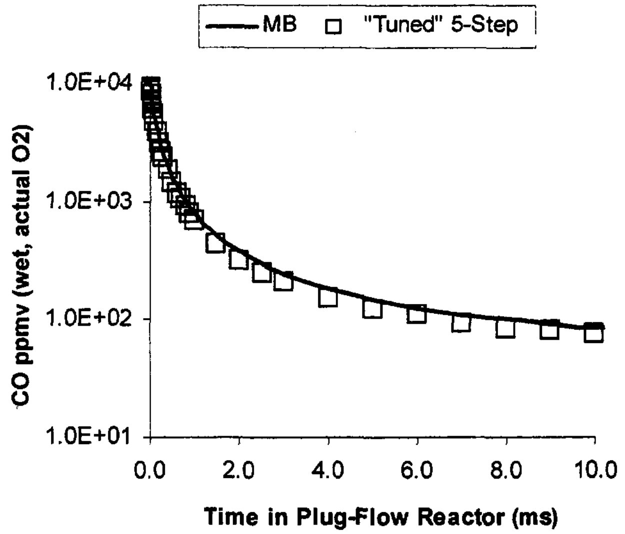

Fig. 4 Comparison of predicted carbon monoxide concentrations using CRM in the PSR (0.5 ms residence time) + PFR configuration at a pressure of 1 atm, a 650 K inlet temperature, and a 0.55 fuel-air equivalence ratio. Results are shown for the full Miller and Bowman (MB) and the "tuned" five-step global mechanism.

The global mechanism "tuning" procedure detailed in Nicol (1995) involves selecting a chemical reactor arrangement consisting of an adiabatic PSR followed by an adiabatic PFR for determining the species formation rates. It is shown in that work that although the "tuned" mechanism developed using the CRM configuration agrees well (less than 15 percent relative error) with the full MB mechanism, the activation temperatures of the "tuned" global mechanism are higher than those listed in Table 1. While not presenting any difficulties in chemical reactor modeling, this increase in activation temperature can become a source of difficulty in CFD applications due to the fact that the range of temperatures encountered in CFD is much wider than with the adiabatic PSR + PFR CRM configuration. For example during preliminary testing of the global mechanism using CFD, combustion failed to occur if the activation temperature of the first global reaction, $CH_4 + 3/2O_2 \Rightarrow CO + 2H_2O$, exceeded 25000 K.

In an effort to broaden the temperature range over which the regression analysis is performed, and, hence, to lessen the global rate expression's sensitivity to temperature and to reduce the reaction rate activation temperatures, a chemical reactor configuration consisting of a single PSR operated nonadiabatically (i.e., a PSR run at an assigned temperature) is chosen for use in this study. The range of assigned temperatures varies from "partial" oxidation of the fuel (corresponding to the consumption of approximately 75 percent (by mole) of the fuel in the PSR) to the adiabatic equilibrium flame temperature. Selection of a nonadiabatic PSR permits the species formation rate data to be generated over a significantly wider temperature range than if an adiabatic PSR is selected. That is, the maximum temperature range for the nonadiabatic PSR is approximately 600 K; whereas, the adiabatic PSR temperature range, confined between blowout of the PSR and equilibrium, is generally less than about 100 K for the conditions used in this study. Additionally, as the global mechanisms developed herein are to be used in CFD applications in which the temperature covers the entire range from inlet to adiabatic equilibrium, the choice of a nonadiabatic PSR should ensure a broader applicable temperature range for the global mechanism fit parameters.

As detailed in Nicol (1995), the global mechanism for methane to CO_2 oxidation found to yield the closest agreement with full kinetic mechanisms under typical gas turbine operating conditions involves the first three reactions and general rate expressions listed in Table 2. The two-step global NO formation mechanism consisting of reactions 4 and 5 is proposed herein to approximate full mechanism NO formation rates. The fourth reaction accounts for NO formation via the nonthermal pathways, while the fifth reaction accounts for thermally formed NO. Thus, a five-step global mechanism of the form shown in Table 2 is used as the starting point for optimization in this study.

The net production/destruction rate for each species in the global mechanism is found in terms of an algebraic sum of the R_i's listed above. That is,

$$\frac{d[CH_4]}{dt} = -R_1, \quad \frac{d[CO]}{dt} = R_1 + R_3 - R_2,$$

$$\frac{d[CO_2]}{dt} = R_2 - R_3, \quad \frac{d[NO]}{dt} = 2R_4 + 2R_5$$

One Atmosphere Five-Step Global Mechanism Results

The matrix of operating conditions used in this study to provide the data for the regression/optimization analysis of the global rate input parameters is as follows: pressure of 1 atm, inlet temperature of 650 K, fuel-air equivalence ratio range of 0.45 to 0.70, assigned PSR residence time range of incipient extinction (nominally 0.055 to 0.23 ms) to 5.0 ms, and assigned PSR temperature range of about 1250 K to adiabatic equilibrium (nominally 1665 to 2090 K for the stated fuel-air equivalence ratio range).

The five-step global mechanism resulting from the regression/optimization analysis of the MB mechanism data is shown in Table 3.

Figures 3, 4, and 5 show a comparison of the "tuned" global mechanism with the full MB mechanism for CH_4, CO, and NO, respectively. Chemical reactor modeling consisting of a PSR (with a 0.5 ms residence time) followed by a PFR configuration and using the nominal design operating conditions of this study (i.e., 1.0 atm pressure, 650 K inlet temperature, 0.55 fuel-air equivalence ratio) is used to generate the species comparisons shown in these figures. At these operating conditions at the shortest times, NO formation occurs mainly via nonthermal pathways; however, as time increases the amount of thermal NO formed also increases. In Figs. 3 through 5, the leftmost

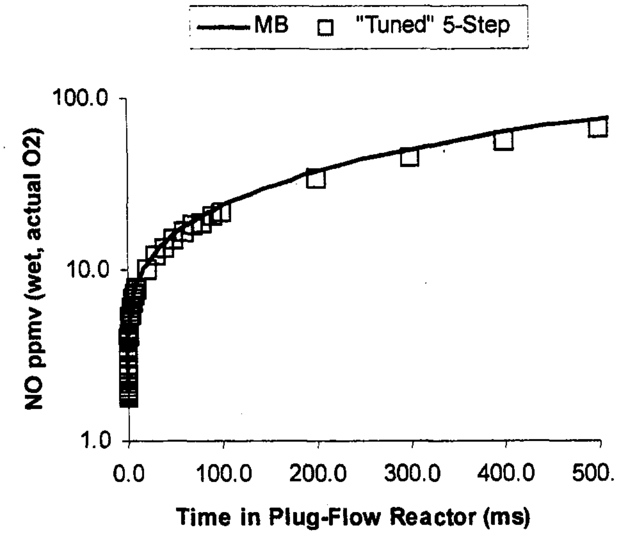

Fig. 5 Comparison of predicted nitric oxide concentrations using CRM in the PSR (0.5 ms residence time) + PFR configuration at a pressure of 1 atm, a 650 K inlet temperature, and a 0.55 fuel-air equivalence ratio. Results are shown for the full Miller and Bowman (MB) and the "tuned" five-step global mechanism.

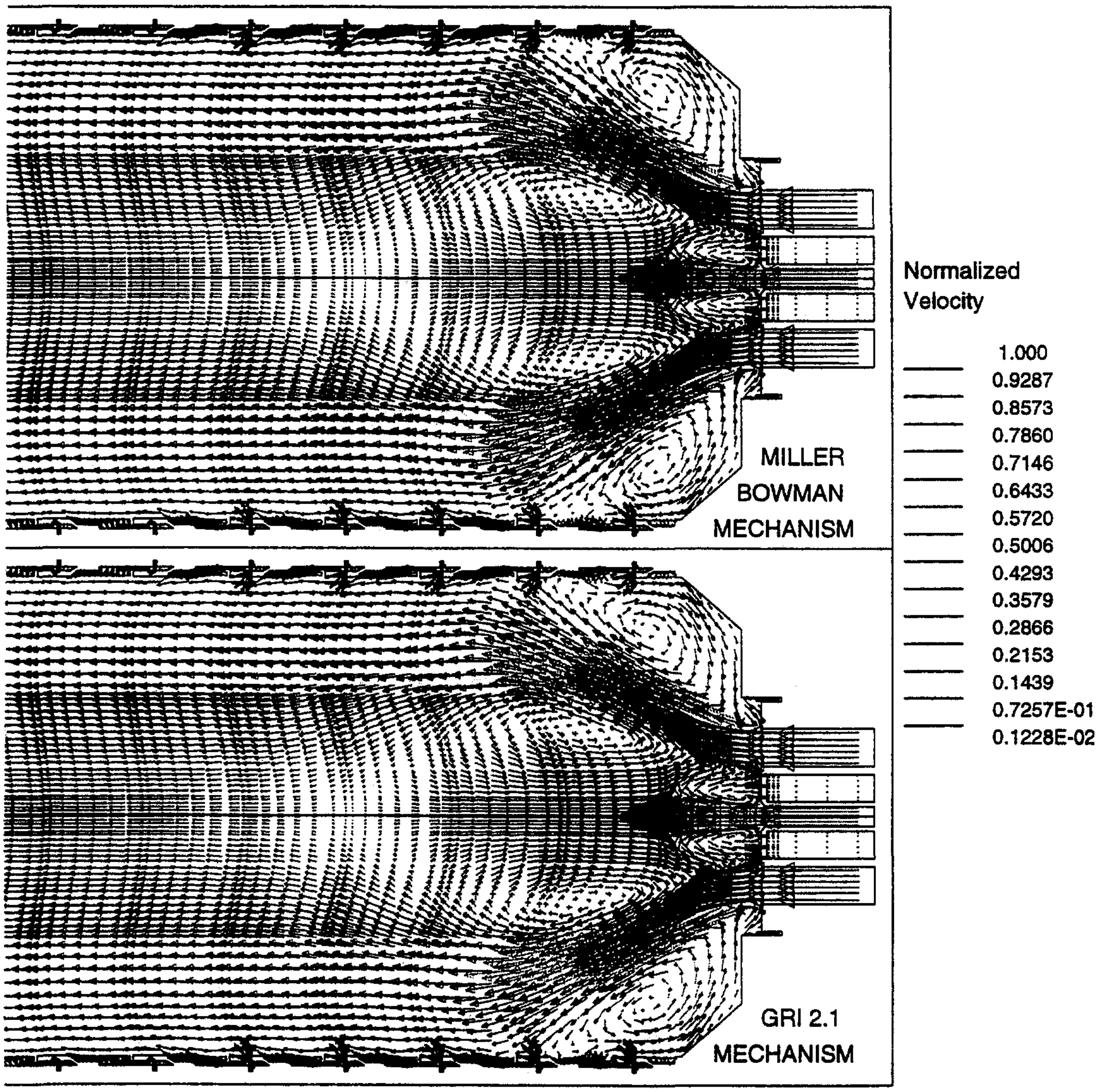

Fig. 6 Predicted velocity field using CFD modeling of a commercial lean-premixed gas turbine combustor using the "tuned" five-step global mechanisms. Results using the global mechanism "tuned" to the Miller and Bowman mechanism are shown top; results using the global mechanism "tuned" to the GRI 2.11 mechanism are shown bottom. CFD simulation at a pressure of 10 atm, an inlet temperature of 650 K, and a premixer mean fuel-air equivalence ratio of 0.6.

point (i.e., shortest time) corresponds to the conditions existing at the PSR exit. All other points shown in the figures correspond to the conditions existing in the PFR section used to model the post-flame zone. From these figures, it can be seen that the predicted methane, carbon monoxide, and NO species concentrations of the "tuned" mechanism closely agree with the full mechanism values for both the flame and post-flame zones.

Although a comparison of the "tuned" and full mechanism is shown for only one particular operating condition, the "tuned" mechanism has been verified over the entire range of inlet operating conditions (i.e., pressure of 1 atm, inlet temperature of 650 K, fuel-air equivalence ratio range of 0.45 to 0.70). The maximum difference between predicted "tuned" and full mechanism species concentrations observed is approximately 20 percent and the difference is generally less than 5 percent for all species in the global mechanism.

Elevated Pressure Five-Step Global Mechanism Results

The "tuning" procedure detailed in the preceding section is used to develop two five-step global mechanisms at nominal lean-premixed gas turbine operating conditions (i.e., elevated pressure, 650 K inlet temperature, 0.45 to 0.70 nominal mean fuel-air equivalence ratio). One global mechanism is based on the Miller and Bowman (1989) mechanism and the other is based on the GRI 2.11 mechanism. The numerical values of the "tuned" reaction rate parameters of the elevated pressure global mechanisms are not listed herein due to proprietary constraints. However, the agreement between the elevated pressure global mechanisms and the full mechanisms on which they are based is comparable to that shown for the 1 atm global mechanism. Over the range of design conditions, the maximum difference between the predicted "tuned" global and full mechanisms species concentrations observed is approximately 20 percent and the difference is generally less than 5 percent for all species in the global mechanism.

An industrial lean-premixed gas turbine engine combustor is modeled herein using the "tuned" elevated pressure five-step global mechanisms in conjunction with a two-dimensional axisymmetric CFD code (Gosman, 1996) with 3515 computational cells. In this study, this combustor is configured such that perfectly premixed fuel and air enter the combustor through the main inlet port, but only air enters the combustor through the pilot port (i.e., there is no fuel in the pilot). Additional air enters the combustor through liner cooling ports along its length.

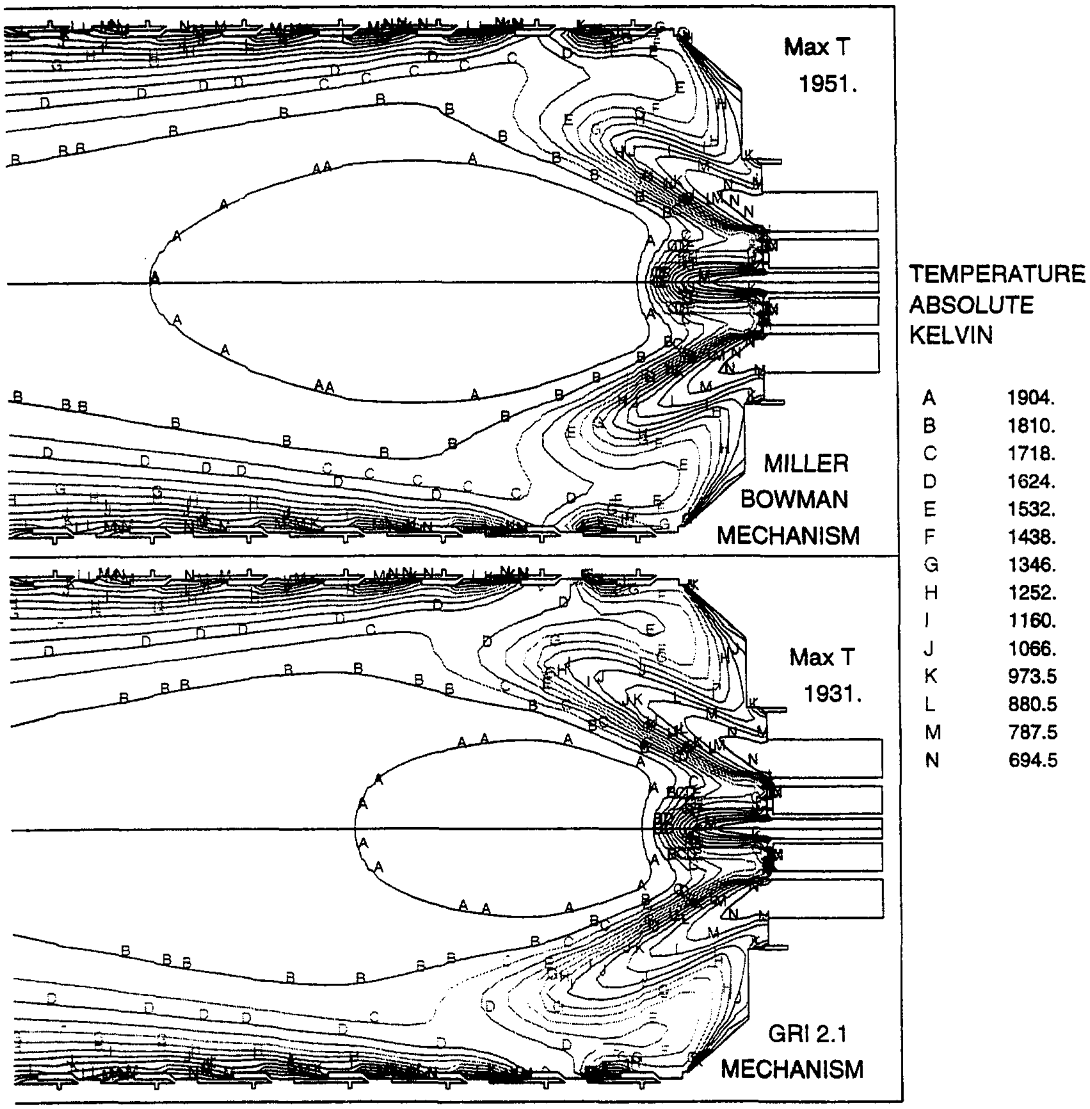

Fig. 7 Predicted temperature field using CFD modeling of a commercial lean-premixed gas turbine combustor using the "tuned" five-step global mechanisms. Results using the global mechanism "tuned" to the Miller and Bowman mechanism are shown top; results using the global mechanism "tuned" to the GRI 2.11 mechanism are shown bottom. CFD simulation at a pressure of 10 atm, an inlet temperature of 650 K, and a premixer mean fuel-air equivalence ratio of 0.6.

The boundaries for which boundary conditions were specified include the swirling uniform premixed fuel-air inlet, the liner cooling air inlet, the dome cooling air inlet, the pilot air inlet without fuel, and the fuel nozzle cooling air inlet. The two standard equation k-epsilon turbulence model is used and the following dependent variables are solved for u, v, and w velocities, pressure, temperature, kinetic energy, dissipation of kinetic energy, and species mass fractions. The nominal operating conditions of the combustor consist of a pressure of 10 atm, an inlet temperature of 650 K, and a nominal fuel-air equivalence ratio of 0.6 (corresponding to an air flow rate of 1.2 kg/sec and a fuel flow rate of 70 kg/hr). The results of the CFD modeling are shown in Figs. 6 through 9. Figures 6 and 7, respectively, present the predicted fluid velocity and temperature profiles existing in the combustor. Figures 8 and 9, respectively, show the carbon monoxide and nitric oxide mass fraction contours within the combustor. In each figure, the upper plot shows the results of the CFD modeling using the five-step global mechanism based on the Miller and Bowman mechanism, and the lower plot shows the results of the CFD modeling using the global mechanism based on the GRI 2.11 mechanism. The actual local reaction rate used in the CFD modeling is the minimum of that predicted by the eddy break-up model (fluid mixing controlled) and by the global mechanism (chemical controlled).

The normalized velocity profiles shown in Fig. 6 may be used to visualize the flow field within the combustor. The velocity profiles indicate that two large recirculation zones exist in the combustor; one occurring along the centerline, the other occurring in the dome region. An additional smaller recirculation zone is created between the main and pilot ports. The large dome recirculation zone is capable of convecting liner cooling air into the flame zone, thus affecting the primary combustion stoichiometry. Differences in the size of this dome recirculation zone can be seen between the MB and the GRI 2.11 results. The MB results indicate a smaller dome recirculation zone than is shown in the GRI 2.11 results.

In Figure 7, this difference in dome recirculation zone size can be seen to have a two-fold effect on the predicted temperature behavior in the combustor. First, the peak temperature predicted by the MB global mechanism (with the smaller dome recirculation zone, and hence less liner cooling air influence on combustion) is 1951 K compared to a peak temperature of 1931 K predicted by the GRI global mechanism (with the larger dome recirculation zone). Second, the volume of the combustor

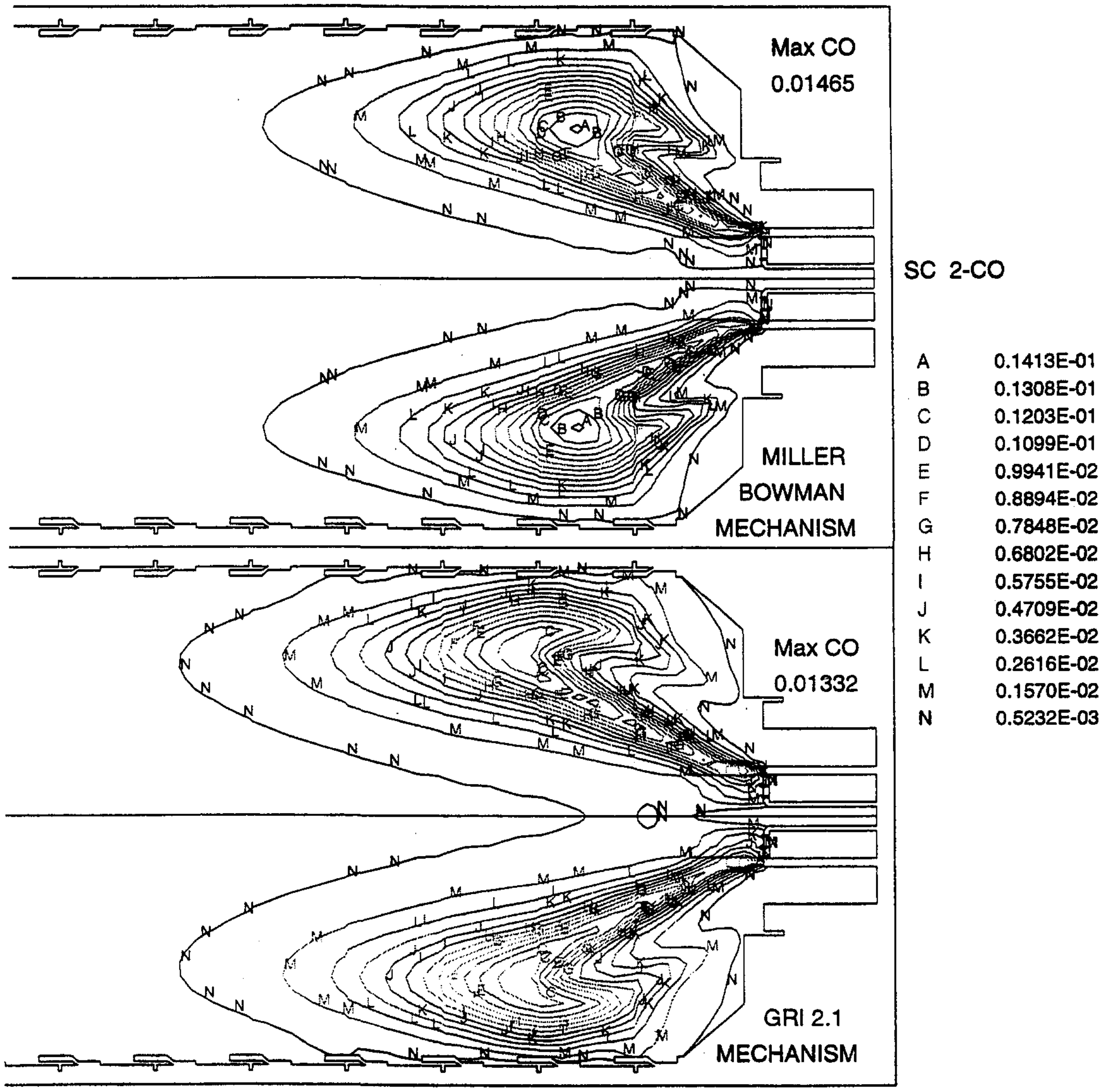

Fig. 8 Predicted CO mass fractions using CFD modeling of a commercial lean-premixed gas turbine combustor using the "tuned" five-step global mechanisms. Results using the global mechanism "tuned" to the Miller and Bowman mechanism are shown top; results using the global mechanism "tuned" to the GRI 2.11 mechanism are shown bottom. CFD simulation at a pressure of 10 atm, an inlet temperature of 650 K, and a premixer mean fuel-air equivalence ratio of 0.6.

encountering elevated temperatures is significantly larger in the MB results than in the GRI results.

The difference in dome recirculation zone size can also be seen to have an effect on the CO and NO mass fractions predicted by the global mechanisms "tuned" to the MB and to the GRI 2.11 mechanisms. As shown in Fig. 8, the MB global mechanism predicts a more intense flame zone as indicated by the more compact region of CO and by the greater peak CO mass fraction (0.01465 for the MB global mechanism versus 0.01332 for the GRI global mechanism). The GRI global mechanism, on the other hand, predicts a somewhat less compact flame which allows for greater liner air quenching of the CO and hence yields a slightly greater exit plane CO emission (35 ppm (dry, 15 percent O_2) for the GRI global mechanism versus 10 ppm (dry, 15 percent O_2) for the MB global mechanism). The measured exit plane CO emission for the combustor operating at the nominal test conditions is 11 ppm (dry, 15 percent O_2) (Mellor, 1996). Thus, the predicted CO emission, particularly that found using the MB global mechanism, is seen to agree well with the measured value.

From Fig. 9 *it can be seen that the more intense flame zone* predicted by the MB global mechanism also results in a greater peak NO mass fraction (9.7E-05 for the MB global mechanism versus 4.8E-05 for the GRI global mechanism). As the reaction rate for NO formation via nonthermal pathways (i.e., reaction 4) is proportional to the CO concentration, it is expected that the larger peak CO emissions and higher temperatures predicted by the MB global mechanism should produce correspondingly larger overall NO formation rates. For both mechanism results, the peak NO mass fraction occurs in the large centerline recirculation zone due to residence time effects. The highest NO formation rates occur in the regions just downstream of the highest CO values. In these regions, the combination of high temperature and high free-radical concentration (i.e., CO) is optimal for NO formation. The MB global mechanism also predicts a greater exit plane NO emission (19 ppm (dry, 15 percent O_2) for the MB global mechanism versus 9 ppm (dry, 15 percent O_2) for the GRI global mechanism). This factor of two difference in NO emission is also seen using the full MB and GRI 2.11 mechanisms with CRM at the lean-premixed combustor test conditions. The measured exit plane NO emission for the combustor operating at the nominal test pressure and inlet temperature is 32 ppm (dry, 15 percent O_2) for the test fuel-air equivalence ratio of 0.6 and 22 ppm (dry, 15 percent O_2) for a fuel-

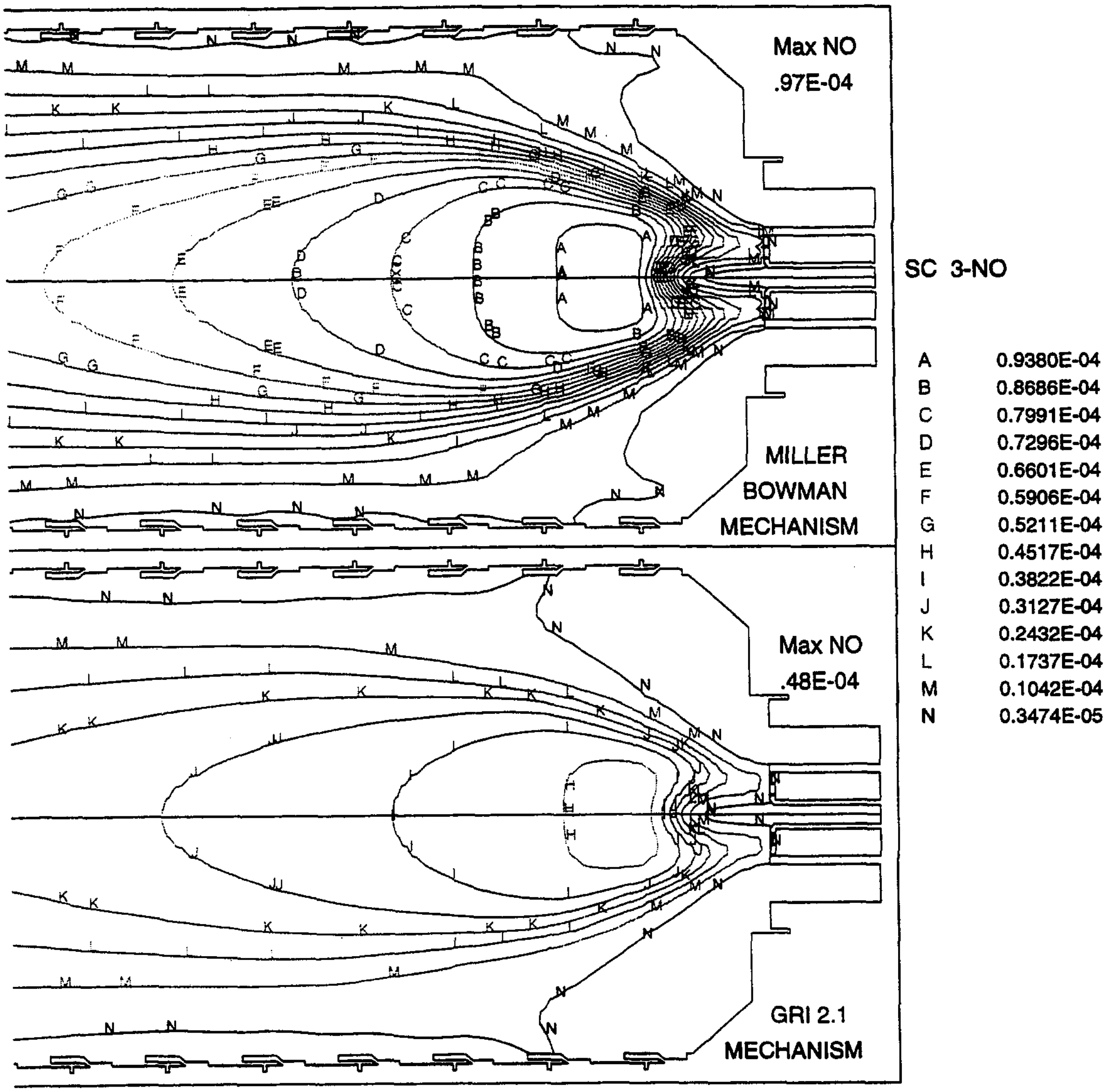

Fig. 9 Predicted NO mass fractions using CFD modeling of a commercial lean-premixed gas turbine combustor using the "tuned" five-step global mechanisms. Results using the global mechanism "tuned" to the Miller and Bowman mechanism are shown top; results using the global mechanism "tuned" to the GRI 2.11 mechanism are shown bottom. CFD simulation at a pressure of 10 atm, an inlet temperature of 650 K, and a premixer mean fuel-air equivalence ratio of 0.6.

air equivalence ratio of 0.57 (Mellor, 1996). The fact that the NO emission is underpredicted by the CFD-global mechanism model may be explained by considering that in the CFD model, the inlet fuel-air stream is assumed to be perfectly premixed (i.e., with no inlet unmixedness) while the measured NO emission occurs in a combustor with imperfect premixing. It is shown in Nicol et al. (1997) using CRM to simulate the combustor under current study that even a small degree of unmixedness in the inlet fuel-air stream results in a significant (e.g., greater than 100 percent) increase in predicted NO emission at the present test conditions.

Hamer and Roby (1997) and Mori (1998) have conducted further testing of the five-step global mechanisms. In both of these studies, the five-step global mechanisms are used with a commercial CFD code to model lean-premixed gas turbine engine combustion. Hamer and Roby use a two-dimensional axisymmetric code (STAR*CD) with a standard *k*-epsilon turbulence model and 12016 computational cells at a pressure of 10 atm and over a range fuel-air equivalence ratios (0.51 to 0.82). Comparison between integrated exit plane emission predictions and laboratory measurements is shown to give good agreement for both NO and CO over the applicable range of fuel-air equivalence ratios (i.e., 0.45 to 0.70). For example, using the elevated pressure GRI global mechanism at a fuel-air equivalence ratio of 0.63, Hamer and Roby report a predicted to measured emission ratio of 0.7 for NO and of 6.9 for CO. (Hamer and Roby attribute the discrepancy of the predicted CO emission primarily to quenching of the CO by liner cooling air at the wall.) Mori uses a three-dimensional code (FLUENT) with a standard *k*-epsilon turbulence model and 80000 computational cells. Mori indicates a predicted to measured emission ratio of 0.93 for NO and comparably good agreement for CO.

Model Improvements

By its zero-dimensional nature, chemical reactor modeling is unable to predict certain flame properties such as flame speeds and induction times. As these properties can play an important role in CFD modeling of gas turbine combustion, other numerical models could be used to further refine and improve the global mechanisms developed in this study, and to verify the robustness that the global mechanisms must have in order to cover the entire range of conditions experienced during combustion in a gas turbine engine. These numerical models include the laminar one-dimensional flame model (i.e., CHEMKIN), the finite-rate mixing model of Tonouchi and Pratt (1996), and possibly laminar two-dimensional CFD codes. In addition to providing such additional information as laminar flame speed, these models would allow for the testing of the global mechanisms over the entire temperature range from inlet to adiabatic equilibrium, and, hence, would provide a more rigorous environment for determining the general applicability of the global mechanisms developed herein. Furthermore, this may lead to reduction in the activation temperatures of the global rates.

The five-step global mechanisms for CH_4 oxidation with NO formation developed in this study are limited by their test conditions to a fuel-air equivalence ratio range of 0.45 to 0.70. Outside of this range, the global mechanism has not been fully validated, and, hence, it cannot be expected that it will continue to predict emissions satisfactorily at richer fuel-air equivalence ratios. Thus, this global mechanism will not, in all probability, be valid for examining the combustion conditions found in piloted lean-premixed combustion and for examining the effects of incomplete premixing in lean-premixed combustors. Alternate, more complex global mechanisms will need to be developed to accommodate the broader range of fuel-air equivalence ratios encountered in these situations.

The robustness and generality of the ''fine-tuning'' procedure used to generate the global mechanisms should be investigated further by examining other input design conditions. That is, different pressures and different inlet temperatures should be tested. If equally satisfactory results are obtained at these new conditions, the premise behind the global mechanism ''tuning'' procedure will be further strengthened and shown to be universally applicable.

Conclusions

Previously published global methane oxidation mechanisms are shown to have difficulty accurately predicting CH_4 and CO concentrations under typical lean-premixed combustion turbine operating conditions. In this work five-step global mechanisms, consisting of a three-step oxidation mechanism and a two-step mechanism for NO formation, are developed for lean-premixed combustion using a simple linear least-squares data fit optimization method for tuning the reaction rate parameters. Chemical reactor and, more importantly, CFD models can be easily adapted to incorporate the five-step global mechanisms. Using CRM, the five-step global mechanisms are shown to give good agreement with the full MB and GRI 2.11 chemical mechanisms. The maximum difference in species concentrations is approximately 20 percent, but the difference is generally less than 5 percent for all species in the global mechanism. The five-step global mechanisms are used with CFD to model an industrial lean-premixed gas turbine engine combustor. Results from this analysis indicate that the five-step global mechanisms successfully predict the measured CO and NO emissions. The ratio of predicted to measured emissions range from 0.91 (MB) to 3.18 (GRI) for CO and from 0.28 (GRI) to 0.60 (MB) for NO. Other researchers (Hamer and Roby, 1997; Mori, 1998) have also demonstrated the usefulness and applicability of the five-step global mechanisms for modeling lean-premixed gas turbine combustion.

References

Dryer, F. L., and Glassman, I., 1973, Proceedings, Fourteenth Symposium (International) on Combustion, The Combustion Institute, Pittsburgh, PA, p. 987.

DuPont, V., Pourkashanian, M., and Williams, A., 1993, ''Modeling of Process Heaters Fired by Natural Gas,'' *Journ. of the Inst. of Energy,* Vol. 66, p. 20.

Gosman, D., 1996, *STAR*CD Version 2.3 Users Manual,* Computational Dynamics, London, England.

GRI MECH 2.11, 1995, World Wide Web Site: ''http://www.me.berkeley.edu/gri_mech/''.

Hamer, A. J., and Roby, R. J., 1997, ''CFD Modeling of a Gas Turbine Combustor Using Reduced Chemical Kinetic Mechanisms,'' AIAA Paper No. 97-3242.

Jones, W. P., and Lindstedt, R. P., 1988, *Combust. and Flame,* Vol. 73, p. 233.

Mellor, A. M., ed., 1996, *NO_x and CO Emissions Models for Gas-Fired, Lean Premixed Combustion Turbines: Final Report,* Vanderbilt University, Nashville, TN.

Miller, J. A., and Bowman, C. T., 1987, ''Mechanism and Modeling of Nitrogen Chemistry in Combustion,'' *Prog. in Energy and Combust. Science,* Vol. 15, p. 287.

Mori, G., 1998, Personal Correspondence with Ansaldo Ricerche.

Nicol, D. G., 1995, ''A Chemical and Numerical Study of NO_x and Pollutant Formation in Low-Emissions Combustion,'' PhD dissertation, University of Washington, St. Louis, MO.

Nicol, D. G., Rutar, T., Martin, S. M., Malte, P. C., and Pratt, D. T., 1997, ''Chemical Reactor Modeling Applied to the Production of Pollutant Emission in LP Combustors,'' AIAA Paper No. 97-2711.

Nicol, D. G., Steele, R. C., Marinov, N. M., and Malte, P. C., 1995, ''The Importance of the Nitrous Oxide Pathway to NO_x in Lean-Premixed Combustion,'' ASME JOURNAL OF ENGINEERING FOR GAS TURBINES AND POWER, Vol. 117, p. 100.

Steele, R. C., Malte, P. C., Nicol, D. G., and Kramlich, J. C., 1995, *Combust. and Flame,* Vol. 100, p. 440.

Steele, R. C., Jarrett, A. C., Malte, P. C., Tonouchi, J. H., and Nicol, D. G., 1997, ASME JOURNAL OF ENGINEERING FOR GAS TURBINES AND POWER, Vol. 119, p. 102.

Tonouchi, J. H., 1996, ''Macromixing and Micromixing in Lean Premixed Combustion,'' PhD dissertation, University of Washington, St. Louis, MO.

Westbrook, C. K. and Dryer, F. L., 1984, ''Chemical Kinetic Modeling of Hydrocarbon Combustion,'' *Prog. in Energy and Combust. Science,* Vol. 10, p. 1.

J. M. Cohen

N. M. Rey

C. A. Jacobson

T. J. Anderson

United Technologies Research Center,
411 Silver Lane, MS 129-19,
East Hartford, CT 06108

Active Control of Combustion Instability in a Liquid-Fueled Low-NOx Combustor

A practical active control system for the mitigation of combustion instability has been designed and demonstrated in a lean, premixed, single-nozzle combustor at realistic engine operating conditions. A full-scale engine fuel nozzle was modified to incorporate a simple fuel flow actuator. Results indicate that the system was capable of reducing pressure fluctuations by 82 percent (15 dB or 5.6×) while maintaining or reducing NO_x and CO emissions levels.

Introduction

Emphasis on reducing the levels of pollutants created by gas turbine combustors has led to the development of lean, premixed combustor designs, especially for industrial applications. Premixing large amounts of air with the fuel prior to its injection into the combustor greatly reduces peak temperatures within the combustor and leads to lower NO_x emissions. Premixed combustors are often susceptible to thermoacoustic combustion instabilities, which can lead to large pressure oscillations in the combustor. These pressure oscillations result in increased noise and decreased durability due to vibration and flame motion.

In a DARPA (Defense Advanced Research Projects Agency) funded program, United Technologies Research Center (UTRC) investigated the feasibility of attenuating combustion instability using active control techniques. Because of DARPA's interest in marine applications (which typically use liquid fuel), the initial focus of this research was on a liquid-fueled low-NO_x combustor. This combustor exhibited a large-amplitude ($p'/p \sim 10$ percent) instability at a frequency of approximately 200 Hz. The goal of the research was to develop a practical active control system that would reduce the magnitude of the pressure fluctuations caused by the instability without adversely affecting NO_x levels. The effort stressed the practicality of the system and its ability to work with full-scale engine hardware at realistic operating conditions.

Experiment and Instrumentation

Experiments were conducted in a single-nozzle, flametube combustor (see Fig. 1). The nominal energy conversion rate of the single-nozzle combustor was 4 MW. The combustor used fuel nozzles designed for engine use and ran at engine operating conditions (pressure, temperature, and flow rate per injector). The fuel nozzles were designed to provide a high degree of fuel-air mixing and have been discussed thoroughly in previous papers (Snyder et al., 1994). Figure 2 shows a schematic of the fuel nozzle. Liquid fuel (No. 2 Diesel fuel) was injected through six axially oriented "spokes" protruding from the nozzle centerbody. High-pressure-drop spray tips were installed at the end of each spoke. The 15.2 cm diameter combustor test section was water cooled with a thermal barrier coating on the inner wall. A pilot fuel injector was located 2.5 cm. downstream of the combustor dump plane. A water-cooled orifice plate provided a choke point to simulate the acoustic boundary of the engine's turbine inlet guide vanes. Upstream of the combustor, the air flow rate was metered using a choked venturi.

After passing through the venturi, the air flow was split between the fuel nozzle and a bypass leg. The air that flowed through the bypass leg was injected at the downstream end of the combustor (upstream of the orifice plate), representing combustor dilution air.

The volumes and lengths of the combustor, diffuser region upstream of the fuel nozzle and bypass leg were set in order to reproduce the instability observed in a full-annular engine combustor.

An array of six gas-sampling probes, located upstream of the bypass air injection was used to measure NO_x and CO concentrations as well as combustor fuel/air ratio and combustion efficiency. Species concentrations are reported here in ppm on a 15 percent oxygen basis for a ganged probe arrangement. High-response data were collected at a rate of 5 kHz on a simultaneous sample-hold data acquisition system. The analog signals were low-pass filtered at 2 kHz to prevent aliasing. Fluctuating pressures were measured at two locations in the combustor using high-response pressure transducers. A photomultiplier tube (PMT) was used to measure the intensity of CH and CO radical emissions in the combustor. Light was collected using a fiber optic probe "looking" upstream through the orifice plate at the fuel nozzle (see Fig. 3). This orientation allowed the PMT to "see" the majority of the combustor. A 200 μm diameter quartz fiber with a numerical aperture of 0.37 viewed through a flange in the exit plenum and was directly coupled to the PMT. With a small amount of air purge, this probe required minimal access to the combustor and provided sufficient signal to monitor the emissions from the flame. A bandpass optical filter was installed to selectively admit only those wavelengths associated with CH and CO emissions (430 nm). The intensity of these emissions has been shown to linearly track the rate of heat release in premixed systems (John and Summerfield, 1957; Samaniego et al., 1995). As such, this measurement yields a time-responsive volume-averaged measurement of the combustor heat release rate. Control signals, indicating the commands sent to the actuation system, were also recorded.

Characterization of the Instability

The frequency of the primary mode of instability varied from 180 Hz to 220 Hz, depending on the test conditions. Secondary modes are present at higher frequencies, but are smaller in magnitude and of less interest here. Figure 4 shows power-spectral density (PSD) plots of the combustor pressure and the heat release rate during instability. These data are presented on a decibel scale, where the fluctuations are normalized by a reference value and represented on a logarithmic scale as follows:

Contributed by the International Gas Turbine Institute and presented at the International Gas Turbine and Aeroengine Congress and Exhibition, Stockholm, Sweden, June 2–5, 1998. Manuscript received by the ASME Headquarters April 1, 1998. Paper No. 98-GT-267. Associate Technical Editor: R. Kielb.

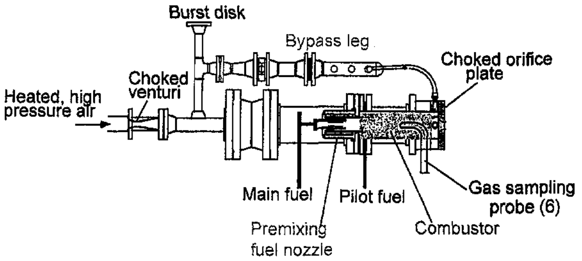

Fig. 1 Schematic of single-nozzle combustor rig. Test section diameter = 15.2 cm. For clarity, only one of the 6 sampling probes is shown.

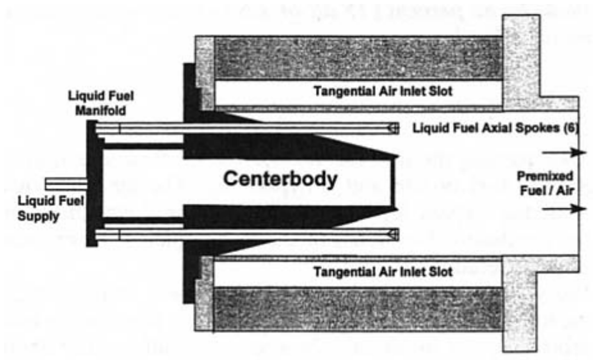

Fig. 2 Schematic of tangential-entry fuel nozzle, showing liquid fuel injection spokes

$$dB = 20 \log_{10}\left(\frac{P'}{P_{\text{ref}}}\right).$$

A similar expression was employed for the heat release values.

For fixed inlet pressure and temperature, the magnitude of the instability grew with decreasing fuel/air ratio, as shown in Fig. 5. This feature of the instability limited the leanness of the usable mixture, and therefore the level to which the NO_x emissions could be reduced. Application of a steady, sidewall diffusion flame pilot reduced the magnitude of the instability, but resulted in increased NO_x emissions.

The instability mode of interest (~200 Hz) was a bulk mode, characterized as a Helmholtz resonator/spring-mass system in which the combustor volume represented the spring and the masses of gas in the fuel nozzle and the exit orifice represented the masses. Pressure fluctuations were coupled with the heat release process through their effect on the flow rate of air delivered through the fuel nozzle. Time-varying air flow rate led to time-varying equivalence ratio, and, therefore, time-varying heat release rate. This conceptual model of the instability is discussed in more detail in Peracchio and Proscia (1998). Additional control-oriented modeling is currently being performed at UTRC using describing function analyses.

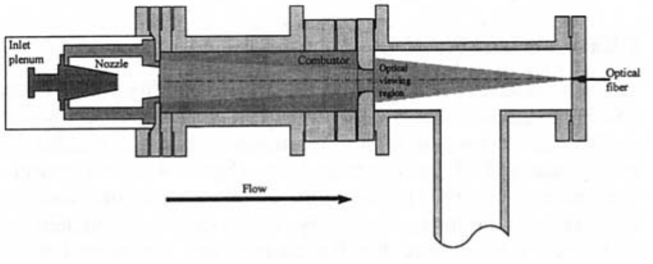

Fig. 3 Layout of fiber-optic viewing region for measurement of combustor heat release rate

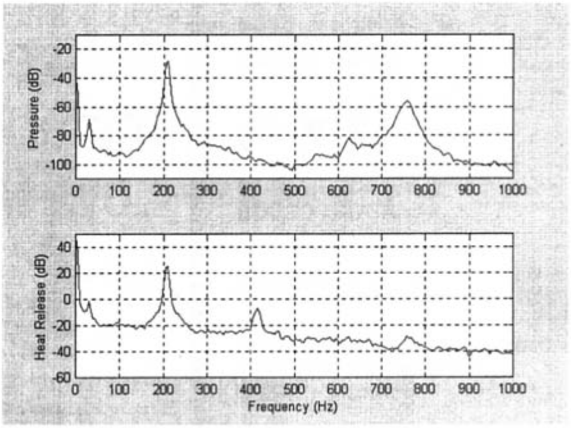

Fig. 4 Combustor pressure and heat release spectra for uncontrolled combustion at an equivalence ratio of 0.51

Description of the Control System

The control system consisted of three parts: a sensor to measure the state of the system, a control algorithm to determine the required action, and an actuator to achieve that action. The high-response measurements of combustor pressure and heat release rate had illustrated their capability for tracking the instability with high signal/noise ratio and were both available as control sensors. A variety of control algorithms, ranging from simple phase-shifting algorithms to more complex adaptive algorithms were available for implementation, depending on the need. It was apparent that the critical component was the actuator.

The initial requirements for the actuator were two-fold: it had to be able to affect the dynamics of the combustor system at the 200 Hz frequency and it had to be able to endure the operating environment in which it was placed. In addition, it was preferable that the device be simple and easy to control. Previous applications of active control to combustors have been in lab-scale devices operating at capacities, pressures, and temperatures significantly lower than those considered in this study (see Yu, 1997; Billoud, 1992; McManus, 1997; Richards, 1995; Zinn, 1997; Hantschk, 1996).

The high power output (4 MW per nozzle), inlet operating pressure (1.7 MPa) and temperature (730 K) of this application eliminated many of the actuation concepts used in these studies from consideration. Actuation of the combustor air flow rate was considered, but it was determined that the durability of this scheme would be inadequate, again due to the high operating temperature. Other, more sophisticated actuators were discarded

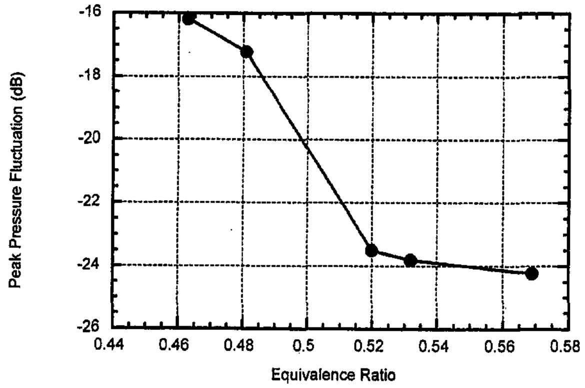

Fig. 5 Effect of equivalence ratio on level of combustor pressure fluctuation in the 200 Hz mode

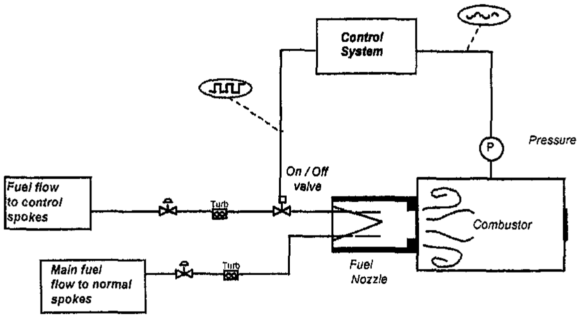

Fig. 6 Schematic of fuel control system with block diagram of controller

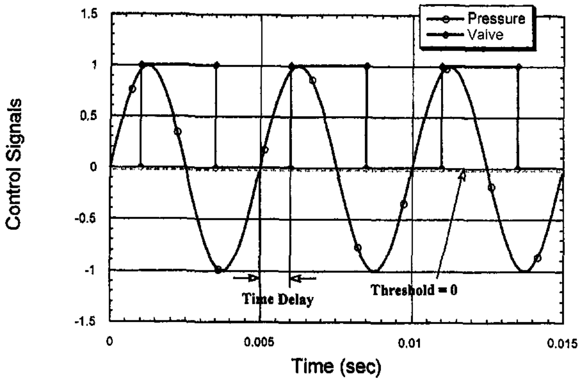

Fig. 8 Threshold control algorithm schematic with illustration of delay and threshold settings

due to the level of complexity they introduced into the problem. Actuation of the fuel flow remained as a viable candidate. Several configurations of fuel actuation were designed and tested. Only one will be discussed in this paper.

One of the six spokes delivering fuel into the premixing fuel nozzle was disconnected from the main fuel system and was connected to a separately metered fuel system (see Fig. 6). A high-speed solenoid valve was installed in this system external to the combustor rig, so as to isolate it from the high operating temperature. The volume of tubing between the valve and the fuel injection location was minimized in order to reduce attenuation and time lag due to capacitive effects. An accumulator was installed immediately upstream of the solenoid valve to minimize supply pressure variations. No direct measurement of the time-varying fuel flow rate was made. Open-loop testing of the flow system indicated that the valve responded at frequencies up to approximately 250 Hz, which determined the maximum operating frequency.

Open-loop actuator authority tests were conducted under reacting conditions. In these tests $\frac{1}{6}$ of the total fuel flow rate (time averaged) was delivered through the control fuel system. The remainder of the fuel was delivered through the other five spokes. The solenoid valve was driven at different frequencies, independently of the combustor behavior, using a signal generator. The on/off duty cycle was maintained at 50 percent. The response of the combustor pressure and heat release rate were then measured. Figure 7 shows the results of open-loop forcing at 100 Hz. Note that the 200 Hz instability was still present. It was not possible to obtain a nonresonant situation under reacting conditions, although these tests were conducted at the highest practical fuel/air ratio in order to reduce the magnitude of the 200 Hz instability.

For diagnostic purposes, a simple threshold control algorithm was designed. The principle of its operation is shown in Fig. 8. Whenever the control sensor signal crossed an established threshold level, a command was sent to the solenoid valve. On positive-direction crossings, the valve was opened and on negative-direction crossings, it was closed. A time delay between the moment of crossing and the valve command was also imposed. The same delay was used for both opening and closing commands. The threshold level and time delay were manipulated via a user interface to the control algorithm. Because the opening and closing of the valve was tied to the pressure signal, the algorithm was self-tuning over the frequency range of interest (100–300 Hz).

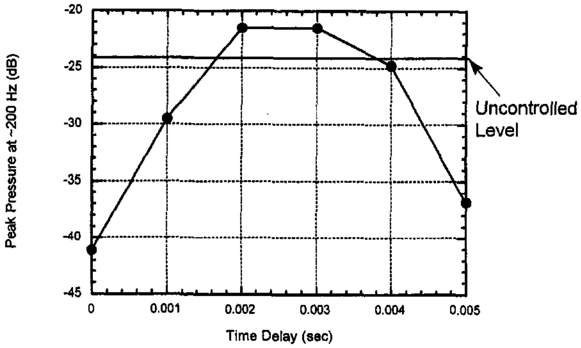

Fig. 9 Effect of control delay time on attenuation of pressure fluctuations of 200 Hz mode at an equivalence ratio of 0.56

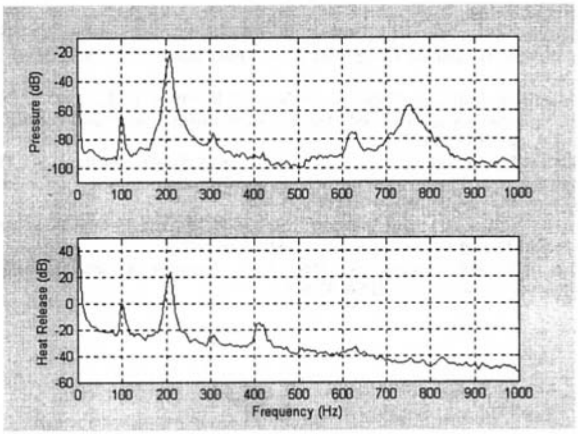

Fig. 7 Pressure and heat release spectra at an equivalence ratio of 0.56 with open-loop forcing at 100 Hz

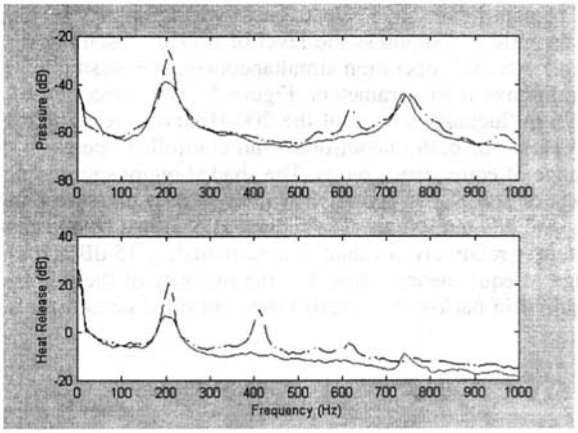

Fig. 10 Spectra of pressure and heat release during controlled (solid lines) and uncontrolled (dashed lines) at an equivalence ratio of 0.51 with optimum delay

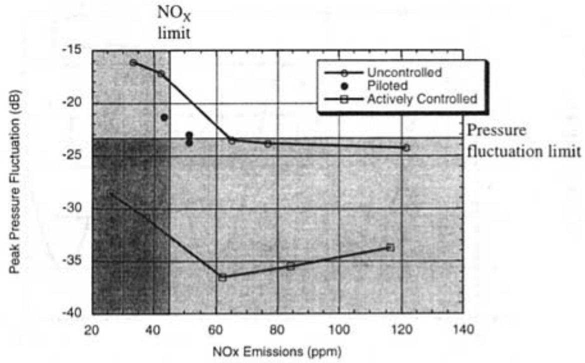

Fig. 11 Cross-plot of pressure fluctuation level versus NO$_x$ emissions. Points represent equivalence ratios of 0.47, 0.49, 0.51, 0.53, and 0.56 from left to right on each curve. Piloted points are for operation at 0.49 with 2.5, 5.0, and 6.5 percent sidewall pilot, top to bottom (percentage of total fuel flow rate).

Results of Controlled Combustion

Tests with the threshold controller and spoke actuation were conducted using the bandpass-filtered (100–300 Hz) combustor pressure as the control signal. In all the cases discussed here, the threshold level was set at zero, nominally yielding a 50 percent duty cycle. These tests were conducted at a combustor pressure of 1.56 MPa and a combustor inlet temperature of 730 K. The nominal power output of the test combustor was 4 MW. The fuel/air equivalence ratio was varied over a wide range of values, down to near-blowout conditions.

Figure 9 shows the behavior of the controlled combustor as the delay time was varied. Proper choice of the time delay yielded significant reductions in the level of pressure oscillations. (Note that the control system was capable of increasing the magnitude of the instability as well as attenuating it.) This exercise was conducted at five equivalence ratios between 0.47 and 0.56 (based on nozzle air flow). The optimum time delay was constant at 0 ms across this range, and also across a range of air flow rates. This value has no physical significance, in that it represents only a control system time delay and not the acoustic, convective or kinetic time delays involved in the mixing and combustion of the actuated fuel flow. These parameters were not directly measured.

Figure 10 shows PSD's of the uncontrolled and controlled combustor pressure and heat release rate at an equivalence ratio of 0.51. The magnitude of the 200 Hz mode was attenuated by 15 dB (5.6× or 82 percent) using the optimum time delay. The overall RMS pressure level was reduced from 29.2 kPa to 11.5 kPa.

The control system's effectiveness will ultimately be judged by its ability to suppress the level of pressure oscillations and enable low-NO$_x$ operation simultaneously. It is desirable, then, to minimize both parameters. Figure 11 is a cross plot of the pressure fluctuation level of the 200 Hz mode versus the NO$_x$ emissions for both uncontrolled and controlled operation over a range of equivalence ratios. The shaded regions represent the limits of acceptable operation with respect to pressure fluctuation and NO$_x$ emissions. The reduction obtained by the control system is relatively constant at approximately 15 dB across the range of equivalence ratios. For the majority of the points (all acquired in back-to-back tests) the controlled combustor actually created less NO$_x$ than the uncontrolled combustor. It is believed that this is because temporal ''hot spots'' created by the fuel/air fluctuations have been removed by the control system.

Also shown in Fig. 11 is a comparison of the controlled system to piloted operation. Piloted data were collected at an overall equivalence ratio of 0.49. While diffusion flame piloting reduced the level of pressure fluctuations, it increased the NO$_x$ emissions. Only the actively controlled system was capable of delivering simultaneous low NO$_x$ and low pressure fluctuations. Low CO emissions were also maintained and, especially at low equivalence ratios, lowered using control.

Summary

A practical active combustion control system for application to liquid-fueled, lean, premixed combustion systems has been designed and demonstrated in a single-nozzle combustor at realistic engine operating conditions. A full-scale engine fuel nozzle was minimally modified to incorporate a simple actuation system using an off-the-shelf high-speed solenoid valve. Investigation of the controlled system behavior indicated that a fixed time delay between the input signal and the control signal to the valve yielded optimum effectiveness over a wide range of combustor equivalence ratios. Suppression of the instability by as much as 15 dB was typical. The control system was self-tuning over the 100–300 Hz frequency range, enabling it to track changes in frequency with changing operating conditions. The system demonstrated simultaneous achievement of both NO$_x$ and pressure fluctuation goals and demonstrated its superiority to diffusion-flame piloting.

Acknowledgments

The authors wish to thank DARPA for their sponsorship of this work. The contract monitor is Dr. William Scheuren. The contributions of Drs. Thomas Rosfjord, Aldo Peracchio, John McVey, and Gonzalo Rey, Messrs. William Proscia, Jeffrey Walker, Timothy Snyder and Frederick Padget and Ms. Luu Vu were key to the success of this demonstration.

Bibliography

Billoud, G., Galland, M.A., Huynh Huu, C., and Candel, S., 1992, ''Adaptive Active Control of Combustion Instabilities,'' *Combustion Science and Technology*, Vol. 81, pp. 257–283.

Hantschk, C., Hermann, J., and Vortmeyer, D., 1996, ''Active Instability Control with Direct Drive Servo Valves in Liquid-Fuelled Combustion Systems,'' paper presented at the 26th International Symposium on Combustion, Naples, Italy.

John, R. R., and Summerfield, M., 1957, ''Effect of Turbulence on Radiation Intensity from Propane Air Flames,'' *Jet Propulsion*, Vol. 27, pp. 169–179.

McManus, K.R., Magill, J.C., Miller, M.F., and Allen, M.G., 1997, ''Closed-Loop System for Stability Control in Gas Turbine Combustors,'' Paper AIAA-97-0463.

Peracchio, A.A., and Proscia, W., 1998, ''Nonlinear Heat-Release/Acoustic Model for Thermoacoustic Instability in Lean Premixed Combustors,'' ASME Paper 98-GT-269.

Richards, G.A., Yip, M.J., Robey, E., Cowell, L., and Rawlins, D., 1995, ''Combustion Oscillation Control By Cyclic Fuel Injection,'' ASME Paper 95-GT-224.

Samaniego, J.-M., Egolfopoulos, F. N., and Bowman, C. T., 1995, ''CO2* Chemiluminescence in Premixed Flames,'' *Combustion Science and Technology*, Vol. 109, pp. 183–203.

Snyder, T.S., Rosfjord, T.J., McVey, J.B., and L.M. Chiappetta, L.M., 1994, ''Comparison of Liquid Fuel/Air Mixing and NO$_x$ Emissions for a Tangential Entry Nozzle,'' ASME Paper 94-GT-283.

Yu, K., Wilson, K.J., and Schadow, K.C., 1997, ''Active Combustion Control in a Liquid-Fueled Dump Combustor,'' AIAA-97-0462.

Zinn, B.T., and Neumeier, Y., 1997, ''An Overview of Active Control of Combustion Instabilities,'' AIAA-97-0461.

Y. Liao
Department of Aerospace Engineering

A. T. Sakman
Department of Mechanical Engineering

S. M. Jeng
Department of Aerospace Engineering

M. A. Jog
Department of Mechanical Engineering

University of Cincinnati,
Cincinnati, OH 45221

M. A. Benjamin
Gas Turbine Fuel Systems Division,
Parker Hannifin Corporation,
Mentor, OH 44060

A Comprehensive Model to Predict Simplex Atomizer Performance

The pressure swirl atomizer, or simplex atomizer, is widely used in liquid fuel combustion devices in the aerospace and power generation industries. A computational, experimental, and theoretical study was conducted to predict its performance. The Arbitrary-Lagrangian-Eulerian method with a finite-volume scheme is employed in the CFD model. Internal flow characteristics of the simplex atomizer, as well as its performance parameters such as discharge coefficient, spray angle and film thickness, are predicted. A temporal linear stability analysis is performed for cylindrical liquid sheets under three-dimensional disturbances. The model incorporates the swirling velocity component, finite film thickness and radius that are essential features of conical liquid sheets emanating from simplex atomizers. It is observed that the relative velocity between the liquid and gas phases, density ratio and surface curvature enhance the interfacial aerodynamic instability. The combination of axial and swirling velocity components is more effective than only the axial component for disintegration of liquid sheet. For both large and small-scale fuel nozzles, mean droplet sizes are predicted based on the linear stability analysis and the proposed breakup model. The predictions agree well with experimental data at both large and small scale.

1 Introduction

Atomization is a process of generating a large number of droplets from a bulk liquid. The performance of a liquid fuel atomizer has direct effects on combustion efficiency, pollutant emissions, and combustion stability. Understanding the underlying mechanisms of the atomization process is crucial for improvements in liquid-spray combustion. Because of its advantages such as small power consumption, good spray quality, and simple geometry (Bayvel, 1993), the pressure swirl atomizer, or simplex atomizer, is widely used in gas turbine engines and in furnaces in the power generation industry. Figure 1 shows a typical geometry of a simplex atomizer. High pressure liquid enters through the swirler inlet slots. Due to the swirling motion of the liquid, an air core is developed inside the nozzle and liquid emanates in the form of a conical liquid sheet. The flow features inside the nozzle and the disintegration of the liquid sheet determine the characteristics of the resultant spray. Since the spray angle, mean drop size and droplet size distribution from the liquid sheet disintegration control the subsequent heat and mass transfer in a convection environment such as in spray combustion, they have a direct effect on combustion efficiency, pollutant emission, and stability. Understanding factors that affect the atomizer performance parameters is important for both practical atomizer design and improvement. However, predictions of the atomizer performance still remain a challenge.

According to Giffen and Muraszew's (1953) maximum flow principle, discharge coefficient, spray angle and film thickness depend only on the geometry constant K, which is defined as $K = A_p/D_s d_o$. Although the theory provides correct trends, it is based on the assumption of inviscid flow and the features of the internal flow are ignored. Recent studies (Yule et al., 1997; Holtzclaw et al., 1997) show that the performance parameters depend not only on nozzle geometry but also on internal flow features.

Mean droplet size and the size distribution are even more difficult to predict theoretically or numerically than other performance parameters mentioned above as the physics of the complex atomization process is not clearly understood. So far, in most spray applications, empirical correlations for mean drop sizes are employed, which are discussed in Lefebvre (1989).

The understanding of the atomization process has benefited greatly by the pioneering work of instability analysis of liquid sheets by Squire (1953). Extensive research has been conducted thereafter, for example, Hagerty and Shea (1955), Dombrowski and Johns (1962), Clark and Dombrowski (1972), and Li and Tankin (1991). Forces such as the inertial force, surface tension, aerodynamic force, viscous force, and centrifugal force are involved in the disintegration process. Some of them resist the disintegration process while others promote it. It is the competition among these forces that determines the stability of liquid sheets. It is now generally agreed that the aerodynamic instability of the liquid sheet is responsible for the disintegration process. Based on linear stability theory, Dombrowski and Johns (1963) proposed a breakup model for a plane liquid sheet. The predicted mean drop sizes agree well with experimental measurement. The two-dimensional instability model was extended later by Crapper et al. (1975), Meyer and Weihs (1987), Lee and Chen (1991), Dumouchel et al. (1993), Panchagnula et al. (1996), and Shen and Li (1996) for annular liquid sheets.

The objective of the present paper is to develop a comprehensive model to predict the performance of a simplex atomizer. In the CFD model, the Arbitrary-Lagrangian-Eulerian method with a finite-volume scheme is employed to compute the internal flow field and the initial properties of the liquid sheet emanating from the nozzle. Discharge coefficient, spray angle, film thickness, and velocity at the nozzle exit are predicted. The computational model has been validated by comparisons with experimental measurements (Holtzclaw et al., 1997; Jeng et al., 1998). The instability model considers an inviscid, swirling annular liquid sheet under three-dimensional disturbances and different gas velocities. A parametric study has been carried out to understand the specific roles of various forces, fluid properties and geometrical conditions in the disintegration process. By incorporating the essential features such as axial and tangential

---

Contributed by the Gas Turbine Division of THE AMERICAL SOCIETY OF MECHANICAL ENGINEERS for publication in the ASME JOURNAL OF ENGINEERING FOR GAS TURBINES AND POWER.

Manuscript received by the Gas Turbine Division June 30, 1998; final revision received by the ASME Headquarters February 10, 1999. Associate Technical Editor: J. E. Peters.

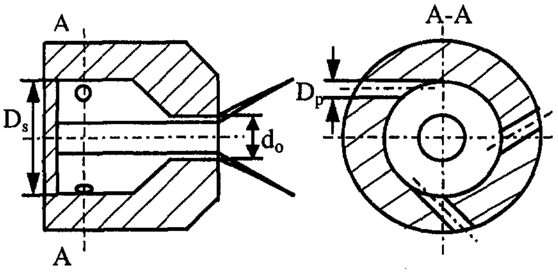

Fig. 1 Typical geometry of a simplex atomizer

velocity, attenuating film thickness and finite radius of the liquid sheet issuing out from a simplex nozzle, the present model is used to calculate the maximum growth rates and the most unstable wave number (wavelength). This wavelength is then incorporated into the breakup model, based on Rayleigh's theory, to predict mean droplet sizes, while the maximum growth rate is employed to determine the location of the liquid sheet breakup.

2 Mathematical Formulation

2.1 Computational Model. The flow is assumed to be axisymmetric and incompressible. The governing equations are the continuity and Reynolds averaged Navier-Stokes equations expressed below.

$$\frac{\partial(\rho U)}{\partial x}+\frac{\partial(r\rho V)}{r\partial r}=0 \qquad (1)$$

$$\rho\frac{\partial U}{\partial t}+\rho U\frac{\partial U}{\partial x}+\frac{\rho V}{r}\frac{\partial U}{\partial r} = (\mu_t+\mu)\left(\frac{\partial^2 U}{\partial x^2}+\frac{\partial\left(r\frac{\partial U}{\partial r}\right)}{r\partial r}\right)-\frac{\partial p}{\partial x} \qquad (2)$$

$$\rho\frac{\partial V}{\partial t}+\rho U\frac{\partial V}{\partial x}+\frac{\rho V}{r}\frac{\partial V}{\partial r} = (\mu_t+\mu)\left(\frac{\partial^2 V}{\partial x^2}+\frac{\partial\left(r\frac{\partial V}{\partial r}\right)}{r\partial r}\right) -\frac{\partial p}{\partial r}+\rho\frac{W^2}{r}-2(\mu_t+\mu)\frac{V}{r} \qquad (3)$$

$$\rho\frac{\partial W}{\partial t}+\rho U\frac{\partial W}{\partial x}+\frac{\rho V}{r}\frac{\partial W}{\partial r} = (\mu_t+\mu)\left(\frac{\partial^2 W}{\partial x^2}+\frac{\partial\left(r\frac{\partial W}{\partial r}\right)}{r\partial r}\right)-\rho\frac{VW}{r} \qquad (4)$$

The turbulent eddy viscosity is determined by the algebraic equation model proposed by Baldwin and Lomax (1978).

Boundary conditions are prescribed at the swirl chamber inlet, tip (outflow of computational domain), solid boundary and liquid/gas interface. To compare the CFD model with the experimental configuration comprised of a finite number of square inlet slots, the radial and tangential velocities and the width of the equivalent annular inlet slot are determined by equating the total mass flow rate, angular momentum and kinetic energy of the two cases. No-slip boundary conditions are prescribed at the solid boundary. At the tip, the second derivative of pressure with respect to x is set to 0. At the gas-liquid interface, the normal stress is balanced as

$$P=P_\infty+\sigma(1/R_1+1/R_2), \qquad (5)$$

where P_∞ is the ambient air pressure and R_1, R_2 are the principal radii of curvature at the interface. The velocity gradients of liquid normal to the interface are assumed to be zero since shear stress is small due to the large density and viscosity ratios between the liquid and gas phases.

The above governing equations and boundary conditions are discretized by a finite-volume scheme. The Arbitrary-Lagrangian-Eulerian method (ALE) with an adaptive grid generation technique is used to track the position of the interface. The details of the computational procedures of ALE are described in Jeng et al. (1998) and are not repeated here for brevity. The steady state solution is achieved when the normal velocity component at the interface becomes zero.

2.2 Linear Stability Analysis. A swirling annular liquid sheet subject to concurrent inner and outer air streams is considered. The geometrical and flow conditions are shown in Fig. 2. Both the liquid and gas phases are assumed to be inviscid and incompressible. The inviscid assumption is based on Shen and Li's study (1996), which found that viscosity has only a small influence on the growth rates of disturbances at high Weber number. Basic flow velocities for the liquid and inner and outer gas are assumed to be $(U_l, 0, A/r)$, $(U_i, 0, 0)$, and $(U_o, 0, 0)$, respectively. A temporal linear instability analysis is performed

Nomenclature

A = vortex strength, m^2/s
A_p = total inlet area, m^2
C_d = discharge coefficient
D = mean droplet diameter, m
D_L = ligament diameter, m
D_p = inlet slot diameter, m
D_s = swirl chamber diameter, m
d_o = exit orifice diameter, m
FN = flow number ($=\dot{m}_l/\sqrt{\Delta p\rho_l}$), m^2
g = density ratio between gas and liquid
h = ratio of inner and outer radii
K = atomizer geometric constant
k = axial wave number, 1/m
$\dot{m}_l$ = mass flow rate, kg/s
n = azimuthal wave number
P = mean pressure, N/m^2
p = disturbance pressure, N/m^2
Δp = pressure differential, N/m^2
R_a, R_b = inner and outer radius of liquid sheet, m
R_1, R_2 = radii of curvature, m
r = radial coordinate, m
t = time, s
t_s = film thickness at breakup, m
U = mean axial velocity, m/s
V = mean radial velocity, m/s
W = mean tangential velocity, m/s
u = disturbance axial velocity, m/s
v = disturbance radial velocity, m/s
w = disturbance tangential velocity, m/s
We = Weber number (We $=\rho U^2 R/\sigma$)
x = axial coordinate, m

Greek Letters

η = displacement disturbance, m
λ = wave length, m
θ = azimuthal angle or spray cone half angle radian or degree
ρ = fluid density, kg/m^3
ω = temporal frequency, 1/s

Subscripts

l = liquid phase
i = inner gas
o = outer gas
$*$ = at maximum condition
s = based on swirling component

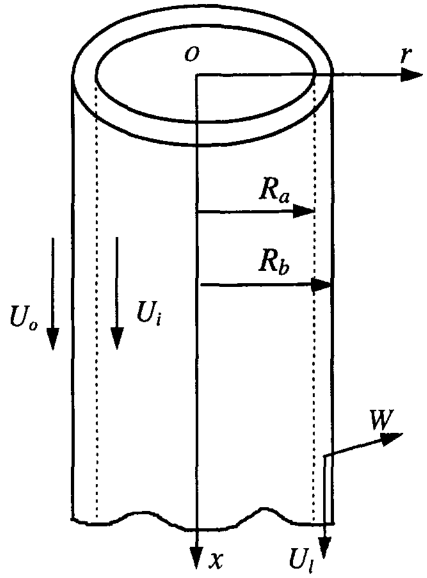

Fig. 2 Schematic of an annular liquid sheet

for the annular liquid sheet under three-dimensional disturbances with the normal mode method. The approach to the problem is similar to that of Panchagnula et al. (1996).

The governing equations in a cylindrical coordinate system are

$$\frac{V}{r} + \frac{\partial V}{\partial r} + \frac{1}{r}\frac{\partial W}{\partial \theta} + \frac{\partial U}{\partial x} = 0 \tag{6}$$

$$\frac{\partial U}{\partial t} + V\frac{\partial U}{\partial r} + \frac{W}{r}\frac{\partial U}{\partial \theta} + U\frac{\partial U}{\partial x} = -\frac{1}{\rho}\frac{\partial p}{\partial x} \tag{7}$$

$$\frac{\partial V}{\partial t} + V\frac{\partial V}{\partial r} + \frac{W}{r}\frac{\partial V}{\partial \theta} + U\frac{\partial V}{\partial x} - \frac{W^2}{r} = -\frac{1}{\rho}\frac{\partial p}{\partial r} \tag{8}$$

$$\frac{\partial W}{\partial t} + V\frac{\partial W}{\partial r} + \frac{W}{r}\frac{\partial W}{\partial \theta} + U\frac{\partial W}{\partial x} + \frac{VW}{r} = -\frac{1}{\rho}\frac{\partial p}{r\partial \theta} \tag{9}$$

The disturbances are assumed to have the forms of

$$(u, v, w, p') = (\hat{u}(r), \hat{v}(r), \hat{w}(r), \hat{p}(r))e^{i(kx+n\theta-\omega t)}, \tag{10}$$

where $\hat{}$ indicates the disturbance amplitude which is a function of r only. For the temporal instability analysis, the wave number k and n are real while frequency ω is complex. The imaginary part of ω reflects the growth rate of the disturbance. The displacement disturbance at the inner and outer interfaces are

$$\eta_j(x, \theta, t) = \hat{\eta}_j e^{i(kx+n\theta-\omega t)} \quad j = i, o. \tag{11}$$

To obtain linearized disturbed equations, let

$$U = \bar{U} + u, \quad V = v, \quad W = \bar{W} + w, \quad p = P + p', \tag{12}$$

where the over bar represents the assumed mean flow quantities and prime indicates disturbance. Substituting Eq. (12) into Eq. (6), (7), (8), and (9) and neglecting second order terms, we get the linearized disturbed equations for the liquid flow as

$$\frac{v}{r} + \frac{\partial v}{\partial r} + \frac{1}{r}\frac{\partial w}{\partial \theta} + \frac{\partial u}{\partial x} = 0 \tag{13}$$

$$\frac{\partial u}{\partial t} + \frac{A}{r^2}\frac{\partial u}{\partial \theta} + U_l\frac{\partial u}{\partial x} = -\frac{1}{\rho_l}\frac{\partial p'_l}{\partial x} \tag{14}$$

$$\frac{\partial v}{\partial t} + \frac{A}{r^2}\frac{\partial v}{\partial \theta} + U_l\frac{\partial u}{\partial x} - \frac{2Aw}{r^2} = -\frac{1}{\rho_l}\frac{\partial p'_l}{\partial r} \tag{15}$$

$$\frac{\partial w}{\partial t} + \frac{A}{r^2}\frac{\partial w}{\partial \theta} + U_l\frac{\partial w}{\partial x} = -\frac{1}{\rho_l}\frac{\partial p'_l}{r\partial \theta}. \tag{16}$$

The linearized disturbed equations for the inner and outer gas flow can be written in vector form as

$$\nabla \cdot \vec{u}_j = 0 \tag{17}$$

$$\frac{\partial \vec{u}_j}{\partial t} + U_j\frac{\partial \vec{u}_j}{\partial x} = -\frac{1}{\rho_j}\nabla p'_j \quad j = i, o, \tag{18}$$

where $\vec{u}_j = (u \quad v \quad w)$.

The boundary conditions are

For the Inner Gas,

$$v = \frac{D\eta_i}{Dt} = \frac{\partial \eta_i}{\partial t} + U_i\frac{\partial \eta_i}{\partial x} \quad \text{at } r = R_a \tag{19}$$

For the Outer Gas,

$$v = \frac{D\eta_o}{Dt} = \frac{\partial \eta_o}{\partial t} + U_o\frac{\partial \eta_o}{\partial x} \quad \text{at } r = R_b \tag{20}$$

For the Liquid Phase,

$$v = \frac{D\eta_i}{Dt} = \frac{\partial \eta_i}{\partial t} + \frac{A}{r^2}\frac{\partial \eta_i}{\partial \theta} + U_l\frac{\partial \eta_i}{\partial x} \quad \text{at } r = R_a \tag{21}$$

$$v = \frac{D\eta_o}{Dt} = \frac{\partial \eta_o}{\partial t} + \frac{A}{r^2}\frac{\partial \eta_o}{\partial \theta} + U_l\frac{\partial \eta_o}{\partial x} \quad \text{at } r = R_b \tag{22}$$

The dynamic boundary conditions are

$$p'_l - p'_i = \sigma\left(\frac{\eta_i}{R_a^2} + \frac{1}{R_a^2}\frac{\partial^2 \eta_i}{\partial \theta^2} + \frac{\partial^2 \eta_i}{\partial x^2}\right) - \frac{\rho_l A^2 \eta_i}{R_a^3} \tag{23}$$

$$p'_l - p'_o = -\sigma\left(\frac{\eta_o}{R_b^2} + \frac{1}{R_b^2}\frac{\partial^2 \eta_o}{\partial \theta^2} + \frac{\partial^2 \eta_o}{\partial x^2}\right) - \frac{\rho_l A^2 \eta_o}{R_b^3} \tag{24}$$

In order to determine the role of the various forces, fluid properties and geometric parameters, the above equations are nondimensionalized by introducing the following dimensionless parameters:

$$\mathrm{We}_i = \frac{\rho_i U_i^2 R_a}{\sigma}, \quad \mathrm{We}_o = \frac{\rho_o U_o^2 R_b}{\sigma}$$

$$\mathrm{We}_s = \frac{\rho_l W^2 R_b}{\sigma} = \frac{\rho_l A^2}{\sigma R_b}, \quad \mathrm{We}_l = \frac{\rho_l U_l^2 R_b}{\sigma}$$

$$g_i = \frac{\rho_i}{\rho_l}, \quad g_o = \frac{\rho_o}{\rho_l}, \quad h = \frac{R_a}{R_b}, \quad \bar{k} = kR_b, \quad \bar{\omega} = \frac{\omega R_b}{U_l}$$

$$\frac{U_i}{U_l} = \sqrt{\frac{\mathrm{We}_i}{\mathrm{We}_l}\frac{1}{g_i h}}, \quad \frac{U_o}{U_l} = \sqrt{\frac{\mathrm{We}_o}{\mathrm{We}_l}\frac{1}{g_o}}, \quad \frac{A}{U_l R_b} = \sqrt{\frac{\mathrm{We}_s}{\mathrm{We}_l}} \tag{25}$$

The final dispersion equation is a polynomial of fourth order of the form

$$a_4\bar{\omega}^4 + a_3\bar{\omega}^3 + a_2\bar{\omega}^2 + a_1\bar{\omega} + a_0 = 0. \tag{26}$$

The detailed derivation of the above dispersion equation is available in Liao (1999). The coefficients $\{a_i\}$ depend on wave number $\bar{k}$ and n, flow conditions, fluid properties, and geometric parameters and are given in the appendix. The dispersion equation is solved using Mathematica™. For each pair of $(\bar{k}, n)$ and given dimensionless parameters, we look for the root with the maximum imaginary part which represents the growth rate of the disturbance.

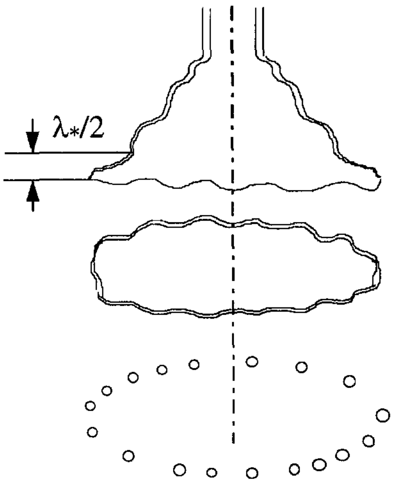

Fig. 3 Disintegration scheme of a conical liquid sheet

2.3 Breakup Model. The breakup model of a conical liquid sheet is essential for understanding the atomization process and the prediction of droplet sizes in practical simplex atomizers. The current breakup model assumes that the most unstable wave is detached at troughs to form a ring of half wavelength width ($\lambda_*/2$) as shown in Fig. 3. Dombrowski and Johns (1963) originally proposed this assumption for the breakup of plane liquid sheets. The most unstable wavelength is determined by the above instability model. The ring immediately evolves into a ligament of diameter D_L. Drops of equal diameter are formed from one wavelength intervals on the resultant ligament (Rayleigh, 1879). By conservation of liquid mass, the diameter of the ligament is given by

$$D_L = \left(\frac{2}{\pi}\lambda_* t_s\right)^{0.5} = 2\left(\frac{t_s}{k_*}\right)^{0.5} \qquad (27)$$

and the mean drop diameter is related to the diameter of the ligament as (Lefebvre, 1989)

$$D = 1.89 D_L. \qquad (28)$$

Substituting Eq. (27) into Eq. (28) leads to the equation of mean drop diameter as follows:

$$D = 3.78\left(\frac{t_s}{k_*}\right)^{0.5}. \qquad (29)$$

It should be noted that t_s in Eq. (29) represents the film thickness at the point of breakup. The breakup length is first calculated based on the maximum growth rate. Knowing the spray cone angle, the film thickness at the point of breakup is then determined through conservation of mass.

3 Results and Discussions

3.1 Computational Model. The CFD model was first validated by detailed comparison with experimental data. All the experiments to validate the CFD model were carried out on large size prototype atomizers with an exit orifice diameter of 18 mm and a swirl chamber diameter of 76 mm. The working fluid was water. The Reynolds number for the flow based on the exit orifice diameter and the mean exit velocity varied from 2.7×10^5 to 3.5×10^5. The corresponding pressure drop in the injector varied from 69 to 345 kPa. The details of the apparatus and the experimental methodology are available in Holtzclaw et al. (1997) and are not repeated here for brevity.

The computational results were obtained with a grid of 71 points in the x-direction and 21 points in the r-direction. In the radial direction, the grid points are distributed nonuniformly with a fine grid near the wall and at the gas-liquid interface where higher gradients are expected; a coarser grid is used in the central region. In the x-direction, the grid points are distributed as follows: seven in the inlet section, 29 in spin chamber, 22 in the converging section, six in the exit orifice section, and seven outside the nozzle orifice. In the Lagrangian step, the solution was considered converged if the maximum relative error in cell mass between two iterations was less than 10^{-7}. To test grid independence of the computational solutions, results were obtained by doubling the grid in both directions for two cases corresponding to the minimum and the maximum value of the atomizer constant. The results for film thickness, spray cone angle and the discharge coefficient were essentially unchanged (less than 1 percent).

Figure 4(a) shows that the mean film thickness at the orifice is directly proportional to K. Note that the experimental and computational results match to a good extent, while the analytical model (Rizk and Lefebvre, 1985) clearly underestimates both. In Fig. 4(b), it is observed that spray cone half angle decreases with increasing K. Note that the experimental and CFD results are in good agreement, while the analytical model (Giffen and Muraszew, 1953) overestimates the results for this case. An increase in the atomizer constant can be effected by increasing the inlet swirl slot area. For a given mass flow rate, this results in decreasing the swirl inside the spin chamber resulting in lower centrifugal force and corresponding lower cone angle and higher film thickness. Giffen and Muraszew's model is based on an inviscid flow assumption, and therefore it does not provide accurate predictions. Figure 4(c) shows that the discharge coefficient increases with increasing K. Again, an excellent agreement between the computational and experimental results is clearly evident, and this validates our computational model.

We note that the dimensionless flow parameter governing the flow phenomena inside the atomizer is the Reynolds number. The range of Reynolds number considered here is the same as that typically encountered in small-scale fuel injectors in aircraft engines. Therefore, the results of the computational model are also valid for small-scale atomizers.

It is evident from Fig. 4 that the geometry parameter K plays an important role in determining the atomizer performance. Other dimensionless geometry parameters such as L_s/D_s and D_s/d_o also influence the atomizer performance. We have used the validated computational code to evaluate the effect of two such parameters L_s/D_s and D_s/d_o on the film thickness at the orifice exit. L_s/D_s was varied from 0.1 to 1.5 and D_s/d_o from 3.5 to 6.5. For these cases, the mass flow rate, inlet slot area and the exit diameter were all held constant. Figure 5(a) shows the variation of film thickness with L_s/D_s. The film thickness is seen to increase with this parameter. At low values of L_s/D_s, there is a sharp increase in film thickness with L_s/D_s followed by a gradual increase. For a given spin chamber diameter, increasing L_s may result in high friction losses and therefore lower exit velocities and corresponding higher film thickness. Figure 5(b) shows the variation of D_s/d_o with the film thickness. It is seen from the figure that the film thickness increases with decreasing D_s/d_o. For a given D_s, a decrease in D_s/d_o can be achieved by increasing d_o. With a large d_o, fluid is no longer squeezed through a narrow orifice and the film thickness increases. At present, reliable correlations are not available to predict the influence of these geometric parameters on the performance of the atomizer. The CFD model allows us to predict the effect of geometry changes on the film thickness, spray cone angle, and in conjunction with the stability analysis and the breakup model, the mean drop sizes.

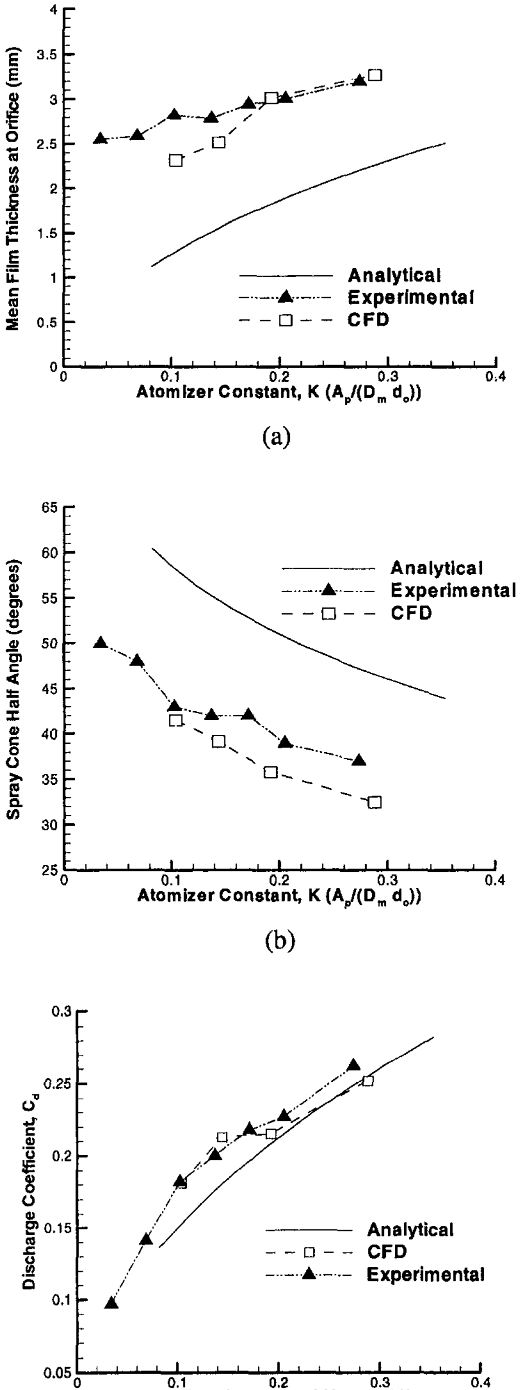

(a)

(b)

(c)

Fig. 4 (*a*) Film thickness versus *K*, (*b*) spray cone half angle versus *K*, and (*c*) discharge coefficient versus *K*

3.2 Linear Stability Analysis. Based on the derived dispersion equation, a parametric study has been carried out to isolate the effects of the axial and swirl velocity, gas-to-liquid density ratio, and surface curvature on the instability of liquid sheets. The frequency with the maximum imaginary part is the most unstable mode, hence, it will dominate the liquid sheet breakup process. For the simplex atomizer using this model, the inner and outer gas velocities are set equal to zero. The disturbance growth rate $\bar{\omega}$ is plotted in terms of dimensionless parameters such as axial Weber number, We_l, swirl Weber number, We_s, axial wave number, $\bar{k}$, azimuthal wave number, n, the ratio of inner and outer radii, h, and the gas-to-liquid density ratio, g_o.

It is seen from Fig. 6, that there exists a finite range of wave numbers with positive growth rate. The wave number that corresponds to the maximum growth rate is called the most unstable wave number. This behavior is explained as follows. The instability mechanism can be thought of as a frequency-selective amplifier. The mean flow is its energy supply, and its gain and frequency characteristics depend upon flow conditions and fluid properties. When the axial velocity is very low, the axisymmetric mode ($n = 0$) dominates the competition of disturbance growth. As the axial velocity increases, both the maximum growth rate and the range of wave numbers with positive growth rate (unstable wave number range) increase. The corresponding most unstable wave number or frequency shifts to a higher value. Furthermore, the importance of helical modes become comparable with the axisymmetric mode. This behavior has also been validated by previous studies (e.g., Panchagnula et al., 1996).

Figure 7 shows the instability of a purely swirling (i.e., with a zero axial velocity component) annular liquid sheet. As the swirl strength increases, i.e., as the swirl Weber number increases, the aerodynamic force increases, thus, promoting instability. This is manifested in the increased growth rate and the increased range of unstable wave number. More interestingly, the dominating mode shifts from the axisymmetric mode to the helical mode at moderate swirl Weber number. This is explained by the fact that the helical mode extracts more energy from the

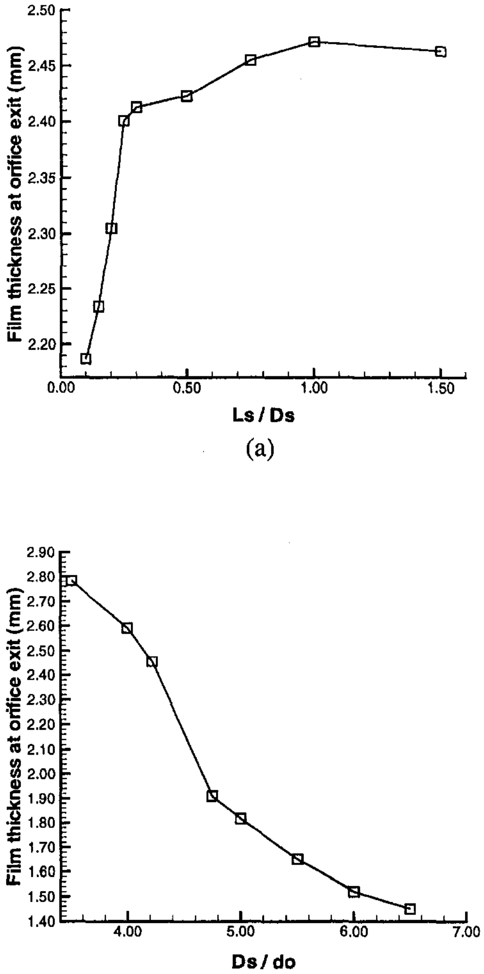

(a)

(b)

Fig. 5 Variation of film thickness with (*a*) L_s/D_s and (*b*) D_s/d_o

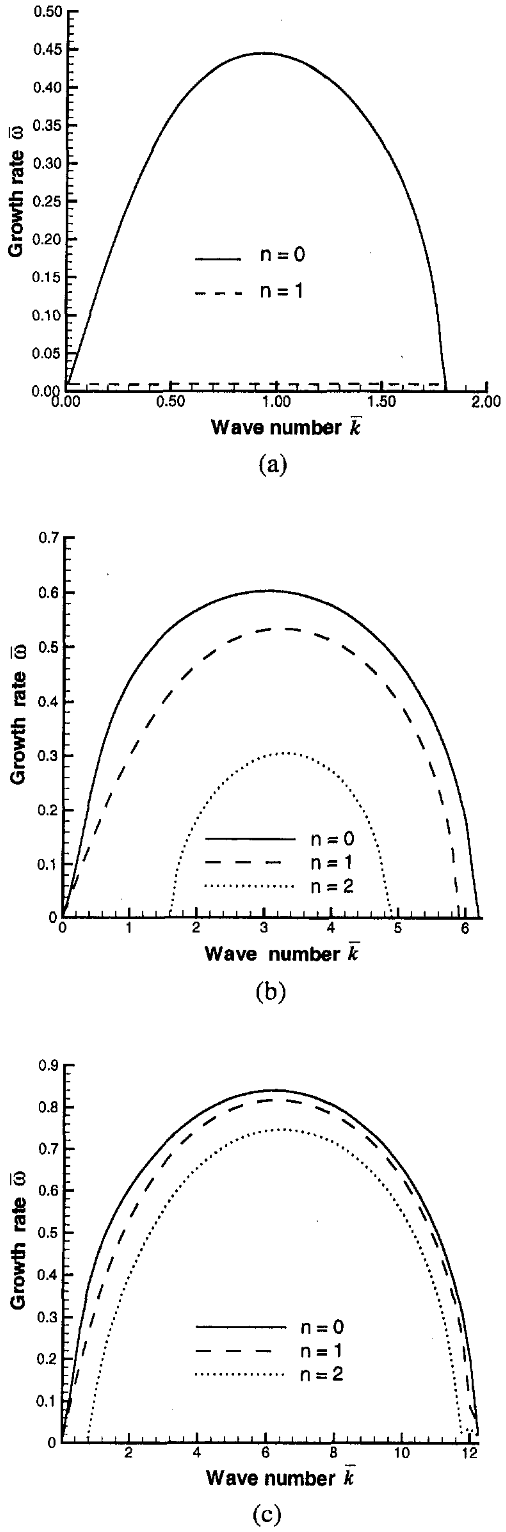

Fig. 6 Growth rate versus wave number for $n = 0, 1, 2$ mode at $We_s = 0$, $g_o = 0.00123$, $h = 0.99$: (*a*) $We_l = 1000$, (*b*) $We_l = 5000$, and (*c*) $We_l = 10000$

mean swirling flow field than the axisymmetric mode for the case where swirl is stronger. This illustrates the superior performance, at moderate injection pressure differential, of a simplex atomizer compared to plain pressure atomizer where liquid swirl is absent. This performance is partly due to the destabilizing effect of swirl.

The influence of the gas-to-liquid density ratio on the instability of the annular liquid sheet is presented in Fig. 8. Both the unstable wave number range and the growth rates increase with increasing gas density. Since an increase in gas density increases the aerodynamic force, it enhances the aerodynamic instability of liquid sheets as expected. This implies that the higher the ambient pressure, the smaller the drops produced. This conclu-

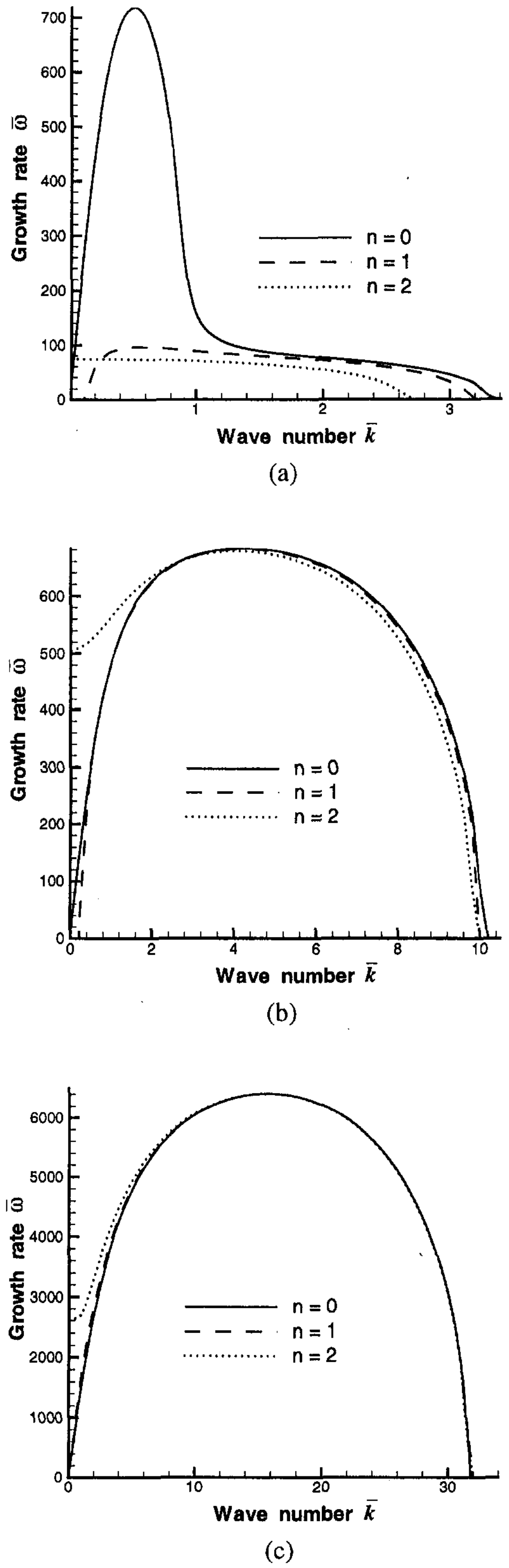

Fig. 7 Growth rate versus wave number for $n = 0, 1, 2$ mode at $We_l = 0$, $g_o = 0.00123$, $h = 0.99$. (*a*) $We_s = 10$, (*b*) $We_s = 100$, and (*c*) $We_s = 1000$

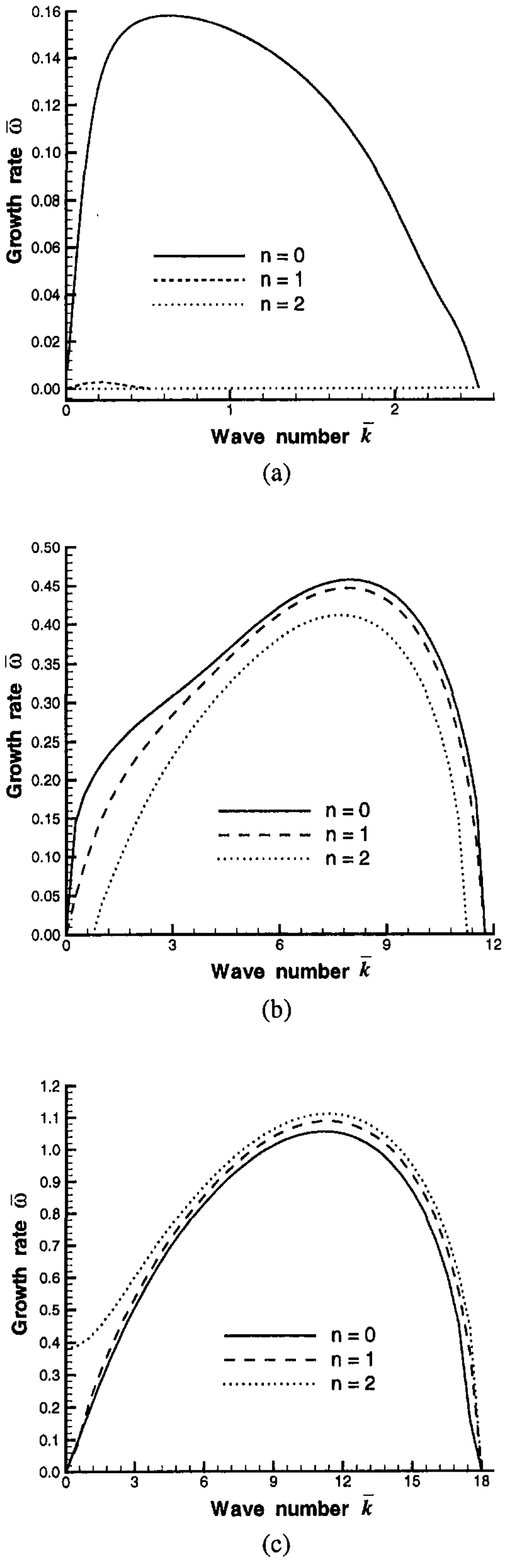

(a)

(b)

(c)

Fig. 8 Growth rate versus wave number for $n = 0, 1, 2$ mode at $h = 0.77$: (a) $g_o = 0.00123$, $We_l = 1000$, $We_s = 0$, (b) $g_o = 0.0123$, $We_l = 1000$, $We_s = 0$, and (c) $g_o = 0.0123$, $We_l = 1000$, $We_s = 100$

sion has been proved by Dombrowski and Hooper's (1963) experimental study of the effect of ambient density on drop size formation. Furthermore, when there is no swirl and gas density increases, the importance of helical modes becomes comparable with the axisymmetric mode. However, for weak swirl, helical modes become the dominating mode and are responsible for the disintegration of the liquid sheet.

Surface curvature has a remarkable effect on the growth rate of unstable waves as shown in Fig. 9. For both axisymmetric and helical modes and decreasing inner radius (for fixed outer radius), the growth rate increases, while the unstable wave

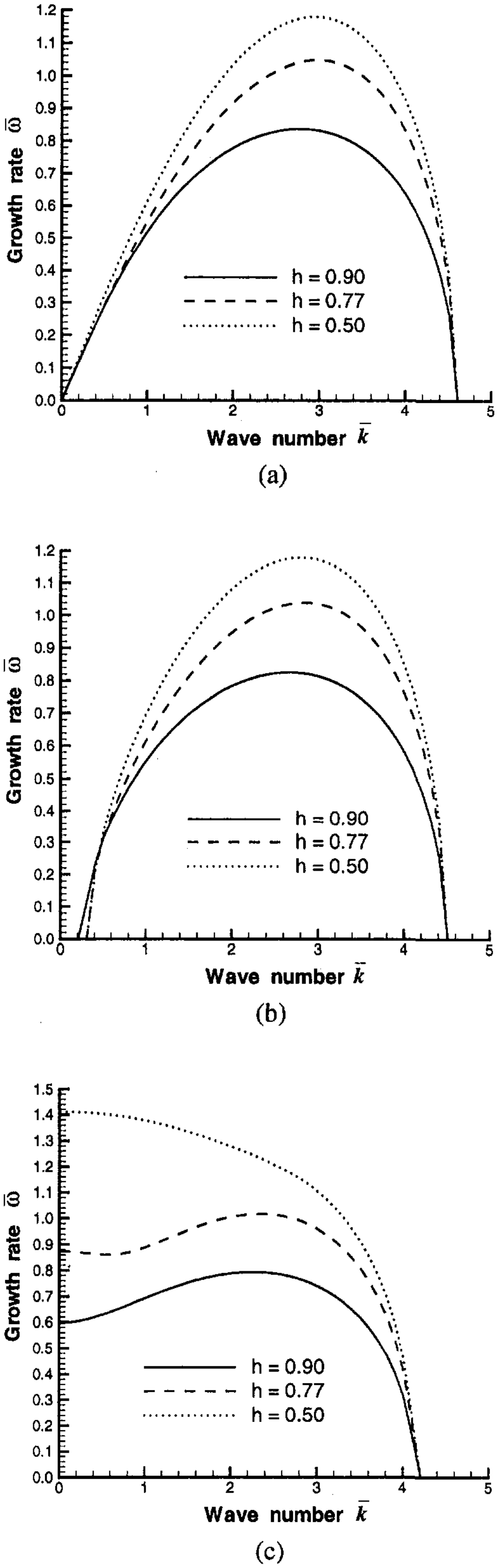

(a)

(b)

(c)

Fig. 9 Effect of surface curvature on instability for first three modes at $g_o = 0.00123$, $We_l = 20$, $We_s = 20$: (a) $n = 0$, (b) $n = 1$, and (c) $n = 2$

Table 1 Geometry details and performance parameters of three large scale atomizers

Case No.	Atomizer constant	Orifice diameter (mm)	Pressure differential (Pa)	Mass flow rate (kg/s)	Spray cone angle (degree)	Orifice film thickness (mm)	Breakup location (mm)
1	0.092	28.85	31026	0.63	78.5	2.56	152.4
2	0.092	28.85	134449	1.26	90.0	2.48	88.9
3	0.092	28.85	286134	1.89	90.3	2.30	50.8
4	0.214	24.89	48264	0.945	70.0	2.89	101.6
5	0.214	24.89	199949	1.89	75.7	2.84	76.2
6	0.214	24.89	361977	2.52	78.8	2.86	63.5
7	0.370	14.43	31026	0.504	52.5	2.41	158.75
8	0.370	14.43	175817	1.08	57.3	2.37	76.2
9	0.370	14.43	361977	1.512	57.1	2.40	50.6

number range is unaffected. These results are consistent with Lee and Chen (1991) and Shen and Li (1996). However, Crapper et al. (1975) claims the unstable range also changes with increasing surface curvature.

3.3 Mean Drop Size Prediction. Using the CFD model, the stability analysis and the breakup model, we have calculated mean drop sizes for both large scale and small scale (aero-engine scale) atomizers. The large-scale results were compared with our experimental data for a number of atomizer geometries and flow conditions. For the small-scale results, extensive comparisons of our predictions have been carried with correlations and experimental data available in the literature for small-scale atomizers. Properties of water ($\mu_l = 0.001$ kg/ms, $\sigma = 0.0734$ kg/s^2, $\rho_l = 1000$ kg/m^3) were used in the predictions of mean droplet sizes for both large and small-scale atomizers.

3.3.1 Large Scale. The mean droplet size and spray cone angle were measured by optical techniques and the liquid film thickness at the orifice exit was measured by an ultrasonic transducer. The film thickness and spray cone angle measurements were used to validate the CFD model as described earlier. A video recording of droplets was obtained using a high speed CCD camera at a vertical distance of approximately 0.5 meter from the nozzle orifice. This distance was chosen to assure that liquid sheets were well atomized and no ligaments were present in the measurement window. The size of measurement window varied from case to case and had a value of about 30 mm by 30 mm. A large number of images were analyzed to obtain the sauter mean diameter (SMD). The spray angle was determined by digitizing and processing images of the spray obtained by the CCD camera. An ultrasound transducer was mounted at the nozzle exit. The liquid film thickness measurements were based on the time delay in signal reflected from the water-Plexiglas interface and that from the water-air interface. The details of the experimental apparatus and procedure are available in Benjamin et al. (1998).

The axial and tangential velocity components, film thickness and cone angle were taken from the CFD results. The breakup point of the liquid sheet was located experimentally by observing the occurrence of discontinuities in the liquid sheet with stroboscopic lighting at 450 Hz and by analyzing spray images. The mean drop sizes were then calculated using the breakup model.

Table 1 summarizes the performance parameters of three large-scale atomizers under three different operating conditions. We note that the liquid film thickness at the orifice exit were rather large (about 2 mm) due to large orifice diameters (15–29 mm). Also the breakup length shortens as pressure differential (discharge velocity) increases.

In Table 2, the predicted SMD values obtained using the present theory are compared with measurement data and with those by Couto et al. theory (1997) and existing empirical correlations (Lefebvre 1989). It is seen that the present theory correctly predicts the trend for SMD; that is, the SMD decreases with increasing mass flow rate. Quantitatively, the present theory gives an overall error of about 20%. The discrepancy at the lowest flow cases may be caused by non-stationary flow at very low pressure. However, SMD is significantly overestimated by the Babu et al. correlation and significantly underestimated by the Couto et al. theory and correlations of Jasuja, Lefebvre, and Wang, and Lefebvre. It is evident from Table 2 that, for large-scale atomizers, Radcliffe's correlation and the present theory give the best predictions.

3.3.2 Small Scale. There is considerable experimental data at small scale for film thickness, spray cone angle, and drop sizes available in the literature. Unfortunately, these studies do not provide geometric details of the small-scale atomizers used. Therefore, the CFD code could not be utilized to calculate the properties of the liquid sheet emanating from the atomizer. These were obtained from the available data as follows. The axial and tangential velocity components were calculated using Eq. (30) and (31), respectively.

$$U = \frac{\dot{m}_l}{\rho_l(A_o - A_a)} = \frac{4\dot{m}_l}{\rho_l \pi (4d_o t - 4t^2)} \tag{30}$$

$$W = U \tan(\theta), \tag{31}$$

where t is the film thickness at orifice exit and is estimated by the equation below (Lefebvre, 1989).

Table 2 Comparison of SMD predicted by existing theory and empirical correlations

Case No.	Measured SMD (μm)	Present theory (μm)	Radcliffe's correlation (μm)	Jasuja's correlation (μm)	Babu et al. Correlation (μm)	Lefebvre's correlation (μm)	Wang and Lefebvre's correlation(μm)	Couto et al. Theory (μm)
1	1161	1556	1367	1064	4060	990	843	776
2	997	1152	904	660	2842	566	519	414
3	768	1028	739	521	2440	429	401	306
4	1169	1615	1268	962	4138	878	847	783
5	1052	1166	854	608	2968	513	557	461
6	902	1004	773	539	2825	445	492	391
7	1190	1029	1293	1013	3517	936	896	907
8	1002	829	769	560	2128	468	546	490
9	913	758	637	449	1860	360	455	390

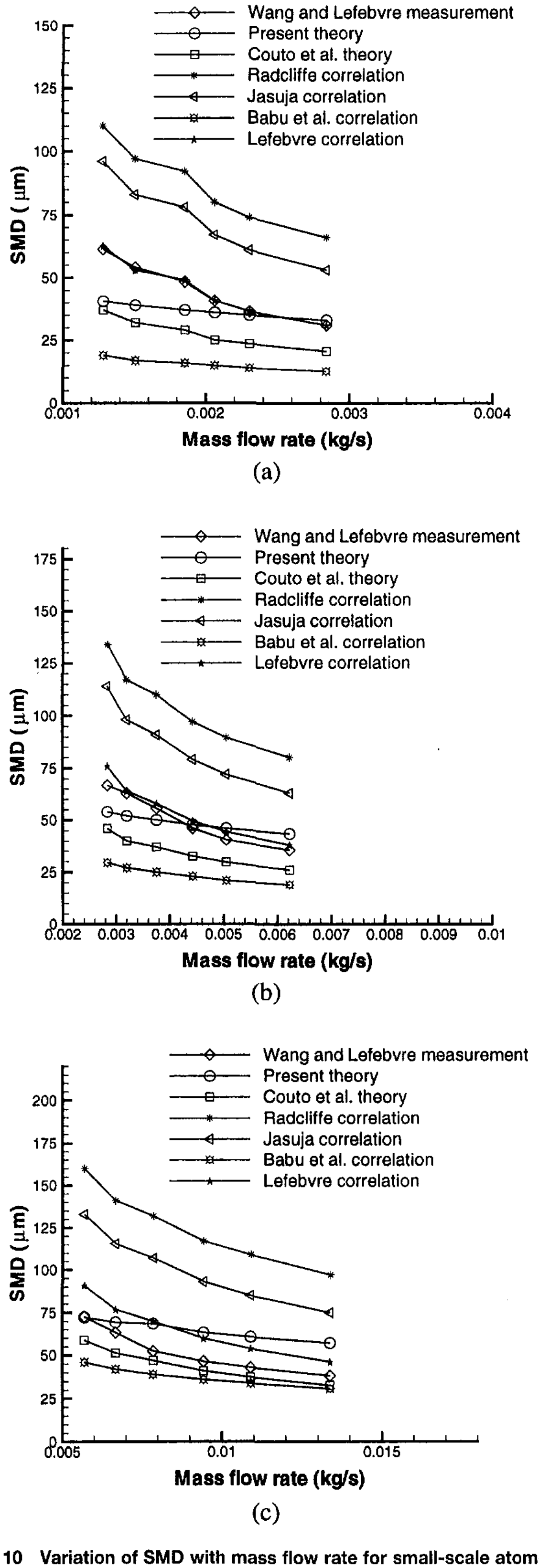

Fig. 10 Variation of SMD with mass flow rate for small-scale atomizer: (*a*) FN = 6.25 × 10^{-8} m^2, (*b*) FN = 12.5 × 10^{-8} m^2, and (*c*) FN = 25 × 10^{-8} m^2

$$t = \frac{0.00805\mathrm{FN}\rho_l^{0.5}}{d_o \cos(\theta)} \tag{32}$$

Further, it was assumed that the breakup of the liquid sheet occurs when the ratio of the disturbance amplitude to the initial amplitude reaches e^{12} as suggested by Dombrowski and Johns (1963). Hence, the breakup length (or time) can be readily calculated from the maximum growth rate and the film thickness at the breakup point is thus determined via conservation of mass. The effect of attenuating film thickness is considered in the breakup model by employing the film thickness at the point of breakup in Eq. (29).

The present model was employed to predict SMD for small-scale atomizers and compared with the experimental data of Wang and Lefebvre (1987), the aforementioned theory and correlations. The three small atomizers used by Wang and Lefebvre had a 60 deg spray cone angle with flow numbers of 6.25, 12.5, and 25 × 10^{-8} m^2, respectively. The pressure differential varies from 0.35 MPa to 2.07 MPa. As shown in Fig. 10(*a*) and 10(*b*), for atomizers with the FN of 6.25 × 10^{-8} and 12.5 × 10^{-8}, SMD predictions by Lefebvre's correlation and the present theory are very close to experimental data while others either significantly overestimate or underestimate them. For the atomizer with the FN of 25 × 10^{-8}, as shown in Fig. 10(*c*), the discrepancy between Lefebvre's correlation and measurement data becomes larger than those in Fig. 10(*a*) and (*b*). Our model predicts drop sizes in agreement with experimental data with a somewhat more gradual variation of SMD with mass flow rate than that measured. This is because the slope of the curve is highly dependent on the predicted film thickness from the correlation. Therefore, accurate film thickness measurements at small-scale would improve the agreement. We note that Radcliffe's correlation, which appears to provide reasonable prediction at large scale, gives errors of over 100 percent at the small scale! Results from present analysis are consistently close to measurement data for both large and small-scale atomizers.

4 Conclusions

A comprehensive model to predict the performance of a simplex atomizer has been established. The CFD model based on the ALE method can accurately predict the internal flow features and properties of the liquid sheet emanating from the nozzle. It is found that the atomizer geometric constant ($K = A_p/(D_s d_o)$) and other geometric parameters (L_s/D_s and D_s/d_o) significantly affect the atomizer performance. As atomizer geometric constant increases, discharge coefficient and film thickness at the orifice increases while spray angle decreases. The film thickness was found to increase with L_s/D_s and decrease with D_s/d_o.

A temporal linear stability analysis was performed for cylindrical liquid sheets under three-dimensional disturbances. The instability model incorporates swirling velocity components, finite film thickness and radii that are essential features of conical liquid sheets emanating from simplex atomizer. It is observed that the relative velocity between the liquid and gas phases, gas-liquid density ratio, and surface curvature enhance the interfacial aerodynamic instability. As Weber number and density ratio increase, both the wave growth rate and unstable wave number range increases. The combination of axial and swirling velocity components is more effective than the single axial component for disintegration of the liquid sheet. It not only enhances the interfacial instability, but also shifts the dominating mode from axisymmetric to the helical mode. Based on the proposed breakup model and stability analysis, mean drop sizes are predicted for both large and small-scale atomizers. Our predictions agree well with experimental data at both large and small scales.

Acknowledgment

This work is supported by Parker Hannifin Corporation and by NASA LeRC under grant NAG3-1987.

References

Ahmadi, M., and Sellens, R. W., 1993, "A Simplified Maximum Entropy Based Drop Size Distribution," *Atomisation and Sprays,* Vol. 3, pp. 291–310.

Baldwin, B., and Lomax, H., 1978, "Thin Layer Approximation and Algebraic Model for Separated Turbulent Flow," AIAA Paper 78-0257.

Bayvel, L., and Orzechowski, Z., 1993, *Liquid Atomization,* Taylor and Francis, Washington, DC, pp. 172–178.

Benjamin, M., Mansour, A., Samant, U., Jha, S., Liao, Y., Harris, T., and Jeng, S. M., 1998, "Film Thickness, Droplet Size and Correlations for Large Pressure-Swirl Atomizers," Paper No. 98-IG-537, ASME/IGTI Conference and Exhibition, Stockholm, Sweden.

Clark, C. J., and Dombrowski, N., 1972, "Aerodynamic Instability and Disintegration of Inviscid Liquid Sheets," *Proceeding of Royal Society London A,* Vol. 329, pp. 467–478.

Couto, H. S., Carvalho, J. A., and Netto, D. B., 1997, "Theoretical Formulation for Sauter Mean Diameter of Pressure-Swirl Atomizers," *Journal of Propulsion and Power,* Vol. 13, No. 5, pp. 691–696.

Crapper, G. D., Dombrowski, N., and Pyott, G. A. D., 1975, "Kevin-Helmholtz Wave Growth on Cylindrical Sheets," *Journal of Fluid Mechanics,* Vol. 68, pp. 497–502.

Dombrowski, N., and Hooper, P. C., 1962, "The Effect of Ambient Density on Drop Formation in Sprays," *Chemical Engineering Science,* Vol. 17, pp. 291–305.

Dombrowski, N., and Johns, W. R., 1962, "The Aerodynamic Instability and Disintegration of Viscous Liquid Sheets," *Chemical Engineering Science,* Vol. 18, pp. 203–214.

Dombrowski, N., and Johns, W. R., 1963, "The Aerodynamic Insdtability and Disintegration of Viscous Liquid Sheets," *Chemical Engineering Science,* Vol. 18, pp. 203–214.

Dumouchel, C., Ledoux, M., Bloor, M. I. G., Dombrowski, N., and Ingham, D. B., 1990, "The Design of Pressure Swirl Atomizers," Proceedings, 23th Symposium (International) on Combustion, The Combustion Institute, Pittsburgh, PA, pp. 1461–1467.

Giffen, E., and Muraszew, A., 1953, *The Atomization of Liquid Fuels,* Chapman & Hall Ltd., London, pp. 100–116.

Hagerty, W. W., and Shea, J. F., 1955, "A Study of the Stability of Plane Fluid Sheets," *Journal of Applied Mechanics,* Vol. 22, No. 4, pp. 509–514.

Holtzclaw, D., Sakman, T., Jeng, S. M., Jog, M. A., and Benjamin, M., 1997, "Investigation of Flow in a Simplex Fuel Nozzle," AIAA Paper 97-2970.

Jeng, S. M., Jog, M. A., and Benjamin, M. A., 1998, "Computational and Experimental Study of Liquid Sheet Emanating from Simplex Fuel Nozzle," *AIAA Journal,* Vol. 36, No. 2, pp. 201–207.

Lee, J. G., and Chen, L.-D., 1991, "Linear Stability Analysis of Gas-Liquid Interface," *AIAA Journal,* Vol. 29, No. 10, pp. 1589–1595.

Lefebvre, A. H., 1989, *Atomization and Sprays,* Hemisphere Publishing Corp., Bristol, PA, pp. 82–90.

Li, X., and Tankin, R. S., 1991, "On the Temporal Instability of a Two-Dimensional Viscous Liquid Sheet," *Journal Fluid Mechanics,* Vol. 226, pp. 425–443.

Liao, Y., 1999, "Instability and Breakup of Liquid Sheets and Liquid Jets," Ph.D thesis, University of Cincinnati, Ohio.

Meyer, J., and Weihs, D., 1987, "Capillary Instability of An Annular Liquid Jet," *Journal of Fluid Mechanics,* Vol. 179, pp. 531–545.

Panchagnula, M. V., Sojka, P. E., and Santangelo, P. J., 1996, "On the Three-Dimensional Instability of a Swirling, Annular, Inviscid Liquid Sheet Subject to Unequal Gas Velocities," *Physics of Fluids,* Vol. 8, No. 12, pp. 3000–3312.

Rayleigh, L., 1879, "On the Instability of Jets," *Proceedings of the London Mathematical Society,* Vol. 10, pp. 4–13.

Rizk, N. K., and Lefebvre, A. H., 1985, "Internal Flow Characteristics of Simplex Swirl Atomizers," *Journal of Propulsion and Power,* Vol. 1, pp. 193–199.

Shen, J., and Li, X., 1996, "Instability of an Annular Viscous Liquid Jet," *ACTA Mechanica,* Vol. 114, pp. 167–183.

Squire, H. B., 1953, "Investigation of the Instability of a Moving Liquid Film," *British Journal of Applied Physics,* Vol. 4, pp. 167–169.

Yule, A. J., and Chinn, J. J., 1997, "Pressure Swirl Atomizer Internal Flow and Performance," Proceedings, 10th Annual Conference on Liquid and Spray Systems, ILASS-Americas, Irvine, CA, pp. 90–94.

Wang, X. F., and Lefebvre, A. H., 1987, "Mean Drop Sizes from Pressure-Swirl Nozzles," *Journal of Propulsion and Power,* Vol. 3, No. 1, pp. 11–18.

APPENDIX

Coefficients in the dispersion equation, Eq. (26), are listed below.

$$a_4 = C_1C_4 + C_7C_{10} \quad a_3 = C_1C_5 - C_2C_4 - C_7C_{11} - C_8C_{10}$$

$$a_2 = -C_1C_6 - C_7C_{12} + C_8C_{11} - C_2C_5 - C_3C_4 - C_9C_{10}$$

$$a_1 = C_2C_6 - C_3C_5 + C_8C_{12} + C_9C_{11} \quad a_0 = C_3C_6 + C_9C_{12}$$

$$C_1 = -B_n + g_oG_n$$

$$C_2 = 2\bar{k}G_n\sqrt{\frac{g_o\mathrm{We}_o}{\mathrm{We}_l}} - 2\left(n\sqrt{\frac{\mathrm{We}_s}{\mathrm{We}_l}} + \bar{k}\right)B_n$$

$$C_3 = -\bar{k}^2G_n\frac{\mathrm{We}_o}{\mathrm{We}_l} + \left(n\sqrt{\frac{\mathrm{We}_s}{\mathrm{We}_l}} + \bar{k}\right)^2 B_n + \frac{\bar{k}}{\mathrm{We}_l}(1 - n^2 - \bar{k}^2) + \frac{\mathrm{We}_s}{\mathrm{We}_l}\bar{k}$$

$$C_4 = -g_iH_n - C_n$$

$$C_5 = 2g_i\bar{k}H_n\sqrt{\frac{g_i\mathrm{We}_i}{\mathrm{We}_l h}} + 2\left(\frac{n}{h^2}\sqrt{\frac{\mathrm{We}_s}{\mathrm{We}_l}} + \bar{k}\right)C_n$$

$$C_6 = \frac{\bar{k}^2H_n}{h}\frac{\mathrm{We}_i}{\mathrm{We}_l} + \left(\frac{n}{h^2}\sqrt{\frac{\mathrm{We}_s}{\mathrm{We}_l}} + \bar{k}\right)^2 C_n + \frac{\bar{k}}{h^2\mathrm{We}_l}(1 - n^2 - h^2\bar{k}^2) - \frac{\bar{k}}{h^3}\frac{\mathrm{We}_s}{\mathrm{We}_l}$$

$$C_7 = S_n \quad C_8 = \left(\frac{n}{h^2}\sqrt{\frac{\mathrm{We}_s}{\mathrm{We}_l}} + n\sqrt{\frac{\mathrm{We}_s}{\mathrm{We}_l}} + 2\bar{k}\right)S_n$$

$$C_9 = -\left(\frac{n}{h^2}\sqrt{\frac{\mathrm{We}_s}{\mathrm{We}_l}} + \bar{k}\right)\left(n\sqrt{\frac{\mathrm{We}_s}{\mathrm{We}_l}} + \bar{k}\right) \quad C_{10} = Q_n$$

$$C_{11} = \left(\frac{n}{h^2}\sqrt{\frac{\mathrm{We}_s}{\mathrm{We}_l}} + n\sqrt{\frac{\mathrm{We}_s}{\mathrm{We}_l}} + 2\bar{k}\right)Q_n$$

$$C_{12} = -\left(\frac{n}{h^2}\sqrt{\frac{\mathrm{We}_s}{\mathrm{We}_l}} + \bar{k}\right)\left(n\sqrt{\frac{\mathrm{We}_s}{\mathrm{We}_l}} + \bar{k}\right)Q_n$$

$$H_n = \frac{I_n(kR_a)}{I_n'(kR_a)} \quad G_n = \frac{K_n(kR_b)}{K_n'(kR_b)}$$

$$B_n = \frac{I_n'(kR_a)K_n(kR_b) - I_n(kR_b)K_n'(kR_a)}{I_n'(kR_a)K_n'(kR_b) - I_n'(kR_b)K_n'(kR_a)}$$

$$C_n = \frac{I_n'(kR_b)K_n(kR_a) - I_n(kR_a)K_n'(kR_b)}{I_n'(kR_a)K_n'(kR_b) - I_n'(kR_b)K_n'(kR_a)}$$

$$S_n = \frac{I_n'(kR_b)K_n(kR_b) - I_n(kR_b)K_n'(kR_b)}{I_n'(kR_a)K_n'(kR_b) - I_n'(kR_b)K_n'(kR_a)}$$

$$Q_n = \frac{I_n(kR_a)K_n'(kR_a) - I_n'(kR_a)K_n(kR_a)}{I_n'(kR_a)K_n'(kR_b) - I_n'(kR_b)K_n'(kR_a)}$$

Shift Reactors and Physical Absorption for Low-CO_2 Emission IGCCs

P. Chiesa
pchiesa@clausius.energ.polimi.it

S. Consonni
stefano.consonni@polimi.it

Dipartimento di Energetica,
Politecnico di Milano,
Piazza Leonardo da Vinci 32,
Milan 20133,
Italy

Integrated gasification combined cycles (IGCC) exhibit conditions particularly favourable to the sequestration of CO_2. The concept pursued in this paper is the generation of syngas low in carbon, where most of the heating value of the coal fuel is carried by hydrogen. Catalytic shift reactors convert most of the CO in the syngas into CO_2, which is subsequently removed by physical absorption and then compressed to make it suitable for transport and permanent storage. Energy balances, performance, and cost of electricity are evaluated for two plants based on a Texaco gasifier and a large, heavy-duty gas turbine giving an overall IGCC power output between 350 and 400 MW. In one plant, the raw syngas exiting the gasifier is cooled in a high-temperature, radiative cooler; in the other it is quenched by the injection of liquid water. With respect to "conventional" Texaco IGCCs, the reduction of specific CO_2 emissions by 90 percent reduces LHV efficiency from 5 to 7 percentage points and increases the cost of electricity of about 40 percent. These penalties can be reduced by accepting lower reductions of CO_2 emissions. Compared to the semi-closed cycle considered by other authors, where CO_2 is the main component of the gas turbine working fluid, the plants analyzed here exhibit higher efficiency over the whole range of specific CO_2 emissions.

1 Background and Scope

Concerns about climate changes induced by the emission of greenhouse gases call for new strategies toward the use of fossil fuels. Carbon dioxide emissions from the combustion of fossil fuels now account for more than 50 percent of the incremental greenhouse effect attributed to anthropogenic activities (Houghton et al., 1990); without corrective measures such percentage will increase, because the ongoing phase-out of CFCs will be paralleled by increased fossil fuel burning resulting from growth in population and incomes.

Renewable and nuclear energy could virtually eliminate all CO_2 emissions related to the production of power or heat. However, the widespread use of renewable energy is subject to technical, economic, and infrastructural challenges, while a massive diffusion of nuclear reactors faces critical security, environmental, and political issues (Turkenburg, 1997). Deep reductions in CO_2 emissions can be achieved most effectively by an appropriate combination of various low CO_2 emission technologies (Johansson et al., 1996). One of them is carbon sequestration, whereby part (or even all) of the carbon in the fossil fuel is diverted to an appropriate site for permanent storage, typically as liquid CO_2 (Turkenburg, 1997); appropriate storage sites are depleted oil or natural gas wells, aquifers, salt caves, or deep oceanic waters (*Capture,* 1993; Holloway, 1997; Freund and Ormerod, 1997). The carbon emitted by a power plant can be sequestered according to three basic concepts:

1 Remove CO_2 from combustion gases through an end-of-pipe separation process placed ahead of the stack, with no or minimal modications of the existing plant. Most suitable technology appears chemical absorption (Smelser et al., 1991); physical absorption is unattractive due to the low pressure of the combustion gases to be treated (Kohl and Riesenfeld, 1985, chap. 14; Weiss, 1997); even more so cryogenic separation (*Capture,* 1993); other technologies like membranes require further development and testing (Van der Sluijs et al., 1992; Feron et al., 1992; Kubek et al., 1997).

2 Restructure the energy conversion process so that carbon (as CO_2) can be removed at a convenient stage of the process. Generally, this strategy cannot be applied to existing plants. The most suitable separation technology must be selected based on the type of process and the operating conditions at the point where CO_2 is removed.

3 "Decarbonize," the fuel, i.e., remove carbon (also in this case as CO_2) to produce hydrogen (Blok et al., 1997; Socolow, 1997). Hydrogen can then be used as a substitute of the original fossil fuel with minor modifications of the existing plants; yet it can allow the use of more efficient and more environmentally benign technologies like fuel cells.

These three concepts share the potential for achieving substantial reductions of CO_2 emissions without radical changes of the systems now used for power production and without abrupt cuts of fossil fuel usage.

This paper concentrates on two schemes following concept (2), i.e., two "restructured" large scale, coal-fired IGCCs. These plants are particularly suitable to the application of concept (2) because: (i) the cost and complexity of CO_2 separation, transport and storage make it feasible only at large scale, (ii) carbon sequestration is most interesting for coal, which exhibits the highest CO_2 production per net electric kWh, and (iii) in a IGCC it is relatively simple to carry out CO_2 removal under favorable conditions. In the plants proposed here, most of the carbon in the coal fuel is discharged as pressurized, liquid CO_2; emissions to the atmosphere comprise water vapour, the excess air required for adequate combustion conditions and some CO_2.

2 Plant Configurations

In order to attain carbon sequestration, an IGCC can be "restructured" according to two basic concepts:

a Make CO_2 the main component of the gas turbine working fluid by burning the fuel into pure oxygen. In this case there

---

Contributed by the International Gas Turbine Institute and presented at the International Gas Turbine and Aeroengine Congress and Exhibition, Stockholm, Sweden, June 2–5, 1998. Manuscript received by the ASME Headquarters April 1, 1998. Paper No. 98-GT-396. Associate Technical Editor: R. Kielb.

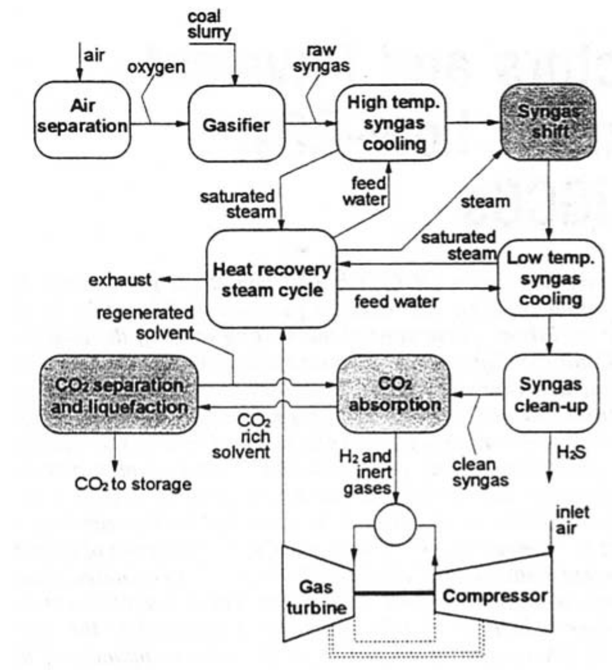

Fig. 1 Schematic of the IGCC with shift reaction and CO_2 removal considered in the paper. Shaded blocks denote subsystems extraneous to conventional IGCCs. The raw syngas exiting the gasifier can be cooled either through a heat exchanger generating HP steam or by quenching it with liquid water.

is no need for a separation process: CO_2 is removed by bleeding part (or all) of the working fluid at an appropriate point of the cycle.

b Keep ambient air as the basic working fluid and remove CO_2 by a separation process conveniently located along the cycle.

Concept (a) translates into the semi-closed cycle analyzed by Mathieu and De Ruick (1993), Ulizar and Pilidis (1997), and Chiesa and Lozza (1998). Rather than being vented to the atmosphere, the gas turbine exhausts—almost exclusively comprised of CO_2 and H_2O—are cooled (thereby condensing most of the water), deprived of the CO_2 generated in the combustor and then sent back to the gas turbine compressor. This configuration, which can be adapted to any fuel, suffers from the following two caveats: (i) large auxiliary power consumption and investment cost; and (ii) the need to adapt the gas turbine to a working fluid (mainly CO_2 and H_2O) rather different from that of commercial engines. Since the use of unmodified commercial engines is crucial in determining the success of novel plant arrangements, the second handicap is very severe.

This work focuses on configurations following concept (b), i.e., schemes involving minimal changes to the gas turbine. The schematic of the plant configuration is shown in Fig. 1. Compared to "conventional" IGCCs, the system includes the following three additional components:

a) a shift reactor placed downstream of the syngas cooler (or the quench chamber), which converts almost all the CO in the syngas into CO_2 according to the water-gas shift reaction:

$$\mathrm{CO} + \mathrm{H_2O_{vap}} \rightarrow \mathrm{CO_2} + \mathrm{H_2} + 44.477\ \mathrm{MJ/Mol_{CO}} \qquad (1)$$

b) a physical absorption unit, where CO_2 is dissolved into a selective liquid solvent like, for example, Selexol

c) a separation and liquefaction unit, where CO_2 is released from the solvent and then brought to the conditions required for its transport and storage

Given the extensive operating experience accumulated in the chemical industry, none of these three components requires specific technological development, nor do they require substantial changes to other components of the IGCC.

The exotermic conversion of CO into CO_2 taking place in the shift reactor "charges" most of the syngas heating value to hydrogen; in fact, the two Moles on the left hand side of Eq. (1) ($CO + H_2O_{vap}$) exhibit a LHV of 282.985 MJ, while the LHV of the two moles on the right hand side ($CO_2 + H_2$) is 238.508 MJ[1]. The heat developed in the reaction—at the reference temperature of 25°C, 44.477 MJ/Mol_{CO}—is recovered in the steam cycle. The "relocation" of heating value from CO to H_2 allows maintaining good thermodynamic performance; despite the removal of carbon, most of the chemical energy of the coal fuel remains in the H_2-rich syngas, whereby it can be used most efficiently in the combined cycle.

The CO_2 generated in the shift reactor is most efficiently removed downstream of low temperature syngas clean-up, where the combination of low temperature, relatively high molar concentrations, and high pressure[2] is particularly favorable to physical absorption into a liquid. CO_2 and other gases captured in the absorber are then stripped in a separation unit which regenerates the solvent for further use, while CO_2 is compressed and liquefied to make it ready for transport and storage.

CO_2 emissions are determined by the amount of CO and CO_2 in the clean syngas fed to the gas turbine combustor; in turn, the amount of CO is controlled by the conversion of CO to CO_2 in the shift reactors, while the amount of CO_2 depends on the removal efficiency of the absorption system[3]. Low CO_2 emissions require both high CO to CO_2 conversion and high CO_2 removal efficiency; since both these requirements penalize performances, there exist a trade-off between CO_2 emissions and electric efficiency.

2.1 Syngas Cooler Versus Quench. Figures 2 and 3 illustrate two plants embodying the concept of Fig. 1. Both plants are centered around a pressurized, oxygen-blown, entrained-

Nomenclature

m = mass flow rate, kg/s
p = pressure, bar
T = temperature, °C or K
V = volumetric flow rate, m^3/s
μ = ratio between mass flow of steam (or water) added ahead of shift reactors and coal mass flow

Acronyms

HHV, LHV = higher/lower heating value
HP, MP, LP = high/medium/lower pressure
IGCC = integrated gasification combined cycle
NGCC = natural gas fired combined cycle
PCSC = pulverized coal steam cycle

---

[1] Heat of reactions and heating values are evaluated according to the JANAF Tables (Stull and Prophet, 1971).

[2] Basically, all gasification technologies of interest produce syngas at a pressure at least equal to the pressure required for injection into the gas turbine combustor.

[3] Since the solvent also captures some CO, the CO concentration in the gas turbine fuel also depends on the absorption system. However, in most cases the influence of the absorber on CO is minimal, even more when the separation unit includes provisions to recycle non-CO_2 gases.

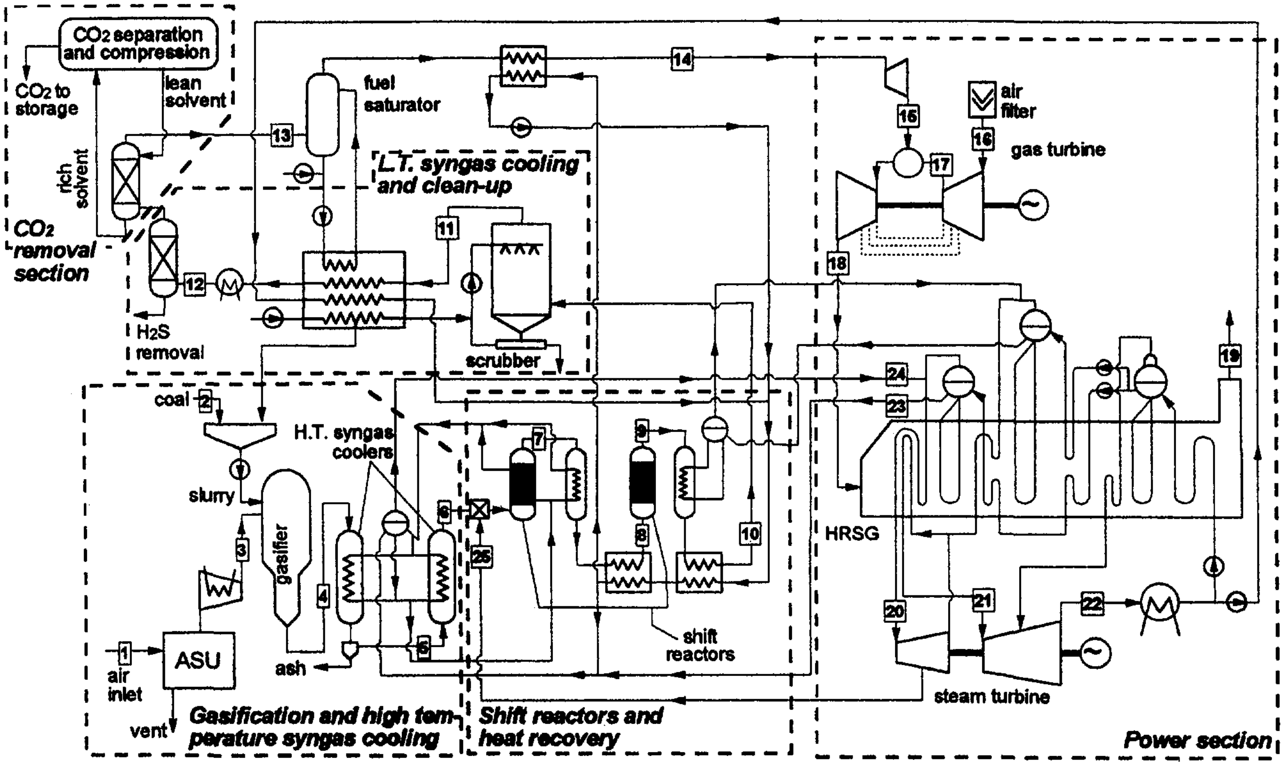

Fig. 2 Plant with high temperature radiative syngas coolers

flow gasifier fed with a slurry of coal and water, the technology developed by Texaco with many applications in the production of synthesis gas and IGCCs (Black and McDaniel, 1996; Hough et al., 1997). Application to other entrained-flow gasifiers would not entail relevant variations, except for what required to guarantee an adequate amount of water in the syngas that

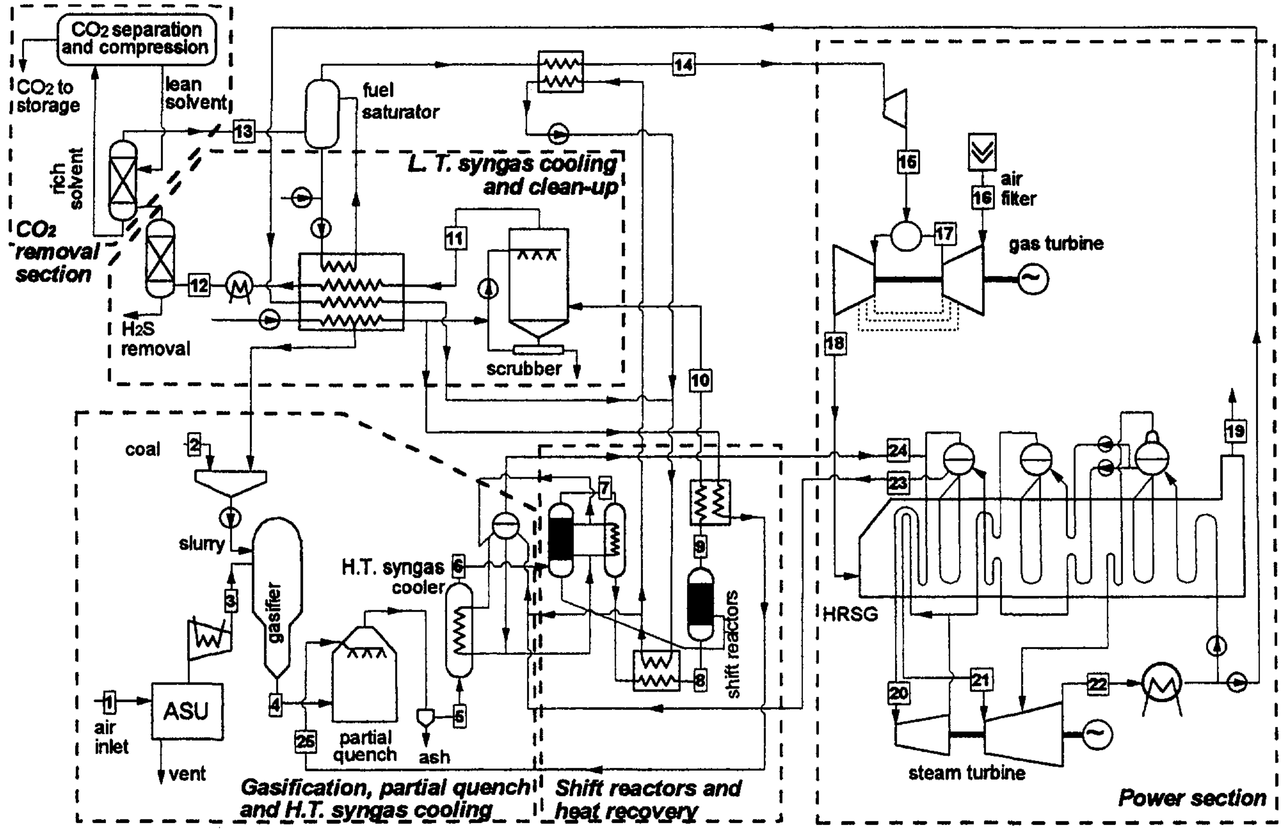

Fig. 3 Plant with partial quench and medium-temperature convective cooling of the raw syngas

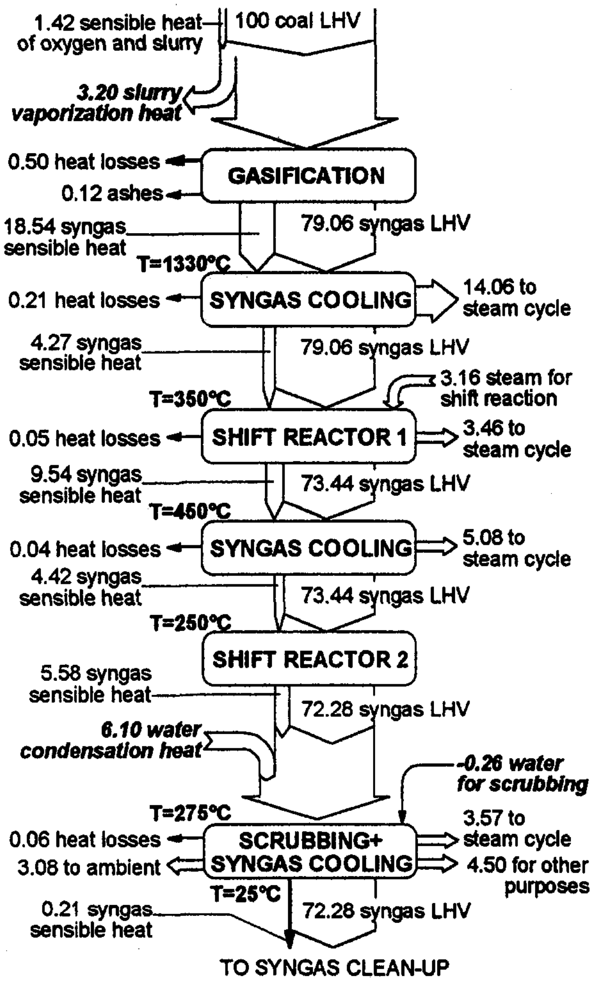

Fig. 4 Energy balance of gasification, shift reactions and syngas cooling. Bold items represent latent heat of evaporation or condensation, which by definition cannot be included into the LHV.

enters the shift reactor[4]. Application to fluidized bed or fixed bed gasifiers may require significant changes of plant arrangement and/or operating parameters.

In both schemes in Fig. 2 and 3 the gasifier generates raw syngas at 1327°C (1600 K), 60 bar; oxygen is provided by a nonintegrated air separation unit and pressurized by an intercooled compressor; the water vapour content in the raw syngas is significant (17.7 percent by volume) but insufficient to carry out a complete conversion of CO to CO_2. The conversion of CO to CO_2 is split between two reactors in series: one at about 450°C, the other at about 250°C. The heat released by the first reactor generates HP steam; the heat released by the second reactor generates MP steam (scheme with syngas cooler) or hot, pressurized water (scheme with quench). With a single reactor, high CO to CO_2 conversion would require operation at the lowest temperature of 250°C (see Chap. 3), whereby no generation of HP steam and detrimental effects on overall efficiency. The syngas exiting the lower temperature shift reactor is scrubbed with water to remove solids and soluble contaminants, cooled to 25°C, and then passed through two physical absorption columns to remove H_2S and CO_2. The CO_2-free clean syngas is then saturated, superheated, depressurized in a turbo-expander and finally injected into the gas turbine combustor. Low temperature heat released by the saturated syngas exiting the scrubber (at about 180°C) is used to heat water for the coal slurry, saturate the clean syngas, preheat HP feedwater.

The basic difference between the schemes in Fig. 2 and 3 lies in the technique used to cool the raw syngas below the ash melting point (approximately 1050 ÷ 1100°C). The scheme in Fig. 2 features a high-temperature radiative heat exchanger that cools the syngas to 900°C, followed by a convective heat exchanger that cools it further down to 350°C; the cool syngas is then mixed with steam bled from the steam turbine to insure an adequate amount of water for a complete shift reaction. In the scheme in Fig. 3 the extra-water needed to achieve the required CO to CO_2 conversion is injected into the raw syngas at the gasifier exit as liquid water (previously heated with syngas exiting the clean-up system and with heat released after the second shift reactor). As long as the amount of liquid water injected into the syngas is enough to lower its temperature below the ash melting point, this practice allows eliminating the expensive (and often troublesome) high-temperature radiative coolers. In all situations analyzed here, the amount of liquid water that warrants the required CO to CO_2 conversion does

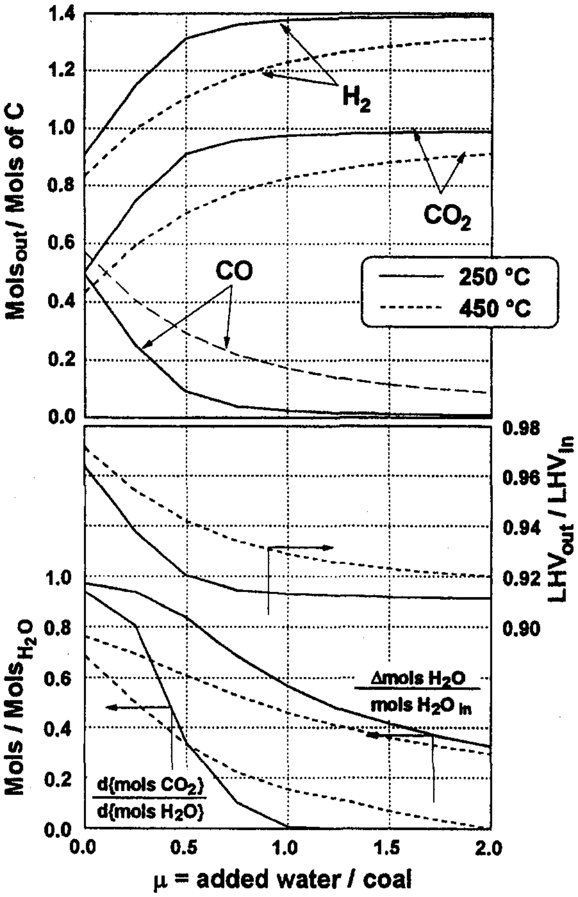

Fig. 5 Evolution of shift reaction versus μ. The mixture entering the shift reactor comprises raw syngas produced by the gasifier and the amount of water shown on the abscissa axis; the mixture at outlet is the one corresponding to chemical equilibrium at 250°C and 450°C. Since chemical equilibrium depends only on temperature and atomic population, diagrams apply both to plants with syngas cooler (Fig. 2) and with partial quench (Fig. 3). The ratio $\Delta\{mol_{H_2O}\}/\{mol_{H_2O,in}\}$ shows how many of the moles of water entering the reactor are converted to H_2. The derivative $d\{mol_{CO_2}\}/d\{mol_{H_2O}\}$ shows how many additional mols of CO_2 are produced as a result of an infinitesimal increase of the water content in the mixture entering the reactor. LHV_{IN} and LHV_{OUT} are both expressed as MJ per kg of gas entering the reactor, so that their ratio is nondimensional.

---

[4] In a dry-feed system like the Shell gasifier, the water in the raw syngas is much less, whereby the amount to be injected ahead of the shift reactors to insure adequate CO to CO_2 conversion is much larger. Injecting more water (or steam) penalizes the overall cycle performance.

Table 1 Assumptions maintained throughout all calculations

POWER CYCLE	
Air mass flow at gas turbine inlet, kg/s	600
Pressure ratio	15
Gas turbine inlet temperature, °C	1280
Inlet pressure losses (filter), kPa	1
Maximum steam evaporation pressure, bar	110
Steam temperature at admission, °C	538
Condensation pressure, bar	0.05
HRSG gas side pressure losses, kPa	3
GASIFICATION SECTION	
Water/coal ratio in slurry	0.323
Gasification pressure, bar	60
Syngas temperature at gasifier exit, K	1600
Heat losses in gasifier, % of input LHV	0.5
Syngas cooler heat losses, % of heat exchanged	1.5
Overall pressure losses along syngas path, bar	~10
Auxiliary power consumption, % of input LHV	1
Coal composition (Illinois#6), % by weight: Carbon: 61.27; Hydrogen: 4.69; Oxygen: 8.83, Nitrogen: 1.10; Sulfur: 3.41; Moisture: 12.00; Ash: 8.70 LHV: 24.83 MJ/kg; HHV: 26.14MJ/kg	

actually cool the syngas below the ash melting point, although it does not bring the syngas to saturation. Therefore, the proper designation of the configuration in Fig. 3 is ''partial quench''. Ahead of the shift reactors, the unsaturated, partially quenched syngas is cooled in a convective HP evaporator arranged in parallel with the evaporator of the higher temperature (450°C) shift reactor. The heat released by the lower temperature (250°C) shift reactor is used most effectively to heat the pressurized water to be injected in the quench chamber.

3 The Shift Reactor

The shift reactor ''relocates'' most of the chemical energy of the coal fuel to molecular hydrogen. At the conditions reported in Table 3 (corresponding to $\mu = 1$), each kg of coal with a LHV of 24.826 MJ generates 0.497 kg of H_2-rich saturated syngas with a LHV of 17.225 MJ (34.663 MJ per kg of syngas). This means that about 70 percent of the chemical energy of the coal fuel becomes the input to the combined cycle; the remaining 30 percent turned into heat is ''recycled'' to the steam cycle and partially dissipated to ambient (see Fig. 4).

The shift reaction is well known and widely practiced throughout the chemical industry. A typical application is in plants for hydrogen production by natural gas reforming, where the shift reactor converts the CO left downstream of the steam reformer. Being exotermic, the reaction is favored by low temperatures; on the other hand, low temperatures decrease the speed of reaction, thereby imposing the use of a catalyst to limit the size of the reactor. Although many of the catalysts now used in commercial plants (e.g., chromium promoted iron on alumina) can be poisoned by even very small amount of sulfur, ample experience has been accumulated with sulfur-tolerant catalysts suitable to coal gasification plants. One catalyst developed by Haldor Topsoe has been extensively operated in the 70s and the 80s in Texaco coal gasification plants producing hydrogen for ammonia synthesis in Sweden, Denmark, and the Canary Islands (Storgaard, 1997); rather than being poisoned by sulfur compounds, the catalyst used in those plants does require sulfur (up to 1–1.5% by volume) to operate properly.

Due to the catalyst, the concentrations of CO, CO_2, H_2, and H_2O at the exit of the reactor are always very close to equilibrium. Figure 5 reports equilibrium concentrations, heating value and fraction of water consumed in the reaction as a function of the amount of steam added to the reacting mixture, for two temperatures of the mixture at equilibrium exiting the shift reactor. The conversion to CO_2 of the carbon in the coal fuel is enhanced by low temperatures (the reaction is exotermic) and by excess amounts of steam. At 250°C, the conversion to CO_2 of 90 percent of total carbon requires the addition of 0.5 kg of steam per kg of coal, which become about 1.75 kg_{steam}/kg_{coal} at 450°C; such 90 percent carbon conversion to CO_2 causes a reduction of about 8 percent of the lower heating value.

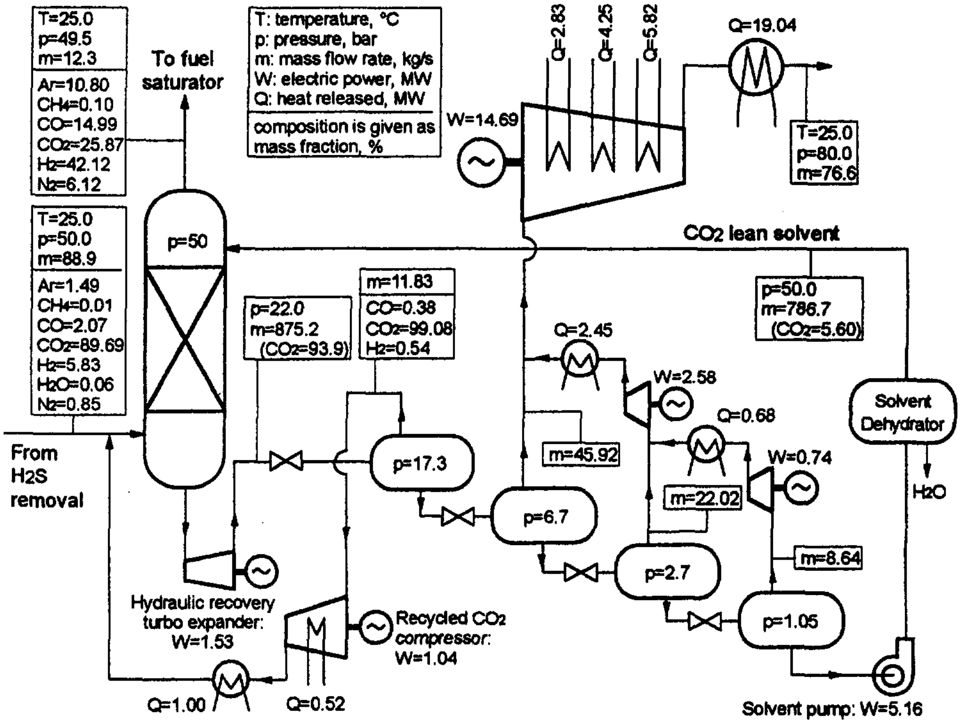

Fig. 6 Configuration of CO_2 removal, compression, and liquefaction section. Mass flows, pressures, and power consumptions refer to the operating conditions in Table 3 (syngas cooler plant in Fig. 2).

Table 2 Performances of a natural-gas-fired combined cycle based on the same heavy-duty turbine assumed to assess IGCCs (assumptions listed in Table 1)

Fuel LHV, MJ/kg	44.77
Gas turbine power, MW	215.3
Steam cycle power, MW	123.4
Plant net output, MW	338.7
Plant net efficiency,%	55.10
T at turbine outlet, °C	596.2
T at stack, °C	85.7
$m_{fuel}/m_{compressor\ inlet}$	0.023
V_{fuel}, Nm^3/s	17.52
m steam at turbine inlet, kg/s	69.4
m steam at turbine outlet, kg/s	94.2
CO_2 emissions, kg/kWh_{el}	0.358

The higher μ the smaller the fraction of H_2O converted to H_2. At 250°C and $\mu = 0.5$, more than 80 percent of the water in the mixture entering the reactor participates to the conversion of CO, turning to CO_2 about 90 percent of the carbon. With $\mu = 2$ carbon conversion to CO_2 increases to 99 percent, but only one third of the water is effectively consumed in the reaction; the other two thirds act as an inert diluent. Since water addition penalizes cycle efficiency, a large fraction of unreacted water should be avoided. The derivative $d\{mol_{CO2}\}/d\{mol_{H2O}\}$ in the lower diagram of Fig. 5 is the marginal production of CO_2 made possible by the addition of water; its behavior makes clear that at 250°C the addition of water beyond 1 kg_{H2O} per kg of coal is useless, because the extra water would not generate any extra CO_2; at 450°C the addition of water keeps increasing the CO to CO_2 conversion up to about $\mu = 2$.

4 CO_2 Removal

The two most experienced commercial technologies for the separation of CO_2 from gaseous streams are chemical absorption (typically based on aqueous solutions of ethanolamines) and physical absorption (Kohl and Riesenfeld, 1985, chps. 2 and 14). In both cases the capture of CO_2 is favored by low temperature, which increases CO_2 solubility, and requires that the gas is free of contaminants that could impair the solvent properties. For these reasons, the most suitable arrangement of CO_2 removal is downstream of a cold clean-up system.

In the IGCC considered here, the partial pressure of CO_2 in the cold, clean syngas is 13 ÷ 20 bar (total pressure about 50 bar and mol fraction 26–40 percent), a situation particularly favourable to physical absorption (Schütz et al., 1992). In fact, physical absorption is typically proposed also for the removal of H_2S. The plants in Fig. 2 and 3 include two physical absorption systems operating at 25°C placed downstream of the low temperature syngas coolers: the first removes H_2S, the second removes CO_2[5]. The power consumption for the removal of H_2S is small and can simply be considered as part of auxiliary power consumption (in our case 1 percent of gross thermal input, see Table 1). On the contrary, the power consumption for the removal and compression of CO_2 can be very relevant, and must be explicitly accounted for; the estimates presented here refer to the Selexol solvent commercialized by Union Carbide, for which there is large operating experience on H_2S-rich and CO_2-rich gases (Bucklin and Schendel, 1984).

4.1 Operating Conditions. The operating temperature of the absorption column should be optimized to find the best trade-off between investment and O&M cost; higher temperatures reduce cost and heat losses of syngas cooling (downstream of the scrubber), but require larger solvent flow and larger power consumption due to lower CO_2 solubility. Optimization has not been attempted because it requires accurate estimates of investment cost and detailed knowledge of the thermo-physical characteristics of the solvent, which are proprietary[6]. The results presented here are based on data given by Bucklin and Schendel (1984) for an absorption temperature of 25°C, a value typical of Selexol applications.

Figure 6 reports configuration and operating parameters of the CO_2 removal and compression section for the case with syngas cooler and $\mu = 1$. Clean syngas enters the bottom of the absorption tower and flows upward counter-current to Selexol. The CO_2-rich solvent collected at the bottom of the tower goes to four flash drums connected in series, where CO_2 is deabsorbed as a consequence of lower pressure. Lean Selexol exiting the last drum is pumped back to the top of the tower. The pressure drop between the absorption column and the first

Table 3 Operating conditions of plants in Figs. 2 and 3 for $\mu = 1$. Numbers in leftward column refer to state points in the figures.

	Syngas cooler (fig. 2)			Partial quench (fig. 3)		
Pt	T,°C	p,bar	m,kg/s	T,°C	p,bar	m,kg/s
1	15.0	1.01	129.1	15.0	1.01	128.3
2	15.0	1.01	37.2	15.0	60.00	37.0
3	337.0	72.00	29.7	337.0	72.00	29.5
4	1326.9	60.00	78.9	1326.8	60.00	78.4
5	900.0	58.80	75.7	623.3	57.00	112.2
6	350.0	57.00	75.7	350.0	57.00	112.2
7	450.0	55.86	112.9	450.0	55.86	112.2
8	225.0	55.30	112.9	225.0	55.30	112.2
9	275.2	54.75	112.9	275.2	54.75	112.2
10	200.0	53.66	112.9	200.0	53.66	112.2
11	186.3	53.12	114.2	186.3	53.12	113.5
12	25.0	49.95	91.2	25.0	49.95	90.6
13	25.0	49.95	12.3	25.0	49.95	12.2
14	250.0	48.60	18.5	250.0	48.60	16.9
15	131.5	17.31	18.5	132.1	17.31	16.9
16	15.0	1.00	600.0	15.0	1.00	600.0
17	398.4	15.05	530.0	398.4	15.05	530.4
18	592.8	1.04	618.5	592.3	1.04	616.9
19	80.0	1.01	618.5	80.0	1.01	616.9
20	538.0	101.20	151.7	538.0	101.20	112.5
21	538.0	18.40	123.8	538.0	18.40	124.1
22	32.9	0.05	127.6	32.9	0.05	131.9
23	318.0	110.00	116.0	318.0	110.00	62.3
24	319.0	110.00	146.5	319.0	110.00	83.1
25	454.4	60.00	37.2	261.3	60.00	37.0

CYCLE PERFORMANCE	Syngas Cooler	Partial quench
Gas turbine power, MW	236.4	234.4
Steam cycle power, MW	185.9	183.9
Syngas expander, MW	10.8	10.3
ASU power absorption, MW	42.1	41.8
Other auxiliaries power, MW	10.1	10.1
CO_2 separation and compression, MW	22.7	22.5
Plant net output, MW	358.2	354.2
Plant net efficiency, %	38.77	38.59
CO_2 specific emissions, kg/kWh_{el}	0.070	0.070
CO_2 removal efficiency, %	91.7	91.7

---

[5] H_2S and CO_2 could be removed together in a single absorption column; however, this would raise issues on the disposal of the CO_2–H_2S mixture.

[6] According to the licensor of Selexol, general purpose thermodynamic models like those included into the ASPEN code (*ASPEN PLUS*, 1996), do not give an adequate description of a mixture of homolog hydrocarbons like Selexol (Echt, 1998).

Table 4 Comparison between the performances of "conventional" IGCCs and those of the two configurations with CO_2 removal proposed here

	Syngas cooler (fig. 2)				Partial quench (fig. 3)		
	CO_2 removal				CO_2 removal		
	no	yes	yes	yes	no	yes	yes
μ=added water (or steam)/coal ratio	-	1	0.5	0	1	1	0.5
Air mass flow at GT inlet, kg/s	600	600	600	600	600	600	600
Gas turbine power, MW	241.9	236.4	229.1	227.6	239.6	234.4	228.5
Steam cycle power, MW	199.1	185.9	193.7	197.8	180.2	184.0	192.9
Cycle auxiliaries power, MW	38.2	41.4	40.9	39.6	38.4	41.7	41.0
Cycle net output, MW	402.9	380.9	381.9	385.8	381.4	376.7	380.4
Cycle thermal input (LHW), MW	878.5	923.8	894.8	861.7	872.2	917.9	892.9
Gas turbine thermal input (LHV), MW	668.3	640.8	628.1	631.5	663.7	636.7	627.0
Syngas LHV / Coal fuel LHV	0.761	0.694	0.702	0.733	0.761	0.694	0.702
Cycle net efficiency, %	45.86	41.23	42.68	44.77	43.73	41.04	42.60
CO_2 separation and compression, MW	-	22.7	20.0	12.7	-	22.5	19.9
Plant net output, MW	402.9	358.2	361.9	373.1	381.4	354.2	360.5
Plant net efficiency, %	45.86	38.77	40.44	43.30	43.73	38.59	40.37
$m_{syngas}/m_{compressor\ inlet}$	0.108	0.031	0.029	0.052	0.105	0.028	0.028
V_{syngas} (gasif. sec. outlet), Nm^3/s	64.09	60.46	58.66	56.46	63.63	60.08	58.54
V_{syngas} (satur. at comb.inlet), Nm^3/s	71.69	72.06	63.18	58.16	69.05	69.83	62.54
m steam at turbine inlet, kg/s	127.9	151.7	139.7	127.5	98.6	112.5	123.8
m steam at turbine outlet, kg/s	139.4	127.6	134.1	138.0	147.6	131.9	135.2
Last flash drum pressure, bar	-	1.05	1.05	1.05	-	1.05	1.05
CO_2 absorption removal efficiency, %	-	96.0	95.5	92.3	-	96.0	95.5
Overall CO_2 removal efficiency*, %	0	91.7	81.7	45.6	0	91.7	81.9
CO_2 emissions, kg/s	79.45	6.97	14.66	42.39	78.88	6.91	14.62
CO_2 specific emissions, kg/kWh_{el}	0.710	0.070	0.146	0.409	0.745	0.070	0.146
Temperature at quench outlet, °C	-	-	-	-	626.6	623.3	932.1

* Ratio between CO_2 removed and the amount of CO_2 generated by the oxidation of the coal fuel.

drum is accomplished through an hydraulic turbine to recover at least part of the pumping work. The CO_2 released in each drum enters a series of compressors and intercoolers which bring it to the pressure required for transport and storage.

Since the solubility of H_2 and CO in the Selexol solvent is small but not irrelevant, the amount of H_2 and CO captured together with CO_2 is enough to reduce significantly the syngas heating value[7]. This loss can be avoided by recycling the gas de-absorbed in the first drum as shown in Fig. 6. Since the mol fractions of H_2 and CO in the gas de-absorbed in the first drum are much lower than those in the absorption tower, virtually all the H_2 and CO are released in the first flash drum. Recycling the gas liberated in the first drum restores almost completely the syngas heating value, but increases auxiliary power consumption due to (i) recompression of recycle gas, (ii) release of CO_2 at lower pressure from drums two, three, and four, and (iii) larger CO_2 flow in the tower, whereby larger solvent flow and pumping power. For the cycle parameters considered here, the additional power consumption due to these effects is lower than the additional power output generated by the increase of about 8 MW of syngas heating value.

Drum pressures have been set as follows: (i) the first one (17.3 bar) is the value that limits the fraction of hydrogen carried away by the solvent to 0.1 percent; and (ii) the last one (1.05 bar) insures that the whole plant is above atmospheric pressure; (iii) the remaining two (6.7 and 2.7 bar) are the values giving a constant expansion ratio between two subsequent drums. A sensitivity analysis has shown that the power consumption of the separation and compression section does not change appreciably when these pressures are varied.

The optimal configuration for CO_2 removal and compression also depends on the pressure required by the transport system. The supercritical value of 80 bar chosen here warrants high CO_2 density and, thus, a limited diameter of the pipe for its transport and disposal in oceanic water; this pressure also assures the head required for discharge at a depth between 1000 and 1500 m, where the density of the clathrates formed by CO_2 is higher than the density of oceanic water and thus the probability of CO_2 ascending to the surface is remote (*Capture,* 1993, chp. 2).

5 Calculation Model and Main Assumptions

IGCC efficiency and power output have been estimated by a computer code designed to evaluate heat and mass balances of complex gas-turbine-based power plants, which is extensively described elsewhere (Lozza, 1990; Consonni, 1992; Chiesa et al., 1993; Macchi et al., 1995). Thanks to its modular structure, the code can easily be adapted to analyze unconventional cycles like those considered here; further examples of the capabilities of the model can be found in Consonni et al. (1997), Larson and Consonni (1997), and Chiesa and Lozza (1998).

The power and mass balances of the CO_2 removal and compression section (i.e., the subsystem in Fig. 6) have been estimated by a new, separate piece of software, whereby it is assumed that all the species in the syngas follow Henry's law and the heat of solution is negligible (see the appendix for details). Given the peculiar characteristics of Selexol, a more sophisticated model like ASPEN did not warrant higher accuracy. The

---

[7] At 25°C and same partial pressure, Selexol captures 0.013 mols of H_2 and 0.028 mols of CO for each mol of CO_2 (Bucklin and Schendel, 1984). The mol fraction of H_2 in the syngas entering the absorber is 1.4 to 1.8 times the mol fraction of CO_2 (depending on the water injected ahead of the shift reactors); consequently, at 25°C the absorber captures between 0.018 to 0.023 mols of H_2 for each mol of CO_2.

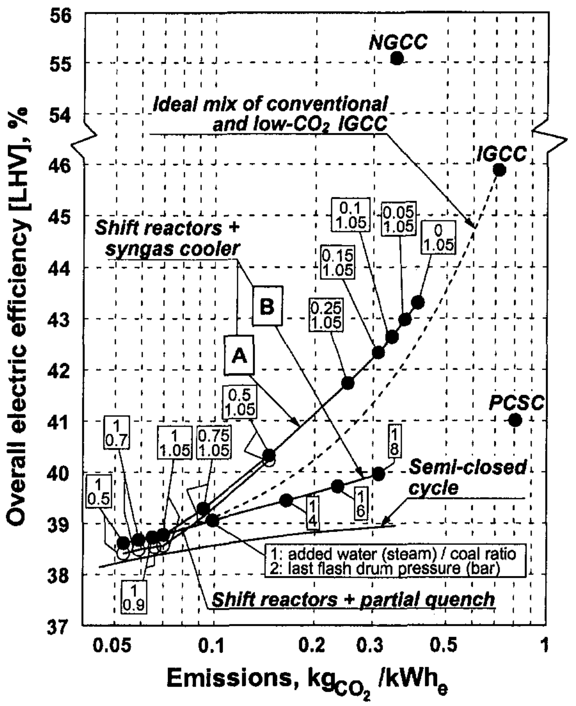

Fig. 7 Efficiency versus CO_2 emissions. All calculations of plants with CO_2 removal assume a CO_2 delivery pressure of 80 bar; numbers in boxes report μ and pressure of last flash drum of plants with physical absorption. The dashed curve refers to a mix of conventional IGCCs (most rightward dot on the curve) and IGCCs with syngas cooler and maximum CO_2 removal (most leftward dot on the curve). The curve for semi-closed cycles is taken from Chiesa and Lozza (1998) and is based on the same assumptions adopted here.

appropriateness of the simplified model described in appendix has been supported by Echt (1998).

The most relevant assumptions adopted to generate the results are summarized in Table 1. The basic characteristics of the gas turbine (air flow, turbine inlet temperature, pressure ratio) are representative of state-of-the-art, large heavy-duties, i.e., what is commonly called ''F'' technology. Steam conditions conform to advanced combined cycle practice: higher pressure and temperature could slighty increase efficiency, but would also entail higher costs and complexity. In the context of such complicated plants, the adoption of conservative steam conditions seems more adequate. The performances achievable by a combined cycle fired with natural gas are reported in Table 2. The scale of the IGCC plant is set by the flow rate of 600 kg/s at the inlet of the gas turbine compressor.

6 Efficiency Versus CO_2 Emissions

Table 3 reports operating conditions and overall performances of the two configurations in Figs. 2 and 3 when μ = 1; based on the calculation procedure outlined in the appendix, about 92 percent of the CO_2 generated by the oxidation of coal is sequestered[8].

Given the penalties incurred by the almost complete removal of CO_2, one may think of reducing them by accepting the removal of only part of the CO_2. Table 4 shows the implications of varying the degree of CO_2 removal, by varying μ. The syngas cooler also includes the case with $\mu = 0$ because the water vapor in the raw syngas is enough to promote the conversion to CO_2 of about half of the carbon; without the syngas cooler, some water must necessarily be injected to cool the gas at least below the ash melting point. Allowing higher CO_2 emissions has marginal effects on power output, but produces substantial efficiency gains.

The penalty due to CO_2 removal is much more severe with the syngas cooler. To achieve a 90 percent reduction of specific CO_2 emissions (kg_{CO2}/kWh_{el}), the net efficiency of the syngas cooler plant drops by about 7 percentage points; with partial quench the drop is about 5 percentage points. Accepting a 80 percent rather than 90 percent reduction of specific CO_2 emissions reduces these penalties to about 5.5 and 3.5 percentage points, respectively. For the assumed CO_2 delivery pressure of 80 bar, the CO_2 separation and compression section illustrated in Fig. 6 requires between 3.4 to 6 percent of the cycle net power.

The enrichment in hydrogen of the syngas allows maintaining the mass flow of syngas to few percent of the compressor air flow (see Table 4), thereby preventing compressor stall. On the other hand, Table 4 also shows that the volume flow of syngas is about equal to the one of ''conventional'' IGCCs; this implies that engines designed for operation on natural gas would require modifications to the fuel nozzles and the combustor chamber.

With the syngas cooler the steam flow at the steam turbine inlet is larger than the flow at outlet, because part of the flow is bled at medium pressure and used for the shift reaction; the opposite with partial quench, where a large amount of low temperature heat is used to generate LP steam.

7 Comparison With Other Concepts

Figure 7 shows the trade-off between efficiency and CO_2 emissions for the following situations:

—Plant with syngas cooler, where CO_2 emissions are varied by varying either μ (curve A) or the removal efficiency (curve B); the latter is varied by changing the pressure of the last flash drum (see the appendix).
—Plant with partial quench and varying μ;
—Semi-closed cycle considered by Chiesa and Lozza (1998);

Table 5 Cost of CO_2 storage. Bold characters denote the data used to calculate the cost of electricity in Table 6 and Fig. 8. Figures do not include ground transmission, i.e., the power plant is located at the well (underground injection) or on the shore. Rightward column (mill\$/kWh) refers to the plant of Fig. 2 with μ = 1.

Storage option	Cost of storage	
	\$/ton CO_2	mill\$/kWh
Depleted natural gas field (Hendricks, 1994)	0.5÷2.8	0.41÷2.27
Acquifer, 2 km depth (Hendricks, 1994)	1.8÷7.2	1.46÷5.83
Acquifer (Freund and Ormerod, 1997)	4.7	3.81
Submerged pipeline and dispersion in ocean (Fujioka et al., 1997)	**10**	**8.10**
Submerged pipeline and dispersion in ocean (Freund and Ormerod, 1997)	4.1÷21	3.32÷17.0

---

[8] Specific CO_2 emissions (kg_{CO2}/kWh_{el}) decrease to a lesser extent due to lower efficiency. Consequently, the reduction of specific CO_2 emissions is always lower than the fraction of removed carbon.

Table 6 Preliminary estimates of the cost of electricity. Investment costs have been levelized at 8 percent interest rate, 25 year plant life, straight-line depreciation, 40 percent tax (capital carrying charge 14.9 percent) and 7000 hours/yr of operation. The contribution of the cost of fuel is calculated from the heat rates in row 3, which are 5 percent higher than those corresponding to the efficiencies in row 2 to account for ageing, fouling, part-load behavior, etc. Values for PCSCs are representative of supercritical plants. Cost of electricity for plants with CO_2 removal includes a cost for storage of 8.1 mills/kWh (see Table 5). (FGD: Flue Gas Desulfurization)

	NGCC	PCSC +FGD	IGCC without CO_2 removal		IGCC with CO_2 removal	
			syngas cooler	partial quench	syngas cooler	partial quench
Net power plant, MW	338.7	400.0	402.9	381.4	358.2	353.8
Net efficiency, %	55.10	41.00	45.86	43.73	38.77	38.59
Heat rate, kJ/kWh	6877	9243	8263	8666	9774	9820
Emissions, kg_{CO2}/kWh	0.377	0.836	0.747	0.784	0.074	0.074
Power section cost, M\$ CO_2 removal/compression cost, M\$	193	508	624	553	624 82.0	553 81.6
Overall cost, \$/kW	570	1270	1550	1450	1972	1794
Interest during construction, %	6	11	16	16	16	16
Fuel cost, \$/GJ	3.30	1.70	1.70	1.70	1.70	1.70
O&M costs, mill\$/kWh	2.19	6.95	5.75	5.41	7.16	6.56
Cost of electricity, mill\$/kWh	37.79	52.76	58.19	56.06	80.73	75.82
Recovery costs, \$/ton avoided CO_2	-	-	-	-	33.47	27.86

—An ideal mix between conventional IGCCs and the IGCC with the highest (92.5 percent) reduction of specific CO_2 emissions.

The knees in syngas cooler curve A and the curve for partial quench corresponds to $\mu = 1$; as discussed in chap. 3 (see Fig. 5) further increases of μ have negligible effects on CO to CO_2 conversion, whereby further reductions of CO_2 emissions are possible only by increasing the removal efficiency (decrease pressure of last CO_2 separation drum).

The figure, which also reports conventional supercritical pulverized coal steam cycles (PCSC) and natural gas-fired combine cycles (NGCC), shows that (1) varying μ is a much more efficient way to control CO_2 emissions than varying the removal efficiency through the pressure of the last flash drum, (2) when requiring an almost complete CO_2 removal, all IGCC configurations give about the same efficiency; and (3) When requiring only partial CO_2 removal, the configurations presented in this paper with moderate values of μ are superior to all other configurations. The IGCCs analyzed here can achieve the same net LHV efficiency of conventional PCSCs (around 41 percent) with specific CO_2 emissions around 0.2 kg_{CO2}/kWh_{el}, about 60 percent the specific emissions of NGCCs—or less than 30 percent of those of PCSCs.

8 Cost of Electricity

Tables 5 and 6 report basic assumptions and main results of a preliminary economic analysis. The cost of CO_2 storage can vary over a very wide range depending on storage site; the cost of electricity in Table 6 includes a cost of 8.1 mills/kWh for storage in deep oceanic waters via a submerged pipeline (power plant placed by the sea shore). Plant costs interpret indications and trends reported in the literature (*TAG,* 1993; Todd and Stoll, 1997; McMullan et al., 1995; West and Ereaut, 1997); fuel costs are meant to represent medium term trends for the European market (Hagedorn and Paul, 1997; Häuser and Herzog, 1997; Wondergem, 1997); where applicable, O&M costs are coherent with EPRI estimates (*TAG,* 1993). The investment for CO_2 removal (HP steam bleed, shift reactors, CO_2 absorption and compression) is scaled down from estimates of Hendricks (1994), assuming a scale factor of $\frac{2}{3}$ with respect to the plant thermal input.

Conventional IGCCs give a cost of electricity 6–10 percent higher than that of supercritical PCSCs. With CO_2 removal, the cost of electricity of IGCCs increases by about 40 percent, bringing it in the range 75–80 mills/kWh. This 40 percent cost increase is only slightly higher than that estimated by Göttlicher and Pruscheck (1996) and the final cost of electricity and the cost per ton of CO_2 avoided (33.5 and 27.9 $\$/ton_{CO2}$) are about the same.

Despite its higher heat rate, the scheme with partial quench is advantaged due to its lower investment cost. Figure 8 reports the sensitivity of the cost of electricity to a hypothetical carbon tax proportional to the actual emissions of CO_2 to the atmosphere. The lines for the plants with CO_2 removal refer to the conditions giving about 90 percent reduction of specific emissions ($\mu = 1$, see Table 4); CO_2 removal becomes competitive with conventional pulverized coal and IGCC plants for a carbon tax around 35 $mills/kg_{CO2}$—which would bring the price of coal to almost 5 \$/GJ. Competitiveness with natural gas fired combined cycles requires a carbon tax around 100 $mills/kg_{CO2}$.

9 Conclusions

An appropriate integration of shift reactors and physical absorption into IGCC plants can reduce specific CO_2 emissions over 90 percent. With respect to "conventional" IGCCs, CO_2 removal penalizes efficiency by 5 to 7 percentage points, bringing it down to 38–39 percent (LHV), and increases the cost of electricity by about 45 percent, bringing it to 55–57 mills/kWh (storage into oceanic waters via pipeline). These penalties can be substantially reduced by accepting higher CO_2 emissions. Compared to other concepts proposed to reduce IGCC CO_2 emissions, the schemes proposed here exhibit higher efficiencies over the whole range of specific emissions; in addition, they are compatible with standard, commercial gas turbines and do

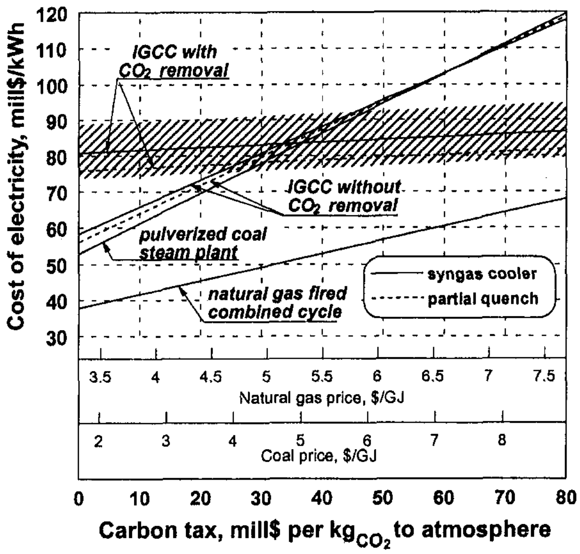

Fig. 8 Cost of electricity versus carbon tax. Lines for IGCC with CO_2 removal refer to a cost for storage of 8.1 mill$/kWh. The shaded area reports the range covered by variations in storage cost from 1 to 20 $/ton CO_2 according to values in Table 5.

not require the development of new technologies nor new components.

References

ASPEN PLUS release 9.3, Reference Manual—Volume 2, 1996, "Physical Property Methods and Models," Aspen Technology Inc., Cambridge, MA.

Black, C. R., McDaniel, J. E., 1996, "Polk Power Station IGCC Projects," Proc. of "Gasification Technologies Conference," San Francisco, CA.

Blok, K., Williams, R. H., Katofski, R. E., and Hendricks, C. A., 1997, "Hydrogen Production from Natural Gas, Sequestration of Recovered CO_2 in Depleted Gas Wells and Enhanced Natural Gas Recovery," *Energy,* Vol. 22, pp. 161–168.

Bucklin, R. W., and Schendel, R. L., 1984, "Comparison of Fluor Solvent and Selexol Processes," *Energy Progress,* Vol. 4, No. 3, pp. 137–142.

The Capture, Utilization and Disposal of Carbon Dioxide from Fossil Fuel-Fired Power Plants, 1993 report prepared for U.S. Dep. of Energy, contract No. DE-FG02-92ER30194.A000, July 1993.

Chiesa, P., Consonni, S., Lozza, G., and Macchi, E., 1993, "Predicting the Ultimate Performance of Advanced Power Cycles Based on Very High Temperature Gas Turbine Engines," ASME Paper 93-GT-223.

Chiesa, P., and Lozza, G., 1998, "CO_2 Emission Abatement in IGCC Power Plant by Semiclosed Cycles. Part A: With Oxygen-Blown Combustion," ASME paper 98-GT-384.

Consonni, S., 1992, "Performance Prediction of Gas/Steam Cycles for Power Generation," Ph.D. thesis No. 1893-T, Mechanical and Aerospace Engineering Dept., Princeton University, Princeton, NJ.

Consonni, S., Larson, E., Kreutz, T. and Berglin N., 1997, "Black Liquor-Gasifier/Gas Turbine Cogeneration," ASME Paper 97-GT-273.

Echt, W. I., 1998, personal communication, Union Carbide Corporation Danbury, CT.

Feron, P. H. M., Jansen, A. E., and Klaassen, R., 1992, "Membrane Technology in Carbon Dioxide Removal," *Energy Convers. Mgmt.,* Vol. 33, No. 5–8, pp. 421–428.

Freund, P. and Ormerod, W. G., 1997, "Progress Toward Storage of Carbon Dioxide," *Energy Convers. Mgmt.,* Vol. 38, Suppl., pp. S199–S204.

Fujioka, Y., et al., 1997, "Cost Comparison in Various CO_2 Ocean Disposal Options," *Energy Convers. Mgmt.,* Vol. 38, Suppl., pp. S273–S277.

Göttlicher, G. and Pruscheck, R., 1996, "Comparison of CO_2 Removal Systems for Fossil-Fuelled Power Plant Processes," *Energy Convers. Mgmt.,* Vol. 38, Suppl., pp. S173–S178.

Hagerdon, G., and Paul, I., 1997, "Innovative Steam Power Plant Technology: New Solution for the Benefit of Customer Worldwide," Proceedings, Power-Gen Europe '97, Madrid, Spain, June 1997., Vol. III, PennWell, Utrecht, The Netherlands, pp. 383–404.

Häuser, U., and Herzog, M., 1997, "Design Data of Steam Power Plants: An Economic and Environmental Evaluation," Proceedings, Power-Gen Europe '97, Vol. III, PennWell, Utrecht, The Netherlands, pp. 335–357.

Hendriks, C., 1994, "Carbon Dioxide Removal from Coal-Fired Power Plants," Ph.D. thesis, University of Utrecht, The Netherlands.

Holloway, S., 1997, "An Overview of the Underground Disposal of Carbon Dioxide," *Energy Convers. Mgmt.,* Vol. 38, Suppl., pp. S193–S198.

Hough, M. F., Kelty, F. J., O'Keefe, L. F., Thone, P. W., and Weissman, R. C. (1997), "The Bottomless Refinery: Gasification as The Optimum Solution to Maximum Refinery," presented at the Gasification Technology in Practice, February 26–27, 1997, Milan, Italy.

Houghton, J. T., Jenkins, G. J., and Ephraums, J. J., eds., 1990, *Climate Change: The IPCC Scientific Assessment,* Cambridge University Press, Cambridge, UK.

Johansson, T. B., Williams, R. H., Ishitani, H., and Edmonds, J. A., 1996, "Options for Reducing CO_2 Emissions for the Energy Supply Sector," *Energy Policy,* Vol. 24, pp. 985–1003.

Kohl, A., and Riesenfeld, F., 1985, *Gas Purification,* 4th ed., Gulf Publishing Company, Houston, TX.

Kubek, D. J., Polla, E., and Wilcher, F. P., 1997, "Purification and Recovery Options for Gasification," Proceedings, Gasification Technology in Practice, Gulf Publishing Company, Houston, TX.

Larson, E., and Consonni, S., 1997, "Performance of Black Liquor Gasifier/Gas Turbine Combined Cycle Cogeneration in the Kraft Pulp and Paper Industry," Proceedings, 3rd Biomass Conference of the Americas, Montreal, Canada, Pergamon-Elsevier Science, New York.

Lozza, G., 1990, "Bottoming Steam Cycles for Combined Gas-Steam Power Plants: A Theoretical Estimation of Steam Turbine Performance and Cycle Analysis," Proceedings, 1990 ASME Cogen-Turbo, ASME, New York, pp. 83–92.

Macchi, E., Consonni, S., Lozza, G., Chiesa, P., 1995, "An Assessment of the Thermodynamic Performance of Mixed Gas-Steam Cycles—Part A: Intercooled and Steam-Injected Cycles," ASME JOURNAL OF ENGINEERING FOR GAS TURBINES AND POWER, Vol. 117, pp. 489–498.

Mathieu, P., De Ruick, J., 1993, "CO_2 Capture in CC and IGCC Power Plants Using a CO_2 Gas Turbine," Proceedings, IGTI Cogen-Turbo Congress, ASME, New York, pp. 77–84.

McMullan, J. T., et al., 1995, "Techno-Economic Assessment Studies of Fossil Fuels and Fuel Woods Power Generation Technologies," Joule II Programme, R&D in Clean Coal Technology, report to the European Commission, Brussels, Belgium, CIEMAT, Madrid, Spain.

Schütz, M., Daun, M., Weinspach, P. M., Krumbeck, M., and Hein, K. R. G., 1992, "Study on the CO_2 Recovery from an IGCC Plant," *Energy Convers. Mgmt.,* Vol. 33, No. 5–8, pp. 357–363.

Smelser, S. C., Stock, R. M., McCleary, G. J., 1991, "Engineering and Economic Evaluation of CO_2 Removal from Fossil-Fuel-Fired Power Plant," EPRI Report IE-7365, Palo Alto, CA.

Socolow, R. H., ed., 1997, "Fuels Decarbonization and Carbon Sequestration: Report of a Workshop," PU/CEES Report No. 302, Princeton University, Princeton, NJ.

Storgaard, L., 1997, personal communication, Haldor Topsoe, Lyngby, Denmark.

Stull, D. R., and Prophet, H., project directors, 1971, *JANAF Thermochemical Tables,* 2nd ed., U.S. National Bureau of Standards, Washington D.C.

TAG—Technical Assessment Guide (electric supply), 1993 EPRI Report TR-102275 Vol. 1, Rev. 7, Palo Alto, CA.

Todd, D. M., and Stoll, H., 1997, "Integrated Gasification Combined Cycle—The Preferred Power Technology of a Variety of Applications," Proceedings, Power-Gen Europe '97, Vol. III, PennWell, Utrecht, The Netherlands, pp. 365–384.

Treybal, 1980, *Mass-Transfer Operations,* Mc-Graw-Hill, New York.

Turkemburg, W., 1997, "Sustainable Development, Climate Change and Carbon Dioxide Removal (CDR)," *Energy Convers. Mgmt.,* Vol. 38, Suppl., pp. S3–S12.

Ulizar, I., and Pilidis, P., 1997, "Design of a Semiclosed Cycle Gas Turbine with Carbon Dioxide-Argon as Working Fluid," ASME Paper 97-GT-125.

Van der Sluijs, J. P., Hendricks, C. A., Blok, K., 1992, "Feasibility of Polymer Membranes for Carbon Dioxide Recovery from Flue Gas," *Energy Convers. Mgmt.,* Vol. 33, No. 5–8, pp. 429–436.

Weiss, M. M., 1997, "Selection of the Acid Gas Removal Process for IGCC Applications," Proceedings, Gasification Technology in Practice.

West, S. S., and Ereaut, P. R., 1997, "Air-Blown or Oxygen Blown Gasification for Power Generation?" Proceedings, Gasification Technology in Practice.

Wondergem, A., 1997, "Selection of Gas Turbine(s) for a 110 MW Power Station," Proceedings, Power-Gen Europe '97, Vol. III, PennWell, Utrecht, The Netherlands, pp. 47–55.

APPENDIX

Absorption Process

Figure A1 illustrates the operating plane of the absorption tower. Following the convention adopted by Treybal (1980), the abscissa X is the molar ratio between the CO_2 in the liquid and the solvent ($\text{kmol}_{CO2}/\text{kmol}_{\text{Selexol}}$), while the ordinate Y is the molar ratio between the CO_2 in the gas and all species other than CO_2 in the gas ($\text{kmol}_{CO2}/\text{kmol}_{\text{gas}*}$, where "gas*" refers to the gas deprived of the CO_2).

CO_2 removal efficiency and solvent flow are evaluated as follows. Except when specified otherwise, the pressure of the last drum is set to 1.05 bar[9], whereby the concentration in the solvent entering the top of the tower (X_{in}) can be calculated from Henry's law as the asymptote of the equilibrium curve at 1.05 bar. To ensure an adequate driving force at the top of the column, the concentration of the gas exiting the top of the tower (Y_{ex}) is set to 1.25 times the one corresponding to X_{in} on the equilibrium curve at 50 bar; this allows calculating the mass flow of CO_2 absorbed in the column (relative to the flow of solvent) and the corresponding CO_2 removal efficiency. The solvent flow is determined by setting it to 1.25 times the minimum admissible value (corresponding to a tower with infinite height) given by the slope of the dotted line in Fig. A1, which connects point A representing the conditions at the top of the tower with point B, the point on the equilibrium curve with Y equal to the one of the gas at inlet (Y_{in}).

Under the hypotheses mentioned above, the CO_2 removal efficiency ranges from 92.5 ($\mu = 0$) to 96 percent ($\mu = 1$) of the CO_2 concentration in the gas at inlet (Y_{in}, which in turn depends on the amount of H_2O injected ahead of the shift reactors). The cases with reduced removal efficiency (curve B in Fig. 7) have been calculated by increasing the pressure of the last flash drum, whereby point A moves rightward and the CO_2 concentration in the gas exiting the tower (Y_{ex}) increases; while the power of the solvent pump remains virtually unchanged, the power of the CO_2 compressors decreases, because the mass flow to be compressed is lower and the drum pressures are higher.

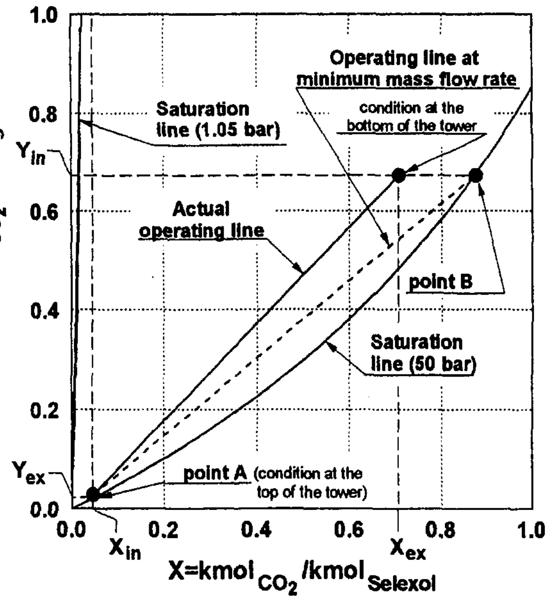

Fig. A1 Operating diagram of the CO_2 absorption column

---

[9] The lower the pressure of the last flash drum, the higher the purity of the solvent introduced at the top of the column and, given the absorber pressure and the solvent/gas mass flow ratio, the higher the removal efficiency. On the other hand, lowering the pressure of the final flash drum increases capital cost (due to larger volume flows) and pumping power requirements. The minimum pressure of 1.05 bar allows operating the whole CO_2 system above atmospheric pressure.

J. Ling
jling01@fiu.edu

Y. Cao
Department of Mechanical Engineering,
Florida International University,
Miami, FL 33199

W. S. Chang
Propulsion Directorate,
Air Force Research Laboratory,
Wright-Patterson AFB, OH 45433

Analyses of Radially Rotating High-Temperature Heat Pipes for Turbomachinery Applications

A set of closed-form solutions for the liquid film distributions in the condenser section of a radially rotating miniature heat pipe and for the vapor temperature drop along the heat pipe length are derived. The heat transfer limitations of the heat pipe are analyzed under turbine blade cooling conditions. Analytical results indicate that the condenser heat transfer limitation normally encountered by low-temperature heat pipes no longer exists for the high-temperature rotating heat pipes that are employed for turbine blade cooling. It is found that the heat pipe diameter, radially rotating speed, and operating temperature are very important to the performance of the heat pipe. Heat transfer limitations may be encountered for an increased heat input and rotating speed, or a decreased hydraulic diameter. Based on the extensive analytical evaluations, it is concluded that the radially rotating miniature heat pipe studied in this paper is feasible for turbine blade cooling applications.

Introduction

Aerospace turboengines present a great challenge to many heat transfer scientists and engineers. Designers in this field are seeking the best design to transform the chemical energy of the fuel into the useful work of propulsive thrust at a maximum efficiency (Shepherd, 1972). To this aim, aerospace turboengines must operate at very high temperatures and pressures with very little heat losses. As a result, gas turbine blades are subject to severe operating conditions (Wagner et al., 1991).

Traditional air cooling or film cooling may be safe, convenient, and effective. However, they not only need about several percentages of the total air flow rate from the compressor, but also adversely affect the aerodynamic and thermodynamic performance of the aerospace turboengines. Heat pipe technology provides a potential means of cooling structures exposed to high heat fluxes (Dunn and Reay, 1982; Faghri, 1995). Combining the air cooling technology with radially rotating miniature heat pipes for the blade cooling is a new attempt and challenge. The application of radially rotating miniature heat pipes for cooling the trailing edge of rotor blades has been proposed and investigated (Cao, 1996). A possible heat pipe disposition in the blade has also been illustrated in the same reference. Before the heat pipe is actually applied to the turbine blade, however, the fundamental transport phenomena related to various heat transfer limitations must be fully understood.

A radially rotating heat pipe, which rotates about the axis of revolution, is a wickless heat pipe that is comprised of an air-evacuated hollow container and an amount of working fluid sealed within the container. The centrifugal force generated by the rotating motion of the heat pipe is utilized for the return of the liquid condensate from the condenser to the evaporator (Faghri, 1995; Cao and Chang, 1997). Rotating heat pipes have been studied extensively in the past (Gray, 1969; Daniels et al., 1975; Marto, 1976; Maezawa et al., 1981; and Harley and Faghri, 1995). Some closed-form solutions and experimental data are also available in the literature. The aforementioned studies, however, concentrated mainly on low-temperature rotating heat pipes with relatively low rotating speeds. The effect of the centrifugal force on the vapor flow was also neglected. However, for radially rotating miniature heat pipes with a high operating temperature and high rotating speed in a turbomachinery application, the effects of vapor centrifugal force should be taken into account. In this paper, the performance characteristics of radially rotating heat pipes under turbine cooling conditions are studied. Analytical solutions for the liquid film distribution and vapor flow along the heat pipe length are derived. The various heat transfer limitations and the suitable operating conditions that could avoid these heat transfer limitations are also evaluated for heat pipe design considerations.

Generalized Solutions of Liquid Film Distributions in Radially Rotating Heat Pipes

Figure 1 schematically illustrates a radially rotating heat pipe with a tilt angle, ϕ, and its interior working conditions. The assumptions of general Nusselt-type thin-film condensation analysis are applied in the following derivation, and the thermocapillary flow effects are negligible in the presence of a large body force field.

A cylindrically differential control volume in the condensate liquid film for a radially rotating heat pipe is shown in Fig. 2, where the liquid centrifugal force is $f_c = 2\pi\rho_l\omega^2 Zrdrdz$, gravitational force is $f_g = 2\pi\rho_l grdrdz$. ϕ in the figure is the tilt angle of the heat pipe, which should be close to 90 deg to take advantages of a strong centrifugal force for the liquid return from the condenser section to the evaporator section. Static force balances in the z-direction result in the following relation:

$$p_l 2\pi r dr - \left(p_l + \frac{\partial p_l}{\partial z} dz\right) 2\pi r dr + \tau_l 2\pi r dz - 2\pi(r + dr)dz\left(\tau_l + \frac{\partial \tau_l}{\partial r} dr\right) + \rho_l(\omega^2 Z - g)\sin\phi\, 2\pi r dr dz = 0, \quad (1)$$

where the revolving radius of the heat pipe is $Z \approx z_0 + z \sin \phi$, and z_0 is the revolving radius of the coordinate origin.

For the control volume in the liquid film, dr is an infinitesimal quantity and much smaller than r. The assumption of $dr \ll r$ is applied to simplify the problem in this analysis. Therefore, $2\pi(r + dr)dz \approx 2\pi r dz$. Plugging it in Eq. (1) and rearranging it, we get

Manuscript received by the ASME Headquarters October 20, 1998. Associate Technical Editor: T. Simon.

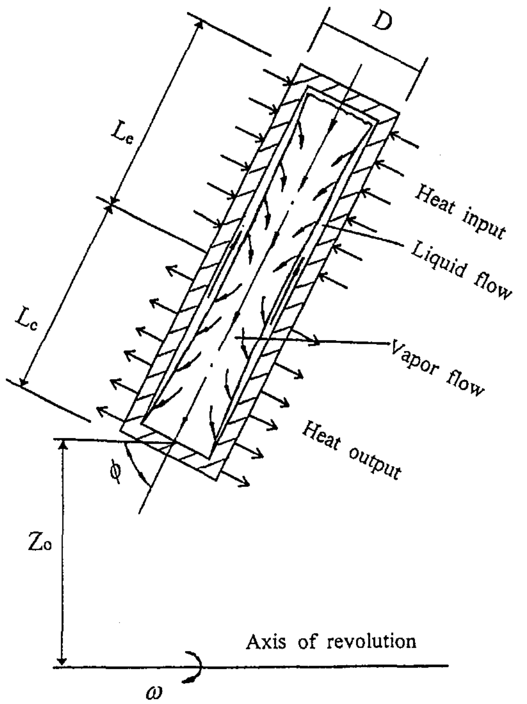

Fig. 1 Schematic of a radially rotating heat pipe with a tilt angle

$$\frac{\partial \tau_l}{\partial r} = -\frac{\partial p_l}{\partial z} - \rho_l(\omega^2 Z - g)\sin\phi. \tag{2}$$

Similarly, static force balances in r direction result in the following relation:

$$\frac{\partial p_l}{\partial r} = -\rho_l(\omega^2 Z - g)\cos\phi. \tag{3}$$

Integrating Eq. (3) from r to $R - \delta$, and recasting it, we obtain

$$p_l = p_{l,R-\delta} + \rho_l(\omega^2 Z - g)\cos\phi(r - R + \delta). \tag{4}$$

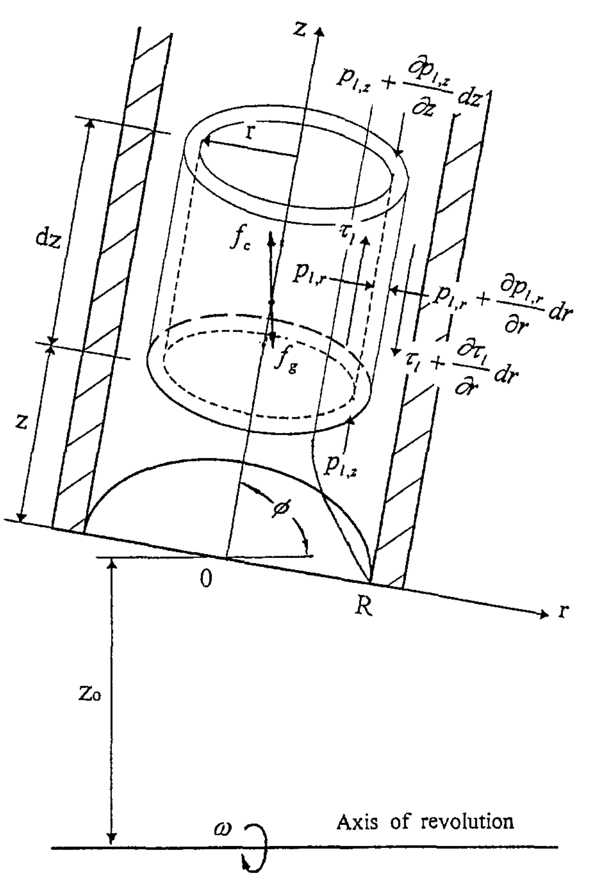

Fig. 2 Schematic of differential control volume of condensate liquid film

Differentiating Eq. (4) with respect to z, and assuming that the liquid pressure, $p_{l,R-\delta}$, is equal to the vapor pressure, p_v, at the liquid-vapor interface, we have

$$\frac{\partial p_l}{\partial z} = \frac{\partial p_v}{\partial z} + \rho_l\omega^2 \sin\phi\cos\phi(r - R + \delta) + \rho_l(\omega^2 Z - g)\cos\phi\,\frac{d\delta}{dz}. \tag{5}$$

Substituting Eq. (5) into Eq. (2) gives

$$\frac{\partial \tau_l}{\partial r} = -\frac{\partial p_v}{\partial z} + \rho_l(\omega^2 Z - g)\left(\sin\phi - \cos\phi\,\frac{d\delta}{dz}\right) - \rho_l\omega^2 \sin\phi\cos\phi(r - R + \delta). \tag{6}$$

Nomenclature

A = cross-sectional area, m^2
Bo = Bond number
C_w = empirical constant in Wallis' correlation
D = heat pipe diameter, m
F_v = frictional coefficient
f = skin-friction coefficient
g = gravitational acceleration, m/s^2
h_{fg} = latent heat of evaporation, J/kg
k = thermal conductivity, W/m-K
L = length of the heat pipe, m
L_a = adiabatic length, m
L_c = condenser length, m
L_e = evaporator length, m
L_{eff} = effective length of the heat pipe, m
$\dot{m}$ = mass flow rate, kg/s
p = pressure, N/m^2
Q = heat transfer rate, W
q'' = heat flux, W/m^2
Re = Reynolds number
R = heat pipe radius, m
T = temperature, K
w = axial velocity, m/s
x = axial coordinate, m
ϕ = tilt angle between the heat pipe centerline and the engine radial line, degree
z = axial location of the control volume, m
Z = revolving radius of the heat pipe, m
Γ = liquid mass flow rate per unit circumferential length, kg/m-s
δ = thickness of liquid film, m
σ = surface tension, N/m
ρ = density, kg/m^3
μ = dynamic viscosity, kg/m-s
τ = shear stress, N/m^2
ω = angular velocity, rad/s

Subscripts

a = adiabatic section
c = condenser
e = evaporator
ent = entrainment
eff = effective
w = heat pipe wall
l = liquid phase
v = vapor phase
R-δ = liquid-vapor interface

The boundary conditions for the above equation are

$$w_l = 0 \quad \text{at } r = R \tag{7}$$

and

$$\tau_{l,R-\delta} = -\tau_{v,R-\delta} \quad \text{at } r = R - \delta. \tag{8}$$

Integrating Eq. (6) with the boundary conditions given by Eqs. (7) and (8), and noting that $\sin\phi - \cos\phi(d\delta/dz) \approx \sin\phi$, the following relation for the axial velocity distribution in the liquid film is obtained:

$$w_l = \frac{1}{\mu_l}\left[\frac{\partial p_v}{\partial z} - \rho_l(\omega^2 Z - g)\sin\phi\right]\left[(R-\delta)(R - r) - \frac{1}{2}(R^2 - r^2)\right] - \frac{1}{\mu_l}\tau_{v,R-\delta}(R - r) - \frac{\rho_l}{\mu_l}\omega^2\sin\phi\cos\phi\left[\frac{1}{2}(R-\delta)^2(R-r) - \frac{1}{2}(R - \delta)(R^2 - r^2) + \frac{1}{6}(R^3 - r^3)\right]. \tag{9}$$

The liquid mass flow rate per unit circumferential length, Γ_l, can then be evaluated as follows:

$$\Gamma_l = \frac{m_l}{\pi D} = \frac{1}{2\pi R}\int_{R-\delta}^{R} \rho_l w_l 2\pi r dr = \frac{\rho_l}{\mu_l R}\left\{\left[\frac{\partial p_v}{\partial z} - \rho_l(\omega^2 Z - g)\sin\phi\right]\left(-\frac{1}{3}R\delta^3 + \frac{5}{24}\delta^4\right) - \tau_{v,R-\delta}\left(\frac{1}{2}R\delta^2 - \frac{1}{3}\delta^3\right) - \rho_l\omega^2\sin\phi\cos\phi\left(\frac{1}{8}R\delta^4 - \frac{3}{40}\delta^5\right)\right\} \tag{10}$$

since

$$\Gamma_l = \int_0^z \frac{q_c''}{h_{fg}}dz = \frac{\bar{q}_c''}{h_{fg}}z \tag{11}$$

where $\bar{q}_c''$ is the average heat flux. Substituting Eq. (11) into Eq. (10) yields

$$\frac{\bar{q}_c'' z}{h_{fg}} = \frac{\rho_l}{\mu_l R}\left\{\left[\frac{\partial p_v}{\partial z} - \rho_l(\omega^2 Z - g)\sin\phi\right] \times \left(-\frac{1}{3}R\delta^3 + \frac{5}{24}\delta^4\right) - \tau_{v,R-\delta}\left(\frac{1}{2}R\delta^2 - \frac{1}{3}\delta^3\right) - \rho_l\omega^2\sin\phi\cos\phi\left(\frac{1}{8}R\delta^4 - \frac{3}{40}\delta^5\right)\right\}. \tag{12}$$

Rearranging Eq. (12), the following general solution for the liquid film thickness, δ, is obtained:

$$-\frac{3h_{fg}}{40\mu_l R\bar{q}_c'' z}\rho_l^2\omega^2\sin\phi\cos\phi\delta^5 + \frac{5h_{fg}\rho_l}{24\mu_l R\bar{q}_c'' z}\left[\rho_l(\omega^2 Z - g)\sin\phi - \frac{\partial p_v}{\partial z}\right]\delta^4 - \frac{h_{fg}\rho_l}{3\mu_l R\bar{q}_c'' z}\delta^3 + \frac{h_{fg}}{8\mu_l q_c'' z}\rho_l^2\omega^2\sin\phi\cos\phi\delta^4 - \frac{h_{fg}\rho_l}{3\mu_l\bar{q}_c'' z}\left[\rho_l(\omega^2 Z - g)\sin\phi - \frac{\partial p_v}{\partial z}\right]\delta^3 + \frac{h_{fg}\rho_l}{2\mu_l\bar{q}_c'' z}\tau_{v,R-\delta}\delta^2 + 1 = 0. \tag{13}$$

Once the film thickness is obtained, the temperature drop across the liquid film thickness can be calculated as follows:

$$\Delta T_l = T_\delta - T_w = \frac{\bar{q}_c'' \ln\dfrac{R-\delta}{R}}{k_l}. \tag{14}$$

For a radially rotating heat pipe with a high speed, the liquid film thickness, δ, is much smaller compared to the heat pipe radius, R. Therefore, Eq. (10) can be simplified to

$$\Gamma_l = \frac{m_l}{\pi D} \approx \int_{R-\delta}^{R}\rho_l w_l dr = \frac{\rho_l}{\mu_l}\left\{-\rho_l\omega^2\sin\phi\cos\phi\frac{\delta^4}{8} - \left[\frac{\partial p_v}{\partial z} - \rho_l(\omega^2 Z - g)\sin\phi\right]\frac{\delta^3}{3} - \tau_{v,R-\delta}\frac{\delta^2}{2}\right\}. \tag{15}$$

Accordingly, the equation for the liquid film thickness can be simplified to

$$\frac{h_{fg}}{8\mu_l\bar{q}_c'' z}\rho_l^2\omega^2\sin\phi\cos\phi\delta^4 - \frac{h_{fg}\rho_l}{3\mu_l\bar{q}_c'' z}\left[\rho_l(\omega^2 Z - g)\sin\phi - \frac{\partial p_v}{\partial z}\right]\delta^3 + \frac{h_{fg}\rho_l}{2\mu_l\bar{q}_c'' z}\tau_{v,R-\delta}\delta^2 + 1 = 0. \tag{16}$$

If the tilt angle, ϕ, is equal to 90 deg, Eq. (16) is reduced to

$$-\frac{h_{fg}\rho_l}{3\mu_l\bar{q}_c'' z}\left[\rho_l(\omega^2 Z - g) - \frac{\partial p_v}{\partial z}\right]\delta^3 + \frac{h_{fg}\rho_l}{2\mu_l\bar{q}_c'' z}\tau_{v,R-\delta}\delta^2 + 1 = 0. \tag{17}$$

Comparing Eq. (16) with Eq. (13), it is clear that Eq. (16) can be obtained from Eq. (13) if the first, second and third terms on the left-hand side of Eq. (13) are dropped. Also, Eq. (17) is obtained from Eq. (16) with ϕ = 90 deg. For these reasons, Eqs. (16) and (17) are two special cases of Eq. (13). In other words, Eq. (13) is a more general relation for liquid film distributions in radially rotating heat pipes.

For a disk-shaped heat pipe, a relation similar to Eq. (16) can be derived (Cao and Chang, 1997). The closed-form analytical solution of the liquid film for a disk-shaped heat pipe thus obtained is

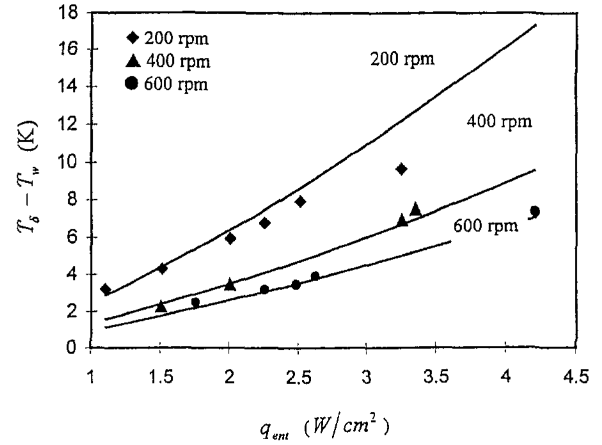

Fig. 3 Comparison of the analytical predictions and the experimental data from Maezawa et al. (1981)

$$2\,\frac{h_{fg}\rho_l^2\omega^2\sin\phi\cos\phi}{8\mu_l\bar{q}_c''x}\,\delta^4 + 2\left[-\,\frac{h_{fg}\rho_l^2(r\omega^2-g)\sin\phi}{3\mu_l\bar{q}_c''x} + \frac{h_{fg}\rho_l}{3\mu_l\bar{q}_c''x}\,\frac{dp_v}{dx}\right]\delta^3 + \frac{h_{fg}\rho_l\tau_{v,\delta}}{\mu_l\bar{q}_c''x}\,\delta^2 + 1 = 0, \quad (18)$$

where x is the axial coordinate.

To verify the analysis presented in this section, Eq. (18) is compared in Fig. 3 with relevant experimental data from Maezawa et al. (1981), when the effects of the friction and vapor gradient are neglected. As can be seen, the agreement between the experimental data and analytical prediction is generally good.

Axial Vapor Temperature Distributions in Radially Rotating Heat Pipes

In the foregoing analytical solutions for the liquid film distributions on the heat pipe wall, both the shear stress at the liquid-vapor interface and the vapor pressure gradient along the heat pipe length are present. To complete the analysis, solutions for the vapor flow must be obtained. Also, as mentioned in the introduction, the centrifugal force may play an important role in the vapor temperature drop along the heat pipe length. In some extreme cases, this temperature may present a heat transfer limitation for the heat pipe performance (Cao and Chang, 1997). Consider one-dimensional laminar and incompressible vapor flow along the heat pipe length under the steady-state working condition. The following relations for the vapor pressure gradient and shear stress are derived:

$$\frac{dp_v}{dz} = \frac{2}{R_v}\,\tau_{v,R-\delta} + \rho_l(\omega^2 Z - g) - \frac{d}{dz}\,(\dot{m}_v\bar{w}_v) \quad (19)$$

$$\tau_{v,R-\delta} = (f\,\mathrm{Re})_v\,\frac{\mu_v\bar{q}_c''z}{2R_v^2\rho_v h_{fg}} \quad (20)$$

$$\frac{d(\dot{m}_v\bar{w}_v)}{dz} = \frac{8\pi\bar{q}_c''^2 z}{\rho_v h_{fg}^2}, \quad (21)$$

where $R_v = R - \delta$ is the vapor space radius in the heat pipe, m_v is vapor mass flow rate, $\bar{w}_v$ is average vapor velocity over the heat pipe cross-sectional area, and f is the laminar vapor skin-friction coefficient. In general, the above two equations are valid when the following two conditions in terms of the vapor Reynolds number and Mach number are satisfied:

$$\mathrm{Re}_v = \frac{2R_vQ}{A_v\mu_v h_{fg}} \le 2300 \quad (22)$$

$$M_v = \frac{Q}{A_v\rho_v h_{fg}\sqrt{\gamma_v R_g T_v}} \le 0.2, \quad (23)$$

where A_v is the cross-sectional area of vapor space, γ_v is the vapor specific heat ratio, and R_g is the gas constant of the vapor (Chi, 1976). These two conditions are usually satisfied for high-temperature heat pipes having a small diameter and operating at a steady state.

Substituting Eqs. (20) and (21) into Eq. (19) yields

$$\frac{dp_v}{dz} = (f\,\mathrm{Re})_v\,\frac{\mu_v\bar{q}_c''z}{R_v^3\rho_v h_{fg}} + \rho_v(\omega^2 Z - g) - \frac{8\pi\bar{q}_c''^2 z}{\rho_v h_{fg}^2}. \quad (24)$$

Assuming that the heat addition along the evaporator and the heat removal along the condenser are constant, and integrating Eq. (24) along the heat pipe length, the following relation for the vapor pressure drop along the heat pipe is obtained:

$$\Delta p_v = F_v L_{\mathrm{eff}}(\pi D L_c\bar{q}_c'') + \rho_v\omega^2 L\bar{Z} - \rho_v g L \approx F_v L_{\mathrm{eff}} Q + \rho_v\omega^2 L\bar{Z}, \quad (25)$$

where $L = L_e + L_a + L_c$ is the total heat pipe length, $L_{\mathrm{eff}} = 1/2(L_c + 2L_a + L_e)$ is the heat pipe effective length, L_a is the adiabatic length of the heat pipe, $\bar{Z} = z_0 + 1/2L$ is the average revolving radius, $F_v = (f\,\mathrm{Re})_v\mu_v/2\pi R_v^4\rho_v h_{fg}$ is the vapor frictional coefficient, and Q is the total heat input.

As mentioned earlier, the vapor Reynolds number is in general less than 2300. But with an increase of the total heat input Q, the Mach number may be greater than 0.2 when the heat pipe operating temperature is relatively low. In this situation, the vapor compressibility should be taken into consideration. Employing the ratio of the drag coefficient, $f_{v,c}$, for a compressible flow to that for an incompressible flow, $f_{v,i}$, the vapor Reynolds number can be corrected by the following equation:

$$\frac{f_{v,c}}{f_{v,i}} = \left(1 + \frac{\gamma_v - 1}{2}\,M_v^2\right)^{-1/2}. \quad (26)$$

Substituting Eq. (26) into the relation for the vapor frictional

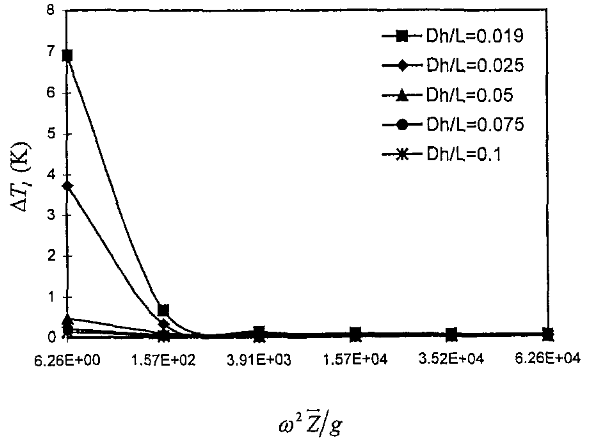

Fig. 4 Maximum temperature drops across the liquid film for sodium as the working fluid (T_v = 1100 K, Q = 200 W)

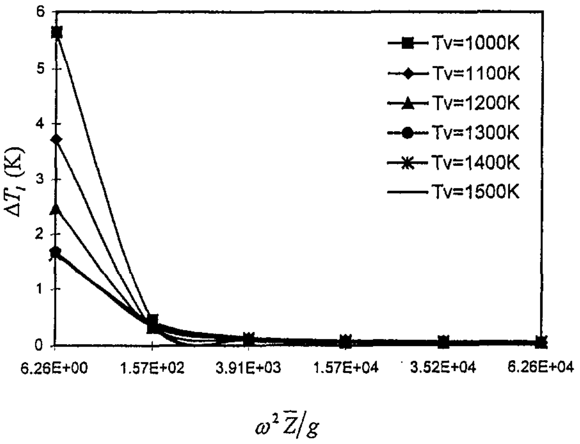

Fig. 5 Maximum temperature drops across the liquid film for sodium as the working fluid (D_h/L = 0.025, Q = 200 W)

coefficient, the following modified vapor friction coefficient is obtained:

$$F_v = \frac{(f\mathrm{Re}_v)\mu_v}{2\pi R_v^4 \rho_v h_{fg}}\left(1 + \frac{\gamma_v + 1}{2} M_v^2\right)^{-1/2}, \qquad (27)$$

where the value of ($f\mathrm{Re}_v$) is the same as that for the incompressible laminar flow (Chi, 1976).

To obtain a relation for the vapor temperature drop along the heat pipe length, the vapor is assumed to be saturated and the Clapeyron equation that relates the saturated temperature with the saturated pressure is employed. The dimensionless temperature drop thus obtained from Eq. (25) is as follows:

$$\frac{\Delta T_v}{T_v} \approx \frac{F_v L_{\mathrm{eff}}(\pi D L_c \bar{q}_c'')}{\rho_v h_{fg}} + \frac{\omega^2 \bar{Z} L}{h_{fg}} = \Delta T_{v,f} + \Delta T_{v,c}, \qquad (28)$$

where T_v is the operating temperature of the heat pipe, $\Delta T_{v,f}$ is the dimensionless temperature drop due to the friction at the liquid-vapor interface, and $\Delta T_{v,c}$ is the dimensionless temperature drop due to the vapor centrifugal force.

Analytical Results for the Temperature Drops and Heat Transfer Limitations

Temperature drops across the liquid film or along the heat pipe length are very important criteria for designing radially rotating heat pipes with a high operating temperature and a high rotating speed. In this paper, analytical results are presented for radially rotating miniature heat pipes working under high heat flux and high rotating speed conditions. The ranges of heat inputs, geometric dimensions, and the rotating speeds are as follows: $40 \leq Q \leq 200$ W, $1.0 \leq D_h \leq 8.0$ mm, $6.26 \leq \omega^2\bar{Z}/g \leq 6.26 \times 10^4$, $L = 80$ mm, $L_c = L_e$, $L_a = 0$, and $\phi = 90$ deg. It should be pointed out that the above ranges only give some typical values and may not represent the values for a specific engine design (Harman, 1981). It is clear that, according to Eqs. (17) through (28), the liquid film thickness, temperature drop across the liquid film, and vapor temperature drop along the heat pipe length are mainly the function of shear stresses, heat fluxes, liquid and vapor thermophysical properties,

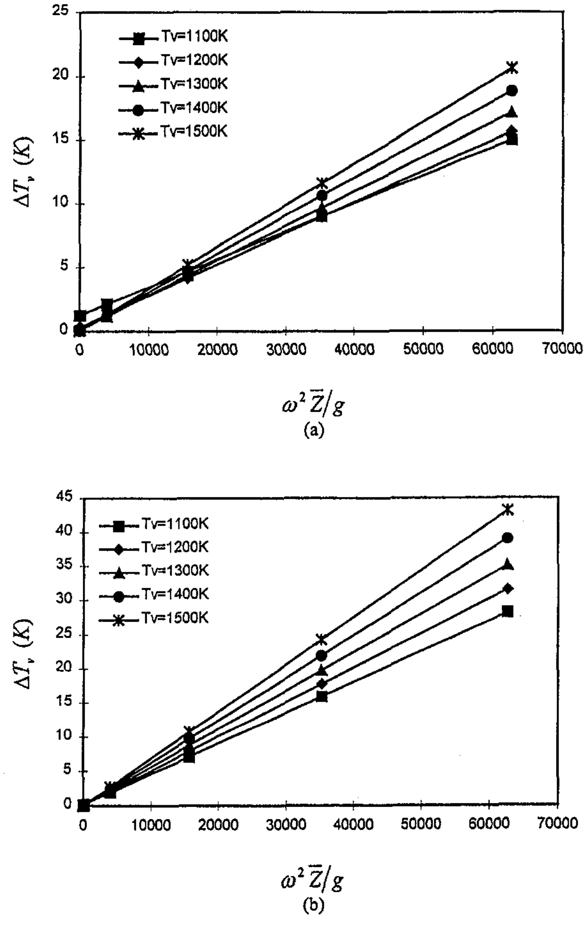

Fig. 6 Vapor temperature drops along the heat pipe length at different rotating speeds (D_h/L = 0.025, Q = 200 W): (*a*) sodium; (*b*) potassium

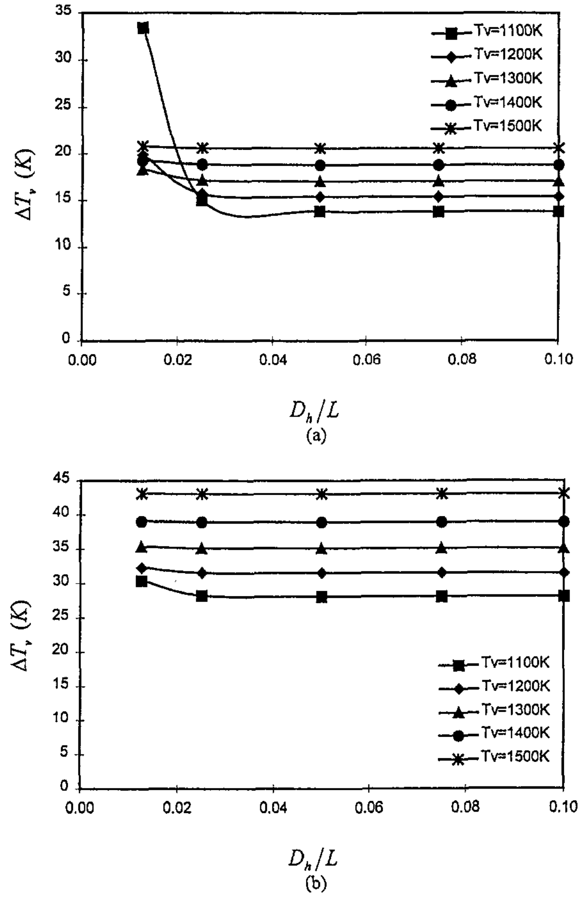

Fig. 7 Vapor temperature drops along the heat pipe length at different heat pipe dimensionless sizes (Q = 200 W, $\omega^2\bar{Z}/g$ = 6.26*E*04): (*a*) sodium; (*b*) potassium

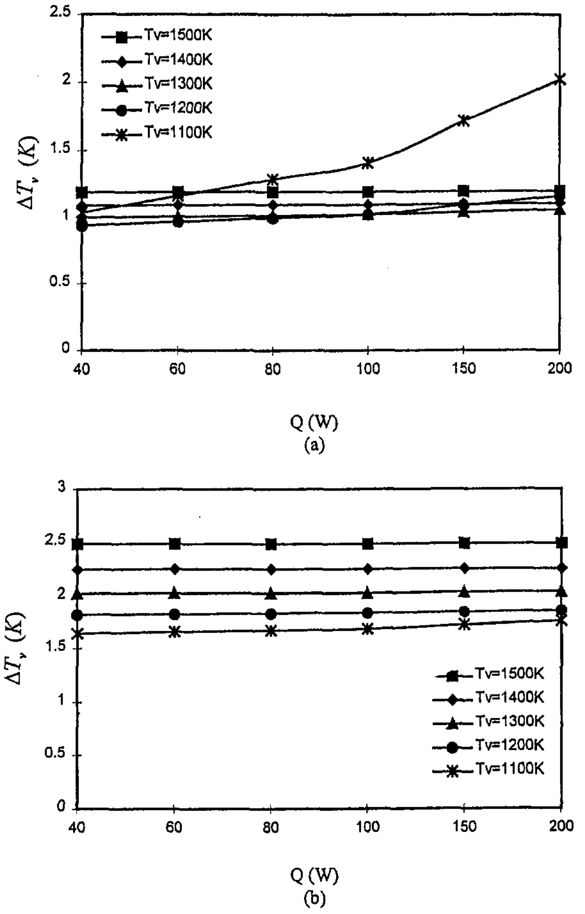

Fig. 8 Vapor temperature drops along the heat pipe length at the different heat inputs (D/L = 0.025, $\omega^2\bar{Z}/g$ = 3.91 × 10^3): (*a*) sodium; (*b*) potassium

liquid and vapor centrifugal forces, heat pipe sizes, and heat pipe operating temperatures. The operation of a heat pipe depends on the heat load at the evaporator and the cooling condition at the condenser. In general, the operating temperature, T_v, of a heat pipe can be controlled by the flow rate of cooling air at the condenser section and the heat input at the evaporator section. The operating temperature, T_v, will be going up if the flow rate of cooling air is reduced or the heat input is increased.

Figure 4 illustrates the maximum temperature drops across the liquid film versus the dimensionless centrifugal forces, $\omega^2\bar{Z}/g$, for sodium as the working fluid. The working temperature, T_v, and the total heat input, Q, are kept as constants at 1100 K and 200 W, respectively. The dimensionless geometric parameter, D_h/L, is treated as a variable. For the results presented in Fig. 5, however, D_h/L is kept as a constant, and the operating temperature is considered to be a variable. It is observed from Figs. 4 and 5 that at a relatively high rotating speed or large revolving radius, $\omega^2\bar{Z}/g > 150$, the maximum temperature drop across the liquid film is negligible. However, a smaller heat pipe diameter or a lower heat pipe operating temperature may increase the temperature drop. Still, under normal turbine working conditions, the maximum temperature drop is much less than 1 K. This means that the commonly encountered condenser limitation for low-temperature heat pipes would never be a serious problem for the high-temperature heat pipes studied in this paper.

Calculations are then made for the vapor temperature drops along the heat pipe length with sodium and potassium as the working fluids. Figure 6 shows vapor temperature drops as a function of dimensionless centrifugal forces at different operating temperatures. The dimensionless heat pipe geometric parameter and the total heat input are kept as constants (D_h/L = 0.025 and Q = 200 W). It is clear from the figure that the vapor temperature drops increase with an increase in the centrifugal force or in the operating temperature. At the same time, it can be seen that a heat pipe with sodium as the working fluid would have a smaller vapor temperature drop than the heat pipe with potassium as the working fluid. For many cases, the vapor temperature drop is on the order of 10–40 K. This temperature drop is considerably high for a low-temperature heat pipe. However, for the high-temperature heat pipes studied in this paper, this temperature drop is relatively small compared to the average heat pipe operating temperature level.

The vapor temperature drops as a function of heat pipe operating temperature and dimensionless size are shown in Fig. 7. At a given heat pipe operating temperature, the vapor temperature drop is increased when the heat pipe diameter is decreased due to a higher friction at the liquid-vapor interface. If the heat pipe operating temperature is less than 1100 K, the vapor temperature drops for the miniature heat pipe with D_h/L = 0.0125 would increase sharply. However, for a heat pipe with D_h/L greater than 0.02 or D_h greater than 1.5 mm, the influence of the operating temperature level on the vapor temperature drop is relatively small.

Figure 8 illustrates the influence of the heat input on the vapor temperature drop along the heat pipe length. In general, the influence of the heat input on the vapor temperature drop is relatively small when the operating temperature level of the heat pipe is relatively high. However, for a heat pipe operating at a relatively low temperature level, the vapor temperature is substantially increased when the heat input is high.

According to Eq. (28), the total vapor temperature drop is due to the contribution of friction at the liquid-vapor interface and the contribution of the vapor centrifugal force. The contri-

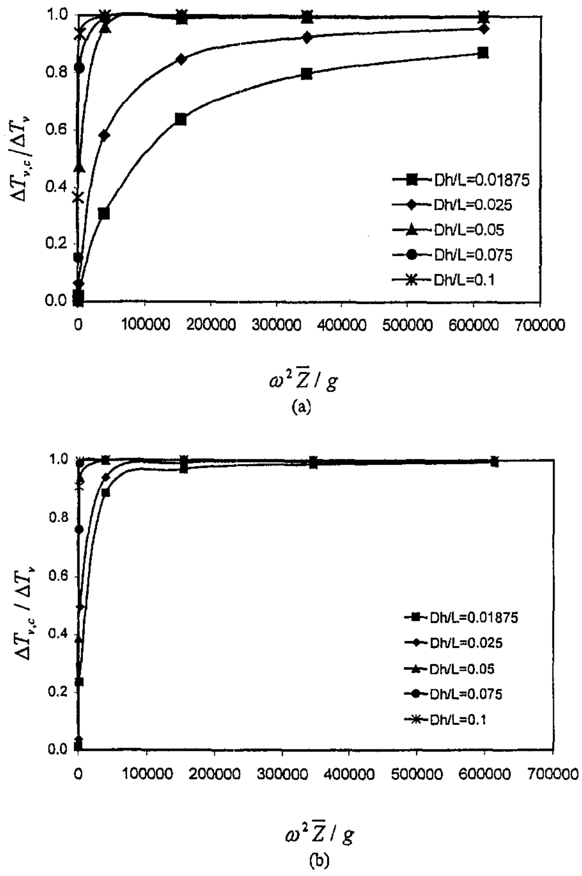

Fig. 9 Ratio of vapor temperature drops due to the centrifugal force to the total temperature drops (T_v = 1100 K, Q = 200 W): (*a*) sodium; (*b*) potassium

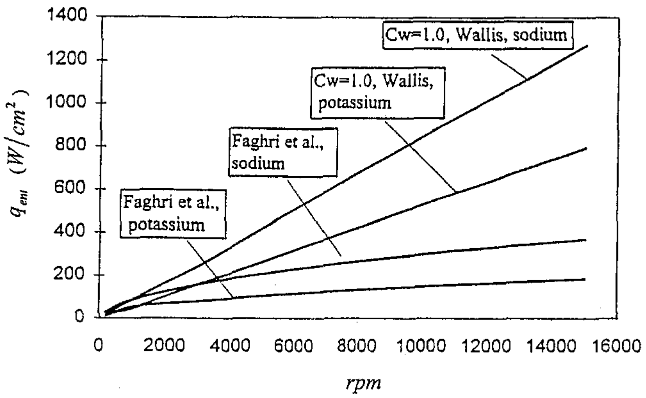

Fig. 10 Entrainment limitation as a function of rotating speeds (T_{ref} = 937 K for potassium and T_{ref} = 1073 K for sodium)

bution of the centrifugal force is illustrated in Fig. 9 as the ratio of the vapor temperature drop due to the vapor centrifugal force to the total vapor temperature drop. At a low rotating speed, the contribution of the centrifugal force is relatively small, but at a high rotating speed, the contribution of centrifugal force becomes a dominant factor. This is especially obvious for a heat pipe having a relatively large diameter.

As illustrated by the foregoing analytical results, the vapor temperature drop along the heat pipe length may present a heat transfer limitation when the heat pipe is of very small diameter, with a relatively low operating temperature level and high rotating speed. However, for a miniature heat pipe having a diameter on the order of 1.5 to 2 mm, the heat transfer limitation would not be encountered at normal rotating speeds and operating temperature levels. This indicates that the radially rotating miniature heat pipe is feasible for the turbine blade cooling application.

The entrainment limit is due to the interaction between the countercurrent liquid and vapor flows occurring at the liquid-vapor interface. This limit may be a major concern when the heat input is high and the heat pipe dimensionless sizes are small. In this case, the shear stresses at the liquid-vapor interface retard the return of the liquid from the condenser to the evaporator section. The heat pipe is said to have reached the entrainment limit when the liquid is prohibited from returning to the evaporator section. A comprehensive review regarding the entrainment limit for two-phase closed thermosyphons is given by Faghri (1995) and Peterson (1994). Various correlations for the evaluation of this limit are also included in the literature. For current wickless rotating heat pipes, the mechanism of the entrainment limit should be similar to that of thermosyphons with the gravitational force being replaced by the rotating centrifugal force. Figure 10 shows the entrainment limits for the same heat pipe studied earlier at different rotating speeds. The calculation was made based on Wallis' correlation (Faghri, 1995)

$$\frac{Q_{\text{ent}}}{A} = \frac{C_w^2 h_{fg}\sqrt{(r_o + x)\omega^2 D(\rho_l - \rho_v)\rho_v}}{[1 + (\rho_v/\rho_l)^{1/4}]^2} \tag{29}$$

and the correlation from Faghri et al. (1989)

$$\frac{Q_{\text{ent}}}{A} = (\rho_l/\rho_v)^{0.14}(\tanh^2 Bo^{1/4}) \times h_{fg}[(r_o + x)\omega^2\sigma(\rho_l - \rho_v)]^{1/4}[\rho^{-1/4} + \rho^{-1/4}]^{-2} \tag{30}$$

for sodium and potassium as the working fluids. For the rotating heat pipe with a small dimensionless size, $D_h/L = 0.0125$, the entrainment limit is very sensitive to the rotating speed, and it may be a concern when the rotating speed is very low. However, when the rotating speed is moderately high, the entrainment limit is increased to more than 100 W/cm^2, which is acceptable for turbomachinery applications. The values of the entrainment limit that are calculated by the Wallis' correlation are close to those from Faghri et al. (1989), when the rotating speed is low. However, at high rotating speeds, large deviation occurs with both working fluids. A similar trend was observed also by Faghri (1995) for thermosyphons.

Conclusions

Closed-form analytical solutions for the liquid film distributions and vapor flow in a radially rotating miniature heat pipe operating at a high rotating speed and high temperature have been derived. The heat transfer limitations of the heat pipe have been evaluated under different operating conditions with sodium and potassium as the working fluids. Analytical results indicate that the condenser heat transfer limitation commonly associated with low-temperature heat pipes no longer exists for high-temperature rotating heat pipes. However, the heat pipe hydraulic diameter or operating temperature level may present a new heat transfer limitation. The vapor temperature drop associated with the vapor pressure drop along the heat pipe length is considerably higher for high-speed rotating heat pipes. Still, this vapor temperature drop, which is on the order of 10–40 K in the normal operating range of turbomachinery, is relatively small compared to the operating temperature level of the heat pipe and is tolerable for turbomachinery applications. When the rotating speed is very low, the entrainment limit may be a serious concern due to the high friction at the liquid-vapor interface. At a moderately high rotating speed, however, this limitation would disappear. Therefore, high-temperature rotating miniature heat pipes with a radius on the order of 1.5 mm are feasible for the turbomachinery applications without encountering any serious heat transfer limitations.

Acknowledgments

The authors would like to thank the Air Force Office of Scientific Research for the financial support and Dr. James McMichael of AFOSR for his interest in this research project.

References

Cao, Y., 1996, "Rotating Micro/Miniature Heat Pipes for Turbine Blade Cooling Applications," paper presented at the AFOSR Contractor and Grantee Meeting on Turbulence and Internal Flows, Atlanta, GA.

Cao, Y., and Chang, W. S., 1997, "Analyses of Heat Transfer Limitations of Radially Rotating Heat Pipe for Turbomachinery Applications," AIAA 97-2542.

Chi, S. W., 1976, *Heat Pipe Theory and Practice: A Sourcebook*, Hemisphere Publishing Corporation, New York.

Daniels, T., and Al-Jumaily, F., 1975, "Investigations of the Factors Affecting the Performance of a Rotating Heat Pipe," *Int. J. Heat Mass Transfer*, Vol. 18, pp. 961–973.

Dunn, P. D., and Reay, D. A., 1982, *Heat Pipe*, Pergamon Press, Oxford, New York.

Faghri, A., Chen, M. M., and Morgan, M., 1989, "Heat Transfer in Two-Phase Closed Conventional and Concentric Annular Thermosphon," ASME *Journal of Heat Transfer*, Vol. 111, pp. 611–618.

Faghri, A., 1995, *Heat Pipe Science and Technology*, Taylor & Francis, Washington, DC.

Gray, V. H., 1969, "The Rotating Heat Pipe—A Wickless, Hollow Shaft for Transferring Heat Fluxes," ASME Paper No. 69T-19, Proceedings, ASME/AIChE Heat Transfer Conf., pp. 1–5.

Harley, C., and Faghri, A., 1995, "Two-Dimensional Rotating Heat Pipe Analysis," *ASME Journal of Heat Transfer*, Vol. 117, No. 1, pp. 418–426.

Harman, R. T. C., 1981, *Gas Turbine Engineering*, John Wiley & Sons, Inc., New York.

Maezawa, S., Suzuki, Y., and Tsuchida, A., 1981, "Heat Transfer Characteristics of Disk-Shaped Rotating, Wickless Heat Pipes," Proceedings, 4th Int. Heat Pipe Conf., pp. 725–733.

Marto, P., 1976, "Performance Characteristics of Rotating Wickless Heat Pipes," Proceedings, 2nd Int. Heat Pipe Conf., pp. 281–291.

Peterson, G. P., 1994, *An Introduction to Heat Pipes*, John Wiley & Sons, Inc., New York.

Shepherd, D. G., 1972, *Aerospace Propulsion*, American Esevier Publishing, New York, London.

Wagner, J. H., Johnson, B. V., and Hajek, T. J., 1991, "Heat Transfer in Passages With Smooth Walls and Radial Outward Flow," ASME *Journal of Heat Transfer*, Vol. 113, pp. 42–51.

Inhibition of Interdiffusion From MCrAlY Overlay Coatings by Application of a Ni-Re Interlayer

R. A. Page

G. R. Leverant

Southwest Research Institute,
Materials and Structures Division,
6220 Culebra,
San Antonio, TX 78238-5166

The durability of protective coatings on combustion turbine blades and vanes is a critical issue in the power generation industry. Coating life usually dictates the refurbishment intervals for these components, and these intervals have generally been of shorter duration than desired by the operators of the equipment. Both MCrAlY and aluminide type coatings protect against oxidation and hot corrosion by forming a protective Al_2O_3 surface layer. Degradation of the coatings occurs by depletion of the aluminum content of the coating through interdiffusion with the substrate and through the formation and spallation of an external Al_2O_3 scale. The results obtained in this study clearly show that the application of a thin interlayer of Ni-Re beneath the MCrAlY coating can significantly decrease the growth rate of the inner β-NiAl depletion zone. Order of magnitude reductions in the inner depletion zone thickness formed at 1000 h were obtained with both the Ni-32 wt.% Re and the Ni-47 wt.% Re interlayer coatings. Since formation of the inner depletion zone is believed to result from interdiffusion with the substrate, these results suggest that the Ni-Re interlayer provided a significant impediment to the inward diffusion of Al into the substrate.

Introduction

The durability of protective coatings on combustion turbine blades and vanes is a critical issue in the power generation industry. Coating life usually dictates the refurbishment intervals for these components, and these intervals have generally been of shorter duration than desired by the operators of the equipment. The excessive downtime associated with this maintenance is quite costly as either less efficient power generation equipment must be brought on line or replacement power must be purchased. Furthermore, breaching of the coating by oxygen can lead to severe attack of the superalloy substrate, such that sets of blades or vanes must be purchased to replace unrepairable parts. The cost of a set of air-cooled, nickel-base superalloy blades can range up to $1,000,000.

For both aluminide and MCrAlY coatings, the life of the coating is controlled by maintaining a reservoir of Al that forms a protective Al_2O_3 scale on the surface. Loss of Al from the coating occurs by spallation of the Al_2O_3 due to thermal cycling and, also, by interdiffusion of the coating and substrate. That is, Ni diffuses from the substrate into the coating, and Al diffuses from the coating into the substrate. All of these factors reduce the Al concentration of the coating to levels where it can no longer form Al_2O_3 and is, therefore, no longer protective.

It would be desirable to suppress interdiffusion that leads to loss of Al to the substrate and ingress of Ni from the substrate. This could be accomplished by the presence of a diffusion barrier that locally slows down diffusional processes. One approach might be the introduction of a completely new material near the interface between the coating and substrate. However, a more direct approach would be to develop an in-situ "barrier" using an element that is already indigenous to superalloy systems.

Leverant (1976) demonstrated that the element rhenium (Re) significantly reduces the creep rate of nickel-base superalloys. Since Re is a very large atom, and since creep is known to be controlled by diffusion, it has been thought that Re significantly reduces diffusion rates. The exact mechanism by which Re enhances creep resistance remains a controversial subject (Giamei and Anton, 1985; Blavette, et al., 1986; Lahrman, et al., 1981; Neubauer, et al., 1994), but all theories involve mechanisms that suppress thermally activated processes. Therefore, it is hypothesized that the local introduction of Re into the superalloy substrate adjacent to the coating could reduce interdiffusion that leads to dilution of the coating Al concentration.

The objective of this work was to evaluate the feasibility of introducing the element rhenium as an in-situ diffusion barrier to reduce the loss of aluminum from oxidation-resistant protective coatings to the superalloy substrate. A relatively simple and cost effective means of introducing Re into the superalloy substrate adjacent to the coating would be to deposit a thin Re or Ni-Re coating on the superalloy substrate prior to the formation of the aluminide or MCrAlY coating. The results of a series of experiments designed to determine if such a Re or Ni-Re coating would decrease interdiffusion are presented in this paper.

Experimental Procedures

Substrate Material. A representative blade alloy, IN738LC, was selected as the substrate for this coating study. Rectangular oxidation coupons (2.54 cm × 1.27 cm × 1.5 mm thick) were machined from an IN738LC blade using a wire electro-discharge-machining (EDM) process. The surfaces of the coupons were lapped following machining to remove the melt layer produced by the EDM process.

Ni-Re Coatings. The Ni-Re coatings were deposited by sputter deposition. Initial sputter deposition runs were performed using 6 keV nitrogen ion sputtering of a melt solutionized Ni-8 wt. % Re target. Sputter deposition rates and film thicknesses were determined using a quartz crystal thickness monitor. Evaluation of the sputtered films indicated that Re was being incorporated into the film. At this point, a change was made from nitrogen ions to krypton ions for the sputtering process. As shown in Table 1, use of the heavier krypton ions

---

Contributed by the International Gas Turbine Institute and presented at the International Gas Turbine and Aeroengine Congress and Exhibition, Stockholm, Sweden, June 2–5, 1998. Manuscript received by the ASME Headquarters April 1, 1998. Paper No. 98-GT-375. Associate Technical Editor: R. Kielb.

Table 1 Calculated Ni/Re sputter yield (atoms/incident ion)

Beam Energy	N Ions	Kr Ions
1 keV	0.78/0.38	2.1/1.9
5 keV	1.1/0.64	4.8/4.5
10 keV	1.1/0.67	6.1/5.8

instead of the lighter nitrogen ions provides both a better overall sputter yield and closer to a one-to-one Ni/Re sputter ratio. EDS measurements of the coatings confirmed that their Re content matched that of the sputter target.

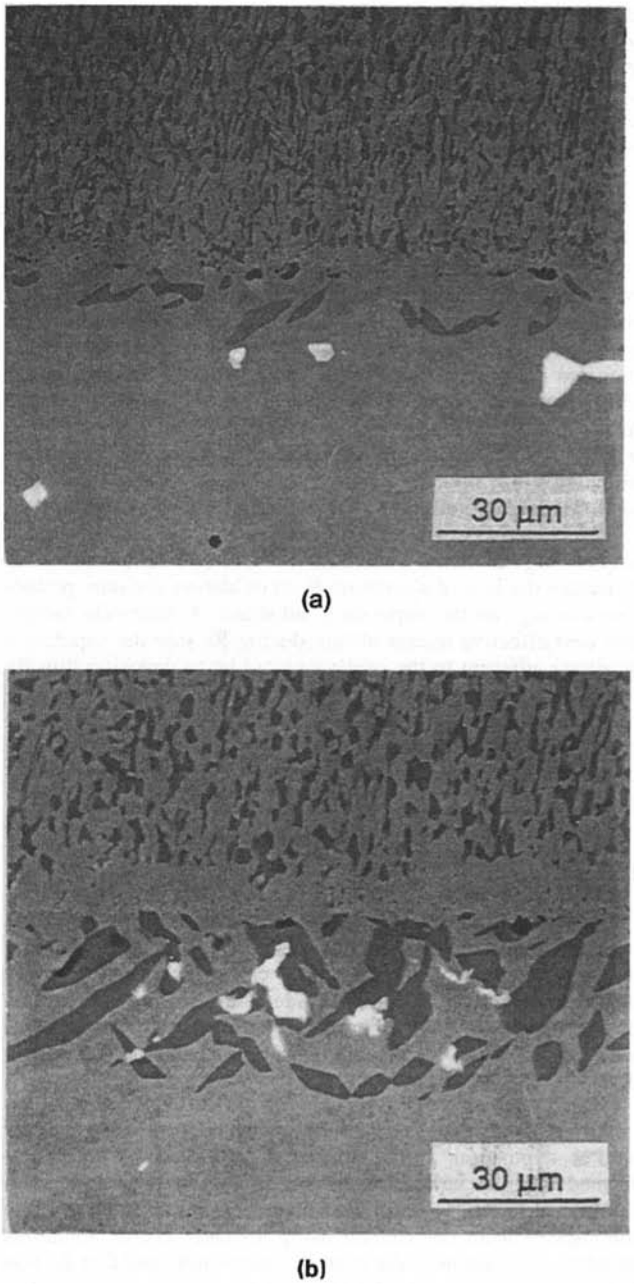

Fig. 1 Scanning electron micrograph of the baseline, i.e., no Re addition, CoCrAlY/IN738 interface in the (*a*) as-deposited condition and (*b*) following a 1000 hr oxidation treatment at 926°C (1700°F)

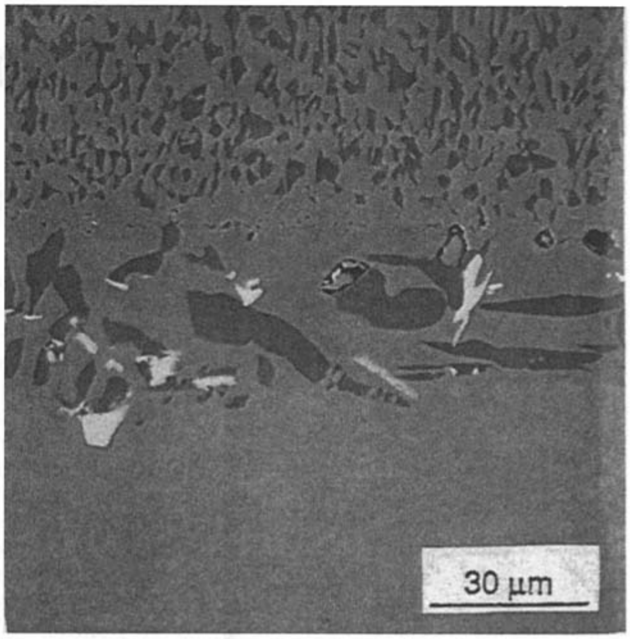

Fig. 2 Scanning electron micrograph, collected with backscattered electrons to optimize elemental contrast, of the CoCrAlY/IN738 interface on a sample with a Ni-47 percent Re interlayer following a 1000 hour oxidation treatment at 926°C (1700°F)

Table 2 CoCrAlY diffusion zone and β-NiAl depletion zone thickness

Re Content	Thermal Anneal	Oxidation Time at 926°C (hours)	Average Diffusion Zone Thickness (μm)	Average β-NiAl Depleted Layer Thickness (μm)
None	–	None, as coated	14	2
None	–	1,000	33	9
8%	No	1,000	29	4
8%	Yes	1,000	27	4
8%	No	2,000	48	10
8%	Yes	2,000	47	11
32%	No	1,000	29	1
32%	Yes	1,000	31	0.9
32%	No	2,000	45	6.5
32%	Yes	2,000	47	6
47%	No	1,000	31	0.7
47%	Yes	1,000	33	0.8
47%	No	2,000	47	7.5
47%	Yes	2,000	51	5

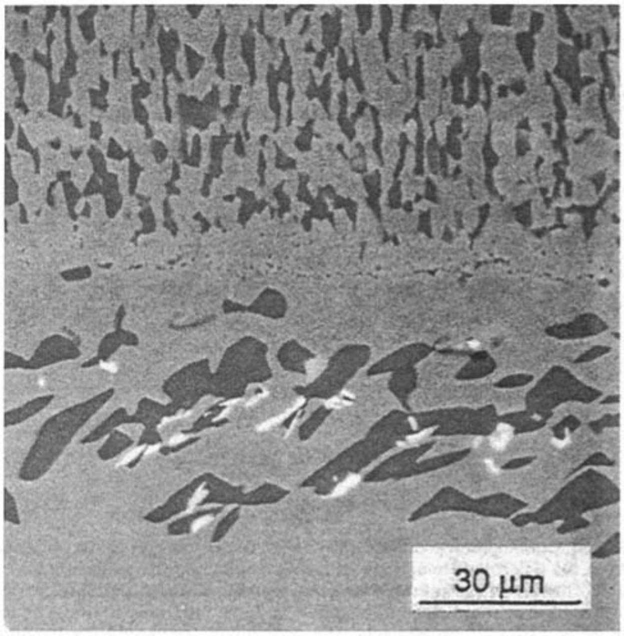

Fig. 3 Scanning electron micrograph, collected with backscattered electrons to optimize elemental contrast, of the CoCrAlY/IN738 interface on a sample with a Ni-47 percent Re interlayer following a 2000 hour oxidation treatment at 926°C (1700°F)

Based on the positive results obtained with the Ni-8% Re target, 6 IN738LC oxidation coupons were given 0.5 μm thick sputter deposited Ni-Re coatings. Two of the coupons were coated with Ni-8% Re, two with Ni-32% Re, and two with Ni-47% Re. EDS spectra obtained from the three compositions of sputter deposited coatings confirmed that they mirrored the compositions of the targets. Following the sputter deposition, half of the coupons, one of each coating composition, were given a one-hour vacuum thermal anneal at 1080°C (1975°F). The other coupons were left in the as-sputter deposited condition.

MCrAlY Coatings. Following the application of the sputter deposited Ni-Re coatings, the oxidation coupons were sent to Chromalloy Turbine Technologies where they were given a CoCrAlY coating by an electron-beam physical vapor deposition process.

Oxidation Exposures. Following the application of the CoCrAlY coatings, static oxidation tests were conducted. These oxidation tests consisted of 1000 and 2000 hour exposures at 926°C (1700°F) in laboratory air. During the oxidation exposures, the specimens were supported on alumina platens with the test surface facing upward. Temperature was monitored by a thermocouple placed directly above the specimens and recorded continuously. The time and temperature for these exposures were selected based on evaluation of literature data on diffusion of Re in Ni (Neubauer, et al., 1994) and degradation rates of MCrAlY coatings (Srinivasan, et al., 1995).

Metallographic and Microprobe Evaluations. Following the oxidation exposures, each of the specimens was sectioned along its centerline, mounted in a conductive mounting media, and metallographically polished. The microstructures exhibited in the coatings and diffusion zones were examined in the scanning electron microscope. The samples were examined in the unetched condition using backscattered electrons to provide contrast due to compositional differences. A Cameca microprobe at Howmet Corporation was used to determine the composition of the various phases present and to measure composition profiles from the coating, across the diffusion zone and into the base metal. The measurements within the composition profiles were made at 2 μm increments. A total of 53 points covering a distance of 104 μm was used for each of the CoCrAlY coated samples.

Results

Microstructural Evaluations. The microstructure present along the coating substrate interface in the as-deposited condition is shown in Fig. 1(*a*). The two phase nature of the CoCrAlY coating is evident with the β-NiAl phase appearing dark in the backscattered images. Voids at the edge of the CoCrAlY coating clearly mark the coating substrate boundary. A two phase diffusion zone, approximately 14 μm thick, is apparent beneath these voids. A dark, presumably Al rich, second phase is evident within the diffusion zone. The extremely bright particles in the micrographs are carbides within the IN738LC substrate.

The microstructure observed in the baseline CoCrAlY coated samples, i.e., no Ni-Re interlayer, after 1000 hours at 926°C (1700°F) is shown in Fig. 1(*b*). Three prominent differences are apparent between the as coated microstructure and the microstructure after the 1000 hour exposure. First, the β-NiAl phase within the coating had coarsened. Second, the diffusion zone had grown, increasing to approximately 30 μm, and the amount of the darker phase within the diffusion zone had in-

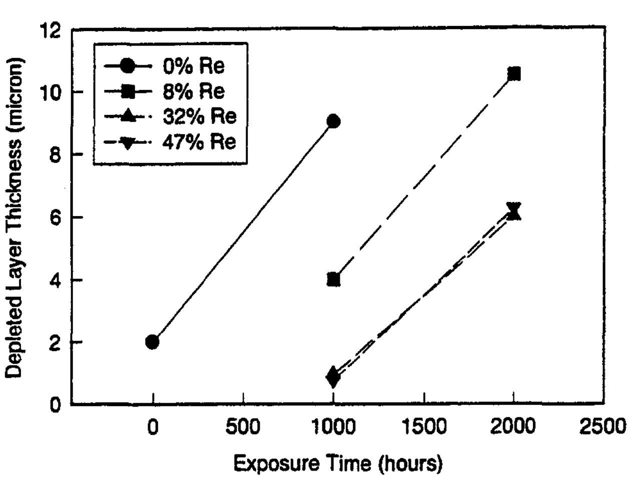

Fig. 4 Effect of exposure time at 926°C (1700°F) on the β-NiAl depleted layer thickness

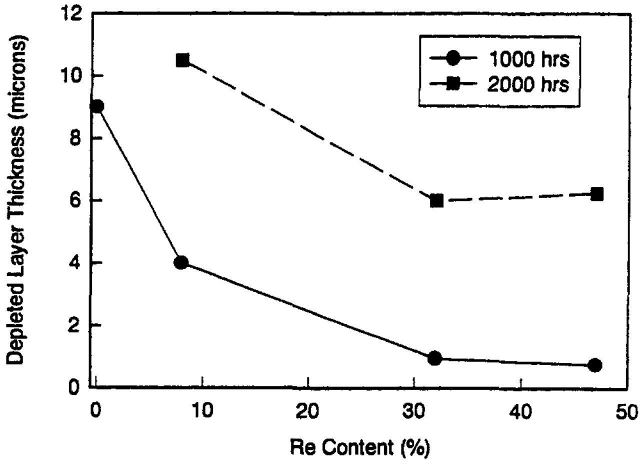

Fig. 5 Effect of Re content on the β-NiAl depleted layer thickness

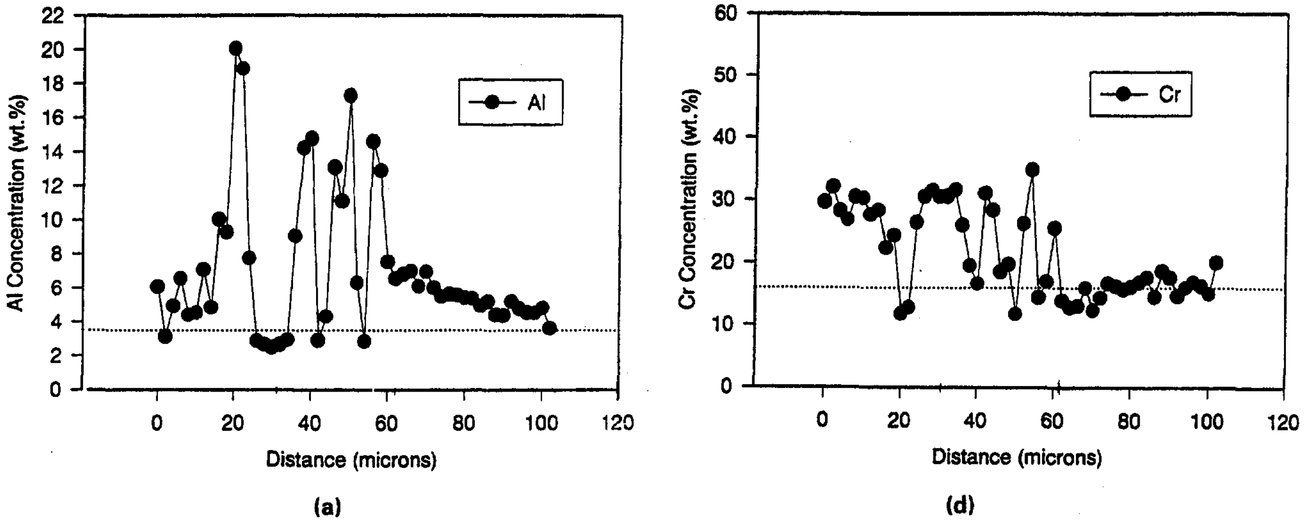

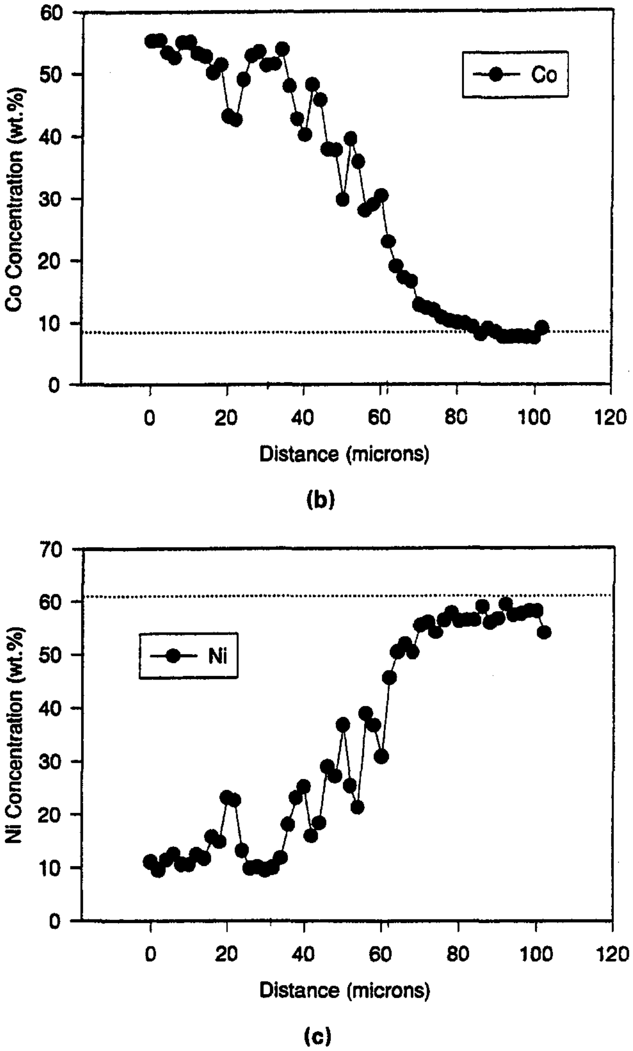

Fig. 6 Composition profiles for (*a*) Al, (*b*) Co, (*c*) Ni, and (*d*) Cr obtained from the 8 percent Re sample following a 1000 hour oxidation exposure at 926°C (1700°F). The transitions between the CoCrAlY coating and the diffusion zone and between the diffusion zone and the base metal occur at 32 and 62 μm, respectively. The dotted lines represent the average concentration in the substrate.

creased. Third, a zone in which the β-NiAl phase was depleted had formed in the CoCrAlY coating adjacent to the IN738LC substrate. Although not shown in the micrographs, a β-NiAl depletion zone also formed along the outer surface of the coating during the 1000 hour oxidation treatment.

After 1000 hours at 926°C (1700°F), the three CoCrAlY samples containing a Ni-Re interlayer, Fig. 2, exhibited the same microstructural features as the baseline Re-free sample. The thickness of the diffusion zones, Table 2, appeared to be unaffected by the Re additions. The only difference observed between the Re containing samples and the Re-free baseline was the thickness of the β-NiAl depletion zone. As shown in Table 2, the Ni-Re interlayer appeared to decrease the thickness of the depletion zone.

A typical microstructure observed after 2000 hours at 926°C (1700°F) is shown in Fig. 3. The additional 1000 hour exposure resulted in growth of both the diffusion zone and the β-NiAl depleted layer. No changes in the general microstructural features were observed, however.

Since the formation of a β-NiAl depletion zone along the coating/substrate interface is thought to be due to the diffusion of Al from the coating into the substrate, the effect of Re on the growth of this layer is an indication of the effect of Re on the inward diffusion of Al. When the depletion zone thickness is plotted versus exposure time, as shown in Fig. 4, three separate curves are obtained. The Re-free sample exhibited the most rapid growth of the depletion layer, the 8 wt. % Re samples exhibited intermediate growth rates, and the 32 wt. % Re and 47 Wt. % Re samples exhibited the slowest, and virtually identical, growth rates. The decrease in β-NiAl depletion layer thickness with increasing Re content can be seen in Fig. 5.

Microprobe Evaluations. The microprobe results confirmed that the coating was indeed a CoCrAlY with approximately 8 wt.% Al. The results also confirmed that the dark phase present in the backscattered images of the diffusion zone was an aluminum rich phase (16–20 wt. % Al). The continuous matrix phase within the diffusion zone was low in Al (3–4 wt. %Al) and the compositions of both diffusion zone phases transitioned across the diffusion zone. The composition of the β-NiAl depleted zone matched that of the adjacent diffusion zone matrix phase.

Profiles for Al, Co, Ni, and Cr concentration across the coating/substrate interface for the 8, 32, and 47 wt. % Re samples following the 1000 hour oxidation treatment are shown in Figs. 6 through 8. Measurements were not performed on the Re-free baseline sample due to its unavailability at the time of the microprobe measurements. Interpretation of these profiles is complicated by the multiphase nature of both the CoCrAlY coating and the diffusion zone. Nonetheless, two observations are apparent. First, the amount of Re present did not seem to

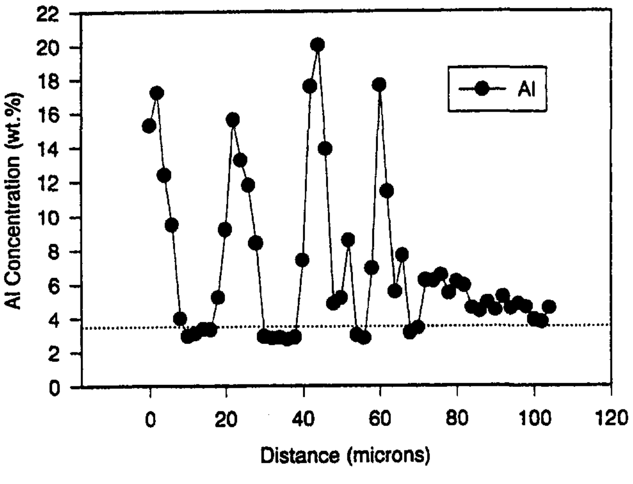

(a)

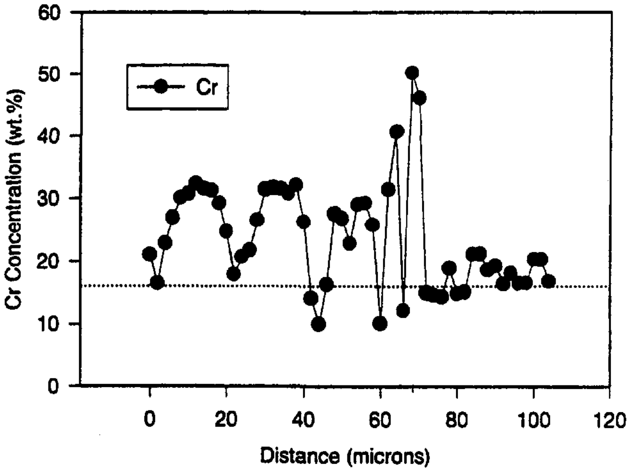

(d)

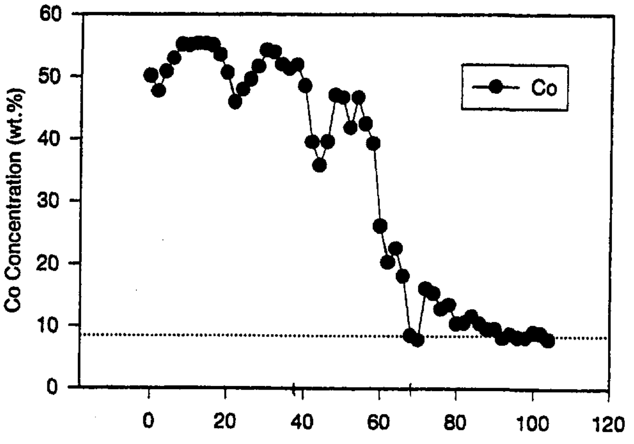

(b)

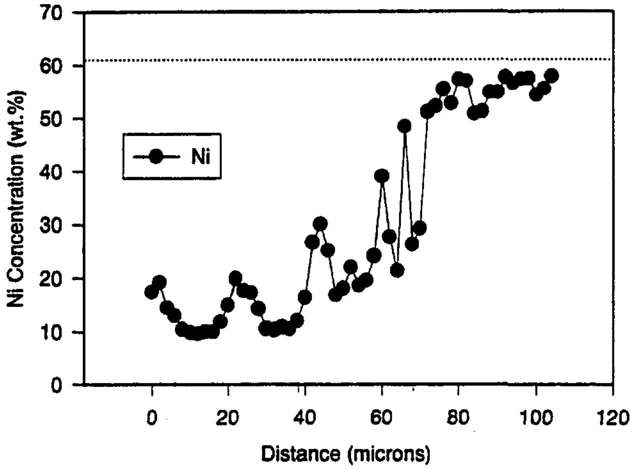

(c)

Fig. 7 Composition profiles for (*a*) Al, (*b*) Co, (*c*) Ni, and (*d*) Cr obtained from the 32 percent Re sample following a 1000 hour oxidation exposure at 926°C (1700°F). ***The transitions between the CoCrAlY coating and the diffusion zone and between the diffusion zone and the base metal occur*** **at 38 and 68 μm, respectively. The dotted lines represent the average concentration in the substrate.**

significantly alter any of the profiles. Second, the presence of elevated levels of Al and Co in the IN738LC matrix for at least 20 μm beyond the two-phase diffusion zone was evident in each of the samples. The Al enhancement appeared to extend to a greater depth than the Co enhancement; however, no obvious effect of Re on the depth of either the Al or the Co enhancement was observed.

Discussion

Both MCrAlY and aluminide type coatings protect against oxidation and hot corrosion by forming a protective Al_2O_3 surface layer. Degradation of the coatings occurs by depletion of the aluminum content of the coating through interdiffusion with the substrate and through the formation and spallation of an external oxide scale. For MCrAlY type coatings, aluminum depletion leads to depletion of the aluminum rich β-NiAl particles, with interdiffusion producing an inner depletion zone at the coating/substrate interface, and oxide formation and spallation producing an outer depletion zone at the outer coating boundary. The relationships between aluminum depletion, formation of the β-NiAl depletion zone, and coating deterioration are so strong that the depleted zone widths have been used as an indicator of coating condition (Cheruvu et al., 1996) and to predict the operational temperature of service exposed blades (Srinivasan et al., 1995).

The results obtained in this study, Table 2 and Figs. 4 and 5, clearly show that the application of a thin interlayer of Ni-Re beneath the MCrAlY coating can significantly decrease the growth rate of the inner β-NiAl depletion zone. Order of magnitude reductions in the inner depletion zone thickness formed at 1000 hours were obtained with both the Ni-32 wt.% Re and the Ni-47 wt.% Re interlayer coatings. Since formation of the inner depletion zone is believed to result from interdiffusion with the substrate, these results suggest that the Ni-Re interlayer provided a significant impediment to the inward diffusion of aluminum into the substrate.

The identification of rhenium as a potent strengthener in nickel-base superalloys (Anton and Lemkey, 1984) has led to a number of studies of its role in creep and diffusion processes. The results of these studies are worth reviewing since they may help explain the beneficial results obtained with the Ni-Re interlayers. Giamei and Anton (1985), Lahrman et al. (1988), and Murakami et al., (1994) have shown that rhenium partitions to the γ phase. Coarsening of the γ' during thermal exposure would thus require that rhenium diffuse away. It has been postulated that the necessary diffusion of rhenium away from the growing γ' coupled with a slow diffusion rate for rhenium in the γ was responsible for the decreased γ' coarsening kinetics in the presence of rhenium (Giamei and Anton, 1985). Recent measurements of diffusion in the nickel-rhenium system (Neu-

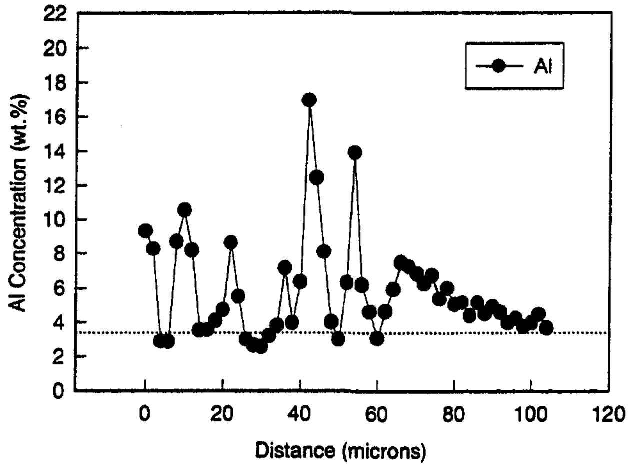

(a)

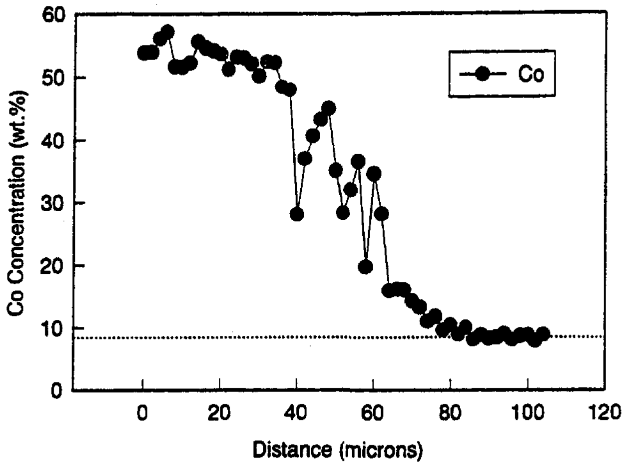

(b)

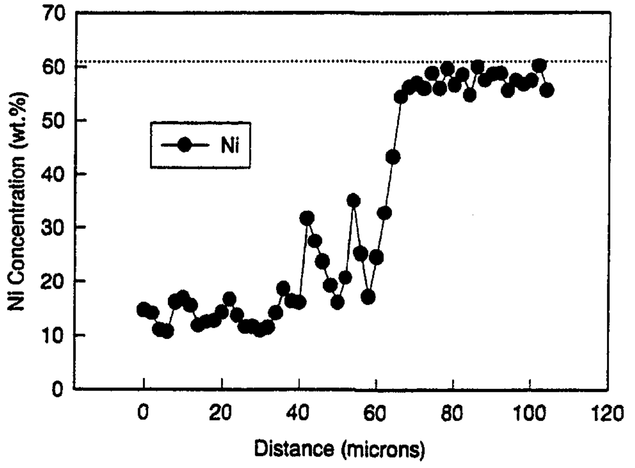

(c)

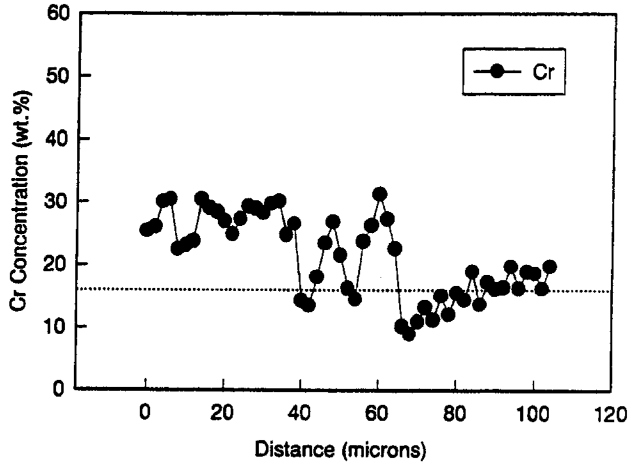

(d)

Fig. 8 Composition profiles for (*a*) Al, (*b*) Co, (*c*) Ni, and (*d*) Cr obtained from the 47 percent Re sample following a 1000 hour oxidation exposure at 926°C (1700°F). The transitions between the CoCrAlY coating and the diffusion zone and between the diffusion zone and the base metal occur at 35 and 65 μm, respectively. The dotted lines represent the average composition in the substrate.

bauer et al., 1994), finding relatively low activation energies for the diffusion of rhenium in nickel, have not supported the early theories. These low activation energies, however, were thought to be due to pipe and/or grain boundary diffusion. More recent atom probe measurements have shown that the creep strengthening produced by rhenium may be due to the formation of short range order by the rhenium in the γ.

Rhenium's ability to retard γ' growth could certainly play a role in reducing inward diffusion of aluminum since the inward diffusing aluminum would likely result in growth of the γ'. However, for the IN738LC substrate used in this study, most of the inward diffusing aluminum was incorporated in a zone devoid of γ'; only the tail of the diffusion profile extended into the γ/γ' phase region. The γ' appeared to dissolve, possibly due to diffusion induced compositional changes, at the front of the advancing diffusion zone. The benefits of retarded γ' coarsening would not be expected to be large under such conditions. The mechanism by which rhenium retarded the inward diffusion of aluminum is, thus, still unknown.

Conclusions

The following conclusions can be drawn from the results obtained in this investigation:

1 The presence of a thin Ni-Re interlayer decreased the growth rate of the inner β-NiAl depletion zone in a CoCrAlY coating by about an order of magnitude.

2 The reduction of the inner β-NiAl depletion zone thickness indicates that Re can be an effective barrier to the inward diffusion of aluminum. The mechanism for this enhancement has yet to be identified.

Acknowledgments

This work was supported by the Electric Power Research Institute under contract number W.O. 9005-03.

References

Anton, D. L. and Lemkey, F. D., 1984, "Quinary Alloy Modifications of the Eutectic Superalloy γ/γ' + Cr_3C_2," *Superalloys 1984*, M. Gell, C. S. Kortovich, R. H. Bricknell, W. B. Kent, and J. F. Radavich, eds., AIME, Warrendale, PA, pp. 601–610.

Blavette, D., Caron, P., and Khan, T., 1986, "An Atom Probe Investigation of the Role of Rhenium Additions in Improving Creep Resistance of Ni-Base Superalloys," *Scripta Metallurgica*, Vol. 20, pp. 1395–1400.

Cheruvu, N. S., Carr, T. J., Dworak, J., and Coyle, J., 1996, "The In-Service Degradation of Corrosion-Resistant Coatings," *Journal of Materials*, pp. 34–38.

Giamei, A. F., and Anton, D. L., 1985, ''Rhenium Additions to a Ni-Base Superalloy: Effects on Microstructure,'' *Metallurgical Transactions*, Vol. 16A, pp. 1997–2005.

Lahrman, D. F., Field, D. R., Darolia, R., and Fraser, H. L., 1988, ''Investigation of Techniques for Measuring Lattice Mismatch in a Rhenium Containing Nickel Base Superalloy,'' *Acta Metallurgica*, Vol. 36, pp. 1309–1320.

Leverant, G. R., 1976, Air Force Contract F44620-76-C-0028, unpublished research.

Murakami, H., Harada, H., and Bhadeshia, H. K. D. H., 1994, ''The Location of Atoms in Re and V-Containing Multicomponent Nickel-Base Single-Crystal Superalloys,'' *Applied Surface Science*, Vol. 76/77, pp. 177–183.

Neubauer, C. M., Mari, D., and Dunand, D. C., 1994, ''Diffusion in the Nickel-Rhenium System,'' *Scripta Metallurgica et Materialia*, Vol. 31, pp. 99–104.

Srinivasan, V., Cheruvu, N. S., Carr, T. J., and O'Brien, C. M., 1995, ''Degradation of MCrAlY Coating and Substrate Superalloy During Long Term Thermal Exposure,'' *Materials and Manufacturing Processes*, Vol. 10, pp. 955–959.

P. Martin
Machinery Department,
Det Norske Veritas,
(DTP 303) 1 Veritasveien,
1332 Hovik, Norway

Det Norske Veritas Rule Philosophy With Regard to Gas Turbines for Marine Propulsion

1 Introduction

Det Norske Veritas (DNV) has been in the process of updating its rules for marine use for some time now. Regulatory bodies such as the International Maritime Organization (IMO), Norwegian Petroleum Directorate (NPD), and many others, change their requirements from time to time. IMO has introduced a revised code a few years ago. The requirements of these codes/standards and the implications are often very difficult to understand and implement, both for the manufacturers and the class societies such as ours. Further, the rule requirements of DNV need to be understood and acceptable world-wide if the gas turbine industry and the maritime industry, as a whole, is to function in a rational, safe, and profitable manner. This paper is mainly based on ''DNV Rules of January 1996, Part 4, Chapter 2, Section 4—Gas Turbines,'' and is intended to at least open the dialogue between the gas turbine industry and DNV.

There is a need for design approval and manufacturing inspection process systematic and testing procedures to match the standards of the industry. We need to understand the role and expectations imposed on us by owners, the authorities, insurance agencies, etc. These expectations often have technical implications that may go against the normal procedures and practices of the gas turbine industry, and could have cost impacts.

The question of DNV acceptance criteria has been asked many times, with respect to gas turbines. We rely a great deal on the manufacturer to provide the basis for the design criteria, manufacturing, and testing criteria of the gas turbine. However, we add our knowledge and experience to this, and check that the documentation presented to us by the manufacturer is technically acceptable. Generally, a high level of the state-of-the-art theoretical documentation is required to support the design of modern gas turbines.

A proper understanding of the rule philosophy of DNV could prove to be useful in developing better gas turbines systems, which fulfill the rule requirements, and at the same time save resources such as money and time. It is important for gas turbine manufacturers to understand the intent of our rules since it is the intent that needs to be fulfilled. Further, our rules do have the principle of equivalence, which means that there is full freedom in how one fulfills the intent of the rules, as long as DNV accepts the solution.

2 High Speed And Light Craft Rules—Propulsion Systems

The high speed light craft (HSLC) rules are intended for vessels that normally run at speeds in excess of 30 knots. In theory, these vessels could be propelled by any system such as an open propeller, a surface piercing propeller, or a waterjet. The most popular propulsion system is a waterjet, and this paper will address such a system.

The rules address three main elements in the process of acceptance of gas turbines known as the ''certification'' process. The fourth element, namely the in-service inspection, will help in determining if any design changes need to be made as a result of the service life of the gas turbine. This closes the loop, and forms a feedback system to the certification process.

The four main elements of the certification process are:

1-Design Assessment
2-Components Manufacturing Inspection
3-Testing of Gas turbines
4-In-Service Inspection

Design Assessment. As it is not possible to go into all the details of all the rules for gas turbines, we will address only the principles of the design assessment, some parts of the current rules, and some intended future rules.

Drawings. As a minimum, drawings are to indicate dimension, material specification, finish, and coatings, where applicable. Equivalent methods are acceptable, such as references to other documents made on the drawings that will, in turn, fulfill our requirements. The documents sent to DNV need to be controlled documents, at least in relation to DNV. That is, changes to the approved drawings need to be sent to DNV for acceptance, what changes need to be reported (e.g., Class 1 change), and when these drawings need to be sent shall be agreed upon by DNV and the manufacturer.

Strength and Vibration Calculations of Components. Our rule requirements are based on the knowledge that prior to the manufacture of components such as blades, disks, rotors, nozzles, casing, etc. the manufacturer does rigorous technical studies to ensure that the elements will survive the running conditions they will be subjected to and for a reasonable amount of hours. We also assume that there are applicable safety factors built into the design acceptance criteria of the manufacturer. Calculations are to be documented in sufficient detail to fulfill the intention of verifying the specified rules.

Example (Vibration Calculations): Blade and Disk Vibration Analysis; Methods Used and Results. In this case, the documentation should include details of the method used, e.g., the finite element method, boundary conditions of the model, material properties, and expected forcing frequencies. Results should include the natural frequencies (within the range seen necessary by the manufacturer), modal deformation related to the respective frequencies, Campbell Diagram, and a conclusion.

Components Manufacturing Inspection. The manufacturing process needs to be inspected by DNV in order to ensure that the product is manufactured in accordance with practices normally specified by the manufacturer and accepted by DNV.

Testing of Gas Turbines. Testing of the gas turbine is to be conducted according to the approved test specifications of the manufacturer and DNV, including the requirements stated in

---

Contributed by the International Gas Turbine Institute and presented at the ASIA '97 Congress and Exhibition, September 30–October 2, 1997. Manuscript received by the ASME Headquarters June 24, 1997. Paper No. 97-AA-116. Associate Technical Editor: H. A. Kidd.

the rules. The testing, which is the final acceptance test (FAT), is to be witnessed by a DNV surveyor.

In-Service Inspection. In-Service inspection is normally to be carried out by a DNV surveyor. However, DNV is in the process of working with the industry to find a solution, which would interface the maintenance manual of the manufacturers with the inspection schedule and the changes to be made, based on the results of the inspection.

The main requirements for a gas turbine to be certified according to DNV Rules are as follows:

Documentation	(A200, ref. 1)
The gas turbine is type approved	(A103, ref. 1)
The gas turbine manufacturer is ISO 9001 certified	(B101, ref. 1)
A manufacturing survey arrangement (MSA) is made between DNV and the gas turbine manufacturer	(B102, ref. 1)
Borescope inspection	(B104, ref. 1)
Enclosure for the gas turbine	(B106, ref. 1)
Periodic audits are conducted	(B301, ref. 1)
Type testing is witnessed by DNV	(B400, ref. 1)
Certification testing is witnessed by DNV	(B500, ref. 1)
Control system to be type approved	(B505, ref. 1)

2.1 Documentation. Documentation requirements are specified in the rules and normally do not need interpretation. In general, where we have encountered problems is a mutual understanding as to the level of documentation required. In this case, we would like to state that DNV needs to know the basis for the design to the same extent as the designer, with relation to strength, vibration, fatigue, etc. Further, the documentation requirements as stated in the rules are very specific, and as DNV normally does not verify the results of calculations or testing with calculations of their own, we depend greatly on the documentation of the manufacturer. Therefore, in order for DNV to evaluate these calculations, they need to be of sufficient detail. If we consider finite element analysis for blade strength, we need the mesh, the boundary conditions, the assumed loads, and the point of application of the load.

Performance is not the essential part of our work at this point, although there appears to be some pressure from the end-users to help with this aspect. For the moment, the focus of DNV is on strength, as this ties in directly with the integrity of the gas turbine, and is of the greatest importance with respect to safety. DNV requirements for performance is limited, unless otherwise stated, to the level of power required to maneuver the vessel. This power level is essential.

2.2 Type Approval. The gas turbine is normally to be type approved. From our experience, the time and effort required to obtain a design assessment on a case-by-case basis for a gas turbine is enormous. The time spent is due to the effort needed to assemble the correct documentation in terms of drawings and calculations needed to substantiate the design of the gas turbine.

In many cases DNV has found background design information poorly or not at all documented. This has been to some extent due to the age of the initial model of the gas turbine, and DNV documentation requires modern and thorough calculations, which may not have existed at the time of the original design. However, from the point of view of DNV we do not have a valid basis for approval of current models based on mature models with insufficient documentation. In certain cases the application for the mature model is unlike the current intended application, e.g., power generation was the original intention, and the current application is modern ferry service. As gas turbine manufacturers and DNV are learning, this type of extrapolation could be erroneous.

We believe that the design of gas turbines is to a considerable extent application dependent and may require additional checks due to DNV rules or rules required by other bodies that DNV is authorized to represent. We also believe that extrapolation of power on mature models should be conducted in a cautious manner.

Considering the conditions we are faced with, type approval is found to be the only reasonable method of design assessment. Most manufacturers have consented to this approach. We have also noticed that buyers are interested to have type approved gas turbines, as this assures them of technical acceptance by the authorities.

Further, the gas turbine manufacturer is motivated to complete the type approval, as this is a formal agreement between DNV and the manufacturer and is mandatory in our rules. Therefore, there is greater interest and motivation to comply with our documentation requirements.

2.3 ISO 9001. The manufacturer needs to be ISO 9001 certified. ISO 9001 is a system certification. As such, there is no control on the technical aspects of the turbine, but only that written procedures exist and that these procedures are followed.

As a result, we suggest that prior to the start of the certification, a review of the quality system is done with a technical content. This design related audit will enable DNV and the manufacturer to have a better understanding in order to write a proper manufacturing survey arrangement (MSA).

2.4 MSA. An MSA should be set up between DNV and the manufacturer. Without this, the certification process cannot take place in a rational, cost effective manner. An MSA is an agreement between the manufacturer and DNV. The intention is to formalize the processes that need to be set in place to ensure that the design initiated manufacturing process is carried out in the form of technical instructions, testing, etc. In a normal DNV certification process, a DNV surveyor would be required to witness testing and inspection of all major components such as pressure testing of casings, dimension testing of blades, etc. For gas turbines, this would be an impossible and costly process. In order to simplify this, an MSA is written with spot checks witnessed by DNV surveyors on a product audit basis at intervals mutually agreed upon by DNV and the manufacturer (normally twice a year). Within a four year period, all components mentioned in the rules should have been audited.

2.5 Borescope Inspection—In-Service Inspection. Borescope inspection is required by the Rules after testing of the gas turbines. That is after Type Testing, Certification Testing, and after a certain amount of time spent running the turbines at sea (e.g. 2500 hours).

DNV believes that borescope inspections with modern technology could be very useful in determining the condition of gas turbines. What we expect from the manufacturers is the use of correct tools and documented acceptance criteria that could enable qualified personnel, either DNV, representatives of the manufacturer, or bodies authorized by the manufacturers and accepted by DNV, to conduct professional assessment of gas turbines. Where we see a problem is in extending the life of components. This has a significant bearing on the cost, and, therefore, may lead to hasty decisions. It is here we need the support/understanding of the manufacturers and end user/owner to see that extending the life of certain components which should not be extended could actually cost more and could lead to serious consequential damages.

DNV requires that all acceptance criteria such as crack lengths, etc., be documented by theoretical or other methods, besides experience of the manufacturer. The reason for DNV taking the extra precautions, is that the marine industry does not have a body similar to the Federal Aviation Authorities, which have the resources and power to monitor, world wide, the conditions of gas turbines and to stop if necessary, turbines from being used or have them opened up for inspection on short notice. This is stated from the practical side. Theoretically, DNV may have authority to do this, in certain cases, but it may be difficult to implement this with respect to owners.

2.6 Enclosure for the Gas Turbine. The gas turbine is to be enclosed. The intention is not with respect to containment, but with respect to minimizing the possibility of fire and to prevent flammable fluids from other components to come into contact with the hot surfaces of the gas turbine. From our experience with enclosures, fire detection/prevention/control has proven to be much faster to react, and actually saved the gas turbine from damage in a certain case, where a fuel pipe came loose and sprayed fuel on the gas turbine.

2.7 Product Audits. Periodic audits are needed to check that components such as those mentioned below (2.11) comply with the requirements assumed in the design documentation, the material requirements, the manufacturing processes laid down by the manufacturer (which DNV agrees with), and the testing requirements of the manufacturer.

2.8 Type Testing. Type Testing is an integral part of the design assessment, as aspects which cannot or have not been documented by calculations or other analytical methods, are demonstrated by testing or verified by testing. In certain cases DNV may require that calculations submitted for approval are to be verified through measurements.

2.9 Certification Testing. Certification testing is required by our rules to be witnessed by our surveyors. In addition to the type testing of a particular design, each delivery has to be run through a test to receive a product certificate. The test will normally follow the specification of the engine manufacturer.

2.10 Control System Certification. DNV considers the control system to be an integral part of the gas turbine. The control system is to be type approved and tested prior to being tested together with the gas turbine.

3.0 The Sequential Certification Process

In the previous section, elements of the certification process were described. One possible method that has been adopted with success can be seen in the figure given below (Fig. 1).

The manufacturers of gas turbines are required to be ISO9001 certified. This is the first step in the process. The next step is to have the gas turbine type approved. This is followed by a manufacturing survey arrangement, product audits, and testing. This process will lead to each gas turbine that requires a DNV certification being issued a ''product certificate''.

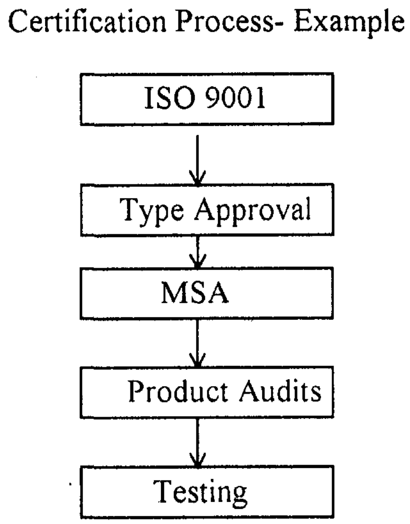

Fig. 1

However, from experience, this process does not take place as intended. It appears that most of the time, following a firm contract, manufacturers set our process in motion. These different activities begin to take place simultaneously; hence, the first turbines go through the system with great difficulty to both the manufacturers and DNV.

If we are to better this situation, we would suggest that, whenever possible, manufacturers seek type approval for their gas turbines prior to a contract for delivery. Further, as the certification process needs to be set for one single engine as for several, it may be in the interest of the manufacturer to be proactive in setting up this system, especially for manufacturers that are new to DNV. Adding engines to an already existing certification system is a relatively simple process. Following the type approval of the additional gas turbine, relevant changes need to made to the MSA, product audit, etc., and with that the certification process will follow the prescribed course.

An important aspect that needs to be stressed is that the terms and conditions on certificates such as power, speed, drawings numbers, etc., should not be changed without written consent from DNV. If so, the certificates automatically become invalid.

Further, ''major changes'' in the design, the definition of which should be agreed upon at the design assessment stage, should be notified to DNV prior to the change actually taking place. By major changes, DNV normally means changes to components in the gas flow path.

3.1 List of Critical Components. The main components focused on the testing of components mentioned in the rules, and checked during the certification process are as follows:

Blades
Impellers
Disks
Shafts
Interstage coupling
Tie Bolts
Combustors
Nozzles
Gas generator casings
Power turbine casing
Gas generator rotor assembly
Power turbine rotor assembly
Control Systems

The main characteristics of components for certification are as follows:

Material Specification Physical/Chemical
Dimensions
Repair Procedures
Air flow in blades (Cooling)
Casting procedure
Heat Treatment
Balancing of rotors

4.0 Gas Turbine—Part of a Propulsion System

The gas turbine in propulsion systems for marine use is a part of a system. Therefore, the question of integration becomes increasingly relevant. DNV rules are intended to address these needs as well. In marine application and in particular the high speed and light craft (HSLC) application, the gas turbine, the gearbox, and the waterjet need to be compatible and function together. The central unit that normally takes care of this is the control system.

Figure 2 is a representation of a HSLC propulsion system consisting of two gas turbines driving two waterjets through a reduction gearbox. In the future, it is very likely that the system could become even more complicated as the vessel owners wish to have greater flexibility in using their propulsion power capabilities in conjunction with economical fuel consumption, maximum use of turbine maintenance limits, etc.

The control system in these propulsion systems are being utilized to maximize the range of the propulsion system; for example, tuning the turbine acceleration to suit the maximum vessel/waterjet capabilities, synchronize the functionality of the different elements (such as limiting the torque to the waterjets), monitor the system for high vibrations, and to some extent log the running of the gas turbines, such that it is possible to calculate equivalent hours, etc.

5 Discussion on Certain Existing Rules

Certain aspects of the rules may need some special attention both for DNV and the gas turbine industry, some of these will be discussed in this section.

Containment With Regard to Blade Loss. The question often arises as to what is meant by this requirement one blade out, a part of a blade, or several blades. We normally agree on this during discussions based on the experience of the manufacturer with blade losses that they have witnessed. Otherwise, it is blade failure at the root. What is not addressed normally is that blade loss need not be single blades from one disk. Sometimes the blade, on its exit route, will take some other blades with it. This by itself is not necessarily a problem; however, in certain cases, the blade loss, together with other blades coming free, could destabilize the rotor. This aspect needs to be addressed by a gas turbine manufacturer, as consequential loss of other components or the turbine or other equipment, is not acceptable. By loss we mean loss that results in hazardous conditions to the vessel or its occupants. Containment is a requirement not only from DNV but also from IMO.

Modified/Upgraded Gas Turbines. In general, the approval of modification of engines already approved by us is relatively simple. Where we seem to have problems is the extent of our involvement. The manufacturers give us the impression that the upgrading of gas turbines is a relatively standard procedure in the industry, and we accept this. However, from our point of view we see this as stretching the envelope of the performance, and, in some form, lowering the safety margins (assuming upgrading the power is the purpose). Even though the manufacturer sees this as relatively simple, DNV needs to be sure that the intended point on the extrapolated curve is sufficiently justified by theoretical and/or experimental documentation.

To clarify this point, if a gas turbine is to be upgraded in power by 10 percent. DNV would like to have documentation, in form of calculations (vibrations, FEM, etc.), testing, etc., that would justify this power increase.

Novel Gas Turbine Design. DNV treats gas turbines that have been used in one application, and intended to be used in another, as a novel design. An example is industrial gas turbines being considered for marine use. The reason for this is that from our experience, the marine fast ferry environment has surprised us and many manufacturers due to its mission cycle. Therefore, we have altered our position with regard to accepting gas turbines used for fast ferry use. That is, we will accept the gas turbine only after they have exhibited an acceptable performance in this particular application, for a period of time. This is due to the fact that the gas turbines had not experienced this type of environment, and, hence, we consider it as a novel design with regard to its application.

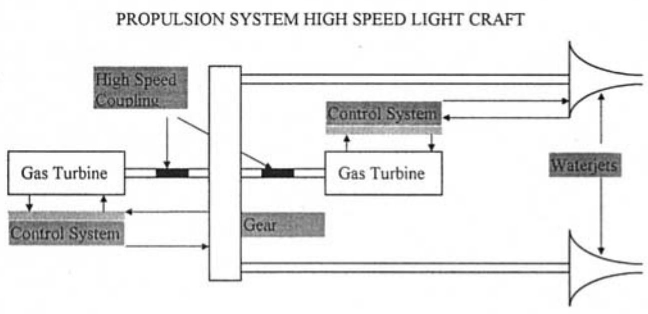

Fig. 2

Failure Mode and Effect Analysis (FMEA). Documentation is required by DNV on FMEA. This is also an IMO requirement. What is difficult to determine is the extent of the FMEA for the gas turbine. In general, what DNV is looking for is the result of one failure at a time. Each anticipated failure should result in an effect that is controlled. In most cases, the manufacturer and DNV have come to an agreement on the extent of this documentation.

Preventive Maintenance. Preventive maintenance programs are seen as very important by DNV, it is these programs that will determine whether gas turbines will prove to be successful or not. We have had feedback from the owners of high-speed vessels that propulsion machinery breakdowns are not looked after well by the Society. This has proved costly, due to breakdowns that are unscheduled. This condition actually could be improved if there is a good preventive maintenance programs.

DNV is encouraging owners to have close contact with manufacturers regarding maintenance programs. We have observed many owners having maintenance contracts with manufacturers, e.g., power by the hour. For the present, we see this as positive, as DNV is not in a position to have competent personnel all over the world, just for gas turbines inspection. In the future, our positions may change.

Control System. Control systems for gas turbines need to be type approved and certified prior to being coupled to the gas turbine. In certain cases, this has not been an easy task to follow up. An example is that specifications were found that were not updated with the model changes within the quality system. There was, however, internal documentation with regard to the changes. In one case, the control system was full of bugs, which had to be debugged during sea trials. This was, as expected, unpopular with all parties.

Further changes that are made to the logic or the limits (alarm/trip) of the control system are to be documented to DNV, with reasons for the changes. The basic philosophy is the same as for other components: if changes are made to the control system without the acceptance of DNV, our certificate (product certificate) is automatically not valid.

In Fig. 3, an example of the routing of functional signals is presented. The intention of this figure is to present the interaction between the components of the propulsion machinery in terms of the monitoring, safety, and control parameters. Examples of sampling parameters are speed, torque, temperature, etc. This is considered the lower level, as there is a higher level, which is the Bridge Control System.

The gas turbine is the source of power to the propulsion system that is capable of delivering varying amounts of power. In certain cases, much more power than the rest of the propulsion system is designed to withstand. Therefore, there is a need for cross-talk between the components, taking into consideration the different limiting parameters.

The gas turbine manufacturer, together with the system integrator, needs to take into consideration the rest of the propulsion system. Normally, the shipyard is the system integrator for HSLC vessels.

6 Discussion on Possible New Rules

Monitoring of Accumulated Life. DNV is considering using the control and monitoring system or other systems to regis-

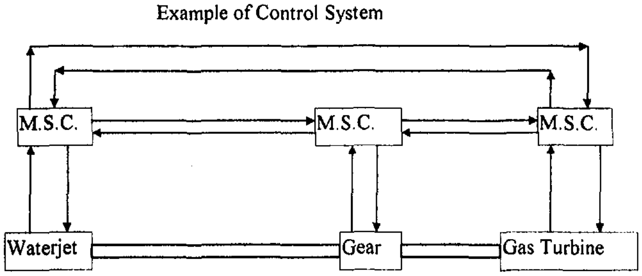

M.S.C = Monitoring / Safety /Control

Fig. 3

ter the actual accumulated life of the gas turbine. The general principle is already being tried out in existing vessels by some manufacturers of gas turbines. The power produced by the gas turbine and associated characteristics such as duration of power over the normal rating, the mission cycle (including rate of change of parameters such as temperature), speed, number of cold starts, etc., are registered. This information is transformed using the manufacturers own formula to result in an equivalent accumulated life. DNV intends to monitor this information, and use the information to estimate remaining life in critical components. DNV will require replacement of the relevant components at or close to the time when the life of the component will expire.

As the monitoring is to be done by the control system, the control system needs to be such that the version number of the software is to be registered by DNV. Further, it may be necessary to register the date of entering the software for a change and recording the actual software change. Resetting the accumulated hours should at the least be restricted.

DNV Acceptance of Overhaul Depots. With the growing use of fast ferries all over the world, there appears to be a need for replacement of components of gas turbines to be undertaken by competent workshops/depots. Most gas turbine manufacturers have depots to support their turbines the world over. DNV does not see any objections to using these depots to overhaul components, or change them. However, in order to maintain traceability of components and assure ourselves that proper components are used in our vessels, we would require that these overhaul facilities/depots comply with certain requirements such as ISO 9002, etc. DNV will need to accept these depots prior to them being allowed to overhaul DNV certified gas turbines.

7 Prototype Gas Turbines

Prototype gas turbines have not been easy to certify. The authorities often do not permit the turbines to be tested at sea without the turbines being certified. However, we are not in a position to issue a certificate due to the fact that the turbine has not proved itself. This does prove to be a bit of a problem. What we do in such cases is to issue interim certificate that will permit the turbine to be tested and fulfill its mandatory 2500 hours prior to our acceptance.

We need the close cooperation of the manufactures to get through this process in a safe and defensible manner. This is one of the areas where we see that DNV, the authorities, and the manufacturers need to discuss how to get through these problem areas, without adding enormous unnecessary effort to the project.

8 Refurbished Gas Turbines

Refurbished gas turbines are not addressed in the current rules in a direct manner. Our general position today is that we will accept gas turbines that have documented evidence to prove complete traceability of all critical components to the same extent as we would a new engine. This applies to replacement of already existing gas turbines on vessels that are in service. We do not accept refurbished engines for new vessels.

We are aware that the industry may need us to be more flexible to enable the replacement of gas turbines for overhaul purposes, replace modules that have unscheduled breakdowns, etc. We are willing to accept modular changes of turbines that are within our certification process. By this, we mean turbines that have been certified by DNV and are logged with respect to time and damages; in short, we have a certain amount of traceability.

9 Conclusion

The objective of this paper has been to inform the gas turbine industry of our philosophy and initiate a dialogue between DNV, gas turbine manufacturers, and other interested parties. In our opinion, there needs to be more informed gathering of the different parties (manufacturers, owners, class societies, authorities, and others) so that a global approach may be possible. Today, we see barriers that could be in existence purely due to insufficient knowledge or contact between the various parties.

We hope that this paper will open possibilities for other members of this industry to share their opinions on our rules and discuss them with us so that the rules can better serve the industry and the main purpose of its existence—safety at sea.

Reference

Det Norske Veritas Rules for Classification of High Speed and Light Craft Part 4, 1996, Chap. 2, Section 4, Jan.

Energy Input of a Centrifugal Stage Into the Attached Piping System During Mild Surge

B. Ribi[1]

G. Gyarmathy

ETH Swiss Federal Institute
of Technology Zurich,
Zurich, CH-8092,
Switzerland

Subjected to an oscillating flow rate, a compressor may feed additional (excitational) energy into the attached piping system. The relation between this additional energy input and the instantaneous behavior of a centrifugal compressor stage is dealt in a first part. Modeling the stage behavior by taking into account either inertia of the enclosed fluid mass or a first-order transient element or transient stall in any component leads to a different energy input. The energy input at a flow rate oscillation of given frequency and amplitude was calculated as a function of the slope of the characteristic and the reduced frequency applying a previously published model to describe the instantaneous behavior of the stage. In this model transient stall in the diffuser is taken into account. At reduced frequencies above unity the energy input of the diffuser was reduced by a considerable amount due to the specified instantaneous behavior of the diffuser. This indicates a potential to reduce the additional energy input of the diffuser either by increasing the time constant of the stall process or by increasing the mild surge frequency. For the investigated diffuser size the required reduced frequencies imply mild surge frequencies in a range being too high for industrial application (>200 Hz). Still, this method turned out to give useful insight into the link between the instantaneous behavior of the compressor and its energy input. In a second part for the same centrifugal compressor the energy contribution of several stage segments during mild surge oscillations was determined from detailed instantaneous measurements. As a result, the contribution of each stage segment to the conservation of the mild surge pulsation emerges. Although at the investigated mild surge frequencies the stage segments no longer behave strictly quasi-steadily, their contribution to the additional energy input is found to be mainly determined by the slope of their quasi-steady characteristic.

Introduction

In the context of compressor flow range enlarging, the field of active surge control by suitable devices has been widely discussed. Despite its experimentally proven potential the use of additional equipment such as sensors, controllers, and actuators is undesirable in industrial application. In addition, the limitations of active surge control for large installations in terms of large B-parameter are evident (e.g., Simon et al., 1992).

In order to find means to enlarge the flow range, compressor manufacturers would like to act on the compressor stage itself, rather than on the attached piping system. Therefore, in operating points with system instability such as mild surge, the question is how the additional energy fed into the system by the compressor can be lowered, rather than how this energy can be damped out by the system.

In a previous paper by Ribi and Gyarmathy (1991), it was shown how deep surge was preceded by mild surge. The transition from one system instability into the other will be delayed if the growth of the mild surge amplitude is prevented.[2] The mild surge amplitude is a function of both the additional energy input of the stage resulting from the mild surge oscillations and the ability of the attached duct work to dissipate this energy. As a consequence, the additional energy input of the stage has to be minimized.

Hunziker and Gyarmathy (1991) considered the slope of the stage component and subcomponent characteristics in order to quantify their tendency towards dynamic instability. Once the system became dynamically unstable (i.e., mild surge oscillations are present), this slope was taken as a measure to assess the component's contribution to the conservation of the oscillations. As long as the components behave quasi-steadily, the slope determined by time-averaged pressure measurements is an adequate measure for this. However, the situation is different when the components do not behave quasi-steadily. Then their contribution to conserve the oscillations has to be determined in another way.

Part I Stage Behavior and Energy Input

Assume a compressor system as shown in Fig. 1 consisting of a compressor, a duct where all flow inertia is taken into account, and a plenum allowing transient mass storage and a throttle ("Helmholtz resonator analogue"). In this system the compressor acts as an energy feeding element while the throttling device and the piping friction are the damping elements.

The theory about dynamic instability (see Greitzer, 1981) states that additional energy can be fed into the compression system as soon as the slope of the compressor characteristic is positive. As long as the compressor behaves quasi-steadily, any variation of mass flow rate leads to a simultaneous variation of the associated pressure rise that is either exactly in phase (Fig. 2, left) or 180 deg out of phase (Fig. 2, right)—depending whether the pressure rise characteristic is positively or negatively sloped. The integrated value of the product of mass flow perturbation times pressure rise perturbation is the net produc-

---

[1] Current address: Sulzer Turbo Ltd., Zurich, Switzerland.

[2] It was found that this transition is caused by impeller rotating stall. Although the mean time operating point is far above the limit for rotating stall, this stall was intermittently triggered when during mild surge oscillations the instantaneous flow rate dropped below the associated limit.

Contributed by the International Gas Turbine Institute and presented at the International Gas Turbine and Aeroengine Congress and Exhibition, Orlando, FL, June 2–5, 1997. Manuscript received by the ASME Headquarters March 1, 1997. Paper No. 97-GT-84. Associate Technical Editor: H. A. Kidd.

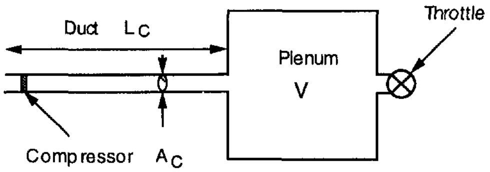

Fig. 1 Helmholtz resonator analogue

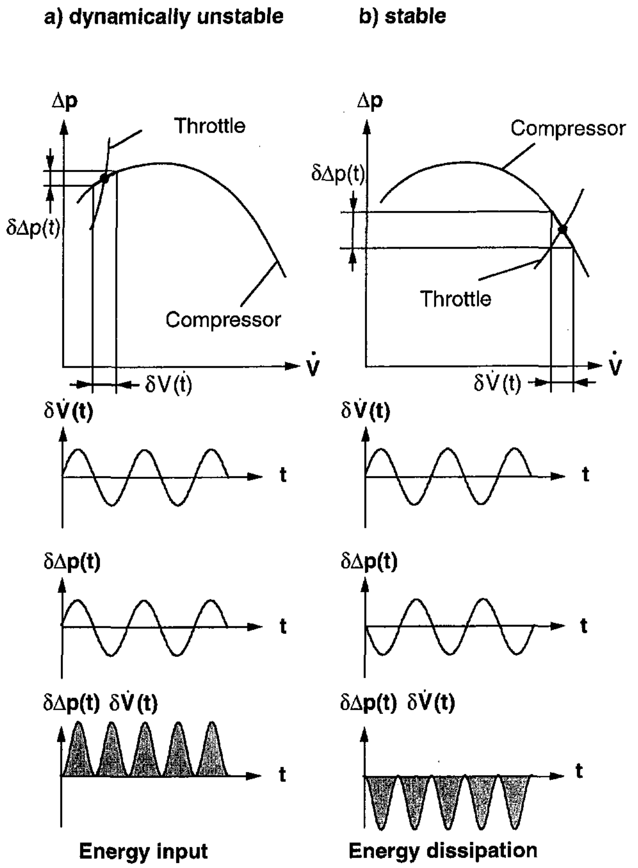

Fig. 2 Relation between pressure rise slope and additional energy due to any oscillation

tion of additional energy per cycle. With a negative slope, this product is negative too. The compressor assists in damping out any flow oscillations. In contrast, a positive product is found in case of positive slopes. As a consequence, additional energy is fed into the compression system. If this additional energy cannot be dissipated by the throttling device small disturbances will grow in time in an exponential manner until nonlinear effects limit their amplitude.

Whether the additional energy can be damped out or not depends on the system in which the stage is embedded. Greitzer (1981) showed that the ratio of pressure forces to inertial forces has to be examined by viewing the stability parameter B. However, focusing only on the stage itself, in this paper the influence of the system will not be discussed.

Quasi-Steadiness and Non-Quasi-Steadiness. So far it is obvious that there is a relation between the additional energy fed into the compression system during any flow oscillation and the way the compressor behaves. At a positive slope of the pressure rise characteristic, this amount is positive and it reaches its maximum for a given flow rate perturbation when the associated pressure rise perturbation $\delta\Delta p(t)$ is in phase with the flow rate perturbation $\delta\dot{V}(t)$; i.e., if the stage behaves quasi-steadily. In this case, the amount of additional energy is proportional to the slope.

However, it is well known that above a certain oscillation frequency the stage no longer behaves in a quasi-steady manner. The flow rate perturbation and pressure rise perturbation will no longer be in phase. The amount of net energy is altered. The question how far it is altered is strongly linked to the compressor behavior. There are several attempts to take nonquasi-steadiness into account.

Inertia of the Enclosed Fluid Mass. Abdel-Hamid (1985), for example, published some investigations performed on a centrifugal blower. He proposed to model the stage by adding an inertia element of an effective length of 0.4 times the impeller circumference. As shown below, the influence of inertia depends on the enclosed fluid mass; i.e., the flow path length of the segment considered and, therefore, does not change the additional energy input.

First-Order Transient Model. In addition to accounting for mass inertia, being usually significant in the inlet and exit flow paths of the compressor, the behavior of the stage itself is often described by a first-order transient model involving a time constant T_0 (e.g., Greitzer, 1975). While some authors bring

Nomenclature

A = area
A_{rel} = relative distance from the stability line
a = velocity of sound
B = stability parameter as defined by Greitzer (1981) as $B = u_2/2\omega_H L_C = (u_2/2a)\sqrt{V/L_C A_C}$
Bl = blockage
D = diameter
Dp = nondimensional pressure rise $Dp = \Delta p/\rho_E/2u_2^2$
f = frequency
h = enthalpy
L = length
$\dot{m}$ = flow rate
Mu_2 = peripheral Mach number $\text{Mu}_2 = u_2/\sqrt{\kappa R T_E^o}$
p = pressure
R = gas constant
T^o = stagnation temperature
T_p = period
T_0 = time constant
t = time
V = volume
$\dot{V}$ = volumetric flow rate
r = radius
u_2 = impeller tip speed

Greek Symbols

α_{2D} = diffuser vane angle setting
δ = perturbation quantity
δE = energy input per time
ϵ = phase shift
ϕ = flow coefficient $\phi = \dot{m}/\rho_E u_2 D_2^2$
ψ_s = isentropic head coefficient
κ = isentropic coefficient
ρ = density
Ω = reduced frequency
ω = angular velocity

Subscripts

A = stage exit
B = leading edge of the diffuser vanes
C = diffuser throat
C = referring to the compressor
E = stage entry
H = referring to the Helmholtz resonator analogue
i = referring to segment i
MS = referring to mild surge
tot = total
0 = normalized
1 = impeller inlet
2 = impeller outlet
3 = diffuser channel leading edge

T_0 to agreement with their experiments trying to find a corresponding flow path length with a representative velocity (e.g., Hansen et al., 1981; Bons, 1994; Fink et al., 1991), T_0 is chosen for example by Löhle (1986) as the time needed to change the circulation around the blades. However, in all these publications, the influence of transient stall is neglected. By assuming, for simplicity, a linear quasi-steady characteristic over the flow range of interest, this approach results in symmetric deviations of the instantaneous pressure rise around the steady operating point at the mean flow rate.

The influence of a compressor behaving as a first-order transient element (inertia being neglected) on the additional energy input during any flow oscillation can easily be shown. For simplification, it is assumed that the compressor is subjected to a sinusoidal flow fluctuation of a given frequency f_{MS} and amplitude $\delta\phi$. It is further assumed that the time delay can be expressed as a phase shift ϵ between $\phi(t)$ and the associated isentropic head coefficient $\psi_s(t)$. $\psi_s(t)$ is chosen instead of the pressure rise $\Delta p(t)$ in order to avoid nonlinear terms. Then the instantaneous characteristic $\psi_s(t) = f(\phi(t))$ can be expressed by the quasi-steady characteristic plus the phase shift ϵ. As shown in Appendix A, the following expression is found for the nondimensional energy input per time δE_0 after linearizing:

$$\delta E_0 = \frac{1}{T_p}\frac{\partial\psi_s}{\partial\phi}\,\delta\phi^2\left\{\int_t^{t+T_p}\cos\omega t\,\cos(\omega t-\epsilon)\,dt\right\}$$

$$= \frac{1}{2}\frac{\partial\psi_s}{\partial\phi}\,\delta\phi^2\cos\epsilon. \qquad (1)$$

Thus, the amount of δE_0 is proportional to the slope of the quasi-steady characteristic $\partial\psi_s/\partial\phi$ and the cosine of the phase shift ϵ between $\phi(t)$ and $\psi_s(t)$. As long as the slope $\partial\psi_s/\partial\phi$ is positive, δE_0 is positive also and vice versa. If ϵ is ± 90 deg, δE_0 is zero – regardless of $\partial\psi_s/\partial\phi$. By dividing the equation by the factor $\delta\phi^2$, the influence of the amplitude vanishes. The resulting amount of energy, $\delta E_0/\delta\phi^2$, is termed "normalized" energy input per time. As a consequence of normalizing this parameter, the resulting values of $\delta E_0/\delta\phi^2$ of any characteristic or any amplitude $\delta\phi$ can be plotted on the same $\partial\psi_s/\partial\phi$ versus ϵ field.

The dependence of $\delta E_0/\delta\phi^2$ is shown in Fig. 3 for the slope $\partial\psi_s/\partial\phi$ varying between ± 4.0 (according to a quasi-steady characteristic given by an arbitrarily chosen polynomial) and the phase shift ϵ varying between 0 deg and 90 deg.

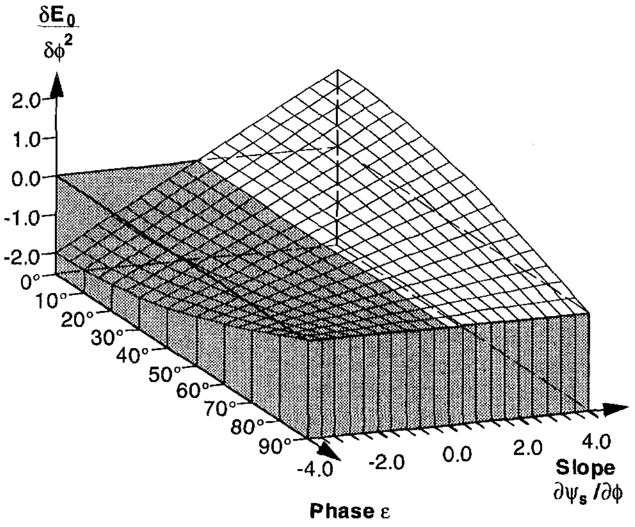

Fig. 3 Additional energy input as a function of the slope of the isentropic head coefficient and the phase shift between flow rate oscillation and isentropic head oscillation

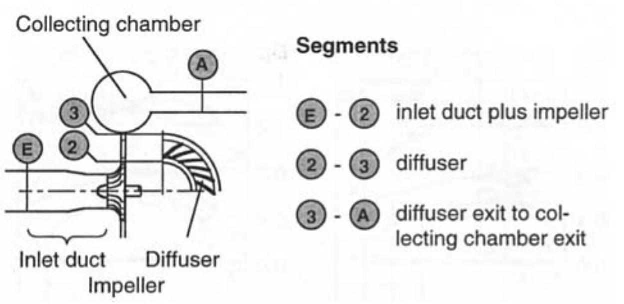

Fig. 4 Subdivision of the stage into segments in order to determine their instantaneous behavior

At a given positive slope $\partial\psi_s/\partial\phi$, the amount of the normalized energy input per time $\delta E_0/\delta\phi^2$ can be reduced by increasing the phase shift ϵ. This phase shift increases with a higher oscillation frequency. As a consequence a compressor behaving as a first-order transient element will feed less energy into the attached piping system when operating at a higher mild surge frequency f_{MS}.

Transient Stall. The deviations of the instantaneous pressure rise or isentropic head coefficient around the steady operating point at the mean flow rate are no longer symmetric if transient stall is present. Therefore, the behavior of $\delta E_0/\delta\phi^2$ with respect to a delayed pressure build up is expected to be different too.

Ribi and Gyarmathy (1995) investigated and modeled the behavior of a centrifugal compressor stage during mild surge oscillation. It is by no means postulated that the model is of general validity for all centrifugal compressors. However, this model helps to elucidate the influence of transient stall on the additional energy input. Therefore, the model is briefly sketched without further details.[3]

Stage Segments and Measured Instantaneous Behavior. In order to determine the instantaneous behavior of the compressor, the stage was subdivided into individual segments that were defined as a result of the particular location of the pressure transducers (see. Fig. 4). These are

— inlet duct and impeller ($E - 2$),
— impeller exit to diffuser exit ($2 - 3$), and
— diffuser exit to collecting chamber exit ($3 - A$).

Due to the position of the sensors, a suction pipe element of 930 mm length was comprised in $E - 2$, and an exit pipe element of about 1050 mm length in $3 - A$.

With this arrangement it was possible to determine separately the instantaneous pressure rise across these segments during a given flow rate oscillation (imposed by the piping system and variable by changing its configuration, see Fig. 10). As a typical result, Fig. 5 shows the instantaneous pressure rise versus flow rate traces (cycles) for the stage and its segments at an oscillation frequency of about 20 Hz. The results refer to one stage configuration ($\alpha_{2D} = 25$ deg, see Part II) measured at four speeds ($Mu_2 = 0.4, 0.6, 0.75$, and 0.9). The dots represent the normalized instantaneous pressure rise $Dp(t)$ during flow oscillations around a mean value $\bar{\phi}$. The full lines are the time-averaged characteristics $Dp(\bar{\phi})$ known from measurement by pneumatic devices. (Most lines fall off to the left of the maximum of the stage head Dp_{EA}, where time-averaged measurements yield a lower value due to mild surge fluctuations.) The largest instantaneous deviations from the pneumatically deter-

---

[3] As outlined by Davies et al. (1995), for axial compressors a possibility is given to take transient stall into account by the use of the "Dynamic Turbine Engine Compressor Code" (DYNTECC) in combination with the wide-range compressor stage performance model described by Bloch and O'Brien (1992).

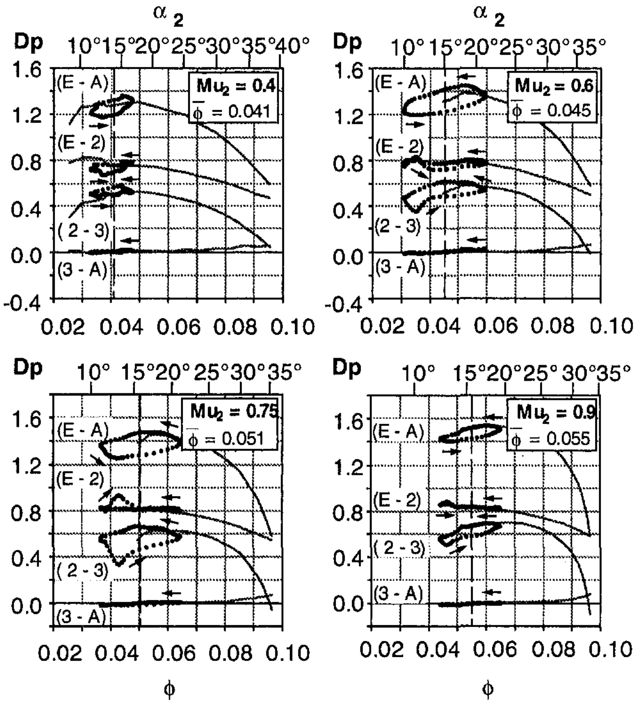

Fig. 5 Cycles described by the different stage segments in a Dp-ϕ-map during mild surge oscillations

mined characteristic are seen to occur in the diffuser $(2 - 3)$, while the inlet duct plus impeller $(E - 2)$ seems to follow closely this line with the exception at $\mathrm{Mu}_2 = 0.4$. No deviation appears in the collecting chamber plus exit duct. All cycles are run through counter clockwise.

Based on such measurements, the determination of the instantaneous behavior was possible. The following was found:

1. The pressure rise oscillations recorded in the impeller-plus-inlet-duct segment $(E - 2)$, are fully explained by the inertia of the air column comprised in the inlet duct.[4] Therefore, at least at the investigated frequencies (max. 20 Hz) the impeller itself is seen to follow the mild surge pulsations in a quasi-steady way.
2. However, the pressure rise oscillations in the diffuser segment $2 - 3$, exceed the pertinent inertial effect by far. The unsteady behavior of the diffuser is likely to be governed by noninertial (i.e., kinematic-type) flow phenomena.

As outlined by Ribi and Gyarmathy (1995), this noninertial flow phenomena can be explained by transient stall either in the vaneless or in the vaned part of the diffuser. This is sketched in Fig. 6.

If a region of stalled fluid is developed (time t_1), it takes a while for the healthy stream to carry this fluid out of the diffuser channel. In the meantime (time t_2), the stalled fluid restricts the flow area in the diffuser throat and channel. As a result the pressure recovery is reduced.

Description of the Model. The behavior of both the impeller-plus-inlet-duct segment and the diffuser segment was described by a simple mathematical model.

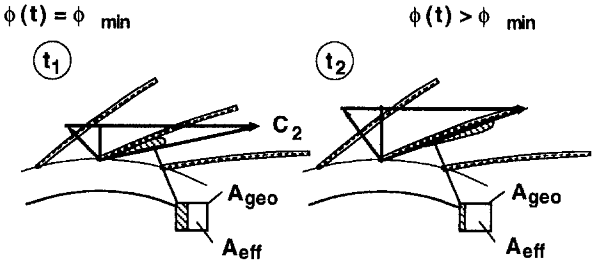

Fig. 6 Model to take into account transient stall in the diffuser

In the impeller-plus-inlet-duct segment the quasi-steady characteristic known from measurements is modeled by a polynomial. To model the instantaneous pressure head for this segment, mass inertia is assumed to be the principal influence, resulting in an additional term to the polynomial.

For the diffuser, steady flow diffuser correlations published in literature are used as a guideline.[5] For the instantaneous pressure rise, inertia is neglected due to the fact that these effects are comparatively small. However, it is assumed that the cycle is governed by kinematic effects as previously sketched. Based on the guideline to get the steady-state pressure recovery, the influence of a zone of stalled fluid was expressed by a delayed blockage in the diffuser throat, Bl_C. (This blockage may, as during quasi-steady conditions, increase with increasing incidence angle but after having reached the maximum of incidence, Bl_C may be delayed by a function of first order. The needed time scale T_0 may be proportional to the time the fluid needs to pass the diffuser channel.)

Additional Energy Input Due to Flow Rate Oscillation. Based on this model, it is possible to describe the behavior of the stage, and, hence, its energy input at any mild surge frequency. The energy input is examined separately for the impeller-plus-inlet-duct and the diffuser. The model is not adapted to take into account inertia effects in the diffuser segment or any transient stall in the impeller at higher frequencies. This allows quantifying the two influences separately.

As an example, one of the measured set of characteristics was modeled and subjected to an oscillating flow rate at a given frequency, f_{MS}, and a given amplitude, $\delta\phi$. The normalized energy input per time for the impeller-plus-inlet-duct segment, $\delta E_{0\,E-2}/\delta\phi^2$, and for the diffuser segment, $\delta E_{0\,2-3}/\delta\phi^2$, were then calculated at mean flow rates giving different slopes $\partial\psi_S/\partial\phi$. The oscillation frequency, f_{MS}, was varied in a range yielding reduced frequencies Ω for the first segment as high as 100 and in the much shorter diffuser element up to 10. (Ω is the transit time through the segment times the angular velocity of the oscillation.) For the amplitude, the following three values were selected: $\delta\phi/\bar{\phi} = 0.05$, 0.1, and 0.2, while the four slopes were $\partial\psi_s/\partial\phi = -0.2$, $+0.2$, $+0.4$, and $+0.6$.

Since the phase shift ϵ is a function of both the inertia and the slope, the normalized energy input per time, $\delta E_0/\delta\phi^2$, is plotted against the reduced frequency Ω instead of ϵ. Figure 7 shows the findings for the impeller-plus-inlet-duct segment on the left and those for the diffuser segment on the right.

For the impeller-plus-inlet-duct segment the normalized energy input per time, $\delta E_{0\,E-2}/\delta\phi^2$, reveals to be independent of the reduced frequency.[6] Since inertia is taken into account for this segment, the reduced frequency Ω is governed by the flow path length considered. This length is arbitrarily fixed by the

---

[4] Pressure excursions near the left ends of both loops, impeller-plus-inlet-duct and diffuser are due to intermittent rotating stall triggered below a critical flow rate. These excursions are nonreal apparent effects caused by the use of a single pressure sensor at some point of the circumference for measuring the impeller exit. Although this instrumentation is sufficient whenever the flow is uniform all around, it is not any more representative for the average impeller exit pressure in case of distorted flows as the ones associated with rotating stall phenomena.

[5] The required correlations between pressure recovery and throat blockage or throat blockage and diffuser vane incidence angle were taken, e.g., from Kenny (1972), Verdonk (1978), Stein (1986), Japikse (1987), Clements and Artt (1987) or Hunziker (1993).

[6] By virtue of the chosen quasi-steady characteristic given by a polynomial of second order $\delta E_{0E-2}/\delta\phi^2$ is independent of the amplitude $\delta\phi/\bar{\phi}$ too.

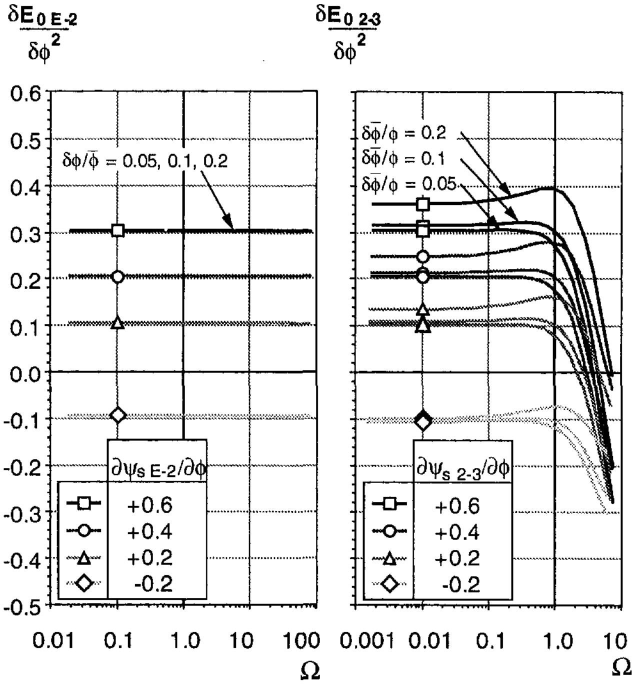

Fig. 7 Influence of the slope and the reduced frequency on the normalized energy input determined by the model—left: impeller; right: diffuser.

instrumentation and not the result of a physical mechanism. Therefore, $\delta E_{0E-2}/\delta\phi^2$ is not influenced by Ω. However, $\delta E_{0\,E-2}/\delta\phi^2$ is a function of $\partial\psi_s/\partial\phi$.

For the diffuser segment, where only transient stall was taken into account, an additional strong dependence of the reduced frequency Ω emerges for $\delta E_{0\,2-3}/\delta\phi^2$. As soon as Ω exceeds unity, $\delta E_{0\,2-3}/\delta\phi^2$ begins to decay regardless whether the slope is positive or negative. At very high values of Ω, the amount of $\delta E_{0\,2-3}/\delta\phi^2$ becomes negative although the slope is positive. Observing the associated cycle in a ψ_s-ϕ-plot reveals how the strong delay of $\psi_s(t)$ against $\phi(t)$ overturns the cycle so strongly that it resembles a forced cycle in an operating point with negative slope. The influence of the amplitude $\delta\phi/\bar{\phi}$ becomes very important at $\Omega \approx 1$ since it determines whether $\delta E_{0\,2-3}/\delta\phi^2$ already begins to decay or increases slightly prior to the drop.

The influence of inertia on the one hand and of transient stall on the other hand may emerge more clearly by examining the energy input of the segments while subjecting the compressor to a given flow rate oscillation at various degrees of throttling along a speed line. For this, the varying time mean operating point $\bar{\phi}$, the amplitude of flow rate $\delta\phi$ and the oscillation frequency f_{MS} are needed. While the amplitude $\delta\phi$ was kept constant (=0.01), the oscillation frequency f_{MS} was set to 20, 50, 100, and 200 Hz.

In any given time-mean operating point the normalized energy input per time, $\delta E_0/\delta\phi^2$, is related to the slope of the characteristic $\partial\psi_s/\partial\phi$ and the reduced frequency Ω, as shown in Figs. 8 and 9, again for the two stage segments. Taking one frequency (i.e., 20 Hz), during the throttling process one moves from negative slopes to positive slopes; because of the decreasing flow rate, Ω increases slightly. At higher oscillation frequencies, Ω is shifted to higher values. With increasing oscillation frequency the energy supplied by the impeller-plus-inlet-duct segment, $\delta E_{0\,E-2}/\delta\phi^2$, does not change since only inertia effects were considered.

This is no longer valid for the diffuser segment. At oscillating frequencies yielding $\Omega > 1$, $\delta E_{0\,2-3}/\delta\phi^2$ becomes significantly lower at positive slopes. As a consequence, the same diffuser feeds less energy into the piping system if it is forced to oscillate at a higher frequency. However, the problem is that in most applications it might be impossible to realize a piping system provoking a self-induced oscillation with such high frequencies. For the compressor examined in this paper a useful reduction in $\delta E_{0\,2-3}/\delta\phi^2$ is found for oscillation frequencies f_{MS} of about 200 Hz, which is definitively too high to be realized as the natural frequency of an appropriate piping system. Therefore, an increase of the reduced frequency has to be performed by increasing the diffuser time constant T_0 rather than the oscillation frequency. This might be achieved by slowing down the process of flow reattachment in the diffuser.

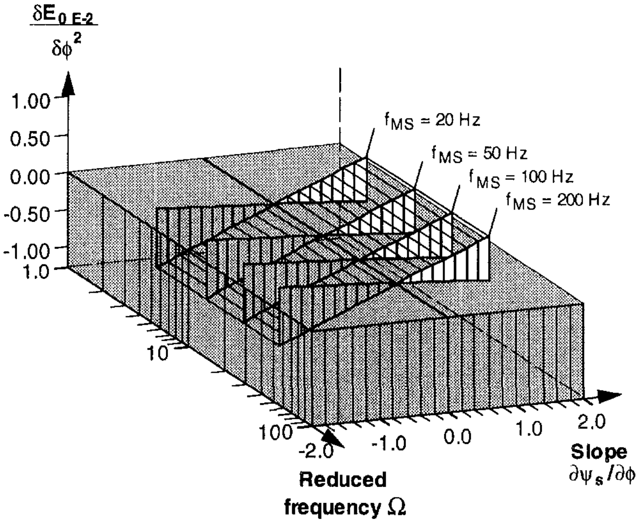

Fig. 8 Amount of the normalized energy input per time of the impeller $\delta E_{0\,E-2}/\delta\phi^2$ during throttling (reduction of Ω_{E-2}) for different oscillation frequencies f_{MS} due to the modeled instantaneous behavior (inertia taken into account)

Part II Measurements

Experimental Set-Up. The centrifugal stage of the Laboratory for Turbomachines at the ETH (Zurich) is described in detail by Hunziker and Gyarmathy (1993). The impeller was combined with different diffusers varying the diffuser vane angle setting α_{2D} (see reference). In order to vary the mild

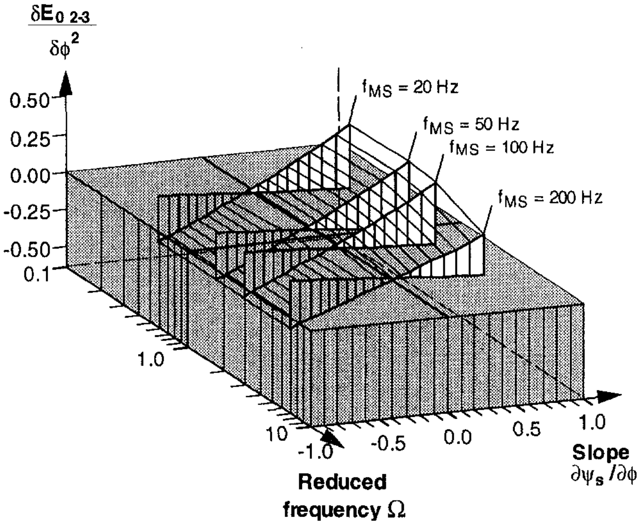

Fig. 9 Amount of the normalized energy input per time of the diffuser $\delta E_{0\,2-3}/\delta\phi^2$ during throttling (reduction of Ω_{2-3}) for different oscillation frequencies f_{MS} due to the modeled instantaneous behavior (transient stall taken into account)

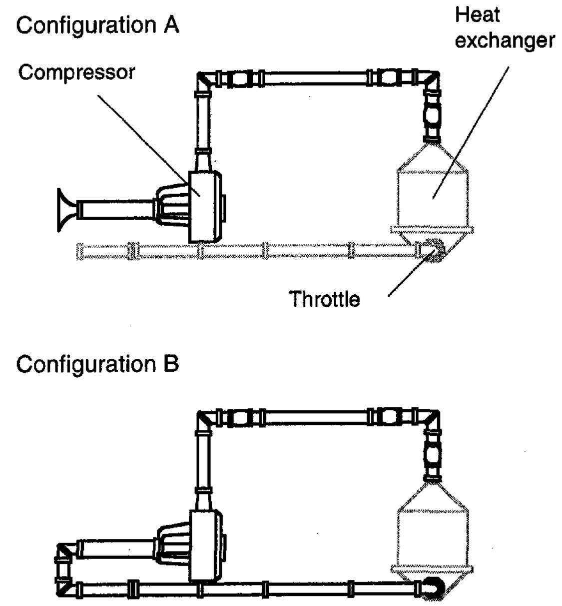

Fig. 10 Compression system configurations yielding different mild surge frequencies

surge frequency f_{MS} these stages were operated in two different compression systems termed as configuration A and B. Due to the different arrangement of ducts and volumes the two systems lead to the excitation of different acoustic modes during mild surge. As a result mild surge frequencies of 10.5 Hz (Configuration A), 17–20 Hz (Configuration B), respectively were found. The two configurations are sketched in Fig. 10. (Those parts which are not relevant for determining the acoustical mode are drawn with shaded lines.)

Measurements.

Segments. In order to capture the different instantaneous mechanisms, so far the compressor stage was divided into one segment containing the impeller-plus-inlet-duct and another segment containing the diffuser. To experimentally analyze the energy input, the diffuser was then further subdivided using additional transducers. The following may be identified as segments:

- impeller-plus-inlet-duct ($E - 2$),
- vaneless space ($2 - B$),
- semi-vaneless space ($B - C$),
- diffuser channel plus downstream vaneless space ($C - 3$), and
- collecting chamber ($3 - A$).

Compared to the theoretical analysis in Part I, this results in a subdivision of the diffuser into three additional segments.

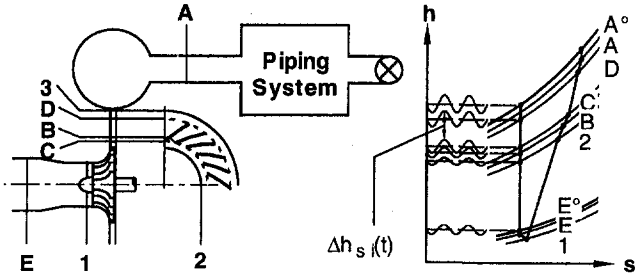

Fig. 11 Subdivision of the stage into segments in order to define the individual amount of additional energy input due to mild surge oscillations

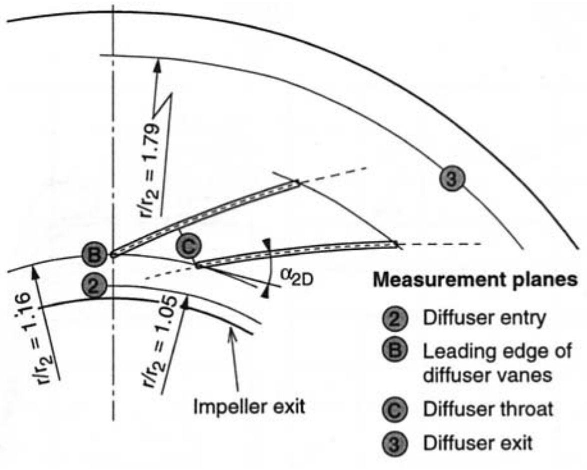

Fig. 12 Diffuser geometry and inside segments

Figure 11 is a sketch of the subdivided stage and the related isentropic enthalpy rise. Figure 12 shows more details of the diffuser geometry ($\alpha_{2D} = 25$ deg) and the location of the segments.

The individual energy input δE_i of these segments was then examined. As a result a distinction between the segments providing a positive contribution to the additional energy input and those with a negative contribution is possible. In addition, the results can be compared with the findings reported by Hunziker and Gyarmathy (1993) or Hunziker (1993), where the energy input was assessed based on the quasi-steady slope alone.

Since a suitable device to measure the instantaneous flow rate was only provided at stage entry (E), the assumption of the same mass flow at time t in any segment is a prerequisite. It can easily be shown that mass storage is negligible in the segments from E to 3 for the given oscillation frequencies. However, in the last segment (the collecting chamber) mass storage is probable. Therefore, the results for δE_{3-A} may not be fully reliable.

In Appendix B it is shown how the normalized energy input per time of an individual segment, $\delta E_{0i}/\delta\phi^2$, can be expressed as

$$\frac{\delta E_{0i}}{\delta\phi^2} = \frac{1}{T_p \delta\phi^2} \int_t^{t+T_p} \delta\phi(t)\delta\psi_{s\,i}(t)dt, \tag{2}$$

provided that the oscillation of the mass flow and of the isentropic enthalpy rise can be expressed as the sum of a stationary part and a time variant part.

Instrumentation and Data Handling. Signals were recorded from all pressure transducers as well as from a fast response pitot probe giving the instantaneous flow rate.[7] With in-house software running in a VMS environment, the stored pressure readings were analyzed by phase locked conditional sampling (over 46 to 98 periods, each with 50 to 60 values), and, subsequently, further processed to get the instantaneous flow rate $\phi(t)$ and the instantaneous isentropic head coefficient $\psi_{s\,i}(t)$ produced in the individual segments. After integrating these values, $\delta E_{0\,i}/\delta\phi^2$ was calculated.

All data were taken from operating points with steady mild surge oscillations just beyond the stability line. A nearly con-

---

[7] The pitot probe was located in the inlet duct at a radius ratio of $0.761 R_{\text{duct}}$ (with R_{duct} as duct radius). It can be shown that the instantaneous velocity profile of a flow oscillating at the given mild surge frequencies and the given viscosity of the fluid is almost constant across the given duct diameter. As a result at the chosen position the instantaneous average velocity can be determined with adequate accuracy. The length and diameter of the probe itself were selected to allow the detection of flow fluctuations by the in-built transducer up to the expected mild surge frequencies without any phase lag or amplitude attenuation.

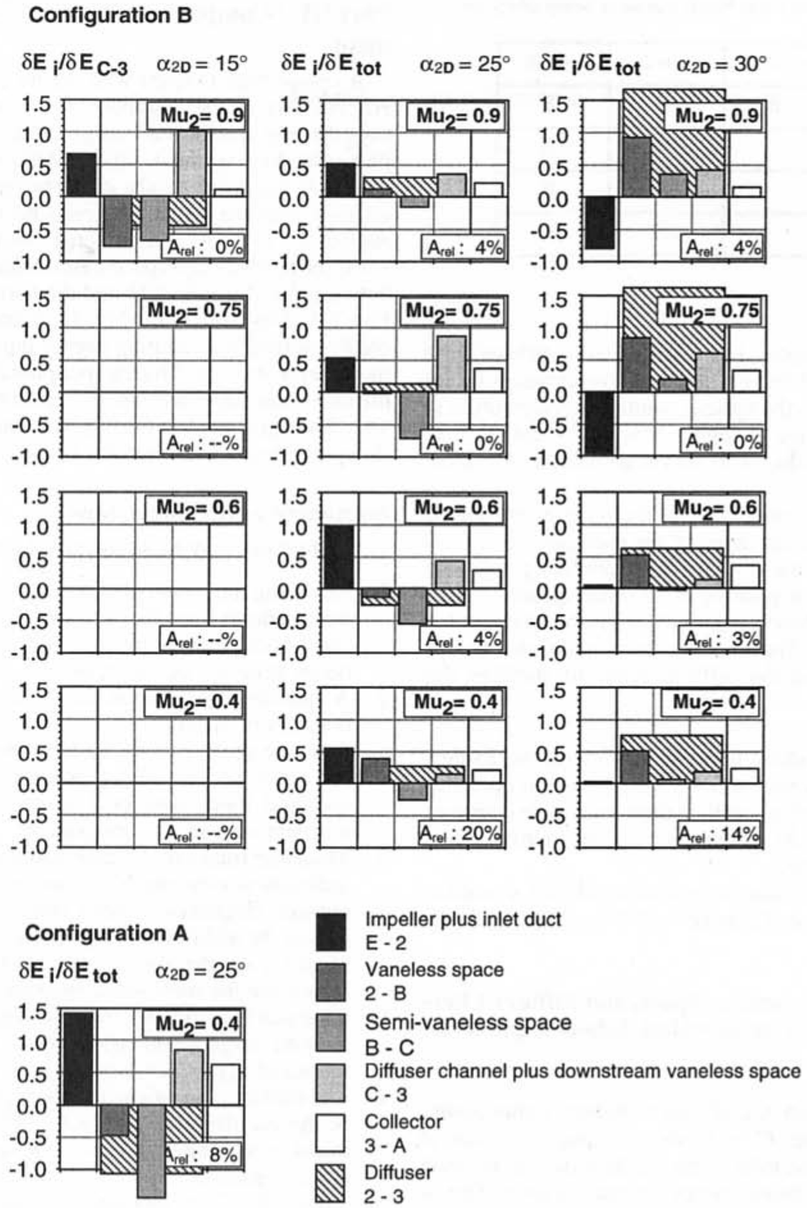

Fig. 13 Contributions of the individual stage segments to the total amount of additional energy fed into the piping system during mild surge oscillations

stant amplitude $\delta\phi$ was ensured by this procedure without the risk of triggering rotating stall and running into deep surge. The relative distance from the stability line A_{rel}, defined as

$$A_{\text{rel}} = \frac{\phi_{MS} - \bar{\phi}}{\phi_{MS}} \tag{3}$$

is given as percentage value (see Fig. 13).

Table 1 reveals which stages (α_{2D}) and peripheral Mach numbers (Mu_2) have been analyzed in which configurations (A or B). In configuration A, only one stage configuration was tested ($\alpha_{2D} = 25$ deg) at $\text{Mu}_2 = 0.4$. At higher Mu_2, the compressor encountered surge without the required amount of mild surge cycles. For the diffuser vane angle settings $\alpha_{2D} = 15$ deg in configuration B stable mild surge was only found at $\text{Mu}_2 = 0.9$.

Results. Figure 13 is a bar diagram showing the contribution of each segment to the additional energy input. The height of a bar indicates the relative amount of the segment to the total of the energy input produced in the compressor, δE_{tot}. Therefore, their sum equals unity with the exception of the stage with $\alpha_{2D} = 15$ deg, where the contributions were normalized by the amount produced in the diffuser channel δE_{C-3}. The three segments vaneless space $(2 - B)$, semi-vaneless space $(B - C)$, and channel plus downstream vaneless space $(C - 3)$ form the diffuser $(2 - 3)$. The sum of this segment is also shown in Fig. 13.

Impeller, Diffuser, Collector. Referring to the upper bar diagrams in Fig. 13 (Configuration B), first consider the whole diffuser as one segment. Consequently, the contributions of impeller, diffuser, and collector are examined, bearing in mind that the contribution of the collector may be inaccurate due to the possibility of mass storage.

It is seen that with increasing α_{2D} the main contribution to δE_{tot} is produced by the diffuser rather than by the impeller. Since the observed operating points are only slightly beyond the stability line (A_{rel} small) this behavior agrees with the findings of Hunziker and Gyarmathy (1993), where the quasi-steady slopes were analyzed near the stability line. The following can be seen:

Table 1 Stages and peripheral Mach numbers being analyzed

	$\alpha_{2D} = 15°$	$\alpha_{2D} = 25°$	$\alpha_{2D} = 30°$
$Mu_2 = 0.9$	B	B	B
$Mu_2 = 0.75$		B	B
$Mu_2 = 0.6$		B	B
$Mu_2 = 0.4$		A/B	B

1 With an "open" diffuser; i.e., a rather large diffuser vane angle setting ($\alpha_{2D} = 30$ deg), it is the diffuser which brings additional energy into the system, while the contribution of the impeller is negative at higher Mu_2 (0.75 and 0.9), or almost zero at lower Mu_2. This was also concluded by Hunziker (1993).

2 At $\alpha_{2D} = 25$ deg, the impeller and the diffuser are jointly responsible for the conservation of the oscillation ($\delta E_{E-2} > 0$).[8] At $Mu_2 = 0.6$, the diffuser is a stabilizing segment; however, its amount is positive at all other speeds.

3 With a "closed" diffuser ($\alpha_{2D} = 15$ deg), the situation has completely changed. The impeller feeds additional energy into the system,[9] and the diffuser tends to stabilize this situation.

For configuration *A* (where only the stage with the 25 deg-diffuser was measured at $Mu_2 = 0.4$), the time-mean operating point is closer to the stability line than the comparable operating point in configuration *B*. As a consequence, the contribution of the diffuser is still negative.

The contribution of the collector is always positive. Considering the quasi-steady slope, Hunziker (1993) predicted almost zero energy input.

Vaneless Space, Semi-vaneless Space, and Diffuser Channel. The contributions of the individual diffuser segments are evaluated as follows:

1 In every configuration the diffuser channel (plus downstream vaneless space, $C - 3$) shows a positive value of δE_{C-3}. Subjected to the mild surge oscillations, this segment obviously feeds additional energy into the system. This is again expected because of the positive slope of the diffuser channel segment (Hunziker and Gyarmathy, 1993).

2 Considering the semi-vaneless space ($B - C$), a negative value of the energy δE_{B-C} is found in all configurations except the ones measured with the 30 deg-diffuser at higher Mu_2. Focusing on one example (Configuration B, 25 deg-diffuser at $Mu_2 = 0.75$), also Hunziker found this segment being still stabilizing near the stability line (i.e., negative slope).

3 The vaneless space ($2 - B$), is almost neutral in the example reported by Hunziker. This also agrees with the amount of energy measured in the same configuration. In many cases, however, this segment plays an important role in determining whether the total amount of the additional energy is positive or negative. With the 30 deg-diffuser δE_{2-B} is always positive while negative values are found for $\alpha_{2D} = 15$ deg. In between, $\alpha_{2D} = 25$ deg, δE_{2-B} is either positive or negative.

Part III Comparison Between Theory and Measurement

A cross-check is made with the measured energy input at 20 Hz. As long as the amplitude $\delta\phi$ is small enough, the model says that the normalized energy input per time of the impeller-plus-inlet-duct segment, $\delta E_{0\,E-2}/\delta\phi^2$, will depend only on the slope of the quasi-steady characteristic. This is true for the diffuser segment too, if the reduced frequency Ω_{2-3} is small enough (<1.0). At a mild surge frequency of 20 Hz Ω_{2-3} is <1.0 for all measured speeds. According to the model the factor between the slope $\partial\psi_s/\partial\phi$ and the normalized energy input per time $\delta E_{0\,i}/\delta\phi^2$ is 0.5 (see Fig. 7). A comparison is made possible by plotting the resulting energy inputs gained from different measurements with different peripheral Mach numbers Mu_2 or diffuser vane angle settings α_{2D} against the slope $\partial\psi_s/\partial\phi$ (Fig. 14). The agreement is fairly good, indicating that the slope of the quasi-steady characteristic is a determinant factor.

Summary and Conclusions

The findings may be summarized and interpreted as follows:

1 Assessing the potential of a compressor stage to feed excitational energy into the attached piping system during mild surge oscillations requires the knowledge about the instantaneous behavior of the stage.

2 A considerably different energy input is predicted when the behavior of the given stage (being subjected to an oscillating flow rate of given reduced frequency) is modeled in different ways; i.e., by taking into account either inertia of the enclosed fluid mass or a first-order transient element or transient stall in any component.

3 Modeling transient diffuser stall in the diffuser investigated indicates a considerable reduction of the energy input at reduced frequencies above unity. Therefore, a potential to reduce the additional energy input by the diffuser must exist by delaying the flow reattachment in the diffuser or by increasing the mild surge frequency. However, for the diffuser size investigated, reduced frequencies above unity lead to mild surge frequencies in a range being too high for industrial application (>200 Hz).

4 The contribution of each stage segment to the conservation of the oscillations was identified by determining the additional energy input of the several stage segments by instantaneous measurements during mild surge oscillations.

5 Although at the investigated mild surge frequencies, the stage segments no longer behave quasi-steadily their contribution to the additional energy input is mainly determined by the slope of their quasi-steady characteristic. As a result,

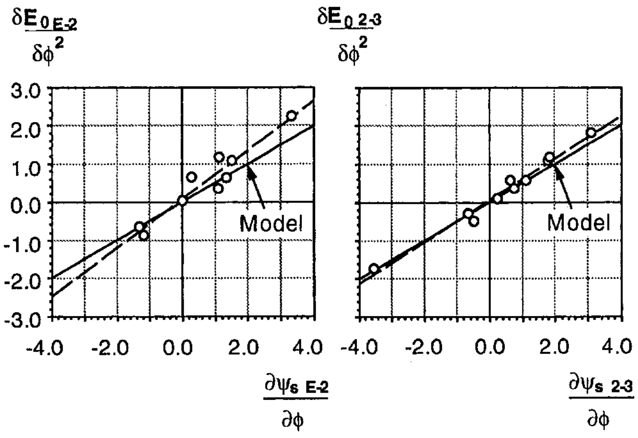

Fig. 14 Measured normalized energy input per time $\delta E_{0i}/\delta\phi^2$ and its dependence on the slope $\partial\psi_s/\partial\phi$—left: impeller; right: diffuser.

---

[8] At $Mu_2 = 0.4$ and 0.6 the time mean operating point lies below $\bar{\phi} = 0.05$ where a strong flow recirculation at impeller inlet leads to a positively sloped impeller characteristic.

[9] The impeller characteristic is again positive due to the flow recirculation at impeller inlet.

the findings agree with those concluded from examining the quasi-steady slope of each segment close to the stability line as reported by Hunziker and Gyarmathy (1993). Therefore, the following behavior is found:

- By "closing" the diffuser (i.e., decreasing the diffuser camber line angle from circumferential direction), the main contribution to the additional energy is shifted from the diffuser to the impeller.
- The diffuser channel was found to be a segment that always provides additional energy and, therefore, amplifies any oscillation.
- For the semi-vaneless space, a negative energy contribution was found in all configurations except the ones measured with the most "open" diffuser.
- In many cases the vaneless space plays an important role in determining whether the total amount of additional energy is positive or negative.

Acknowledgment

The authors would like to thank the Swiss "Kommission für die Förderung der Wissenschaftlichen Forschung" (KWF) for the financial support and ABB Turbo Systems, Sulzer Turbo and Sulzer Innotec for their technical cooperation and their financial support.

References

Abdel-Hamid, A. N., 1985, "Dynamic Response of a Centrifugal Blower to Periodic Flow Fluctuations," ASME Paper No. 85-GT-195.

Bons, J. P., 1994, "Dynamic Surge Behavior of a Centrifugal Pumping System," ASME Paper No. 94-GT-150.

Clements, W. W. and Artt, D. W., 1987, "The Influence of Diffuser Channel Geometry on the Flow Range and Efficiency of a Centrifugal Compressor," Proceedings, Inst. IMechE, Vol. 201 No. A2 (C41/8).

Bloch, G. S. and O'Brien, W. F., 1992, "A Wide-Range Axial-Flow Compressor Stage Performance Model," ASME Paper No. 92-GT-58.

Davies, M. W. Jr., Owen, A. K., O'Brien, W. F., and Cousins, W. T., 1995, "Joint Dynamic Airbreathing Propulsion Simulations Partnerships (JDAPS)," ASME Paper No. 95-GT-279.

Fink, D. A., Cumpsty, N. A., and Greitzer, E. M., 1991, "Surge Dynamics in a Free-Spool Centrifugal Compressor System," ASME Paper No. 91-GT-31.

Greitzer, E. M., 1975, "Surge and Rotating Stall in Axial Flow Compressors: Part I—Theoretical Compression System Model," ASME Paper No. 75-GT-9.

Greitzer, E. M., 1981, "The Stability of Pumping Systems—The Freeman Scholar Lecture," ASME *Journal of Fluids Engineering*, Vol. 103, pp. 193–242.

Hansen, K. E., Jørgensen, P., and Larsen, P. S., 1981, "Experimental and Theoretical Study of Surge in a Small Centrifugal Compressor," ASME *Journal of Fluids Engineering*, Vol. 103, pp. 391–395.

Hunziker, R., and Gyarmathy, G., 1993, "The Operational Stability of a Centrifugal Compressor and its Dependence on the Characteristics of the Subcomponents," ASME Paper No. 93-GT-284.

Hunziker, R., 1993, "Einfluss der Diffusorgeometrie auf die Instabilitätsgrenze des Radialverdichters," Thesis, ETH Nr. 10252, ETH Zürich.

Japikse, D., 1987, "The Technology of Centrifugal Compressors: A Design Approach and New Goals for Research," lecture notes on the flow in centrifugal compressors, Von Karman Institute, Brussels.

Kenny, D. P., 1972, "Lectures on the radial compressor," Von Karman Institute, Brussels.

Löhle, M., 1986, "Experimentelle und theoretische Untersuchung des dynamischen Betriebsverhaltens eines dreistufigen Radialverdichters," Thesis, Universität Stuttgart, Germany.

Ribi, B., and Gyarmathy, G., 1993, "Impeller Rotating Stall as a Trigger for the Transition from Mild to Deep Surge in a Subsonic Centrifugal Compressor," ASME Paper No. 93-GT-234.

Ribi, B., and Gyarmathy, G., 1995, "The Behavior of a Centrifugal Compressor Stage during Mild Surge," paper presented at the 1rst European Conf. Turbomachinery—Fluid Dynamic and Thermodynamic Aspects, VDI Berichte Nr. 1186.

Simon, J. S., Valavani, L., Epstein, A. H., and Greitzer, E. M., 1992, "Evaluation of Approaches to Active Compressor Surge Stabilization," ASME Paper No. 92-GT-182.

Stein, W., 1986, "Beitrag zur Analyze der gegenseitigen Beeinflussung von Laufrad und Diffusorbeschaufelung in Radialverdichtern," Thesis, Hannover.

Verdonk, G., 1978, "Theoretical and Experimental Investigation of the Flow at the Inlet of the Vaned Diffuser for a High Pressure Ratio Centrifugal Compressor," Technical Note 125, Von Karman Institute, Brussels.

APPENDIX A

Influence of a First-Order Transient Element on the Additional Energy Input Due to Flow Oscillations

The quasi-steady characteristic of a compressor is assumed to be known. Then the additional energy per cycle with the period T_p is given by:

$$\delta E = \int_t^{t+T_p} \dot{m}(t)\Delta h_s(t)dt - \bar{\dot{m}}\overline{\Delta h_s}T_p \tag{A1}$$

The term to the far right of Eq. (A1) is the quasi-steady energy input while the term to the left is the energy input during the oscillations with the period T_p. The difference between these two terms corresponds to the additional energy fed into the piping system by the oscillation. With the definitions

$$\psi_s \equiv \frac{\Delta h_s}{u_2^2} \quad \text{and} \quad \phi \equiv \frac{\dot{m}}{\rho_E D_2^2 u^2}$$

Eq. (A1) can be written as:

$$\delta E = u_2^3 \rho_E D_2^2 \left\{ \int_t^{t+T_p} \phi(t)\psi_s(t)dt - \bar{\phi}\bar{\psi}_s T_p \right\} \tag{A2}$$

provided that there are neither pressure nor temperature fluctuations at the stage entry. Then the non-dimensional energy input per time (net power input) is:

$$\delta E_0 = \frac{1}{T_p}\left\{ \int_t^{t+T_p} \phi(t)\psi_s(t)dt - \bar{\phi}\bar{\psi}_s T_p \right\} \tag{A3}$$

The oscillation of flow coefficient $\phi(t)$ is assumed to be sinusoidal while the associated isentropic head rise may be delayed by a phase shift ϵ:

$$\phi(t) = \bar{\phi} + \delta\phi \cos \omega t$$

and

$$\psi_s(t) = f(\phi(t - T_0))$$
$$\psi_s(t) = f(\bar{\phi} + \delta\phi \cos(\omega t - \epsilon))$$

These expressions are inserted in Eq. (A3). After the multiplication those integrals with an odd power of the perturbation quantities $\delta\phi$ or $\delta\psi_s$ vanish and as a result

$$\delta E_0 = \frac{1}{T_p}\left\{ \int_t^{t+T_p} \delta\phi(t)\delta\psi_s(t)dt \right\}$$
$$= \frac{1}{T_p}\left\{ \int_t^{t+T_p} \delta\phi \cos \omega t \delta\psi_s \cos(\omega t - \epsilon)dt \right\} \tag{A4}$$

is found. A further simplification occurs by linearizing $\delta\psi_s$ with the slope $\partial\psi_s/\partial\phi$:

$$\delta E_0 = \frac{1}{T_p}\frac{\partial\psi_s}{\partial\phi}\delta\phi^2 \left\{ \int_t^{t+T_p} \cos \omega t \cos(\omega t - \epsilon)dt \right\}$$
$$= \frac{1}{T_p}\frac{\partial\psi_s}{\partial\phi}\delta\phi^2 \cos \epsilon \tag{A5}$$

In order to exhibit the dependence of δE_0 on the slope and the phase shift an arbitrarily characteristic given by

$$\bar{\psi}_s = f(\bar{\phi}) = a\bar{\phi}^2 + b\bar{\phi}$$

is chosen while the slope $\delta\psi_s/\partial\phi$ is varied between ±4 and the phase shift ϵ between 0° and 90°.

APPENDIX B

Separation of the Total Amount of Energy Input Into the Contribution of Each Component

The additional energy which is fed into the attached piping system by the stage from $E - A$ due to the oscillation during the period T_p is (see Eq. (A1)):

$$\delta E = \int_t^{t+T_p} \dot{m}(t)\Delta h_{s\,E^\circ-A^\circ}(t)dt - \bar{\dot{m}}\overline{\Delta h}_{s\,E^\circ-A^\circ}T_p \quad \text{(B1)}$$

At all times it is:

$$\overline{\Delta h}_{s\,E^\circ-A^\circ} = \overline{\Delta h}_{s\,E^\circ-2} + \overline{\Delta h}_{s\,2-B} + \ldots + \overline{\Delta h}_{s\,D-A^\circ} = \sum_{i=1}^{5} \overline{\Delta h}_{s\,i} \quad \text{(B2)}$$

and at time t:

$$\delta h_{s\,E^\circ-A^\circ}(t) = \Delta h_{s\,E^\circ-2}(t) + \Delta h_{s\,2-C}(t) + \ldots + \Delta h_{s\,D-A^\circ}(t) = \sum_{i=1}^{5} \Delta h_{s\,i}(t) \quad \text{(B3)}$$

and so:

$$\delta E = \sum_{i=1}^{5} \int_t^{t+T_p} \dot{m}(t)\Delta h_{s\,i}(t)dt - \bar{\dot{m}}\overline{\Delta h}_{s\,i}T_p \quad \text{(B4)}$$

As a consequence the amount of energy can be subdivided into the contribution of each component:

$$\delta E = \sum_{i=1}^{5} \int_t^{t+T_p} \dot{m}(t)\Delta h_{s\,i}(t)dt - \bar{\dot{m}}\overline{\Delta h}_{s\,i}T_p \quad \text{(B5)}$$

If $\dot{m}(t)$ and $\Delta h_{s\,i}(t)$ can be expressed as the sum of a stationary part and a time variant part; i.e.,

$$\dot{m}(t) = \bar{\dot{m}} + \delta\dot{m}(t) \quad \text{and} \quad \Delta h_{s\,i}(t) = \overline{\Delta h}_{s\,i} + \delta\Delta h_{s\,i}(t) \quad \text{(B6)}$$

then (B5) can be written as:

$$\delta E_i = \int_t^{t+T_p} \delta\dot{m}(t)\delta\Delta h_{s\,i}(t)dt = u_2^3 D_2 \rho_E \int_t^{t+T_p} \delta\phi(t)\delta\psi_{s\,i}(t)dt \quad \text{(B7)}$$

Mode Localization of a Cracked Blade Disk

J. H. Kuang
kuang@mail.nsysu.edu.tw

B. W. Huang

Department of Mechanical Engineering,
National Sun Yat-Sen University,
Kaohsiung, Taiwan,
Republic of China

In this paper, the effect of blade crack on the mode localization of a rotating blade disk is studied. Pretwisted taper beams are used to simulate blades of a blade disk. The crack on the blade can be regarded as a local disorder of this periodically coupled blades system. An application of Hamilton's principle and Galerkin's method is used to formulate the equations of motion of the mistuned system. Effects of pretwisted angle, rotating speed, and crack depth of the blade on the in-plane and off-plane mode localizations of a rotating system are investigated. Numerical results indicate that the increase of rotating speed, pretwisted angle, and crack depth could enhance the localization phenomenon significantly.

1 Introduction

The localization phenomenon may be observed in a weakly coupled periodic structure with local structural or material irregularities. Such localization may in turn localize the vibrational modes and thereby confine the vibrational energy. A number of studies were conducted to introduce the mode localization phenomenon in mistuned periodic structures (Bendiksen, 1987; Pierre and Dowell, 1987; Wei and Pierre, 1988a, 1988b). However, different models and parameter values used in the above analyses have yielded different and even conflicting conclusions.

Due to manufacturing flaws or cyclic fatigue during operation, cracks frequently appear in the rotating machinery. Especially for the turbodisk, numerous cracks were observed after severe operation (Bernstein and Alien, 1992; Walls et al., 1997). The local structural irregularity caused by cracks on the blade may change the dynamic behavior of this mistuned system. The effect of crack on the dynamic and static behaviors of structures have been studied by a number of papers (Rizos et al., 1990; Broke, 1986; Tada et al., 1973). More recent papers by Chen et al. (1988) and Grabowski (1980) also deal with the effect of crack on a rotating machinery. The shrouded bladed disk of a turborotor can be regarded as a periodic system if all the blades are assembled periodically. The dynamic behavior of such shrouded blade–disk system has been studied by Cottney and Ewins (1974), whereas the fundamental aspects of mode localization in mistuned turbomachinery rotors have been studied by Bendiksen (1984) and Kaneko et al. (1994). More recent studies by Cha and Pierre (1991), and Orgun and Tongue (1994) have dealt with vibrational localization in the mistuned system with multimode subsystem.

Design of turbomachinery trend toward more and more high efficiency, so complex shape of blade in turbomachinery is unavoidable. To consider the shape effect of blade on the dynamic behaviors of a turbodisk, periodically coupled taper beams are used herein to simulate blades of the turbodisk. For the sake of simplicity, the tapered pretwisted beams are approximated as Euler–Bernoulli beams. Similar models were proposed by those of Rao (1977) and Young (1991). Most of these studies on mode localization are limited to stationary mistuned structures. The shrouded effect, commonly treated as a massless spring effect, is considered in this study in order to introduce the constraint between blades. The effects of crack size, pretwisted angle, and rotation speed on the in-plane and off-plane mode localizations in the shrouded blade–disk have been investigated in this study.

2 Equations of Motion

The periodic shrouded blade structure at a constant rotating speed Ω is shown in Fig. 1(*a*). It consists of a rigid hub with radius R_h and a cyclic assembly of N coupled blades. Each blade is coupled with the adjacent one through a shroud. The length of cantilever beam is L, and every blade is coupled by a shroud ring to the adjacent one at position r_c. The individual blade modeled as the tapered pretwisted beam is displayed in Fig. 1(*b*). The thickness and breadth at the root of the blade are t_0 and b_0. The deflection components $v_s(r, t)$ and $u_s(r, t)$ denote, respectively, the transverse flexible deflection of the sth blade in the rotational plane and perpendicular to the rotational plane.

2.1 Blades Without Crack. In this paper, it is assumed that the cross section of the blade is symmetric about two principle axes, and only the flexural bending is able to occur. The kinetic energy, due to the bending vibration, of the rotating sth taper blade is given by

$$T_s = \frac{1}{2}\int_0^L \rho A\{[\dot{u}_s(r, t)]^2 + [\dot{v}_s(r, t)]^2 + [\Omega v_s(r, t)]^2\}dr. \tag{1}$$

The cross-sectional area of the taper beam at position r is

$$A(r) = b_0 t_0\left(1 - \alpha\frac{r}{L}\right)\left(1 - \beta\frac{r}{L}\right) \tag{2}$$

and

$$\alpha = \frac{b_0 - b_1}{b_0} \tag{3}$$

$$\beta = \frac{t_0 - t_1}{t_0}, \tag{4}$$

where b_1 and t_1 denote, respectively, the breadth and thickness at the blade tip.

The total strain energy of the sth blade consists of three terms, and each will be considered separately. The first is due to the bending moment and is

$$U_s^e = \frac{1}{2}\int_0^L E[I_{yy}(u_s'')^2 + 2I_{xy}(u_s'')(v_s'') + I_{xx}(v_s'')^2]dr, \tag{5}$$

where a symbol prime (′) denotes a partial derivative with respect to r. In this equation, E is the Young's modulus of the blade and I_{xx}, I_{yy}, and I_{xy} are the moments of area. Consider the

---

Contributed by the International Gas Turbine Institute and presented at the International Gas Turbine and Aeroengine Congress and Exhibition, Stockholm, Sweden, June 2–5, 1998. Manuscript received by the ASME Headquarters April 1, 1998. Paper No. 98-GT-105. Associate Technical Editor: R. Kielb.

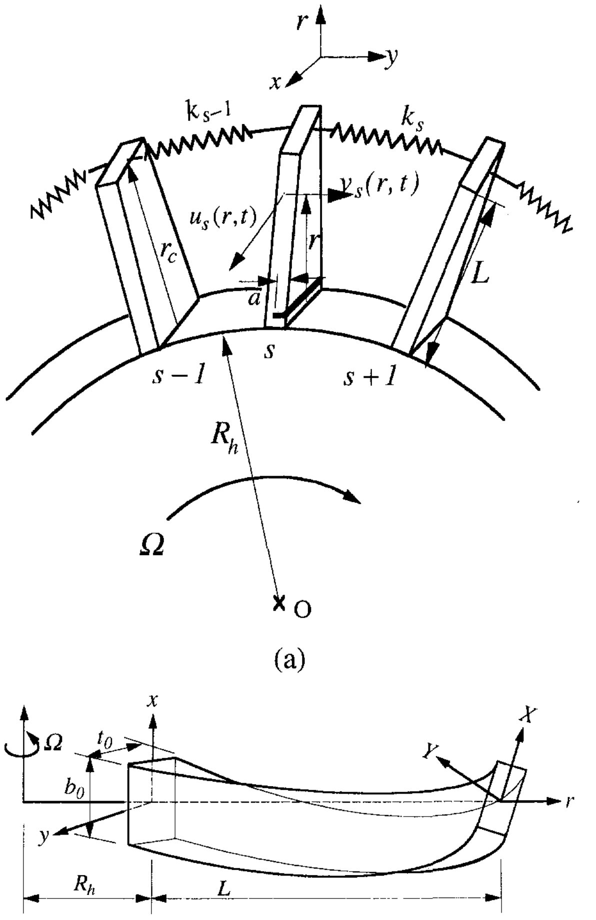

(a)

(b)

Fig. 1 (*a*) Geometry of the blade-disk system; (*b*) geometry of the pretwisted taper blade

taper beam to be pretwisted with a uniform twist angle θ, and then the moments of area at the position r can be derived as

$$I_{xx} = I_{XX}\cos^2\left(\frac{r}{L}\theta\right) + I_{YY}\sin^2\left(\frac{r}{L}\theta\right) \tag{6a}$$

$$I_{yy} = I_{XX}\sin^2\left(\frac{r}{L}\theta\right) + I_{YY}\cos^2\left(\frac{r}{L}\theta\right) \tag{6b}$$

$$I_{xy} = (I_{YY} - I_{XX})\sin\left(\frac{r}{L}\theta\right)\cos\left(\frac{r}{L}\theta\right), \tag{6c}$$

where

$$I_{XX} = \frac{b_0 t_0^3}{12}\left(1 - \alpha\frac{r}{L}\right)\left(1 - \beta\frac{r}{L}\right)^3 \tag{7a}$$

$$I_{YY} = \frac{b_0^3 t_0}{12}\left(1 - \alpha\frac{r}{L}\right)^3\left(1 - \beta\frac{r}{L}\right). \tag{7b}$$

The strain energy component due to the centrifugal force caused by the rotational speed Ω can be derived as

$$U_s^{\Omega} = \frac{1}{2}\int_r^L p^*\,[(u_s')^2 + (v_s')^2]dr, \tag{8}$$

where p^* is the centrifugal force, and is written by

$$p^* = \int_r^L \rho A \Omega^2 (r + R_h)dr. \tag{9}$$

The third and last term is the strain energy due to the elastic deformation of the shroud constrainer. This part is

$$U_s^k = \frac{k_s}{2}[v_{s+1}(r_c) - v_s(r_c)]^2. \tag{10}$$

Combining the three terms, the total strain energy of the sth blade can be obtained as follows,

$$U_s = U_s^e + U_s^{\Omega} + U_s^k. \tag{11}$$

By means of Hamilton's principle, the equation of motion of the sth blade can be derived as

$$\rho A\ddot{u}_s - \rho\Omega^2\left[\int_r^L A(r + R_h)dr u_s'\right]' + E(I_{yy}u_s'' + I_{xy}v_s'')'' = 0 \tag{12a}$$

Nomenclature

A = cross section area of the each blade
a = depth of crack
b_0 = width at the root of the blade
b_1 = width at the tip of the blade
E = Young's modulus of material of blade
$\{\bar{F}\}$ = external force vector
k_s = the stiffness of coupling for sth blade
L = length of blade
N = total number of blades
P_b = bending monent at crack
$p_i^s(t)$, $q_i^s(t)$ = determined coefficient for transverse direction for the sth blade, $i = 1, 2, \ldots, m$
r = arbitrary position on the blade
r_c = position of coupled spring
r^* = cracked position on the blade
R_h = inner diameter of disk
r = arbitrary position on the blade
s = the number of blade
t_0 = thickness at the root of the blade
t_1 = thickness at the tip of the blade
$u_s(r, t)$, $v_s(r, t)$ = deflection in transverse direction of the sth blade for the rotational plane and out of plane
$u_\xi(r, t)$, $v_\xi(r, t)$ = deflection in transverse direction of the cracked blade for the rotational plane and out of plane
$\phi_i^s(r)$ = comparison functions for the sth blade
λ_i = coefficient
μ = Poisson's Ratio
ξ = the number of cracked blade
θ = the pretwisted angle of blade
ρ = density of blade
Ω = rotation speed
ω = excitating frequency on the system
ω_0, ω_n = reference and natural frequency of the system

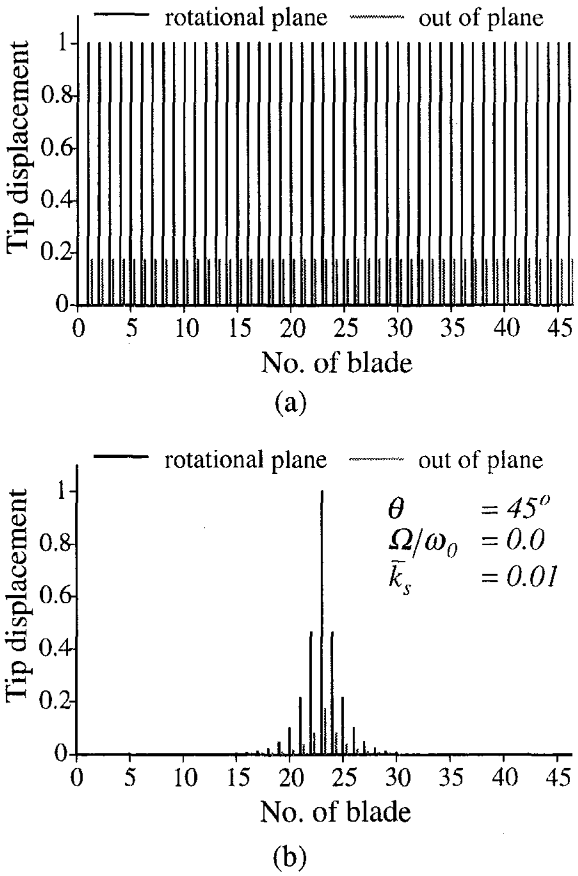

(a)

(b)

Fig. 2 *(a)* **System without crack ($\bar{\gamma}$ = 0.0, ω_1/ω_0 = 2.303); *(b)* system with a crack ($\bar{\gamma}$ = 0.1, ω_1/ω_0 = 2.299)**

$$\rho A \ddot{v}_s - \rho\Omega^2\left\{ A v_s + \left[\int_r^L A(r+R_h)\,dr\,v_s' \right]' \right\}$$
$$+ E(I_{xx}v_s'' + I_{xy}u_s'')'' + (k_s + k_{s-1})v_s\delta(r - r_c)$$
$$- k_s v_{s+1}\delta(r - r_c) - k_{s-1}v_{s-1}\delta(r - r_c) = 0 \quad (12b)$$

and the boundary conditions are

$$u_s = v_s = u_s' = v_s' = 0, \quad \text{at} \quad r = 0 \quad (13a)$$

$$u_s'' = v_s'' = u_s''' = v_s''' = 0, \quad \text{at} \quad r = L. \quad (13b)$$

Solutions of the above eigenvalue problem, i.e., Eqs. (12*a*) and (12*b*), are assumed in the form

$$u_s(r,t) = \sum_{i=1}^{m} p_i^s(t)\phi_i^s(r) \quad (14a)$$

$$v_s(r,t) = \sum_{i=1}^{m} q_i^s(t)\phi_i^s(r), \quad (14b)$$

where $p_i^s(t)$ and $q_i^s(t)$ are coefficients to be determined and $\phi_i^s(r)$ are comparison functions. In order to simplify the notations, two dimensionless variables $\bar{r} = r/L$ and $\bar{r}_c = r_c/L$ are introduced. The deflection modes are used to approximate the comparison functions $\phi_i^s(\bar{r})$ in this article. They are

$$\phi_i^s(\bar{r}) = (\cosh\lambda_i\bar{r} - \cos\lambda_i\bar{r})$$
$$- \frac{\cos\lambda_i + \cosh\lambda_i}{\sin\lambda_i + \sinh\lambda_i}(\sinh\lambda_i\bar{r} - \sin\lambda_i\bar{r}) \quad (15)$$

and

$$\cos\lambda_i\bar{r}\cosh\lambda_i\bar{r} + 1 = 0 \quad \text{for} \quad i = 1, 2, \ldots, m. \quad (16)$$

By using the Galerkin's method, the equation of motion of the *s*th blade can be derived in matrix form as

$$[m]_s\begin{Bmatrix}\ddot{p}\\ \ddot{q}\end{Bmatrix}_s + ([k^e]_s + [k^\Omega]_s)\begin{Bmatrix}p\\ q\end{Bmatrix}_s - k_{s-1}[\Lambda^{s-1}]\begin{Bmatrix}p\\ q\end{Bmatrix}_{s-1}$$
$$+ (k_s + k_{s-1})[\Lambda^s]\begin{Bmatrix}p\\ q\end{Bmatrix}_s - k_s[\Lambda^{s+1}]\begin{Bmatrix}p\\ q\end{Bmatrix}_{s+1} = 0$$
$$\text{for } s = 1, 2, \ldots, N, \quad (17)$$

where matrices $[m]_s$, $[k^e]_s$, and $[k^\Omega]_s$ are given as

$$[m]_s = \begin{bmatrix}[m]^u & 0\\ 0 & [m]^v\end{bmatrix}_s \quad (18a)$$

$$[k^e]_s = \begin{bmatrix}[k^e]^u & [k^e]^{uv}\\ [k^e]^{uv} & [k^e]^v\end{bmatrix}_s \quad (18b)$$

$$[k^\Omega]_s = \begin{bmatrix}[k^\Omega]^u & 0\\ 0 & [k^\Omega]^v\end{bmatrix}_s \quad (18c)$$

with

$$(m)_{ij}^u = (m)_{ij}^v = \int_0^1 A(\bar{r})\phi_i(\bar{r})\phi_j(\bar{r})\,d\bar{r} \quad (19a)$$

$$(k^e)_{ij}^u = \frac{E}{L^4}\int_0^1 I_{yy}(\bar{r})\phi_i''(\bar{r})\phi_j''(\bar{r})\,d\bar{r} \quad (19b)$$

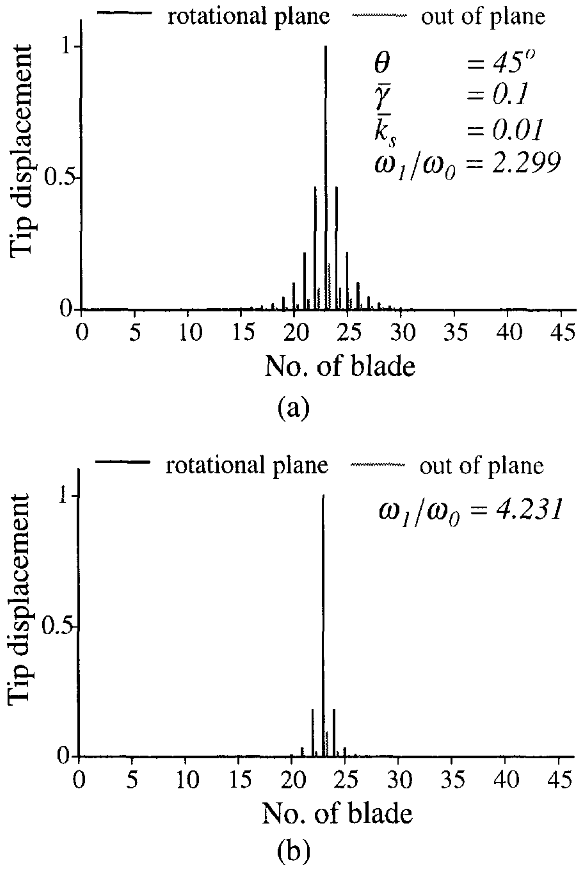

(a)

(b)

Fig. 3 *(a)* **At speed Ω/ω_0 = 0.0; *(b)* at speed Ω/ω_0 = 5.0**

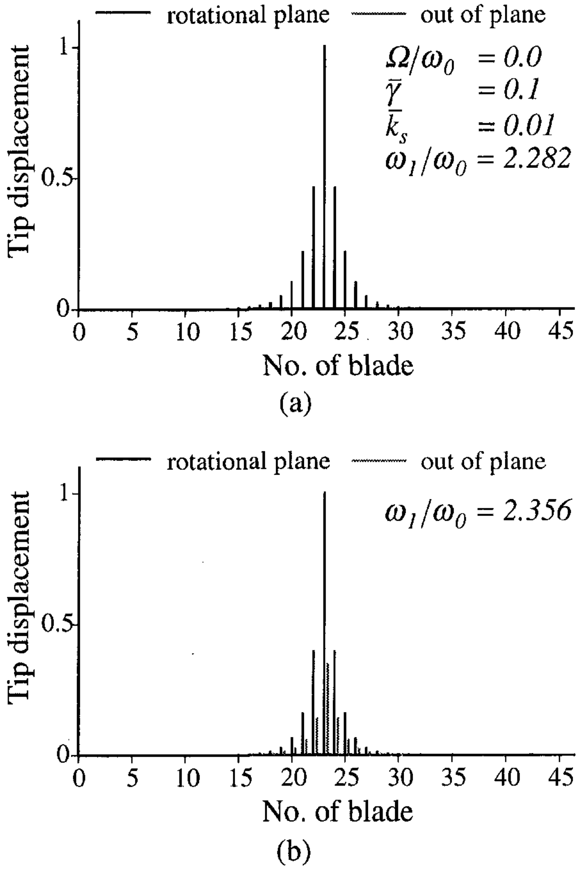

Fig. 4 (*a*) Pretwisted angle $\theta = 0$ deg; (*b*) pretwisted angle $\theta = 90$ deg

$$(k^e)^v_{ij} = \frac{E}{L^4}\int_0^1 I_{xx}(\bar r)\phi_i''(\bar r)\phi_j''(\bar r)d\bar r \qquad (19c)$$

$$(k^e)^{uv}_{ij} = \frac{E}{L^4}\int_0^1 I_{xy}(\bar r)\phi_i''(\bar r)\phi_j''(\bar r)d\bar r \qquad (19d)$$

$$(k^\Omega)^u_{ij} = \frac{\rho\Omega^2}{L^2}\int_0^1 p^*(\bar r)\phi_i'(\bar r)\phi_j'(\bar r)d\bar r \qquad (19e)$$

$$(k^\Omega)^v_{ij} = \frac{\rho\Omega^2}{L^2}\int_0^1 [p^*(\bar r)\phi_i'(\bar r)\phi_j'(\bar r) - L^2A(\bar r)\phi_i(\bar r)\phi_j(\bar r)]d\bar r. \qquad (19f)$$

For the sake of convenience, the same comparison function is assumed for the individual blade of disk, i.e., $\phi_j^s(\bar r) \equiv \phi_j(\bar r)$. So, matrices $[\Lambda^{s-1}]$, $[\Lambda^s]$, and $[\Lambda^{s+1}]$ are identical, and the vector $\{\phi(\bar r)\}_s = [\phi_1^s(\bar r), \phi_2^s(\bar r), \ldots, \phi_m^s(\bar r)]^T$ defined. They can be rewritten as

$$[\Lambda^{s-1}] = [\Lambda^s] = [\Lambda^{s+1}] = [\Lambda] \qquad (20)$$

$$[\Lambda] = \left[\begin{matrix} 0 & 0 \\ 0 & \{\phi\}_s\{\phi\}_s^T \end{matrix}\right]\Bigg|_{\bar r = \bar r_c}. \qquad (21)$$

2.2 Blade With a Crack. Considering a crack be located at $\bar r = \bar r^*$ of the ξth blade, it may be regarded as a mistuned system. The total strain energy of the defective blade will consist of four terms.

$$U_\xi = U_\xi^e + U_\xi^\Omega + U_\xi^k - U_\xi^c, \qquad (22)$$

where U_ξ^c is the released energy of the crack for the ξ blade. If the crack is initiated by the bending fatigue, the mode *I* loading will dominate the stress field. According to Dimarogonas's (1983) and Krawczuk's (1993) investigations, alteration of elastic deformation energy in places of the crack caused by bending moment is the only important change in the case of slender beams. Therefore, the released energy of this crack may be written in the following form:

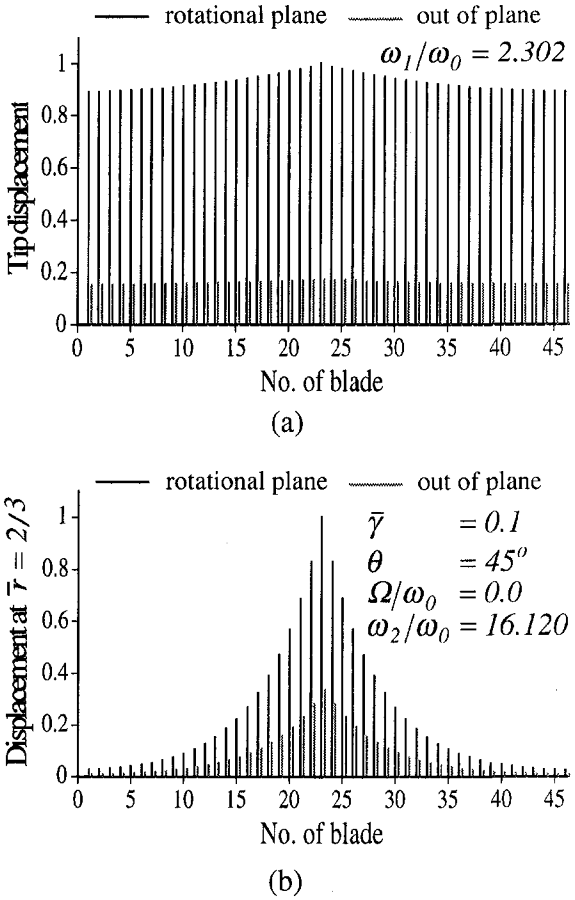

Fig. 5 (*a*) First order mode for $\bar k_s = 1.0$; (*b*) second order mode for $\bar k_s = 1.0$

$$U_\xi^c = b_0(1 - \alpha\bar r^*)\int_0^a \frac{(1-\mu^2)}{E} K_I^2 da, \qquad (23)$$

where a and μ are the depth of crack and the Poisson's ratio

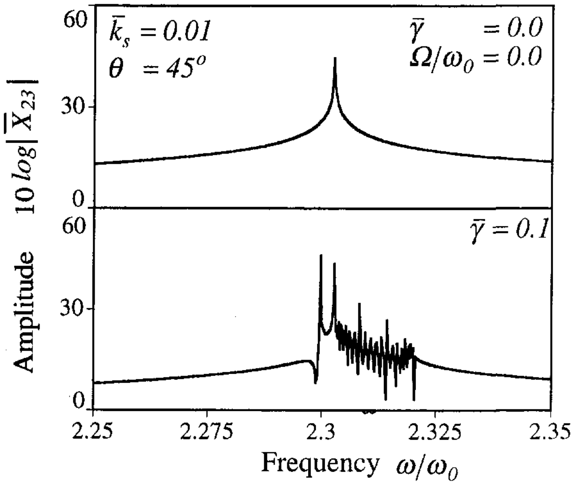

Fig. 6 Variation of frequency response of systems with and without a crack

of blade, respectively, and K_I is the stress intensity factor under mode I loading. In this case, the mode I stress intensity factor K_I can be approximated by the Tada et al. (1973) equation as

$$K_I = \frac{6p_b}{t_0^2 b_0(1 - \alpha\bar{r}^*)(1 - \beta\bar{r}^*)^2} \times \sqrt{\pi\bar{\gamma} t_0(1 - \beta\bar{r}^*)}\, F_I(\bar{\gamma}), \quad (24)$$

where

$$p_b = EI_{xx} v_\xi'' \,|_{\bar{r}=\bar{r}^*} \quad (25)$$

$$\bar{\gamma} = \frac{a}{t_0(1 - \beta\bar{r}^*)} \quad (26)$$

$$F_I(\bar{\gamma}) = \sqrt{\frac{2}{\pi\bar{\gamma}} \tan\left(\frac{\pi\bar{\gamma}}{2}\right)}\, \frac{0.923 + 0.199\left[1 - \sin\left(\frac{\pi\bar{\gamma}}{2}\right)\right]^4}{\cos\left(\frac{\pi\bar{\gamma}}{2}\right)}. \quad (27)$$

Adapting Eq. (23) gives

$$U_\xi^c = 3E(1 - \mu^2)t_0(1 - \beta\bar{r}^*) \times \int_0^1 I_{xx} Q(\bar{\gamma})(v_\xi'')^2 \delta(\bar{r} - \bar{r}^*)d\bar{r}, \quad (28)$$

where $\delta(\bar{r} - \bar{r}^*)$ is the delta function and

$$Q(\bar{\gamma}) = \int_0^{\bar{\gamma}} \pi\bar{\gamma} F_1^2(\bar{\gamma})d\bar{\gamma}. \quad (29)$$

Similarly, equations of motion for the ξth cracked blade can be derived by using Hamilton's principle. It leads to

$$\rho A\ddot{u}_\xi - \rho\Omega^2\left[\int_r^L A(r + R_h)dr u_\xi'\right]' + E(I_{yy}u_\xi'' + I_{xy}v_\xi'')'' = 0 \quad (30a)$$

$$\rho A\ddot{v}_\xi - \rho\Omega^2\left\{Av_\xi + \left[\int_r^L A(r + R_h)dr v_\xi'\right]'\right\}$$
$$+ (k_\xi + k_{\xi-1})v_\xi\delta(r - r_c) - k_\xi v_{\xi+1}\delta(r - r_c)$$
$$- k_{\xi-1}v_{\xi-1}\delta(r - r_c)$$
$$- 6EI_{xx}(1 - \mu^2)t_0(1 - \beta\bar{r}^*)Q(\bar{\gamma})[v_\xi''\delta(\bar{r} - \bar{r}^*)]''$$
$$+ E(I_{xx}v_\xi'' + I_{xy}u_\xi'')'' = 0. \quad (30b)$$

Boundary conditions of Eqs. (30a) and (30b) are the same as the sth blade, i.e., the blade without crack. Based on the Galerkin method, the equation of motion of the ξth cracked blade can be rewritten in matrix form as follows:

$$[m]_\xi \begin{Bmatrix} \ddot{p} \\ \ddot{q} \end{Bmatrix}_\xi + ([k^e]_\xi + [k^\Omega]_\xi - [k^c]_\xi)\begin{Bmatrix} p \\ q \end{Bmatrix}_\xi$$
$$- k_{\xi-1}[\Lambda^{\xi-1}]\begin{Bmatrix} p \\ q \end{Bmatrix}_{\xi-1} + (k_\xi + k_{\xi-1})[\Lambda^\xi]\begin{Bmatrix} p \\ q \end{Bmatrix}_\xi$$
$$- k_\xi[\Lambda^{\xi+1}]\begin{Bmatrix} p \\ q \end{Bmatrix}_{\xi+1} = 0, \quad (31)$$

where

$$[k^c]_s = \begin{bmatrix} 0 & 0 \\ 0 & [k^{cv}] \end{bmatrix}_s \quad (32)$$

and

$$k_{ij}^{cv} = 6\frac{EI_{xx}}{L^4}(1 - \mu^2)\frac{t_0}{L}(1 - \beta\bar{r}^*) \times Q(\bar{\gamma})[\phi_i''(\bar{r})\phi_j''(\bar{r})]_{\bar{r}=\bar{r}^*}. \quad (33)$$

2.3 Equation of Motion of the Mistuned System. For simplicity, the same comparison function is assumed for each blade. The equation of motion of the entire disk system can be expressed as

$$[M]\{\ddot{X}\} + [K]\{X\} = 0. \quad (34)$$

The system mass matrix $[M]$ and the system stiffness matrix $[K]$ are

$$[M] = \begin{bmatrix} [m]_1 & 0 & 0 & \cdot & 0 & 0 & 0 \\ 0 & [m]_2 & 0 & \cdot & 0 & 0 & 0 \\ 0 & 0 & [m]_3 & \cdot & 0 & 0 & 0 \\ \cdot & \cdot & \cdot & \cdot & \cdot & \cdot & \cdot \\ 0 & 0 & 0 & \cdot & [m]_{N-2} & 0 & 0 \\ 0 & 0 & 0 & \cdot & 0 & [m]_{N-1} & 0 \\ 0 & 0 & 0 & \cdot & 0 & 0 & [m]_N \end{bmatrix} \quad (35a)$$

$$[K] = \begin{bmatrix} [\alpha]_1 & -k_1[\Lambda] & 0 & \cdot & 0 & 0 & -k_N[\Lambda] \\ -k_1[\Lambda] & [\alpha]_2 & -k_2[\Lambda] & \cdot & 0 & 0 & 0 \\ 0 & -k_2[\Lambda] & [\alpha]_3 & \cdot & 0 & 0 & 0 \\ \cdot & \cdot & \cdot & \cdot & \cdot & \cdot & \cdot \\ 0 & 0 & 0 & \cdot & [\alpha]_{N-2} & -k_{N-2}[\Lambda] & 0 \\ 0 & 0 & 0 & \cdot & -k_{N-2}[\Lambda] & [\alpha]_{N-1} & -k_{N-1}[\Lambda] \\ -k_N[\Lambda] & 0 & 0 & \cdot & 0 & -k_{N-1}[\Lambda] & [\alpha]_N \end{bmatrix} \quad (35b)$$

$$\{X\} = \left[\begin{Bmatrix} p \\ q \end{Bmatrix}_1^T, \begin{Bmatrix} p \\ q \end{Bmatrix}_2^T, \ldots, \begin{Bmatrix} p \\ q \end{Bmatrix}_{N-1}^T, \begin{Bmatrix} p \\ q \end{Bmatrix}_N^T\right]^T \quad (35c)$$

$$\{X\} = \{\bar{X}\}e^{i\omega t}. \quad (35d)$$

Due to the cyclic arrangement of blades, it leads to

$$\begin{Bmatrix} p \\ q \end{Bmatrix}_{N+1} = \begin{Bmatrix} p \\ q \end{Bmatrix}_1$$

and

$$[\alpha]_s = [k^e]_s + [k^\Omega]_s - [k^c]_s + k_s[\Lambda] + k_{s-1}[\Lambda] \quad (36)$$

$$k_0 = k_N \quad (37)$$

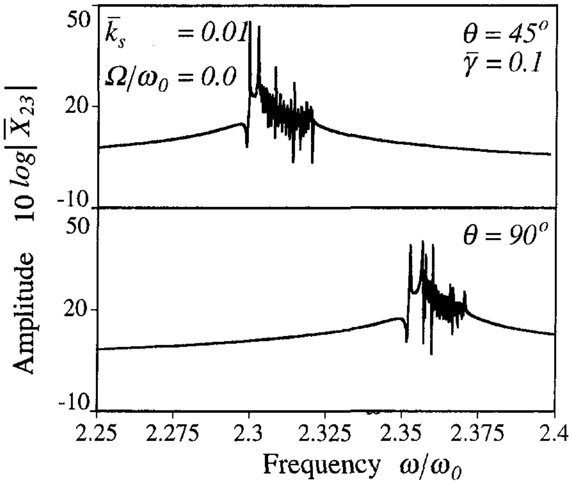

Fig. 7 Variation of frequency response of systems with and without considering the rotational speed effect

3 Numerical Results and Discussions

A rigid hub attached to 46 uniform blades, which are modeled as tapered pretwisted beams, is used to approximate the bladed disk. In this article, the existence of mode localization for a mistuned, tapered pretwisted blade–disk system with a cracked blade is studied. The effects of rotational speed, depth of the crack, and pretwisted angle of the blade on the mode localization have also been studied. The following nondimensional parameters $(R_h/L) = 0.2$, $(b_o/L) = 0.1$, $(t_0/L) = 0.02$, $\alpha = \beta = 0.25$, $\theta = 45$ deg, and $\bar{r}^* = 0$ are specified for the blade. For the convenience of specifying the mode localization frequency, a nondimensional frequency ratio ω_n/ω_0 is employed. The frequency ω_n is the natural frequency of the mistuned system, and ω_0 is a reference frequency that is defined as $\omega_0 = 0.01\sqrt{E/\rho L^2}$.

As a crack propagates on a blade, it may not only alter the dynamic behavior of this blade, but may also introduce the so called mode localization phenomenon in the whole mistuned system. In this numerical example, a crack is assumed at the root of the 23rd blade.

3.1 Free Vibration Analysis. An assembly of 46 pretwisted taper beams interconnected at blade tip is considered, i.e., $\bar{r}_c = 1$. An interblade coupling stiffness $\bar{k}_s = 0.01$ is assumed for the shroud ring. The dimensionless stiffness is defined as $\bar{k}_s = (12k_sL^3)/Eb_0t_0^3$. The vibration of this pretwisted blade–disk system consists of two parts, one of which is vibrated in the rotational plane and the other is in the out-of-plane. Blade tip displacement patterns of the tuned system at the lowest natural frequency are illustrated in Fig. 2(a). The figure shows that the magnitude of tip displacement of the individual blade in a tuned system is the same. Figure 2(b) is illustration of the occurrence of modal localization in this mistuned system. Results indicate that the tip displacement pattern may change from a weak localization to a strong localization as the crack depth γ is increased. Figures 3(a) and (b) display that the mode localization is affected by the rotational speed. As expected, because of the centrifugal force, the localization frequency ω_1 of the mistuned system is increased. It is also observed that the localization vibration in the rotational plane is enhanced, and the vibration in the out-of-plane is depressed simultaneously as the rotational speed is increased. The effect of pretwisted angle on the mode localization has also been studied in this investigation. Figures 4(a) and (b) display the variation of the tip displacement pattern for blades with different pretwisted angle. It indicates that the localization in the out of plane is enhanced as the pretwisted angle is increased.

As noted in a number of papers, the degree of localization depends significantly upon the magnitude of disorder and the modal coupling effect. The modal coupling effect in this blade–disk system is determined by the spring stiffness constant $\bar{k}_s$, the blade mode number, and the modal deflection at the blade tip. The above study has shown that strong localization occurs in all modes for a small coupling stiffness, e.g., $\bar{k}_s = 0.01$ in this case. It is of interest to investigate what happens in the large coupling case. Figures 5(a) and (b) display selected mistuned systems connected at their tips for $\bar{k}_s = 1.0$. As the coupling stiffness is increased up to $\bar{k}_s = 1.0$, localization may turn out to be weak at the first order frequency ω_1, as shown in Fig. 5(a). However, strong localization may reappear in the groups of modes whose primary component mode has a node near the constraint location $\bar{r}_c = 1$. Figure 5(b) shows the localization at the second order frequency and it shows a strong localization occurs in this mode.

3.2 Forced Response. The response of the mistuned blade–disk system depends upon the disk structure, the excitation frequency and magnitude, the crack depth, and the interblade coupling. The effects of blade twist angle, crack depth, and rotating speed on the localization response have been studied. Consider a uniformly distributed harmonic force $\{\bar{F}\}e^{i\omega t}$ being applied on the tapered pretwisted blades of the mistuned system. The maximum amplitude responses of the tuned and mistuned systems are shown in Fig. 6. Only a single peak at $(\omega_1/\omega_0) = 2.303$ is observed for the tuned system. It indicates that every individual blade possesses identical frequency at this peak. Contrary to the single peak in the tuned system, multiple peaks are found for the cracked blade. A group of peak amplitudes are appeared for this mistuned system in a wider frequency range. The lowest resonance frequency of this mistuned system, i.e., the so-called localization frequency $(\omega_1/\omega_0) = 2.299$ is close, but lower than the corresponding lowest natural frequency of a tuned system. From the tip pattern as shown in Fig. 2(b), it shows that the vibration at localization frequency is confined only in a few numbers of blades.

Figure 7 displays the displacement frequency responses of the mistuned system with different pretwisted angles. Results indicate that the higher localization frequency is observed for the mistuned system with large pretwisted angle. Figure 4 shows the corresponding tip displacement patterns. It show that the localization in the out of plane has been enhanced for the mistuned system with a larger pretwisted angle.

4 Conclusions

The effect of crack depth, twist angle and rotational speed on mode localization in a pretwisted blade–disk system has been investigated. The following conclusions can be drawn from this study.

1 It can be observed that the localization phenomenon of a pretwisted shrouded blade–disk system may be introduced by a cracked blade. The strong localization appears for the mistuned system with weak interblade coupling. This localization may disappear as the interblade coupling is increased, but it will reappear in the higher modes.

2 The depth of a crack is one of the important parameters for the modal localization of a rotating blade–disk system. Results indicate that the localization may be enhanced as the depth of the crack is increased.

3 The rotational speed of the mistuned disk has a significant influence on the localization frequency; it will shift the localization frequency towards a higher frequency. The centrifugal force introduced by the rotational speed may enhance the localization in the rotational plane and depress it in the out of plane.

4 The twist angle of the blade may also affect localization in the mistuned pretwisted blade–disk system. A large twist angle will enhance modal localization in the out of plane.

Acknowledgments

The authors would like to acknowledge the support of the National Science Council, R. O. C., through Grant No. NSC87-2212-E-110-004.

5 Reference

Bendiksen, O. O., 1984, "Flutter of Mistuned Turbo Machinery Rotors," ASME Journal of Engineering for Gas Turbines and Power, Vol. 106, pp. 25–23.

Bendiksen, O. O., 1987, "Mode Localization Phenomena in Large Space Structures," *AIAA Journal*, Vol. 25, pp. 1241–1248.

Bernstein, H. L., and Alien, J. M., 1992, "Analysis of Cracked Gas Turbine Blades," ASME Journal of Engineering for Gas Turbines and Power, Vol. 114, pp. 293–301.

Broek, D., 1986, *Elementary Engineering Fracture Mechanics*, Martinus Nijhoff Publishers, Dordrecht, The Netherlands.

Cha, P. D., and Pierre, C., 1991, "Vibration Localization by Disorder in Assemblies of Monocoupled, Multimode Component Systems," *ASME Journal of Applied Mechanics*, Vol. 58, pp. 1072–1081.

Chen, L., and Chen, C., 1988, "Vibration and Stability of Cracked Thick Rotating Blade," *Computers & Structures*, Vol. 28, No. 1, pp. 67–74.

Cottney, D. J., and Ewins, D. J., 1974, "Towards the Efficient Vibration Analysis of Shrouded Bladed Disk Assemblies," *ASME Journal of Engineering for Industry*, Vol. 96B, pp. 1054–1059.

Dimarogonas, A. D., and Paipetis, S. A., 1983, *Analytical Methods in Rotor Dynamics*, Applied Science Publishers, New York.

Grabowski, B., 1980, "The Vibrational Behavior of a Turbine Rotor Containing a Transverse Crack," *ASME Journal of Mechanic Design*, Vol. 102, pp. 140–146.

Kaneko, Y., Mase, M., Fujita, K., and Nagashima, T., 1994, "Vibration Response Analysis of Mistuned Bladed Disk," *JSME International Journal Series C*, Vol. 37, No. 1, pp. 33–40.

Krawczuk, M., and Ostachowicz, W. M., 1993, "Transverse Natural Vibrations of a Cracked Beam Loaded With a Constant Axial Force," *ASME Journal of Vibration and Acoustics*, Vol. 115, pp. 524–528.

Orgun, C. O., and Tongue, B. H., 1994, "Mode Localization in Coupled Circular Plates," *ASME Journal of Vibration and Acoustics*, Vol. 116, pp. 286–294.

Pierre, C., and Dowell, E. H., 1987, "Localization of Vibrations by Structural Irregularity," *Journal of Sound and Vibration*, Vol. 114, No. 3, pp. 549–564.

Rao, J. S., 1977, "Vibration of Rotating, Pretwisted and Tapered Blades," *Mechanism and Machine Theory*, Vol. 12, pp. 331–337.

Rizos, P. F., Aspragathos, N., and Dimarogonas, A. D., 1990, "Identification of Crack Location and Magnitude in a Cantilever Beam from the Vibration Mode," *Journal of Sound and Vibration*, Vol. 138, pp. 381–388.

Tada, H., Paris, P., and Irwin, G., 1973, *The Stress Analysis of Crack Handbook*, Del Research Corporation, Hellertown, PA.

Walls, D. P., deLaneuville, R. E., and Cunningham, S. E., 1997, "Damage Tolerance Based Life Prediction in Gas Turbine Engine Blades under Vibratory High Cycle Fatigue," ASME Journal of Engineering for Gas Turbines and Power, Vol. 119, pp. 143–146.

Wei, S. T., and Pierre, C., 1988, "Localization Phenomena in Mistuned Assemblies With Cyclic Symmetry Part I: Free Vibrations," *ASME Journal of Vibration, Acoustics, Stress, and Reliability in Design*, Vol. 110, pp. 429–438.

Wei, S. T., and Pierre, C., 1988, "Localization Phenomena in Mistuned Assemblies with Cyclic Symmetry Part II: Forced Vibrations," *ASME Journal of Vibration, Acoustics, Stress, and Reliability in Design*, Vol. 110, pp. 439–449.

Young, T. H., 1991, "Dynamic Response of A Pretwisted, Tapered Beam With Non-Constant Rotating Speed," *Journal of Sound and Vibration*, Vol. 150, No. 3, pp. 435–446.

Qualitative Characterization of Anti-Swirl Gas Dampers

N. L. Zirkelback[1]
George W. Woodruff School
of Mechanical Engineering,
Georgia Institute of Technology,
Atlanta, GA 30332-0405

Anti-swirl gas dampers have applications in high-temperature turbomachinery. Nozzles comprising the circumference of the damper inject air against the direction of shaft rotation, providing a force tangential to the rotor surface that acts to damp rotor vibration. The present work involves prediction of experiments by using direct damping and cross-coupled stiffness coefficients given in Vance and Handy (1997) that characterize the rotordynamic performance of an anti-swirl damper. Direct stiffness added at the damper location is vital to representing the changes in critical speeds and the onset and cease of backward whirl given in the experiments. This direct stiffness arises due to the release of air axially across the annulus of the damper. With the addition of this significant direct stiffness, experimental results compare well with the present rotordynamic model. Predictions using the experimentally obtained damping coefficients adequately reproduce the reduction in vibration amplitudes at the critical speeds. However, applying the cross-coupled stiffness coefficients in predictions fails to show increases in the speed at which backward whirl begins and does not reproduce the wrecking instability experienced in the tests. A further study investigates the magnitude of the cross-coupled stiffness coefficient necessary to cause instability in the rotor-damper system.

Introduction

Anti-swirl gas dampers represent a viable alternative to squeeze-film dampers applied at bearing locations, especially in high-temperature turbomachinery. Stacked identical nozzles comprising the circumference of the damper inject air anti-rotationally onto the spinning shaft by dissipating air pressure from a plenum area to the damper stator portion. Muszynska (1985) and Muszynska and Bently (1989) demonstrate the damping capabilities of the anti-swirl damper by showing a marked increase in the stability threshold when the nozzles inject air against the direction of shaft rotation. Air injected coincident with the rotor spin direction causes deleterious effects on the rotor response as vibration amplitudes increase, and the threshold of stability actually lessens. Showing similar results, Brown and Hart (1986) study air injection both opposing and coincident with the shaft rotation direction and note large reductions in vibration amplitudes at the critical speeds when air injection opposes the direction of shaft rotation. Another distinct advantage of the anti-swirl damper is the ability to easily control the amount of damping provided to the system by changing the plenum pressure of the damper. Muszynska et al. (1988) elucidate this fact by presenting an elaborate control system to work in conjunction with an anti-swirl damper in successfully reducing vibration amplitudes only when necessary.

In an attempt to quantify anti-swirl damper performance, Handy (1992) and Vance and Handy (1997) determine cross-coupled stiffness and effective damping coefficients for three rotor configurations with varying clearances and surface roughness. Asymmetry of the support stiffness and a lack of internal damping in the test rig caused the first critical speed to split into two distinct critical speeds termed the first split critical speed (FSCS) and the second split critical speed (SSCS). Coastdown tests reveal the onset of backward whirl between the split critical speeds, a well documented and expected occurrence (Vance, 1988). In general, the critical speeds increase with an increase of the plenum pressure in the anti-swirl damper. However, as the plenum pressure of the damper increases, the onset of backward whirl occurs at higher speeds, even at speeds higher than the SSCS for some rotor configurations. At high plenum pressures, instabilities caused damaging crashes in two of the rotor configurations.

The objective of the present work is to predict results submitted by Vance and Handy (1997) that render the rotordynamic effects of an anti-swirl damper. The rotor is modeled, and its eigenvalues and response are reproduced using a popular rotordynamic software package (Murphy, 1995) that employs the polynomial transfer matrix method to quickly obtain prediction of the rotordynamic behavior of the rotor. The section "procedure" of the present work gives a detailed description of the anti-swirl damper setup employed by Handy (1992) and Vance and Handy (1997), while explanation about the experimental setup and procedure used in obtaining the test results appear in their original works. The present results emulate experiments in Vance and Handy (1997) giving both split critical speeds, the onset and cease of backward whirl, and the reduction in amplitude as the plenum pressure of the damper increases.

Analysis

Determining the Whirl Direction. Consider a rotor following a synchronous, elliptical orbit about an equilibrium position with a steady-state frequency (ω). The orbit as described in (x, y) orthogonal directions is

$$X(t) = X_C \cos(\omega t) + X_S \sin(\omega t) \qquad (1a)$$

$$Y(t) = Y_C \cos(\omega t) + Y_S \sin(\omega t), \qquad (1b)$$

where X_C, X_S, Y_C, and Y_S are amplitudes of the motion. Vance (1988) provides the test for the speed of onset and cease of backward whirl as

$$X_C Y_S - Y_C X_S > 0 \qquad (2)$$

Murphy (1995) does not explicitly give these coefficients in response calculations. However, Childs (1993) provides an analysis using the major and minor semi-axes (a and b) of the response ellipse as an indicator of the whirl direction, and these

---

[1] The author performed this work while she studied for a Master of Science degree at Texas A & M University.

Contributed by the International Gas Turbine Institute and presented at the International Gas Turbine and Aeroengine Congress and Exhibition, Stockholm, Sweden, June 2–5, 1998. Manuscript received by the ASME Headquarters April 1, 1998. Paper No. 98-GT-14. Associate Technical Editor: R. Kielb.

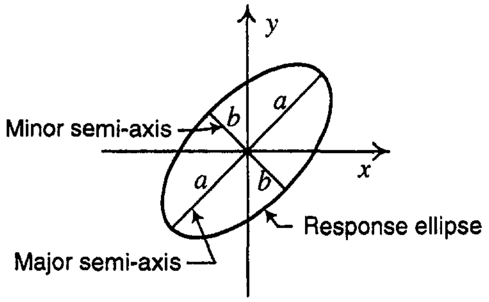

Fig. 1 Shaft response ellipse showing shaft coordinates (*x*, *y*) and major and minor ellipse semi-axes *a* and *b*, respectively

are illustrated in Fig. 1. These two quantities correspond directly to the major and minor amplitudes given in Murphy (1995). Since the minor amplitude (b) is the ratio between ($X_C Y_S - Y_C X_S$) and the major amplitude (a), the condition for backward whirl becomes

$$b = \frac{X_C Y_S - Y_C X_S}{a} > 0. \qquad (3)$$

Thus, a sign change in the minor amplitude in the response predictions indicates the onset or cease of backward whirl.

Explaining the Increase in Critical Speeds. According to Vance and Handy (1997), the anti-rotational injection of air onto the rotor causes cross-coupled stiffness, although their results show only a minute amount of cross-coupled stiffness compared to the support stiffness (<1 percent) and very little actual damping provided to the system. It becomes apparent that the force coefficients provided by Vance and Handy (1997) *cannot explain the marked increase in the critical speed* as the plenum pressure increases. However, significant direct stiffness develops from the release of high pressure gas axially across an annular gap into a low pressure area (e.g., the atmosphere) as in annular seals, and this direct stiffness increases with an increased pressure ratio across the annular gap. This significant direct stiffness associated with the anti-swirl damper accounts for the increase in the critical speeds. Forthcoming results demonstrate this fact.

Procedure

Vance and Handy (1997) use three rotor configurations, and the rotor specifications are listed in Table 1. Vance and Handy (1997) also provide measurements for cross-coupled stiffness and effective damping in a fourth rotor configuration (termed Rotor 3), but critical speed and amplitude measurements are not given. This configuration is not considered in the present work.

It is important to briefly mention the measurement procedure of Vance and Handy (1997) with regard to the present work. After installation of a rotor, a baseline coastdown was performed with zero damper plenum pressure, and measurements of critical speeds, onset and cease of backward whirl, and time of coastdown (for purposes of measuring drag torque) were recorded. Then, the plenum pressure was increased at 6.895 kPa (1 psi) increments (while stability could be maintained), and similar measurements were made. Baseline coastdowns were performed for each rotor configuration since the critical speeds can change slightly with assembly and disassembly.

In the present work, measurements of the rotor provide the geometry for an accurate transfer matrix model, as given in Fig. 2. Mass stations, indicated as vertical lines on the shaft, number 20 for the entire shaft, shown on the figure with circled numbers. Also depicted in Fig. 2 are the end bearings and damper. The rotordynamic model employs generalized bearings, allowing specification of force coefficients for each component. The rotordynamic software (Murphy, 1995) computes mass properties from the input of dimensions for the rotor model, and comparison of the mass properties of the rotor against those given in Handy (1992) are given in Table 2.

Bearing support stiffnesses and internal damping given in Handy (1992) also help to calculate baseline characteristics for each rotor geometry. The support stiffnesses, shown as mass stations 2 and 19 in Fig. 2, are asymmetric in the plane of rotation (x, y), and the left end support (station 2) is much stiffer than the right end support (station 19). The support stiffness as given by Handy (1992) and the support stiffness used to represent the baseline coastdown of each rotor model are compared in Table 3.

Using the analysis in Murphy (1995), these values of support stiffness applied to the model geometry give the FSCS and SSCS as nearly identical to the values provided by Vance and Handy (1997) for the baseline coastdown test having a damper plenum pressure of 0 kPa. The differences in support stiffness between rotor configurations can be attributed to typical changes from test rig disassembly and assembly.

The calculations for each rotor proceeded as follows:

1 determine the support stiffness to reproduce the critical speeds (FSCS and SSCS) for the rotor without the swirl damper (0 kPa), as given in Table 3;

Table 1 Rotor specifications

Rotor	*Radius* [mm (in)]	*Clearance* [µm (mil)]		*Surface Properties*
1	165.1 (6.5)	Tapered:	508 (20) {center} to 1270 (50) {edges}	Smooth
2S	165.3 (6.508)	Uniform:	1016 (40)	Smooth
2K	165.3 (6.508)	Uniform:	1016 (40)	Knurled

Nomenclature

a = major semi-axis of the response ellipse (m)
b = minor semi-axis of the response ellipse (m)
C_{xx}, C_{yy} = direct damping coefficients (N·s/m)
K_{xx}, K_{yy} = direct stiffness coefficients (N/m)
K_{xy}, K_{yx} = cross-coupled stiffness coefficients (N/m)
t = time (s)
$X(t)$, $Y(t)$ = particular solutions in the x and y-directions, respectively (m)
X_C, X_S = amplitudes of the particular solution, $X(t)$ (m)
Y_C, Y_S = amplitudes of the particular solution, $Y(t)$ (m)
ω = shaft angular velocity (rad/s)

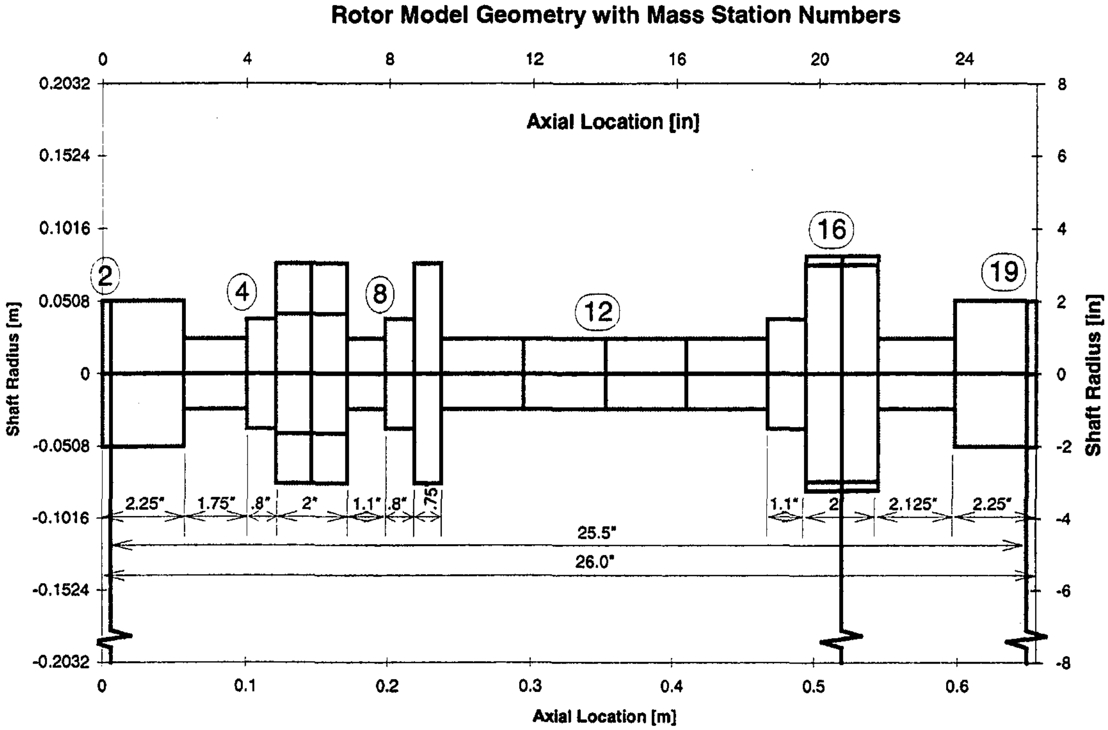

Fig. 2 Rotor geometry and mass matrix model with mass station numbers

Table 2 Mass properties given from transfer matrix model

Mass Property	*Present Work*	*Handy (1992)*	*Percent Difference*
Rotor mass [kg (lbm)]	29.56 (65.175)	29.74 (65.56)	0.59%
Transverse moment of inertia [kg·m^2 (lbm-in^2)]	1.337 (4569)	1.373 (4691)	2.6%
Polar moment of inertia [kg·m^2 (lbm-in^2)]	0.00534 (182.4)	0.00539 (184.1)	0.92%

Table 3 Support stiffness used for each rotor configuration

Rotor	*Mass Station*	*Present Work* K_{xx}, K_{yy} [MN/m (lbf/in)]	*Handy (1992)* K_{xx}, K_{yy} [MN/m (lbf/in)]	*Difference* [%]
1	2	6.284, 6.945	5.236, 6.392	20, 8.6
	(left)	(35880, 39655)	(29900, 36500)	
	19	0.5954, 0.6585	0.5166, 0.6392	15, 3.0
	(right)	(3400, 3760)	(2950, 3650)	
2S	2	5.823, 6.790	5.236, 6.392	11, 6.2
	(left)	(33249, 38770)	(29900, 36500)	
	19	0.5744, 0.6438	0.5166, 0.6392	11, 7.1
	(right)	(3280, 3676)	(2950, 3650)	
2K	2	5.258, 6.291	5.236, 6.392	0.42, 1.5
	(left)	(30026, 35921)	(29900, 36500)	
	19	0.5187, 0.5963	0.5166, 0.6392	0.41, 6.7
	(right)	(2962, 3405)	(2950, 3650)	

2 record the critical speeds, amplitudes at the critical speeds, and the speeds of onset and cease of backward whirl for this condition;
3 for a generic support at the damper location, use the measured cross-coupled stiffness ($-K_{xy} = K_{yx}$) and effective (direct) damping coefficient ($C_{xx} = C_{yy}$) given by Vance and Handy (1997) for a particular plenum pressure;
4 determine the direct stiffnesses (K_{xx}, K_{yy}) at the damper location to match the critical speed given for that plenum pressure;
5 record the critical speeds, amplitudes at the critical speeds, and the speeds of onset and cease of backward whirl as well as the damper force coefficients;
6 repeat the procedure (steps 3–5) for each plenum pressure, then each rotor (steps 1–5).

Results

Figures 3, 4, and 5 show the variation of the FSCS, SSCS, and speeds of onset and cease of backward whirl as the plenum pres-

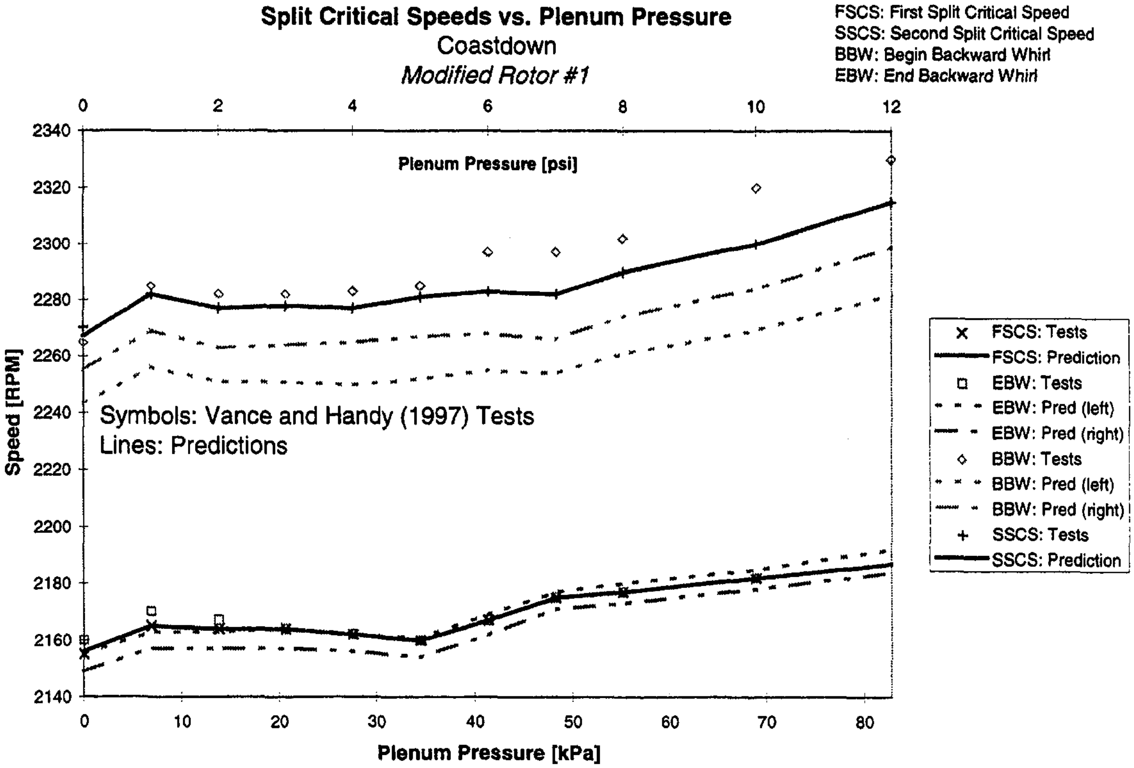

Fig. 3 Variation of critical speeds and backward whirl onset with plenum pressure: Rotor 1

sure increases for Rotors 1, 2S, and 2K, respectively. These figures emulate graphs given in Vance and Handy (1997) where points of speed for each plenum pressure were obtained in coastdown tests. Symbols denote experimental results while lines indicate the present computations. The predictions compare well with tests especially at low plenum pressures. Since the calculated onset and cease of backward whirl always occurs at different speeds for each end of the rotor, trends for both ends are included, indicated as left (station 2) and right (station 19). Calculations of the onset speed of backward whirl tend to follow the trend of SSCS and remain below this speed, while the Vance and Handy (1997) tests show a distinct rise of the onset of backward whirl

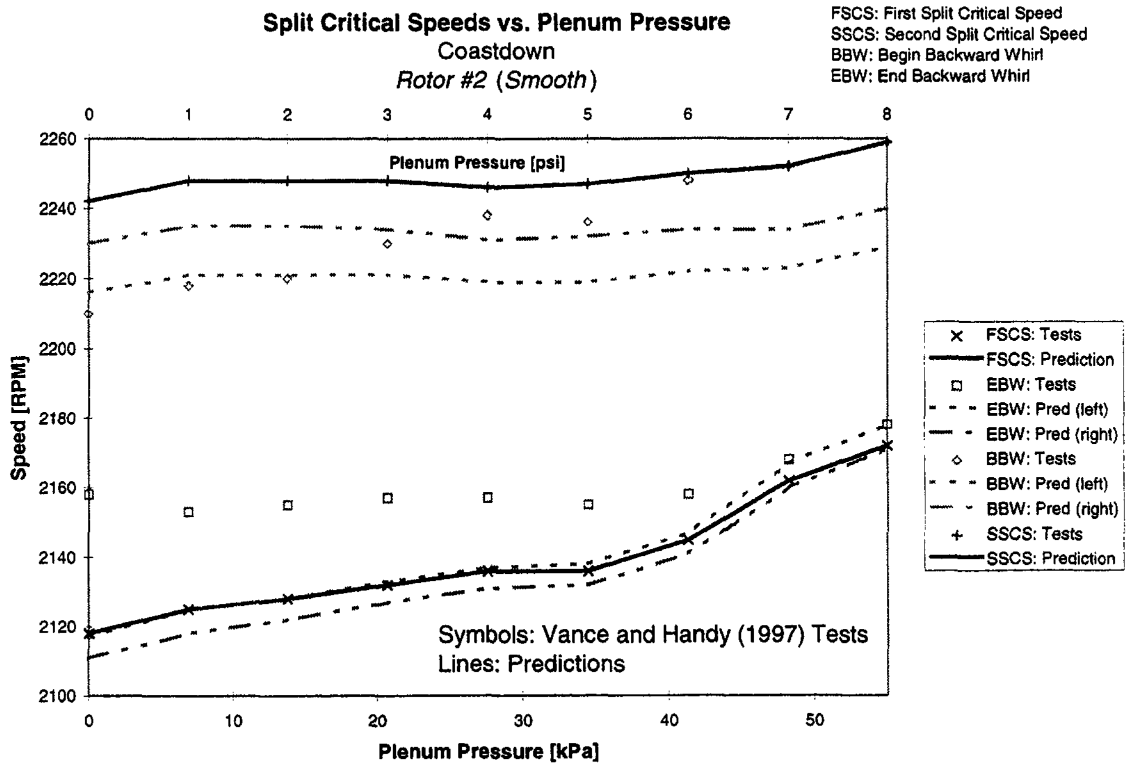

Fig. 4 Variation of critical speeds and backward whirl onset with plenum pressure: Rotor 2 (smooth)

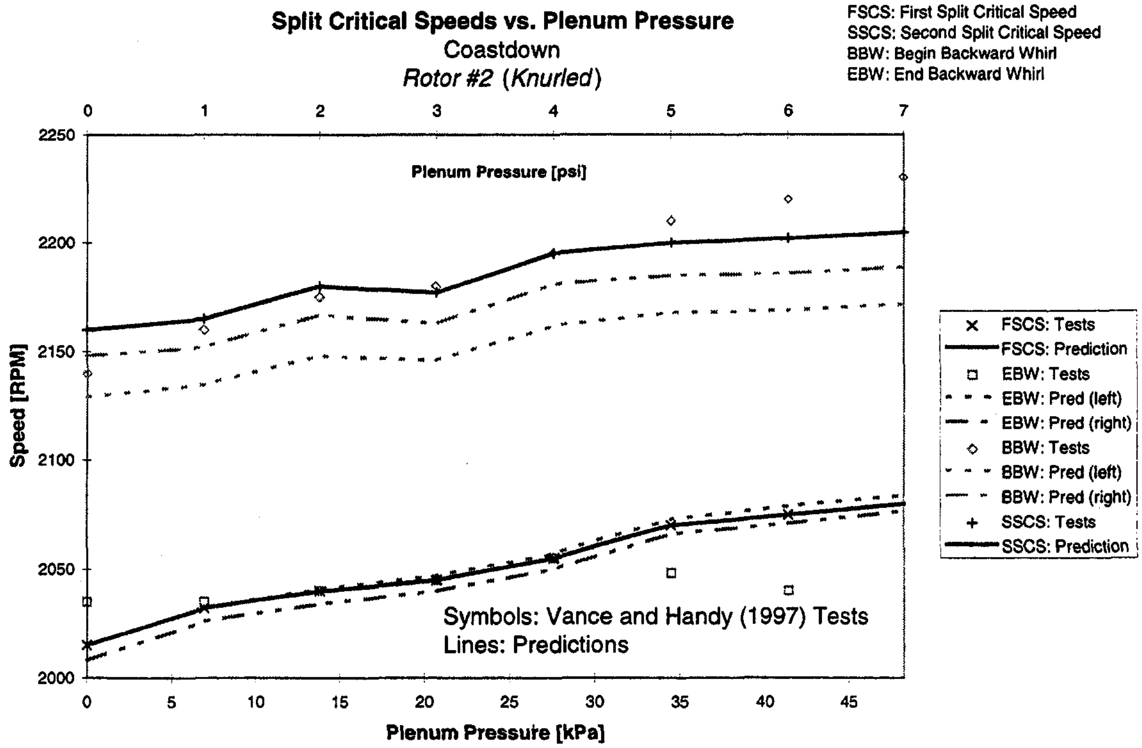

Fig. 5 Variation of critical speeds and backward whirl onset with plenum pressure: Rotor 2 (knurled)

above the SSCS. Neither instability shown by Vance and Handy (1997) for Rotors 1 and 2K was found using the typical calculation procedure since logarithmic decrements always remained positive in eigenvalue calculation, and shaft vibration amplitudes remain well below the size of the clearance.

In Fig. 6, the change in maximum amplitude (as a percentage of the 0 kPa amplitude) with plenum pressure for Rotor 1 generally decreases, indicated by both experiments and prediction. However, the tests insinuate much more dramatic trends. Agreement between measurement and calculations is good considering that the predictions fall exactly between the test points.

The error bars in Fig. 6 show the result of a sensitivity analysis that demonstrates the effects of a ±10 percent change in the direct damping coefficients on the response amplitudes for three

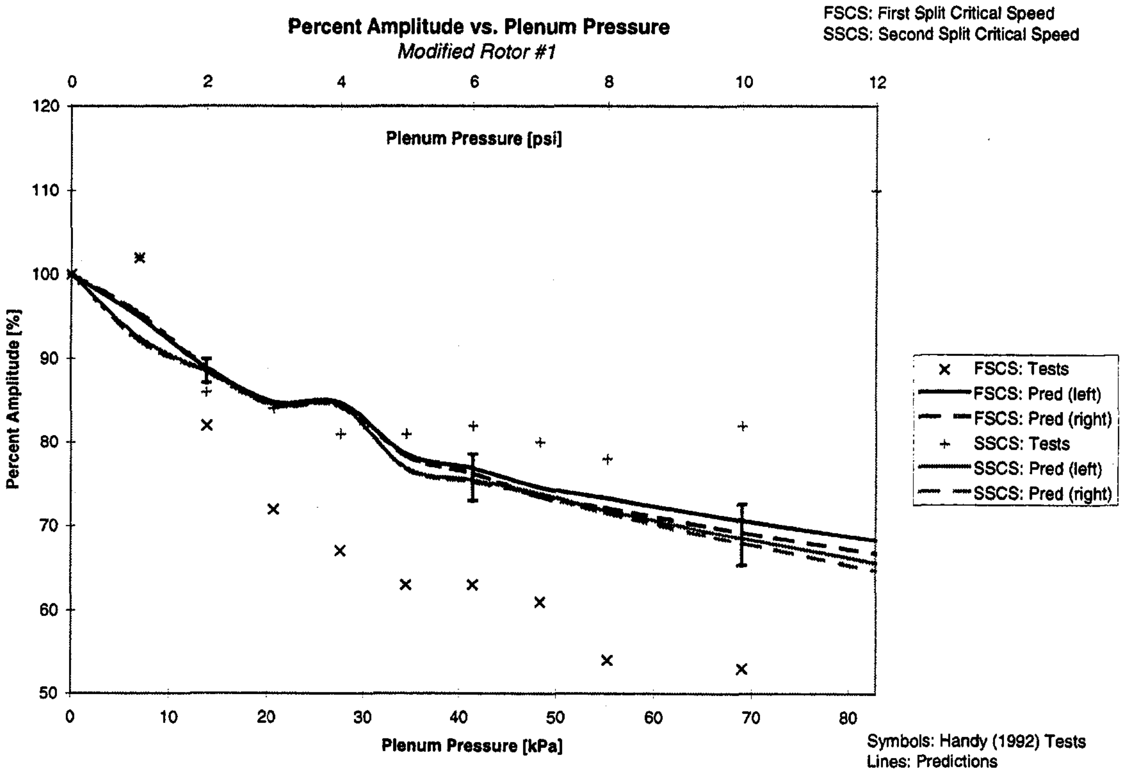

Fig. 6 Change in peak amplitude against plenum pressure: Rotor 1

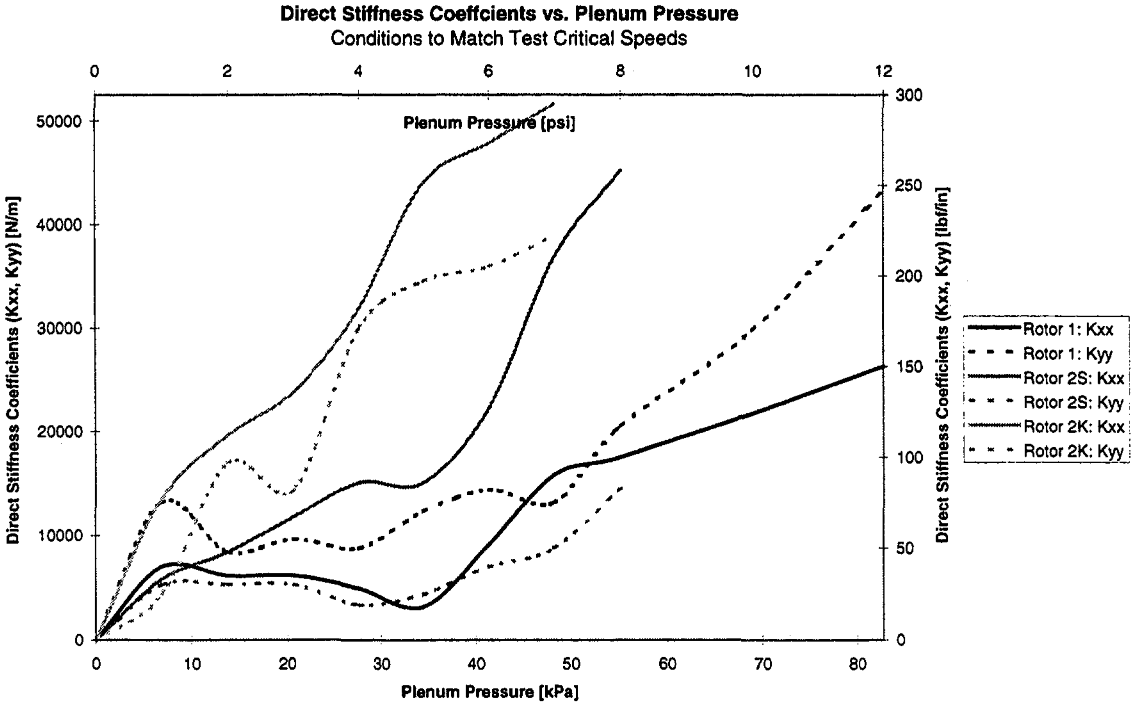

Fig. 7 Direct stiffness at damper location to match test critical speeds

different plenum pressures in Rotor 1. Even with significant changes in the damping coefficients, the test data does not fall within the range of amplitudes given by the predictions. These results indicate that the equivalent direct damping provided by Vance and Handy (1997) is at least of the correct order of magnitude.

Discussion

Although the predictions did not show the marked increase in amplitude (due to instability) that the tests did at the highest plenum pressures, the measurement of effective direct damping provided by the anti-swirl damper is reasonably close. Thus, for moderate levels of plenum pressure, designers of anti-swirl dampers can count on a decrease in vibration amplitude with increased plenum pressures, provided instabilities can be eventually predicted and avoided.

It is clear from the present calculations that the cross-coupled stiffness and direct damping coefficients furnished by Vance and Handy (1997) alone cannot duplicate the behavior of the anti-swirl damper. Direct stiffness provided at the damper location in the present model allow prediction of the two split critical speeds and the onset and cease of backward whirl with good agreement. Figure 7 shows that the amount of added direct stiffness at the damper location rises as the plenum pressure increases. This characteristic behavior as pressure increases demonstrates the strong influence of a pressure drop axially across the annulus of the damper.

Likewise, there exists some backward driving destabilizing effect that causes the wrecking instability and the increase of the onset speed of backward whirl for high plenum pressures. This effect was also misrepresented by the force coefficients given in Vance and Handy (1997). In fact, the steady increase in direct damping implies an increasingly stable rotor configuration, while the cross-coupled stiffness coefficients that could become possible destabilizing force are measured as negligibly small, having virtually no effect on the system eigenvalues or rotordynamic response.

Two circumstances occurring in the tests could have caused the rotor wreck at a damper plenum pressure of 82.757 kPa (12 psi) for Rotor 1, reported by Vance and Handy (1997): a negative log decrement causing system instability or the rotor striking the damper wall. The test data in Fig. 6 shows a much higher amplitude for the SSCS at that damper plenum pressure, and this high amplitude breaks the trend for decreasing critical speed amplitudes with increasing plenum pressure. This fact may indicate the existence of a negative log decrement as the vibration amplitudes become very high in the absence of stable eigenvalues. Figure 6 also indicates that the values of damping provided by Vance and Handy (1997) to be approximate. Since this value of damping largely affects the vibration amplitude at the critical speed, the likelihood that accurate predictions of response amplitudes at critical speeds could be made from these damping coefficients becomes unlikely. Thus, the present work considers wrecking instability to have occurred due to a negative log decrement occurring at the SSCS.

In an attempt to reproduce the conditions causing instability for Rotor 1 at 82.737 kPa (12 psi), cross-coupled stiffness and direct damping coefficients were first extrapolated from the trend of cross-coupled stiffness and damping coefficients for increasing plenum pressures given in Vance and Handy (1997). Since no predicted instability occurred when using this extrapolated value of cross-coupled stiffness, the coefficient was increased by an approximate factor of ten ($-K_{xy} = K_{yx} = 5779$ N/m [33 lbf/in] → 53,764 N/m [307 lbf/in], assuming the damper direct damping remains positive. This caused a negative logarithmic decrement associated with the first eigenvalue. The speed used for eigenvalue calculation, logarithmic decrements, and eigenvalues are shown in Table 4.

The response curve for this configuration shows an extreme increase in the vibration amplitude at 2261 RPM with corresponding amplitudes at this speed that register greater than 500 percent of the baseline amplitude. Although the two eigenvalues seem relatively far apart in speed, the response (not given for brevity) shows no second split critical speed at 2315 RPM, and both horizontal and vertical amplitudes peak at 2260 RPM. With this higher value of backward driving cross-coupled stiffness, backward whirl begins in the right bearing (mass station 19) at a speed higher than the second eigenvalue (2325 RPM), a result predicted in Vance and Handy (1997).

The results giving much higher values of destabilizing cross-coupled stiffness than previously estimated indicates that the

Table 4 Eigenvalues for 82.757 kPa (12 psi) ($-K_{xy} = K_{yx} = 307$ lbf/in)

Speed for Calc. [RPM]	*Log Dec (1)*	*First Eigenvalue* [RPM]	*Log Dec (2)*	*Second Eigenvalue* [RPM]
2000	0.004	2262.7	0.101	2314.1
2315*	-0.00104*	2260.6*		2315.9*
3000	-0.012	2256.7	0.116	2320.0

* Interpolated values

tests by Vance and Handy (1997) did not actually measure cross-coupled stiffness. This presumption results not only from proof given in the predictions above but also by applying engineering rotationale to the experimental results. The highest measured values of cross-coupled stiffness remain less than 1 percent of the lowest value of support stiffness although similar rotor behavior (indicated by oscilloscope traces of the orbit) characterized both the 68.948 kPa (10 psi) case, giving the highest measured value of cross-coupled stiffness, and the 82.737 kPa (12 psi) case, producing the instability (Handy, 1992). Such low values of cross-coupled stiffness measured in Vance and Handy (1997) cannot account for the instability observed in the tests.

An analysis to predict forces and force coefficients in an anti-swirl gas damper is beyond the scope of the present work. However, current analytical tools exist that may allow reasonable estimation of these prameters. The analyses in Yang et al. (1994) and San Andrés (1991) that discuss force coefficients in compressible fluid annular seals can provide a rough but conservative estimate (lower limit) of the direct stiffness. All of the force coefficients in an anti-swirl damper may be obtained from a more refined analysis given in San Andrés and Childs (1997) that considers tangential injection hydrostatic journal bearings (HJBs) operating with compressible fluids. To apply this analysis to anti-swirl dampers, an equivalent HJB orifice diameter can model the anti-swirl damper nozzles. San Andrés and Childs (1997) may also allow prediction of the instability experienced in the anti-swirl damper. Unfortunately, Handy (1992) does not supply sufficient data to apply these tools in the present work. The response curve for this configuration shows an extreme increase in the vibration amplitude at 2261 RPM with corresponding amplitudes at this speed that register greater than 500 percent of the baseline amplitude. Although the two eigenvalues seem relatively far apart in speed, the response (not given for brevity) shows no second split critical speed at 2315 RPM, and both horizontal and vertical amplitudes peak at 2260 RPM. With this higher value of backward driving cross-coupled stiffness, backward whirl begins in the right bearing (mass station 19) at a speed higher than the second eigenvalue (2325 RPM), a result predicted in Vance and Handy (1997).

The results giving much higher values of destabilizing cross-coupled stiffness than previously estimated indicates that the

tests by Vance and Handy (1997) did not actually measure cross-coupled stiffness. This presumption results not only from proof given in the predictions above but also by applying engineering rationale to the experimental results. The highest measured values of cross-coupled stiffness remain less than 1 percent of the lowest value of support stiffness although similar rotor behavior (indicated by oscilloscope traces of the orbit) characterized both the 68.948 kPa (10 psi) case, giving the highest measured value of cross-coupled stiffness, and the 82.737 kPa (12 psi) case, producing the instability (Handy, 1992). Such low values of cross-coupled stiffness measured in Vance and Handy (1997) cannot account for the instability observed in the tests.

An analysis to predict forces and force coefficients in an anti-swirl gas damper is beyond the scope of the present work. However, current analytical tools exist that may allow reasonable estimation of these parameters. The analyses in Yang et al. (1994) and San Andrés (1991) that discuss force coefficients in compressible fluid annular seals can provide a rough but conservative estimate (lower limit) of the direct stiffness. All of the force coefficients in an anti-swirl damper may be obtained from a more refined analysis given in San Andrés and Childs (1997) that considers tangential injection hydrostatic journal bearings (HJBs) operating with compressible fluids. To apply this analysis to anti-swirl dampers, an equivalent HJB orifice diameter can model the anti-swirl damper nozzles. San Andrés and Childs (1997) may also allow prediction of the instability experienced in the anti-swirl damper. Unfortunately, Handy (1992) does not supply sufficient data to apply these tools in the present work.

Conclusions

The rotordynamic behavior of anti-swirl dampers is discussed in the present work. Computations of split critical speeds, speeds of onset and cease of backward whirl, and peak vibration amplitudes rendered for comparison with tests in Vance and Handy (1997) show reasonably good agreement, provided direct stiffness is added at the damper location. Significant direct stiffness arises from a axial pressure ratio across the annular gap in the damper, and as expected, increases with damper plenum pressure. Although prediction of instability did not occur using the direct damping and cross-coupled stiffness coefficients given in Vance and Handy (1997), increasing the cross-coupled stiffness coefficient by a factor of ten reproduced conditions for instability since the logarithmic decrement was found to go negative in the speed range of interest.

Acknowledgments

The author wishes to acknowledge Dr. John Vance for his initial critique of this work and Dr. Luis San Andrés for his helpful advice.

References

Brown, R. D., and Hart, J. A., 1986, "A Novel Form of Damper for Turbo-Machinery," *Rotordynamic Instability Problems in High Performance Turbomachinery*, Texas A&M University, College Station, TX, pp. 325–347 (also NASA C.P. 2443).

Childs, D., 1993, *Turbomachinery Rotordynamics*, John Wiley and Sons, New York.

Handy, S. B., 1992, "An Experimental Investigation of a Swirl Gas Damper for Turbomachinery," Master of Science thesis, Texas A&M University, College Station, TX.

Muszynska, A., 1985, "Anti-Swirling Demonstration," *Instability in Rotating Machinery*, NASA C. P. 2409, pp. 423–426.

Muszynska, A., and Bently, D. E., 1989, "Anti-Swirl Arrangements Prevent Rotor/Seal Instability," *ASME Journal of Vibration, Acoustics, Stress, and Reliability in Design*, Vol. 111, pp. 156–162.

Muszynska, A., Franklin, W. D., and Bently, D. E., 1988, "Rotor Active 'Anti-Swirl' Control," *ASME Journal of Vibration, Acoustics, Stress, and Reliability in Design*, Vol. 110, pp. 143–161.

Murphy, B., 1995, *XLRotor*, rotordynamics software package, Rotating Machinery Analysis, Inc., Austin, TX.

San Andrés, L., 1991, "Analysis of Variable Fluid Properties, Turbulent Annular Seals," *ASME Journal of Tribology*, Vol. 113, pp. 694–702.

San Andrés, L., and D. Childs, 1997, "Angled Injection—Hydrostatic Bearings, Analysis and Comparison to Test Results," *ASME Journal of Tribology*, Vol. 119, No. 1, pp. 179–187.

Vance, J., 1988, *Rotordynamics of Turbomachinery*, John Wiley and Sons, New York.

Vance, J., and Handy, S., 1997, "Rotordynamic Instability from an Anti-Swirl Device," ASME Paper 97-GT-498.

Yang, Z., L. San Andrés, and D. Childs, 1994, "Dynamic Force Performance of Gas Seals at Off-Center Conditions," *STLE Tribology Transactions*, Vol. 37, No. 1, pp. 33–44.

Experimental Rotordynamic Characterization of Annular Seals: Facility and Methodology

J. M. Darden

E. M. Earhart

Marshall Space Flight Center,
MS ED12, Bldg. 4487,
MSFC, AL 35812

G. T. Flowers

Department of Mechanical Engineering,
Auburn University,
Auburn, AL 36849-5341

Annular seals are known to enhance rotordynamic stability margins and minimize vibration response levels in high-speed rotating machinery. Theoretical predictions for the rotordynamic characteristics of annular seals exist but additional experimental data is needed to properly anchor these results. NASA's Marshall Space Flight Center (MSFC) has developed an annular seal test rig and facility to experimentally characterize axially fed annular seals. The objective of MSFC's annular seal test rig is to obtain the rotordynamic coefficients (direct and cross-coupled stiffness, damping, and added mass) for a variety of high Reynolds number annular seals. The MSFC test rig supports centered-seal testing with inlet pressures up to 138 bars (2000 psi) and flow rates of over 946 liters per minute (250 gpm). The rig's shaft is powered by a 186 kilowatt (250 horsepower) steam turbine capable of rotational speeds of over 20,000 revolutions per minute (rpm). A description of the identification process used to obtain rotordynamic coefficients is given as well as procedures for ensuring quality data. Experimental results for a smooth annular seal with an L/D = 0.5 is presented. Excellent agreement between experimental and theoretical results is obtained.

Introduction

Vibration problems on the Space Shuttle Main Engine (SSME) turbomachinery have led engineers to seek ways to enhance rotordynamic stability margins and minimize vibration response levels. One of the most effective ways to enhance the vibration characteristics of the high energy-density SSME turbomachinery is through the use of annular seals. Damping seals, a variation of the typical smooth-stator annular seals (referred to herein as smooth annular seals), were conceived during the development of the SSME High Pressure Turbomachinery. The damping seal, in contrast to the smooth annular seal, employs an intentionally roughened stator to minimize the destabilizing forces through a reduction in the fluid's average tangential velocity within the seal. The concept was developed by von Pragenau (1982), who also performed the first theoretical analysis to yield rotordynamic coefficients for a damping seal. Damping seals are now employed on Rocketdyne's High Pressure Fuel Turbopump (HPFTP) and the High Pressure Oxidizer Turbopump (HPOTP) as well as Pratt & Whitney's Alternate Turbopump (AT) HPFTP and HPOTP.

Background

Experimental rotordynamic coefficient data for smooth annular seals and damping seals is limited in the literature. Childs and Kim (1985) showed damping seals yielded a higher net damping relative to its smooth annular seal counterpart. Of the four stator surface treatments that were tested, the round-hole pattern stator roughness pattern was found to have the highest net damping and lowest leakage. The other three seals included a smooth, knurled and a post-patterned stator surface. Iwatsubo and Sheng (1990) presented experimental work that provided independent rotordynamic coefficients for smooth annular seals as well as damping seals. Three different stator roughness patterns including a smooth seal and two damping seals (both damping seals had an "isogrid" stator roughness pattern but with different cell depths) were evaluated experimentally. Comparisons of the experimental results of the three seals revealed that the smooth annular seal has a higher value of direct stiffness when compared to the damping seals. On the other hand, the whirl frequency ratio of the damping seals was lower than the smooth annular seal indicating a larger capacity to stabilize. The tests were carried out at speeds up to 3600 rpm with maximum seal pressure differentials on the order of 9 bars.

Childs and Hale (1993) presented an excellent description of Texas A&M's hydrostatic bearing test rig and supporting facilities. Experimental data from a modified version of that test rig was presented for smooth annular seals by Marquette, Childs and San Andres (1997). Their work indicated that the rotordynamic coefficients for smooth annular seals are strongly dependent upon eccentricity. The experimental results showed a stronger dependence on eccentricity than the corresponding theoretical predictions. Childs and Fayolle (1997) presented experimental results on two damping seals with a round-hole stator roughness treatment. The difference between the two seals was the depth of the flat bottom holes. Testing revealed that both seals had direct stiffness values much lower than the theoretical predictions. Moreover, the shallow depth hole pattern damping seal had a direct stiffness on the order of zero. The results also showed a general lack of dependence upon seal eccentricity on the experimentally obtained rotordynamic coefficients. Based upon the previously described work, additional experimental results are needed to anchor seal prediction codes.

Test Rig and Facility Description

A cut away view of MSFC's annular seal test rig is shown in Fig. 1. The rig supports testing of seal pressure differentials (ΔP) of up to 138 bars (2000 psi) in deionized water. The test rig's shaft is powered by a 186 kilowatt (250 horsepower) steam turbine which provides a maximum operational speed range of just over 20000 rpm. High pressure deionized water with temperatures typically between 21.1°C to 32.2°C (70°F–90°F) is supplied to the test rig via a 11356 liter (3000 gallon) main water reservoir. The main water reservoir is pressurized by gaseous nitrogen. The water flows from the main reservoir

---

Contributed by the International Gas Turbine Institute and presented at the International Gas Turbine and Aeroengine Congress and Exhibition, Stockholm, Sweden, June 2–5, 1998. Manuscript received by the ASME Headquarters April 1, 1998. Paper No. 98-GT-17. Associate Technical Editor: R. Kielb.

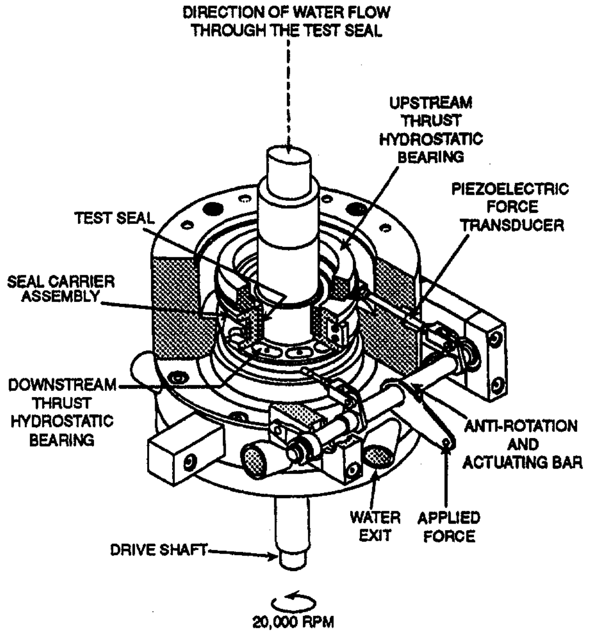

Fig. 1 Cut away view of test rig

through a bank of filters and then to the test rig. The water is routed to the upper and lower slave bearings as well as the test bearing.

As illustrated in Fig. 1, the test rig's shaft is mounted in a vertical position and is supported by a hydrostatic bearing on the lower end of the shaft and damping seal on the upper end of the shaft. The upper shaft bearing is a damping seal with a length of 1.63 cm (0.642 in) and a 8.89 cm (3.5 in) diameter with a radial clearance of 0.0076 cm (0.003 in). The stator surface roughness treatment consists of spherical pockets with a pocket size of 0.305 cm (0.12 in) diameter by 0.152 cm (0.06 in) deep and a hole density of 25 holes per square inch. The lower shaft support bearing is an orifice compensated (6 orifices) hydrostatic bearing with the identical spherical pocket stator surface treatment as previously described for the upper bearing. The length of the hydrostatic bearing is 7.30 cm (2.875 in) and a diameter of 7.62 cm (3.00 in) with a radial clearance of 0.0076 cm (0.003 in). The shaft is supported axially by an orifice compensated thrust hydrostatic bearing located at the lower end of the shaft. The thrust hydrostatic bearing consists of 6 orifices equally spaced on a diameter of 5.15 cm (2.028 in) with a spherical pocket stator surface treatment (pocket size is 0.305 cm (0.12 in) diameter by 0.152 cm (0.06 in) deep). The test bearing is mounted in the seal carrier assembly which is located approximately midspan of the shaft. One of the unique features of MSFC's annular seal test rig is the manner in which the seal carrier assembly (and consequently, the test seal) is isolated from the test rig. The seal carrier assembly is supported axially by upper and lower orifice compensated (each bearing has 6 orifices) thrust hydrostatic bearings. The orifices on the lower thrust bearing are located on a circle with a diameter of 13.65 cm (5.375 in). Likewise, the upper thrust bearing's orifices are located on a circle with a diameter of 12.86 cm (5.062 in). This configuration ensures that the seal carrier assembly remains parallel to the shaft during testing. Pitching of the test seal can adversely affect the experimentally obtained rotordynamic coefficients if not taken into account properly. The primary function of the thrust bearings, however, is to allow translation of the test bearing under an externally applied force without having to account for additional load paths. The hydrostatically supported seal carrier assembly allows for a simple correction to the excitation force. Since the axial hydrostatic bearings allow translation without any significant dynamic impedance, the excitation force needs only to be corrected for the inertial force of the seal carrier assembly. The forces acting on the seal carrier assembly are checked periodically to insure the thrust hydrostatic bearings are operating properly. The inspection is carried out by disconnecting the force linkages (linkages with the piezoelectric force transducers) from the actuating bar and rotating the seal carrier assembly while the rig is at operational pressures. The seal carrier assembly can be easily rotated about the shaft. In addition, an analysis was performed to determine the force exerted by the hydrostatic film on the carrier. Since the force is proportional to velocity, the analysis yielded an equivalent viscous damping coefficient. The value of the equivalent viscous damping coefficient is insignificant when compared to the magnitude of the measured damping coefficients (less than 0.05 percent of the measured damping coefficient).

The excitation forces applied to the seal carrier assembly are provided by an electrodynamic shaker. A stinger extending from the shaker's armature connects the shaker to a lever arm located at the midpoint of the actuating bar as shown in Fig. 1. The excitation forces are measured using a pair of piezoelectric load cells located in the linkage assembly that connects the actuating bar to the seal carrier assembly. Since the load cells are mounted in series with the linkages attached to the seal carrier assembly (illustrated in Fig. 2), the applied excitation load passes directly through the load cells. In addition to a standard calibration, the load cells undergo a static in-situ calibration that is performed before and after each test. If the load cells do not perform up to their specifications prior to a test series, the testing is suspended until corrective action can be taken. The experimental data is invalidated if the load cells do not perform within their specifications following a test.

The relative displacement of the test seal is measured by four inductive probes mounted in 90 degree increments around the

Nomenclature

C_{yy}, C_{yz} = damping coefficients (FT/L)
f_y = measured excitation force (F)
F_y, F_z = Fourier transform of fluid film forces (F)
$G_{F_yF_y}$ = auto spectral density function ((I)(I)/T)
G_{YF_y}, G_{ZF_y}, $G_{F_zF_y}$ = cross spectral density function ((I)(J)/T)
H_{YF_y}, H_{ZF_y}, $H_{F_zF_y}$ = frequency response functions
i = imaginary number ($\sqrt{-1}$)
K_{yy}, K_{yz} = stiffness coefficients (F/L)
m_c = mass of the seal carrier assembly (M)
M_{yy}, M_{yz} = mass coefficients (M)
q_y, q_z = fluid film forces (F)
ω = frequency (rad/T)
ω_s = shaft rotational speed (rad/T)
Ω = whirl frequency ratio
Y, Z = Fourier transform of relative displacements δy, δz (L)
y_s, z_s = absolute seal carrier assembly displacement components (L)
δy, $\delta \mathbf{z}$ = relative displacement components between test seal and shaft (L)
Z_{yy}, Z_{yz} = frequency response (impedance) functions (F/L)
$(\ )^*$ = complex conjugate of complex vector $(\ )$
$(\dot{\ })$ = time derivative $(d(\ )/dt)$
$(\ddot{\ })$ = second time derivative $(d^2(\ )/dt^2)$

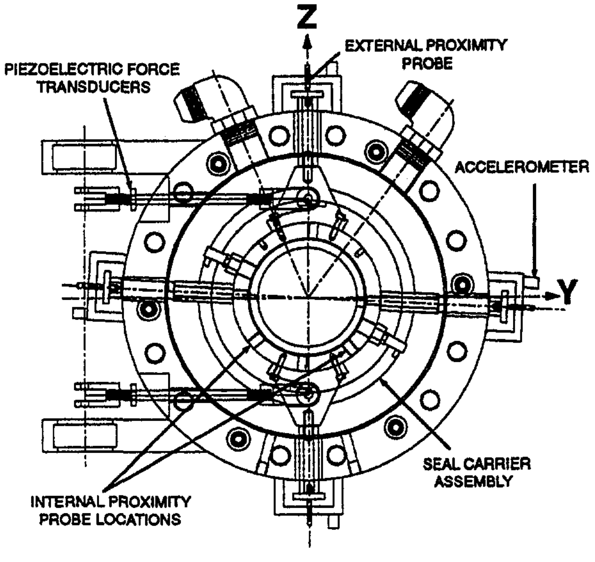

Fig. 2 Top view of the test section

periphery of the seal carrier assembly. This configuration allows direct measurement of the relative displacement of the fluid-film between the test seal and the shaft. These internally mounted proximity probes are employed for redundant relative shaft/test bearing displacement measurements. Two of the four proximity probe locations are identified in Fig. 2. The probes have a measuring range of 0.102 cm (0.040 inches) with a nonlinearity of +/− 0.5 percent of the measuring range and a resolution of 0.0000102 cm (0.000004 inches).

In-situ calibration of the internally mounted proximity probes is accomplished using a custom designed test fixture. Calibration of the proximity probes is carried out with the proximity probes mounted in the seal carrier assembly. The seal carrier assembly is placed on a precision x-y table with a dummy shaft of the exact dimensions and material as the shaft used in the test rig. The table is then swept across the range of the seal radial clearances using a micrometer to record the translation while simultaneously obtaining the corresponding proximity probe voltage levels. Once the calibration is complete, the seal carrier assembly is placed in the test rig for testing without disturbing the setup. Test results confirm the accuracy of the proximity probes and the calibration procedures. Excellent agreement from opposing probes is consistently obtained from dynamic testing.

In addition to the four internally mounted proximity probes, there are four externally mounted proximity probes. The measurements obtained from these probes are used to inertially correct the excitation force applied to the seal carrier assembly by measuring the seal carrier assembly's absolute displacement as illustrated in Fig. 2. Four stingers mounted to the seal carrier assembly extend through the housing. The stingers are designed such that their natural frequencies are well above the excitation frequency range. Attached to the end of each stinger is a flat circular disk that provides an excellent target for a proximity probe in a benign environment. Figure 2 shows that the stingers positioned in line with the excitation are rotated three degrees from the Y-axis. The three degree offset of the probes is necessary because of an interference between the stinger holes and the internal flow passages within the test rig's housing. The stinger offset is accounted for in the data reduction process. The external proximity probes have a measuring range of 0.203 cm (0.08 in) and have a nonlinearity of +/−1.0 percent over the measuring range. The seal carrier assembly's displacements are differentiated in the frequency domain to obtain acceleration. Before the acceleration levels are used to inertially correct the applied force, the acceleration of the test rig housing must be taken into account. Test rig housing acceleration levels are measured using accelerometers mounted on each external proximity probe bracket. These measurements are used in conjunction with the acceleration levels obtained from the proximity probes to ensure that inertial frame acceleration levels are used to correct the applied force.

In addition to recording the parameters necessary for the determination of rotordynamic coefficients, other pertinent measurements are recorded. These include parameters such as seal pressure differential (ΔP), water temperature, leakage flow rate through the test bearing, shaft displacements and various steam turbine measurements.

Test Procedure

A test seal is normally characterized at nine different operating conditions. The operating conditions are comprised of testing at 3 different shaft rotational speeds (5, 10, and 15 krpm) and at 3 different seal pressure differentials ranging from 69 bars to 138 bars (1000 psi to 2000 psi). The applied force is a band-limited random excitation typically between 20–200 Hz. High frequency data, comprised of displacements, forces and pressures, is recorded on an analog tape recorder. The duration at each test condition is approximately 30 seconds. Following a test series, the measured data is digitized from the analog tape at a sampling frequency of 5 kHz. The data is subsequently downloaded to a computer where the data is reduced.

Data Reduction Methodology

After measuring the displacements and forces from the test rig, the individual time histories are transformed to the frequency domain to obtain rotordynamic coefficients. The equations of motion for the seal carrier assembly are written using the coordinate system defined in Fig. 2. In general terms, the equations of motion may be expressed as

$$\text{(applied forces)} - \text{(carrier mass)(carrier acceleration)} = -\text{(fluid film forces)}. \quad (1)$$

The fluid film forces can be modeled as

$$-\begin{Bmatrix} q_y \\ q_z \end{Bmatrix} = \begin{bmatrix} K_{yy}K_{yz} \\ -K_{yz}K_{yy} \end{bmatrix}\begin{Bmatrix} \delta y \\ \delta z \end{Bmatrix} + \begin{bmatrix} C_{yy}C_{yz} \\ -C_{yz}C_{yy} \end{bmatrix}\begin{Bmatrix} \delta \dot{y} \\ \delta \dot{z} \end{Bmatrix} + \begin{bmatrix} M_{yy}M_{yz} \\ -M_{yz}M_{yy} \end{bmatrix}\begin{Bmatrix} \delta \ddot{y} \\ \delta \ddot{z} \end{Bmatrix}, \quad (2)$$

where the rotordynamic coefficients are assumed to be skew-symmetric ($-yz = zy$ and $yy = zz$). The assumption of skew-symmetry is based upon the symmetry of the seal (and flow conditions) as well as the dynamic testing being performed in the centered seal condition. Substituting the appropriate quantities into Eq. (1) yields

$$\begin{Bmatrix} f_y - m_c\ddot{y}_s \\ -m_c\ddot{z}_s \end{Bmatrix} = \begin{bmatrix} K_{yy}K_{yz} \\ -K_{yz}K_{yy} \end{bmatrix}\begin{Bmatrix} \delta y \\ \delta z \end{Bmatrix} + \begin{bmatrix} C_{yy}C_{yz} \\ -C_{yz}C_{yy} \end{bmatrix}\begin{Bmatrix} \delta \dot{y} \\ \delta \dot{z} \end{Bmatrix} + \begin{bmatrix} M_{yy}M_{yz} \\ -M_{yz}M_{yy} \end{bmatrix}\begin{Bmatrix} \delta \ddot{y} \\ \delta \ddot{z} \end{Bmatrix}, \quad (3)$$

where δy, δz are the measured components of relative displacement between the test seal and shaft. $\ddot{y}_s$, $\ddot{z}_s$ are the components of acceleration of the seal carrier assembly, and f_y is the applied force in the y-direction (also a measured quantity). Note that the inertial force generated by the acceleration of the seal carrier assembly is subtracted from the applied force. Since there is no applied load in the z-direction, the only z-component force in the expression is the inertial force of the seal carrier assembly.

Transformation of Eq. (3) to the frequency domain using a Fourier transform yields

$$\begin{Bmatrix} F_y \\ F_z \end{Bmatrix} = \begin{bmatrix} Z_{yy} Z_{yz} \\ -Z_{yz} Z_{yy} \end{bmatrix} \begin{Bmatrix} Y \\ Z \end{Bmatrix}, \tag{4}$$

where capitalization denotes the Fourier transform of a signal. F_y and F_z are the Fourier transforms of the respective inertially corrected force components. Y and Z are the Fourier transforms of the y and z displacements. Z_{yy} and Z_{yz} are defined as frequency response functions. The frequency response functions are assumed to be have the following quadratic form

$$Z_{yy} = K_{yy} + i\omega C_{yy} - \omega^2 M_{yy}$$

$$Z_{yz} = K_{yz} + i\omega C_{yz} - \omega^2 M_{yz}. \tag{5a, b}$$

The applied force used in dynamic testing is a band-limited random signal. The random character of the force signal requires that spectral density methods be employed. Spectral density methods offer excellent noise rejection characteristics that are particularly useful in this type of testing. Typical noise sources include high speed turbulent flow through the test seal, shaft synchronous excitation and other sources that can degrade the coherence between signals. An excellent description of the advantages of spectral density methods is presented by Rouvas and Childs (1993). Equation (4) must be recast to take advantage of the noise rejection characteristics of spectral density methods. The immediate goal is to rewrite Eq. (4) in terms of auto and cross-spectral density functions. To that end, each term in the equation must be post-multiplied by the complex conjugate of the applied force. The following definitions

$$G_{YF_y} = YF_y^*$$

$$G_{ZF_y} = ZF_y^*$$

$$G_{F_zF_y} = F_zF_y^*$$

$$G_{F_yF_y} = F_yF_y^* \tag{6a, b, c, d}$$

are for the resulting auto and cross-spectral density functions. Noise rejection between two signals is accomplished by using the cross-spectral density function. This is due to the cross-spectral density being zero for statistically independent signals (see Bendat and Piersol (1986)). The equations can be written in terms of transfer functions by dividing each term in the equations by the auto-spectral density function $G_{F_yF_y}$. The resulting equations may be written as

$$\begin{bmatrix} H_{YF_y} H_{ZF_y} \\ -H_{YF_y} H_{ZF_y} \end{bmatrix} \begin{Bmatrix} Z_{yy} \\ Z_{yz} \end{Bmatrix} = \begin{Bmatrix} 1 \\ H_{F_zF_y} \end{Bmatrix}, \tag{7}$$

which can be easily solved for the frequency response functions Z_{yy} and Z_{yz}. The rotordynamic coefficients are obtained by a least squares curve fit on the resulting frequency response functions. The curve fits are performed over the frequency range defined by the excitation force. Points that make up the frequency response functions are screened prior to being included in the curve fit. A coherence-based criterion is used to determine the acceptability of each frequency response point. Coherence values are calculated for each frequency within the frequency range of interest using the applied force and the relative displacement in the y-direction. If the value of coherence at a particular frequency is greater than 95 percent, the frequency response function data at that frequency is included in the curve fit. Otherwise, the frequency response function data is discarded. This procedure ensures that quality data is included in the frequency response functions prior to performing the least squares curve fit. This procedure is similar to that used by Wagner and Steff (1996) in their dynamic evaluation of labyrinth seals.

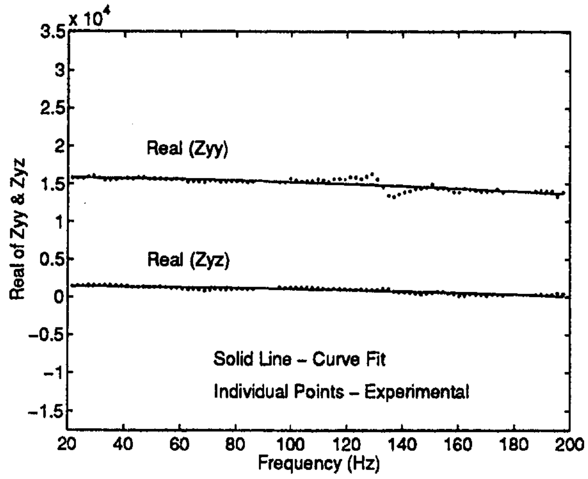

Fig. 3 Frequency response function (5.5 kRPM)

One of the concerns of using a band-limited random excitation force is the potential for leakage. Leakage results in a distortion of a signal's estimated spectra. The data reduction algorithm described in this paper uses estimated spectra in the calculation of the rotordynamic coefficients. Hanning windows are commonly used to minimize the effect of leakage. A comparison study was carried out to determine the effect of leakage on the resulting rotordynamic coefficients. The study was accomplished by using the data reduction code to obtain the rotordynamic coefficient estimates on simulated data. In the comparison study, estimates were obtained with and without the use of a Hanning window. The largest coefficient estimate error without a Hanning window was on the order of three percent. The error using the Hanning window was found to be less than 0.15 percent. Therefore, the error associated with the band-limited random excitation is minimal.

Representative Data for a Smooth Annular Seal

Representative rotordynamic coefficients obtained from MSFC's annular seal test rig for a smooth annular seal are presented. The seal used in the experimental investigation has a length of 4.572 cm (1.8 in) and a diameter of 9.251 cm (3.642 in.) resulting in a L/D of approximately 0.5. The shaft diameter is 9.144 cm (3.6 in.), which produces a radial clearance of 0.533 mm (0.021 in.). Rotordynamic coefficients are presented for three rotational speeds at a seal pressure differential of 93.1 bars (1350 psi). Reynolds numbers on the order of 90000 were achieved during testing. Predicted leakage through the test seal and the leakage values obtain in testing differed by approximately 10 percent. The friction factors used in the theoretical predictions were not adjusted to obtain agreement between predicted leakage rates and the corresponding experimental leakage.

The rotordynamic coefficients are obtained by a least squares curve fit of the experimental frequency response functions. Representative experimental frequency response functions and their corresponding curve fits for the 5500 rpm case are shown in Figs. 3 and 4. A band-limited random excitation (20–200 Hz) was applied to the test bearing. Correspondingly, the frequency response functions are curve fit between 20 Hz and 200 Hz. The figures illustrate the remarkably small scatter of the experimental frequency response functions. The frequency response functions are obtained by using 58 frequency domain averages and are calculated at 1.95 Hz frequency intervals. Frequency response function points that meet the minimum 95 percent

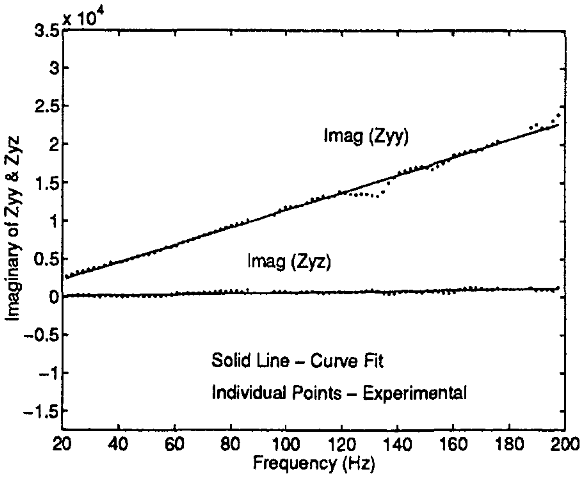

Fig. 4 Frequency response function (5.5 kRPM)

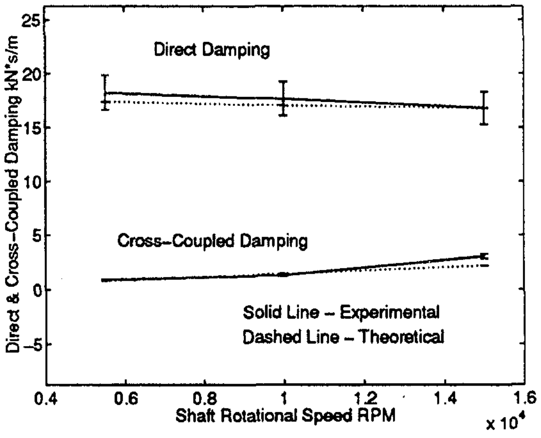

Fig. 6 Damping coefficients versus RPM

coherence criterion (as described earlier) are included in the least square curve fit.

Rotordynamic coefficients are presented in Figs. 5 and 6. The solid lines in both figures represent the experimental values while dashed lines represent the theoretical predictions. The theoretical predictions are obtained using a code developed by Padavala and Palazzolo (1993). The bulk flow model uses a Hir's friction factor model (the value of the constants used in the analysis are $Ms = Mr = -0.217$ and $Ns = Nr = 0.0674$) for a smooth stator and rotor. The theoretical predictions are generated using a fluid preswirl value of 0.23 and an inlet loss factor of 0.1. The fluid preswirl values used in the theoretical predictions are based upon the experimentally obtained whirl frequency ratio since this parameter is not directly measured. The whirl frequency ratio is defined by

$$\Omega = \frac{K_{yz}}{C_{yy}\omega_s}, \qquad (8)$$

where ω_s is the shaft rotational speed (rad/sec). Error bars are included to provide a measure of uncertainty for each experimental value. The uncertainty analysis accounts for the bias errors following the procedure outlined in the ANSI/ASME (1986). The uncertainty in direct terms were largely independent of speed while the uncertainty in the cross-coupled terms exhibited a significant dependence on the shaft rotational speed. The uncertainty value of direct stiffness was no larger than 1210 kN/m (6910 lbf/in). Similarly, the uncertainty value for direct damping had a maximum value of 1.59 kN*s/m (9.1 lbf*s/in). Cross-coupled stiffness uncertainty, on the other hand, was strongly speed dependent (as is the coefficient) but in percentage terms never exceeded 9.2 percent of the experimental value. The uncertainty value for cross-coupled damping terms did not exceed 6.8 percent of the experimental value. The level of uncertainty of the added-mass terms were on the order of 100 percent of the experimental value.

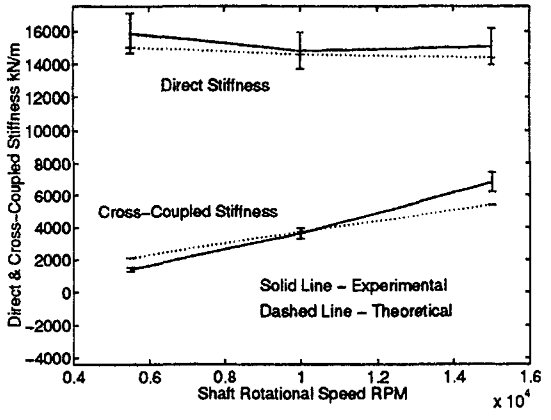

Fig. 5 Stiffness coefficients versus RPM

Figure 5 illustrates the experimental values and theoretical predictions for direct and cross-coupled stiffness at three shaft rotational speeds. Excellent agreement between the experimental values and theoretical predictions is obtained for direct stiffness. Cross-coupled stiffness, on the other hand, shows a slight deviation between the experimental values and theoretical predictions. The experimental values for cross-coupled stiffness have a steeper slope than the corresponding theoretical predictions when plotted as a function of shaft rotational speed.

Comparisons for experimental values of direct and cross-coupled damping and their corresponding theoretical predictions are shown in Fig. 6. Again, the experimental values and theoretical predictions for both direct and cross-coupled damping compare very favorably. Direct damping remains relatively constant versus shaft speed as do the theoretical predictions. Both the experimental values and theoretical predictions for cross-coupled damping increase slightly as a function of shaft speed.

Experimental values of the added-mass coefficients are not presented in graphical form due to relatively high uncertainty values. The values obtained at 5500 rpm are 1.46 kg (0.00832 lbf*s*s/in) and 0.88 kg (0.00502 lbf*s*s/in) for direct and cross-coupled mass, respectively. At 10000 rpm, the direct and cross-coupled added-mass terms were 0.81 kg (0.00464 lbf*s*s/in) and 1.55 kg (0.00886 lbf*s*s/in). For the 15000 rpm case, the values are 1.07 kg (0.00609 lbf*s*s/in) and 0.18 kg (0.00102 lbf*s*s/in) for the direct and cross-coupled added-mass terms, respectively.

Conclusion

The above discussion has described the basic layout and operation of MSFC's annular seal test rig. Instrumentation used in the test rig has been identified and described. Procedures used to enhance the quality of the experimental data such as calibration procedures, various diagnostic tests and frequency response function data qualification are described as well. Since the primary objective of the test rig is to obtain estimates of the rotordynamic coefficients of a given seal, a summary of the data reduction process is presented. Comparisons of experimental data and corresponding theoretical predictions for a smooth annular seal are presented. Overall, excellent agreement is obtained between theoretical predictions and experimental values of rotordynamic coefficients.

References

Bendat, J. S., and Piersol, A. G., 1986, *Random Data Analysis and Measurement Procedures,* 2nd ed., Wiley-Interscience, New York.

Childs, D. W., and Fayolle, P., 1997, "Test Results for Liquid 'Damper' Seals Using a Round-Hole Roughness Pattern for the Stators," unpublished report.

Childs, D. W., and Hale, R. K., 1993, "A Test Apparatus and Facility to Identify the Rotordynamic Coefficients of High-Speed Hydrostatic Bearings," ASME *Journal of Tribology,* Vol. 48.

Childs, D. W., and Kim, C. H., 1985, "Analysis and Testing for Rotordynamic Coefficients of Turbulent Annular Seals With Different, Directionally-Homogeneous Surface-Roughness Treatment for Rotor and Stator Elements," ASME *Journal of Tribology,* Vol. 107, pp. 296–306.

Childs, D. W., and Kim, C. H., 1986, "Test Results for Round-Hole-Pattern Damper Seals: Optimum Configurations and Dimensions for Maximum Net Damping," ASME *Journal of Tribology,* Vol. 108, pp. 605–611.

Coleman, H. W., and Steele, W. G., 1989, *Experimentation and Uncertainty Analysis for Engineers,* Wiley-Interscience, New York.

Iwatsubo, T., and Sheng, B. C., 1990, "An Experimental Study on the Static and Dynamic Characteristics of Damper Seals," Proceedings, 3rd International Conference on Rotordynamics, Lyon, France, September 10–12, 1990, pp. 307–312.

Marquette, O. R., Childs, D. W., and San Andres, L., 1997, "Eccentricity Effects on the Rotordynamic Coefficients of Plain Annular Seals: Theory Versus Experiment," ASME *Journal of Tribology,* Vol. 119, pp. 443–448.

Measurement Uncertainty, 1986, ANSI/ASME PTC 19.1-1985 Part 1.

Murphy, B. T., Scharrer, J. K., and Sutton, R. F., 1990, "The Rocketdyne Multifunction Tester: Part I—Test Method," Proceedings, Workshop on Rotordynamic Instability Problems in High Performance Turbomachinery, Texas A&M University, College Station, TX, pp. 347–359.

O'Donoghue, J. P., 1970, "Design of Annular Multi-Recess Hydrostatic Thrust Bearings," *Machinery and Production Engineering,* November 18, 1970, pp. 830–834.

Padavala, S., Palazzolo, A. B., Vallely, D. P., and Ryan, S., 1993, "Application of an Improved Nelson-Nguyen Analysis to Eccentric, Arbitrary Profile Liquid Annular Seals," Proceedings, Workshop on Rotordynamic Instability Problems in High Performance Turbomachinery, Texas A&M University, College Station, TX, pp. 113–135.

Rouvas, C., and Childs, D. W., 1993, "A Parameter Identification Method for the Rotordynamic Coefficients of a High Reynolds Number Hydrostatic Bearing," ASME *Journal of Vibration and Acoustics,* Vol. 115, pp. 264–270.

Rowe, W. B., 1983, *Hydrostatic and Hybrid Bearing Design,* Butterworths, London, United Kingdom.

von Pragenau, G. L., and Cappel, K. L., 1986, "Damping Seal Tester Progress and Initial Test Results," Proceedings, Advanced Earth-To-Orbit Technology, NASA Conference Publication 2437, Volume 2, May 13–15, 1986, pp. 2–8.

von Pragenau, G. L., 1982, "Damping Seals for Turbomachinery," NASA Technical Paper 1987.

Wagner, N. G., and Steff, K., 1996, "Dynamic Labyrinth Coefficients from a High-Pressure Full-Scale Test Rig Using Magnetic Bearings," Proceedings, Rotordynamic Instability Problems in High-Performance Turbomachinery, NASA Conference Publication 3344, May 6–8, 1996, pp. 95–111.

A Bulk-Flow Analysis of Multiple-Pocket Gas Damper Seals

J. Li

L. San Andrés

J. Vance

Mechanical Engineering Department,
Texas A&M University,
College Station, TX 77843-3123

A bulk-flow model for calculation of the dynamic force characteristics in a single cavity, multiple-pocket gas damper seal is presented. Flow turbulence is accounted for by using turbulent shear stress parameters and Moody's friction factors in the circumferential momentum equation. Zeroth-order-equations describe the isothermal flow field for a centered seal, and first-order equations govern the perturbed flow for small amplitude rotor lateral motions. Comparisons to limited measurements from a four-pocket gas damper seal show the current model to predict well the mass flow rate and the direct damping coefficient. For a reference two-bladed teeth-on-stator labyrinth seal, the current model predicts similar rotordynamic coefficients when compared to results from a two control volume, bulk-flow model. Force coefficients from a reference single-cavity, four pocket gas damper depend on the rotor speed and pressure drop with magnitudes decreasing as the rotor whirl frequency increases. The multiple-pocket gas damper seal provides substantially more damping than a conventional labyrinth seal of the same dimensions. The damper seal cross-coupled stiffness coefficients are small though sensitive to the inlet circumferential preswirl flow.

Introduction

Von Pragenau (1982) first describes damper seals with a roughened stator as elements able to reduce or eliminate destabilizing hydrodynamic forces in turbopumps. One of the advantages of damper seals, as compared to fluid film journal bearings or squeeze film dampers, is that they can be installed along the rotor at locations which have large modal amplitudes. Hence, damper seals have the potential to more effectively suppress rotor vibrations than fluid film bearing dampers.

Childs and Vance (1997) provide an excellent summary of the latest developments in gas seals and detail their influence on the dynamics of rotating machinery. Childs et al. (1989, 1990) verify experimentally that honeycomb seals with a smooth rotor are more stable than annular smooth seals and labyrinth seals. However, Childs and Kleynhans (1993) find that short honeycomb seals ($L \leq 25.4$ mm) do not outperform labyrinth seals rotordynamically. Honeycomb seals with smooth rotors replacing labyrinth seals have been successfully used in industrial compressors for suppressing subsynchronous vibrations (Zeidan et al., 1993). Yu and Childs (1997) have tested a hole-pattern gas damper as an alternative design to honeycomb seals. The experiments show that the hole-pattern gas damper seal in general provides higher effective damping and a reduced leakage rate (−12 percent) when compared to a conventional honeycomb seal.

Murphy and Vance (1980) extend Alford's theory (Alford, 1965) to a multiple-bladed labyrinth seal while neglecting the circumferential flow within the seal. The model predicts a significant equivalent damping coefficient in a seal with a diverging clearance configuration along the axial flow direction. Vance et al. (1993a) conduct extensive coast-down experiments to evaluate the equivalent damping characteristics of labyrinth seals. Both teeth-on-stator and teeth-on-rotor gas seals are tested with different clearance configurations. However, the experimental results demonstrate that the direct damping from various types of labyrinth gas seals is generally very small. The second author later reasoned that the predicted pressure variations in the annular groove of a labyrinth seal can not arise due to the swirl flow induced by rotor spinning.

Vance et al. (1993b) introduce a gas pocket bearing damper as a viable replacement to oil squeeze film dampers in high temperature applications. The gas dynamic pressure in a pocket can be out of phase with the vibratory motion since, the gas flow into and out of the pocket through orifice like restrictions is regulated by the vibratory motion. Therefore, the gas pocket actuator may work like an ideal damper element. An isentropic flow (ideal fluid) model predicts dynamic force coefficients proportional to the supply pressure though strongly dependent on the excitation frequency. A positive damping action occurs if the inlet restriction varies dynamically with the rotor motion. For best results, the outlet or discharge flow restriction must remain invariant to the vibratory motion.

By using the same physical mechanism as in the gas pocket actuator, Vance and Schultz (1993) introduce a novel type of gas damper seal derived from the teeth on stator labyrinth seal. The gas damper seal offers two distinct features that are critical in providing damping. First, the radial rotor to blade clearances must diverge in the direction of axial flow (pressure drop); second, rigid baffles divide the annular circumferential groove into several pockets that generate independent dynamic pressures. A beneficial ancillary effect is a reduction of the circumferential bulk flow. Vance and Li (1996) investigate the rotordynamic characteristics of a two-bladed gas damper seal by coast-down and rap (impact) tests. Experiments show the gas damper seal to have a direct damping coefficient orders of magnitude larger than a labyrinth seal of the same dimensions. However, the measurements also reveal that the leakage rate of the gas damper seal is about 30 percent larger than that of the labyrinth seal. Li and Vance (1995) study experimentally the effects of clearance ratios and number of teeth on short length gas damper seals. Test results demonstrate that the seal damping coefficient decreases with a decrease in the clearance ratio and an increase in the number of teeth. Richards et al. (1995) report of successful applications of multiple-cavity pocket damper seals to eliminate subsynchronous vibration in back-to-back industrial compressors.

The gas pocket damper seal, unlike other dampers commonly used in turbomachinery, does not rely solely on the fluid viscos-

---

Contributed by the International Gas Turbine Institute and presented at the International Gas Turbine and Aeroengine Congress and Exhibition, Stockholm, Sweden, June 2–5, 1998. Manuscript received by the ASME Headquarters April 1, 1998. Paper No. 98-GT-13. Associate Technical Editor: R. Kielb.

ity to dissipate energy. A simplified analysis of gas pocket-damper seal has been advanced (Vance et al., 1993b). The model only accounts for axial flow continuity, neglects the effects of fluid viscosity, flow turbulence, and circumferential flow swirl within the seal pocket, and assumes a uniform pressure within each pocket cavity. Although the model predicts both direct stiffness and damping coefficients with limited accuracy compared to experimental results, it can not provide values of the cross-coupled dynamic force coefficients. Therefore, a more complete flow model is needed to improve the calculation of the damper seal leakage and dynamic force coefficients and to account for more practical operating conditions and desired design features.

Analysis

Figure 1 shows a typical two-bladed (single cavity) gas pocket damper seal and with its radial clearance increasing in the axial flow direction. Radial baffles divide the circumferential groove into several identical pockets. The fluid flow in the gas damper seal is generally fully turbulent due to the large axial pressure gradient across the seal, the high rotor surface speed, and the large seal clearances (Childs, 1993). In seals with a few number of teeth the axial pressure drop can be large enough to induce sonic flow conditions at the seal discharge plane.

The fluid in the seal pocket is regarded as an isothermal ideal gas with density $\rho = P/V*^2$, where $V* = (R_gT)^{1/2}$ is a characteristic velocity proportional to the fluid sonic speed. The pressure in each pocket region varies in the circumferential direction only since the grooves are typically deep and of short axial length. Variations of the pressure in the radial direction are not important as evidenced by three-dimensional CFD results (Guo and Rhode, 1996). The pressure drops across the seal teeth (small clearances) are given by empirical leakage formulae obtained from Childs (1993). The one control volume, bulk-flow model for a two-bladed gas damper seal is shown in Fig. 2.[1] For a gas damper seal divided into N_c identical pockets of angular extent $2\beta = 2\pi/N_c$, the compressible bulk flow in the seal pocket is characterized by the following continuity, circumferential momentum, and axial flow rate equations, as follows:

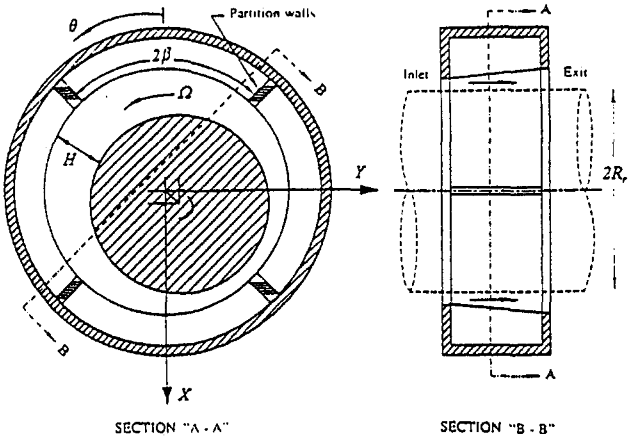

Fig. 1 Schematic of a two-bladed gas damper seal

Nomenclature

$A = L(B + H)$, cross-section area of the pocket (m^2)
B = height of the seal teeth (m)
C_{ij} = damping coefficients (N-s/m), $i, j = X, Y$
$D_h = 2L(B + H)/(L + B + H)$, hydraulic diameter (m)
e_X, e_Y = rotor center displacements in the X and Y directions (m)
e_r, e_s = mean roughness at rotor and stator surfaces (m)
F_j = dynamic seal forces (N), $j = X, Y$
H = seal clearance (m)
K_{ij} = stiffness coefficients (N/m), $i, j = X, Y$
L = axial length of seal pocket (m)
$\dot{M}$ = axial mass flow rate (kg/m-s)
N_c = number of circumferential pockets
P = fluid pressure in seal pocket (N/m^2)
P_b = back pressure at seal exit (N/m^2)
P_s = supply pressure at seal inlet (N/m^2)
$R_a = (R_r + R_s)/2$, average seal radius (m)
R_g = gas constant (J/kg-°K)
R_r = rotor radius (m)
R_s = seal outer radius (m)
$\mathrm{Re}_r = \rho D_h[(U - \Omega R_r)^2 + W^2]^{1/2}/\mu$, local Reynolds number at the rotor surface
$\mathrm{Re}_s = \rho D_h(U^2 + W^2)^{1/2}/\mu$, local Reynolds number at the stator surface
S = baffle thickness between pockets (m)
T = gas temperature (°K)
U = circumferential bulk-flow velocity in seal pocket (m/s)
$U_s = \alpha\Omega R_r$ preswirl velocity of gas flow at seal inlet (m/s)
$V_* = (R_gT)^{1/2}$, characteristic speed of gas (m/s)
W = axial bulk-flow velocity (m/s)
$f_r, f_s = a_m\{1 + [c_m e_{r,s}/(B + H) + b_m/\mathrm{Re}_{r,s}]^{em}\}$ Moody's friction factors at the rotor and stator surfaces $a_m = 0.001375$; $b_m = 10^6$; $c_m = 10^4$; $e_m = \frac{1}{3}$
k_r, $k_s = f_{r,s}\mathrm{Re}_{r,s}$, turbulent shear stress parameters at the rotor and stator surfaces
k_J, $k_x = \zeta_r k_r$, $(\zeta_r k_r)/2 + (\zeta_r L + B_s + B_s)k_s/2L$ dimensionless shear stress factors
α = inlet preswirl velocity ratio
μ_c = "kinetic-energy carryover" factor of gas flow across seal teeth
μ_f = gas flow coefficient across seal teeth
$\Delta\tau_x = -(k_xU - k_J\Omega R_r/2)(\mu L/D_h)$ shear stress difference from seal stator and rotor surfaces
$\zeta_r = R_r/R_a = 2/(1 + R_s/R_r)$
$\zeta_s = R_s/R_a = 2/(1 + R_r/R_s)$
ξ_w = loss coefficient at the baffle
ρ = gas density (kg/m^3)
μ = gas viscosity (N-s/m^2)
γ = ratio of gas specific heats
Ω = angular speed of rotor (rad/s)
ω = angular whirling frequency of the rotor (rad/s)

Subscripts

0 = zeroth-order solution
i, j = first-order solutions ($i, j = X, Y$)
s = seal upstream
b = seal downstream
u = local upstream
d = local downstream
w = baffle wall

---

[1] Current analysis of labyrinth seals accounts for two and three-control volume models. This refinement is not deemed necessary since the advantages of those more complex models are not evident as the existing literature reveals.

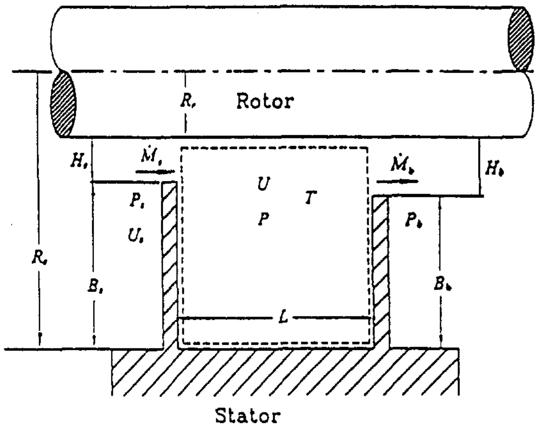

Fig. 2 One control-volume model for gas damper seals with circumferential pockets

$$\frac{1}{V_*^2}\left[\frac{\partial(PA)}{\partial t}+\frac{\partial(PAU)}{R_a\partial\theta}\right]+\zeta_r(\dot{M}_b-\dot{M}_s)=0 \quad (1)$$

$$\frac{1}{V_*^2}\left[\frac{\partial(PAU)}{\partial t}+\frac{1}{R_a}\frac{\partial(PAU^2)}{\partial\theta}\right]+\zeta_r(\dot{M}_bU-\dot{M}_sU_s)$$

$$=-\frac{A}{R_a}\frac{\partial P}{\partial\theta}+\Delta\tau_x \quad (2)$$

$$\dot{M}=\frac{(\mu_c\mu_fH)}{V_*}\sqrt{P_u^2-b_cP_d^2}. \quad (3)$$

Refer to the Nomenclature for an appropriate definition of all variables. P_u and P_d are the local axial upstream and downstream pressures across the seal teeth, respectively. $b_c = 1.0$ for unchoked flow, while $b_c = 0.0$ for choked flow. The shear stress difference $\Delta\tau_x$ combines the contributions of the shear stresses on both seal stator and rotor surfaces (Launder and Leschziner, 1978).

A pressure difference exists at the baffle (dividing two pocket regions) and due to the local acceleration of the flow from the upstream pocket to the downstream pocket. An expression of the pressure at the baffle is given for unchoked flow as

$$P(\beta)=P_d\left[1-\xi_w\left(\frac{P_u-P_d}{P_d}\right)^2\right] \quad (4)$$

where $\xi_w \leq 1$ is an empirical[2] coefficient accounting for the nonisentropic loss effect of the gap between the rotor surface and the tip of the baffle. The circumferential velocity of the flow at the baffle consists of three components due to the rotor surface speed, the upstream preswirl, and the pressure drop across the radial baffle, respectively, i.e.,

$$U(\beta)=\alpha_r\left(\frac{\Omega R_r}{2}\right)+\alpha_sU_s+\alpha_w\left(\frac{D_h(P_u-P_d)}{\mu}\right) \quad (5)$$

where P_u and P_d are the local circumferential upstream and downstream pressure across the partition baffle, respectively. The expressions for the coefficients α_r, α_s, and α_w in the equation above are given in the appendix.

Let the rotor center whirl at frequency (ω) with small amplitude motions (e_X, e_Y) about the seal concentric position. In general, the seal clearance is represented by the following equations:

$$H=H_0+e_jH_je^{i\omega t},\quad i=\sqrt{-1},$$

$$H_X=\cos\theta,\quad H_Y=\sin\theta, \quad (6)$$

where H_0 is the static seal clearance. For small amplitude rotor motions, all flow variables can be expressed as the superposition of steady state and first-order dynamic fields. In general,

$$\Phi=\Phi_0+e_j\Phi_je^{i\omega t},$$

$$\Phi=U,P,k_x,k_J,\mathrm{Re}_r,\mathrm{Re}_s,\ldots,\text{etc.} \quad (7)$$

Substitution of Eqns. (6–7) into the governing equations yields the zeroth and first-order equations describing the equilibrium flow field and the (harmonic) perturbed flow field, respectively. These equations are

$$\frac{1}{V_*^2}\frac{\partial(P_0A_0U_0)}{R_a\partial\theta}+\zeta_r(\dot{M}_{b0}-\dot{M}_{s0})=0 \quad (8)$$

$$\frac{1}{V_*^2}\frac{\partial(P_0A_0U_0^2)}{R_a\partial\theta}+\zeta_r(\dot{M}_{b0}U_0-\dot{M}_{s0}U_{s0})$$

$$=-\frac{A_0}{R_a}\frac{\partial P_0}{\partial\theta}+\Delta\tau_x \quad (9)$$

$$\dot{M}_0=\frac{(\mu_c\mu_fH)_0}{V_*}\sqrt{P_{u0}^2-b_cP_{d0}^2} \quad (10)$$

and

$$\frac{1}{R_aV_*^2}\frac{\partial}{\partial\theta}[P_0A_0U_j+P_0U_0LH_j+U_0A_0P_j]$$

$$+\eta_{mh}H_j+\mu_{mp}P_j\frac{i\omega}{V_*^2}[P_0LH_j+A_0P_j]=0 \quad (11)$$

$$\frac{i\omega}{V_*^2}[P_0A_0U_j]+\frac{1}{R_aV_*^2}[P_0A_0U_j+P_0U_0LH_j+A_0U_0P_j]\frac{\partial U_0}{\partial\theta}$$

$$+\frac{1}{R_aV_*^2}\frac{\partial}{\partial\theta}[P_0U_0U_0U_j]=-\frac{A_0}{R_a}\frac{\partial P_j}{\partial\theta}$$

$$+C_{xu}U_j+C_{xh}H_j+C_{xp}P_j \quad (12)$$

$$\dot{M}_j=\eta_hH_j+\eta_{pu}P_{uj}+\eta_{pd}P_{dj}, \quad (13)$$

where

$$C_{xu}=\eta_{xu}-\eta_{uu}$$

$$C_{xh}=\eta_{xh}-\eta_{uh}+\eta_{mh}U_0+\frac{L}{R_a}\frac{\partial P_0}{\partial\theta}$$

$$C_{xp}=\eta_{xp}-\eta_{up}+\eta_{mp}U_0 \quad (14)$$

and the subscripts "j" ($=X, Y$) denote the directions of rotor motion. The η coefficients given in the appendix arise from the perturbation of the empirical axial leakage terms and turbulent shear stress terms.

Boundary Conditions

The boundary conditions for both the zeroth order and first-order governing equations are given as follows:

1 The pressure at the seal inlet are equal to

$$P_{s0}=P_s,\quad U_{s0}=\alpha\Omega R_r$$

$$P_{sj}=0,\quad U_{sj}=0\quad j=X,Y \quad (15)$$

where α is an inlet preswirl factor. The assumption precludes the case of a perturbation of the circumferential flow upstream of the seal teeth inlet plane.

2 The pressure at the seal discharge plane is equal to

---

[2] This parameter must be extracted from detailed experimental measurements.

Table 1 Two-bladed teeth-on-stator labyrinth seal dimension and operating conditions

R_r = 2.000" (50.8 mm), R_s = 2.180" (55.372 mm)
L = 0.750" (19.05 mm), H_b = 0.004" (0.1016 mm)
H_s = 0.004" (0.1016 mm), B_b = 0.176" (4.4704 mm)
B_s = 0.176" (4.4704 mm), α = 0.5 (preswirl factor)
T = 74 °F (296 °K)
R_g = 639.31 in-lb/lbm-°R (287 J/kg-K) (for air)
P_s = 20-70 psia (1.38-4.83 bar)
P_b = 14.7 psia (1.013 bar)

$$P_{b0} = P_b,$$

$$P_{bj} = 0 \quad j = X, Y. \tag{16}$$

3 At the partition baffle between two pockets, the pressure, and circumferential velocity are expressed as

$$P_j(\beta) = \beta_{jpu} P_{uj} + \beta_{jpd} P_{dj}$$

$$U_j(\beta) = \alpha_{jh} H_j + \alpha_{jpu} P_{uj} + \alpha_{jpd} P_{dj} \quad j = X, Y, \tag{17}$$

where the β_j and α_j coefficients (appendix) arise from the first-order perturbation of the boundary conditions.

The zeroth-order solution determines the steady-state pocket pressure, circumferential velocity fields, and the seal leakage. The first-order solution leads to the determination of the seal dynamic force (stiffness and damping) coefficients by integration of the complex first-order pressure field (P_j) over the rotor surface:

$$(K_{ij} + i\omega C_{ij}) = -LR_r \sum_{n=1}^{N_c} \int_{-\beta}^{+\beta} P_j^n H_i \, d\theta; \quad i, j = X, Y. \tag{18}$$

Note that the seal dynamic force coefficients are frequency dependent since the fluid is compressible. Furthermore, for a seal at its centered position, $K_{YY} = K_{XX}$, and $K_{YX} = -K_{XY}$, etc.

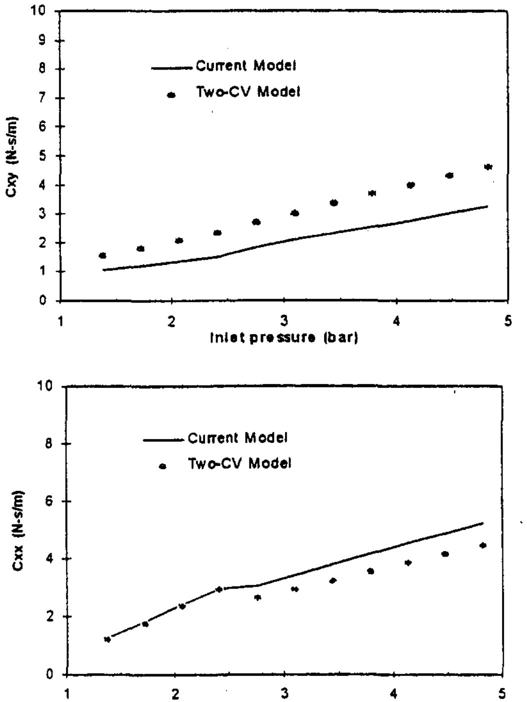

Fig. 3 Damping coefficients of a two-teeth gas labyrinth seal versus inlet pressure (Ω = 4200 rpm, ω = 70 Hz)

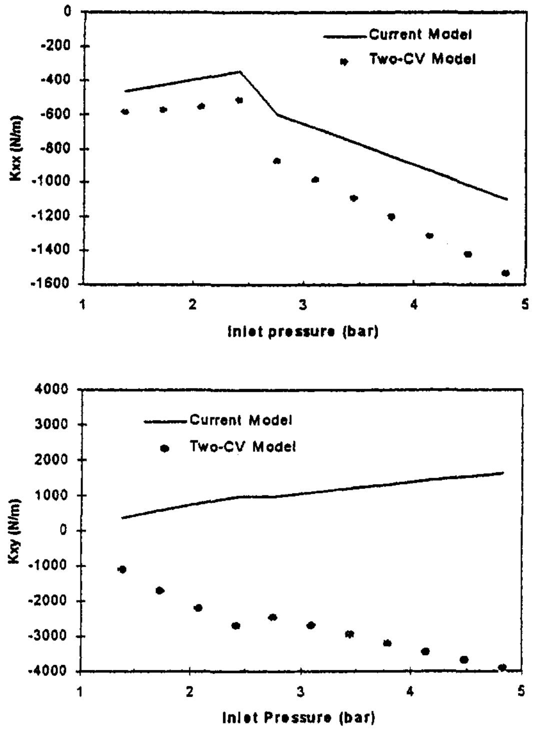

Fig. 4 Stiffness coefficients of a two-teeth gas labyrinth seal versus inlet pressure (Ω = 4200 rpm, ω = 70 Hz)

Numerical Method of Solution

A finite difference scheme is implemented to solve the nonlinear PDEs of mass and momentum transport. The flow field is represented by a series of discrete nodal pressures and circumferential velocities on staggered grids (Patankar, 1980). The velocity nodes are located at points which lie at interfaces midway between the nodes where the pressure is determined. Zeroth order and first-order discrete algebraic equations are derived by integration of the governing equations on finite size control volumes and using the SIMPLEC algorithm of Van Doormaal and Raithby (1984). A full upwinding scheme is used for the advection terms in order to make the algorithm more stable.

Both the steady state and first-order flow fields are numerically calculated based on an iterative procedure. The empirical leakage equation is used to guess an initial uniform pressure field within the seal. The velocity components are first calculated from the circumferential momentum equation using the guessed pressure field, and then a pressure correction equation based on the continuity equation provides corrected pressure and velocity fields. The updated pressure and velocity fields are substituted into the momentum and pressure correction equations again resulting in (generally) more accurate velocity and pressure field solutions. The iterative procedure above is repeated until the maximum difference between two consecutive iterations for the pressure field is less than $1'10^{-6}$ of the seal supply pressure. Also the ratio of the global mass flow residuals to the total mass flow across the seal is used to monitor the convergence of the numerical scheme.

Comparison of Predictions From a Two-Bladed Gas Labyrinth Seal (TOS)

The analysis is developed for two-bladed multiple-pocket gas damper seals and with a few modifications it is also applicable to teeth-on-stator (TOS) labyrinth seals. Wright (1983) presents limited measurements of leakage, radial and tangential forces in a two-bladed (TOS) short labyrinth seal. Li et al. (1997)

Table 2 Two-bladed four pocket gas damper seal dimension and operating conditions (Li, 1995)

R_r = 2.000" (50.8 mm), R_s = 2.180" (55.372 mm)
L = 0.750" (19.05 mm), H_b = 0.008" (0.2032 mm)
H_s = 0.004" (0.1016 mm), B_b = 0.372" (4.3688 mm)
B_s = 0.176" (4.4704 mm), N_c = 4
S = 0.059" (1.5 mm), $\alpha = 0$
T = 74 °F (296 °K), Loss coefficient at the baffle ξ_w = 1.0
R_g = 639.31 in-lb/lbm-°R (287 J/kg-K) (for air)
P_s = 20-60 psia (1.378-4.135 bar), P_b = 14.7 psia (1.013 bar)

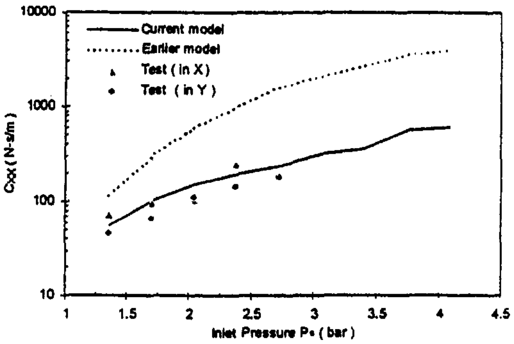

Fig. 6 Direct damping coefficients versus inlet pressure for a two-bladed gas damper seal (Ω = 0.0 rpm, ω = 66 Hz)

include comparisons of these test data to predictions from the current model. Benckert and Wachter (1980), Millsaps and Martinez (1994), and Kwanka and Nagel (1996) report on experimental results for short length labyrinth seals with teeth on rotor. However, these test results are of little relevance to the present development.

Rotordynamic characteristics of a two-bladed gas labyrinth seal are evaluated for comparison to predictions from a two-control volume bulk-flow model (Scharrer, 1988). The gas labyrinth seal has a see-through clearance configuration as detailed in Table 1.

The rotor and stator surfaces are regarded as smooth, and a rotor speed of 4200 rpm is specified. Since synchronous whirl is of major concern in rotating machines, a synchronous excitation frequency (70 Hz) is used to calculate the seal dynamic force coefficients.

As shown in Fig. 3, both computational models predict the same trends in the damping coefficients as the supply pressure increases. The damping coefficients predicted by both models are nearly the same prior to the onset of choked flow at a pressure of 2.75 bars. At higher inlet pressures the predictions diverge slightly. Figure 4 shows the synchronous direct stiffness to be negative for all inlet pressures. At first, the magnitude of the direct stiffness K_{XX} decreases slightly as the supply pressure increases, and then sharply increases above the pressure needed for choked flow. The current bulk-flow model predicts a smaller magnitude of the direct stiffness coefficient than the two-control volume bulk-flow model. The current model predicts positive cross-coupled stiffness coefficients K_{XY} (a destabilizing force mechanism for forward whirl) while the two-control volume model predicts negative values. Since there is no experimental data of the dynamic force coefficient for a two-teeth on stator labyrinth seal, it is difficult to assert reasons explaining the difference in results.

Comparison of Results From Present Analysis With Existing Experimental Data

Comparisons of the predictions from the current model to results from the earlier analysis of Vance et al. (1993b) and experimental values for the direct damping coefficient of a gas damper pocket seal are presented. The test rig description, measurement procedure, and test results are given by Li (1995). The two-bladed seal has four baffles dividing the annular groove into four identical circumferential pockets (see Table 2). Direct damping coefficients are identified from measurements of the logarithm decrement of the decaying free vibration waveforms at null rotor speed. Since the natural frequency of the test rotor is around 66 Hz, a similar excitation frequency is used to calculate the dynamic force coefficients.

Figure 5 shows the current model to predict the mass flow rate reasonably accounting for a ~20 percent uncertainty in the mass flow measurement. However, the model shows an unusual drop in mass flow rate at the choke pressure (~3.25 bars). The predicted behavior is due to the leakage Eq. (3) used in the formulation as obtained directly from Childs (1993). Both theoretical models properly predict the direct damping coefficient (C_{XX}) to increase with the inlet pressure as shown in Fig. 6. The results from the current bulk-flow model correlate well with the test results over the range of test inlet pressures. The earlier (nonviscous) model largely overpredicts the damping coefficient, especially at the largest inlet pressures since it neglects the azimuthal flow within the seal. Nonetheless, Vance and Schultz (1993) also report test damping values where the simplified model underpredicts the damping magnitude at high inlet pressures. An explanation may reside on the test damper element which has a deeper cavity than the seal investigated here.

Figure 7 illustrates that both theoretical models predict a negative direct stiffness for the two-bladed gas damper seal. This fact has been indirectly confirmed by coastdown tests in which the critical speed of the rotor-seal system decreases with increases in the supply pressure (Li, 1995). Unfortunately, no published test data of the direct stiffness coefficient is available for comparison.

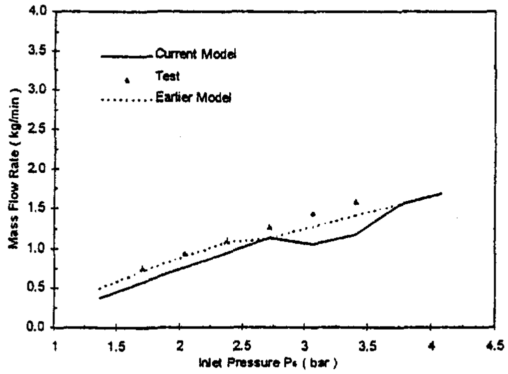

Fig. 5 Mass flow rates versus inlet pressure for a two-bladed gas damper seal

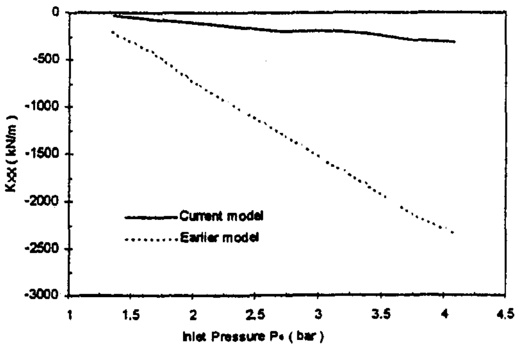

Fig. 7 Direct stiffness coefficients versus inlet pressure for a two-bladed gas damper seal (Ω = 0.0 rpm, ω = 66 Hz)

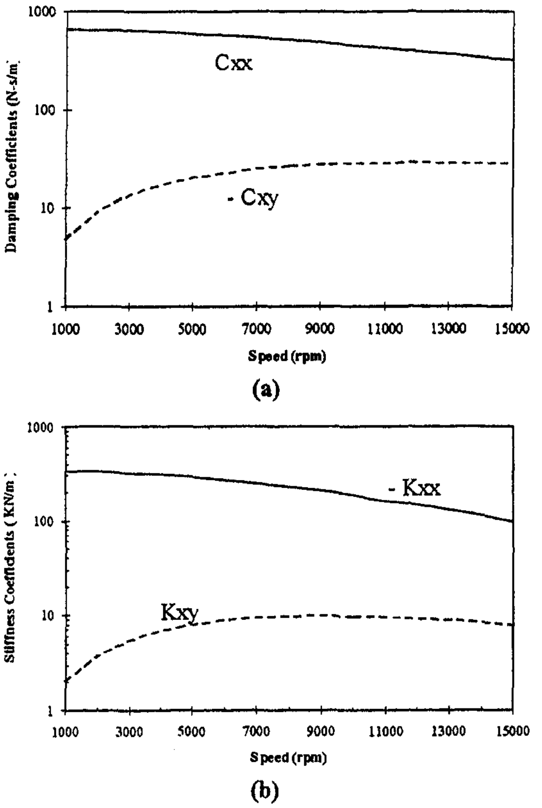

Fig. 8 Dynamic force coefficients of a two-bladed gas damper seal versus rotor speed (inlet pressure = 4.1347 bar, preswirl ratio = 0.0): (*a*) damping coefficients and (*b*) stiffness coefficients

Dynamic Performance of a Two-Blade on Stator, Four-Pocket Gas Damper Seal

The effects of rotor speed, preswirl ratio and excitation frequency on the dynamic force coefficients of a four pocket damper seal are investigated. The geometry of the reference damper seal is given in Table 1, although the exit clearance (H_b) is twice the given value. In the following, the rotordynamic force coefficients are evaluated at the synchronous whirl frequency unless otherwise noted.

Figure 8 shows the seal force coefficients of the two-bladed gas damper seal as the rotational speed increases from 1000 rpm to 15,000 rpm. Note that the synchronous excitation frequency (ω) also increases with rotor speed. In all cases, the direct stiffness coefficient (K_{XX}) is negative and its magnitude decreases as the rotor speed increases. On the other hand, the cross-coupled stiffness coefficient (K_{XY}) is positive, first increases rapidly, and then remains nearly constant at higher rotor speeds. However, the magnitude of the cross-coupled stiffness is much smaller than that of the direct stiffness because the circumferential flow is greatly blocked by the radial baffles. The direct damping coefficient (C_{XX}) is positive, and decreases slightly with increases in the rotor speed. The cross-coupled damping (C_{XY}) follows a similar trend as the cross-coupled stiffness. The whirl frequency ratio ($K_{XY}/C_{XX}\Omega$) of the damper seal decreases from 0.028 to 0.015 as the rotational speed increases from 1000 rpm to 15,000 rpm. Note the large magnitude of the direct damping coefficient (C_{XX}) when compared to the labyrinth seal predictions given in Fig. 3.

Figure 9 depicts the rotordynamic force coefficients of the gas damper seal versus the inlet preswirl ratio at a specified rotational speed of 4,200 rpm and synchronous excitation frequency (70 Hz). The direct force coefficients (K_{XX}, C_{XX}) are insensitive to the inlet circumferential preswirl ratio. The cross-coupled stiffness coefficient (K_{XY}) increases linearly with the preswirl ratio while the cross-coupled damping coefficient (C_{XY}) decreases. Correspondingly, the whirl frequency ratio of the damper seal changes from −0.16 to 0.21 as the inlet preswirl ratio changes from −1 to 1. Compared with the direct force coefficients, the magnitude of the cross-coupled force coefficients always remains at a lower level.

Figure 10 shows the direct force coefficients to be strongly dependent on the excitation whirl frequency (rotor speed of 4200 rpm). The magnitude of the direct force coefficients (K_{XX}, C_{XX}) decreases as the excitation frequency increases. The cross-coupled force coefficients (K_{XY}, C_{XY}) follow a similar trend as the direct force coefficients.

Conclusions

An isothermal bulk-flow analysis for calculation of the leakage and rotordynamic force coefficients in two-bladed, multiple-pocket gas damper seals is presented. The one control-volume model accounts for the effects of fluid viscosity, flow turbulence, and circumferential flow in the seal cavities. Zeroth and first-order bulk-flow equations describe the flow fields for the seal centered position and for small amplitude rotor motions, respectively.

Comparisons to limited measurements from a two-bladed (TOS), four pocket gas damper seal show the current model to predict well the mass flow rate and the direct damping coefficient. The analysis also renders similar rotordynamic coefficients for a reference two-teeth on stator gas labyrinth seal when compared to a two control-volume bulk-flow model. Typically, the dynamic force coefficients of the gas damper seal are much larger than those of a labyrinth seal with identical geometry. The accuracy of the model to predict stiffness coefficients remains to be verified by experiments. Fortunately, a test program is currently under development to fully identify and characterize the dynamic force coefficients of multiple-pocket gas damper seals (Ransom, 1997).

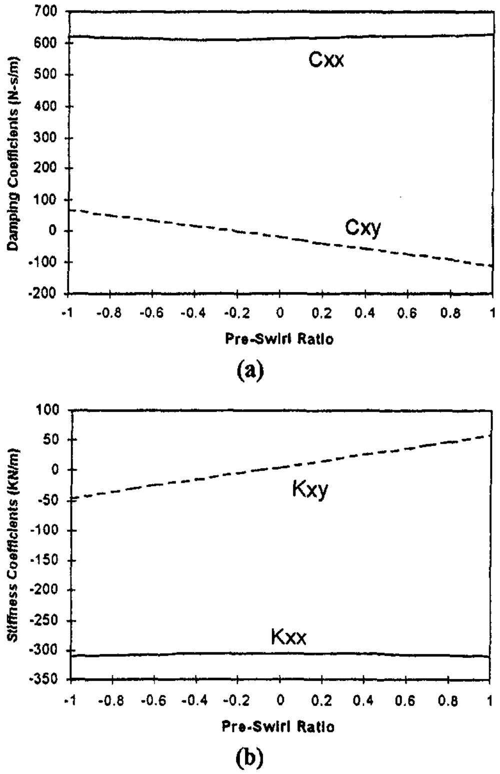

Fig. 9 Dynamic force coefficients of a two-bladed gas damper seal versus inlet preswirl ratio (inlet pressure = 4.1347 bar, Ω = 4,200 rpm): (*a*) damping coefficients and (*b*) stiffness coefficients

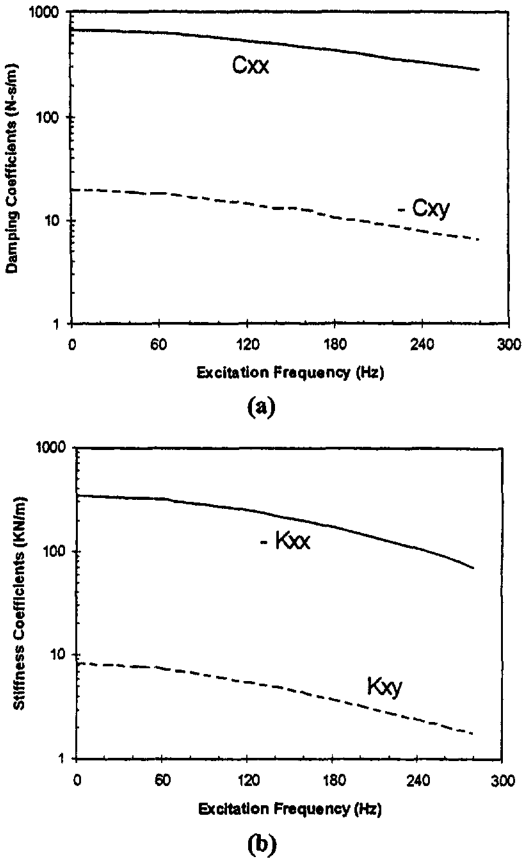

Fig. 10 Dynamic force coefficients of a two-bladed gas damper seal versus excitation frequency (inlet pressure = 4.1347 bar, preswirl ratio = 0.0, Ω = 4,200 rpm): (*a*) damping coefficients and (*b*) stiffness coefficients

A parametric investigation conducted for a reference two-bladed, four pocket gas damper seal provides insight into the rotordynamic characteristics of the novel gas damper seal. The magnitudes of the seal force coefficients decrease with increases in the rotor whirl frequency. The direct force coefficients are insensitive to the inlet preswirl (circumferential) velocity while the cross-coupled dynamic force coefficients are proportional to this parameter. The whirl frequency ratio of the damper seal decreases as the rotational speed increases. Gas pocket damper seals provide larger magnitudes of direct damping when compared to conventional labyrinth seals.

Acknowledgments

The support of the State of Texas Advanced Technology Program is gratefully acknowledged.

References

Alford, J. S., 1965, "Protecting Turbomachinery From Self-Excited Rotor Whirl," ASME *Journal of Engineering for Power*, pp. 333–344.

Benckert, H., and Wachter, J., 1980, "Flow Induced Spring Coefficients of Labyrinth Seals For Application in Rotordynamics," NASA CP 2133, pp. 189–212.

Childs, D. W., 1993, "Turbomachinery Rotordynamics: Phenomena, Modeling, & Analysis," John Wiley & Sons, Inc., New York, pp. 300.

Childs, D. W., and Kleynhans, G., 1993, "Theory Versus Experiment for Short ($L/D = \frac{1}{6}$) Honeycomb and Smooth Annular Pressure Seals," Proceedings, 14th ASME Vibration and Noise Conference, ASME, New York, pp. 173–179.

Childs, D. W., and Vance, J. M., 1997, "Annular Seals and the Rotordynamics of Compressors and Turbines," Proceedings, 26th Turbomachinery Symposium, ASME, New York, pp. 201–220.

Childs, D. W., Elrod, D., and Hals, K., 1989, "Annular Honeycomb Seals: Test Results for Leakage and Rotordynamic Coefficients; Comparisons to Labyrinth and Smooth Configurations," ASME *Journal of Tribology*, Vol. 111, pp. 293–301.

Childs, D. W., Elrod, D., and Ramsey, C., 1990, "Annular Honeycomb Seals: Additional Test Results for Leakage and Rotordynamic Coefficients," Proceedings, Third International Conference on Rotordynamics in IFToMM, pp. 303–312.

Guo, Z., and Rhode, D., 1996, "Assessment of Two and Three-Dimensional κ-ϵ Models for Rotating Cavity Flows," ASME *Journal of Turbomachinery*, Vol. 118, pp. 826–834.

Kwanka, K. T., and Nagel, M., 1996, "Experimental Rotordynamic Coefficients of Short Labyrinth Gas Seals," NASA CP 3344, pp. 135–144.

Laundar, B. E., and Leschziner, M., 1978, "Flow in Finite-Width, Thrust Bearings Including Inertial Effects: I—Laminar Flow: II—Turbulent Flow," ASME *Journal of Lubrication Technology*, Vol. 100, pp. 330–345.

Li, J., 1995, "The Effect of A New Damper Seal on Rotordynamics," Master's thesis, Texas A&M University, College Station, TX.

Li, J., and Vance, J. M., 1995, "Effects of Clearance and Clearance Ratio on Two and Three Bladed TAMSEALs," TRC-Seal-4-95, Turbomachinery Laboratory Research Progress Report, Texas A&M University, College Station, TX.

Li, J., San Andrés, L., and Vance, J. M., 1997, "A Bulk-Flow Analysis of A Novel Gas Damper Seal," TL-Seal-2-97, Turbomachinery Laboratory Research Progress Report, Texas A&M University, College Station, TX.

Millsaps, K. T., and Martinez, M., 1994, "Dynamic Forces From Single Gland Labyrinth Seals: Part I—Ideal and Viscous Decomposition," ASME *Journal of Turbomachinery*, Vol. 119, pp. 686–694.

Murphy, B. T., and Vance, J. M., 1980, "Labyrinth Seal Effects on Rotor Whirl Instability," Proceedings, 2nd International Conference on Vibrations in Rotating Machinery, #C306/80, ImechE, London, U.K. pp. 369–373.

Patankar, S. V., 1980, *Numerical Heat Transfer And Fluid Flow*, Hemisphere Publishing Corporation, McGraw-Hill, New York.

Ransom, D. L., 1997, "Identification of Dynamic Force Coefficients of a Labyrinth and Gas Damper Seal Using Impact Load Excitations," Master's thesis, Texas A&M University, College Station, TX.

Richards, R. L., Vance, J. M., and Zeidan, F. Y., 1995, "Using a Damper Seal to Eliminate Subsynchronous Vibrations in Three Back-to-Back Compressors," Proceedings, 24th Turbomachinery Symposium, Houston, September, pp. 59–71.

Scharrer, J. K., 1988, "Theory Versus Experiment for the Rotordynamic Coefficient of Labyrinth Gas Seals: Part I—A Two Control Volume Model," *ASME Journal of Vibration, Acoustic, Stress, and Reliability in Design*, Vol. 110, pp. 270–280.

Van Doormaal, J. P., and Raithby, G. D., 1984, "Enhancements of the SIMPLE Method for Predicting Incompressible Fluid Flows," *Numerical Heat Transfer*, Vol. 7, pp. 147–163.

Vance, J. M., and Li, J., 1996, "Test Results of A New Damper Seal for Vibration Reduction in Turbomachinery," ASME JOURNAL OF ENGINEERING FOR GAS TURBINES AND POWER, Vol. 118, pp. 843–846.

Vance, J. M., and Schultz, R. R., 1993, "A New Damper Seal for Turbomachinery," *Vibration of Rotating System*, Proceedings, 14th Vibration and Noise Conference, ASME DE-Vol. 60, ASME, New York, pp. 139–148.

Vance, J. M., Zierer, J. J., and Conway, E. M., 1993a, "Effect of Straight Through Labyrinth Seals on Rotordynamics," *Vibration of Rotating Systems*, Proceedings, 14th Vibration and Noise Conference, ASME DE-Vol. 60, ASME, New York, pp. 159–171.

Vance, J. M., Cardon, B. P., San Andres, L. A., and Storace, A. F., 1993b, "A Gas-Operated Bearing Damper for Turbomachinery," ASME JOURNAL OF ENGINEERING FOR GAS TURBINES AND POWER, Vol. 115, pp. 383–389.

Von Pragenau, G. L., 1982, "Damping Seals for Turbomachinery," NASA Technical Paper 1987.

Wright, D. V., 1983, "Labyrinth Seal Forces on A Whirling Rotor," *Rotordynamic Instability*, Proceedings, ASME Applied Mech., Bioeng. and Fluids Engineering Conference, ASME, New York, pp. 19–31.

Yu, Z., and Childs, D. W., 1997, "A Comparison of Experimental Rotordynamic Coefficients and Leakage Characteristics Between Hole-Pattern Gas Damper Seals and a Honeycomb Seal," ASME Paper 97-GT-9.

Zeidan, F. Y., Perez, R. X., and Stephenson, E. M., 1993, "The Use of Honeycomb Seals in Stabilizing Two Centrifugal Compressors," Proceedings, 22nd Turbomachinery Symposium, ASME, New York, pp. 3–15.

APPENDIX

Expressions for Flow Coefficients in Bulk-Flow Equations at the Partition Baffles (Eq. 5)

$$\alpha_r = \frac{k_J}{k_x + \zeta_r \dot{m}_b D_h/\mu L}, \quad \alpha_s = \frac{\zeta_r \dot{m}_s D_h/\mu L}{k_x + \zeta_r \dot{m}_b D_h/\mu L}$$

$$\alpha_w = \frac{H_w/S}{k_x + \zeta_r \dot{m}_b D_h/\mu L},$$

where H_w is the gap between the tip of the radial baffle wall and the rotor surface.

First-Order Bulk-Flow Equations (Eqs. 11–14).

$$\eta_{mh} = \zeta_r(\eta_{hb} - \eta_{hs}), \; \eta_{mp} = \zeta_r(\eta_{pb} - \eta_{ps}),$$

where

$$\eta_{hs} = \eta_h)_{\text{upstream}}, \quad \eta_{ps} = \eta_{pd})_{\text{upstream}}$$

$$\eta_{hb} = \eta_h)_{\text{downstream}}, \quad \eta_{pb} = \eta_{pu})_{\text{downstream}}$$

$$\eta_h = \mu_{f0} D_{p0} C_{hc}/V_*, \quad \eta_{pu} = H_0 \mu_{c0} C_{fu}/V_*, \quad \eta_{pd} = H_0 \mu_{c0} C_{fd}/V_*$$

$$C_{fu} = \mu_{f0} b_{pu} + D_{p0} a_{fu}, \quad C_{fd} = \mu_{f0} b_{pd} + D_{p0} a_{fd}$$

$$C_{hc} = H_0 a_c + \mu_{c0} a_h, \quad D_p = \sqrt{P_u^2 - b_c P_d^2},$$

where $b_c = 1$ for unchoked flow and $b_c = 0$ for choked flow.

$$b_{pu} = \frac{\partial D_p}{\partial P_u}\bigg)_0 \quad b_{pd} = \frac{\partial D_p}{\partial P_d}\bigg)_0 \quad a_{fu} = \frac{\partial \mu_f}{\partial P_u}\bigg)_0 \quad a_{fd} = \frac{\partial \mu_f}{\partial P_d}\bigg)_0$$

$a_h = 1$ for variable clearance and $a_h = 0$ for fixed clearance.

$a_c = a_h \dfrac{\partial \mu_c}{\partial H}\bigg)_0$ for other teeth and $a_c = 0$ for the first tooth.

Note that μ_f and μ_c are the flow coefficient and "carry-over" factor, respectively, as defined by Childs (1993).

$$C_{xu} = \eta_{xu} - \eta_{uu}, \quad C_{xp} = \eta_{xp} - \eta_{up} + \eta_{mp} U_0$$

$$C_{xh} = \eta_{xh} - \eta_{uh} + \eta_{mh} U_0 + \frac{L}{R_a} \frac{\partial P_0}{\partial \theta},$$

where

$$\eta_{uh} = \zeta_r (U_0 \eta_{hb} - U_s \eta_{hs}), \quad \eta_{uu} = \zeta_r \dot{m}_{b0}$$

$$\eta_{up} = \zeta_r (U_0 \eta_{pb} - U_s \eta_{ps})$$

$$\eta_{xh} = \gamma_{xD} \gamma_{Dh} + \gamma_{xx} (\eta_r b_{rh} + \eta_s b_{sh}) + \gamma_{xJ} b_{rh} \zeta_r$$

$$\eta_{xu} = \gamma_{xu} + \gamma_{xx} (\eta_r b_{ru} + \eta_s b_{su}) + \gamma_{xJ} b_{ru} \zeta_r$$

$$\eta_{xp} = \gamma_{xx} (\eta_r b_{rp} + \eta_s b_{sp}) + \gamma_{xJ} b_{rp} \zeta_r$$

$$\eta_r = \frac{1}{2} \zeta_r, \quad \eta_s = \frac{(\zeta_s L + B_s + B_b)}{2L}$$

$$\gamma_{xu} = \frac{\partial(\Delta\tau_x)}{\partial U} = -\left(\frac{\mu L k_x}{D_h}\right)_0, \quad \gamma_{xx} = \frac{\partial(\Delta\tau_x)}{\partial k_x} = -\left(\frac{\mu L U}{D_h}\right)_0$$

$$\gamma_{xJ} = \frac{\partial(\Delta\tau_x)}{\partial k_J} = -\left(\frac{\mu L}{D_h} \frac{\Omega R_r}{2}\right)_0$$

$$\gamma_{xD} = \frac{\partial(\Delta\tau_x)}{\partial D_h} = -\left(\frac{\mu L}{D_h^2}\left[k_x U - k_J \frac{\Omega R_r}{2}\right]\right)_0$$

$$b_{ru} = \gamma_{ru}\left(\text{Re}_r \frac{\partial f_r}{\partial\, \text{Re}_r} + f_r\right)_0, \quad b_{sp} = a_{sp}\left(\text{Re}_s \frac{\partial f_s}{\partial \text{Re}_s} + f_s\right)_0$$

$$b_{su} = \gamma_{su}\left(\text{Re}_s \frac{\partial f_s}{\partial \text{Re}_s} + f_s\right)_0, \quad b_{rp} = a_{rp}\left(\text{Re}_r \frac{\partial f_r}{\partial \text{Re}_r} + f_r\right)_0$$

$$b_{rh} = \left\{\text{Re}_r \frac{\partial f_r}{\partial H} + a_{rh}\left(\text{Re}_r \frac{\partial f_r}{\partial \text{Re}_r} + f_r\right)\right\}_0$$

$$b_{sh} = \left\{\text{Re}_s \frac{\partial f_s}{\partial H} + a_{sh}\left(\text{Re}_s \frac{\partial f_s}{\partial \text{Re}_s} + f_s\right)\right\}_0$$

$$a_{rh} = \gamma_{rD} \gamma_{Dh} + \gamma_{rw} \gamma_{wm} \eta_{hs} + \gamma_{rw} \gamma_{wh}$$

$$a_{rp} = \gamma_{rp} + \gamma_{rw} \gamma_{wm} \eta_{ps} + \gamma_{rw} \gamma_{wp}$$

$$a_{sh} = \gamma_{sD} \gamma_{Dh} + \gamma_{sw} \gamma_{wm} \eta_{hs} + \gamma_{sw} \gamma_{wh}$$

$$a_{sp} = \gamma_{sp} + \gamma_{sw} \gamma_{wm} \eta_{ps} + \gamma_{sw} \gamma_{wp}$$

$$\gamma_{ru} = \frac{\partial \text{Re}_r}{\partial U}\bigg)_0, \quad \gamma_{rp} = \frac{\partial \text{Re}_r}{\partial P}\bigg)_0, \quad \gamma_{rD} = \frac{\partial \text{Re}_r}{\partial D_h}\bigg)_0,$$

$$\gamma_{rw} = \frac{\partial \text{Re}_r}{\partial W}\bigg)_0$$

$$\gamma_{su} = \frac{\partial \text{Re}_s}{\partial U}\bigg)_0, \quad \gamma_{sp} = \frac{\partial \text{Re}_s}{\partial P}\bigg)_0, \quad \gamma_{sD} = \frac{\partial \text{Re}_s}{\partial D_h}\bigg)_0,$$

$$\gamma_{sw} = \frac{\partial \text{Re}_s}{\partial W}\bigg)_0$$

$$\gamma_{wm} = \frac{\partial W}{\partial \dot{m}}\bigg)_0, \quad \gamma_{wp} = \frac{\partial W}{\partial P}\bigg)_0, \quad \gamma_{wh} = \frac{\partial W}{\partial H}\bigg)_0, \quad \gamma_{Dh} = \frac{\partial D_h}{\partial H}\bigg)_0$$

First-Order Boundary Conditions (Eq. 17).

$$\beta_{jpu} = \frac{\partial P_j(\beta)}{\partial P_u} = -\frac{2\xi_w (P_u - P_d)}{P_d}$$

$$\beta_{jpd} = \frac{\partial P_j(\beta)}{\partial P_d}$$

$$= \left[1 - \xi_w \left(\frac{P_u - P_d}{P_d}\right)^2\right] + 2\xi_w \left(\frac{P_u - P_d}{P_d}\right)\left(\frac{P_u}{P_d}\right)$$

and

$$\alpha_{jh} = (\gamma_{jhw} + \gamma_{jhr} + \gamma_{jhs})/[1 - (\gamma_{jur} + \gamma_{jus} + \gamma_{juw})]$$

$$\alpha_{jpu} = (\gamma_{jpuw} + \gamma_{jpur} + \gamma_{jpus})/[1 - (\gamma_{jur} + \gamma_{jus} + \gamma_{juw})]$$

$$\alpha_{jpd} = (\gamma_{jpdw} + \gamma_{jpdr} + \gamma_{jpds})/[1 - (\gamma_{jur} + \gamma_{jus} + \gamma_{juw})],$$

where

$$\gamma_{jur} = (\gamma_{arkr} b_{ru} + \gamma_{arks} b_{su})_w \left(\frac{\Omega R_r}{2}\right)$$

$$\gamma_{jus} = U_s (\gamma_{askr} b_{ru} + \gamma_{asks} b_{su})_w$$

$$\gamma_{juw} = (\gamma_{awkr} b_{ru} + \gamma_{awks} b_{su})_w \left(\frac{D_h (P_u - P_d)}{\mu}\right)_w$$

$$\gamma_{jhr} = (\gamma_{arkr} b_{rh} + \gamma_{arks} b_{sh} + \gamma_{arDh} \gamma_{Dh} + \gamma_{armb} \eta_{hb})_w \left(\frac{\Omega R_r}{2}\right)$$

$$\gamma_{jhs} = U_s (\gamma_{askr} b_{rh} + \gamma_{asks} b_{sh} + \gamma_{asDh} \gamma_{Dh} + \gamma_{asms} \eta_{hs} + \gamma_{asmb} \eta_{hb})_w$$

$$\gamma_{jhw} = (D_h (\gamma_{awkr} b_{rh} + \gamma_{awks} b_{sh} + \gamma_{awDh} \gamma_{Dh} + \gamma_{awmb} \gamma_{hb}$$
$$+ \gamma_{awh}) + \alpha_w \gamma_{Dh})_w \left(\frac{D_h (P_u - P_d)}{\mu}\right)_w$$

$$\gamma_{jpr} = (\gamma_{arkr} b_{rp} + \gamma_{arks} b_{sp} + \gamma_{armb} \eta_{pu})_w$$

$$\gamma_{jps} = (\gamma_{askr} b_{rp} + \gamma_{asks} b_{sp} + \gamma_{asms} \eta_{pd} + \gamma_{asmb} \eta_{pu})_w$$

$$\gamma_{jpw} = (\gamma_{awkr} b_{rp} + \gamma_{awks} b_{sp} + \gamma_{awmb} \eta_{pu})_w$$

$$\gamma_{jpur} = \gamma_{jpr} \beta_{jpu}, \quad \gamma_{jpdr} = \gamma_{jpr} \beta_{jpd}$$

$$\gamma_{jpus} = \gamma_{jps} \beta_{jpu}, \quad \gamma_{jpds} = \gamma_{jps} \beta_{jpd}$$

$$\gamma_{jpuw} = [\alpha_w + (P_u - P_d) \gamma_{jpw} \beta_{jpu}] \left(\frac{D_h}{\mu}\right)_w$$

$$\gamma_{jpdw} = [-\alpha_w + (P_u - P_d)\gamma_{jpw}\beta_{jpd}]\left(\frac{D_h}{\mu}\right)_w$$

$$\gamma_{arkr} = \left.\frac{\partial \alpha_r}{\partial k_r}\right)_0, \quad \gamma_{arks} = \left.\frac{\partial \alpha_r}{\partial k_s}\right)_0, \quad \gamma_{arDh} = \left.\frac{\partial \alpha_r}{\partial D_h}\right)_0,$$

$$\gamma_{armb} = \left.\frac{\partial \alpha_r}{\partial \dot{m}_b}\right)_0$$

$$\gamma_{askr} = \left.\frac{\partial \alpha_s}{\partial k_r}\right)_0, \quad \gamma_{asks} = \left.\frac{\partial \alpha_s}{\partial k_s}\right)_0, \quad \gamma_{asDh} = \left.\frac{\partial \alpha_s}{\partial D_h}\right)_0,$$

$$\gamma_{asmb} = \left.\frac{\partial \alpha_s}{\partial \dot{m}_b}\right)_0$$

$$\gamma_{asms} = \left.\frac{\partial \alpha_s}{\partial \dot{m}_s}\right)_0$$

$$\gamma_{awkr} = \left.\frac{\partial \alpha_w}{\partial k_r}\right)_0, \quad \gamma_{awks} = \left.\frac{\partial \alpha_w}{\partial k_s}\right)_0,$$

$$\gamma_{awDh} = \left.\frac{\partial \alpha_w}{\partial D_h}\right)_0, \quad \gamma_{awmb} = \left.\frac{\partial \alpha_w}{\partial \dot{m}_b}\right)_0$$

$$\gamma_{awh} = \left.\frac{\partial \alpha_w}{\partial H_w}\right)_0 .$$

Experimental and Three-Dimensional CFD Investigation in a Gas Turbine Exhaust System

B. K. Sultanian
General Electric Company,
GE Power Systems,
1 River Raod, Bldg. 53-227,
Schenectady, NY 12345

S. Nagao

T. Sakamoto

Toshiba Corporation,
Heavy Apparatus Engineering Lab,
Tsurumi-ku,
Yokohama-shi 230,
Japan

Both experimental and three-dimensional CFD investigations are carried out in a scale model of an industrial gas turbine exhaust system to better understand its complex flow field and to validate CFD prediction capabilities for improved design applications. The model consists of an annular diffuser passage with struts, followed by turning vanes and a rectangular plenum with side exhaust. Precise measurements of total/static pressure and flow velocity distributions at the model inlet, strut outlet and model outlet are made using aerodynamic probes and locally a Laser Doppler Velocimeter (LDV). Numerical analyses of the model internal flow field are performed utilizing a three-dimensional Navier-Stokes (N-S) calculation method with the industry standard k-ε turbulence model. Both the experiments and computations are carried out for three load conditions: full speed no load (FSNL), full speed mid load (FSML, 57 percent load), and full speed full load (FSFL). Based on the overall comparison between the measurements and CFD predictions, this study concludes that the applied N-S method is capable of predicting complicated gas turbine exhaust system flows for design applications.

Introduction

Turbulent flow diffusion and pressure recovery processes occurring in a typical industrial gas turbine exhaust system are rather complex and three-dimensional in nature. With a growing trend towards higher efficiency combined-cycle (steam and gas turbine) power plants, both aerodynamic and thermodynamic management of gas turbine exhaust for improved performance is receiving its due attention in more recent designs. In most early designs, diffuser section was mainly targeted for most of the pressure recovery and almost all the remaining dynamic pressure was lost in the downstream ducting. For a given compressor discharge pressure and nearly ambient pressure at the inlet to the heat recovery steam generator (HRSG) unit in a combined cycle operation, higher pressure recovery in the exhaust system means lower pressure at the turbine outlet plane. This translates into higher overall pressure ratio across the turbine, giving higher power output and efficiency. A high-pressure-recovery exhaust system generally also favors a nearly uniform flow velocity (or dynamic pressure) and lower turbulence levels into the downstream silencer and HRSG units. It may be noted here that peaky velocity distribution and high turbulence level adversely impact silencer performance. An important feature of an industrial gas turbine exhaust system is that its inlet flow conditions such as mass flow rate and flow angle vary widely with turbine load under design and off-design operations. These considerations form the basis for the present experimental and CFD investigations into a scale model of GE's MS9001E exhaust system, being one of the most complex designs in the existing product line.

The analysis of three-dimensional diffusion in an exhaust system is extremely complicated by the presence of too many geometric and inlet flow parameters. Available test data and analysis results are rather limited to guide practical designs, and are generally applicable for two-dimensional simple geometries. A number of mostly experimental and some analytical attempts have been made to improve industrial turbine exhaust system performance. Xingsu et al. (1981), for example, tested marine gas turbine exhaust volute to select optimum geometric parameters. From the analysis of their experimental data, they also propose the basic design criteria of exhaust volutes. Mao et al. (1987) used the design-of-experiments (DOE) approach to conduct limited model tests to achieve an optimized axial turbine exhaust hood configuration. Fleischer et al. (1989) used scale model of a complete gas turbine exhaust system to test out suitable design of various flow-distributing devices for acceptable quality of exhaust velocity distribution. Desideri and Manfrida (1995) conducted extensive tests on the model of a gas turbine exhaust diffuser to map out detailed distributions of mean velocities, flow angles, and turbulence quantities.

Some of the early work in delineating the diffuser flow regimes are due to Kline and his coworkers at Stanford University (Kline et al., 1959; Fox and Kline, 1962; Reneau et al., 1967). They found that the maximum pressure recovery in a straight-walled two-dimensional diffuser with thin turbulent inlet boundary layer occurs when short-duration flow reversal propagates up and down the diffuser walls, a condition generally known as transitory stall. In practice, exhaust system diffusers are seldom designed for maximum pressure recovery under transitory stall condition because of a small margin to permanent wall boundary layer separation. The latter, if occurs, results in a marked deterioration in the diffuser pressure recovery performance. Ghose and Kline (1976) presents a method of predicting transitory stall in two-dimensional diffusers. Experimental work of Howard et al. (1967) also provides details on various flow regimes and their relation to annular diffuser performance and so does the investigation by Takehira et al. (1977). Japikse and Pampreen (1979) used a boundary layer calculation procedure to predict pressure recovery in an automotive gas turbine annular diffuser and compared with test data. Kanemoto et al. (1982) report CFD validation quality data in an annular diffuser.

Test results of Kelnhofer and Derick (1971) indicate that pressure recovery normally increases when a rectangular diffuser is fitted with a straight constant-area tailpipe instead of a plenum chamber. Senoo and Kawaguchi (1983) found that a plenum chamber at the end of an annular curved diffuser reduced the pressure recovery. The design was improved with a bigger size plenum and by incorporating vanes to reduce the swirl.

Contributed by the International Gas Turbine Institute and presented at the International Gas Turbine and Aeroengine Congress and Exhibition, Stockholm, Sweden, June 2–5, 1998. Manuscript received by the ASME Headquarters April 1, 1998. Paper No. 98-GT-111. Associate Technical Editor: R. Kielb.

Influence of inlet conditions on annular diffuser performance has been the subject of experimental studies by Wolf and Johnston (1969) and Adenubi (1975). The incoming swirl which varies significantly between design and off-design operating conditions has a dramatic influence on exhaust system performance. A moderate swirl level generally improves boundary layer separation at the diffuser outer wall and hence, the diffuser performance. Beyond a critical swirl level, flow reversal, called vortex breakdown, at the inner radius occurs resulting in significant performance loss. The investigation by Srinath (1968) addresses in detail the issue of swirl effects on annular diffuser performance. Unsteady effects by way of vortex shedding behind struts in an annular diffuser form important design considerations especially under FSNL operating conditions. Fric et al. (1996) through their extensive experimental work report the benefits of using tapered struts to minimize the problem.

Kawagishi and Sakamoto (1992) used a commercial CFD code STAR-CD to successfully validate predictions against measurements in a steam turbine exhaust hood. Raab et al. (1996) used another commercial CFD code TASCflow to evolve an optimal aerodynamic design for the whole gas turbine diffusion system. The exhaust system flow fields considered in the present investigation, due to both geometry and inlet flow conditions, are much more complex than those considered in these two studies.

Present Contribution. In view of the joint nature of this technology development program, it was decided at the outset not to use any of the company proprietary in-house CFD codes for validation of N-S calculation method with an advanced industrial turbulence model. Instead, an approach to utilize available leading commercial technology for both high quality grid generation and three-dimensional CFD simulation is used. The emphasis throughout this investigation has been on (1) accurate scale model of complex geometry of the selected gas turbine exhaust system, (2) benchmark quality measurements to investigate detailed flow field in the exhaust system, (3) understanding of the flow field under widely varied load (inlet) conditions, and (4) CFD method validation under these load conditions to confirm the usefulness of the method for design applications.

Experimental Method

Experimental Facility. The experimental program was planned to obtain detailed flow measurements for CFD validation in a $\frac{1}{10}$ size scale model of the exhaust system of an industrial gas turbine (GE-MS9001E type). The model cross-section in the horizontal plane is shown in Fig. 1. It consists of an annular diffuser, 10 struts with an airfoil cross-section located inside the diffuser passage, axisymmetric turning vanes with three-dimensional curved surfaces to deflect the flow from axial to radial direction, held together by 16 tie rods and stiffening plates, and the rectangular plenum. This exhaust system is a ''side-exhaust'' type where discharge from the last stage turbine flows axially in the annular diffuser, enters the rectangular plenum via turning vanes, and exhausts from the plenum at 90 deg in the horizontal plane. It thus features a very complex flow field under all load conditions. The model geometry simulates the prototype design in detail. The inner and outer diameters at the model inlet section are 178 mm and 274 mm, respectively. The model outlet cross-section is 310 mm in width and 526 mm in height. At 160 mm upstream of the model inlet plane, 16 movable guide vanes are installed to generate desired inlet flow swirl for each load condition. The model was assembled in a high-speed air test stand. It is shown here in the photograph in Fig. 2. Compressed air (maximum pressure of about 3 atmosphere) was cooled in a heat exchanger and supplied to the test section through a control valve. The exhaust from the test section was discharged into the atmosphere through an outlet pipe and a stack. The flow diagram of the air test stand is described in Fig. 3.

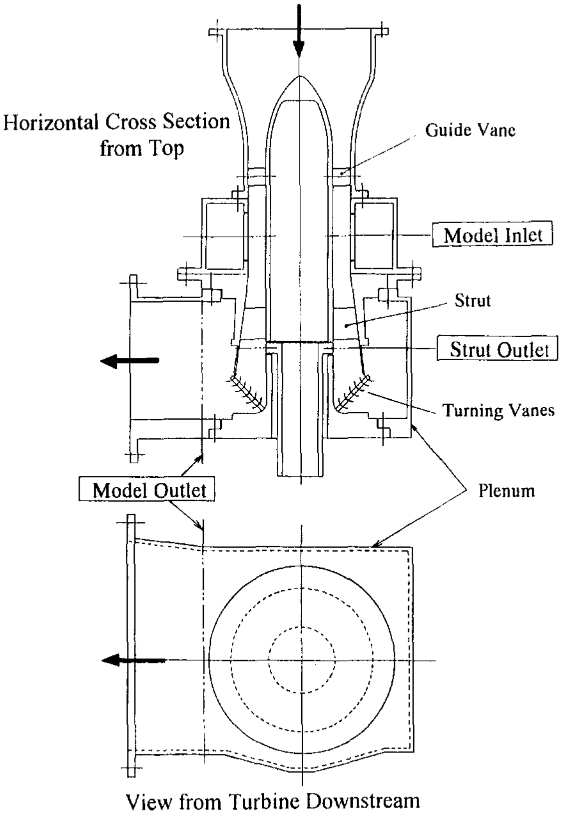

Fig. 1 Test model configuration

Test Conditions. Tests were carried out for the following three load conditions: full speed no load (FSNL); full speed mid load (FSML); and full speed full load (FSFL). Main flow parameters for each of the three load conditions are given in Table 1, which shows a wide variation in both mass flow rate and inlet swirl angle from FSNL to FSFL. In the experiment, both the model inlet Mach number and the swirl angle, simulating the actual turbine outlet conditions, were adjusted by controlling the mass flow rate and the upstream vane angle. The outlet pressure was constant at the atmosphere value, and the model inlet and outlet pressure levels as well as the pressure ratio were almost the same as in the actual combined-cycle

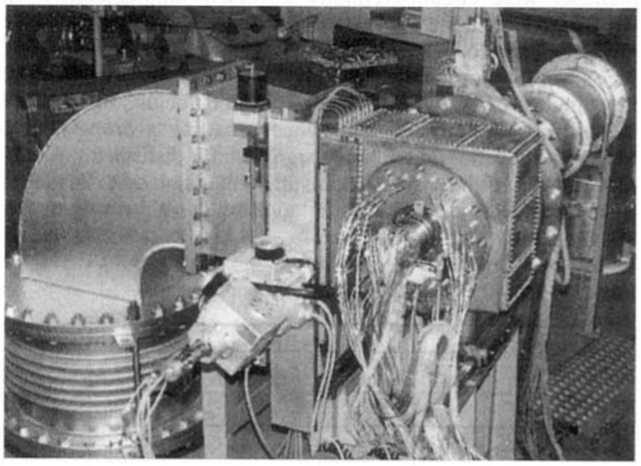

Fig. 2 Test stand overview

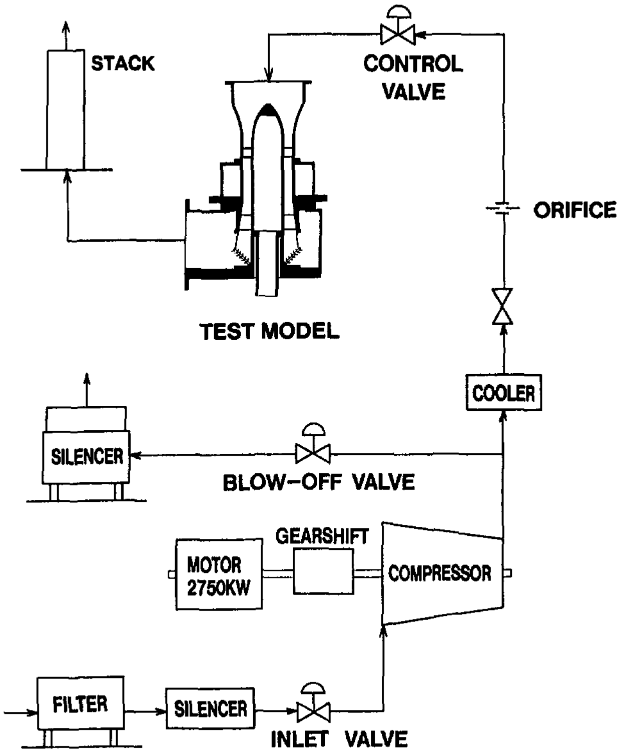

Fig. 3 Test stand flow diagram

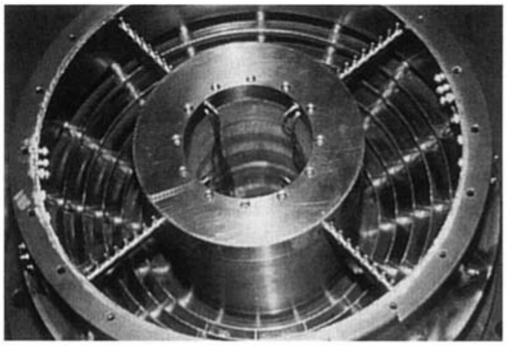

Strut Outlet Traverse Probes

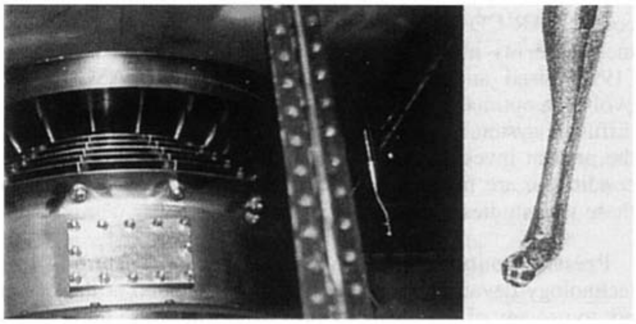

Model Outlet Traverse Probe 5-Hole Probe Head

Fig. 4 Measuring probes

condition. Since this program mainly concerned an aerodynamic investigation and CFD validation, the inlet air temperature was not simulated to correspond to the turbine exhaust condition. In the scale model, the inlet flow Reynolds number, based on the strut chord length, was in the range $0.6-1.1 \times 10^6$, which are about $\frac{1}{3}$–$\frac{1}{5}$ of the prototype values.

Measurement Instrumentation and Error Estimation. Aerodynamic measurements were done at the following four locations: model inlet, around struts, strut outlet, and model outlet. At the model inlet and outlet planes, five-hole pressure probes with a head of 2.4 mm diameter were traversed to measure the distribution of total and static pressures, pitch angle, and yaw angle. Pressure from each hole was detected by piezo-resistive-type pressure transducers. The probes were calibrated in advance in an open-type wind tunnel under atmospheric condition. Total temperature probes were also traversed together with the five-hole pressure probes. At the strut outlet, four rake-type probes with total pressure and temperature heads of 3 mm diameter were circumferentially traversed simultaneously. In this arrangement, the probe heads were nominally fixed in axial direction, but could span about ±60 deg laterally. A 5-Watt argon-ion two-dimensional/three-dimensional Laser Doppler velocimeter (Aeromertics) was also used locally to measure velocity vectors around strut, since installing a probe in this measuring location would have significantly disturbed the flow field. Only two-dimensional measurements in blade-to-blade region were made due to the limitation of the viewing window size on the tip wall. Pure water was sprayed upstream to create droplets of about 5 micron diameter for seeding in the LDV measurements. A hot film probe with a sensor of about 50 micron diameter and 1 mm length was traversed at the model inlet plane for measuring the turbulence intensity distribution, which formed a part of the inlet boundary condition specification in the calculations. Probes used for strut outlet and model outlet are shown in Fig. 4. Measurement procedures, except the LDV measurements, were programmed and automatically controlled on an HP-9000 engineering workstation.

Table 1 Overall test conditions

Load	Mass Flow Rate (kg/s)	Model Inlet Conditions					Model Outlet Static Press. (MPa)
		Swirl Angle (deg)	Absolute Mach Number	Static Press. (MPa)	Total Temp. (deg.C)	Reynolds Number	
FSNL	3.9	-50.8	0.452	0.107	43.1	0.64×10^6	0.102
FSML	5.8	-4.9	0.463	0.095	47.7	0.90×10^6	0.099
FSFL	6.8	13.6	0.567	0.09	44.3	1.07×10^6	0.101

The accuracy of measurements was checked by several methods. At the model outlet plane, velocities were measured by the following two different methods: (1) using the total and static pressures by the pressure probe, and (2) LDV. Comparison shown in Fig. 5 indicates fairly good agreement between the two sets of velocity measurements. The integrated mass flow rate through the model inlet, strut outlet, and the model outlet derived from the pressure-probe measurements were also compared with that measured by the orifice pressure-difference in the upstream lead pipe. The mass flow rate deviations from the orifice-based values were mostly within 3 percent in relative and 5 percent maximum. Considering the complex nature of the flow field through these measuring planes with a nonuniform flow distribution and separation, this accuracy is considered within an acceptable range. Estimated error in both total and static pressures is about 0.2 percent. With this error in pressure, the maximum relative errors in pressure-recovery and total pressure loss coefficients become 2 percent and 7 percent, respectively, for FSNL, 4 percent and 9 percent for FSML, and 4 percent and 4 percent for FSFL.

Computational Method

Strategy. At the outset of this joint program, a computational strategy for the validation of the state-of-the-art CFD technology was adopted and followed throughout the investiga-

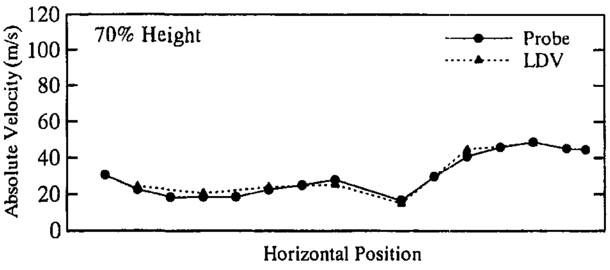

(a) FSNL

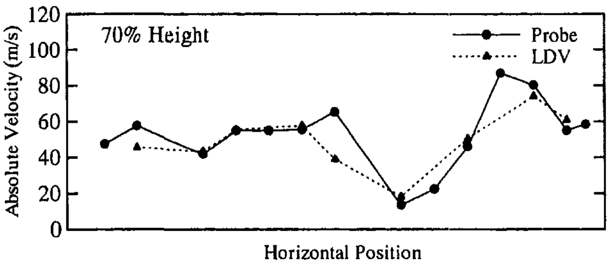

(b) FSFL

Fig. 5 Comparison of measured velocities at model outlet plane by probe and LDV

tion. Three key elements of this strategy are: (1) choice of a turbulence model, (2) choice of computational grid, and (3) choice of commercial N-S code. Each of the three elements are briefly discussed here.

Choice of Turbulence Model. In a recent study, Hirsch and Khodak (1995) compared different turbulence models—standard high-Reynolds-number k-ε model, and an explicit nonlinear algebraic Reynolds stress closure model (ASM) to predict an S-shaped diffusing duct flow. Although, ASM is found to give some improvements in predicting flow details, the overall flow parameters obtained with different turbulence models are close to each other. In an earlier study, Sultanian and Mongia (1986) found that the flow predictions using standard high-Reynolds-number k-ε model with wall functions compared very well with the measurements of Kanemoto et al. (1982) in an annular diffuser. In view of these and other investigations and overall accumulated experience with this model, it was decided to stay with the standard high-Reynolds-number k-ε model with wall functions, simply called the k-ε model, in the present investigation.

Choice of Computational Grid. The geometric complexity of the present computational domain favored the choice of an unstructured grid mainly from the speed of grid generation. However, from the considerations of computational accuracy and available solver speed, this choice was not made. Instead, it was decided to go for a multiblock high quality structured grid as discussed in the grid generation section below.

Choice of Commercial N-S Code. Based on a number of in-house benchmarking and other validation studies of different leading commercial CFD codes, STAR-CD was selected as the N-S solver in this investigation, since it required less memory to run the present model with 1.2 million cells on a highend HP workstation. This choice minimized the overall cost of CFD runs to simulate the three-load conditions used in the experiments.

Grid Generation. Generation of high quality CFD grid in a complex computational domain remains to be one of the most challenging tasks in most applications in gas turbine design engineering. For generating multiblock structured grid in the scale model of the gas turbine exhaust system considered here, the native grid generation capability of STAR-CD was found inadequate and time consuming. An evaluation of commercially

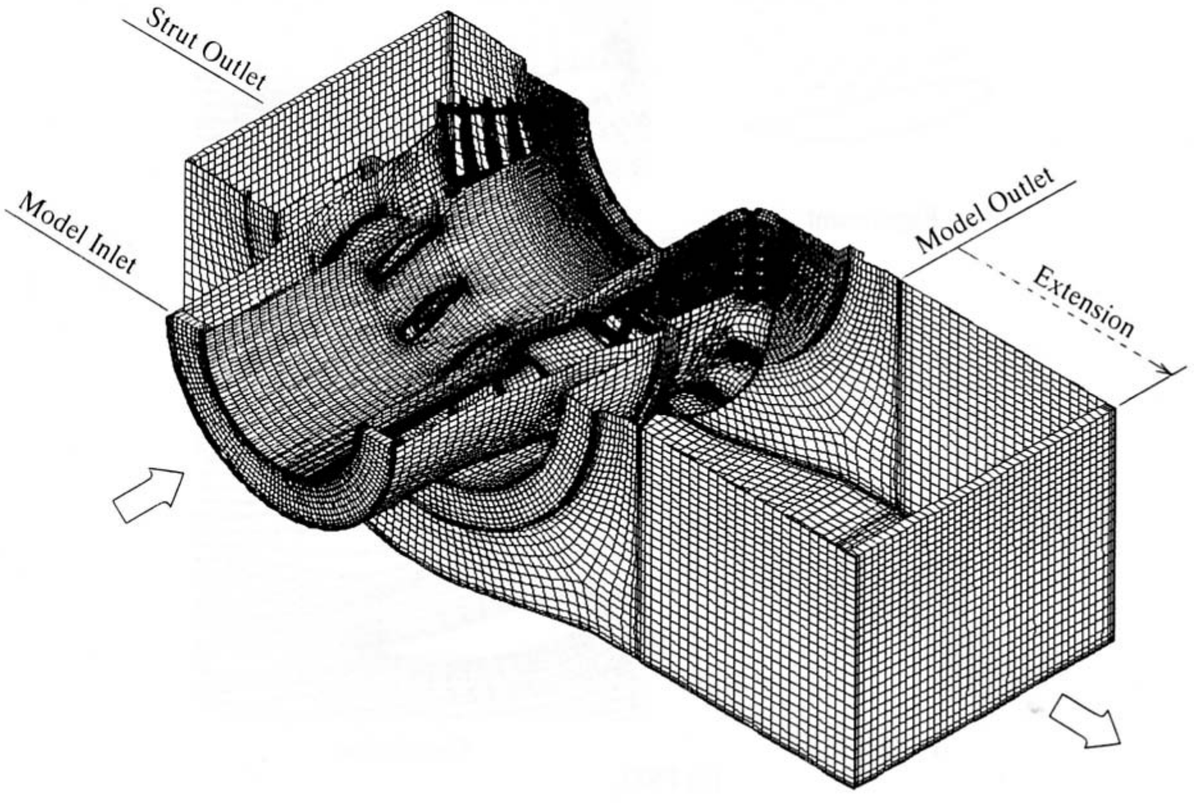

Fig. 6 Lower half of calculation grid

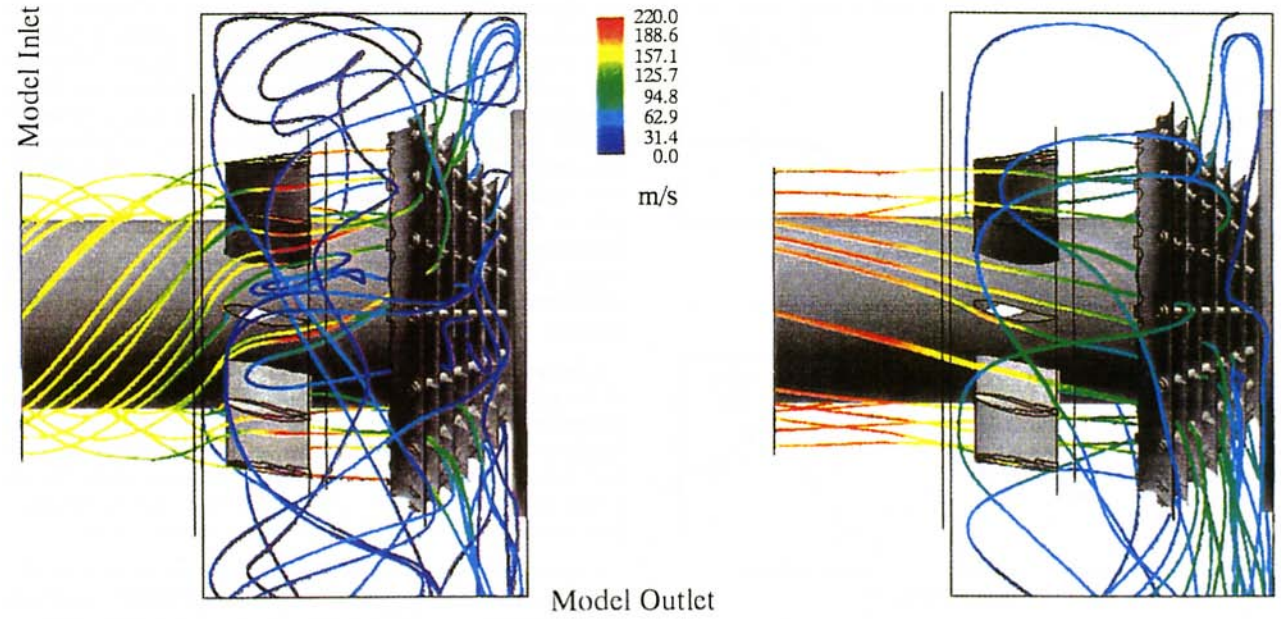

(a) FSNL

(b)FSFL

Fig. 7 Streamlines in entire model (calculation)

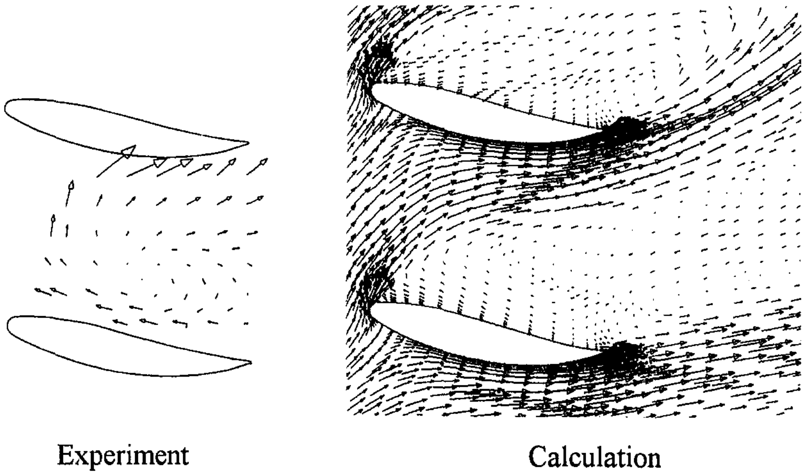

(a)FSNL

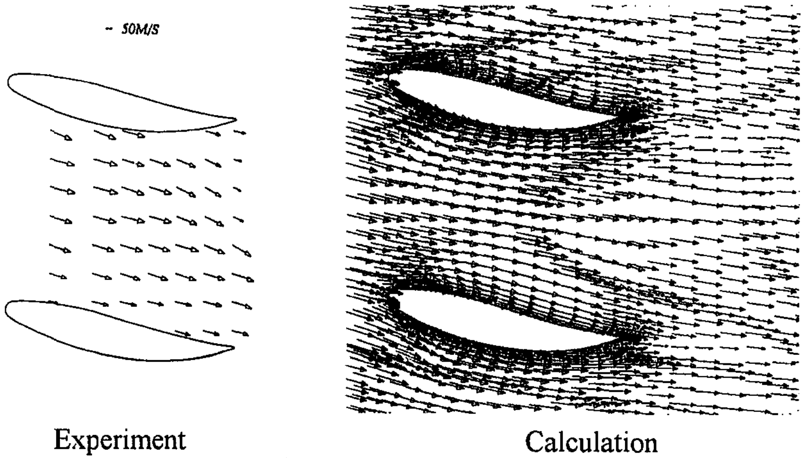

(b) FSFL

Fig. 8 Velocity vectors around struts

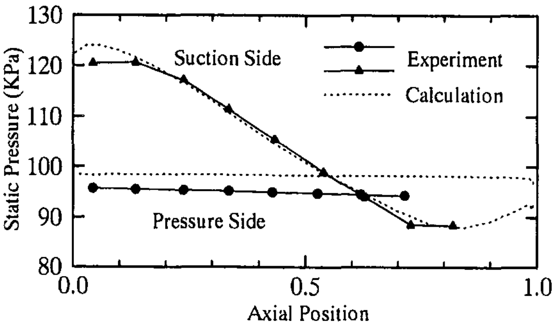

(a) FSNL

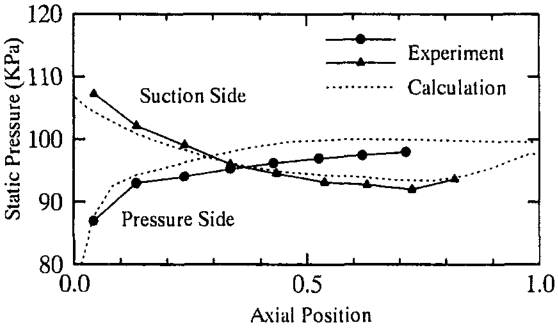

(b) FSML

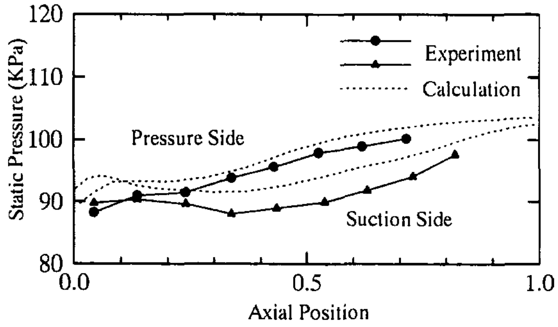

(c) FSFL

Fig. 9 Static pressure distributions on strut surface

available grid generation technologies led to the superior gridding package GridPro/az3000. Details on this grid generation technology may be found in Eiseman (1995) and Cheng and Eiseman (1996). It suffices here to mention that the selection was made on the basis of three key criteria: grid quality, speed of grid generation in a complex domain, and compatibility with the chosen CFD solver.

The overall grid generation process is based upon a top-down concept whereby a coarse wire frame is optimally mapped onto a smooth, nearly orthogonal multiblock grid. The purpose of the wire frame, which is a sequence of corners and linkages that form a coarse unstructured quadrilateral (two-dimensional) and hexahedral (three-dimensional) grid, is to define the pattern of grid points that cover the computational domain under consideration. The wire frame corners are generally placed in a loose fashion relative to the associated region boundaries and are appropriately assigned to the corresponding parts of these boundaries. With the glue of surface assignment, the wire frame represents a grid pattern for the region called grid topology that represents the minimal information needed to generate a multiblock grid. Organization for this information is given by the Topology Input Language (TIL), which is an object oriented language as discussed in Eiseman (1995). The multiblock grids are then automatically generated by compiling and running TIL codes. In this process, gridding on the bounding surfaces and their common intersections are also generated automatically.

The surface grid for the entire computational domain generated using GridPro is shown in Fig. 6, which is showing lower half of the model geometry only; the whole geometry, however, was used in the flow simulations. In spite of a very complex geometry of the exhaust system, the figure shows that the grid lines are virtually perpendicular to each other, and transition of grid cells are smooth and gradual. There are about 1.2 million computational cells in this model. Clustering specifications have been used to ensure that first nodes from the wall region fall within the logarithmic region for proper applicability of the wall function boundary conditions used here. Computed $y+$ values are found typically in the range of 30–160 for most wall surfaces.

Governing Equations. The governing conservation equations of both the mean flow and the standard high-Reynolds-number k-ε turbulence model to compute three-dimensional compressible flow in this study are, for example, given in Lakshminarayana (1996) with the turbulence model constants from Launder and Spalding (1974).

Boundary Conditions. The three-dimensional computational model used here involves three types of boundaries: inflow (inlet plane), outflow (outlet plane), and no flow (solid walls). Each type of boundary condition is briefly discussed here.

Inflow (Inlet Plane). Detailed measurements of the mean flow and the turbulence field are used as inlet boundary conditions for all the three load conditions. Flow quantities such as total pressure, total temperature, flow angle, turbulent kinetic energy, turbulence dissipation rate (obtained from local equilibrium with a suitable length scale), and mass flow rate are specified at the inlet computational cell faces.

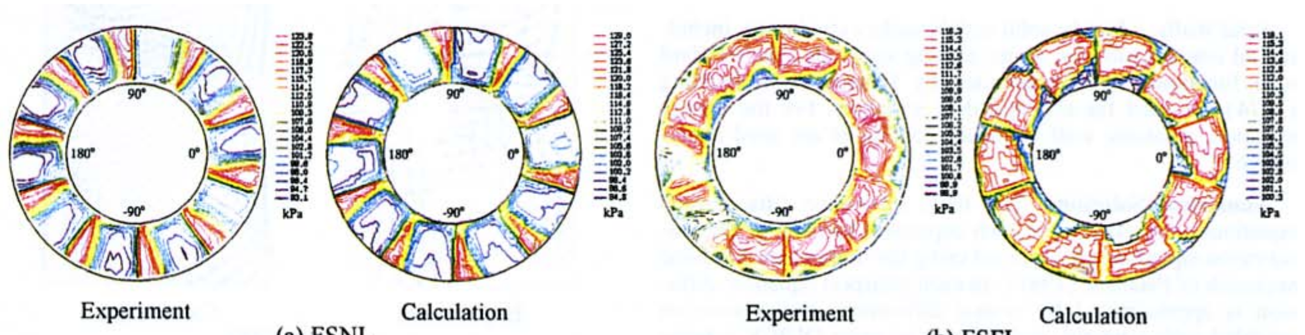

(a) FSNL (b) FSFL

Fig. 10 Total pressure contours at strut outlet (view from downstream)

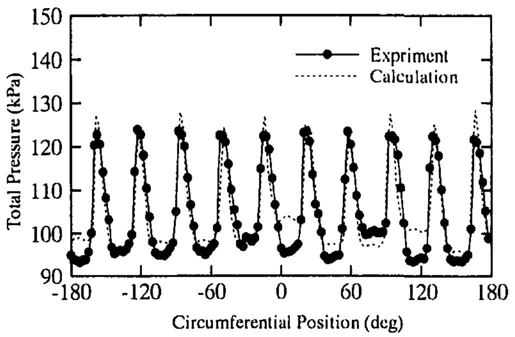

(a) FSNL

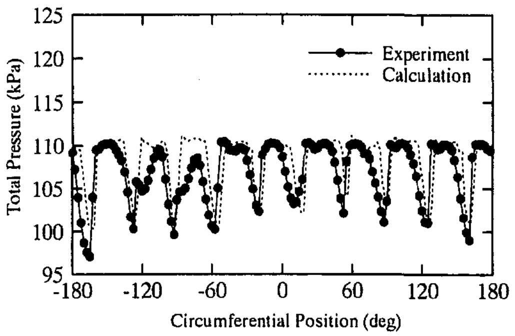

(b) FSML

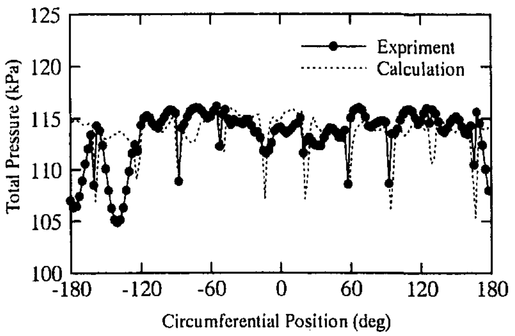

(c) FSFL

Fig. 11 Circumferential distributions of total pressure at strut outlet

Outflow (Outlet Plane). The boundary conditions at the outlet plane correspond to zero axial gradient for all the dependent variables. Note in Fig. 6 that the computational model is extended to facilitate such a boundary condition and to avoid any inflow at the outflow boundary due to flow recirculation. During the computations, however, the N-S solver modifies the outflow quantities to conserve net air flow rate entering the computational domain.

Solid Walls. For the solid wall boundary conditions, including all internal surfaces, struts, turning vanes etc., the standard wall functions as recommended by Launder and Spalding (1974) are used for all dependent variables. For the energy equation, adiabatic wall boundary conditions are used everywhere.

Numerical Solution. The finite difference (discretized) equations corresponding to each dependent variable of the conservation equations are obtained using the finite control volume approach of Patankar (1981). In each transport equation, diffusion is approximated by central differences and convection modeled with a nearly second order accurate QUICK scheme of Leonard (1979). This is done to primarily minimize false numerical diffusion errors in the computation. The N-S solver uses the semi-implicit pressure-linked equations (SIMPLE) approach of Patankar (1981) to obtain numerical solution of the resulting system of algebraic equations.

Results and Discussion

Calculation results from three-dimensional CFD simulations for the three load conditions are compared with the measurements in the diffuser strut region, strut outlet plane, and model outlet plane. In addition, comparison between the calculated and measured overall performance of the exhaust system in terms of total pressure loss and static pressure recovery is also made. These results are discussed in the following sections.

Flow Field in the Entire Model. Figure 7 shows computed streamlines in the whole model from inlet to outlet, looking from top. This gives a good understanding of the overall flow characteristics. At FSNL, shown in Fig. 7(*a*), the inlet flow with a high swirl angle hits the struts and creates large separations in the inter-strut passage, suggesting a large pressure drop in this area. The largest velocities are observed around the strut outlet as shown in red color, accompanied with a sudden deceleration at downstream. Streamlines in the plenum also indicate to have large vortices. On the contrary, flow field in FSFL, shown in Fig. 7(*b*), the highest velocity is observed at the diffuser inlet, decelerating along the diffuser passage much more smoothly compared with FSNL. This conversion of dynamic pressure into flow static pressure (pressure recovery) takes place along the whole passage from the model inlet to the plenum outlet.

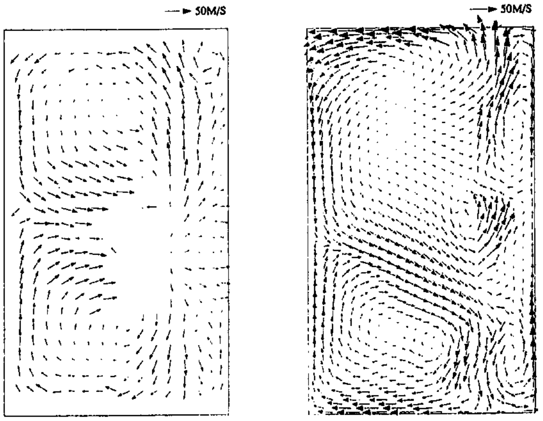

Experiment Calculation

(a) FSNL

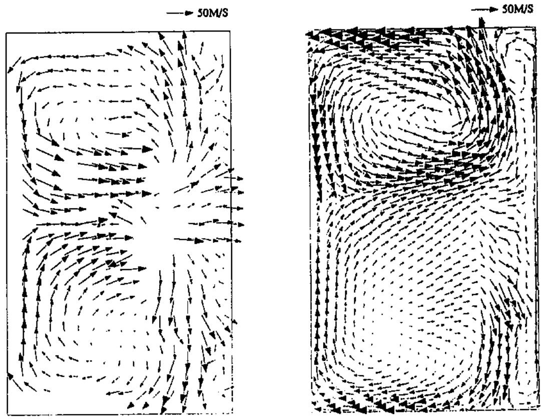

Experiment Calculation

(b) FSFL

Fig. 12 Velocity vectors in model outlet plane (view from downstream)

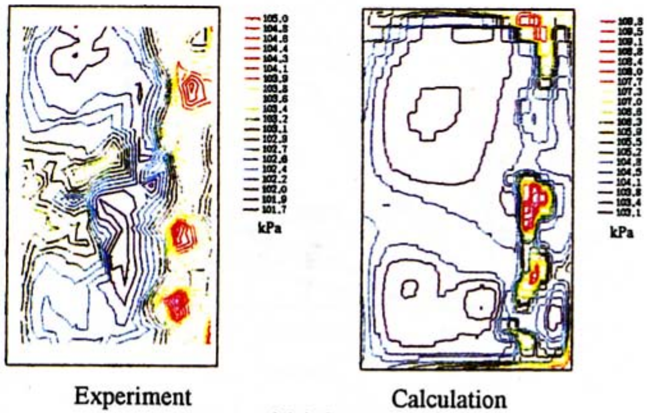

(a) FSNL

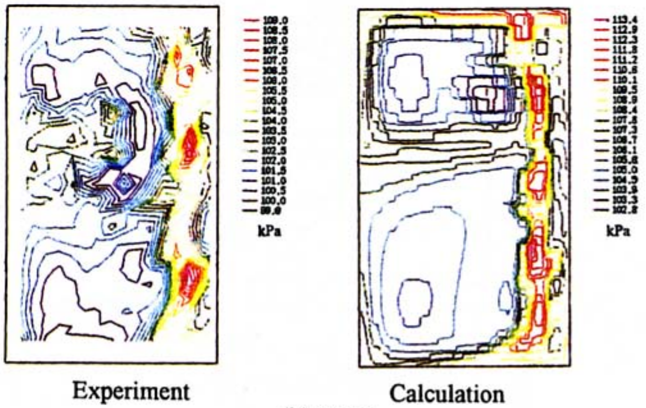

(b) FSFL

Fig. 13 Total pressure contours at model outlet (view from downstream)

Flow Field in the Diffuser Section and Around Struts.

Velocity Vectors Around Strut. Figure 8 shows velocity vectors around a diffuser strut at mid-span from both calculations and LDV measurements for both FSNL and FSFL. At FSNL, shown in Fig. 8(*a*), flow approaches the strut leading edge (suction side) with the swirl angle of −50 deg. This leads to a large flow separation region covering the entire pressure surface, extending further downstream. Key features of these low-load-flow phenomena are well predicted by calculation; the center position of the secondary flow vortex from calculations almost coincides with that obtained from measurements. The velocity vectors in the passage upstream region, however, show some discrepancies. At FSFL, shown in Fig. 8(*b*), the incoming flow has negligible incidence angle with the strut leading edge, and it moderately turns to the axial direction in the passage without creating any large flow separation. Agreement between calculation and the LDV measurement is reasonable for both flow direction and velocity magnitude.

Static Pressure Distribution on Strut Surface. Figure 9 shows static pressure distribution on strut surface. At FSNL, shown in Fig. 9(*a*), the large inflow angle to the suction side causes a higher pressure in the front half than that on the pressure side. This tendency is quite well predicted, though the calculated static pressure is slightly higher than measurement on pressure side. For FSML, shown in Fig. 9(*b*), the flow still has large incidence at the suction side leading to a high suction-side pressure at the front end. Calculations again agree fairly well with the measurements on both sides for FSML. For FSFL, shown in Fig. 9(*c*), pressure distributions on both sides assume the normal strut airfoil design condition, and the overall distribution is well predicted. Pressure level is also reasonably calculated although it is 1–2 kPa higher than experiment for pressure side and 2–3 kPa for suction side.

Total Pressure Contour at Strut Outlet. Figure 10 compares measured and calculated total-pressure contours at the strut outlet plane. At FSNL, shown in Fig. 10(*a*), outlet total pressure

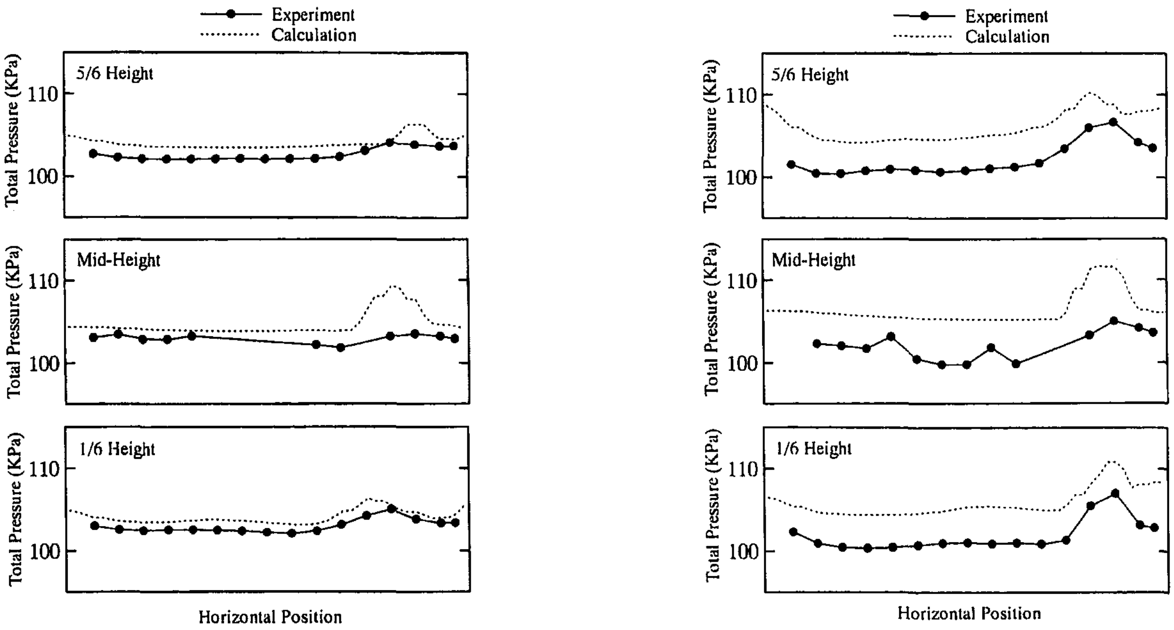

(a) FSNL

(b) FSFL

Fig. 14 Total pressure distribution at model outlet is high downstream of the suction side as the flow deflects to this side at low load, and low downstream of the separated reversed flow region earlier presented in Fig. 8(*a*). A comparison of calculation and measurement shows that this flow field is well predicted. For FSFL, shown in Fig. 10(*b*), the high pressure region corresponding to each inter-strut passage almost connects circumferentially with that from adjacent passage. This indicates that the flow velocities are fairly large even in the wakes, except in the root and tip regions.

Circumferential Distribution of Total Pressure at Strut Outlet. Figure 11(*a*) shows that for FSNL the mid-span circumferential distribution of total pressure at the strut outlet plane features sharp peaks of high total pressure region and flat bottoms of low pressure regions. This behavior results from flow concentration toward a very narrow stream on the strut suction side and flow separation in the remaining region. Positions of these peaks are correctly predicted by calculations. The total pressure difference between the peak and bottom predicted by the calculation matches reasonably with the experiment. For FSML, shown in Fig. 11(*b*), flow expands to almost full pitch of inter-strut passage except in the wake region. The wider top and very narrow bottom are, therefore, observed in the circumferential distribution of total pressure unlike in the case of FSNL. The total pressure difference between the peak and bottom is again quite well predicted by the calculations. For FSFL, shown in Fig. 11(*c*), calculations do predict the experimentally observed narrow and sharp wakes. The test data, however, show larger unsymmetry in circumferential direction than calculations. This circumferential asymmetry is possibly caused by a 90-deg complex flow turning in the plenum. Some of the small wakes observed in measurements indicate that the traverse interval used in testing was still too large to capture some of the narrower wakes in FSFL.

Flow Field Exiting the Plenum.

Velocity Vectors in the Model Outlet Plane. Figure 12 shows velocity vectors in the model outlet plane for both FSNL and FSFL, comparing experiments (5-hole probe measurements) and calculations. The calculation well predicts the existence of two large counter-rotating vortices in upper and lower halves, including the rough location of their centers. The direction of vortices coincides with that of secondary flow generated by turning from diffuser to plenum outflow. Calculated velocity vectors in the region between the two counter-rotating vortices differ from the experimental data that exhibit greater symmetry between the upper and lower halves. For FSFL, shown in Fig. 12(*b*), the direction of calculated vectors in the region between the two vortices becomes nearly horizontal and the two vortices come closer to being symmetric. This reproduces the measured velocity pattern fairly well.

Total Pressure Distribution in the Outlet Plane. Figure 13 shows total-pressure contours at the model outlet plane at both FSNL and FSFL. At FSNL, shown in Fig. 13(*a*), the pattern of the total pressure distribution is roughly predicted. The high-pressure region is seen along the right endwall spanning from top to bottom. Weak and broad pressure peaks are seen in each upper and lower half in the low velocity regions from center to the left side. For FSFL, shown in Fig. 13(*b*), again flow pattern is roughly reproduced by calculation as in FSNL. In this flow condition, several pressure peaks are found along the right endwall with large and weak peaks in the upper and lower halves corresponding to the low velocity regions. The calculated range of total pressure variation is about 10 kPa, which is the same as experiment, but the calculated mean level is 3–4 kPa higher than experiment.

Figure 14 shows line plots of total pressure distribution at the model outlet plane at three different heights for both FSNL and FSFL. In FSNL, calculation predicts total pressure level 1–2 kPa larger than experiment, except for a big peak observed in the right side at mid height. In FSFL, the discrepancy between calculation and experiment becomes larger to be 3–5 kPa. The tendency that the model outlet pressures are calculated larger than measurements is seen more or less for all load conditions.

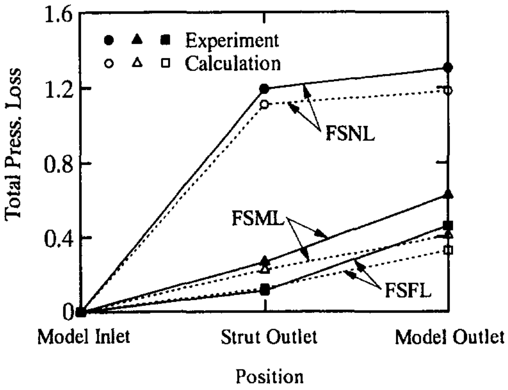

(a) Total Pressure Loss

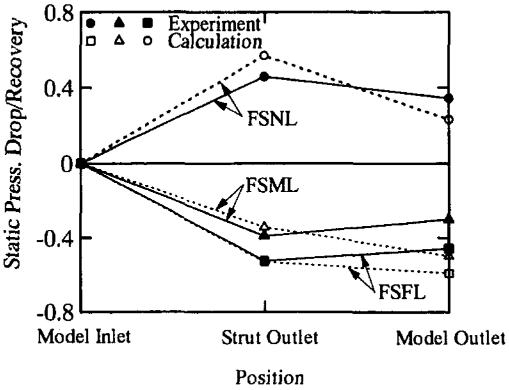

(b) Static Pressure Drop

Fig. 15 Total pressure loss and static pressure drop distribution

Total-Pressure Loss and Static-Pressure Drop/Recovery. Figure 15 describes the variation of mean total pressure loss and static pressure drop/recovery along the flow passage from the model inlet to strut outlet, and to model outlet, derived from both experiment and calculation. Definitions of the both parameters are as follows:

$$\text{total pressure loss coefficient} = (P_{01} - P_{0L})/(P_{01} - P_1)$$
$$\text{static pressure drop coefficient} = (P_1 - P_L)/(P_{01} - P_1)$$

where P_0 is total pressure, P is static pressure, subscript 1 is at the model inlet, and L indicates local mean value for each location. For the total pressure loss distribution shown in Fig. 15(*a*), the following observations are made:

1. In FSNL, most of the total pressure loss occurs in the front part or diffuser passage from model inlet to strut outlet. This is clearly due to large separation around the strut.
2. In FSML and FSFL, the loss in the front part reduces significantly, and is smallest for FSFL. Loss in the back part (from strut outlet to model outlet) in FSML and FSFL is a little larger than in FSNL, which is considered due to increased velocities in this region. For the whole passage, total-pressure loss is the smallest for FSFL.
3. Comparing the calculation with experiment, predicted losses for the front part agree fairly well with experiment for all loads, while the differences for the back part become larger.

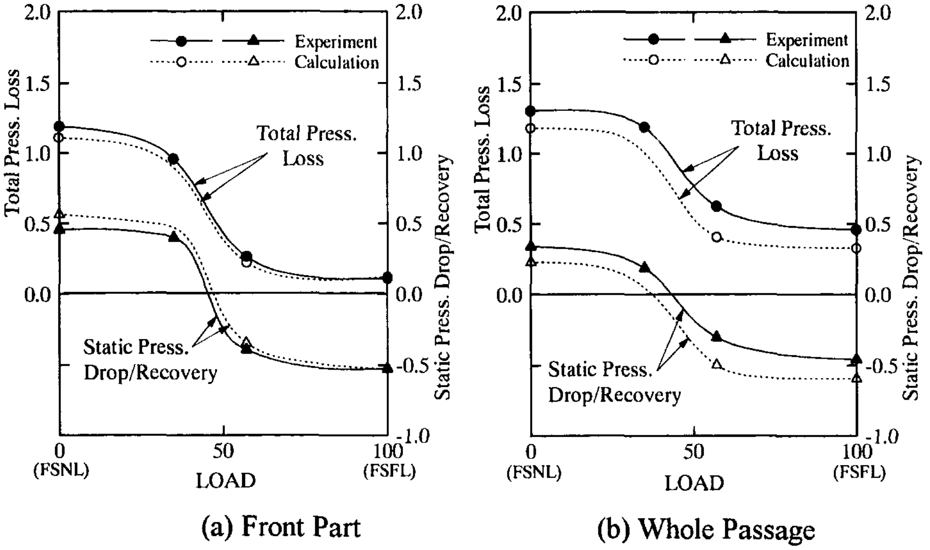

Fig. 16 Total pressure loss and static pressure drop with load

For the static pressure drop or recovery shown in Fig. 15(*b*), principal observations are as follows:

1. In FSNL, large static-pressure drop is observed in the front part, which indicates the diffuser does not function with full efficiency in this no load condition.
2. For FSML and FSFL, large negative pressure drop or positive pressure recovery is obtained in the diffuser, suggesting a satisfactory diffuser performance. The entire pressure recovery is largest when the exhaust system operates under FSFL.
3. Calculated values again agree well with experiment for the front part, the comparison in back part shows larger discrepancies for each load.

The variation of the total pressure loss and static pressure drop with change in load condition from FSNL to FSFL is depicted in Fig. 16 for both the front part (from model inlet to strut outlet) and the whole passage (from model inlet to model outlet). Both the total pressure loss and static pressure drop decrease significantly near the mid load operating condition. A better agreement between calculation and experiment in the front part for all load conditions is also seen here. It is important to note here that even with larger discrepancy in the model exit plane, a certain tendency important to design application is clearly observed that the calculation always underpredicts total pressure losses and static pressure drops compared with measurements.

In a gas turbine exhaust system, most of the total pressure loss is associated with the secondary flows in the stalled regions. Relatively, only a small part of the overall loss can be attributed to friction in the wall boundary layers. Therefore, it is logical to assume that any further improvement in the near-wall treatment, such as using a two-layer model instead of the wall-functions, will only marginally improve predictions. However, capturing the flow behavior away from the wall using a more advanced turbulence model to accurately simulate effects of streamline curvature and turbulence anisotropy due to flow separation and widely varying swirl could further bring predictions closer to measurements. Taking into consideration the need for computational efficiency for industrial design applications, a Reynolds stress transport model that combines accuracy with speed is desirable. Based on a recent study by Hirsch and Khodak (1995) and an earlier study by Sultanian et al. (1986), ASM seems to be a promising turbulence model for further improvement in CFD predictions in the stalled regions of a gas turbine exhaust system where pressure loss is primarily due to secondary flows.

Conclusions

This paper presents the results of both experimental and three-dimensional CFD investigations in a scale model of an industrial gas turbine exhaust system (GE-MS9001E type) to better understand its complex flow field and to validate CFD prediction capabilities. Principal conclusions of this study are as follows:

1. The flow field in the present exhaust system largely varies with the gas turbine operating load condition. The trends of such variation in total pressure loss and static pressure recovery as well as the local flow features are reasonably predicted by the three-dimensional CFD calculations.
2. In a quantitative comparison, CFD predictions are found to compare well with the experiments for strut surface pressure and strut outlet total pressure in the front part (diffuser section) of the model. At the model outlet plane, pressure levels are calculated somewhat higher than experiment, indicating that secondary flow losses in regions of turning vanes and the plenum are not fully captured by the turbulence model.
3. Results indicate satisfactory prediction accuracy for total pressure loss and static pressure recovery in the diffuser section. For the entire exhaust system including the plenum, the CFD predictions of these values are found consistently somewhat less accurate under wide operating load variations from full-speed-no-load (FSNL) to full-speed–full-load (FSFL).
4. Overall, the applied CFD method offers a useful design engineering tool capable of predicting complex gas turbine exhaust system flows including the quantitative prediction of the total pressure loss and static pressure recovery.

Acknowledgment

Authors are grateful to Ron Wesorick, Alan Walker, Dincer Ozgur, and Tom Taylor of General Electric Company and Takashi Ikeda, Shoichi Hisa, Tädashi Kobayashi, and Tadashi Tanuma of Toshiba Corporation for their continued support and teaming during the course of this joint technology program, and also to the two companies for their permission to publish this work.

References

Adenubi, S. O., 1975, "Performance and Flow Regime of Annuar Diffusers with Axial-Turbomachine-Discharge Inlet Conditions," Paper 75-WA/FE 5, ASME, New York.

Desideri, U., and Manfrida, G., 1995, ''Flow and Turbulence Survey for a Model of Gas Turbine Exhaust Diffuser,'' ASME Paper 95-GT-139.

Cheng, Z., and Eiseman, P. R., 1996, ''Interactive Topology Generation and Grid Viewer for GridPro/az3000,'' in Numerical Grid Generation in Computational Field Simulations, Proceedings, Of the 5th International Conference, B. Soni, J. F. Thompson, J. Hauser, and P. R. Eiseman, eds., Mississippi State University Press, pp. 413–422.

Eiseman, P. R., 1995, ''Automatic Structured Grid Generation,'' *Computational Fluid Dynamics Review 1995,* Wiley, New York, pp. 54–69.

Fleischer, F., Koerner, C., and Mann, J., 1989, ''Flow Guiding and Distributing Devices on Exhaust Side of Stationary Gas Turbines,'' ASME Paper 89-GT-214.

Fox, R. W., and Kline, S. J., 1962, ''Flow Regime Data and Design Methods for Curved Subsonic Diffusers,'' *ASME Journal of Basic Engineering,* Series D, Vol. 84, No. 3, Sept., pp. 303–312.

Fric, T. F., Villarreal, R., Auer, R. O., James, M. L., Ozgur, D., and Staley, T. K., 1996, ''Vortex Shedding From Struts in an Annular Exhaust Diffuser,'' ASME Paper 96-GT-475.

Ghose, S., and Kline, S. J., 1976, ''Prediction of Transitory Stall in Two Dimensional Diffusers,'' Report MD-36, Thermosciences Div., Dept. of Mech. Engrg., Stanford University, Stanford, CA.

Hirsch, C., and Khodak, A. E., 1995, ''Application of Different Turbulence Models for Duct Flow Simulation with Reduced and Full Navier-Stokes Equations,'' ASME Paper 95-GT-145.

Howard, J. H. G., Henseller, H. J., and Thornton-Trump, A. B., 1967, ''Performance and Flow Regimes for Annular Diffusers,'' ASME Paper 67-WA/FE-21.

Japikse, D., and Pampreen, R., 1979, ''Annular Diffuser Performance for an Automotive Gas Turbine,'' *ASME Journal of Engineering Power,* Vol. 101, July, pp. 358–372.

Kanemoto, T., Toyokura, and Kurokawa, J., 1982, ''Flow in Annular Diffuser,'' *Bulletin JSME,* Vol. 25, No. 204, pp. 912–918.

Kawagishi, H., and Sakamoto, T., 1992, ''Performance and Flow Analysis of Steam Turbine Exhaust Hood,'' JSME 920-78, pp. 213–215 (in Japanese).

Kelnhofer, W. J., and Derick, C. T., 1971, ''Tailpipe Effects on Gas-Turbine-Diffuser Performance With Fully Devoted Inlet Conditions,'' ASME *Journal of Engineering for Power,* Vol. 93 Jan., pp. 57–62.

Kline, S. J., Abbott, D. E., and Fox, R. W., 1959, ''Optimum Design of Straight-Walled Diffusers,'' ASME *Journal of Basic Engineering,* Vol. 81, pp. 321–330.

Lakshminarayana, B., 1996, ''Fluid Dynamics and Heat Transfer of Turbomachinery,'' John Wiley & Sons, Inc., New York.

Launder, B. E., and Spalding, D. B., 1974, ''The Numerical Calculation of Turbulent Flow,'' *Computer Methods in Applied Mechanics and Engineering,* Vol. 3, pp. 269–289.

Leonard, B. P., 1979, ''A Stable and Accurate Convective Modeling Procedure Based on Quadratic Upstream Interpolation,'' *Computer Methods Appl. Mech. Eng.,* Vol. 19, pp. 59–98.

Mao, S. K., Wei, Y. Z., and May, Y. L., 1987, ''Aerodynamic Characteristics Optimization of an Axial Turbine Exhaust Hood by Tests Based on an Orthogonal Design Approach,'' ASME Paper 87-GT-149.

Patankar, S. V., 1980, ''Numerical Heat Transfer and Fluid Flow,'' McGraw-Hill, New York.

Raab, I., Dirk, L., and Hennecke, D. K., 1996, ''A New Concept for The Design of Turbine Diffusers,'' ASME Paper 96-GT-450.

Reneau, L. R., Johnston, J. P., and Kline, S. J., 1967, ''Performance and Design of Straight Two-Dimensional Diffusers,'' *ASME Journal of Basic Engineering,* Vol. 89 D, pp. 141–150.

Senoo, Y., and Kawaguchi, N., 1983, ''Pressure Recovery of Collectors with Annuar Curved Diffusers,'' ASME Paper 83-GT-35.

Srinath, T., 1968, ''An Investigation of the Effects of Swirl on Flow Regimes and Performance of Annular Diffusers with Equal Inner and Outer Cone Angles,'' M.S. thesis, Mechanical Engineering Department, University of Waterloo, Waterloo, Ontario.

Sultanian, B. K., and Mongia, H. C., 1986, ''Fuel Nozzle Air Flow Modeling,'' AIAA-86-1667.

Sultanian, B. K., Neitzel, G. P., and Metzger, D. E., 1986, ''A Study of Sudden Expansion Pipe Flow Using an Algebraic Stress Model of Turbulence,'' AIAA-86-1062.

Takehira, A., Tanaka, M., Kawashima, T., and Hanabusa, H., 1977, ''An Experimental Study of the Annular Diffusers in Axial-Flow Compressors and Turbines,'' Paper No. 39, Japan Society of Mechanical Engineers.

Wolf, S., and Johnston, J. P., 1969, ''Effects of Nonuniform Inlet Velocity Profiles on Flow Regimes and Performance in Two-Dimensional Diffusers,'' ASME *Journal of Basic Engineering,* Sept., pp. 462–474.

Xingsu, L., Kunyuan, P., and Zuomin, W., 1981, ''Aerodynamic Design and Experimental Study of Marine Gas Turbine Exhaust Volutes,'' ASME Paper 81-GT-143.